

RESEARCH Monograph - 21



Imaging in Alcohol Research



U.S. DEPARTMENT OF HEALTH AND HUMAN SERVICES
Public Health Service
Alcohol, Drug Abuse, and Mental Health Administration

Research Monograph No. 21



Imaging in Alcohol Research

Proceedings of a Workshop on Imaging in Alcohol Research

May 9-11, 1991

Wild Dunes, South Carolina

Sponsored by:

National Institute on Alcohol Abuse and Alcoholism

Edited by:

Sam Zakhari, Ph.D.

Ellen Witt, Ph.D.

NATIONAL INSTITUTES OF HEALTH
NIH LIBRARY
SEP 26 2007

BLDG 10, 10 CENTER DR
BETHESDA, MD 20892-1150

U.S. DEPARTMENT OF HEALTH AND HUMAN SERVICES

Public Health Service

Alcohol, Drug Abuse, and Mental Health Administration

National Institute on Alcohol Abuse and Alcoholism

5600 Fishers Lane

Rockville, MD 20857

The Editors: Sam Zakhari, Ph.D., is currently Chief of the Biomedical Research Branch in the Division of Basic Research at the National Institute on Alcohol Abuse and Alcoholism (NIAAA). Prior to his appointment in the Division of Basic Research, Dr. Zakhari was Executive Secretary of the Neuroscience and Behavior Subcommittee at NIAAA. Ellen D. Witt, Ph.D., is a Health Scientist Administrator in the Division of Basic Research, NIAAA, and is responsible for administering the Behavioral Sciences Program in the Neuroscience and Behavioral Research Branch.

NIAAA has obtained permission from the copyright holders to reproduce figures and tables on pages 19, 20, 66-70, 180, 289, 309, and 314-322. Further reproduction of these materials is prohibited without specific permission of the copyright holders. All other material contained in the monograph, except quoted passages from copyrighted sources, is in the public domain and may be reproduced without permission from the Institute or the authors. Citation of the source is appreciated.

The U.S. Government does not endorse or favor any specific commercial product (or commodity, service, or company). Trade or proprietary names (or company names) appearing in this publication are used only because they are considered essential in the context of the studies reported herein.

The opinions expressed herein are the views of the authors and do not necessarily reflect the official position of NIAAA or any other part of the U.S. Department of Health and Human Services.

DHHS Publication No. (ADM)92-1890
Printed 1992

TABLE OF CONTENTS

Foreword	v
Preface.	vii
Participants.	xii

Event-Related Potentials and Magnetoencephalogram Section

1. Can MEG Imaging Be Useful in Alcoholism Research? <i>David Cohen</i>	3
2. The Use of Magnetic Field Tomography in the Study of Acute Alcohol Intoxication <i>R. Llinas and U. Ribary</i>	13
3. Use of Animal Models for Electrophysiological Neural Imaging in Alcohol Research <i>Cindy L. Ehlers</i>	27
4. Brain Electrical Activity: The Promise of New Technologies <i>George Fein, Jonathan Raz, and Bruce Turetsky</i>	49
5. The Topographic Analysis of Model-Referenced Evoked Potential Components <i>John Odencrantz, Sean O'Connor, Henri Begleiter, and Guowang Zhang</i>	79

Nuclear Magnetic Resonance Imaging Section

6. Structural Imaging of the Brain in Chronic Alcoholism <i>Adolf Pfefferbaum, Kelvin O. Lim, and Margaret Rosenbloom</i>	99
7. Studies of Brain Structure in Chronic Alcoholism Using Magnetic Resonance Imaging <i>Terry L. Jernigan, Nelson Butters, and Laird S. Cermak</i>	121

8.	Magnetic Resonance Imaging and Contrast Agents in the Evaluation of Ethanol-Damaged Livers S.W. Young, M. Sidhu, A. Jones, H.H. Muller, and J. Aggeler	135
9.	^{31}P NMR As a Tool To Investigate the Testicular Toxicity of Ethanol In Vivo D.H. Van Thiel, H. Farghali, J.S. Gavaler, and C. Ho	153

Nuclear Magnetic Resonance Spectroscopy Section

10.	Overview of Noninvasive Approaches to Metabolic and Addictive Disease <i>Britton Chance</i>	169
11.	Magnetic Resonance Spectroscopy and Spectroscopic Imaging of Human Liver, Heart, Kidney, and Brain Dieter J. Meyerhoff, Hoby P. Hetherington, James W. Hugg, Gerald B. Matson, George Fein, Andrew Maudsley, and Michael W. Weiner	177
12.	NMR Studies of Cerebral Metabolism Robert G. Shulman, Kevin L. Behar, Douglas L. Rothman, and Graeme F. Mason	195
13.	Alterations in Membrane Metabolism and Physiology in Alzheimer's Disease: Implications for Etiology Jay W. Pettegrew, William E. Klunk, and Richard J. McClure	201
14.	Molecular Insights into Schizophrenia Jay W. Pettegrew and Nancy J. Minshew	215
15.	Influence of Mg^{2+} on Distribution of Ionized Ca^{2+} in Vascular Muscle and on Cellular Bioenergetics and Intracellular Free Mg^{2+} and pH in Perfused Hearts Probed by Digital Imaging Microscopy,	

³¹ P NMR, and Reflectance Spectroscopy Burton M. Altura, Randall L. Barbour, Seth D. Reiner, Amin Zhang, T.P. Cheng, Terry L. Dowd, Raj K. Gupta, Fan Wu, and Bella T. Altura	235
16. In Vivo Measurement of Cerebral Blood Flow and Oxygen Consumption Using ¹⁷ O Magnetic Resonance Imaging Alan C. McLaughlin, James Pekar, Laszlo Ligeti, Zoltan Ruttner, Robbe Lyon, Teresa Sinnwell, Peter van Gelderen, Daniel Fiat, and Chrit T.W. Moonen	273
17. Detection of Ethanol Tolerance in Human Brain With In Vivo Proton Magnetic Resonance Spectroscopy Jack H. Mendelson, Tak-Ming Chiu, Leslie Amass, Nancy K. Mello, Siew Koon Teoh, Bryan Woods, and Erin Rhoades	287

Positron Emission Tomography and Single Photon Emission Computed Tomography Section

18. Advances in SPECT Imaging for Neuropsychiatry Richard Coppola	297
19. SPECT Imaging of the Benzodiazepine Receptor Marc Laruelle, Elzbieta Sybirska, Mohammed Al-Tikriti, Ronald M. Baldwin, and Robert B. Innis	305
20. PET and SPECT Imaging in Cognitive Disorders of Aging and Alcoholism William J. Jagust	333
21. PET Studies of the Myocardium: Prospects for Applications to Studies of Alcoholic Injury James E. Holden	359

22. The Application of Metabolic Mapping Methods to the Identification of the Neural Substrates of the Effects of Alcohol <i>Linda J. Porrino</i>	375
23. Methodological Issues in the Use of PET To Study Drugs of Abuse <i>H. deWit, J. Metz, K. Luh, and M. Cooper</i>	389

FOREWORD

The development of noninvasive imaging techniques over the past decade has provided alcohol researchers with the opportunity to study the effects of alcohol on the internal organs of living individuals. No longer restricted to autopsy studies, researchers can now use imaging tools and techniques to examine alcohol's action in the brain and other organs, including metabolic and structural changes that take place during the various stages of the addiction process (i.e., intoxication, craving, tolerance, and dependence). With this new technology, in fact, we may begin to unravel the mechanisms of addiction, leading to more effective prevention methods and treatments for alcohol-dependent persons.

The potentially important applications of imaging technologies are only beginning to be used in alcohol research. To help integrate the use of these techniques into the alcohol field, the National Institute on Alcohol Abuse and Alcoholism sponsored the workshop entitled "Imaging in Alcohol Research." This workshop, held in Wild Dunes, South Carolina, May 9-11, 1991, brought together leading scientists in alcohol research as well as other fields so that they might become better informed about the potential applications of state-of-the-art noninvasive imaging techniques to the study of alcohol's effects. Experts in imaging technologies presented the latest advances in magnetoencephalography, nuclear magnetic resonance imaging, electroencephalography, single photon emission computed tomography, positron emission tomography, and nuclear magnetic resonance spectroscopy. Leading alcohol researchers who use these techniques presented their research findings. More than 100 scientists attended the 3-day workshop, which included daily roundtable discussions about the possible uses of imaging technology in the study of alcohol-related problems.

I commend the many individuals whose talents and efforts ensured a highly successful workshop experience, including Dr. Sam Zakhari and Dr. Ellen Witt in their roles as workshop co-chairs and the many scientists who contributed to workshop sessions and to this monograph. I hope that these proceedings, which include discussions of the methodology and merits of these highly technical procedures, will stimulate basic scientists to apply these research techniques to reveal the mechanisms underlying the addiction process and alcohol-induced organ damage and, most importantly, to identify individuals who may be at risk for developing alcohol abuse and alcoholism.

Enoch Gordis, M.D.
Director
National Institute on Alcohol Abuse and Alcoholism

PREFACE

Alcohol research is concerned with understanding the consequences of drinking or the damage that alcohol use, particularly heavy use, can cause to internal organs such as the brain and the liver as well as understanding the process that leads to alcoholism, an addictive disorder that evolves over time and produces pervasive metabolic and physiologic effects. Scientists now have the capability to examine the progression of this disease in many organs of the body due to recent advances in noninvasive imaging technologies that enable repeated study of the structure and dynamic function of living tissues. Even more exciting is the potential to measure functional changes induced by alcohol in behaving individuals. If researchers can measure alcohol's effects on mood, emotional states, and cognition while simultaneously assessing metabolic, physiologic, and neurochemical function in the brain, it may be possible to understand the brain mechanisms underlying the addictive process (craving, tolerance, impaired control over alcohol use, and physical dependence). Imaging techniques also provide opportunities to study the acute and chronic effects of alcohol in other organs, including the heart, kidney, gonads, and liver. The contribution of structural and metabolic alterations in these organs to the complications of drinking, and the reversibility of these changes after treatment, can be assessed using these imaging techniques.

The purpose of this monograph is to update scientists about the latest inroads in noninvasive imaging technologies and to encourage the use of these techniques in alcohol research. To accomplish these goals, we invited experts in the respective imaging techniques and preeminent alcohol researchers who are currently using the techniques to give an overview of the technology, including potential applications and limitations; to present research in the use and development of these techniques; and to indicate their possible applications in the alcohol field.

The chapters of the monograph are divided into four sections. The first section deals with the application of brain electrical activity to brain-behavior relationships. Three methods of measuring brain electrical activity are presented: electroencephalography (EEG), magnetoencephalography (MEG), and event-related potentials (ERP). Topics of particular interest are the comparison of EEG and MEG in terms of understanding mechanisms of alcohol's effects on brain function, discussions of the latest mathematical

analyses (e.g., "model-referenced analysis" and "dipole decomposition method") to partition ERP into subcomponents that represent the activity of underlying brain processes, and use of animal models to record ERP from cortical and subcortical structures in an attempt to locate underlying neuro-anatomical and neurochemical systems that generate these potentials.

The second section deals with magnetic resonance imaging (MRI). Advantages of MRI over computed tomography are presented. Using sophisticated computer technology and new contrast agents, MRI studies have made it possible to visualize discrete brain areas and to distinguish between white matter and gray matter abnormalities in chronic alcoholics. However, more studies are needed which relate structural brain changes to functional deficits. The uses of MRI in the early diagnosis of liver disease and in detection of alcohol-induced testicular dysfunction are also discussed.

The third section is devoted to nuclear magnetic resonance (NMR) spectroscopy. NMR can be used to study aberrant energy and lipid metabolism in the brain, liver, heart, and kidney after acute or chronic alcohol exposure. Applications of ^{31}P and ^1H NMR spectroscopy to explore membrane and energy metabolism in brains of Alzheimer and schizophrenic patients are noteworthy, especially if similar analyses can be used to understand the pathogenesis of alcohol-induced brain damage. Development of new NMR techniques to measure glucose metabolism, cerebral blood flow, magnesium, and brain ethanol concentrations are discussed.

The final section concerns positron emission tomography (PET) and single photon emission computed tomography (SPECT). The advantages and disadvantages of both techniques are reviewed. Although PET is usually associated with studies of glucose metabolism and SPECT is ideal for cerebral blood flow investigations, the development of new radioisotopes makes both techniques suitable for studies of *in vivo* receptor pharmacology of alcohol effects. One of the most exciting applications of PET and SPECT technology is the concurrent measurement of alcohol's acute and chronic effects on brain functional activity and behavioral states. The methodological issues relevant to the use of PET and SPECT in the study of drugs of abuse are examined.

In recognition of the extraordinary amount of time and effort that went into the workshop presentations and the chapters in this monograph, we thank the contributors for the excellent, thorough, and comprehensible review of highly technical material. We hope this monograph will provide a useful resource for scientists wishing to apply state-of-the-art imaging techniques to the field of alcohol research.

Sam Zakhari, Ph.D.
Chief
Biomedical Research Branch
Division of Basic Research
National Institute on Alcohol Abuse and Alcoholism

Ellen Witt, Ph.D.
Health Scientist Administrator
Division of Basic Research
National Institute on Alcohol Abuse and Alcoholism



PARTICIPANTS

Burton Altura, Ph.D.

SUNY Health Science Center
at Brooklyn
450 Clarkson Avenue
Brooklyn, NY 11203

Henri Begleiter, Ph.D.

SUNY Health Science Center
at Brooklyn
450 Clarkson Avenue
Brooklyn, NY 11203

Britton Chance, Ph.D., D.Sc.

University of Pennsylvania
School of Medicine
Richards Building D-501
37th and Hamilton Walk
Philadelphia, PA 19104

David Cohen, Ph.D.

Francis Bitter National Magnet
Laboratory
Massachusetts Institute of
Technology
Cambridge, MA 02139

Richard Coppola, D.Sc.

Neuroscience Center
National Institute of Mental Health
William A. White Building
St. Elizabeths Hospital
Washington, DC 20032

Harriet de Wit, Ph.D.

Department of Psychiatry
University of Chicago
Box 411
5841 South Maryland Avenue
Chicago, IL 60637

Enoch Gordis, M.D.

Office of the Director
National Institute on
Alcohol Abuse and Alcoholism
5600 Fishers Lane
Rockville, MD 20857

James E. Holden, Ph.D.

Department of Medical
Physics and Radiology
University of Wisconsin
1530 Medical Sciences Center
1300 University Avenue
Madison, WI 53706

Robert B. Innis, M.D., Ph.D.

Department of Psychiatry
Yale University
Department of Veterans
Affairs Medical Center (116A2)
950 Campbell Avenue
West Haven, CT 06516

William Jagust, M.D.

Department of Research Medicine
55-121 Lawrence Berkeley Laboratory
Berkeley, CA 94720

Terry Jernigan, Ph.D.

Department of Psychiatry (063-P)
University of California, San Diego
La Jolla, CA 92093

Rodolfo R. Llinas, M.D., Ph.D.

Department of Physiology and
Biophysics
New York University Medical Center
550 First Avenue
New York, NY 10016

Jack H. Mendelson, M.D.

Department of Psychiatry
McLean Hospital
115 Mill Street
Belmont, MA 02178

Dieter Meyerhoff, Ph.D.

University of California at
San Francisco
Department of Veterans Affairs
Medical Center, MR Unit (11M)
450 Clement Street
San Francisco, CA 94121

Alan McLaughlin, Ph.D.

Laboratory of Metabolism
National Institute on
Alcohol Abuse and Alcoholism
12501 Washington Avenue
Rockville, MD 20852

Jay W. Pettegrew, M.D.

Graduate School of Public Health
University of Pittsburgh/WPIC
A-710 Crabtree
130 DeSoto Street
Pittsburgh, PA 15261

Adolf Pfefferbaum, M.D.

Department of Psychiatry (116A3)
Department of Veterans Affairs
Medical Center
3801 Miranda Avenue
Palo Alto, CA 94394

Linda Porrino, Ph.D.

Department of Physiology
and Pharmacology
Bowman Gray School of Medicine
300 South Hawthorne Street
Winston-Salem, NC 27103

Robert Shulman, Ph.D.

Department of Molecular Biophysics
and Biochemistry
Yale University School of Medicine
P.O. Box 3333
New Haven, CT 06510

David H. Van Thiel, M.D.

University of Pittsburgh
School of Medicine
3601 Fifth Avenue
Falk Clinic, 5C
Pittsburgh, PA 15213

Charles C. Wood, Ph.D.

Biophysics Group (MS-M715)
Los Alamos National Laboratory
Los Alamos, NM 87545

Stuart W. Young, M.D.

Department of Diagnostic Radiology
and Nuclear Medicine
Stanford University
School of Medicine
Stanford, CA 94305

DISCUSSANTS

Carol Cunningham, Ph.D.

Bowman Gray School of Medicine
Wake Forest University
Winston-Salem, NC 27103

Vincent Dole, M.D.

Rockefeller University
1230 York Avenue
New York, NY 10021

Michael Eckardt, Ph.D.

Section of Clinical Brain Research
National Institute on
Alcohol Abuse and Alcoholism
9000 Rockville Pike
Bethesda, MD 20892

William E.M. Lands, Ph.D.

Division of Basic Research
National Institute on
Alcohol Abuse and Alcoholism
5600 Fishers Lane
Rockville, MD 20857

Marcus A. Rothschild, M.D.

Professor of Medicine
21770 Cypress Drive
Boca Raton, FL 33433

Dean Wong, M.D., Ph.D.

Division of Nuclear Medicine
Johns Hopkins University
School of Medicine
615 North Wolfe Street
Baltimore, MD 21205

CONTRIBUTORS

Cindy L. Ehlers, Ph.D.

Department of
Neuropharmacology
Research Institute
of the Scripps Clinic
10666 North Torrey Pines Road
La Jolla, CA 92037

George Fein, Ph.D.

Psychiatry Service (116R)
Department of Veterans
Affairs Medical Center
4150 Clement Street
San Francisco, CA 94121

Event-Related Potentials and Magnetoencephalogram Section

CAN MEG IMAGING BE USEFUL IN ALCOHOLISM RESEARCH?

David Cohen, Ph.D.¹

This is a brief overview of the magnetoencephalogram (MEG). More lengthy reviews available in the literature include Williamson and Kaufman (1987) and Sato and Smith (1985).

The same electrical currents from the brain that produce the electroencephalogram (EEG) also produce a magnetic field over the head called a neuromagnetic field. A measurement of this field (Cohen 1972) is called an MEG. Because the MEG is produced by the same currents that produce the EEG, an MEG trace (the magnetic field versus time) superficially resembles an EEG trace. However, the MEG samples the currents differently than the EEG, therefore can provide different information about electrical sources in the brain. The MEG is, thus, complementary to the EEG. Stated otherwise, the MEG can provide images of electrical sources in the brain that are complementary to those provided by the EEG.

The neuromagnetic field is very weak, typically at levels below 10^{-12}

tesla. This field is much weaker than the urban magnetic background in the same frequency range (about 10^{-7} tesla), and weaker yet than the earth's steady field (about 10^{-4} tesla). Therefore, the two main requirements for measuring the MEG are a highly sensitive magnetic detector and suppression of magnetic background. The detector used is the superconducting quantum interference device (SQUID), which operates at the cryogenic temperature of about 4 °K and is contained accordingly in a liquid helium dewar. The dewar is shaped to allow field measurements at about 1 cm from the scalp.

ACRONYMS

EEG	electroencephalogram
MEG	magnetoencephalogram
SI and SII	primary and secondary somatosensory cortices
SQUID	superconducting quantum interference device

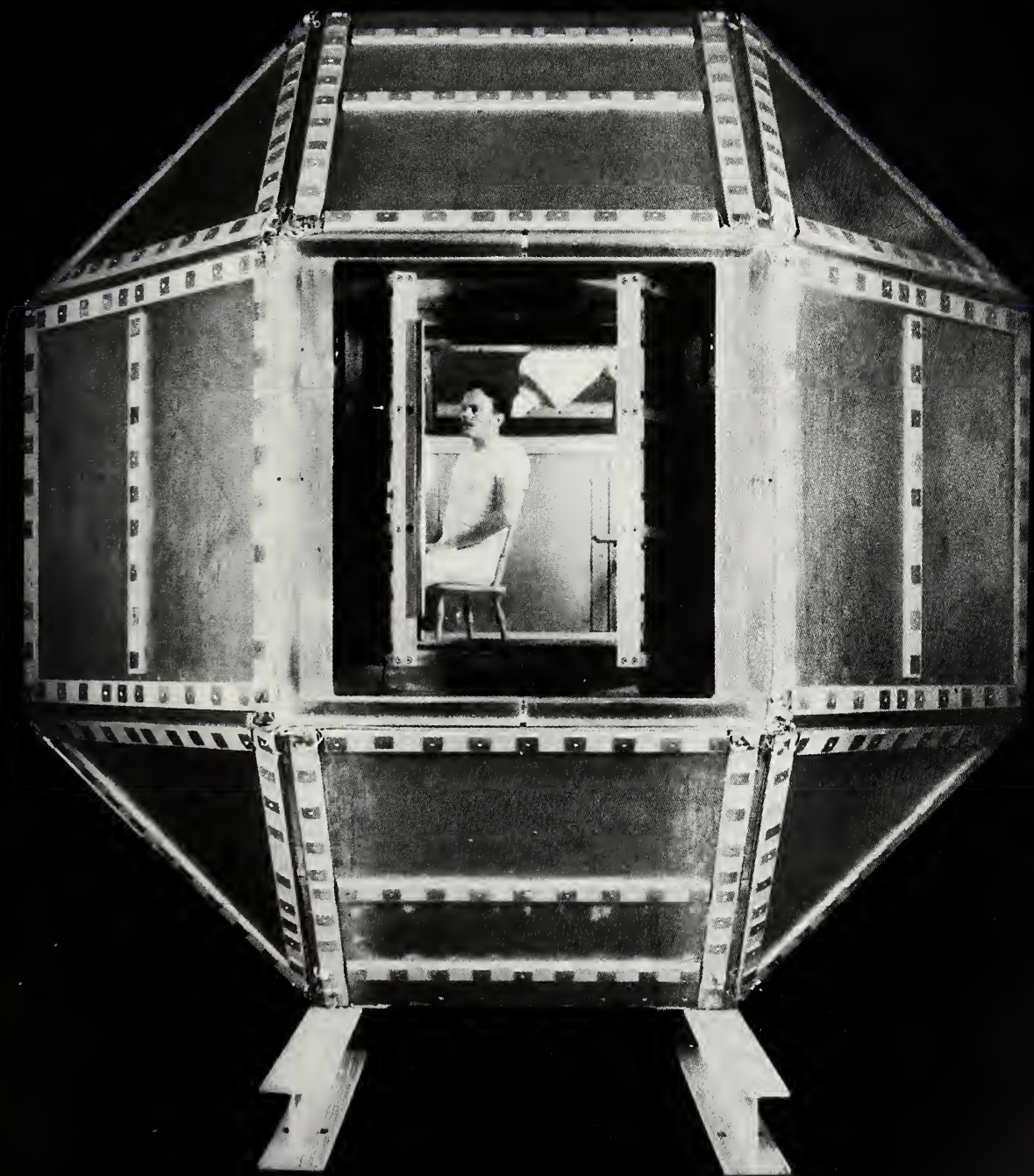
¹Biomagnetism Group Leader, Francis Bitter National Magnet Laboratory, Massachusetts Institute of Technology, Cambridge, MA 02139

The background is suppressed by measuring the MEG in a magnetically shielded room. Figure 1 shows an elaborate shielded room at Massachusetts Institute of Technology (MIT), where some of the first MEG measurements were made (Cohen 1972). More recent shielded rooms are rectangular and simpler. The background is further suppressed by canceling it with an identical detector in the dewar, but spaced further from the head. A good room can eliminate the background almost completely but is expensive, while the canceling method is not as effective. A combination of a modest room plus canceling is increasingly being used. The use of multichannel dewars is also increasing. Although three independent MEG channels are in the dewar shown in figure 1, more recent dewars contain as many as 37 MEG channels, measuring the MEG simultaneously at 37 different locations over the head. However, these systems are expensive. Today a combination of a modest shielded room plus a 37-channel SQUID system may cost more than \$2 million.

About 40 groups around the world are now doing MEG-related work, both clinical and research, and this number is increasing. An increasing number of the signals that have been studied in the EEG are now being studied in the MEG. Of the spontaneous signals, epileptic spikes and the alpha rhythm have been studied using MEG. Studies of epileptic spikes are of clinical interest because of the hope that the MEG may be better than

the EEG, or that the combination of MEG and EEG may be considerably better than the EEG alone, for localization of epileptic foci.

MEG research studies of event-related signals help define and localize sources that are not clear on the EEG. MEGs are being studied, often in combination with the EEG, for both "exogenous" and "endogenous" signals. The exogenous signals include responses evoked by somatosensory, auditory, and visual stimulation. The MEG has produced from exogenous signals a variety of evidence supporting locations of sources in the primary sensory cortices. An example is the well-studied 20-millisecond signal from the human brain in response to peripheral nerve (somatosensory) stimulation. According to the EEG alone, the source of this signal is ambiguous; however, the combination of MEG and EEG maps shows that the source is mostly a tangential dipole in a specific area of the somatosensory cortex (Wood et al. 1985). The MEG has also demonstrated internal organization in some primary areas of the human brain that were previously seen only in the animal brain. Further, MEG has shown the separation of activity between primary and secondary areas, e.g., in primary and secondary somatosensory cortices (SI and SII). Cognitive processes and preparation for movement cloud the MEG evidence from endogenous signals; however, the source distributions are more complex, and these studies are still at an early stage.

FIGURE 1

Magnetically shielded room at MIT, with subject positioned for recording his MEG. The subject's head has been placed at the tail of a liquid helium dewar (large white cylinder). The detector in the tail measures the magnetic field at about 1 cm from the scalp. The subject wears clothes that contain no magnetic material (no zippers, shoes, etc.). Newer MEG dewar systems may be much larger, containing as many as 37 channels within a single dewar.

MEG-EEG DIFFERENCES

Some basic MEG-EEG differences allow the MEG to provide different information about the electrical sources than can the EEG. That is, there are differences which allow the MEG to produce source images in the brain that are complementary to those of the EEG. These basic differences were predicted from electromagnetic theory and later confirmed experimentally. Theoretically, the differences are based on a dipole source in a spherical model of the head, usually with spherical shells representing scalp, skull, etc.

The first difference is that the MEG signals from those electrical sources in the brain that are oriented radially to the skull are highly suppressed. It sees mostly signals from tangentially oriented sources. This is because a radial dipole in a conducting sphere produces zero external magnetic field (Baule 1965). In contrast to the MEG, the EEG sees both radial and tangential sources. Electrical sources in the cortex that are tangential to the skull are mostly located in the sulci whereas radial sources are mostly located in the gyri. It follows that the MEG theoretically sees only the sources in the sulci while the EEG sees both, as illustrated in figure 2. However, the EEG is dominated by the radial sources. Therefore, one consequence of this first difference is that the MEG should see those tangential sources which, on the EEG, are dominated or masked by the radial sources. Detecting tan-

gential sources blocked by radial sources is the main way the MEG is complementary to the EEG in imaging sources. Another consequence of this difference is that the MEG should not see sources near the center of the head because a source (dipole) at the center of a sphere is always a radial source.

The second and third MEG-EEG differences are pattern differences in the MEG and EEG spatial maps over the head. Figure 3 shows that the orientation of the MEG pattern is perpendicular to that of the EEG pattern and that it is smaller than the EEG pattern. The perpendicular difference is due to a basic orthogonality between magnetic and electrical fields causing MEG to localize a source somewhat better in the y direction, while the EEG localizes somewhat better in the x direction. This is another way in which the MEG is complementary to the EEG. The smaller MEG pattern differs from that of the EEG, mainly because the resistivity of the skull spreads the surface current, which can be measured by the EEG but is almost not seen by the MEG. In a purely homogeneous sphere, the MEG and EEG patterns would be about the same size. The consequence of this size difference is that the MEG localizes some 30 percent better in its best direction (y), compared with the EEG in its best direction (x). [The claim, often seen in the literature, that the MEG localizes to within several millimeters (and therefore is much better than the 20 mm reported for the EEG) is

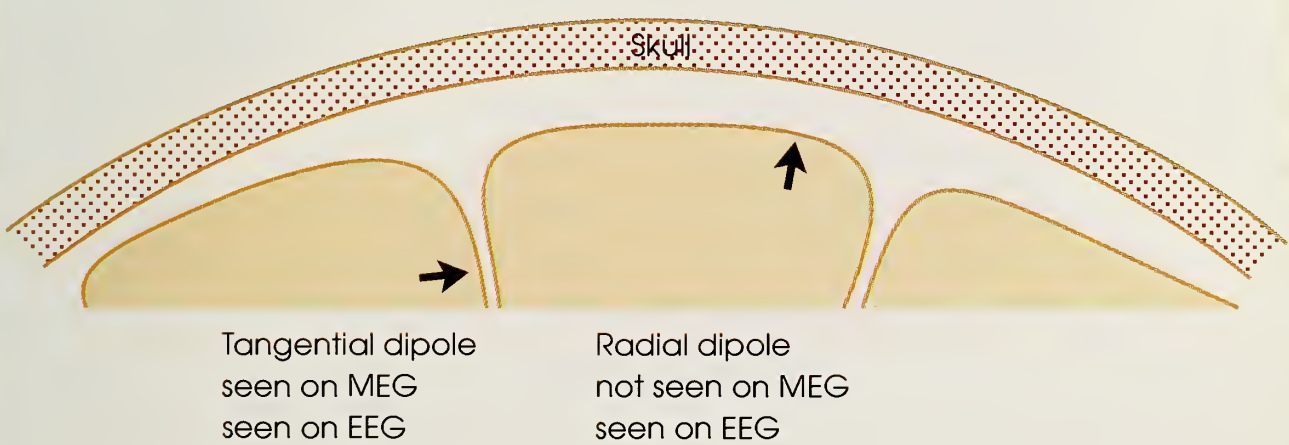
not supported by experimental evidence; both theory and experiment appear to indicate only a small improvement.]

Because the above three theoretical differences have been experimentally confirmed in MEG and EEG maps measured over the actual human head, the human head therefore appears to behave as the spherical-shell model for these purposes. The skull's deviations from sphericity and the fissures of the brain appear to have only minor effects. Of these three differences, the most important MEG-EEG difference for imaging in research on alcoholism is that the MEG sees only a suppressed signal from the radial sources. This difference may allow the MEG to contribute to source imaging in the area of alcoholism research.

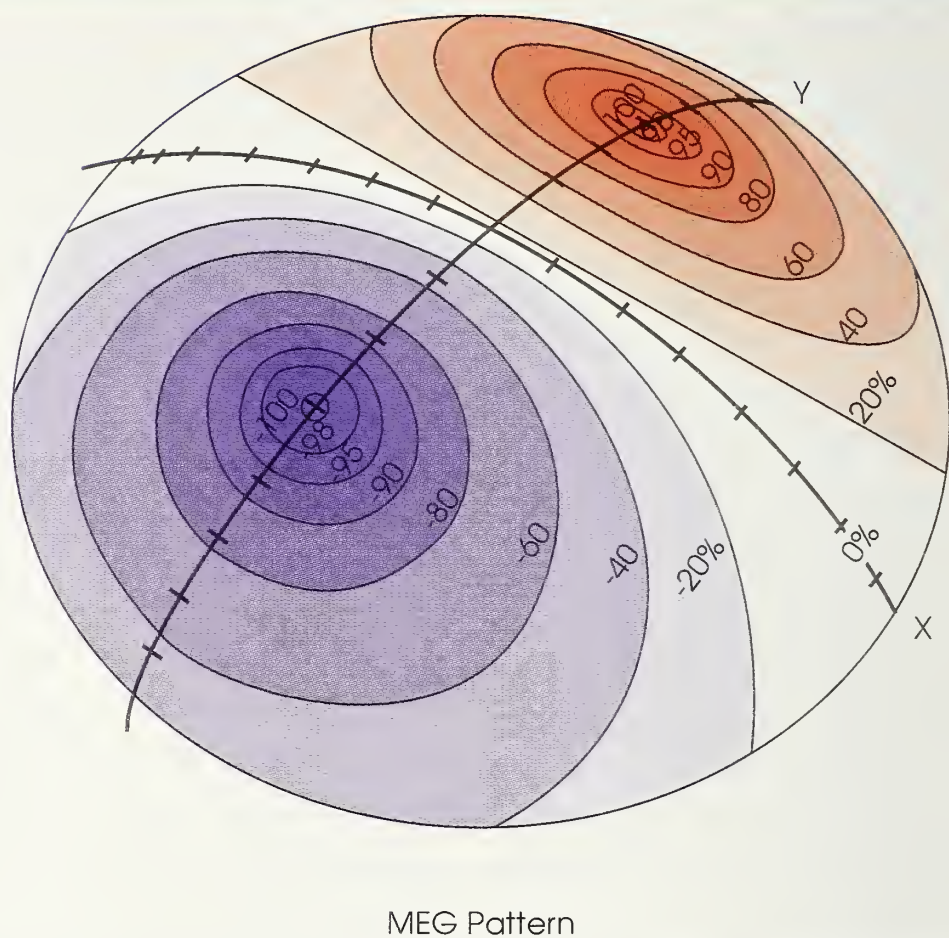
CAN THE MEG HELP WITH THE MAIN EEG ALCOHOLISM MARKER?

The MEG may contribute to alcoholism research in various indirect ways, but perhaps a direct way is to use it in connection with EEG. Had no interesting EEG phenomena been found to be associated with alcoholism, the MEG would probably be of no use. After all, the MEG sees *less* (a subset of the electrical sources). However, Begleiter and his colleagues (1988) and Polich and Bloom (1986) found that the most significant marker identified by the EEG is the P300 component of the event-related potential (Donchin and Coles 1988). However, this component, which is somewhat suppressed in nonalcoholic sons of

FIGURE 2



Two electrical sources in the cortex: one is oriented tangentially to the skull; the other, radially. Each is represented as a current dipole (heavy arrow). Because sources in the cortex are generally oriented perpendicularly to the cortical surface, tangential sources are located in the sulci, while radial sources are located in the gyri. Although the EEG sees both sources, it is dominated by the radial sources in the gyri.

FIGURE 3a

Theoretical MEG map due to a tangential source in a spherical model of the head. The map is shown on a spherical "cap," which has x and y coordinates with ticks at each centimeter. The MEG map is of the component of the magnetic field vector usually measured, perpendicular to the scalp.

alcoholic fathers, is not a perfect marker: There is a significant percentage of false positives, but the MEG may be able to decrease these false values and improve the marker because, by imaging a subset of the generators, it can be more specific. If most of the relevant P300 generators are tangential (i.e., those that are the markers), the MEG would image only those and largely ignore the nonsignificant radial P300 generators. Ideally, the magnetic P300 would be more specific than the EEG P300.

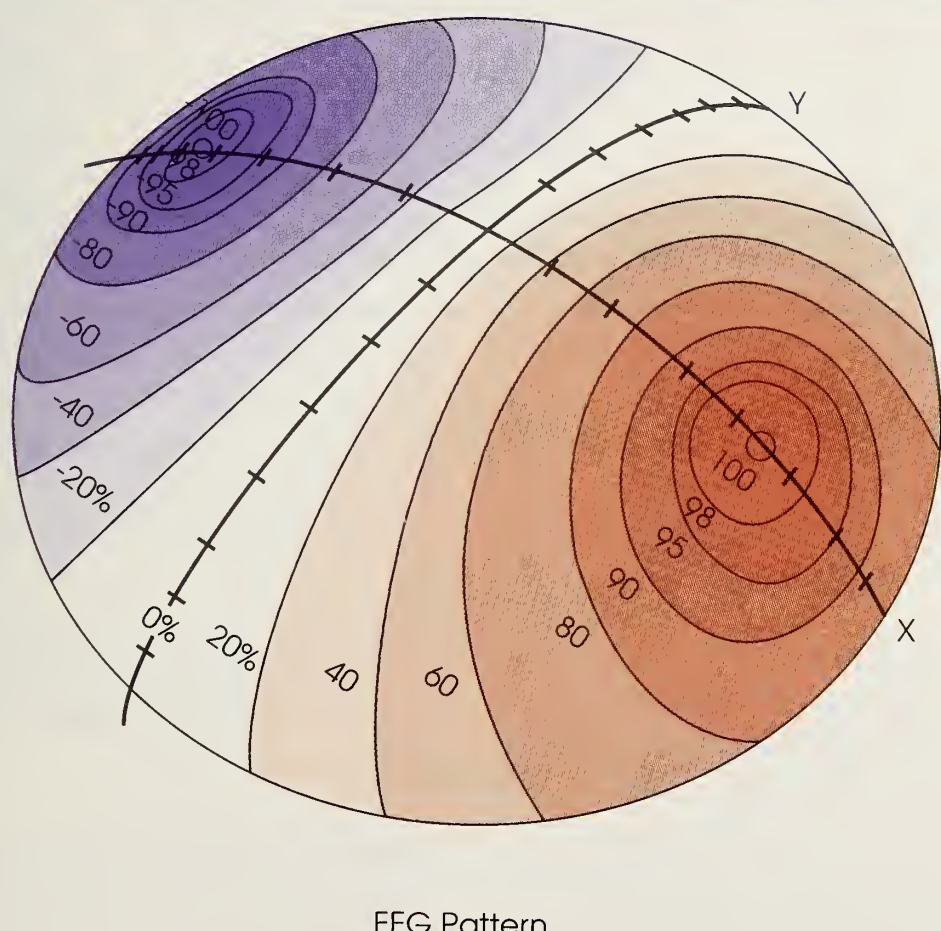
The literature on MEG measurements of P300 contains reports of recent studies by at least two groups (Lewine et al. 1989; Papanicolaou et al. 1990). The results reported by Lewine's group are, on first appearance, discouraging: They found that the variability among normal subjects was greater with the MEG than with the EEG (Lewine, personal communication, 1991). The results of Papanicolaou's research do not appear to conflict with those of the Lewine group although comparison seems difficult.

However, the reports of intersubject P300 variability are supported by previous (unpublished) results in our laboratory. We had found that auditory N100 and P200 (the earlier endogenous components) on the MEG were more variable, subject-to-subject, than on the EEG. If this result is repeated in future MEG P300 work, how could the MEG aid in the identification of markers for alcoholism when it cannot show uniformity among non-alcoholics? The reason for nonuniformity of MEG results must be understood before we can confidently see

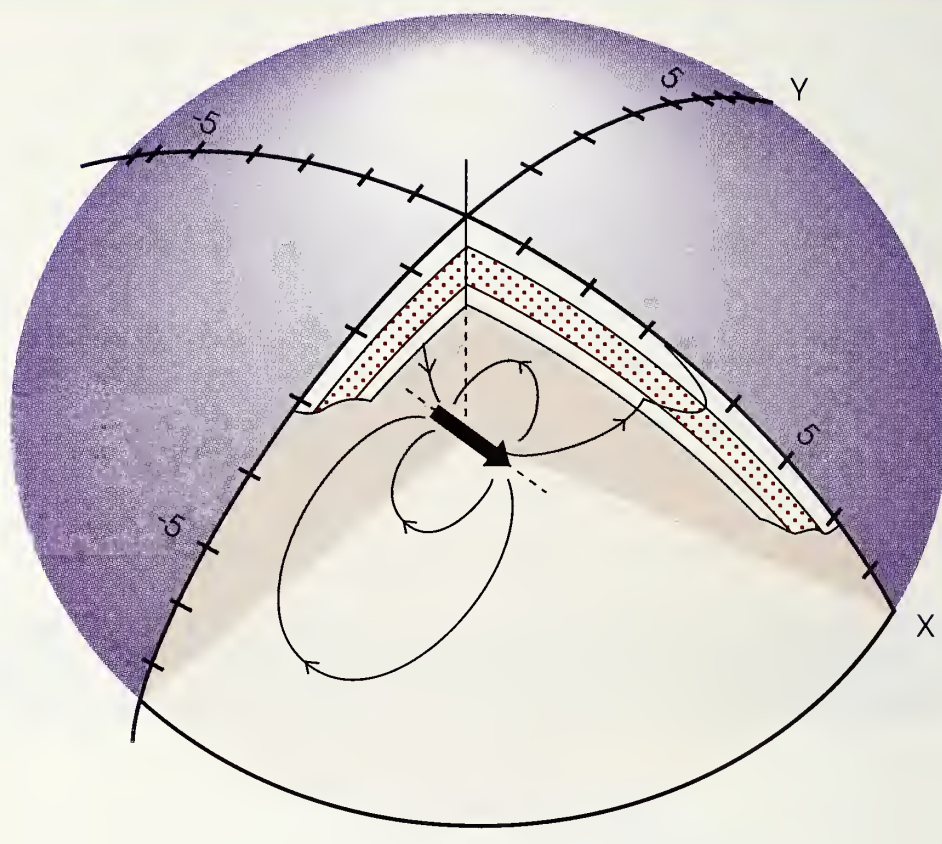
whether the MEG may play a role in alcoholism research.

In that regard, one model may explain the intersubject variability: the model used to explain MEG phenomena seen in the MEG alpha rhythm (Cohen and Cuffin 1979). In that model, continuous sources across a cortical fissure could cause considerable MEG canceling, so that the MEG residue is unusually sensitive to fissure shape, which is different for each subject. There is no such canceling in the EEG. Models such as this could facilitate understanding this phenomenon.

FIGURE 3b



Theoretical EEG map due to a tangential source in a spherical model of the head. The map is shown on a spherical "cap," which has x and y coordinates with ticks at each centimeter. The EEG map is of the surface potential.

FIGURE 3c

Computer Model

The four-layer shell model is shown with the same cap as the MEG and EEG maps. The tangential source (heavy arrow) is a dipole at a depth of 2.7 cm.

REFERENCES

Baule, G., and McFee, R. Theory of magnetic detection of the heart's electrical activity. *J Appl Physics* 36:2066–2073, 1965.

Begleiter, H., and Porjesz, B. Potential biological markers in individuals at high risk for developing alcoholism. *Alcohol Clin Exp* 12(4):488–493, 1988.

Cohen, D. Magnetoencephalography: Detection of the brain's electrical activity with a superconducting magnetometer. *Science* 175:664–666, 1972.

Cohen, D., and Cuffin, B.N. Magnetic measurement and display of current

generators in the brain. Part II: Polarization of the alpha rhythm. XII International Conference on Medical & Biological Engineering, Jerusalem, Israel, August 19–24, 1979, pp. 17–18.

Donchin, E., and Coles, M.G.H. Is the P300 component a manifestation of context updating? *Behav Brain Sci* 11:357, 1988.

Lewine, J.D.; Roeder, S.B.W.; Oakley, M.T.; Arthur, D.L.; Aine, C.J.; George, J.S.; and Flynn, E.R. A modality-specific neuromagnetic P3. In: Williamson, S.J.; Hoke, M.; Stroink, G.; and Kotani, M., eds. *Advances in Biomagnetism*. New York: Plenum Press, 1989. pp. 229–232.

- Papanicolaou, A.; Baumann, S.; Rogers, R.; Saydari, C.; Amparo, E.; and Eisenberg, H. Localization of auditory response sources using magnetoencephalography and magnetic resonance imaging. *Arch Neurol* 47:33-37, 1990.
- Polich, J., and Bloom, F.E. P300 and alcohol consumption in normals and individuals at risk for alcoholism. *Prog Neuropsychopharmacol Biol Psychiatry* 10:201-210, 1986.
- Sato, S., and P.D. Smith. Magnetoencephalography. *J Clin Neurophysiol* 2(2):173-192, 1985.
- Williamson, S.J., and Kaufman, L. Analysis of neuromagnetic signals. In: Gevens, A., and Remond, A., eds. *Handbook of Electroencephalography and Clinical Neurophysiology*. Vol. 3, Chapt. 14. Amsterdam: Elsevier, 1987.
- Wood, C.C.; Cohen, D.; Cuffin, B.N.; Yarita, M.; and Allison, T. Electrical sources in human somatosensory cortex: Identification by combined magnetic and potential field recordings. *Science* 227:1051-1053, 1985.

THE USE OF MAGNETIC FIELD TOMOGRAPHY IN THE STUDY OF ACUTE ALCOHOL INTOXICATION

R. Linas, M.D., Ph.D., and U. Ribary, Ph.D.¹

In the past decade, a significant effort has been invested in the development of noninvasive techniques capable of imaging "real time three-dimensional brain activity" (1 kHz) with sufficient spatial resolution to complement the structural imaging analysis offered by magnetic resonance imaging (MRI; Wehrli et al. 1988) and computed tomography (CT; Brooks and diChiro 1976). However, all imaging techniques, including positron emission tomography (PET; Hoffman and Phelps 1986), fall short of optimal temporal resolution. Other techniques, such as magnetoencephalography (MEG), while providing excellent spatiotemporal resolution (Williamson and Kaufman 1981; Hari and Ilmoniemi 1986; Yamamoto et al. 1988; Ribary et al. 1989; Suk et al. 1991), did not support imaging capability until very recently. Moreover, MEG data analysis has thus far been based solely on the assumption of a single-point

source, the current dipole, which is only valid when the underlying activity is highly localized and uniform.

Recently, we introduced the use of magnetic field tomography (MFT). This noninvasive technique is based on distributed source analysis of MEG data (Ioannides et al. 1989, 1990), which made it possible to demonstrate, for the first time, the three-dimensional reconstruction of dynamic brain activity in

ACRONYMS

CNS	<i>central nervous system</i>
CT	<i>computed tomography</i>
EEG	<i>electroencephalogram</i>
EP	<i>evoked potential</i>
FFT	<i>fast Fourier transformation</i>
IPSP	<i>inhibitory postsynaptic potential</i>
MEG	<i>magnetoencephalogram</i>
MFT	<i>magnetic field tomography</i>
MRI	<i>magnetic resonance imaging</i>
PET	<i>positron emission tomography</i>

¹Department of Physiology and Biophysics, New York University Medical Center, 550 First Avenue, New York, NY 10016

humans. MFT has a temporal resolution <1 millisecond and a spatial accuracy of 2–5 mm at the cortical level, which deteriorates to 1–3 cm at depths of 6 cm or more. This methodology is quite significant because it seems capable of resolving cortical and subcortical electrical activity with sufficient time resolution to match the real-time functioning of the brain. In addition, it appears to be correlated with MRI imaging for anatomical localization.

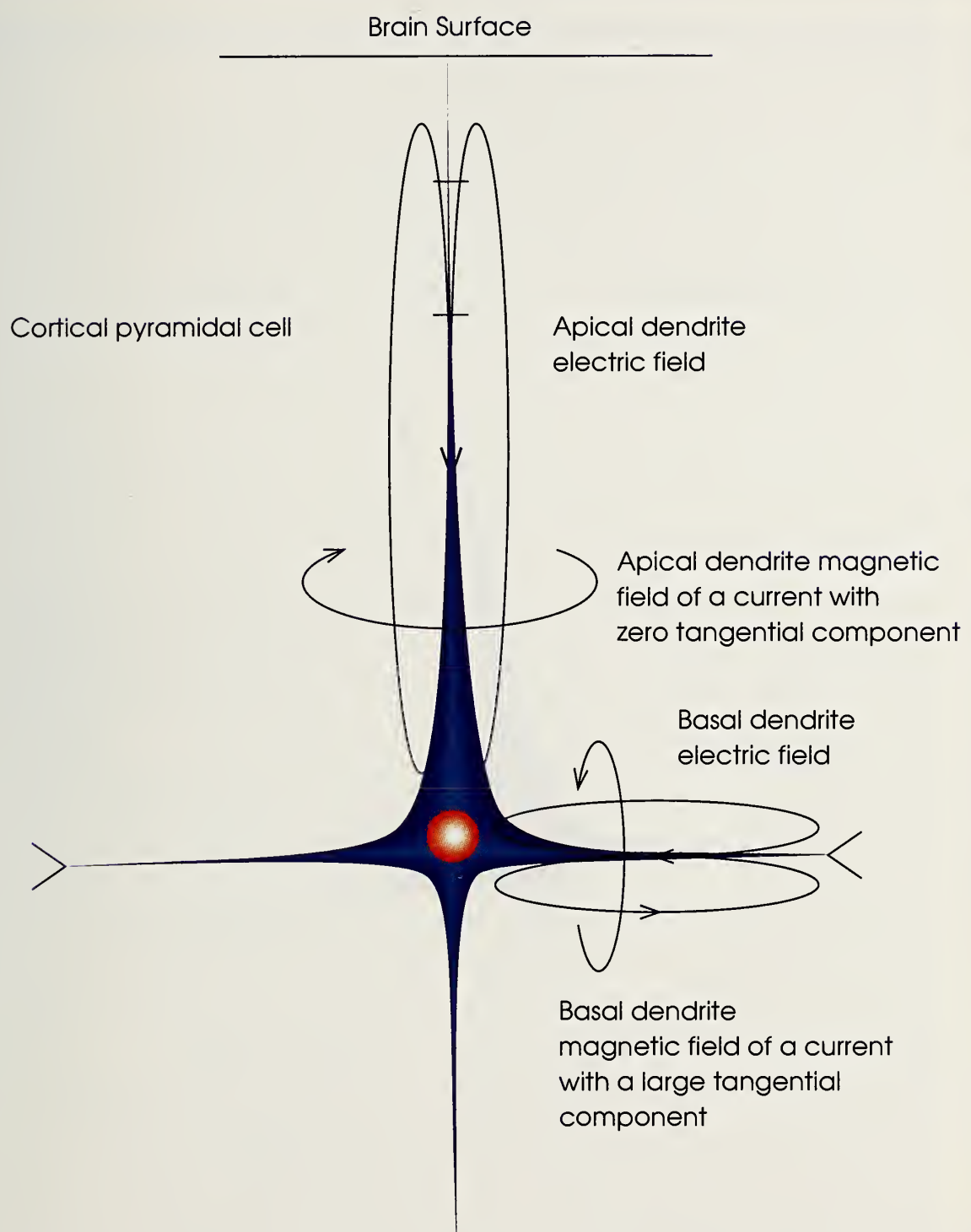
MEG has thus become a most promising technique in the study of normal and pathological central nervous system (CNS) function. Its strengths relate to the following:

- The truly noninvasive nature of the procedure;
- The speed with which results can be gathered (via new multichannel systems, in which many measurements are obtained simultaneously);
- The temporal resolution of the measurements, which is <1 millisecond;
- The spatial resolution for single dipoles, which, in our hands, using modern instruments, is in the millimeter range (Yamamoto et al. 1988; Suk et al. 1991); and
- The new possibility of using MEG as a tomography system.

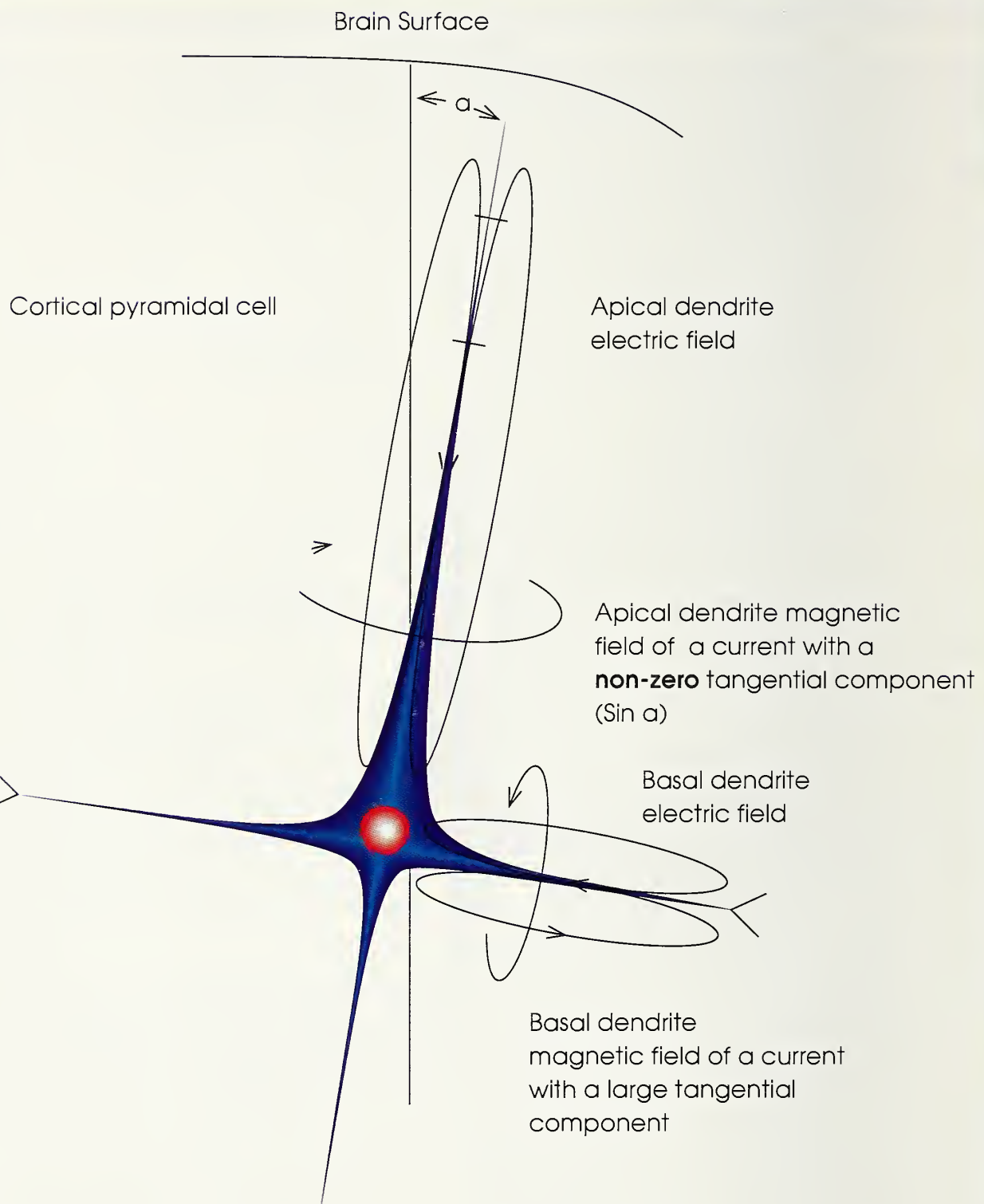
The basic assumption has been that the magnetic fields recorded by MEG are generated by longitudinal intracellular current flowing through the neuronal core conductors organized parallel to the surface of the skull (Cohen and Cuffin

1983). However, only those neurons exactly radial to the skull (figure 1a) generate nonobservable magnetic fields. Any other spatial orientation will have in its current flow a certain tangential vector component (figure 1b) that will generate, in principle, a measurable magnetic field counterpart. This nonradial orientation is very common because the human cortex is continuously folded; only a small portion of the cortical mantle is truly parallel to the outward surface of the scalp. In fact, the amplitude of such a nonzero tangential component is proportional to the sine of the angle of deviation from the purely radial orientation of the neuronal core conductors (figure 1b, angle α). Furthermore, in addition to apical dendrites, there exist significant basal dendritic ramifications, parallel to the surface of the cortex. These basal dendrites, while having radial symmetry in the horizontal direction (and thus a zero isopotential plane at the level of the cell bodies), will generate an open electric field in all other directions and as such should be observable as a magnetic field (figures 1a and b).

This chapter describes how 14- and 37-channel MEG systems (Biomagnetic Technologies Incorporation; BTi) can be used for monitoring and localization of three-dimensional abnormal dynamic patterns of higher frequency components within the human brain during acute alcohol intoxication. The analysis is based on averaged and nonaveraged single-epoch responses obtained before and dur-

FIGURE 1a

Schematic drawing of a cortical pyramidal cell that is exactly radial to the skull and generates an electric field and a nonobservable magnetic field. There is a large tangential component of the current flow within the basal dendrites, which may produce an observable magnetic field. This tangential component, however, represents the sum of all tangential currents in the active basal dendrites. The net current may be close to zero if symmetrical activation of the dendrites occurs due to cancellation within closed electric fields.

FIGURE 1b

Schematic drawing of a cortical pyramidal cell that is slightly deviated from the purely radial orientation with an angle, " α ." This orientation generates an observable magnetic field, created by the tangential component of the current flow, which is proportional to the sine of the angle. There is a large tangential component of the current flow within the basal dendrites, which may produce an observable magnetic field. This tangential component, however, represents the sum of all tangential currents in the active basal dendrites. The net current may be close to zero if symmetrical activation of the dendrites occurs due to cancellation within closed electric fields.

ing auditory processing, offering the possibility of looking at normal and altered brain function in real time.

DYNAMIC PATTERNS OF 40-HZ ACTIVITY

The intrinsic electrical activity of central neurons in the brain seems to be organized in a manner that allows oscillatory events to occur with synchronicity sufficient to generate large functional states (Llinas 1988). The activity thus generated can be recorded with MEG and electroencephalographic (EEG) techniques. This electrical activity, which has been recorded at a single cell level in the mammalian cortex, is correlated with the level of awareness and responsiveness to given sensory inputs in the cortex (Gray and Singer 1989). This correlation suggests that the cortex may function as a tuned oscillator with a peak frequency of 30-45 Hz. This being the case, recognition of the location of these frequencies by magnetic recording could contribute significantly to the study of brain function in normal and pathological states.

Cortical oscillatory activity in the 40-Hz range has been observed in man during cognitive tasks and following sensory stimulation, as analyzed by EEG and MEG (Galambos et al. 1981; Maekelae and Hari 1987; Weinberg et al. 1988; Sheer 1989). Such oscillatory activity is not unique to man but has been seen in many mammalian forms during attentive states (Bouyer et al. 1987) and during physiological stimulation

of the olfactory (Bressler and Freeman 1980) or the visual systems (Eckhorn et al. 1988; Gray and Singer 1989). However, these recordings of 40-Hz activity were restricted to localized brain areas and on occasion to small cell groups, to include a few cortical columns. Even in studies in which EEG and MEG recordings were obtained, data analysis was restricted to a single time slice at the maximum positive or negative peak of an averaged evoked response. Nevertheless, these studies indicate that 40-Hz coherent neuronal activity sufficient to be detected from the scalp is generated during cognitive tasks (Sheer 1989).

We felt, however, that the 40-Hz oscillatory activity observed in various brain regions could reflect certain patterns and share characteristics that are common to much cortical function (Ribary et al. 1988). Indeed, we found a stereotyped dynamic pattern of magnetic activity over the right human hemisphere that was changed during pathological states (Ribary et al. 1989). At each moment in time, we observed a field pattern consisting of positive and negative fields. This pattern "rotated" continuously over the hemisphere, including the frontal, temporal, parietal, and occipital cortices.

More recent studies confirmed these findings and indicated that the recorded 40-Hz activity was a general response during auditory processing, independent of any stimulus parameters (Llinas and Ribary 1991; Ribary et al. 1991). Fast

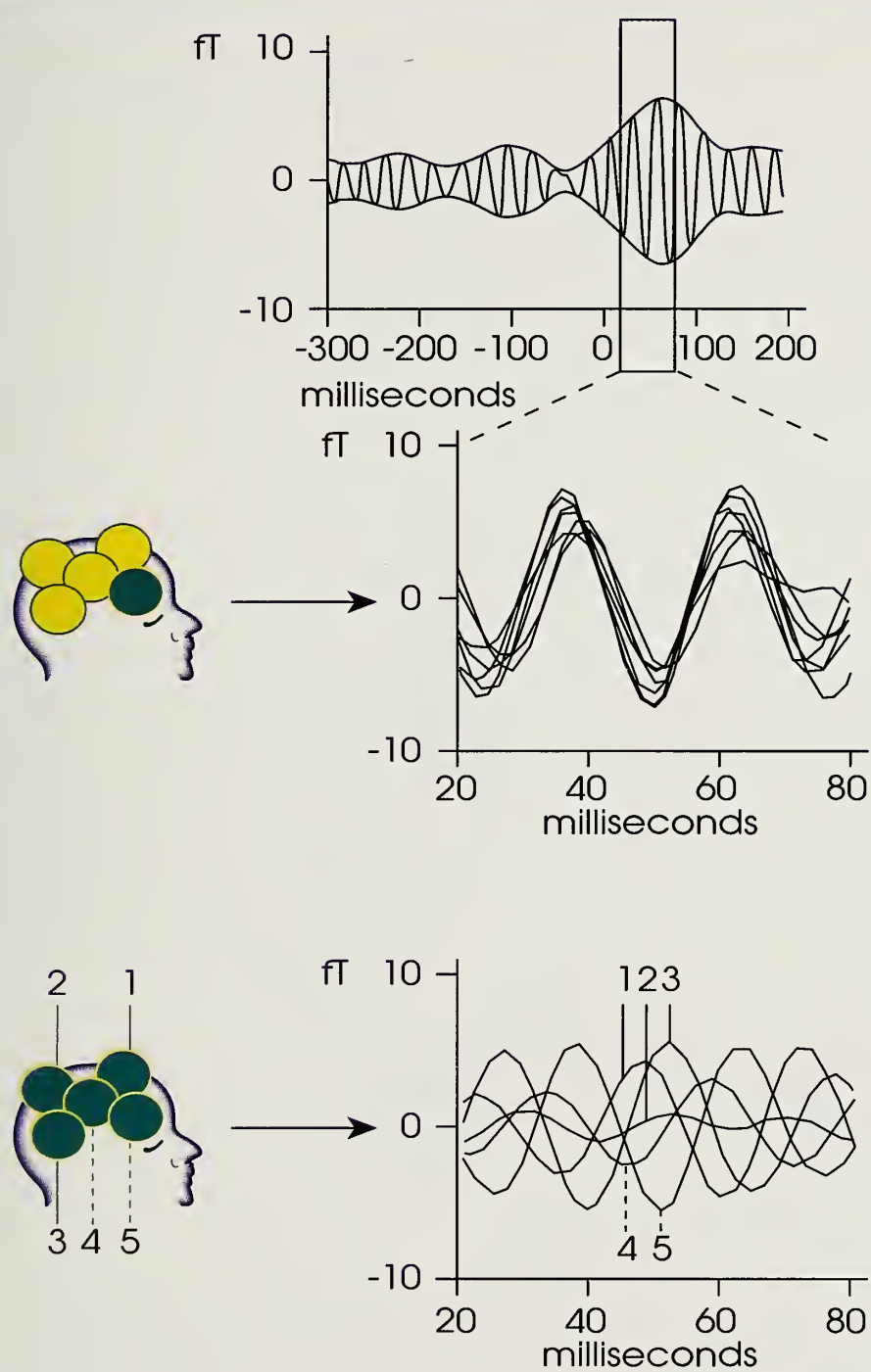
Fourier transformation (FFT) of averaged MEG data showed that during auditory processing, increased activity in the higher frequency range between 30 and 50 Hz peaked around 40 Hz. In addition, filtered data (35–45 Hz) indicated that synchronized 40-Hz activity was recorded over the entire hemisphere during auditory processing. The 40-Hz activity was clearly phase-locked in synchrony among the seven channels of one probe, for periods of over 100–200 milliseconds after onset of stimulus (Llinas and Ribary 1991). Such phase-locking was observable within the area of a single probe (about 25 cm²).

Similar findings, showing temporal and spatial coherence, were obtained for each of the five probe positions located on the subject's right hemisphere. Significantly, large phase differences in the 40-Hz activity were consistently found between the five probe locations; however, small but clear phase shifts among the seven channels of each probe could be followed as continuous events over distance along the entire hemisphere (figure 2). Although these phase shifts were consistent around 40 Hz (35–45 Hz), they disappeared in lower (25–35 Hz) and higher frequency bands (45–55 Hz). This continuous phase shift of the oscillatory activity, within a prime frequency band around 40 Hz, occurred from the frontal to the occipital pole of the hemisphere and corresponded to a shift of the 40-Hz cycle of about 4–6 milliseconds from front to back (Llinas and Ribary 1991). This phase

shifting alone was responsible for the dynamic sweep pattern in 40-Hz magnetic activity along an averaged epoch described above. Such sweep-like activity was also observed in nonaveraged single epochs, using the 37-channel MEG system.

In conjunction with intracellular recordings from cortical interneurons (Llinas et al. 1991), these studies provided further support of the hypothesis that recurrent thalamo-cortico-thalamic activity (figure 3) is involved in organizing and supporting coherent 40-Hz oscillations as a major synchronized event during auditory processing (Llinas 1990; Ribary and Llinas 1990; Llinas and Ribary 1991). This concept is particularly attractive since thalamic neurons *in vivo* have recently been shown to oscillate at 40 Hz (Steriade et al. 1991).

Using MFT on humans, we recently demonstrated that such 40-Hz coherence displayed well-defined cortico-subcortical correlations having a time shift consistent with thalamo-cortical conduction times. In particular, the MFT results indicated that the onset of activity at the thalamic level was followed by widespread activation of the thalamo-cortical system, which resulted in large, coherent thalamo-cortical 40-Hz oscillations that were organized in space and time. We hypothesize that this thalamo-cortical coherence sweeps from the frontal pole to the occipital pole of the brain in order to create from this brain scan a single percept of

FIGURE 2

Phase shift of human magnetic 40-Hz oscillatory activity during auditory processing: The time period between 20 and 80 milliseconds after the start of presentation of the auditory stimuli is shown enlarged in the middle and lower panels. The middle panel shows the superimposition of seven channels (sensors) from one probe (inferior frontal, hatched in sketch at left; simultaneous records) and demonstrates small differences in phase within this region. The bottom panel shows the superimposition of average responses from all sensors in each of the five probe positions (hatched and numbered at left; nonsimultaneous records) and demonstrates large, consistent phase shifts from region to region, indicating a continuous rostro-caudal phase shift over the hemisphere (modified from Llinas and Ribary 1991).

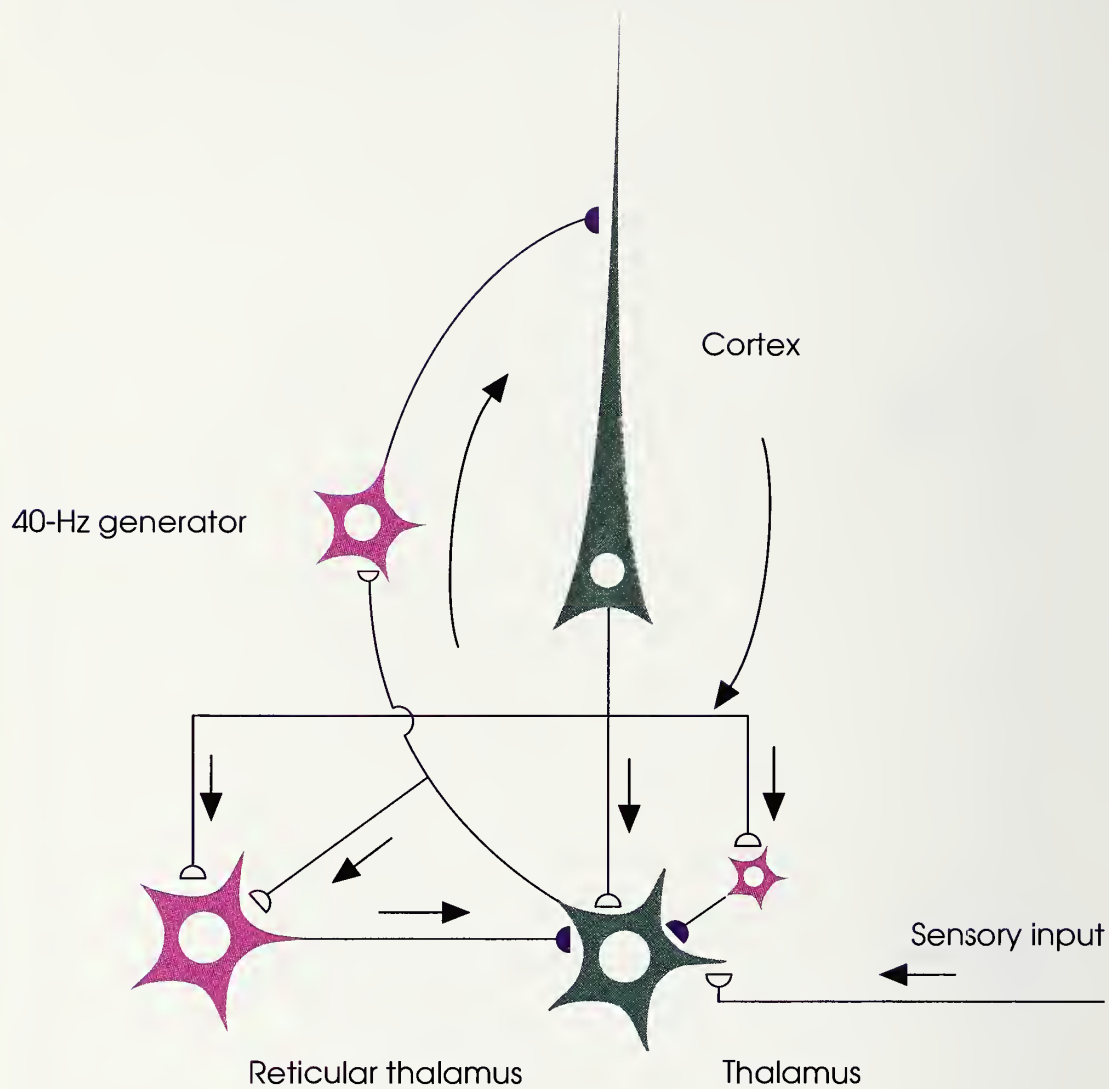
FIGURE 3

Diagram of the proposed cortico-thalamo-cortical reverberating circuit, which may underlay 40-Hz oscillation at the cortex. Thalamic input via projection neurons reaches the neurons of the fourth layer of the cortex that generate 40-Hz oscillation. These cells, which are GABAergic, can generate a 40-Hz IPSP on pyramidal neurons and allow them to fire at 40 Hz as a rebound from abrupt inhibition. Pyramidal cells, in turn, activate via collaterals the thalamic projection neurons as well as the neurons of the reticular thalamus and the interneurons at the thalamus itself. The direct excitatory input (at 40 Hz) to the projection thalamic cells, as well as their disynaptic inhibition via the reticularis and intrathalamic GABAergic neurons, contributes to the thalamic oscillations at 40 Hz. This thalamic oscillation is then signaled back to the cortex, establishing a large, resonant oscillation between the thalamus and the cortex that can recruit sufficient elements to generate the synchronicity observed at both intracellular and extracellular levels in the cortex and thalamus (modified from Llinas and Ribary 1991).

multiple sensory inputs as a basic cognitive function (figure 4).

EXPECTED CHANGES OF DYNAMIC 40-HZ ACTIVITY AFTER ACUTE ALCOHOL INTOXICATION

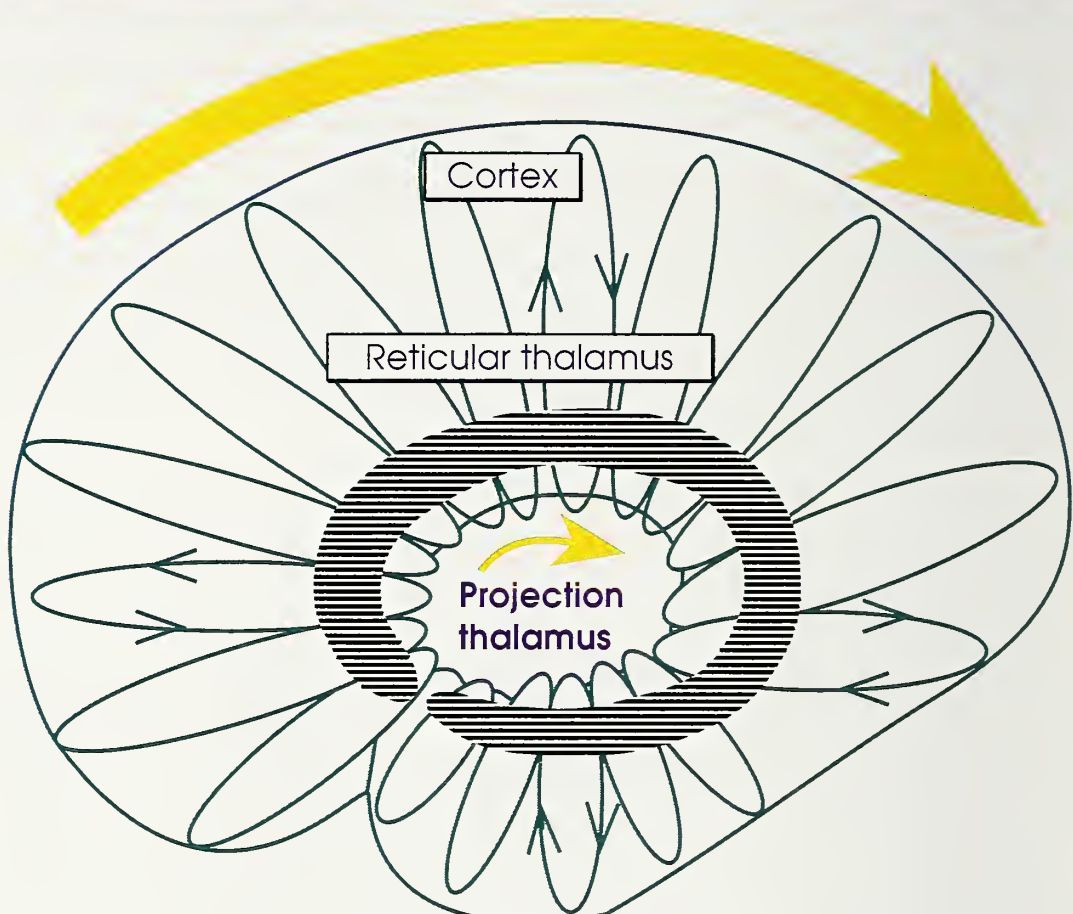
The consumption of alcohol induces several changes in the nervous system and alters behavioral and cognitive states. In general, these include reduced attention, disturbed sensory and cognitive processing, decreased motor control and discharge, and delayed reaction time (Kuschinski and Lullmann 1978). Moderate drinking and chronic alcohol intoxication can further induce irreversible changes within the brain; structural damage ultimately occurs (Harper and Kril 1990). Analyses of the acute and chronic effects of alcohol, as shown by EEG or evoked potential (EP) recordings, have related particular electrical changes to certain cognitive functions during specific sensory tasks. These studies reported generally reduced amplitudes and increased latencies of various short-, middle-, and long-latency components (Begleiter et al. 1981; Pfefferbaum et al. 1987; Oscar-Berman 1987; Meinck et al. 1990). However, only a relatively small fraction of the work dealt with acute alcohol intoxication and its neurophysiological changes, which are not related to an eventual shrinkage or loss of neurons.

To our knowledge, no alcohol studies have been performed using the MEG technique. Unfortunately, in those studies where EEG record-

ings were obtained, data analyses were restricted to single static time slices at the maximum positive or negative peaks of mostly lower-frequency components (below 10 Hz) within averaged evoked responses. However, our studies using the MEG technique focus on the dynamic patterns and interactions of higher frequency components (>20 Hz), analyzed over a certain time period with a temporal resolution of <1 kHz.

All of the findings mentioned suggest that the dynamics of the 40-Hz activity could be altered after an acute administration of alcohol. EEG studies reported delayed auditory brainstem responses in humans (Squires et al. 1978) and indicated a depressive effect of alcohol on neural transmission within brainstem and thalamo-cortical systems. In addition, another study reported an effect of alcohol on GABA-mediated neurotransmission (Kril et al. 1988); however, that study of chronic alcoholics did not demonstrate clearly whether the effect was related to ethanol or to possible cell loss. That report is interesting, however, inasmuch as GABAergic cells reportedly generated a 40-Hz inhibitory postsynaptic potential (IPSP) on pyramidal neurons to allow them to fire at 40 Hz as a rebound from abrupt inhibition (Llinas 1990).

Indeed, preliminary MEG data obtained in our laboratory indicated that the dynamics of the 40-Hz activity during auditory processing were altered following acute intoxication with 0.75 g/kg

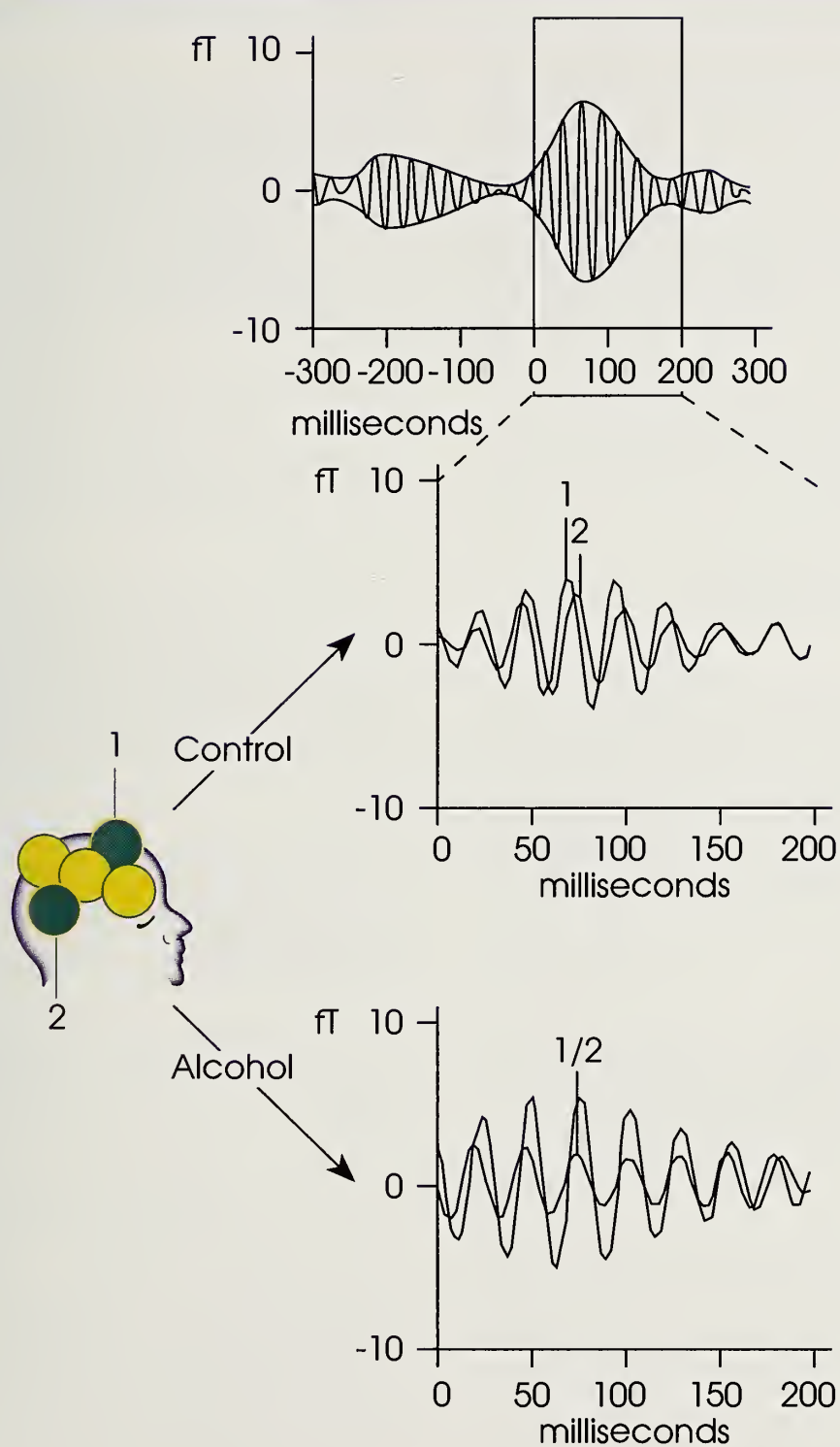
FIGURE 4

Schematic model of a proposed rostro-caudal scan of coherent thalamo-cortical 40-Hz oscillations.

ethanol. Recordings of magnetic fields from frontal and occipital areas of the right hemisphere of an adult healthy subject (figure 5) showed that 30 minutes after alcohol administration, there was clearly decreased coherence within those areas, and it lasted for a shorter time period (50–100 milliseconds) after stimulus start, compared with those in control runs recorded before drug application. In addition, the rostrocaudal phase shift of the 40-Hz activity disappeared (see figure 5), suggesting a more on/off response instead of the stereotypical

spatiotemporal magnetic field pattern described. At 1 hour postadministration, coherence was reduced to a 50-millisecond period in occipital areas but increased in frontal areas. Again, the phase shift from frontal to occipital pole disappeared (figure 5). During the first 50 milliseconds after stimulus start, the phase shift could even be reversed from back to front (figure 5).

These preliminary data suggest complex changes of dynamic 40-Hz activity within thalamo-cortical systems, related to acute alcohol intoxication. With MFT, changes in

FIGURE 5

Phase shift of human magnetic 40-Hz oscillatory activity during auditory processing before and during acute alcohol intoxication. In the middle and lower panels is an enlargement of the time period between 0 and 200 milliseconds after initiation of auditory stimuli, showing the superimposition of average responses from all sensors in each of the two probe positions (hatched and numbered at left; simultaneous records): (i) during the control condition, demonstrating a continuous rostro-caudal phase shift over the hemisphere and (ii) 1 hour after acute alcohol intoxication. The phase shift disappeared after 50 milliseconds of stimulus presentation.

the dynamic patterns of these oscillations can be imaged three dimensionally and characterized with respect to variations in underlying distributed sources and global distribution of magnetic fields over time. Marked abnormalities are expected to be found within the reconstructed three-dimensional brain activity, imaged as a temporal evolution of 1-millisecond steps. One can then correlate these neurophysiological abnormalities with cognitive disturbances during alcohol consumption.

ACKNOWLEDGMENTS

The authors acknowledge the excellent support of R. Jagow, F. Lado, and A. Mogilner of the Center for Neuromagnetism, as well as the continuing support of Biomagnetic Technologies Incorporation (BTi).

REFERENCES

- Begleiter, H.; Porjesz, B.; and Chou, C.L. Auditory brainstem potentials in chronic alcoholics. *Science* 211:1064–1066, 1981.
- Bouyer, J.J.; Montaron, M.F.; Vahnee, J.M.; Albert, M.P.; and Rougeul, A. Anatomical localization of cortical beta rhythms in cat. *Neuroscience* 22:863–869, 1987.
- Bressler, S.L., and Freeman, W.J. Frequency analysis of olfactory system EEG in cat, rabbit and rat. *Electroencephalogr Clin Neurophysiol* 50:19–24, 1980.
- Brooks, R.A., and diChiro, G. Principles of computer assisted tomography (CT) in radiographic and radioisotopic imaging. *Phys Med Biol* 21:689–732, 1976.
- Cohen, D., and Cuffin, N. Demonstration of useful differences between magnetoencephalogram and electroencephalogram. *Electroencephalogr Clin Neurophysiol* 56:38–51, 1983.
- Eckhorn, R.; Bauer, R.; Jordan, W.; Brosch, M.; Kruse, W.; Munk, M.; and Reitboeck, H.J. Coherent oscillations: A mechanism of feature linking in the visual cortex? *Biol Cybern* 60:121–130, 1988.
- Galambos, R.; Makeig, S.; and Talmachoff, P.J. A 40-Hz auditory potential recorded from the human scalp. *Proc Natl Acad Sci USA* 78:2643–2647, 1981.
- Gray, C.M., and Singer, W. Stimulus-specific neuronal oscillations in orientation columns of cat visual cortex. *Proc Natl Acad Sci USA* 86:1698–1702, 1989.
- Hari, R., and Ilmoniemi, R.J. Cerebral magnetic fields. *CRC Crit Rev Biomed Eng* 14:93–126, 1986.
- Harper, C.G., and Kril, J.J. Neuropathology of alcoholism. *Alcohol* 25:207–216, 1990.
- Hoffman, E.J., and Phelps, M.E. Positron emission tomography: Principles and quantization. In: Phelps, M., eds. *Positron Emission Tomography and Autoradiography: Principles and Applications for the Brain and the Heart*. New York: Raven Press, 1986. pp. 237–286.
- Ioannides, A.A.; Bolton, J.P.R.; Hasson, R.; and Clarke, C.J.S. Localized and distributed source solutions for the biomagnetic inverse problem. In: Williamson, S.; Hoke, M.; Stroink, G.; and Kotani, M., eds. *Advances in Biomagnetism*. New York: Plenum Press, 1989. pp. 591–594.

- Ioannides, A.A.; Bolton, J.P.R.; and Clarke, C.J.S. Continuous probabilistic solutions to the biomagnetic inverse problem. *Inverse Prob* 6:1-20, 1990.
- Kril, J.J.; Dodd, P.R.; Gundlach, A.L.; Davies, N.; Watson, W.E.; Johnston, G.A.; and Harper, C.G. Necropsy study of GABA/benzodiazepine receptor binding sites in the brain tissue from chronic alcoholic patients. *Clin Exp Neurol* 25:135-141, 1988.
- Kuschinski, G., and Lullmann, H. *Pharmacology and Toxicology*. Stuttgart, Germany: Thieme Verlag, 1978.
- Llinas, R.R. The intrinsic electrophysiological properties of mammalian neurons: Insights into central nervous system function. *Science* 242:1654-1664, 1988.
- Llinas, R. Intrinsic electrical properties of mammalian neurons and CNS function. *Fidia Research Foundation Neuroscience Award Lectures* 4:173-192, 1990.
- Llinas, R.; Grace, A.A.; and Yarom, Y. In vitro neurons in mammalian cortical layer 4 exhibit intrinsic activity in the 10- to 50-Hz frequency range. *Proc Natl Acad Sci USA* 88:897-901, 1991.
- Llinas, R., and Ribary, U. Rostrocaudal scan in human brain: A global characteristic of the 40-Hz response during sensory input. In: Basar, E., and Bullock, T., eds. *Induced Rhythms in the Brain*. Boston: Birkhauser, 1991, in press.
- Maekelae, J.P., and Hari, R. Evidence for cortical origin of the 40Hz auditory evoked response in man. *Electroencephalogr Clin Neurophysiol* 66:539-546, 1987.
- Meinck, H.M.; Rader, K.; Wieditz, G.; and Adler, L. Afferent information processing in patients with chronic alcoholism: An evoked potential study. *Alcohol* 7:311-313, 1990.
- Oscar-Berman, M. Alcohol-related ERP changes in cognition. *Alcohol* 4:289-292, 1987.
- Pfefferbaum, A.; Rosenblum, M.; and Ford, J.M. Late event-related potential changes in alcoholics. *Alcohol* 4:275-281, 1987.
- Ribary, U., and Llinas, R. The spatial and temporal organization of the 40Hz response in human as analyzed by magnetic recording (MEG). *Eur J Neurosci Suppl* 3:51(Abstr 1229), 1990.
- Ribary, U.; Llinas, R.; Kluger, A.; Suk, J.; and Ferris, S.H. Neuropathological dynamics of magnetic, auditory, steady-state responses in Alzheimer's disease. In: Williamson, S.; Hoke, M.; Stroink, G.; and Kotani, M., eds. *Advances in Biomagnetism*. New York: Plenum Press, 1989. pp. 311-314.
- Ribary, U.; Llinas, R.; Lado, F.; Mogilner, A.; Jagow, R.; Nomura, M.; and Lopez, L. The spatial and temporal organization of the 40Hz response during auditory processing as analyzed by MEG on the human brain. *J Neurosci* 1991, in press.
- Ribary, U.; Weinberg, H.; Cheyne, D.; Johnson, B.; Holliday, S.; and Ancill, R.J. EEG and MEG (magnetoencephalography) mapping for indexing pathological changes in human brain. *Eur J Neurosci Suppl* 1:Abstr 44.17, 1988.
- Sheer, D.E. Sensory and cognitive 40Hz event related potentials: Behavioral correlates, brain function and clinical application. In: Basar, E., and Bullock, T.H., eds. *Brain Dynamics*. Berlin: Springer Verlag, 1989. pp. 339-374.

Squires, K.C.; Chu, N.S.; and Starr, A. Acute effects of alcohol on auditory brainstem potentials in humans. *Science* 201:174–176, 1978.

Steriade, M.; Curro Dossi, R.; Pare, D.; and Oakson, G. Fast oscillations (20–40 Hz) in thalamocortical systems and their potentiation by mesopontine cholinergic nuclei in the cat. *Proc Natl Acad Sci USA* 1991, in press.

Suk, J.; Ribary, U.; Cappell, J.; Yamamoto, T.; and Llinas, R. Anatomical localization revealed by MEG recordings of the human somatosensory system. *Electroencephalogr Clin Neurophysiol* 78:185–196, 1991.

Wehrli, F.W.; Shaw, D.; and Kneeland, J.B. *Biomedical Magnetic Resonance Imaging*:

Principles, Methodology and Applications. New York: VCH Publishers, Inc., 1988.

Weinberg, H.; Cheyne, D.; Brickett, P.; Gordon, R.; and Harrop, R. An interaction of cortical sources associated with simultaneous auditory and somesthetic stimulation. In: Pfurtscheller, G., and Lopes da Silva, F.H., eds. *Functional Brain Imaging*. Toronto: Hans Huber Publishers, 1988. pp. 83–88.

Williamson, S.J., and Kaufman, L. Biomagnetism. *J Magn Magn Materials* 22:129–201, 1981.

Yamamoto, T.; Williamson, S.; Kaufman, L.; Nicholson, C.; and Llinas, R. Magnetic localization of neuronal activity in the human brain. *Proc Natl Acad Sci USA* 85:8732–8736, 1988.

3

USE OF ANIMAL MODELS FOR ELECTROPHYSIOLOGICAL NEURAL IMAGING IN ALCOHOL RESEARCH

Cindy L. Ehlers, Ph.D.¹

Electrophysiological recordings offer one of the few techniques in which split-second neural activity can be assessed, as a function of time, in awake behaving subjects. It is precisely because electrophysiological measures can be rapidly obtained from behaving human and animal subjects that they provide a unique imaging technique for assessing the effects of ethanol use and abuse.

Two electrophysiological techniques have been generally utilized in alcohol research to obtain neural images. One technique is the recording of the spontaneous electroencephalogram (EEG), coupled with the utilization of power spectral techniques to quantitate the precise frequency and amplitude information of the signal. This technique has been applied to studies in human subjects, where it has been found to discriminate between subjects at genetically increased risk for the development

of alcoholism (Gabrielli et al. 1982; Pollock et al. 1983; Ehlers and Schuckit 1988, 1990, 1991). It has also been utilized in human and animal experiments to identify what mechanisms may underlie brain response to acute and chronic administration of alcohol (Begleiter and Platz 1972; Dolce and Decker 1972; Wolf et al. 1981; Young et al. 1982; Ehlers and Reed 1987; Ehlers 1989; Ehlers et al. 1989b; Ehlers and Chaplin 1991; Ehlers et al. 1990, 1991a,c).

The second electrophysiological technique that has provided impor-

ACRONYMS

EEG	electroencephalogram
EPs	evoked potentials
ERPs	event-related potentials
NE	norepinephrine
NMDA	N-methyl-D-aspartate
6-OHDA	6-hydroxydopamine
P and NP	ethanol preferring and nonpreferring
PCPA	parachlorophenylalanine

¹Department of Neuropharmacology, The Scripps Research Institute, La Jolla, CA 92037

tant new measures for the study of factors that may contribute to ethanol abuse is the recording of evoked responses (for a comprehensive review, see Porjesz and Begleiter 1985a). Evoked responses are obtained by recording the EEG following the delivery of a discrete stimulus in a given sensory modality (e.g., auditory, visual, somatosensory). The time-locked EEG responses to the stimuli are recorded and subsequently averaged over several stimulus presentations to produce a series of waves or components with characteristic amplitudes and latencies from the stimulus onset. These waves or components, depending on the stimulus utilized and the location on the brain or surface of the scalp used for recording, represent activity of their neural generators. Early components represent the activity at the sensory end organ whereas middle latency components trace the signal through the brain stem and thalamus. Late components presumably reflect function in limbic and cortical sites (Buchwald and Huang 1975; Stockard and Rossiter 1977; Halgren et al. 1980; McCarthy et al. 1982; Knight et al. 1989).

Simple stimulus paradigms, which consist of single sensory stimulus repetitions, produce brain responses that are labeled evoked potentials (EPs). If a complex stimulus paradigm is utilized, and especially if the subject is required to discriminate one stimulus from another, the brain responses are called event-related potentials (ERPs). ERPs are notable because

they contain late components that reflect the "cognitive processing" of the stimuli in integrative brain sites (Hillyard and Kutas 1983; Donchin et al. 1986).

One late wave ERP component that has been intensively studied in human subjects is the P3 or P300 component. The P3 is a positive going potential that has a latency of about 300 milliseconds when elicited by auditory stimuli in normal, young adults. This component can be averaged from the EEG when a subject is asked to discriminate an infrequent stimulus that is embedded within a series of frequent stimuli (Donchin et al. 1978, 1986). However, the P3 can also be elicited under conditions in which subjects are presented frequently and infrequently occurring tones and are instructed not to respond to them (Polich 1987a).

Quantitative measures of ERP components have been utilized successfully to index cognitive functioning (Donchin et al. 1986) and to assess the functional integrity of different neuroanatomic systems as they relate to clinical pathology syndromes (Polich et al. 1986). Thus, as suggested by Porjesz and Begleiter (1985a), "These powerful EP techniques occupy the interface between cellular neurobiology and the behavioral sciences."

Electrophysiological studies using ERP-imaging techniques have provided a sensitive index whereby the effects of alcohol can be assessed (Porjesz and Begleiter 1985a; Odencrantz et al., Chapter 5). The acute effects of ethanol on ERP

components have been evaluated in human subjects in several studies. When paradigms in which subjects are required to detect "target" stimuli were used, most studies have reported decreases in the amplitude of the N1 and P3 components following acute ethanol administration (Rhodes et al. 1975; Kopell et al. 1978; Pfefferbaum et al. 1980; Campbell et al. 1984; Campbell and Lowick 1987); however, factors such as family history (Elmasion et al. 1982) and attentional effort (Roth et al. 1977) seem to modify responsivity.

In an attempt to assess cognitive and brain functioning in abstinent alcoholics, ERPs have also been recorded. In general, a decrease in the amplitude and an increase in the latency of the P300 component have been reported in some abstinent alcoholics (Emmerson et al. 1987; Patterson et al. 1987; Pfefferbaum et al. 1987; Begleiter et al. 1980b; Porjesz et al. 1980; Porjesz and Begleiter 1981, 1985b). Unexpectedly, however, recent studies have provided evidence to suggest that the decreases observed in the amplitude of the P3 component may have preceded the development of abuse drinking in certain alcoholic populations.

Evaluation of ERPs in the sons of alcoholics, who are at 4–5 times increased risk for the development of alcoholism, and who have not yet developed drinking problems, has revealed that a decrease in the amplitude of the P300 component was also observed in some populations of these subjects (Elmasion et al. 1982; Begleiter et al. 1984; O'Connor

et al. 1986, 1987; Patterson 1987). However, some discrepancies between various studies investigating the P3 and ethanol vulnerability and abuse have been attributed to differences in subject populations and in the ERP tasks and analyses employed in the studies (Pfefferbaum et al. 1979; Polich and Bloom 1986, 1987).

These studies evaluating electrophysiological parameters in human subjects at high risk for the development of alcoholism have helped usher in a new and exciting approach to the understanding of factors that may underlie abusive drinking habits. While the importance of genetic variables in the development of alcoholism has been well documented in family, twin, and adoption studies (Goodwin et al. 1974; Cotton 1979; Cadoret et al. 1980; Cloninger et al. 1984; Goodwin 1985; Schuckit 1985, 1986), the importance of psychosocial variables (Cloninger et al. 1981; Rutter 1986) is difficult to tease out of this multi-factorial system. However, the identification of "biological markers" of genetically influenced brain processes may provide a window by which the biological components important to the development of alcoholism may be identified. To further the understanding of how ERP components might be linked to alcoholism, more information is needed concerning the basic neuroanatomical, neurochemical, and neuropsychological underpinnings of these potentials.

Although the stimulus characteristics required to elicit the P3 com-

ponent (Sutton et al. 1965; Roth 1973; Squires et al. 1975; Donchin et al. 1978; Polich 1987*b*, 1989) and to a certain extent the information-processing activities associated with it (Courchesne 1978*a*; Hillyard and Kutas 1983; Polich and Donchin 1988) are known, less is understood about the neuroanatomical or neurochemical generators of these ERP components. A number of brain areas have been suggested as potential sites of origin of the P3 potential. Cortical areas have been postulated to be important in the generation of the P3 (Courchesne 1978*b*; Goff et al. 1978; Desmedt and Debecker 1979), in particular frontal cortex and temporal-parietal junction (Knight et al. 1989). Convincing evidence for subcortical generators arising from the amygdala or hippocampus has also been provided (Halgren et al. 1980; Wood et al. 1980; McCarthy et al. 1982). Unfortunately, further studies in human subjects may not be able to provide the much needed data on the neuroanatomical and neurochemical contributors to these scalp-recorded potentials.

THE USE OF ANIMAL MODELS

Over the last several years there has been an attempt to develop animal models of long-latency ERPs to probe the psychological, physiological, and anatomical variables that underlie the P3 component. These studies have mostly used cats (Buchwald and Squires 1982; Harrison et al. 1986, 1988) and monkeys (Arthur and Starr 1984; Neville and Foote 1984; Glover et al. 1986;

Pineda et al. 1987; Ehlers 1988, 1989; Paller et al. 1991) for subjects. However, recent studies have reported that a P3 could also be generated in anesthetized (O'Brien 1982) and unanesthetized rats (Hurlbut et al. 1987; Ehlers et al. 1989*a*; Ehlers and Chaplin 1991; Ehlers et al. 1991*a,b,d*).

Various stimulus paradigms and behavioral responses have been used in these investigations to generate ERPs, and most authors have reported that a positive going potential in the 200- to 500-millisecond range could be averaged from the EEG following the presentation of infrequent and/or task-relevant stimuli. A few of these animal models have been utilized in an attempt to identify the neurophysiological mechanisms underlying these potentials. Harrison et al. (1986, 1988) used lesion techniques in a series of studies to evaluate the role of various brain sites in the generation of the P300-like potential in the cat. They found that while primary auditory cortex ablation does not abolish the P3 recorded from the skull surface, septal lesions can produce profound reductions in P3 amplitude. Thus, these data support the concept of a subcortical generator, such as the hippocampus for the P300, as recorded in cats.

One other approach to the understanding of the neuroanatomical generators of ERPs has been to record ERPs from directly within the brain of animals in cortical and subcortical sites instead of merely recording from the surface of the skull or scalp. These studies have been accomplished in rodents, with electrodes chronically implanted in

such areas as the hippocampus, frontal cortex, amygdala, thalamus, and locus coeruleus (Ehlers et al. 1989a; Ehlers et al. 1991d). Results have confirmed that ERP components, which resemble those recorded in human subjects, can be identified in rats using a standard auditory paradigm. In these studies, P3-like potentials were found to occur in limbic sites, amygdala, and hippocampus, but not in cortical brain stem or thalamic areas. Further evaluation of the P3-like potential recorded in hippocampus in the rat also revealed that the amplitude of this potential is significantly affected by changes in stimulus probability, in a manner similar to that observed in human experiments (Ehlers et al. 1989a).

If the P3 potentials recorded on the surface of the scalp in human subjects are indeed generated in limbic sites such as hippocampus and amygdala, as suggested by data from Halgren et al. (1980), this may have further implications for the study of alcoholism. For instance, if P3 amplitudes are indeed linked to genetic variables as well as alcohol abuse, then hippocampal and amygdaloid sites should be considered as important contributors to the behavior.

Yet another approach to the understanding of the origins of these potentials has been to lesion a specific neurotransmitter system and then record the subsequent effects on ERPs. In one study, in which monkeys were used as subjects, Pineda et al. (1989) made electrolytic lesions and knife cuts to the areas of the locus coeruleus and the dor-

sal bundle in order to reduce noradrenergic tone to the forebrain. They found that monkey's P300-like potentials, recorded from the skull, exhibited decreased areas, altered brain-surface distributions, and reduced sensitivity to stimulus probability.

Lesion studies in rats have also provided evidence to support the role for specific neurotransmitters in modifying ERP morphology. 6-Hydroxydopamine (6-OHDA) lesions to the ventral tegmental area, which produced significant reductions in dopamine, were not found to alter rat ERP amplitudes or latencies (Ehlers et al. 1991d). However, reductions in serotonin produced by parachlorophenylalanine (PCPA) administration were found to produce significant reductions in N1 components recorded in hippocampus and cortex (Ehlers et al. 1991d). In further studies, 6-OHDA lesions to the dorsal noradrenergic bundle were also observed to produce reductions in the amplitude of the rat P3, as in the monkey, under certain stimulus conditions (Ehlers et al. 1989a). Thus, it appears that ERP components may have specific neurochemical signatures. Additional investigation of these specific neurochemical systems may give insight into how those systems may be linked to the risk for developing alcoholism.

ALCOHOL EFFECTS ON ANIMAL MODELS OF ERP

Although animal models of ERPs represent a powerful tool for the

understanding of brain function, they have been little used in pharmacological studies in general and alcohol studies in particular. Some studies have evaluated the effects of acute ethanol administration on ERPs, using monkeys (Ehlers 1988, 1989). In these studies, an auditory "oddball plus novel" tone sequence was utilized to elicit late waves including P3-like components from electrodes implanted in the skull. As reported for human subjects, acute oral ethanol administration at low doses (0.75 mg/kg) was found to produce significant decreases in the N1 component, whereas higher doses (1.5 g/kg) were also found to produce decreases in the amplitude of the monkey P3-like component. A modest dose of diazepam (2.5 mg/kg), like alcohol, was found to produce profound reductions in the N1 component; however, it had no effect on the monkey P3 component (Ehlers 1988). These studies suggest that ethanol produces similar effects on ERPs in monkeys and in human subjects. In addition, these studies indirectly suggest that while diazepam can produce some results similar to ethanol on the N1, GABAergic mechanisms as indexed by benzodiazepine administration do not modify the monkey P3 component.

The effects of chronic ethanol exposure have also been assessed in animal models, although most studies have recorded EPs (Begleiter and Coltrera 1975; Porjesz et al. 1976; Begleiter and Porjesz 1977; Chu et al. 1978; Begleiter et al. 1980a; Bierley et al. 1980). In these studies, EP mea-

sures have suggested that prolonged "hyperexcitability" may be observed following withdrawal from chronic ethanol administration. In one study, ERPs were collected (Ehlers and Chaplin 1991). In this study, rats were continuously exposed to ethanol vapors in chambers for 1 month. This treatment produced a mean blood ethanol level of about 180 mg percent. ERPs were collected from control rats and ethanol-treated rats at 10 minutes, 24 hours, and 2 weeks following termination of the ethanol vapor or control chamber exposure. Significant reductions in the N1 and P2 amplitudes of the rat ERPs were found in cortical and hippocampal leads after chronic ethanol exposure. Significant reductions in the amplitude and increases in the latency of the P3 component were also observed. Following 2 weeks' withdrawal, reductions in the N1 and P2 amplitudes in cortex and hippocampus were still evident, as was lengthening of the P3 latency and a trend toward a reduction in P3 amplitude. These data suggest that, in this model, ethanol can produce long-term effects in response to ERP stimuli in a manner similar to that in humans.

The neurochemical basis of this persistent reduction in N1 amplitude of the rat ERP following 2 weeks' withdrawal from ethanol exposure is not known. However, as previously mentioned, depletions of serotonin produced by PCPA have been found to produce reductions in the rat N1 component in this ERP paradigm (Ehlers et al. 1991d). Thus,

the long-term reduction in the N1 component produced by chronic ethanol exposure could theoretically be mediated by serotonergic mechanisms. These data are consistent with those from human studies in which serotonergic reuptake inhibitors have been used in the treatment of alcoholics (Naranjo et al. 1986).

Significant lengthening of rat P3 latencies and a trend toward a decrease in their amplitudes were noted in the hippocampus of rats following 2 weeks' withdrawal from ethanol exposure (Ehlers and Chaplin 1991). Previous studies demonstrated that chronic ethanol exposure can result in morphological alterations in the hippocampus in rodent models (Riley and Walker 1978; Walker et al. 1980, 1981). Thus, it has been suggested that the low voltage or absent P300 components observed in some human alcoholics may indicate a hippocampal deficit (Porjesz and Begleiter 1985a). As previously mentioned, the late positive components of rat ERPs recorded in hippocampus are reduced in amplitude following norepinephrine (NE) depletion (Ehlers and Chaplin 1991). Since NE is known to be changed following chronic ethanol exposure (Nutt and Glue 1986), it could theoretically contribute to the reduction in the amplitude of the rat P3s recorded in hippocampus under those conditions.

More recent investigations have identified another neurotransmitter candidate that may be important in modulating P3 morphology. A se-

ries of studies have provided evidence to suggest that some of the effects of ethanol may be mediated via the glutamate N-methyl-D-aspartate (NMDA) receptor (Hoffman et al. 1990; Gonzales and Hoffman 1991). For instance, in electrophysiological and biochemical experiments, ethanol, at low concentrations, has been shown to inhibit NMDA receptor-mediated events selectively in vitro (Hoffman et al. 1989a,b; Lovinger et al. 1989; Lima-Landman and Albuquerque 1989; Rabe and Tabakoff 1990). Further evidence that the effects of low doses of ethanol may be mediated by glutaminergic neurons comes from studies utilizing the noncompetitive NMDA receptor antagonist MK-801. In behavioral studies, MK-801 has been shown to enhance the anticonvulsant (Shrinivas and Ticku 1989), hypnotic (Wilson et al. 1990), and anxiolytic (Goldberg et al. 1983) effects of ethanol in rodents. MK-801 has also been shown to reduce the seizure score in animals during alcohol withdrawal (Morrisett et al. 1989; Grant et al. 1990).

The effects of MK-801 and ethanol on ERPs have recently been studied in rats (Ehlers et al. 1991a). In this study, evaluation of ERPs obtained from these rats revealed that acute administration of MK-801, in very low doses (0.1 mg/kg), produced significant decreases in the amplitude of the N1 and P2 components in cortex, decreases in the P1 and N2 in thalamus, and a profound decrease in the P3 components' amplitude

recorded in dorsal hippocampus and amygdala. Low doses of ethanol (0.75 mg/kg) were also found to produce decreases in amplitude in the N1 component in cortex, with a trend toward a decrease in amplitude in the P3 in amygdala. Thus, acute administration of ethanol and MK-801 were found to produce some similarities in their effects on ERP components. However, the coadministration of MK-801 and ethanol did not produce significant interactions on ERPs, suggesting that these drugs could be producing similar effects through different mechanisms.

The finding of a highly significant reduction in the rat P3 in hippocampus and amygdala, following administration of low doses of MK-801, further suggests that the glutamate-NMDA receptor system may partially modulate the generation of that component. Some studies in human subjects have suggested that the P3 recorded from human scalp recordings may be associated with memory processes (Donchin et al. 1986). Several studies have also linked the NMDA receptor with some of the neurophysiological mechanisms that underlie memory, such as long-term potentiation (Lynch and Baudry 1984). In addition, administration of MK-801 has been demonstrated to disrupt learning in animals, particularly spatial learning (Whishaw and Auer 1989; McLamb et al. 1990; Wozniak et al. 1990). Thus, the profound reduction in P3 amplitude found in the rat ERP model following acute MK-801 administration lends further

support for a relationship among the P3, the NMDA receptor, and memory processes. Further studies will be necessary to elucidate possible links between alcohol abuse, genetic history, P3 amplitudes, and the NMDA receptor.

THE USE OF ANIMALS SELECTIVELY BRED FOR ETHANOL PREFERENCE FOR ELECTROPHYSIOLOGICAL IMAGING STUDIES

Recently developed animal models offer the opportunity to study genetically influenced differences in drinking behavior (Eriksson 1968; Gentry et al. 1983; Deitrich and Spuhler 1984). Genetic selection breeding studies at Indiana University have produced two lines of rats that differ significantly in their ethanol consumption (Lumeng et al. 1977; Li et al. 1981). Ethanol-preferring (P) rats have been shown, in a free-choice situation, to consume 6–10 g/kg/day of ethanol voluntarily, whereas nonpreferring (NP) rats generally consume less than 1 g/kg/day in the same free-choice situation (Li et al. 1979). The P rats have previously been demonstrated to meet many of the requirements necessary for a suitable animal model for the study of alcoholism. For instance, P rats will work to obtain ethanol, through operant responding, in the presence of food and water (Penn et al. 1978; Murphy et al. 1989). The P rats will also self-infuse ethanol intragastrically (Waller et al. 1984) and have

been shown to develop tolerance and dependence (Waller et al. 1982).

These two rat lines (P and NP) have also been shown to differ on several physiological and biochemical parameters, which may be related to their drinking behavior (Lumeng et al. 1982). For instance, P rats have been shown to differ from NP rats in their steady-state concentrations of certain monoamines in discrete brain regions (Murphy et al. 1982, 1987; McBride et al. 1990). In particular, lowered levels of serotonin and its metabolites have been consistently found in several limbic and cortical brain regions in P rats, in contrast to those in NP rats (Murphy et al. 1982, 1987; McBride et al. 1990).

Recent studies have explored ERP recordings in these animals at baseline and following acute alcohol administration (Ehlers et al. 1991b). In these studies, an auditory "oddball" paradigm was used to record ERP responses at baseline and following several doses of ethanol. The P and NP rats differed at baseline in that P rats had smaller N1-like ERP components and larger P2 waves in both cortex and hippocampus (see figure 1).

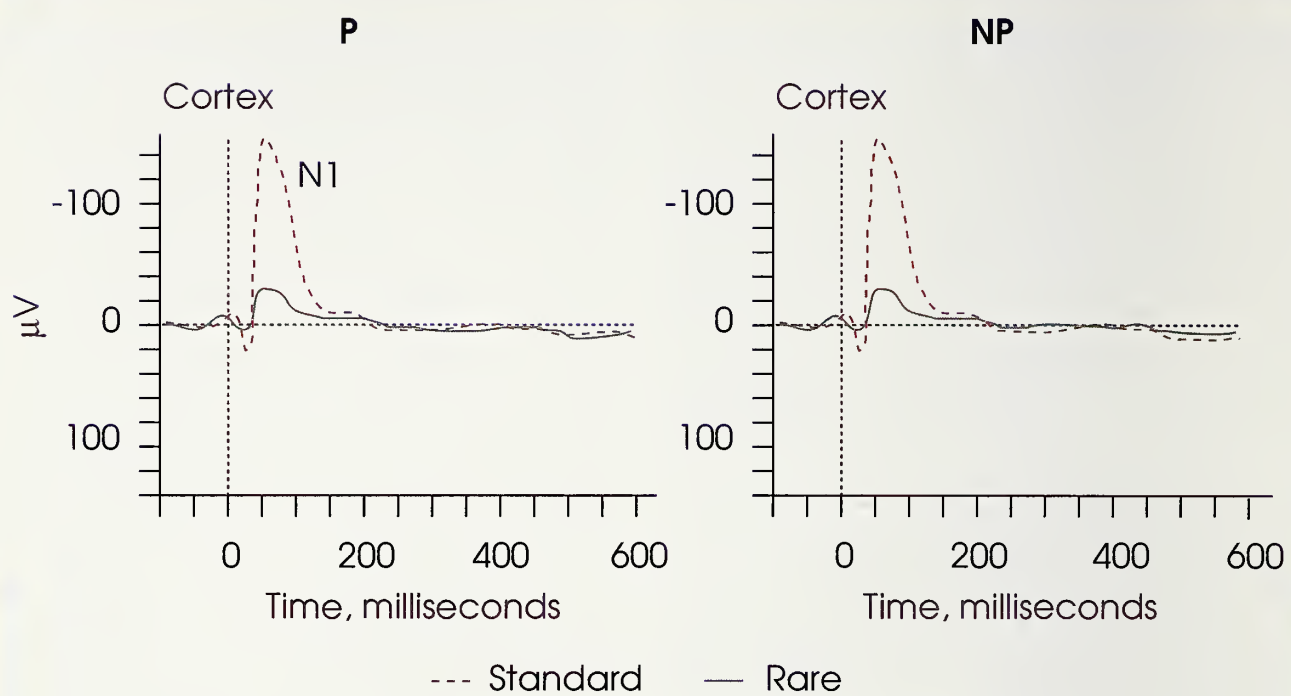
No differences have yet been found between P and NP rats in the amplitude or latency of their P3 responses. The neurochemical basis of the smaller N1-like ERP in P rats is unclear. However, P rats are known to have significantly lower serotonin levels in several brain areas (Murphy et al. 1982), and reductions in serotonin produced by PCPA have been demonstrated to

result in lowered N1 amplitudes in heterozygous Wistars (Ehlers et al. 1991d). Taken together, these studies are consistent with the hypothesis that the inherently reduced serotonin levels in P rats may contribute to the N1 reductions observed in that line.

The P and NP rats have also been found to differ in response to acute ethanol administration. The NP rats have been shown to display dose-dependent reductions in ERP component amplitudes, particularly the N1 recorded from cortical sites. In contrast, P rats do not exhibit such reductions in N1 amplitudes following acute ethanol administration, and, in fact, show increased N1 amplitudes in hippocampal sites (Ehlers et al. 1991b).

Less sedating or mildly arousing responses to ethanol have also been reported to occur in P rats in other electrophysiological and behavioral studies. For instance, Waller et al. (1983) evaluated spontaneous motor activity and found increases after low doses of ethanol administration in P rats, whereas in NP rats locomotion was unaffected. In EEG studies, Morzorati et al. (1988) demonstrated that during non-rapid eye movement sleep, low doses of ethanol produced an increase in EEG spectral power in NP rats; whereas, power in P rats decreased slightly and then returned to baseline. These data suggest that ethanol is capable of producing more deep sleep in NP rats and less deep sleep in P rats. Thus, in that study, as in others, P rats were found to experience a stimulatory

FIGURE 1a



ERP response in P and NP rats.

effect of ethanol, whereas NP rats were more sedated.

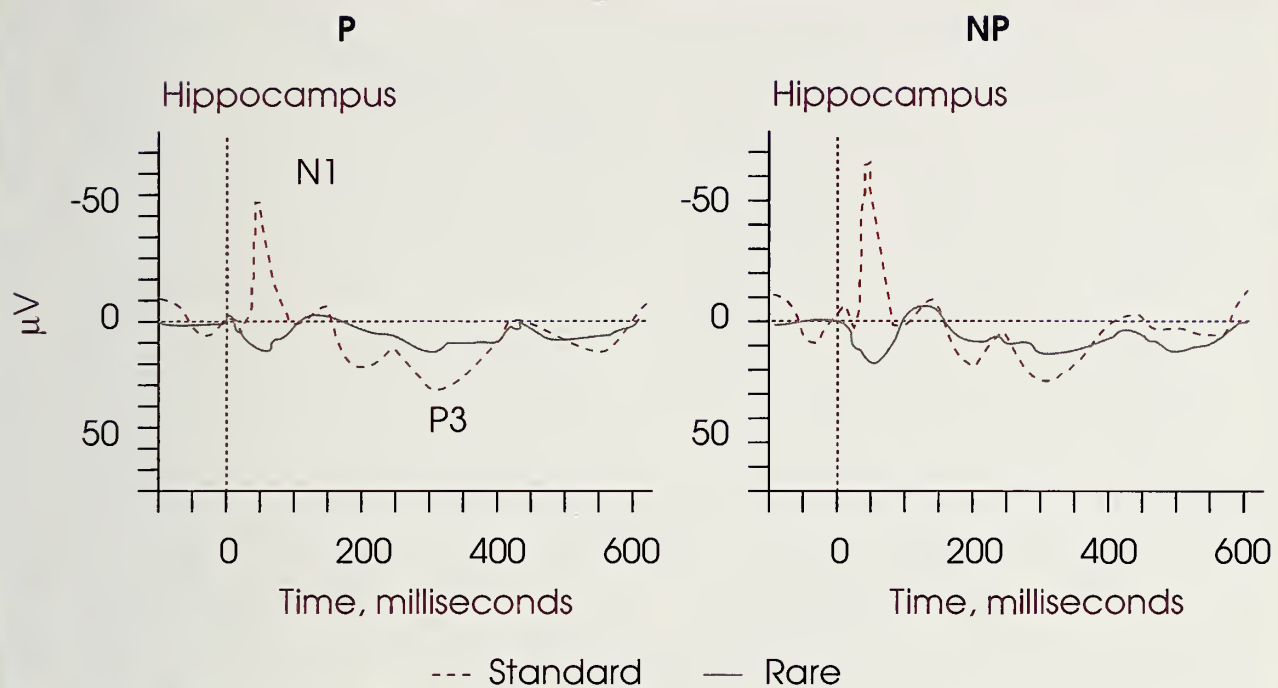
Response to ethanol has also been reported to vary in human subjects, depending on genetic variables. Studies by Schuckit and collaborators have shown that young men with alcoholic fathers have a much less intense response to alcohol, as measured by several subjective and objective measures (Schuckit 1984; Schuckit et al. 1988). In addition, electrophysiological studies have suggested that human subjects with a family history of alcoholism may also experience mild stimulatory effects of alcohol (Ehlers and Schuckit 1988, 1990, 1991).

Thus, animal studies suggest that P rats may possess several at-

tributes of human subjects at increased risk for the development of alcoholism. Further studies of these animals may be fruitful for linking biochemical, behavioral, and electrophysiological variables in the search for mechanisms underlying alcohol use and abuse.

CONCLUSIONS AND FUTURE DIRECTIONS IN THE USE OF ANIMAL MODELS FOR NEURAL IMAGING

The use of electrophysiological imaging techniques has provided important measures by which genetically influenced variables that contribute to abusive drinking behavior can be elucidated. Studies in

FIGURE 1b

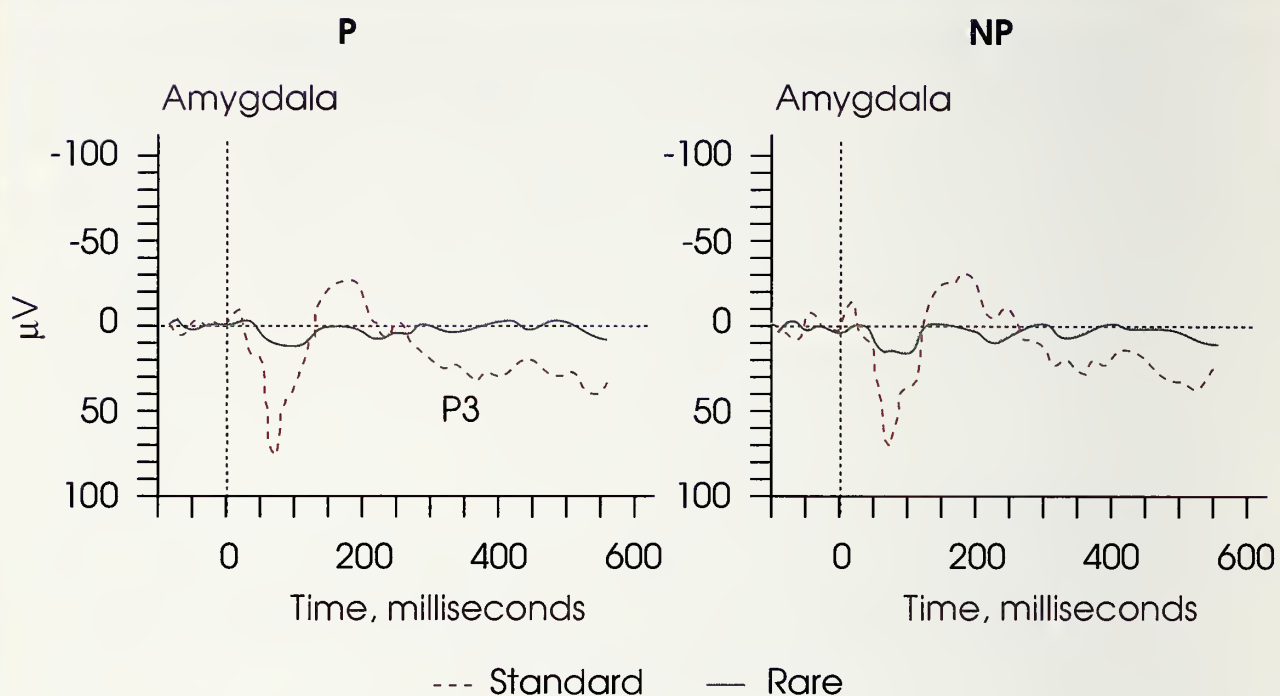
ERP response in P and NP rats.

human subjects have been critical in identifying such variables and linking them to relevant biological and psychosocial concomitants. However, human studies may have some limitations in providing the opportunity to evaluate neurochemical brain mechanisms that may influence the generation of these neural images.

Animal models, while having obvious limitations in lacking complete relevancy to the human condition, do provide the experimental control necessary to search for the mechanisms underlying the neural images of interest to the study of alcoholism. Already some progress has been made in this area. For instance, ERPs that resemble those recorded from humans have been

established to exist in monkeys, cats, and rats. Several studies have also demonstrated that acute and chronic ethanol can produce modifications in these animals' ERPs in a manner similar to that observed in human studies. In addition, investigations in P and NP rats have shown that P rats differ in baseline ERP recordings and that they have a less sedating or more arousing response to alcohol, not unlike what is observed in human high-risk subjects. Thus, relevant animal models of ERPs appear to be emerging for studies in alcoholism.

Additional studies have been conducted in an attempt to identify the neuroanatomical and neurochemical mechanisms underlying these ERPs in animals. So far, all in-

FIGURE 1c

ERP response in P and NP rats.

vestigations in cats, rats, and monkeys suggest a limbic origin for the P300 potential, as supported by direct recordings and lesion studies. While these data are also supported by some human experiments in which direct recordings from these sites have been made, clinical studies of brain pathology also support a role for neocortical sites in the generation of the P300. Undoubtedly, the P300 recorded from the scalp in human subjects has multiple generators. Since non-human primates, cats, and particularly rats have limited cortical development compared with that of humans, these animal species may be especially lacking in the cortical contributions to the P300 and therefore may not provide an

entirely complete model of human ERPs.

Despite these caveats, researchers have begun to utilize animal ERP models in studies evaluating the possible neurotransmitter systems that may contribute to the generation of these potentials. Reductions in dopamine, via lesions to the ventral tegmental area, have thus far not been found to affect ERP amplitudes and latencies. However, successful recordings of ERPs have not been made in dopamine target areas, such as the nucleus accumbens, which are undoubtedly affected by such lesions and may have more relevance to the "rewarding" aspects of alcohol consumption. Depletions of other amines, such as serotonin and NE,

have been shown to have effects on ERP recordings. PCPA-induced reductions in serotonin have been found to cause reductions in the amplitude of the N1 component of the rat ERP. This finding is of particular interest since P rats have been consistently shown to have inherent reductions of serotonin in several brain sites and also display decreased N1 amplitudes.

Several neurotransmitter candidates have been proposed as contributors to the P3 potential. In lesion studies in both monkeys and rats, reductions in NE have been demonstrated to be associated with reductions in P3 amplitude. This finding may have relevance to alcohol research because changes in noradrenergic tone have been described in alcoholics, particularly during withdrawal. Thus, the lowered P3 amplitudes observed in alcoholics could be theoretically linked to altered NE levels. Finally, recent studies have focused on a role for the glutamate-NMDA receptor complex as playing a role in alcohol intoxication. Investigations in rat models have shown that profound reductions in the P3 can be observed following administration of the nonspecific NMDA receptor antagonist, MK-801. However, further studies will be necessary to link these findings to ethanol use and abuse in humans.

While studies in animals are promising, several unanswered questions remain concerning brain mechanisms underlying animal ERPs and their relationship to alcoholism and the risk for alcohol abuse.

More basic studies will be needed in this area to address these questions. For instance, ERPs need to be recorded in many more cortical and subcortical regions in monkeys and cats to verify work in the rat. More studies also are needed using genetic models in which animals have been selected for differences in alcohol consumption and/or differential response to ethanol. In addition, other neurotransmitter systems known to be related to alcohol abuse need to be studied.

A limitation of most of the studies conducted in animal models is that the ERPs were collected under conditions in which the stimuli were passively presented and the subjects were not required to respond to the stimuli. Further studies are necessary where ERPs are collected under conditions in which the animal subjects are required to respond to behaviorally relevant ERP-producing stimuli. One type of study that might be particularly interesting would be the recording of ERPs while animals are operantly responding for alcohol availability. Such studies would thus provide the opportunity to link behaviorally relevant stimuli to the recording of these potentials.

ACKNOWLEDGMENTS

The author recognizes the help of Ms. Susan Lopez in data analysis and reduction. These studies were supported by National Institute on Alcohol Abuse and Alcoholism grants AA00098 and AA06059 to Cindy L. Ehlers and AA04620 to

Floyd E. Bloom, and GCRC grant 00833 to The Scripps Research Institute.

REFERENCES

- Arthur, D.L., and Starr, A. Task-relevant late positive component of the auditory event-related potential in monkeys resembles the P300 in humans. *Science* 223:186–188, 1984.
- Begleiter, H., and Coltrera, M. Evoked potential changes during ethanol withdrawal in rats. *Am J Drug Alcohol Abuse* 2:263–268, 1975.
- Begleiter, H.; DeNoble, V.; and Porjesz, B. Protracted brain dysfunction after alcohol withdrawal in monkeys. In: Begleiter, H., ed. *Biological Effects of Alcohol*. New York: Plenum Press, 1980a. pp. 231–250.
- Begleiter, H., and Platz, A. The effects of alcohol on the central nervous system in humans. In: Kissin, B., and Begleiter, H., eds. *The Biology of Alcoholism*. New York: Plenum Press, 1972. pp. 293–343.
- Begleiter, H., and Porjesz, B. Persistence of brain hyperexcitability following chronic alcohol exposure in rats. *Adv Exp Med Biol* 85B:209–222, 1977.
- Begleiter, H.; Porjesz, B.; Bihari, B.; and Kissin, B. Event-related brain potentials in boys at risk for alcoholism. *Science* 225:1493–1495, 1984.
- Begleiter, H.; Porjesz, B.; and Tenner, M. Neuroradiological and neurophysiological evidence of brain deficits in chronic alcoholics. *Acta Psychiatr Scand* 62(suppl 286):3–13, 1980b.
- Bierley, R.A.; Cannon, D.S.; Wehl, C.K.; and Dustman, R.E. Effects of alcohol on visually evoked responses in rats during addiction and withdrawal. *Pharmacol Biochem Behav* 12:909–915, 1980.
- Buchwald, J.S., and Huang, C.M. Far field acoustic response: Origins in the cat. *Science* 189:382–384, 1975.
- Buchwald, J.S., and Squires, N.S. Endogenous auditory potentials in the cat: A P300 model. In: Woody C., ed. *Conditioning: Representation of Involved Neural Function*. New York: Raven Press, 1982. pp. 503–515.
- Cadoret, R.J.; Cain, C.A.; and Grove, W.M. Development of alcoholism in adoptees raised apart from alcoholic biologic relatives. *Arch Gen Psychiatry* 37:561–563, 1980.
- Campbell, K.B., and Lowick, B.M. Ethanol and event-related potentials: The influence of distractor stimuli. *Alcohol* 4:257–263, 1987.
- Campbell, K.B.; Marois, R.; and Arcand, L. Ethanol and the event related potentials: Effects of rate of stimulus presentation and task difficulty. *Ann NY Acad Sci* 425:551–555, 1984.
- Chu, N.S.; Squires, K.C.; and Starr, A. Auditory brain stem potentials in chronic alcohol intoxication and alcohol withdrawal. *Arch Neurol* 35:596, 1978.
- Cloninger, C.R.; Bohman, M.; and Sigvardsson, S. Inheritance of alcohol abuse. *Arch Gen Psychiatry* 38:861–868, 1981.
- Cloninger, C.R.; Bohman, M.; Sigvardsson, S.; and Von Knorring, A.L. Psychopathology in adopted-out children of alcoholics. In: Galanter, M., ed. *Recent Developments in Alcoholism*. New York: Plenum Press, 1984. pp. 37–51.

- Cotton, N.S. The familial incidence of alcoholism: A review. *J Stud Alcohol* 40:89–116, 1979.
- Courchesne, E. Neurophysiological correlates of cognitive development: Changes in long-latency event-related potentials from childhood to adulthood. *Electroencephalogr Clin Neurophysiol* 45:468–482, 1978a.
- Courchesne, E. Changes in P3 waves with event repetition: Long-term effects on scalp distribution and amplitude. *Electroencephalogr Clin Neurophysiol* 45:754–766, 1978b.
- Deitrich, R.A., and Spuhler, K. Genetics of alcoholism and alcohol actions. In: Smart, R.G.; Capell, H.D.; Glaser, F.B.; Israel, Y.; Kalant, H.; Popham, R.E.; Schmidt, W.; and Sellers, E.R., eds. *Research Advances in Alcohol and Drug Problems*. Vol. 8. New York: Plenum Press, 1984. pp. 47–98.
- Desmedt, J.E., and Debecker, J. Wave form and neural mechanism of the decision P350 elicited without pre-stimulus CNV or readiness potential in random sequences of near-threshold auditory clicks and finger stimuli. *Electroencephalogr Clin Neurophysiol* 47:648–670, 1979.
- Dolce, G., and Decker, H. The effects of ethanol on cortical and subcortical electrical activity in rats. *Res Commun Chem Pathol Pharmacol* 3:523–534, 1972.
- Donchin, E.; Karis, D.; Bashore, T.K.; Coles, M.G.H.; and Gratton, G. Cognitive psychophysiology and human information processing. In: Coles, M.G.H.; Donchin, R.; and Porges, S.W., eds. *Psychophysiology Systems, Processes, and Applications*. New York: Guilford Press, 1986. pp. 244–267.
- Donchin, E.; Ritter, W.; and McCallum, W.C. Cognitive psychophysiology: The endogenous components of the ERP. In: Callaway, E.; Tueting, P.; and Koslow, S.H., eds. *Event Related Brain Potentials in Man*. New York: Academic Press, 1978. pp. 349–411.
- Ehlers, C.L. ERP responses to ethanol and diazepam administration in squirrel monkeys. *Alcohol* 5:315–320, 1988.
- Ehlers, C.L. EEG and ERP responses to naloxone and ethanol in monkeys. *Prog Neuropsychopharmacol Biol Psychiatry* 13:217–228, 1989.
- Ehlers, C.L., and Chaplin, R.I. EEG and ERP response to chronic ethanol exposure in rats. *Psychopharmacology* 104:67–79, 1991.
- Ehlers, C.L.; Chaplin, R.I.; and Kaneko, W. MK-801 and ethanol, effects on the EEG and event related potentials (ERPs) in rats. *Neuropharmacology* 1991a, in press.
- Ehlers, C.L.; Chaplin, R.I.; and Koob, G.F. EEG effects of Ro 15-4513 and FG 7142 alone and in combination with ethanol. *Pharmacol Biochem Behav* 36:607–611, 1990.
- Ehlers, C.L.; Chaplin, R.I.; Lumeng, L.; and Li, T.K. Electrophysiological response to ethanol in P and NP rats. *Alcohol Clin Exp Res* 15(4):739–744, 1991b.
- Ehlers, C.L.; Chaplin, R.I.; Wall, T.L.; Lumeng, L.; Li, T.K.; Owens, M.S.; and Nemeroff, C.B. Corticotropin releasing factor (CRF): Studies in alcohol-preferring and non-preferring rats. *Psychopharmacology* 1991c, in press.
- Ehlers, C.L., and Reed, T.K. Ethanol effects on EEG spectra in monkeys: Comparison to morphine and diazepam. *Electroencephalogr Clin Neurophysiol* 66:317–321, 1987.

- Ehlers, C.L., and Schuckit, M.A. EEG response to ethanol in sons of alcoholics. *Psychopharmacol Bull* 24(3):434–437, 1988.
- Ehlers, C.L., and Schuckit, M.A. EEG fast frequency activity in the sons of alcoholics. *Biol Psychiatry* 27:631–641, 1990.
- Ehlers, C.L., and Schuckit, M.A. Evaluation of EEG alpha activity in sons of alcoholics. *Neuropsychopharmacology* 4(3):199–205, 1991.
- Ehlers, C.L.; Wall, T.L.; and Chaplin, R.I. Long latency event related potentials in rats: Effects of dopaminergic and serotonergic depletions. *Pharmacol Biochem Behav* 38:789–793, 1991d.
- Ehlers, C.L.; Wall, T.L.; and Chaplin, R.I. Auditory long-latency event related potentials in rats: Regional and neurochemical findings. *Soc Neurosci Abstr* 15:1239, 1989a.
- Ehlers, C.L.; Wall, T.L.; and Schuckit, M.A. EEG spectral characteristics following ethanol administration in young men. *Electroencephalogr Clin Neurophysiol* 73:179–187, 1989b.
- Elmasion, R.; Neville, H.; Woods, D.; Schuckit, M.; and Bloom, F.E. Event-related brain potentials are different in individuals at high and low risk for developing alcoholism. *Proc Natl Acad Sci USA* 79:4231–4233, 1982.
- Emmerson, R.Y.; Dustman, R.E.; Shearer, D.E.; and Chamberlain, H.M. EEG, visually evoked and event related potentials in young abstinent alcoholics. *Alcohol* 4:241–248, 1987.
- Eriksson, K. Genetic selection for voluntary alcohol consumption in the albino rat. *Science* 159:739–741, 1968.
- Gabrielli, W.F.; Nednick, S.A.; Volavka, J.; Pollock, B.E.; Schulsinger, F.; and Itil, T.M. Electroencephalograms in children of alcoholic fathers. *Psychophysiology* 19(4):404–407, 1982.
- Gentry, R.T.; Rappaport, M.S.; Ho, A.; Millard, W.J.; and Dole, V.P. Voluntary consumption of ethanol and plasma ethanol concentration in C57BL/6J mice. *Alcohol Clin Exp Res* 7:110, 1983.
- Glover, A.A.; Onofrij, M.C.; Ghilardi, M.F.; and Bodis-Wollner, I. P300-like potentials in the normal monkey using classical conditioning and an auditory "oddball" paradigm. *Electroencephalogr Clin Neurophysiol* 65:231–235, 1986.
- Goff, E.R.; Allison, T.; and Vaughn Jr., H.G. The functional neuroanatomy of event-related potentials. In: Tueting, E.P., and Koslow, S.H., eds. *Event-Related Potentials in Man*. New York: Academic Press, 1978. pp. 1–79.
- Goldberg, M.E.; Salama, A.I.; Patel, J.B.; and Malick, J.B. Novel non-benzodiazepine anxiolytics. *Neuropharmacology* 22:1499–1504, 1983.
- Gonzales, R.A., and Hoffman, P.L. Receptor-gated ion channels may be selective CNS targets for ethanol. *TIPS* 12:1–3, 1991.
- Goodwin, D.W.; Schulsinger, F.; Moller, N.; Hermansen, L.; Winokur, G.; and Guze, S. Drinking problems in adopted and non-adopted sons of alcoholics. *Arch Gen Psychiatry* 31:164–169, 1974.
- Goodwin, D.W. Alcoholism and genetics. *Arch Gen Psychiatry* 42:171–174, 1985.
- Grant, K.A.; Valverius, P.; Hudspith, M.; and Tabakoff, B. Ethanol withdrawal seizures and the NMDA receptor complex. *Eur J Pharmacol* 176:289–296, 1990.

- Halgren, E.; Squires, N.K.; Wilson, C.L.; Rohrbaugh, J.W.; Babb, T.L.; and Crandall, P.H. Endogenous potentials generated in the human hippocampal formation and amygdala by infrequent events. *Science* 210:803–805, 1980.
- Harrison, J.; Buchwald, J.; and Kaga, K. Cat P300 present after primary cortex ablation. *Electroencephalogr Clin Neurophysiol* 63:180–187, 1986.
- Harrison, J.; Buchwald, J.; Kaga, K.; Woolf, N.J.; and Bucher, L. Cat P300 disappears after septal lesions. *Electroencephalogr Clin Neurophysiol* 69:55–64, 1988.
- Hillyard, S.A., and Kutas, M. Electrophysiology of cognitive processing. *Ann Rev Psychol* 34:32–61, 1983.
- Hoffman, P.L.; Moses, F.; and Tabakoff, B. Selective inhibition by ethanol of glutamate-stimulated cyclic GMP production in primary cultures of cerebella granule cells. *Neuropharmacology* 28:1239–1243, 1989a.
- Hoffman, P.L.; Rabe, C.S.; Moses, F.; and Tabakoff, B. N-methyl-D-aspartate receptors and ethanol: Inhibition of calcium flux and cyclic GMP production. *J Neurochem* 52:1927–1940, 1989b.
- Hoffman, P.L.; Rabe, C.S.; Grant, K.A.; Valverius, P.; Hudspith, M.; and Tabakoff, B. Ethanol and the NMDA receptor. *Alcohol* 7:229–231, 1990.
- Hurlbut, B.J.; Jubar, J.F.; and Satterfield, S.M. Auditory elicitation of the P300 event-related potential in the rat. *Physiol Behav* 39:483–487, 1987.
- Knight, R.T.; Scabin, P.; Woods, D.L.; and Clayworth, C.C. Contributions of temporal-parietal junction to the human auditory P3. *Brain Res* 502:109–116, 1989.
- Kopell, B.S.; Roth, W.T.; and Tinglenberg, J.R. Time-course effects of marijuana and ethanol on event-related potentials. *Psychopharmacology (Berl)* 56:15–20, 1978.
- Li, T.K.; Lumeng, L.; McBride, W.J.; Waller, M.B.; and Hawkins, T.D. Progress toward a voluntary oral consumption model of alcoholism. *Drug Alcohol Depend* 4:45–60, 1979.
- Li, T.K.; Lumeng, L.; McBride, W.J.; and Waller, M.B. Indiana selection studies on alcohol related behaviors. In: McClearn, C.E.; Deitrich, R.A.; and Erwin, V.G., eds. *Development of Animal Models as Pharmacogenetic Tools*. NIAAA Research Monograph 6. DHHS Pub. No. (ADM)81-1133. Washington, DC: Supt. of Docs., U.S. Govt. Print. Off., 1981, pp. 171–192.
- Lima-Landman, M.T.R., and Albuquerque, E.X. Ethanol potentiates and blocks NMDA-activated single channel currents in rat hippocampal pyramidal cells. *FEBS Lett* 247:61–67, 1989.
- Lovinger, D.M.; White, G.; and Weight, F.F. Ethanol inhibits NMDA-activated ion current in hippocampal neurons. *Science* 243:1721–1724, 1989.
- Lumeng, L.; Hawkins, T.D.; and Li, T.K. New strains of rats with alcohol preference and nonpreference. In: Thurman, R.G.; Williamson, J.R.; Drott, H.R.; and Chance, B., eds. *Alcohol and Aldehyde Metabolizing Systems*. Vol. 3. New York: Academic Press, 1977. pp. 537–544.
- Lumeng, L.; Waller, M.B.; McBride, W.J.; and Li, T.K. Different sensitivities to ethanol in alcohol-preferring and non-preferring rats. *Pharmacol Biochem Behav* 16:125–130, 1982.

- Lynch, G., and Baudry, M. The biochemistry of memory: A new and specific hypothesis. *Science* 224:1057–1063, 1984.
- McBride, W.J.; Murphy, J.M.; Lumeng, L.; and Li, T.K. Serotonin, dopamine and GABA involvement in alcohol drinking of selectively bred rats. *Alcohol* 7:199–205, 1990.
- McCarthy, G.; Wood, C.C.; Allison, T.; Goff, W.R.; Williamson, P.D.; and Spencer, D.D. Intercranial recordings of event-related potentials in humans engaged in cognitive tasks. *Soc Neurosci Abstr* 8:976, 1982.
- McLamb, R.L.; Williams, L.R.; Nanry, K.P.; Wilson, W.A.; and Tilson, H.A. MK-801 impedes the acquisition of a spatial memory task in rats. *Pharmacol Biochem Behav* 37:41–45, 1990.
- Morrisett, R.A.; Rezvani, A.H.; Overstreet, D.; Janowsky, D.S.; Wilson, W.A.; and Swartzwelder, H.S. MK-801 potently inhibits alcohol withdrawal seizures in rats. *Eur J Pharmacol* 176:103–105, 1989.
- Morazorati, S.; Lamishaw, B.; Lumeng, L.; Li, T.K.; Bemis, K.; and Clemens, J. Effect of low dose ethanol on the EEG of alcohol-preferring and -nonpreferring rats. *Brain Res Bull* 21:101–104, 1988.
- Murphy, J.M.; Gatto, G.J.; McBride, W.J.; Lumeng, L.; and Li, T.K. Operant responding for oral ethanol in the alcohol-preferring (P) and alcohol-nonpreferring (NP) lines of rats. *Alcohol* 6:127–131, 1989.
- Murphy, J.M.; McBride, W.J.; Lumeng, L.; and Li, T.K. Regional brain levels of monoamines in alcohol-preferring and -nonpreferring lines of rats. *Pharmacol Biochem Behav* 16:145–149, 1982.
- Murphy, J.M.; McBride, W.J.; Lumeng, L.; and Li, T.K. Contents of monoamines in forebrain regions of alcohol-preferring (P) and -nonpreferring (NP) lines of rats. *Pharmacol Biochem Behav* 26:389–392, 1987.
- Naranjo, C.A.; Sellers, E.M.; and Lawrin, M.O. Modulation of ethanol intake by serotonin uptake inhibitors. *J Clin Psychiatry* 47(suppl):16–22, 1986.
- Neville, H.J., and Foote, S.L. Auditory event-related potentials in the squirrel monkey: Parallels to human late wave responses. *Brain Res* 298:107–116, 1984.
- Nutt, D., and Glue, P. Monoamines and alcohol. *Br J Addict* 81:327–338, 1986.
- O'Brien, J.H. P300 wave elicited by a stimulus-change paradigm in acutely prepared rats. *Physiol Behav* 28:711–713, 1982.
- O'Connor, S.; Hesselbrock, V.; and Tasman, A. Correlates of increased risk for alcoholism in young men. *Prog Neuropsychopharmacol Biol Psychiatry* 10:211–218, 1986.
- O'Connor, S.; Hesselbrock, V.; Tasman, A.; and DePalma, N. P3 amplitudes in two distinct tasks are decreased in young men with a history of paternal alcoholism. *Alcohol* 4:323–330, 1987.
- Paller, K.A.; Zola-Morgan, S.; Squire, L.R.; and Hillyard, S.A. P3-like brain waves in normal monkeys and monkeys with medial temporal lesions. *Behav Neurosci* 1991, in press.
- Patterson, B.W.; Williams, H.L.; McLean, G.A.; Smith, L.T.; and Schaeffer, K.W. Alcoholism and family history of alcoholism. Effects on visual and auditory event-related potentials. *Alcohol* 4:265–274, 1987.

- Penn, P.E.; McBride, W.J.; Lumeng, L.; Gaff, T.M.; and Li, T.K. Neurochemical and operant behavioral studies of a strain of alcohol-preferring rats. *Pharmacol Behav* 8:475–481, 1978.
- Pfefferbaum, A.; Horvath, T.B.; and Roth, W.T. Event related potentials changes in chronic alcoholics. *Electroencephalogr Clin Neurophysiol* 47:637–647, 1979.
- Pfefferbaum, A.; Horvath, T.B.; Roth, W.T.; Clifford, S.T.; and Kopell, B.S. Acute and chronic effects of ethanol on event-related potentials. In: Begleiter, H., ed. *Biological Effects of Alcohol*. New York: Plenum Press, 1980. pp. 625–640.
- Pfefferbaum, A.; Rosenbloom, M.; and Ford, J.M. Late event-related potential changes in alcoholism. *Alcohol* 4:275–281, 1987.
- Pineda, J.A.; Foote, S.L.; and Neville, H.J. Long-latency event-related potentials in squirrel monkeys: Further characterization of waveform morphology, topography, and functional properties. *Electroencephalogr Clin Neurophysiol* 67:77–90, 1987.
- Pineda, J.A.; Foote, S.L.; and Neville, H.J. Effects of locus coeruleus lesions on auditory, long-latency, event-related potentials in monkeys. *J Neurosci* 9(1):81–89, 1989.
- Polich, J. Comparison of P300 from a passive tone sequence paradigm and an active discrimination task. *Psychophysiology* 24(1):41–46, 1987a.
- Polich, J. Task difficulty, probability, and inter-stimulus interval as determinants of P300 from auditory stimuli. *Electroencephalogr Clin Neurophysiol* 68:311–320, 1987b.
- Polich, J. Frequency, intensity, and duration as determinants of P300 from auditory stimuli. *J Clin Neurophysiol* 6(3):277–286, 1989.
- Polich, J., and Bloom, F.E. P300 and alcohol consumption in normals and individuals at risk for alcoholism. A preliminary report. *Prog Neuropsychopharmacol Biol Psychiatry* 10:201–210, 1986.
- Polich, J., and Bloom, F.E. P300 from normals and adult children of alcoholics. *Alcohol* 4:301–305, 1987.
- Polich, J., and Donchin, E. P300 and the work frequency effect. *Electroencephalogr Clin Neurophysiol* 70:33–45, 1988.
- Polich, J.; Ehlers, C.L.; Otis, S.; Mandell, A.J.; and Bloom, F.E. P300 reflects the degree of cognitive decline in dementing illness. *Electroencephalogr Clin Neurophysiol* 63:138–144, 1986.
- Pollock, M.A.; Volvaka, J.; Goodwin, D.W.; Mednick, S.A.; Gabrielli, W.F.; Knop, J.; and Schulsinger, F. The EEG after alcohol administration in men at risk for alcoholism. *Arch Gen Psychiatry* 40:847–861, 1983.
- Porjesz, B., and Begleiter, H. Human evoked brain potentials and alcohol. *Alcohol Clin Exp Res* 5:304–317, 1981.
- Porjesz, B., and Begleiter, H. Human brain electrophysiology and alcoholism. In: Tarter, R.E., and Van Thiel, D.H., eds. *Alcohol and the Brain: Chronic Effects*. New York: Plenum Press, 1985a. pp. 139–180.
- Porjesz, B., and Begleiter, H. Event related brain potentials to high incentive stimuli in abstinent alcoholics. *Alcohol Clin Exp Res* 9:190, 1985b.
- Porjesz, B.; Begleiter, H.; and Garozzo, R. Visual evoked potentials correlates of

- information processing deficits in chronic alcoholics. In: Begleiter, H., ed. *Biological Effects of Alcohol*. New York: Plenum Press, 1980. pp. 603–623.
- Porjesz, B.; Begleiter, H.; and Horowitz, S. Brain excitability subsequent to alcohol withdrawal in rats. In: Ford, D.H., and Clouet, D.H. eds. *Tissue Responses to Addictive Substances*. New York: Spectrum, 1976. pp. 461–469.
- Rabe, C.S., and Tabakoff, B. Glycine site-directed agonists reverse the actions of ethanol at the N-methyl-D-aspartate receptor. *Mol Pharmacol* 38:753–757, 1990.
- Rhodes, L.E.; Obitz, F.W.; and Creel, D. Effect of alcohol and task on hemispheric asymmetry of visual evoked potentials in man. *Electroencephalogr Clin Neurophysiol* 38:561–568, 1975.
- Riley, J.N., and Walker, D.W. Morphological alterations in hippocampus after long-term alcohol consumption in mice. *Science* 201:711–713, 1978.
- Roth, W.T. Auditory evoked responses to unpredictable stimuli. *Psychophysiology* 10:125–137, 1973.
- Roth, W.T.; Tinklenberg, J.R.; and Kopell, B.S. Ethanol and marijuana effects on event related potentials in a memory retrieval paradigm. *Electroencephalogr Clin Neurophysiol* 42:381–388, 1977.
- Rutter, M. Meyerian psychobiology, personality development and the role of life experiences. *Psychiatry* 143:1077–1087, 1986.
- Schuckit, M.A. Subjective responses to alcohol in sons of alcoholics and control subjects. *Arch Gen Psychiatry* 41:879–884, 1984.
- Schuckit, M.A. Genetics and the risk for alcoholism. *JAMA* 254:2614–2617, 1985.
- Schuckit, M.A. Alcoholism and affective disorders: Genetic and clinical implications. *Am J Psychiatry* 143:140–147, 1986.
- Schuckit, M.A.; Gold, E.R.; and Risch, S.C. A simultaneous evaluation of multiple markers of ethanol/placebo challenges in sons of alcoholics and controls. *Arch Gen Psychiatry* 44:942–945, 1988.
- Shrinivas, K.K., and Ticku, M.K. Interaction between GABAergic anticonvulsants and the NMDA receptor antagonist MK-801 against MES- and picrotoxin-induced convulsions in rats. *Life Sci* 44:1317–1323, 1989.
- Squires, N.K.; Squires, K.C.; and Hillyard, S.A. Two varieties of long-latency positive waves evoked by unpredictable auditory stimuli in man. *Electroencephalogr Clin Neurophysiol* 38:387–401, 1975.
- Stockard, J.J., and Rossiter, V.S. Clinical and pathologic correlates of brainstem auditory response abnormalities. *Neurology* 27:316–325, 1977.
- Sutton, S.; Braren, M.; Zubin, J.; and John, E.R. Evoked-potential correlates of stimulus uncertainty. *Science* 150:1187–1188, 1965.
- Walker, D.W.; Barnes, D.E.; and Zornetzer, S.F. Neuronal loss in hippocampus induced by prolonged ethanol consumption in rat. *Science* 209:711–713, 1980.
- Walker, D.W.; Hunter, B.E.; and Abraham, W.C. Neuroanatomical and functional deficits subsequent to chronic ethanol administration in animals. *Alcohol Clin Exp Res* 5:267–282, 1981.

Waller, M.B.; McBride, W.J.; Lumeng, L.; and Li, T.K. Induction of dependence on ethanol by free-choice drinking in alcohol-preferring rats. *Pharmacol Biochem Behav* 16:501–507, 1982.

Waller, M.B.; McBride, W.J.; Lumeng, L.; and Li, T.K. Initial sensitivity and acute tolerance to ethanol in the P and NP lines of rats. *Pharmacol Biochem Behav* 19:683–686, 1983.

Waller, M.B.; McBride, W.J.; Gatto, G.T.; Lumeng, L.; and Li, T.K. Intragastric self-infusion by ethanol-preferring and nonpreferring lines of rats. *Science* 225:78–80, 1984.

Whishaw, I.Q., and Auer, R.N. Immediate and long-lasting effects of MK-801 on motor activity, spatial navigation in a swimming pool and EEG in the rat. *Psychopharmacology* 98:500–507, 1989.

Wilson, W.R.; Boxy, T.Z.; and Ruth, J.A. NMDA agonists and antagonists alter

the hypnotic response to ethanol in LS and SS mice. *Alcohol* 7:389–395, 1990.

Wolf, D.L.; Young, G.A.; and Khazan, N. Comparison between ethanol-induced and slow-wave sleep synchronous EEG activity utilizing spectral analysis. *Neuropharmacology* 20:687–692, 1981.

Wood, C.C.; Allison, T.; Goff, W.R.; Williamson, P.D.; and Spencer, D.D. On the neural origin of P300 in man. *Prog Brain Res* 54:51–56, 1980.

Wozniak, D.F.; Olney, J.W.; Kettinger III, L.; Price, M.; and Miller, J.P. Behavioral effects of MK-801 in the rat. *Psychopharmacology* 101:47–56, 1990.

Young, G.A.; Wolf, D.L.; and Khazan, N. Relationships between blood ethanol levels and ethanol-induced changes in cortical EEG power spectra in the rat. *Neuropharmacology* 21:721–723, 1982.

BRAIN ELECTRICAL ACTIVITY: THE PROMISE OF NEW TECHNOLOGIES

George Fein, Ph.D.¹ Jonathan Raz, Ph.D.² and Bruce Turetsky, M.D.³

Brain electrical potentials recorded from scalp electrodes represent two separable phenomena: event-related potentials (ERP) and the on-going electroencephalogram (EEG). The study of ERP involves measurement of the brain's response to sensory or cognitive events. One can present physical stimuli and record the brain response to the sensory events, or one can record brain activity associated with the performance of purely cognitive operations. The missing-stimulus paradigm, in which an evoked potential recorded occurs in response to an unexpectedly absent stimulus, provides the clearest illustration that cognitive evoked potentials are not the direct consequences of sensory stimuli. Evoked potentials, which are time-locked to eliciting stimuli or to specific cognitive processes, are embedded in the ongoing EEG. The EEG is not time-locked to specific events. The background EEG, on the other

hand, reflects the level of activation of various brain regions.

The strengths of brain electrical activity recording that make it well suited to the study of neuropsychiatric phenomena are these:

- It is totally noninvasive.
- It has a millisecond resolution in the time domain.
- It is highly sensitive to information-processing operations.
- It has been shown via twin studies (e.g., Stassen et al. 1987) to have a

ACRONYMS

CSD	<i>current source density</i>
DCM	<i>dipole components model</i>
EEG	<i>electroencephalogram</i>
ERP	<i>event-related potentials</i>
MASE	<i>mean average square error</i>
SDM	<i>spatial dipole model</i>
SNR	<i>signal-to-noise ratio</i>
STDM	<i>spatiotemporal dipole model</i>

¹Department of Psychiatry, University of California, San Francisco, San Francisco, CA 94121

²Department of Biostatistics, School of Public Health, University of Michigan, Ann Arbor, MI 48109

³Department of Psychiatry, University of Pennsylvania, Philadelphia, PA 19104

very strongly genetic determination.

Experiments can be performed with subjects performing a wide variety of tasks during data acquisition. Appropriate choice of tasks enables investigators to study sensory processing, memory, vigilance, affect, expectancy, divided attention, and other interesting psychological operations. The technology is also relatively inexpensive, and repeated measures designs are easily implemented.

However, there are a number of problems and limitations in the application of brain electrical activity measures to the study of brain-behavior relationships. It is our belief that many of these limitations reflect the current state of the technology and that new imaging technologies and/or biophysical/statistical models have great promise for moving the field beyond its current limitations. The major limitations are (1) limited spatial resolution, (2) relatively simplistic brain models used in constructing images from EEG and ERP data, (3) less than optimal ability to partition activity from concurrently active brain regions, and (4) sources of artifact (e.g., eye movements or subjects' difficulty in remaining still or paying attention to stimuli in cognitive experiments) that may be associated with subject-selection variables.

The study of brain electrical activity can help answer important questions regarding both the acute effects of alcohol and the long-term

effects of chronic alcohol abuse on brain function. Brain mechanisms that can be investigated are limited only by the ingenuity of the researcher; these include attention, perception, stimulus evaluation, memory, response preparation, response readiness, and response initiation. Also, given the very strong genetic determinants of brain electrical activity, one can compare populations at relatively high versus low risk for alcoholism. Electrophysiological indices of the brain mechanisms mentioned above may prove useful as candidate genetic marker variables. From another perspective, regional differences in the ongoing EEG suggest that differences in the level of activation of various brain systems may indicate genetic behavioral tendencies that may be important in alcoholism and related disorders.

A number of improvements in studies of the ongoing EEG and evoked potential may result from the development and application of more advanced topographic analyses of electrophysiological activity. This developing field is sometimes called "EEG brain imaging." Unfortunately, many popular EEG brain mapping systems use newly developed analytical techniques. Topographic analysis of the EEG holds the promise of (1) more definitive association of electrophysiological findings with specific brain regions, (2) improved partitioning of concurrent activity from multiple brain regions, and (3) improved ability to measure electrophysiological signals via higher signal-to-noise

ratios (SNR), which will result from spatial averaging of the signals across multiple recording sites. Higher SNR are very important because they result in smaller confidence intervals for parameters, increasing the statistical power of experiments, and because they allow for more ecologically valid paradigms via averaging responses to stimuli over fewer trials.

In the sections that follow, some exciting findings in EEG research that have potential application to the study of alcohol abuse and alcoholism will be reviewed. The promise of new and developing EEG data imaging and analytic procedures will also be discussed.

REFLECTING GENETIC BEHAVIORAL TENDENCIES BY BACKGROUND EEG TOPOGRAPHY

Richard Davidson and his colleagues (Davidson and Fox 1989) have reported their work on the association of asymmetries of background EEG activity with behavioral tendencies in adults and children. In their studies, they have not used the brain-imaging methods described here, but rather, have examined asymmetries of standard, common reference EEG recordings. In spite of the relative lack of topographic specificity of common reference recordings, their work has yielded intriguing results. From studies on adults, Henriques and Davidson (1990) reported that EEG alpha asymmetries can distinguish normal subjects from remitted de-

pressives. They found that in comparison to normothymic subjects without a history of depression, normothymic subjects with a history of depression have relatively decreased left- versus right-anterior activation and increased left- versus right-posterior activation, where relatively higher activation is indicated by relatively lower alpha activity. Their hypothesis is that there are deficits in an approach system such that individuals who are more vulnerable to negative affective states evidence decreased left-frontal activation. This EEG pattern is similar to that found in acutely depressed individuals, and it may be a state-independent marker for depression.

Davidson and Fox (1989) extended this work to the study of the association of EEG asymmetry to temperament in infants and very young children. They have found relatively decreased left-frontal activation in the subgroup of infants highly likely to cry when their mothers leave the room. Davidson and Fox interpret these results as suggesting that frontal EEG asymmetries are associated with different thresholds of reactivity to stressful events and different vulnerabilities to particular negative emotions. Following these results, Snidman and Kagan (1990) reported that these EEG asymmetries in infants predict ongoing temperamental traits, such as behavioral inhibition, that persist through childhood.

This work has used relatively crude methodology to measure

asymmetries and regional differences of the ongoing EEG, yet has yielded consistent results regarding the association between background EEG topography and temperamental traits. These studies suggest that the regional pattern of ongoing EEG alpha activity reflects the activation of very basic behavioral and emotional systems that subserve such general traits as approach/avoidance and the propensity for negative versus positive affective states. The application of more sensitive and specific technologies to determine the contribution of various hemispheric brain regions to the surface-recorded EEG will facilitate more precise measurements of the activation of the postulated underlying brain systems. Such developments may increase the power of this approach, eventually leading to the ability to make inferences for individuals, rather than being limited to inferences at the group level.

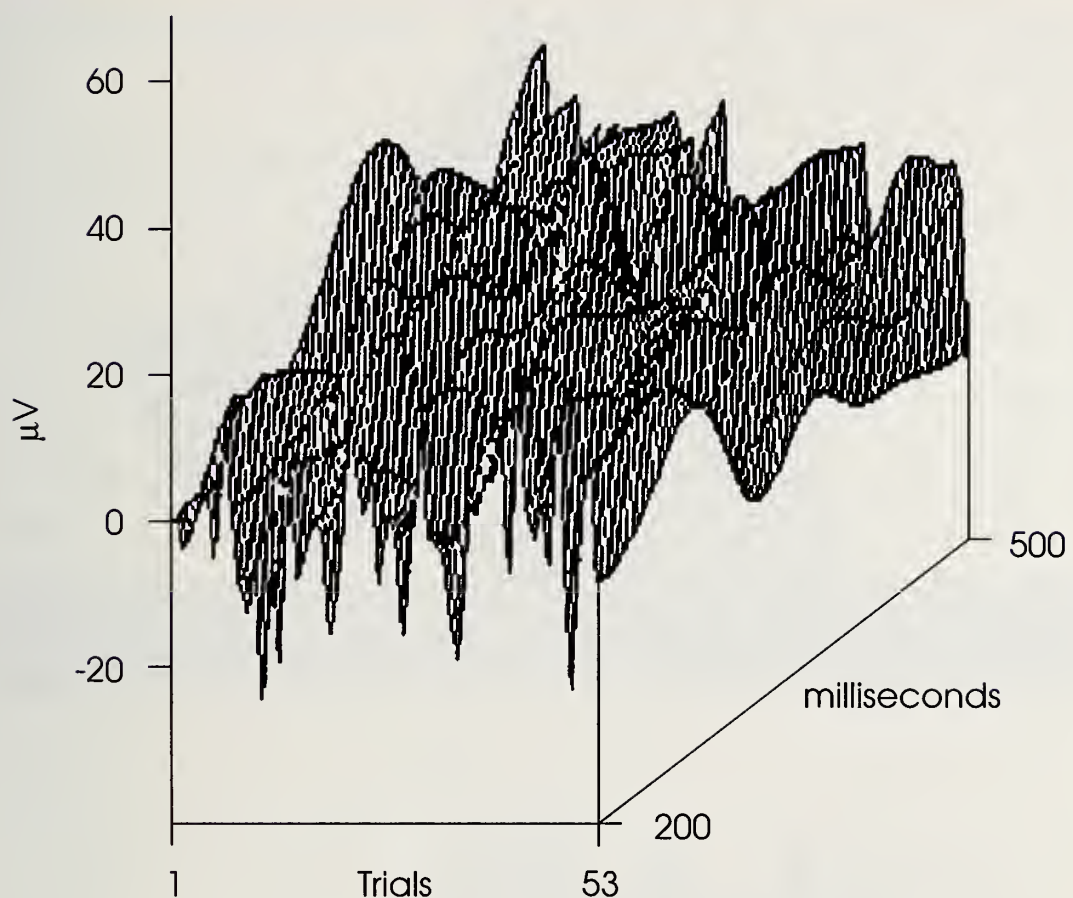
MEASURING HABITUATION OF THE EVOKED POTENTIAL SIGNAL

One of the central assumptions in evoked potential research is that brain responses to all stimuli are the same. This assumption of signal homogeneity underlies the averaging of responses to repetitive stimuli to increase the SNR of the evoked potential signal. The background EEG, which is the primary noise obscuring the evoked potential signal, has a variable time relationship to the stimuli and averages toward zero over the repeated

stimulus events. However, the assumption of signal homogeneity may be violated, for example, if habituation of the evoked potential signal occurs.

Our laboratory has developed statistical methods to test for signal heterogeneity (Raz and Fein 1991) and to estimate evoked potential signals that change slowly over trials (Turetsky et al. 1989; Raz et al. 1989; see also related work by Möcks and colleagues in 1984 and 1988). Figures 1 and 2 illustrate how these procedures can reveal habituation of the P3a response in two asymptomatic HIV-seropositive patients. We believe this technology can be very valuable in studying reduced P300 amplitude in dementia and in alcoholism. It can be used to determine whether the reduced P300 amplitude reflects (1) smaller P300 signals to all stimuli, (2) greater, (3) more rapid habituation of the P300 signal, or (4) a combination of these phenomena.

However, one of the major problems with this analytic technology is that it is SNR limited. For subjects with relatively low SNR, power is insufficient either to distinguish heterogeneous from homogeneous signals or to estimate the degree or pattern of signal heterogeneity. Integration of these methods with the dipole modeling procedures discussed below will likely increase our sensitivity in estimating signal heterogeneity. We believe that with the use of the multielectrode topographic pattern of scalp potentials to estimate the modeled dipole sources, the SNR of the

FIGURE 1a

Raw single-trial data for an asymptomatic HIV-infected subject recorded at Fz for the novel nontarget condition in a three-condition P300 experiment.

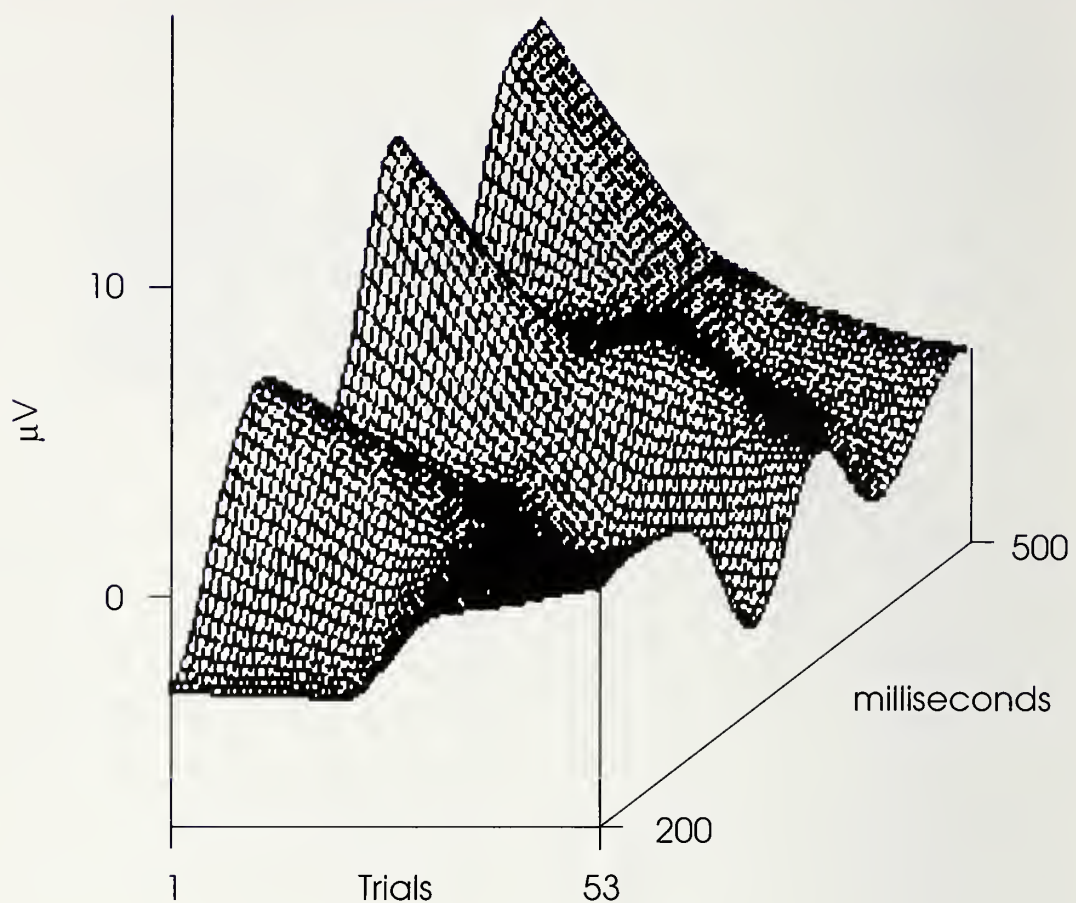
estimated dipole signals will be increased relative to the SNR of single electrode recordings. We will then be able to test for the presence and type of signal heterogeneity in the dipole magnitude function.

ASSESSING SENSORY SYSTEMS VIA HIGH REPETITION RATE STIMULATION

By increasing stimulus repetition rates, one can assess sensory systems during their relative refractory periods, wherein may emerge more

subtle deficits not apparent at low repetition rates. With stimulation during the relative refractory period, sensory evoked potential components show increased latency and decreased amplitude. These changes become greater with increasing repetition rates. Such rapid stimulation paradigms may provide more sensitive assessments of acute alcohol effects on sensory systems.

The utility of such paradigms has been limited: As repetition rates get high enough that their period is less than the duration of the primary sensory evoked potential compo-

FIGURE 1b

Smoothed single-trial data for an asymptomatic HIV-infected subject recorded at Fz for the novel nontarget condition in a three-condition P300 experiment. Data were smoothed using local linear regression and the smoothing span that minimized the estimated mean average square error (MASE; see Raz et al. 1989). The smoothed data reveal habituation of the ERP over trials.

nents, the evoked responses to consecutive stimuli overlap each other, precluding their reliable identification and measurement. Analysis of such data is a vexing problem; various approaches have been suggested for deconvolution of the overlapping responses (e.g., Brillinger 1978; Eysholdt and Schreiner 1982). Recently, Jewett and Silverberg (personal communication, June 1991) have developed such algorithms. In studies of the cat, in which they have

achieved excellent control over the recording environment and sources of noise, these investigators have recovered the response to single auditory stimuli at stimulation rates up to 500 Hz. However, these methods are also SNR limited. As discussed above with reference to signal heterogeneity estimation procedures in the previous section, the integration of these deconvolution algorithms with dipole modeling procedures has promise for increasing the effec-

tive SNR, thereby opening up new paradigms for the assessment of sensory system function.

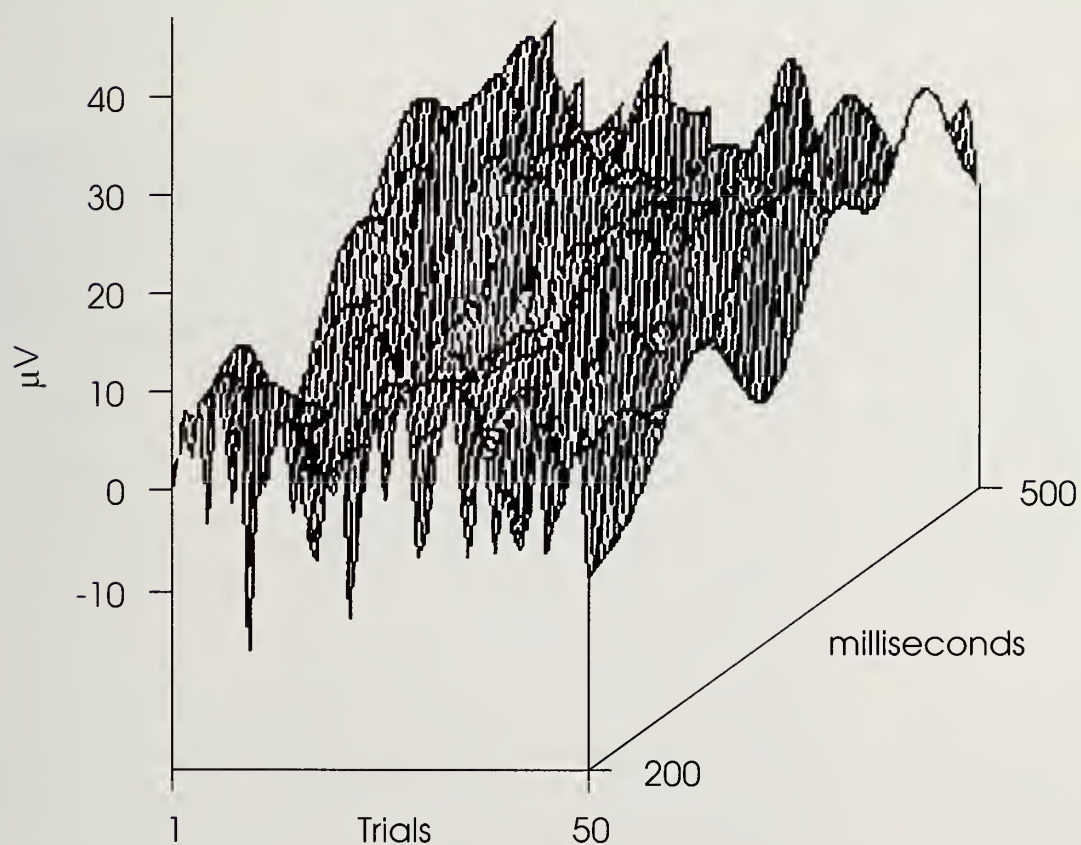
IMAGING BRAIN ELECTRICAL ACTIVITY

Interpolated Referential EEG or Evoked Potential Data

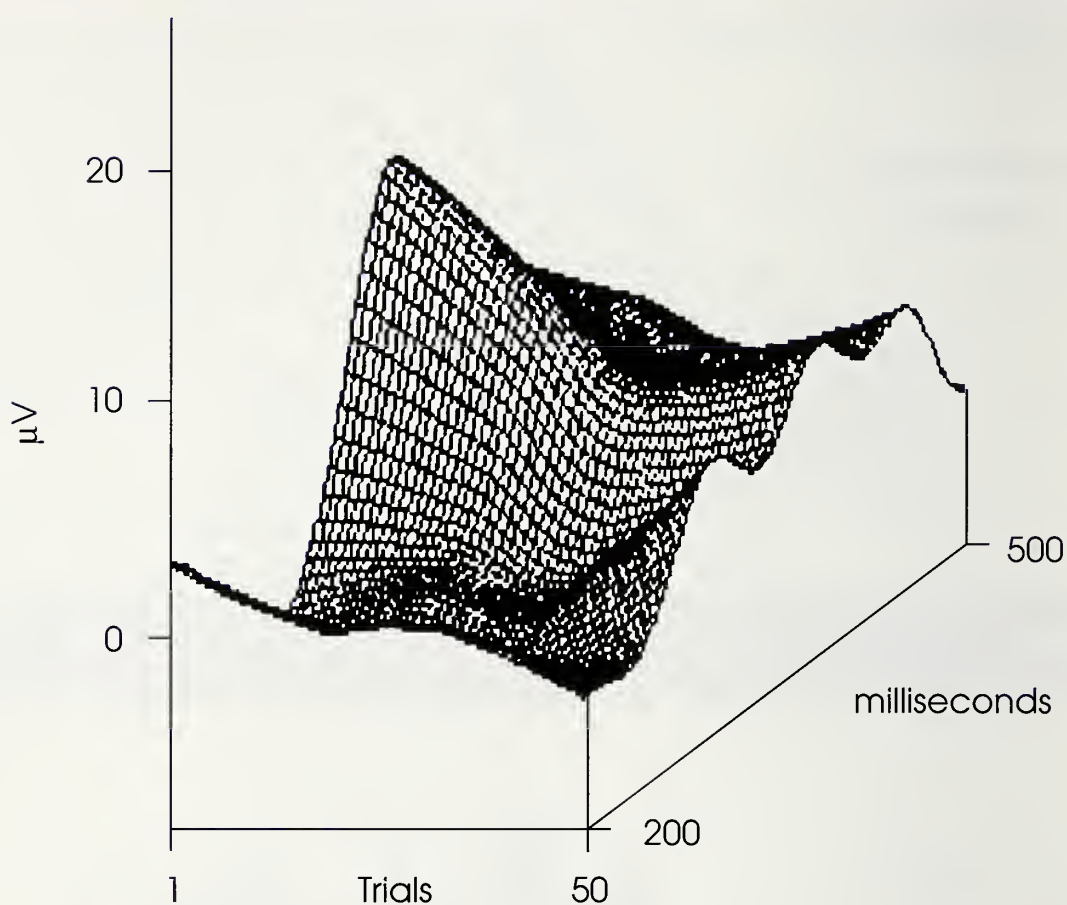
The simplest, or first, level of imaging involves interpolation and display of referential scalp recordings. The display can be either gray scale or color, on either a three-dimensional representation of the head or a two-dimen-

sional (axial or coronal) projection of the head. This type of brain electrical activity image is commercially available from any of a number of companies that advertise in psychophysiological and neuropsychiatric publications. On the surface, these brain-mapping methods appear to represent revolutionary developments in the analysis of brain electrical activity. However, closer examination reveals that they are primarily "window dressing" on the existing, relatively unsophisticated models of brain electrical activity and signal

FIGURE 2a



Raw single-trial data for another asymptomatic HIV-infected subject. As in figure 1, the data were recorded at Fz for the novel nontarget condition in a three-condition P300 experiment.

FIGURE 2b

Smoothed single-trial data for another asymptomatic HIV-infected subject. As in figure 1, the data were recorded at Fz for the novel nontarget condition in a three-condition P300 experiment, and the data were smoothed using local linear regression and the smoothing span that minimized the MASE. This subject's smoothed data also reveal habituation, but with a different ERP morphology over time.

estimation. Brain mapping neither reveals the location of underlying signal sources nor partitions the surface data in terms of those underlying sources.

Laplacian-Transformed EEG or Evoked Potential Data

The second level of brain electrical activity imaging involves estimation and imaging of the Laplacian or current source density (CSD) of the data. The CSD is a measure of

current density perpendicular to the scalp. Images of true CSD are reference free, displaying localized current sources and sinks attributable to appropriate underlying brain regions. Figures 3 and 4 (courtesy of Alan Gevins' EEG Systems Laboratory, San Francisco) illustrate one of the advantages of using Laplacian transformations in imaging regional sources of EEG potential data. The image of inter-

polated linked-ear-referenced data indicates relatively diffuse activation; the map of the same data after Laplacian transformation indicates much more focal activation.

Our laboratory has examined both methods for estimating CSD and the degree to which valid inferences regarding intracranial sources could be made on the basis of CSD-transformed data. We found significant problems regarding distorted topography with certain current approaches to CSD estimation, including spherical spline interpolation (Perrin et al. 1989). Using mathematical analysis and simulations, we have shown that spline interpolation induces artifactually inflated coherences among various brain sites (Biggins

et al. 1991). This problem occurs with any method of CSD estimation that assigns relatively high weights to data from relatively distant electrodes. We note that the Laplacians displayed in figures 3 and 4 (from Gevins' laboratory) were not computed using data from distant electrodes.

An important, if not primary, goal in almost all EEG and evoked potential research is the identification of the brain regions generating the signals. Hjorth and Rodin (1988) claimed that CSD data represent only the activity of superficial (i.e., cortical) generators, while the residual that results from subtracting CSD-transformed data from the original referential data represents only the activity of deep (i.e., subcortical) generators.

Jacobson and Newman (1990) applied that model to analysis of midlatency auditory evoked potentials and made inferences regarding the brain generators of the underlying components. We have recently shown that both the model and the inferences resulting from its application are incorrect (Turetsky and Fein 1991). The basic

FIGURE 3

51 CHANNELS



Interpolated scalp potentials, recorded using the linked-ears reference, reveal a relatively broad left frontocentral focus of activity.

problem is that, even with only superficial sources present, there is a substantial residual when CSD-transformed data are subtracted from referential recordings. Thus, the method leads to artificially high estimates of deep source activity, regardless of whether the sources are radially or tangentially oriented. This example of incorrect application of topographic analysis, together with the example of artifact introduced by spherical spline interpolation, illustrates the importance of careful scrutiny by physicists, engineers, and statisticians before widespread adoption of new methods.

We have used CSD transformations with great success in partitioning data from concurrently active sources. For example, we

examined the effects of the selective alpha-2 noradrenergic agonist clonidine and the alpha-2 antagonist yohimbine on auditory information processing. Our hypothesis was that these pharmacologic agents would have opposite effects on ERP measures associated with the evaluation of relevant signals, implicating norepinephrine in the modulation of such processes. In particular, we hypothesized that the more frontal subcomponent of the P300 (P3a, which denotes the cognitive equivalent of the orienting response to novel stimuli) would be especially affected by these manipulations. We recorded the EEG from a chain of nine equidistant electrodes overlying the midsagittal plane and used a two-dimensional CSD to distinguish the frontal P3a from the overlapping and often larger parietal P3b.

Figures 5 and 6 illustrate how, compared with ear-referenced data (figure 5), CSD transformation (figure 6) facilitates spatial separation of temporally overlapping components. The spatio-temporal contour plots show greater spatial res-

FIGURE 4

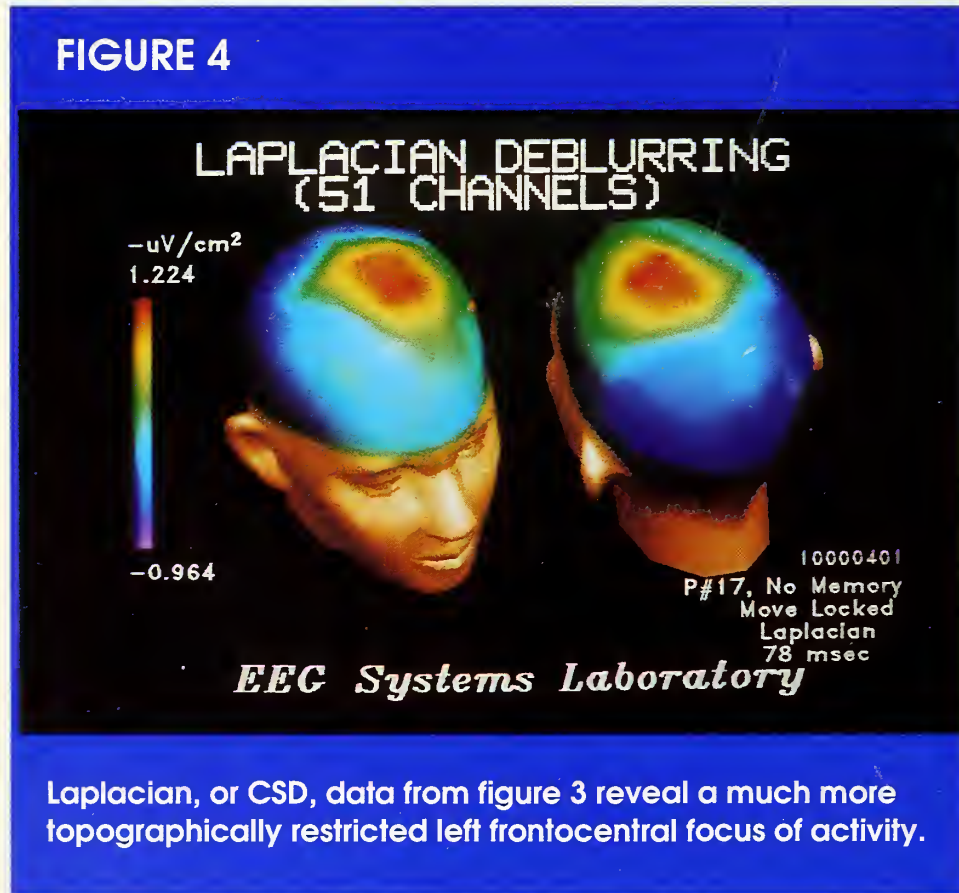
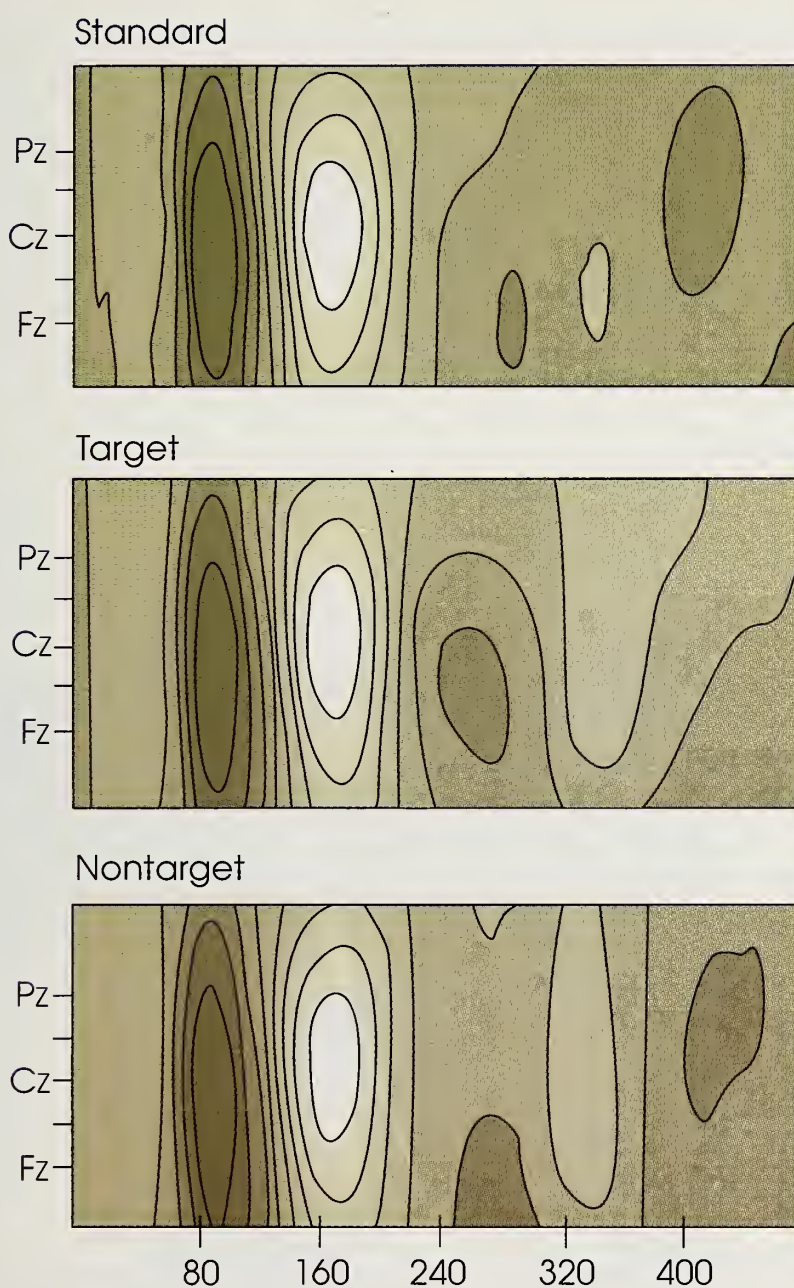
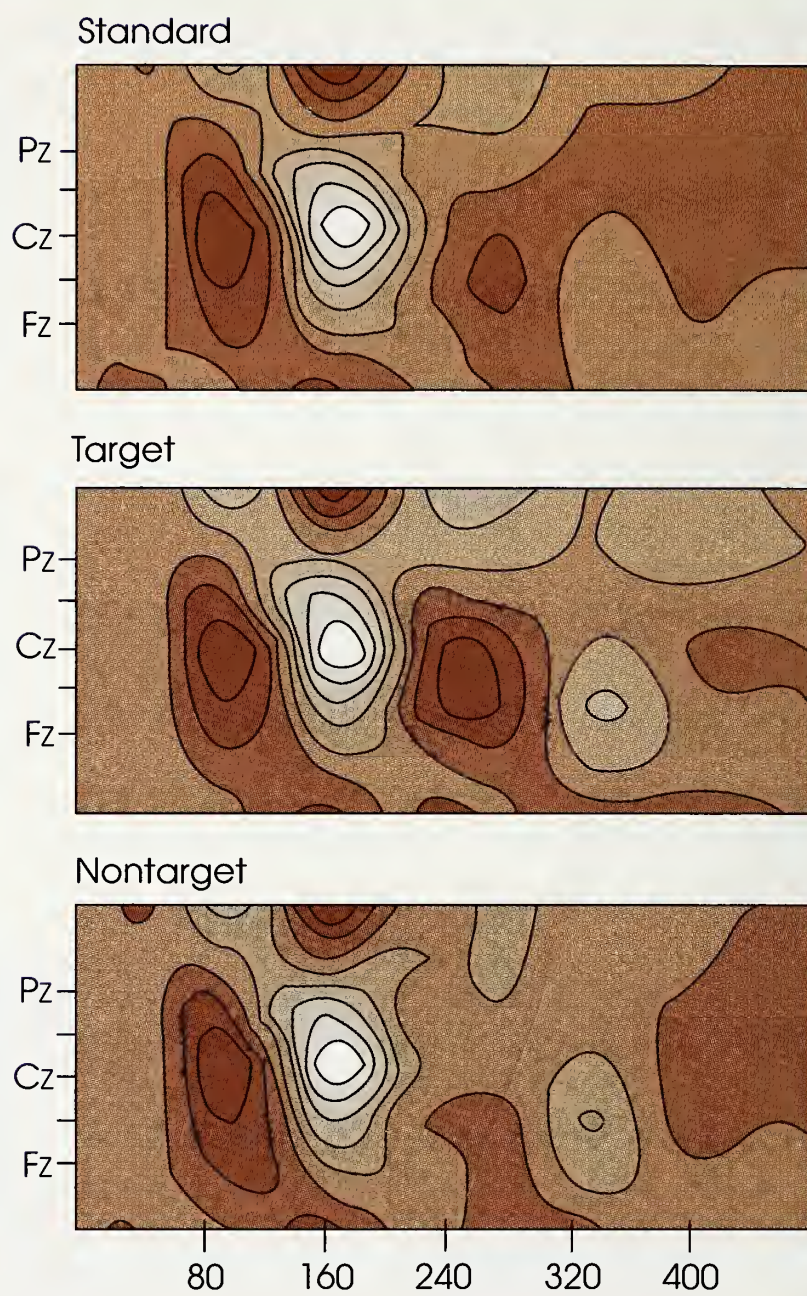


FIGURE 5

Each plot represents the ear-referenced electrical potentials at nine midline electrode sites, from stimulus onset to 480 milliseconds poststimulus. The x-axis represents time from stimulus onset; the y-axis represents the anterior-posterior scalp location. Shaded contour regions correspond to different electrical potentials, darker colors representing negative potentials and lighter colors representing positive potentials. This figure illustrates the relatively broad topographic distribution of the ear-referenced data.

olution of all components after CSD transformation. The N100-P200 complex, for example, appears as a sink-source configuration restricted to

the vicinity of the vertex, rather than broadly distributed across the midline. Similarly, the N250 component is depicted as a relatively lo-

FIGURE 6

Contour plots of the CSD of the data from figure 5 illustrate how the CSD transformation shows greater spatial resolution of components and facilitates spatial separation of temporally overlapping components.

calized frontocentral sink, with the posterior scalp showing some associated source activity.

At the time P300 activity would be expected, there is primarily a frontal source in the nontarget and standard conditions, with little pari-

etal activity; in the target condition, this frontal source is accompanied by a more prominent parietal-occipital source, which overlaps it temporally but is spatially distinct. The delineation of these two sources is less obvious in the ear-

referenced data. When the latencies and amplitudes of these two overlapping sources are disentangled in this way, their patterns of response to experimental effects and drugs are different, reinforcing the notion that these are neuroanatomically and functionally distinct subcomponents of the composite P300. In contrast to P3b latency, which was unaffected by either type of medication, P3a latency was reduced by yohimbine but not by clonidine. Similarly, neither drug affected P3b amplitude, but P3a amplitude was reduced with clonidine and increased with yohimbine.

Maps of Time-Varying Covariance Between Brain Regions

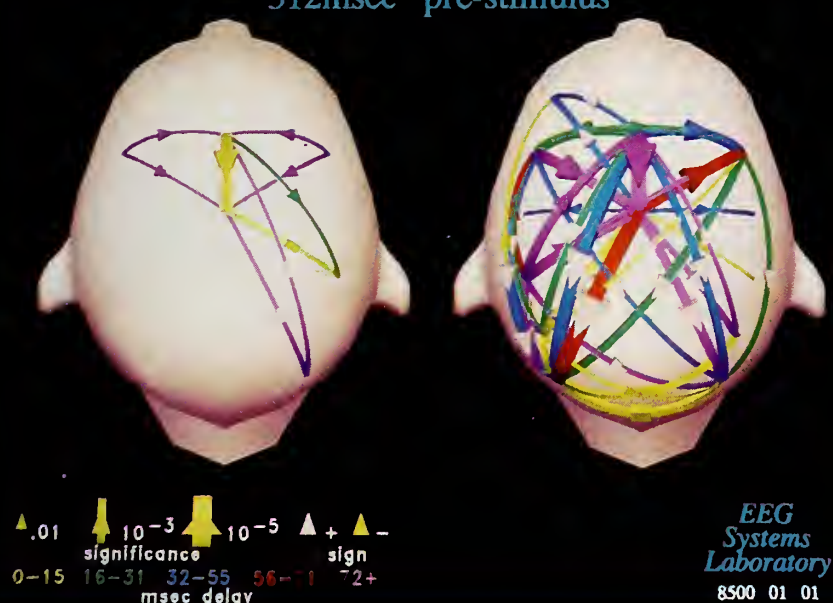
Gevins and colleagues (1987, 1989a,b) have developed intriguing methods for examining time-lagged covariances between Laplacian-transformed potential data recorded over various cortical areas. When studied during task performance, their results are interpreted as reflecting the activity of functional cortical networks. The application of this method to the study of memory load is illustrated in figures 7–9 (Gevins 1990).

The paradigm involved two conditions, in each of which subjects

saw sequential presentations of numeric stimuli. In the memory-load condition, subjects were asked to compare the current stimulus to that presented two stimuli earlier. They were to produce a pressure with the right index finger proportional to the numeric value of the stimulus seen two trials earlier or to inhibit their response if the current stimulus matched the one presented two trials earlier. In the no-memory-load condition, the subjects were to respond by producing

FIGURE 7

NO MEMORY MEMORY 312msec pre-stimulus

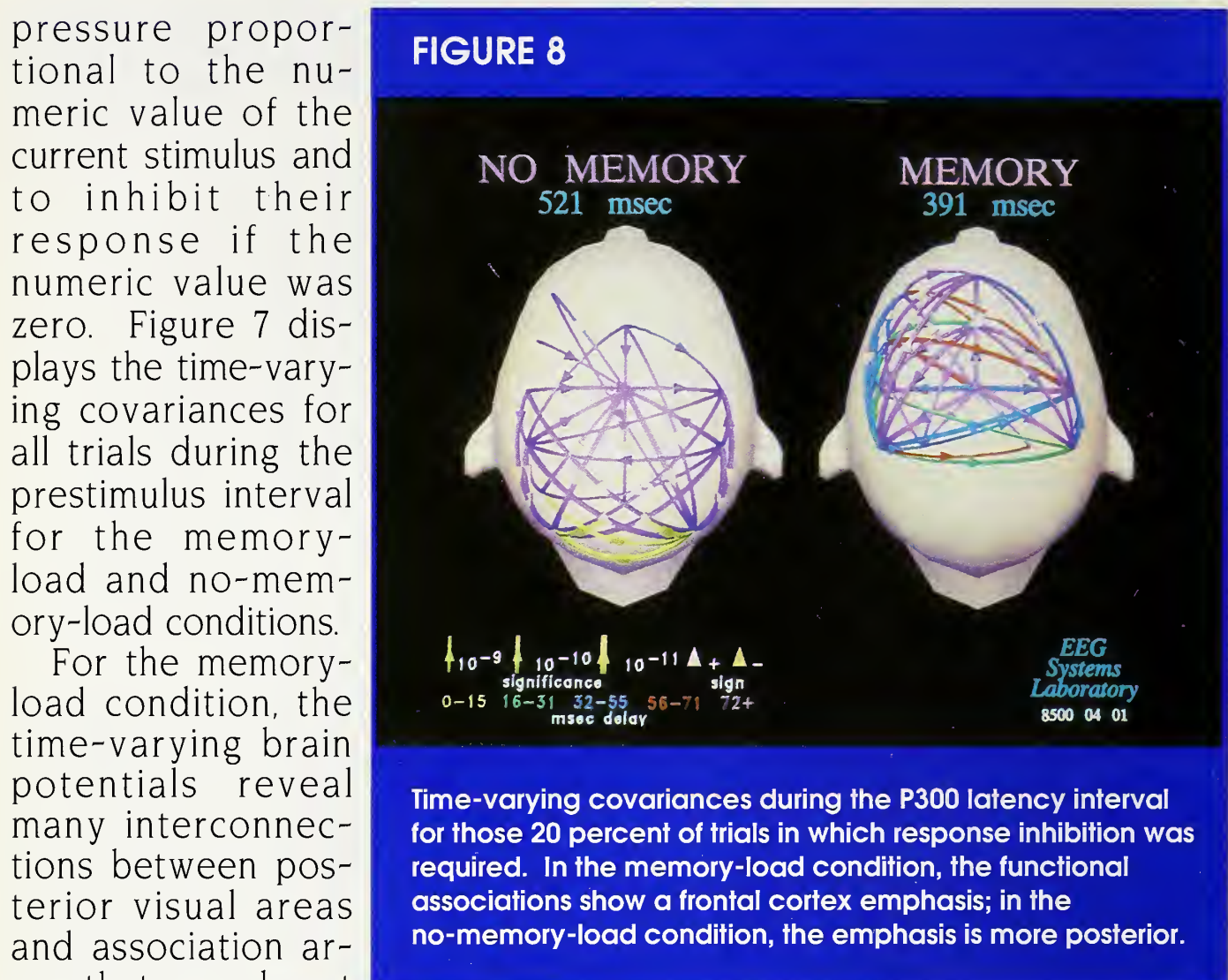


Time-varying covariances for all trials during the prestimulus interval for the memory-load and no-memory-load conditions. For the memory-load condition, time-varying brain potentials reveal many interconnections between posterior visual areas and association areas that are absent in the no-memory-load condition.

pressure proportional to the numeric value of the current stimulus and to inhibit their response if the numeric value was zero. Figure 7 displays the time-varying covariances for all trials during the prestimulus interval for the memory-load and no-memory-load conditions.

For the memory-load condition, the time-varying brain potentials reveal many interconnections between posterior visual areas and association areas that are absent in the no-memory-load condition. Figure 8 displays the time-varying covariances during the P300 latency interval for the 20 percent of trials in which response inhibition was required. In the memory-load condition, the functional associations show a frontal cortex emphasis; in the no-memory-load condition, the emphasis is more posterior.

Figure 9 displays the time-varying covariances during the motor potential and response after-potential time intervals. This figure illustrates that, during the intervals when subjects are responding, virtually no difference is apparent between the memory-load and no-memory-load conditions. Although



to date, the method has been applied primarily to waveforms averaged over subjects, it shows tremendous potential as a technology for studying the activation of brain networks as they function normally and in disease states and as they are affected by drugs and alcohol.

Modeling of Dipole Source Activity

Dipole source localization, in which the ERP is modeled as arising from multiple intracranial electrical dipole sources, has great promise as a method for partitioning ERP waveforms into subprocesses that are anatomically localized and biophysically plausible sources of

electrical activity. There is great excitement among researchers concerning the potential of dipole source localization, and a commercial package (the BESA system; Scherg 1989a) is available to perform dipole source analysis of ERP data.

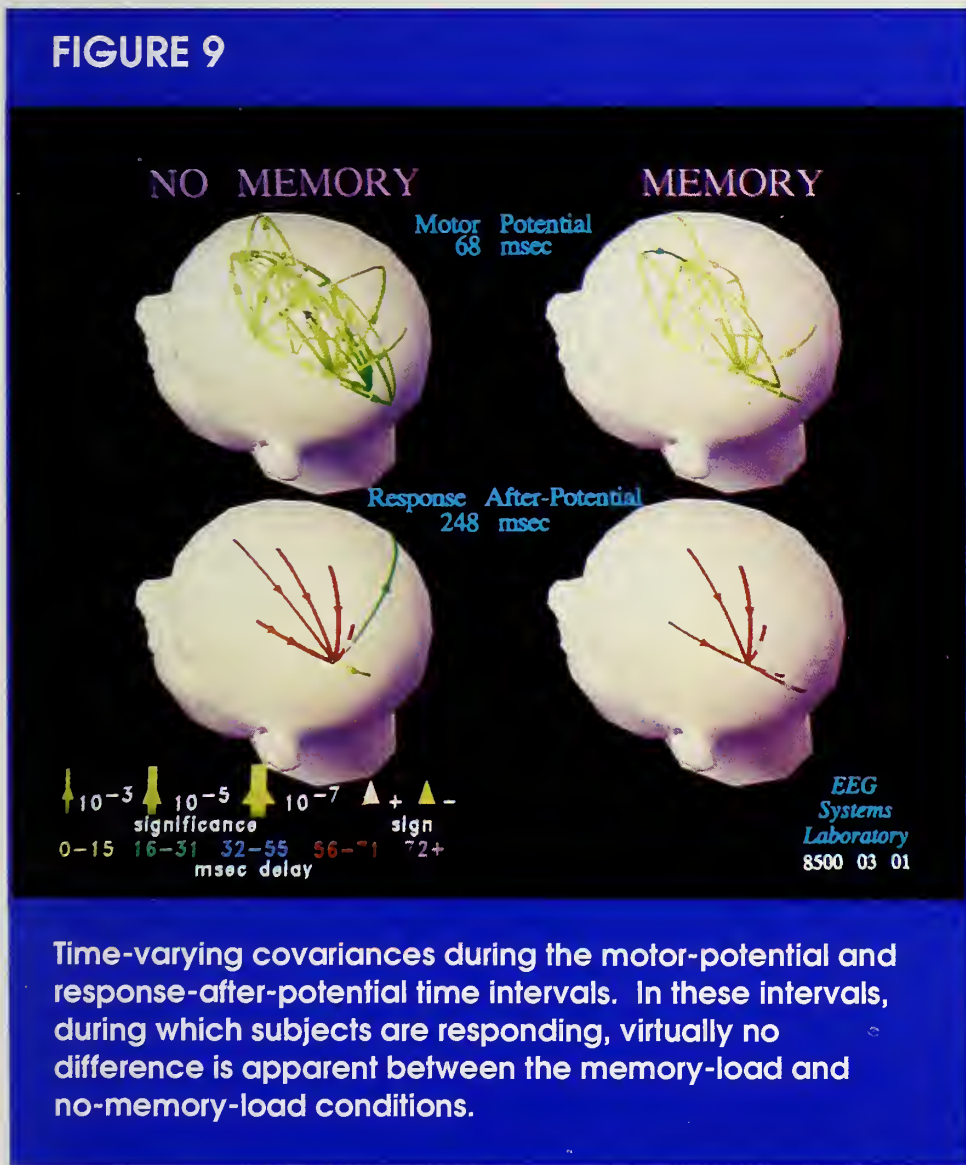
Dipole localization methods assume that ERP are generated by equivalent electrical dipoles. The recorded scalp potentials are modeled as resulting from volume conduction of the dipole source activity; they depend on the location of the dipoles, the dipole moments (i.e., the magnitude of the dipoles in each of the three spatial

dimensions), the locations of the scalp electrodes, and the shape and conductivity of the anatomical structures of the head. This type of modeling should avoid the false lateralization of sources that has occurred with surface EEG (Sammarritano et al. 1987).

Many dipole localization methods are based on the simplifying assumption that the head is a sphere of homogeneous conductivity. For this case, there is an analytical equation for the potentials at the scalp electrodes in terms of the dipole parameters (Brody et al. 1973). Concentric sphere models with uniform conductivity in each layer can also be handled using linear adjustments to the homogeneous sphere solution (Ary et al. 1981). Iterative algorithms (finite element or boundary element) for computing scalp potentials from dipole parameters are required if a nonspherical head shape and/or inhomogeneous conductivity are assumed.

The simplest form of the dipole model, developed by Kavanagh et al. (1978), Fender (1987), and others, assumes a separate set of dipole parameters at

FIGURE 9



every time point. We refer to this as the "spatial dipole model" (SDM) because only the spatial distribution of potentials over the scalp is used for dipole localization. This method is severely limited by the number of degrees of freedom in multichannel data at a single time point. It provides only a small amount of data reduction because separate sets of dipole parameters are derived for each time point.

The spatiotemporal dipole model (STDM; Scherg and Von Cramon 1985, 1986; Scherg 1989*b*) is based on the biologically reasonable assumption that each dipole represents a fixed anatomical structure that is active over a certain interval of time. The great advantage of the STDM over the SDM is that dipole localization for the entire ERP waveform can be achieved with far fewer parameters. The STDM is not a statistical model; therefore, it has a number of limitations as a data analytic tool: (1) It does not allow data from multiple subjects to be included in a single analysis; (2) it ignores variability due to background EEG noise and does not provide confidence intervals for model parameters; (3) it does not include methods for estimating and making inferences about covariate effects; and (4) it does not include procedures for systematically choosing starting parameters for dipole modeling.

The dipole configuration that results from the STDM depends upon the constraints placed on the dipole magnitude time functions. Scherg and colleagues have used two dif-

ferent models of the magnitude function. In early work they used spline functions constrained to resemble the biphasic curves that were being fitted (Scherg and Von Cramon 1985). In more recent work, they acknowledged that the earlier model was arbitrarily restrictive; therefore, they did not constrain the magnitude function, but rather estimated it using linear regression (Scherg and Von Cramon 1986; Scherg 1989*b*). However, this unconstrained function is extremely unparsimonious and thus more susceptible to the effects of noise in the data. Furthermore, this model does not yield summary measures of dipole activity, such as amplitude and latency parameters; thus it has limited utility in analysis of experimental data. We believe a better approach would be a model that is constrained to be smooth but that is less restricted than the biphasic spline model.

The STDM is applied to an individual multichannel ERP data set (e.g., either data from an individual subject or a grand average over a number of subjects), and the resulting equivalent dipole sources are specific to that data set. This application of STDM introduces two problems: First, there is no objective procedure for deciding whether dipoles from two data sets represent the same or different underlying brain processes when their defining parameters are not identical. Then, when the STDM is applied to individual subjects, the correlation structure of the noise in each subject's data can strongly af-

fect the positions and orientations of the dipoles that are fitted (Darcey et al. 1980). Position and orientation parameters are also affected by each subject's unique skull shape, skull thickness, and brain morphology (Ary et al. 1981). Dipole activity may not correlate well with scalp amplitude across individuals.

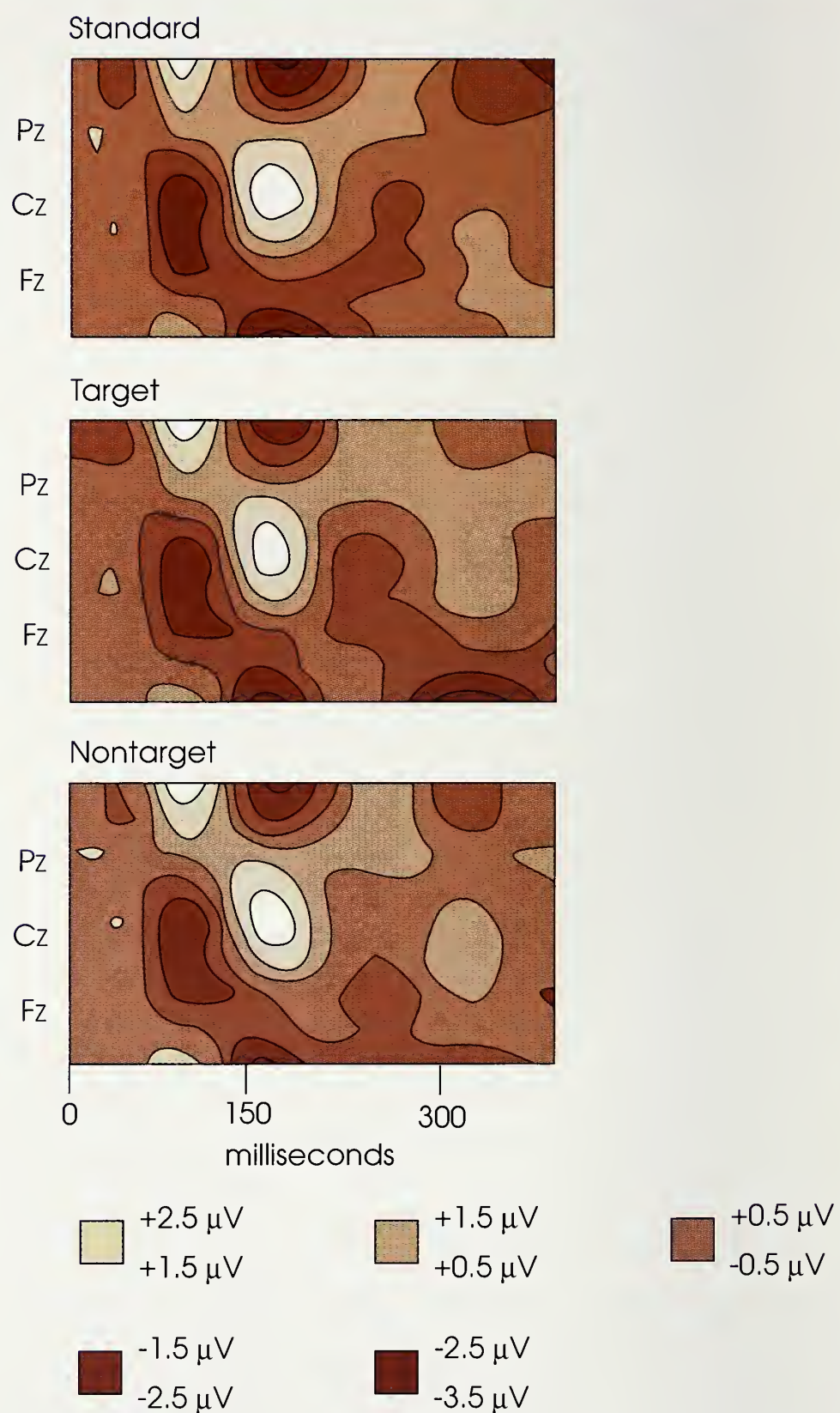
Recently, we have developed two different approaches to overcoming the limitations of the STDM, while taking advantage of its strengths. We first developed the dipole components model (DCM; Turetsky et al. 1990), which applied and extended the statistical framework known as the "topographic components model" (Möcks 1988) to spatiotemporal dipole modeling. In the DCM, dipole locations and orientations are assumed to be constant across time and across subjects, but the time-varying magnitude function of the dipole is modified by subject-specific and condition-specific amplitude and latency parameters ("condition" refers to experimental conditions). The magnitude function is assumed to be a decaying sinusoid with parameters representing the onset time, amplitude decay rate, and oscillation frequency. The great advantage of the DCM is that it allows us to compare the same dipole across subjects and conditions.

We used the simplex procedure (Nelder and Mead 1965) with an ordinary least-squares criterion to fit the dipole components model to the collection of average ERP obtained from the various subjects.

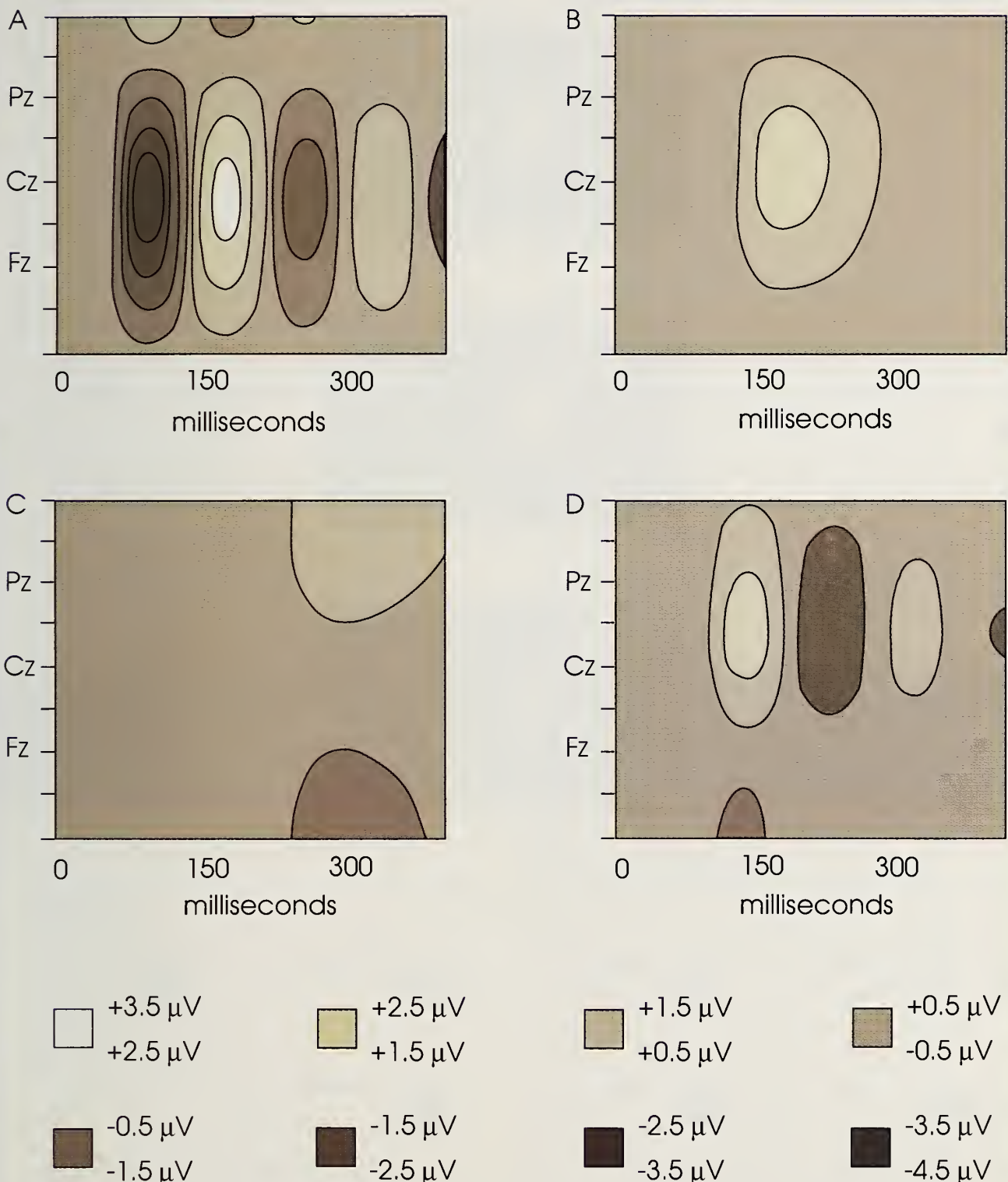
Starting values for this iterative procedure were obtained by fitting various numbers of dipoles with various locations and orientations to the grand average ERP (i.e., the average over all subjects).

We applied the DCM to ERP from 18 subjects performing a three-tone auditory target detection task. Data collected from nine equally spaced electrodes along the midsagittal plane were transformed to the average reference. Inasmuch as dipole parameter estimates are independent of the reference, the average reference was chosen only for convenience. With this electrode array, we were limited to inferences about the projection of the dipoles into the midsagittal plane. No information could be obtained about the laterality of the location and orientation of the dipoles.

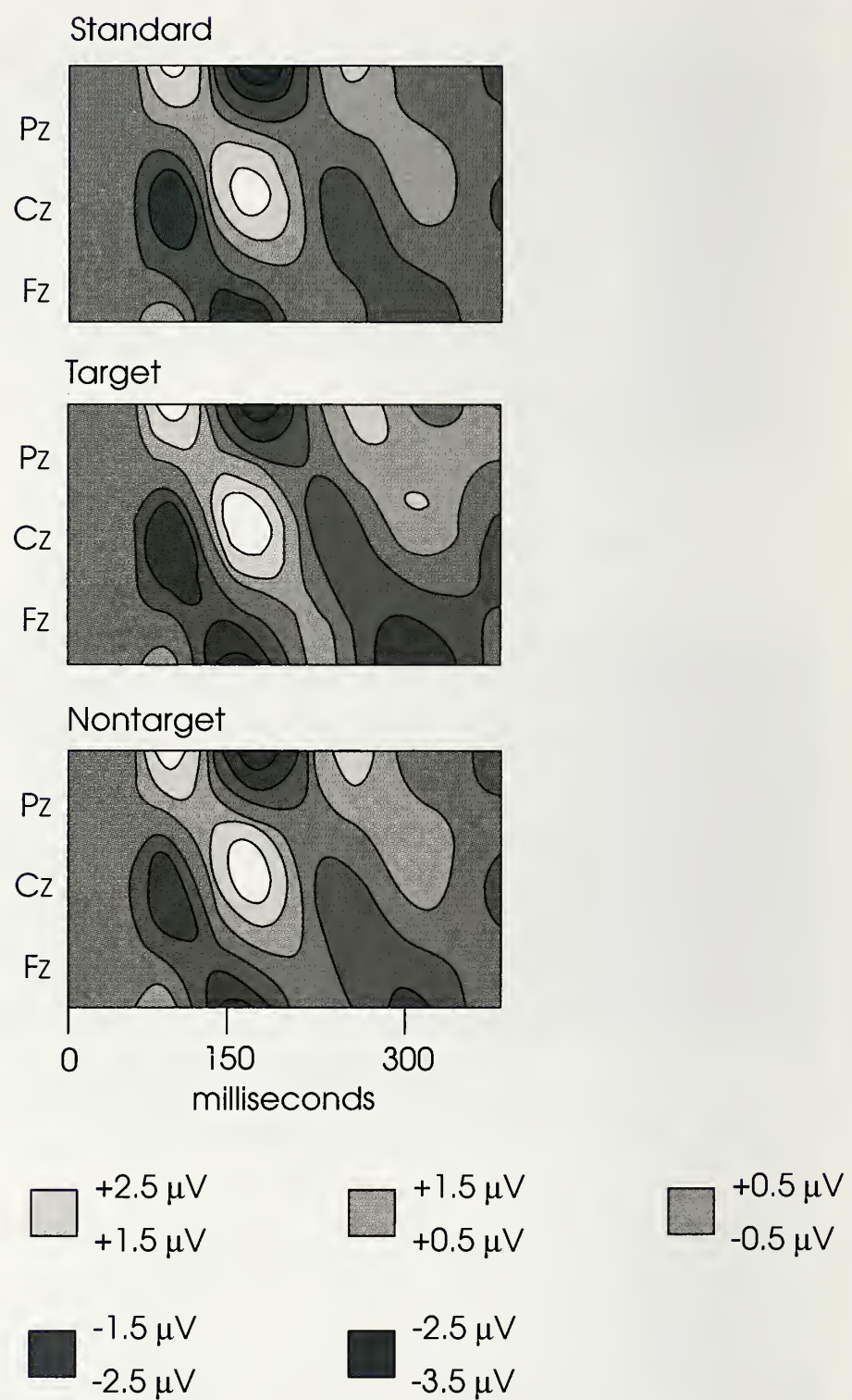
Figure 10 shows spatiotemporal plots of the grand average ERP for the standard, target, and rare non-target conditions. We present the grand average to simplify the presentation; the DCM is actually fitted to average ERP from the various individual subjects and conditions. The model yields a best fit using four dipoles. Figure 11 displays spatiotemporal plots of the average activity from each of the four estimated underlying dipole sources. An interesting result was that the P300 component was generated by a combination of dipoles that were also active at earlier latencies--the P300 could not be represented by any single generator. Figure 12 shows the ERP predicted by the fit-

FIGURE 10

Spatiotemporal contour plots (as in figure 5) of the grand average ERP data from 18 subjects, presented separately for standard, target, and rare nontarget conditions. Shaded contour regions correspond to different electrical potentials, according to the gray scale on the right (from Turetsky et al. 1990).

FIGURE 11

Spatiotemporal contour plots of midline scalp activity arising from each of four equivalent dipole sources. Each plot presents the reference-free electrical potential at nine midline electrode sites, from stimulus onset to 400 milliseconds poststimulus, prior to the inclusion of condition-specific or subject-specific latency and amplitude parameters (from Turetsky et al. 1990).

FIGURE 12

Spatiotemporal contour plots depicting the composite average-referenced scalp activity from four equivalent dipole sources. The composite electrical potential is the sum of the potentials arising from each of the five dipoles displayed in figure 11, after modification of each dipole by its condition-specific latency and amplitude parameters and transformation to the average reference. Comparison of these plots and the grand averages presented in figure 10 illustrates the goodness of fit of the dipole component model (from Turetsky et al. 1990).

ted model, which is a weighted sum of activity of the four underlying equivalent dipoles. The model in figure 12 very closely approximates the plot of original data shown in figure 10.

Because the DCM does not yield confidence intervals for the dipole parameters, we performed randomization tests as statistical checks for experimental effects. The estimated p values associated with differences across conditions in the amplitude [$\ln e_k(m)$] and latency [τ_{km}] parameters of the four dipoles are presented in table 1. There were significant amplitude differences among the experimental conditions for three of the dipoles and a significant latency shift among experimental conditions for one dipole. Thus, the DCM partitioned the ERP

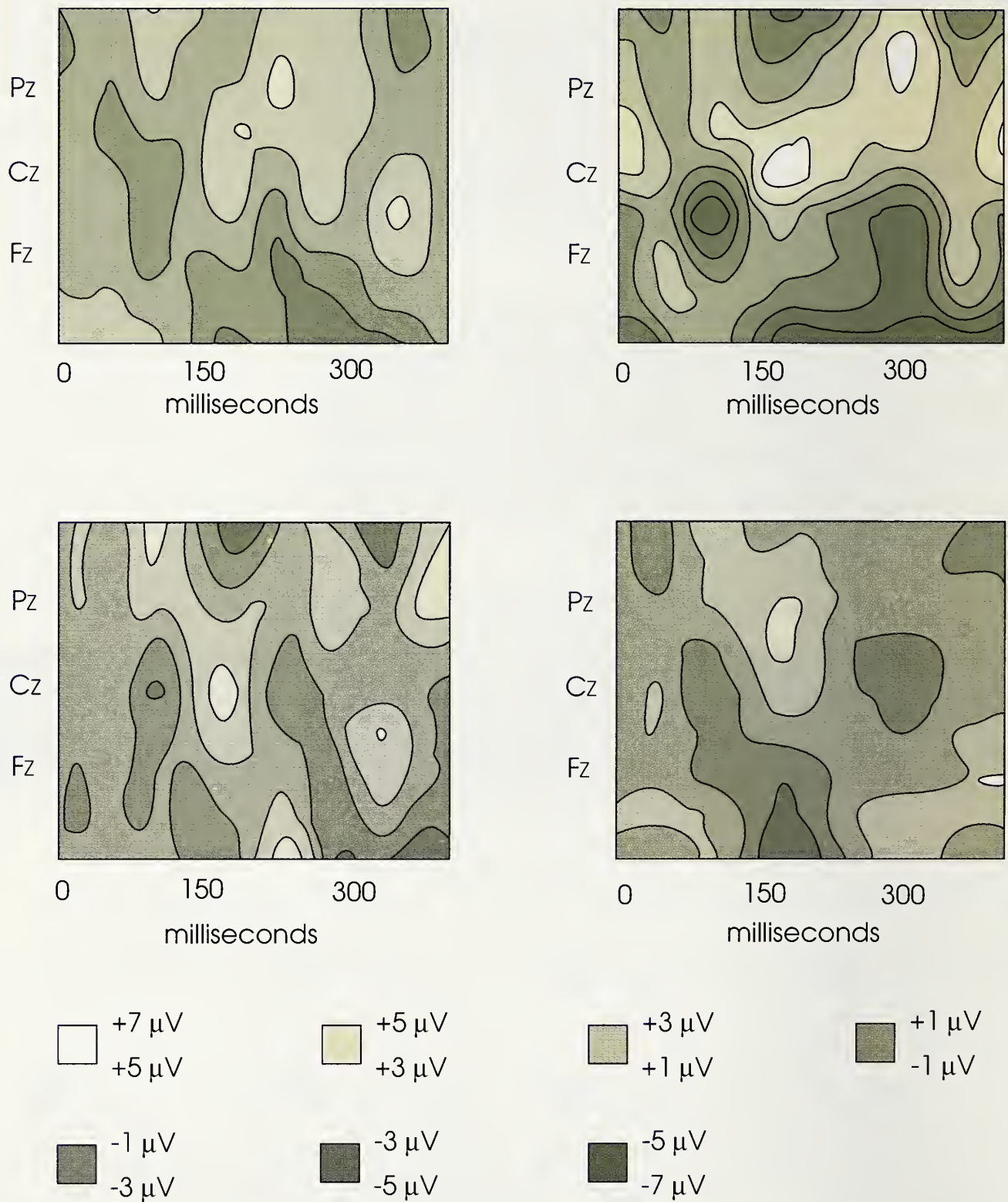
data into components that sensitively distinguished brain electrical responses to various experimental conditions.

One of the important advances in the DCM--the inclusion of subject-specific dipole amplitude and latency parameters and, more recently, subject-specific dipole orientation--is crucial because of the great variability among subjects' evoked potential time-varying topographies. This variability is illustrated in figure 13, which displays the average reference plots for the target condition for four representative subjects. This tremendous intersubject variation must be considered for real progress to be made in understanding the phenomena underlying the brain's response to

Table 1. Dipole component modeling of a three-tone P300 experiment: Tests of significance of condition-specific amplitude and latency parameters

Parameter	Estimated p values			
	Dipole			
	A	B	C	D
Amplitude ($\ln e_k(m)$)	0.215	0.022	0.077	0.007
Paired contrasts				
Standard vs. target		0.030	0.007	0.007
Standard vs. nontarget		0.785	0.111	0.044
Target vs. nontarget		0.007	0.111	0.044
Latency (τ_{km})	0.467	0.089	0.037	0.259
Paired contrasts				
Standard vs. target			0.052	
Standard vs. nontarget			0.882	
Target vs. nontarget			0.022	

From Turetsky et al. 1990.

FIGURE 13

Average-referenced spatiotemporal contour plots of the target response from four randomly selected subjects. Although the plots generally resemble the target grand average (figure 10), they illustrate the substantial intersubject variability that exists in ERP morphology (from Turetsky et al. 1990).

stimuli. The DCM analysis yielded the results presented above, while taking into account this intersubject variability.

Since our initial application of the DCM, we have implemented a program to fit the model to three-dimensional data. In a recent study, we used the three-dimensional dipole model to examine the ability of CSD-transformed potentials to distinguish activity arising from deep versus superficial sources (Turetsky and Fein 1991).

An important disadvantage of the dipole components model stems from the fact that it does not account for the properties of background EEG noise. Specifically, it takes into account neither differences in noise power at different electrode sites and across different subjects nor the coherence of the background EEG among electrode sites due to the common reference, volume conduction, and random subject effects. Without a model for background EEG noise, it is impossible to compute measures of variability of the parameter estimates without resorting to computationally intensive methods such as randomization tests and the bootstrap. Such methods are particularly unwieldy when applied to an estimation procedure that is already highly computational. In fact, the randomization tests used to generate the p value estimates in table 1 required >100 hours of computer time on a 20-MHz 80386-based computer (and that was only a two-dimensional dipole model). Another important disadvantage is

that the time domain model requires a possibly restrictive parametric form for the magnitude function.

To overcome these disadvantages, we have been developing a frequency domain maximum likelihood approach (Raz et al. 1991). In the frequency domain, the spectra and coherences of the noise are easily incorporated as parameters in the model. Elimination of Fourier coefficients at high frequencies leads to substantial data reduction and smoothness constraints on the dipole magnitude function. Using results from statistical time series analysis, we constructed a multivariate complex normal likelihood function (Brillinger 1981) that enabled us to estimate confidence intervals for model parameters. Simulations demonstrated that when the model is correctly specified, precise confidence regions for the dipole parameters can be computed. More work is needed to compute realistic standard errors that account for the nonspherical shape and inhomogeneous conductivity of the head, as well as our lack of knowledge of the true number of dipoles.

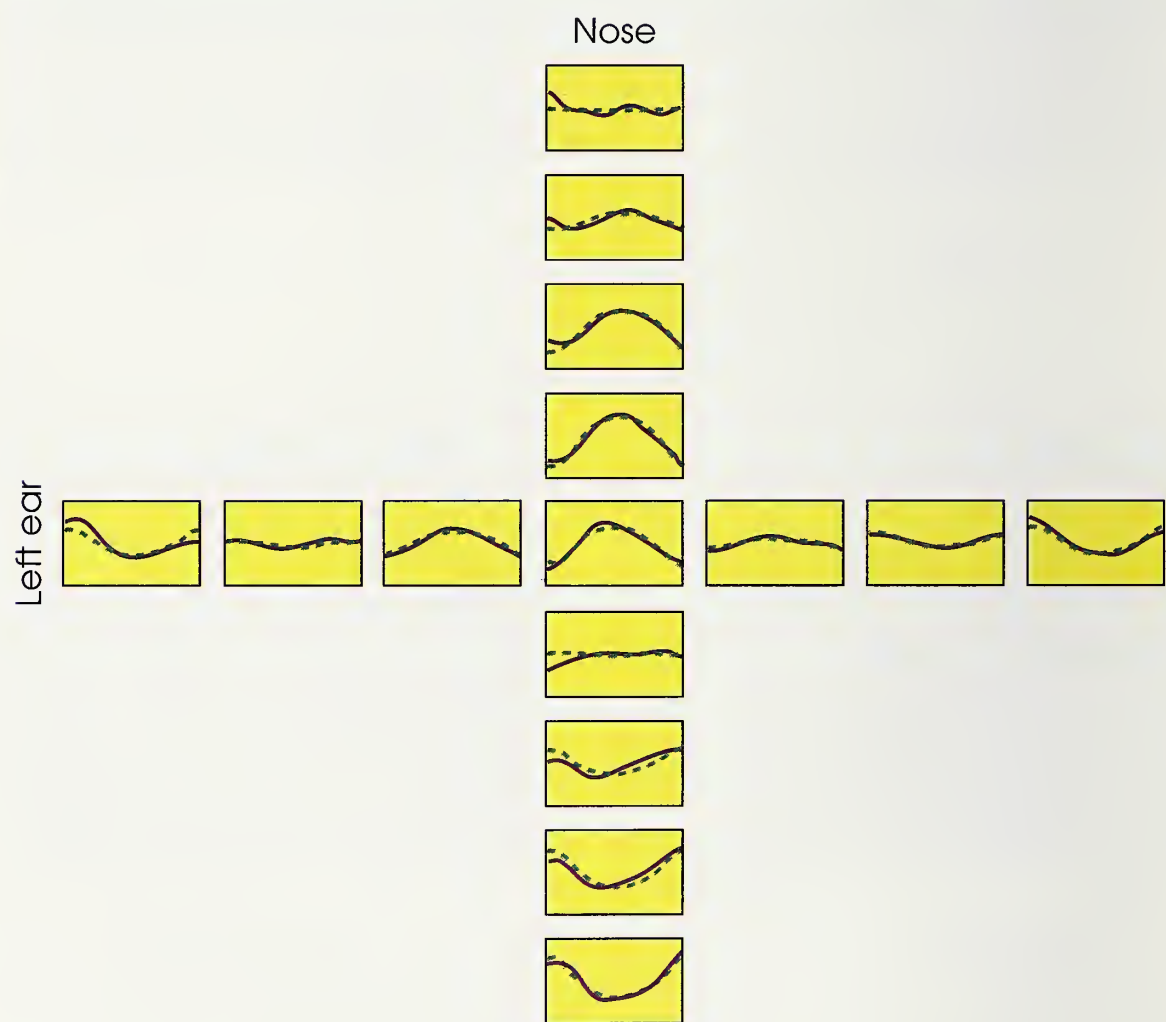
Finally, we applied the frequency domain model to analysis of the P50 response to auditory click stimuli. Assuming that the orientation of the dipole was fixed over time, we computed estimates of the dipole parameters from four subjects' data. The location of the dipoles, which was quite consistent across subjects, corresponds well with evidence that the P50 is generated in the midbrain and/or

diencephalon (Erwin and Buchwald 1987).

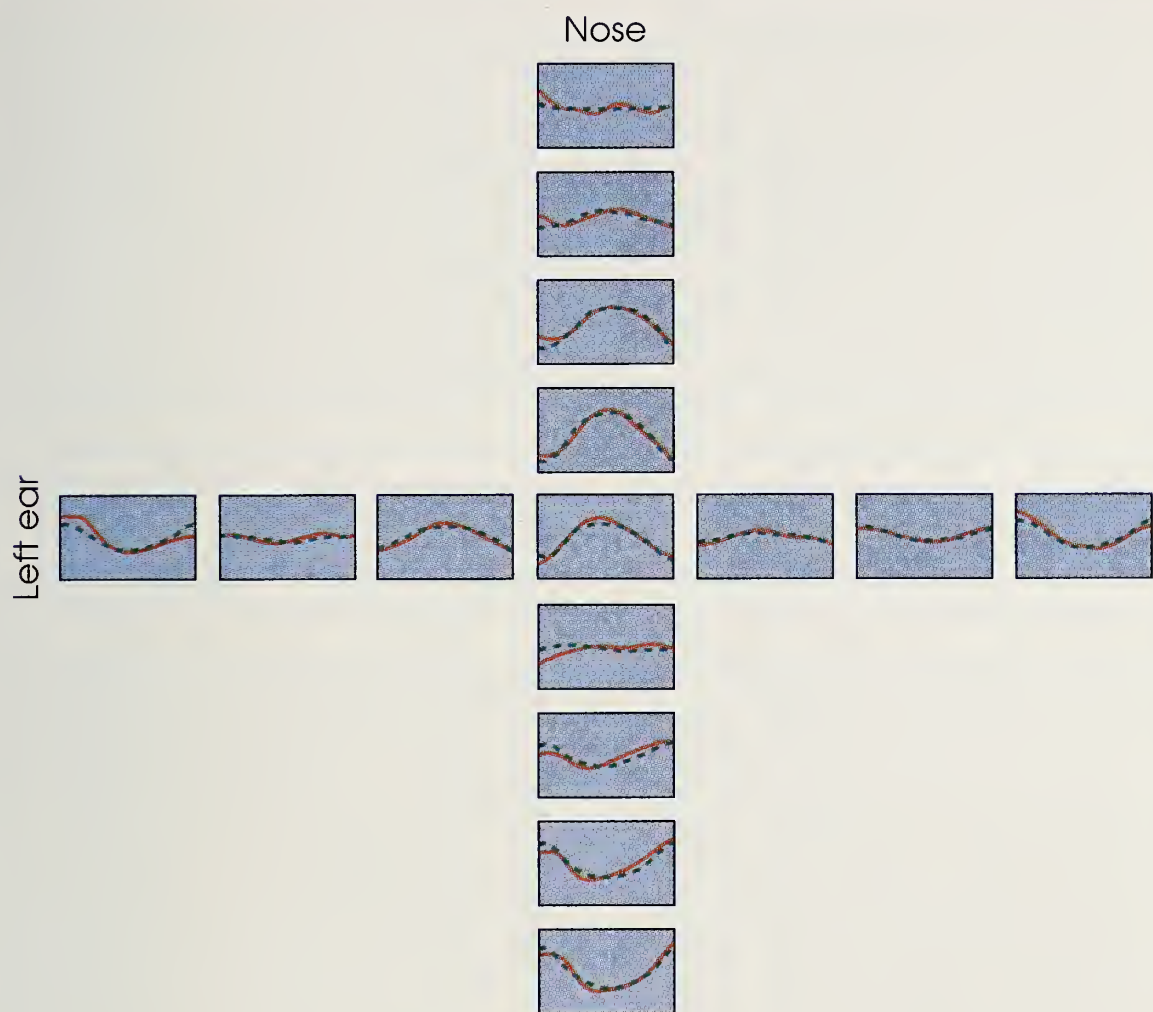
In more recent unpublished work, we have implemented the frequency domain model under the assumption that the orientation

varies over time. In this case, the dipole moment is represented by a time-varying vector of magnitudes in each of the three orthogonal spatial dimensions. Application of the varying orientation model to

FIGURE 14



Recorded evoked potential at 15 scalp electrode locations in a representative subject. The estimated signal is based on the frequency domain model with fixed orientation. Each plot shows the recorded waveform (solid line) and the estimated waveform (dashed line) for a single electrode position. The positions of the plots on the page correspond to the locations of the electrodes on the scalp. The plot in the center of the figure represents the vertex electrode location. The x-axis in each plot represents time from stimulus onset (35 to 66 milliseconds poststimulus). The y-axis is amplitude (-3 to +3 μ V). The recorded evoked potentials are averages of responses to 156 stimuli. The responses were bandpass-filtered between 10 and 100 Hz. The amplitudes displayed are the differences between the potential at the given electrode and the average of all electrodes (average reference).

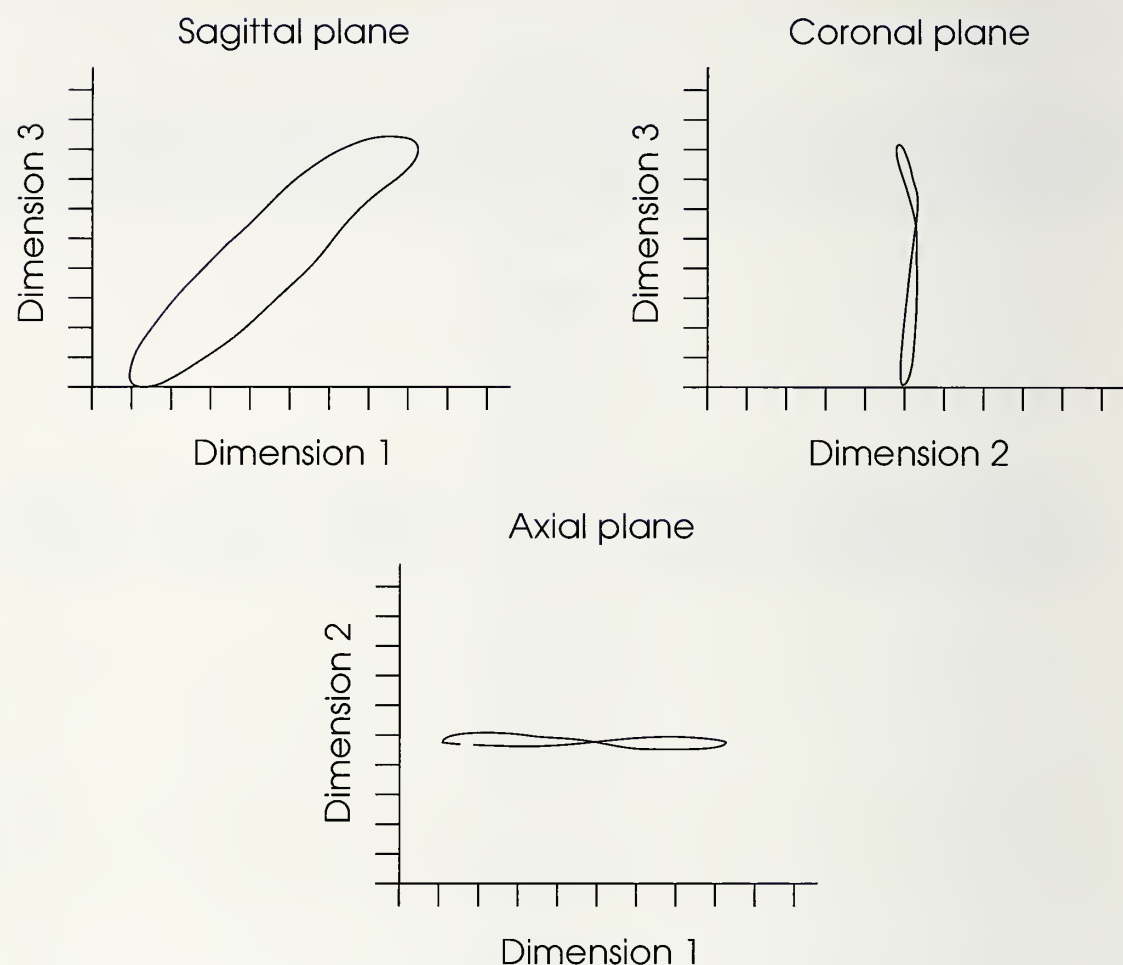
FIGURE 15

Recorded evoked potential at 15 scalp electrode locations for the same subject as in figure 14. The estimated signal is based on the frequency domain model with time-varying orientation. Data represented as those in figure 14, except that the time-varying orientation rather than the fixed-orientation dipole model was used.

the data gave nearly the same location as the fixed orientation. Figure 14 shows the average ERP at each electrode overlaid by the ERP predicted by the fitted fixed orientation model, while figure 15 shows the fit of the varying orientation model.

The fit is slightly better for the varying orientation model because the number of parameters is greater. However, we have ob-

tained evidence that the fixed orientation model is adequate by plotting the three-dimensional Lissajous trajectory of the estimated dipole moment in three two-dimensional projections (figure 16). This plot clearly shows that the orientation is nearly constant over time. We suspect that the departures from the fixed orientation model can be explained by background EEG noise and by de-

FIGURE 16

Projections of the trajectory of the time-varying three-dimensional dipole moment onto the sagittal (upper left), coronal (upper right), and axial (lower) planes. These data are from the subject as in figures 14 and 15. Dimension 1 is defined by a line through the nasion and the inion, dimension 2 by the left and right ears, and dimension 3 by the vertex and center of the head. The tick marks denote arbitrary units that depend on the conductivity and radius of the head. This plot, based on the varying-orientation model, demonstrates that the orientation is essentially fixed over time.

partures from the assumption that the head is a sphere containing a medium of homogeneous conductivity.

CONCLUSIONS

Brain electrical activity is used to study brain processes as they are affected by aging, drugs, changes in

the status of neurotransmitter systems, and dementia or other disease states. Although large, consistent, and potentially important effects on ERP have been documented in alcoholism, dementia, schizophrenia, and other important disease processes, ERP research has not generated the anticipated breakthroughs in the diagnosis of

brain disease or in understanding normal and pathological brain function. This disappointing yield has been attributed to the wide discrepancy between the complexity of the underlying phenomena and the relatively crude technology used to analyze the ERP signals.

Nunez (1981) provided the clearest exposition of the crucial failure of EEG and ERP research methodology to be guided by the biophysics of brain electrical activity. Furthermore, because ERP research requires estimation of relatively small signals embedded in a relatively high-amplitude noise process that has strong time and spatial dependencies, it is equally crucial that ERP analysis methodology rest on a sound statistical basis.

ERP data consist of waveforms recorded at many scalp locations from a number of subjects under various experimental conditions. The waveforms result from the activity of brain processes that occur in response to exogenous stimuli or endogenous brain activity. These waveforms are embedded in background EEG noise. The goal in ERP research is to determine the effects of experimental manipulations and pathology on the brain processes that generate the ERP. To accomplish this goal, one must partition ERP data into subcomponents that represent the activity of the underlying brain processes.

With the advent of inexpensive yet powerful computers, new ERP analysis technologies such as brain mapping have become widely available and are now an integral

part of commercially available clinical ERP machines. The aggressive marketing of these commercial systems has led to a tremendous expansion in the clinical application of ERP testing and to an increase in health care dollars expended for such efforts. On the surface, brain mapping methods appear to represent revolutionary developments in the analysis of brain electrical activity. However, closer examination shows them to be scant improvement over the existing, relatively unsophisticated models of brain electrical activity and signal estimation. Brain mapping neither reveals the location of underlying signal sources nor partitions the surface data in terms of those underlying sources.

Evoked potential research suffers from problems with extracting meaningful and valid data representative of underlying phenomena. These difficulties are especially vexing in the study of later ERP complexes (e.g., P300), partly because these complexes represent activity from multiple brain regions. For example, our clinical research uses the ERP (among other measures) to study the effects of chronic alcohol abuse on central nervous system morbidity with HIV infection. In this work, we have focused on the anterior (P3A) subcomponent of the P300 complex. One of our biggest challenges is to separate anterior from posterior P300 subcomponents such that the resulting measurements have the lowest standard errors, hence optimal sensitivity, as indices of un-

derlying phenomena. Further development of methods for partitioning ERP signals into physiologically meaningful subcomponents will be of tremendous utility in clinical and basic ERP research.

As we have shown, dipole source localization, in which the ERP is modeled as arising from multiple intracranial electrical dipole sources, holds great promise as a method for partitioning ERP waveforms into subprocesses that are anatomically localized and biophysically plausible sources of electrical activity. There is great excitement among researchers concerning the potential of dipole source localization, and Begleiter's group is applying the method to the separation of anterior versus posterior aspects of the P300 complex in the examination of groups at genetic high risk for alcoholism (Odencrantz et al., Chapter 5). This potential may be generators of brain electrical activity and in more precisely measuring (i.e., via higher SNR) the parameters of those intracranial generators.

However, there are important limitations to use of available dipole localization methods. Existing methods to fit a dipole model to multichannel ERP data sets do not include evaluation of the correctness of the model regarding head shape and/or electrical impedance inhomogeneities. Nor do existing methods provide a solid framework for comparing the results of dipole modeling across subjects, groups of subjects, or experimental conditions. Moreover, existing methods do not incorporate statistical pro-

cedures for generating confidence intervals for the dipole parameters or for testing hypotheses about the effects on the dipole parameters of covariates such as experimental manipulations and degree or type of pathology.

The continued development of new methodologies that are closely tied to sound statistical models and to the biophysics of the brain electrical activity is essential if ERP research is to reach its full potential.

ACKNOWLEDGMENTS

The work reported here was supported by General Medical Research funds from the Department of Veterans Affairs.

REFERENCES

- Ary, J.P.; Klein, S.A.; and Fender, D.H. Location of sources of evoked scalp potentials: Corrections for skull and scalp thicknesses. *IEEE Trans Biomed Eng* 28:447–452, 1981.
- Biggins, C.; Raz, J.; Amir, A.; and Fein, G. Artifactualy high coherences result from using spherical spline computation of scalp current density. *Electroencephalogr Clin Neurophysiol* 1991, in press.
- Brillinger, D.R. A note on the estimation of evoked responses. *Biol Cybern* 31:141–144, 1978.
- Brillinger, D.R. *Time Series Data Analysis and Theory*. San Francisco: Holden-Day, 1981.
- Brody, D.A.; Terry, F.H.; and Ideker, R.E. Eccentric dipole in a spherical medium:

- Generalized expression for surface potentials. *IEEE Trans Biomed Eng* 20:141–143, 1973.
- Darcey, T.M.; Ary, J.P.; and Fender, D.H. Methods for localization of electrical sources in the human brain. In: Kornhuber, H.H., and Deecke, L., eds. *Progress in Brain Research*. Vol. 54. Elsevier: Amsterdam, 1980.
- Davidson, R.J., and Fox, N.A. Frontal brain asymmetry predicts infants' response to maternal separation. *J Abnorm Psychol* 98(2):127–131, 1989.
- Erwin, R.J., and Buchwald, J.S. Midlatency auditory evoked responses in the human and the cat model. In: Johnson Jr., R.; Rohrbaugh, J.W.; and Parasuraman, R., eds. *Current Trends in Event-Related Potential Research (EEG Suppl. 40)*. Amsterdam: Elsevier, 1987. pp. 461–467.
- Eysholdt, U., and Schreiner, C. Maximum length sequences--a fast method for measuring brain-stem-evoked responses. *Audiology* 21:242–250, 1982.
- Fender, D. Source localization of brain electrical activity. In: Gevins, A.S., and Remond, A., eds. *Methods of Analysis of Brain Electrical and Magnetic Signals*. EEG Handbook, Vol. I. Amsterdam: Elsevier Science, 1987. pp. 335–403.
- Gevins, A.S. "Advances in Studying Neurocognitive Networks in the Human Brain." President's invited lecture. Society for Neuroscience Annual Meeting, St. Louis, October 31, 1990.
- Gevins, A.S.; Bressler, S.L.; Morgan, N.H.; Cutillo, B.A.; White, R.M.; Greer, D.S.; and Illes, J. Event-related covariances during a bimanual visuomotor task. I. Methods and analysis of stimulus- and response-locked data. *Electroencephalogr Clin Neurophysiol* 74(1):58–75, 1989a.
- Gevins, A.S.; Cutillo, B.A.; Bressler, S.L.; Morgan, N.H.; White, R.M.; Illes, J.; and Greer, D.S. Event-related covariances during a bimanual visuomotor task. II. Preparation and feedback. *Electroencephalogr Clin Neurophysiol* 74(2):147–160, 1989b.
- Gevins, A.S.; Morgan, N.H.; Bressler, S.L.; Cutillo, B.A.; White, R.M.; Illes, J.; Greer, D.S.; Doyle, J.C.; and Zeitlin, G.M. Human neuroelectric patterns predict performance accuracy. *Science* 235(4788):580–585, 1987.
- Henriques, J.B., and Davidson, R.J. Regional brain electrical asymmetries discriminate between previously depressed and healthy control subjects. *J Abnorm Psychol* 99(1):22–31, 1990.
- Hjorth, B., and Rodin, E. Extraction of "deep" components from scalp EEG. *Brain Topog* 1(1):65–69, 1988.
- Jacobson, G.P., and Newman, C.W. The decomposition of the middle latency auditory evoked potential (MLAEP) Pa component into superficial and deep source contributions. *Brain Topog* 2(3):229–236, 1990.
- Kavanagh, R.N.; Darcey, T.M.; Lehmann, D.; and Fender, D.K. Evaluation of methods for 3-dimensional localization of electrical sources in the human brain. *IEEE Trans Biomed Eng* 25:421–429, 1978.
- Möcks, J. Topographic components model for event-related potentials. *IEEE Trans Biomed Eng* 35:482–484, 1988.
- Möcks, J.; Gasser, T.; and Tuan, D.P. Variability of single visual evoked

potentials evaluated by two new statistical tests. *Electroencephalogr Clin Neurophysiol* 57:571–580, 1984.

Möcks, J.; Kohler, W.; Gasser, T.; and Tuan, D.P. Novel approaches to the problem of latency jitter. *Psychophysiology* 25(2):217–226, 1988.

Nelder, J.A., and Mead, R. A simplex method for function minimization. *Computat J* 7:308–313, 1965.

Nunez, P.L. *Electric Fields of the Brain*. New York: Oxford Press, 1981.

Perrin, F.; Pernier, J.; Bertrand, O.; and Echallier, J.F. Spherical splines for scalp potential and current density mapping. *Electroencephalogr Clin Neurophysiol* 72:184–187, 1989.

Raz, J., and Fein, G. Testing for heterogeneity of evoked potential signals using an approximation to an exact permutation test. *Biometrics* 1991, in press.

Raz, J.; Turetsky, B.; and Fein, G. Selecting the smoothing parameter for estimation of smoothly changing evoked potential signals. *Biometrics* 45(3):745–762, 1989.

Raz, J.; Turetsky, B.; and Fein, G. Frequency domain estimation of the parameters of human brain electrical dipoles. *J Am Stat Assoc* 1991, in press.

Sammaritano, M.; de Lotminiere, A.; Andermann, F.; Olivier, A.; Gloor, P.; and Quesney, L.F. False lateralization by surface EEG of seizure onset in patients with temporal lobe epilepsy and gross focal cerebral lesions. *Ann Neurol* 21(4):361–369, 1987.

Scherg, M. *Brain Electrical Source Analysis* (BESA). McLean, VA: Neuroscan, Inc., 1989a.

Scherg, M. Fundamentals of dipoles source potential analysis. In: Hoke, M.; Grandori, F.; and Romani, G.L., eds. *Auditory Evoked Magnetic Fields and Potentials*. Basel: Karger, 1989b.

Scherg, M., and Von Cramon, D. Two bilateral sources of the late AEP as identified by a spatiotemporal dipole model. *Electroencephalogr Clin Neurophysiol* 62:32–44, 1985.

Scherg, M., and Von Cramon, D. Evoked dipole source potentials of the human auditory cortex. *Electroencephalogr Clin Neurophysiol* 65:344–360, 1986.

Snidman, N., and Kagan, J. Infant predictors of inhibited and uninhibited profiles. *Psychophysiology Suppl* 27:S9–S10, 1990.

Stassen, H.H.; Bomben, G.; and Propping, P. Genetic aspects of the EEG: An investigation into the within-pair similarity of monozygotic and dizygotic twins with a new method of analysis. *Electroencephalogr Clin Neurophysiol* 66:489–501, 1987.

Turetsky, B., and Fein, G. Partitioning of deep vs. superficial evoked potential sources using current source densities is not valid. *Brain Topog* 1991, in press.

Turetsky, B.; Raz, J.; and Fein, G. Estimation of trial-to-trial variation in evoked potential signals by smoothing across trials. *Psychophysiology* 26(6):700–712, 1989.

Turetsky, B.; Raz, J.; and Fein, G. Representation of multi-channel evoked potential data using a dipole component model of intra-cranial generators: Application to the auditory P300. *Electroencephalogr Clin Neurophysiol* 76:540–566, 1990.

5

THE TOPOGRAPHIC ANALYSIS OF MODEL-REFERENCED EVOKED POTENTIAL COMPONENTS

John Odencrantz,¹ Sean O'Connor,² Henri Begleiter,¹ and Guowang Zhang¹

Event-related potentials (ERP) have been used to study cognitive processes in the normal human brain as well as to assess brain function in various types of patient populations. ERP offer a unique approach for examining multiple levels of brain functioning. Quantitative measurements of salient features extracted from ERP recordings reflect various aspects of brain function related to sensory as well as higher integrative processes.

For the most part, ERP represent an amalgam of heterogeneous components. Every component is caused by neuronally induced currents in the brain, with each component manifesting spatial and temporal properties distinct from the other components. Identifying the neural origins of each component would provide fundamental information concerning the functions of the brain. Apart from inva-

sive procedures, which are not feasible except in special circumstances, the only means of obtaining information regarding the locations of the generators is knowledge of the scalp current topographies (e.g., Vaughan et al. 1986).

Decomposition of the evoked potential can be achieved via a number of its known or presumed attributes. Among those proposed are stochastic independence (Donchin 1966), homogeneity across subjects of component spatial properties (Mocks 1988), and geometric and electrophysiological properties of generators (Cuffin and

ACRONYMS

EEG	<i>electroencephalogram</i>
ERP	<i>event-related potential</i>
MRA	<i>model-referenced analysis</i>
SPM	<i>significance probability map</i>

¹Department of Psychiatry, SUNY Health Sciences Center, Brooklyn, NY 11203

²Department of Psychiatry, University of Connecticut School of Medicine, Farmington, CT 06032

Cohen 1977; Kavanagh et al. 1978; Sidman et al. 1978).

We propose a topographic analysis based on a combination of two ideas. The first is a representation of the evoked potential over the head as the product of a matrix specifying the spatial features of the evoked potential and temporal characteristics. Formally

$$\Phi_{l,t} = A_l B_t \quad (1)$$

where $\Phi_{l,t}$ is the evoked potential at lead l and time t , A_l is a matrix, each column of which determines the spatial configuration of one component, and B_t is a matrix, each row of which specifies the temporal progression of a component. The matrix product has the effect of making the scalp potential a linear combination of a number of underlying source potentials, each of which may vary in strength over time. Such a decomposition is explicit or implicit in the work of a number of researchers, including Maier et al. (1987), Achim et al. (1988), and Turetsky et al. (1990).

Further restrictions are necessary in order to obtain a unique solution to model 1. Mocks (1988) has proposed a related form that draws the necessary restrictions from considerations of consistency between subjects, while Maier et al. (1987) and Achim et al. (1988) use a combination of orthogonality over time and dipole generator theory over space. This last, the instantaneous dipole model, specifies an explicit functional form for A_l . In this chapter, we consider an alternative approach of specifying a

functional form for the matrix B_t . The resulting decomposition is unique, thus allowing us to examine the topography of various components without making assumptions about the nature and number of sources that generate each.

The functional form for B_t has for each row an exponentially decaying sinusoid

$$B_{i,t} = e^{-\beta(i)t\%} \sin(\omega(i)t) \quad (2)$$

This form is determined from known neuronal interactions. Its physical justification is that it can be derived as a consequence of interacting excitatory and inhibitory nerve masses if nonlinear interactions are excluded. This is similar to Freeman's (1975) model of the evoked potential. O'Connor et al. (1983) derived the single lead model independent of Freeman's earlier work and termed it the "model-referenced analysis" (MRA) of evoked brain potentials.

Practical advantages of this representation include reduction in topographical representation, interpretability, and stability. Representational reduction is a consequence of the fact that a single map is associated with each component, so that a few maps (on the order of five) are sufficient to contain all of the topographic information for a given evoked potential.

Interpretability and stability are both consequences of the fact that MRA components damp quickly in practice, so that each has most of its activity within the time interval of a single evoked potential peak. It is easy to relate MRA components to activities that have been

studied in connection with peak analysis; they tend to be stable from one subject to another.

Analyses based on model 1 can focus either on the spatial properties of the data or their dynamic properties. Our focus is on topography, especially with regard to topographical differences between different brain states. Our primary tool is the significance probability map (SPM), first used in connection with brain research by Duffy et al. (1981). We suggest some multivariate SPM that allows components to be combined. Discriminant analysis is also used as a global means of assessing differences.

For illustration purposes, we have chosen to analyze a set of data in which differences are experimentally induced rather than being the consequence of uncontrollable factors. Evoked potentials were measured in 24 subjects chosen to be homogeneous with regard to their medical background. Each subject was studied under three conditions known to produce specific differences in the ERP, especially in P3. This repeated-measures approach tends to minimize problems arising from extraneous factors. The topography of P3 was of particular interest in this experiment, and two models, differing in how they modeled P3, were implemented and compared.

MATERIALS AND METHODS

Experimental Procedure

The subjects were 24 neurologically intact healthy males between the ages of 18 and 24. None had any

past history of chronic medical problems. Subjects were seated in a sound-attenuated chamber and told to fixate on the center of a CRT 44 cm away. They were presented with three types of stimuli, each consisting of a straight line (42 mm) rotated into one of three possible orientations and passing through the point of visual fixation. The visual angle was 5.46°. The stimuli were presented one at a time in a random rate (2–5 seconds). The nontarget stimuli were frequently occurring vertical lines (75 percent). Two types of rarely occurring target stimuli were used: an easily recognized line that differed from the vertical by 90° (horizontal) and a difficult-to-recognize target that differed from the vertical by only 3°. The targets were each presented 12.5 percent of the time. The subjects' task was to press a button to all nonvertical stimuli as quickly as possible in a target-selection, reaction-time paradigm.

Electrodes

The entire 10/20 International system of electrodes was used (Electro-Cap), with the nasion serving as a reference and the forehead as a ground. Vertical and horizontal eye leads monitored possible eye movement contamination, and trials with excessive eye movement ($>75 \mu\text{V}$) were removed.

Event-Related Potentials

The ERP were amplified 20,000 times and were sampled for 100 milliseconds preceding the stimulus (prestimulus baseline) and for 1,000

milliseconds following the stimulus every 5 milliseconds (200 Hz sampling rate; band width 0.1–100 Hz). On-line digital filtering was performed on the data between 0.1 and 30 Hz.

Decomposing the Evoked Potential (MRA)

Our decomposition was based on the following dynamic model of the evoked potential:

$$\Phi_{l,t} = \sum_i A_{i,l} e^{\beta(i)(t-t(i))} \sin(\omega(i)(t-t(i))) I(t > t(i)) \quad (3)$$

$\Phi_{l,t}$ is the evoked potential at lead l and time point t, and $A_{i,l}$, $\beta(i)$, $\omega(i)$, and $t(i)$ are a set of parameters associated with the i th evoked potential component. The model assumes that each component has the form of an impulse at time $t(i)$ followed by a damped oscillation. The rate of decay is determined by $\beta(i)$, and the rate of oscillation is $\omega(i)/2\pi$. The $\{A_{i,l}\}$ are the gains at individual leads.

Model 2 was fit to each subject's waveforms averaged over all trials for each of the three target stimuli using a nonlinear optimization procedure with a set of 100 randomly generated starting values.

Two decompositions attempted are shown in the next section, entitled Results. One consisted of four components, the bare minimum necessary to model the evoked potential elicited by a visual target paradigm in the interval between 20 and 2,058 milliseconds. The visible activity consists of P1, which was ignored because of its relatively small size, N1, P2, N2, P3, and late slow ac-

tivity concentrated in the frontal leads and probably corresponding to the slow wave. It was omitted from consideration in testing for differences between stimulus conditions.

This activity can be minimally fit by a single component concentrated on N1, a second component for P2 and N2, a third component for P3, and a fourth component for the slow wave late activity. The second model for the evoked potential includes all of the components of the minimal model and an additional second component for P3. This component has higher frequency than the first.

Topographic Analysis

The topographies of individual components are displayed as current source density maps. Current densities were computed by the Laplacian derivatives of the potentials, using the spherical spline approach of Perrin et al. (1989).

An indicator of the possible usefulness of the method is its ability to separate the evoked potentials elicited by different stimulus conditions. With this in mind, statistical tests for differences in component potentials and current source densities between stimulus conditions were carried out. Significance probability maps were constructed from these tests.

The next section, entitled Results, gives examples of the kinds of significance probability maps that are appropriate for this problem. They include both univariate (Student's t) and multivariate (Hotelling's T^2)

maps, the latter used as a means of combining the information for closely associated distance measures. Two examples of the latter are given. The first is distance, based jointly on two or more components, such as those that make up the early (N1-P2-N2) activity. The second is a two-way distance measure among the three target conditions (nontarget versus target, easy target versus hard target). The use of such combined measurements is, like the MRA itself, a means of reducing the amount of visual information to be presented. All tests are based on differences within subjects rather than differences between averages.

Both the statistics themselves and their associated probability measures can be used as bases for maps. The statistics are generally preferable, and we have used them. The Discussion section covers the reason for this.

Hotelling's T^2 and stepwise discriminant analysis were used as global measurements of topographical distances among the stimulus conditions. The Hotelling's T^2 was based on a nine-dimensional random variable constructed by averaging the potentials of laterally symmetric pairs of leads, excluding the frontal and occipital regions. A separate Hotelling's T^2 test was done for each component and for both target/nontarget and easy target/hard target dichotomies. Both three-way (all target conditions) and two-way (target versus nontarget) discriminant analyses were performed. Equal prior prob-

abilities were specified, so that the overall null expected misclassification was two-thirds for the three-way discriminant analysis and one-half for the two-way discriminant analysis. Cross-validation was used as a means of estimating errors.

RESULTS

Two models, one consisting of four exponentially decaying sinusoidal components and the other consisting of five such components, are summarized in table 1, which gives the values of the parameters for the grand mean of the 24 subjects. Each component is specified by three parameters: the time at which its activity begins (t), the rate at which it decays (β), and the frequency at which it oscillates ($\omega/2\pi$). As explained in the beginning of this chapter, these parameters are the same for all leads. We have also included the peak time and the goodness of fit statistic for the model. This last is the ratio of the sum of squares of errors to the sum of squares of total (SSE/SST).

Figure 1 gives the set of topographic maps for the four-component model under the easy target condition. Because of the independence of the dynamic and spatial properties of the model, these maps and the traces of the individual components at any lead carry all the model's information. The topographic map of each component corresponds to its current source density at its peak.

Table 1. Averaged MRA components

	Nontarget			Easy target			Hard target		
	β	ω	t	β	ω	t	β	ω	t
A1	11.384	19.834	.1066	10.593	18.406	.1081	10.548	17.598	.1104
A2	13.368	24.448	.1633	12.155	23.622	.1617	12.073	24.995	.1618
A3	4.828	6.992	.2330	4.131	6.660	.2577	4.292	5.639	.2579
A4	3.349	2.710	.5115	2.657	2.496	.5373	2.748	2.457	.5308
B1	9.522	24.599	.1112	10.424	24.058	.1113	9.254	24.441	.1076
B2	10.619	22.869	.1599	8.589	21.445	.1610	9.574	21.207	.1530
B3	6.551	7.104	.2434	5.627	6.637	.2576	5.972	6.926	.2587
B4	3.472	10.476	.2403	3.218	9.564	.2448	3.524	9.866	.2463
B5	3.009	2.438	.4634	3.332	2.565	.4974	2.662	2.449	.4792

The components of the four-component model are denoted A1 through A4, and the components of the five-component model are denoted B1 through B5. A1 and A2 are essentially identical to B1 and B2. For both models, these fit the early N1-P2-N2 activity, with A1 and B1 essentially fitting N1. As the topographic maps show, these compo-

nents are in the lateral parietal and occipital regions. A4 is also clearly identifiable with B5, both components fitting a slow activity located frontally that follows P3. This component is probably the slow wave.

B3 and B4 correspond jointly to A3, which fits P3. In both its frequency and its topography, B3 resembles A3 much more closely than

FIGURE 1a

Current source densities for four-component MRA model: easy target condition. Blue is maximal negativity; red is maximal positivity.
A1: N1 component.

FIGURE 1b

Current source densities for four-component MRA model: easy target condition. Blue is maximal negativity; red is maximal positivity.
A2: P2/N2 component.

FIGURE 1c

Current source densities for four-component MRA model: easy target condition. Blue is maximal negativity; red is maximal positivity. A3: P3 component.

FIGURE 1d

Current source densities for four-component MRA model: easy target condition. Blue is maximal negativity; red is maximal positivity. A4: late low-frequency activity.

does B4 and may be taken to be the primary P3 component. B4 is a possible secondary P3 component; it seems to be both frontal and parietal but not central. It may reflect the contributions of two distinct generators; alternatively, the parietal activity might be a consequence of the limitations of the

MRA due to nonlinearities. B4 was not used in the statistical analysis.

Table 2 summarizes the results of the Hotelling's T^2 tests both for potential and current source density. A3, which corresponds to P3, showed the greatest differences ($p=0.004$ for potential, $p=0.007$ for current density) between target and nontarget. A2, the joint P2–N2 com-

Table 2. Hotelling's T^2 for global differences

	Nontarget/target			Easy target/hard target		
	F	df	p	F	df	p
A1	1.498 (1.405)	9,16 (9,16)	.230 (.265)	.977 (.852)	9,16 (9,16)	.493 (.583)
A2	3.470 (2.788)	9,16 (9,16)	.015 (.035)	2.675 (2.510)	9,16 (9,16)	.041 (.052)
A3	4.594 (4.034)	9,16 (9,16)	.004 (.007)	.747 (.800)	9,16 (9,16)	.664 (.622)

Entries in parentheses are derived from current source density estimates, and the corresponding potential derived values are above them.

Table 3. Three-way classification

	Resubstitution			Cross-validation		
	Nontarget	Easy target	Hard target	Nontarget	Easy target	Hard target
Nontarget	100.00 (79.19)	0.00 (12.50)	0.00 (8.33)	91.67 (75.00)	4.17 (16.67)	4.17 (8.33)
Easy Target	4.17 (16.67)	83.33 (66.67)	12.50 (16.67)	12.50 (16.67)	58.33 (62.50)	29.17 (20.83)
Hard Target	4.17 (29.17)	8.33 (20.83)	87.50 (50.00)	16.67 (33.33)	20.83 (25.00)	62.50 (41.67)

Entries are percent classified into column. Entries in parentheses are derived from current source density estimates.

ponent, showed appreciable differences both for target/nontarget ($p=0.015$ for potential, $p=0.035$ for current density) and for easy target/hard target ($p=0.041$ for potential, $p=0.052$ for current density). It was the only component to show a strong difference between the two target conditions. A1, the N1 component, showed little difference, either between target and nontarget or between easy and hard target conditions. Significance levels were consistently better for potential than for current source density, but the differences were not large.

Tables 3 and 4 summarize the results of the discriminant analysis. Both two-way and three-way classifications were quite successful; misclassification levels were well below those expected. Classification based on potential was somewhat better than classification based on current source density; for two-way (target versus nontarget) classification, the level of misclassification

for current density was more than twice that for potential.

Figures 1–4 summarize the topography of the MRA components. Figure 1 shows the topography of the four-component model for the easy target condition, and figure 2 shows the topography of the five-component model for the hard target condition. Figures 3 and 4 show the topographies of the components of the four-component model for the nontarget and hard target stimuli, respectively.

Figure 5 shows significance probability maps for component A3 of the four-component model. Figures 5a–c are the individual paired t statistics for each of the three targets, and figure 5d is a map of Hotelling's T^2 statistics.

DISCUSSION

The MRA

The MRA approach is one of a number of possible ways to model

Table 4. Two-way classification

Resubstitution		Cross-validation	
Nontarget	Target	Nontarget	Target
8.33 (20.83)	6.25 (18.75)	8.33 (20.83)	10.42 (25.00)

Entries are percent misclassified. Entries in parentheses are derived from current source density estimates.

and fit the elementary components of an evoked potential. Which method one chooses depends on a number of factors and may well differ from problem to problem. Here, the salient features of the MRA and alternative methods are discussed. The alternative methods we consider are principal components analysis, the intersubject decomposition suggested by Mocks (1988), and dipole-based decomposition methods. It should be noted that these methods are not mutually ex-

clusive: A paper by Turetsky et al. (1990) makes use of both dipole modeling and the MRA.

The distinctive feature of the MRA is that it makes use of a dynamic form that can be derived from a set of differential equations describing neuronal interactions. The multilead form assumes in addition that the time required for the signal to propagate through the head is short, relative to the duration of the evoked potential, and that the temporal and dynamic

FIGURE 2a

Current source densities for five-component MRA model: hard target condition. Blue is maximal negativity; red is maximal positivity. B1: N1 component.

FIGURE 2b

Current source densities for five-component MRA model: hard target condition. Blue is maximal negativity; red is maximal positivity. B2: P2/N2 component.

FIGURE 2c

Current source densities for five-component MRA model: hard target condition. Blue is maximal negativity; red is maximal positivity. B3: low-frequency P3 component.

FIGURE 2d

Current source densities for five-component MRA model: hard target condition. Blue is maximal negativity; red is maximal positivity. B4: high-frequency P3 component.

properties of a specific component are independent of each other.

Principal components analysis, which is the earliest method of decomposing evoked potentials (Donchin 1966), is based on the assumption that components are unrelated in their noise. Since this

assumption is not sufficient to generate a unique solution, additional, more arbitrary constraints must be added. Those used in practice, such as varimax rotation, are drawn from factor analysis.

Mocks' decomposition method is based on the assumption that ERP components differ between subjects only in their relative strengths and not in their individual dynamic or spatial properties. Using this idea, one can replace model 1 with a sum of three-way products:

$$\Phi_{l,s,t} = \sum_j \alpha_{l,j} \beta_{s,j} \gamma_{t,j} \quad (4)$$

where $\Phi_{l,s,t}$ is the ERP for the subject s at lead l and time t, and where the summation is over the set of components. Mocks shows that this decomposition is unique.

Dipole-based decomposition methods were first used extensively by Scherg and his coworkers (1984, 1985a, 1985b, 1989), although a

FIGURE 2e

Current source densities for five-component MRA model: hard target condition. Blue is maximal negativity; red is maximal positivity. B5: late low-frequency activity.

FIGURE 3a

Current source densities for four-component MRA model: nontarget condition. Blue is maximal negativity; red is maximal positivity.
A1: N1 component.

FIGURE 3b

Current source densities for four-component MRA model: nontarget condition. Blue is maximal negativity; red is maximal positivity.
A2: P2/N2 component.

FIGURE 3c

Current source densities for four-component MRA model: nontarget condition. Blue is maximal negativity; red is maximal positivity.
A3: P3 component.

FIGURE 3d

Current source densities for four-component MRA model: nontarget condition. Blue is maximal negativity; red is maximal positivity.
A4: late low-frequency activity.

body of mathematical work pre-dated that. They are based on the assumption that the evoked potential is the product of a small number of sources each of which can be approximated by a mathematical point with a linear charge separation. Depending on the particular

model, the dipole may be regarded as fixed in orientation or free to change direction, and the dynamic change of the dipole charge may similarly be modeled or left free to vary with the data.

The usefulness of a particular approach depends on a number of

FIGURE 4a

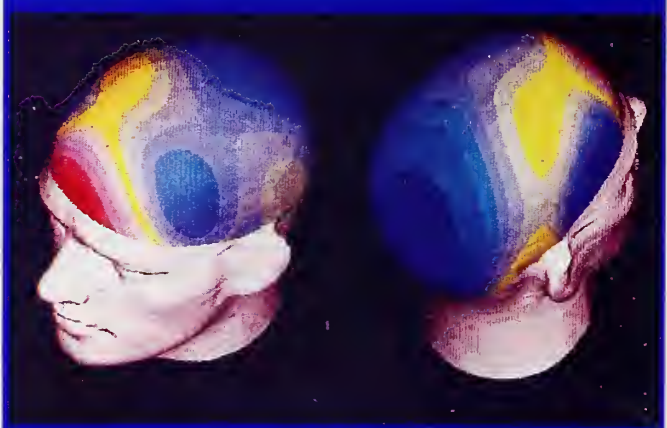
Current source densities for four-component MRA model: hard target condition. Blue is maximal negativity; red is maximal positivity.
A1: N1 component.

FIGURE 4b

Current source densities for four-component MRA model: hard target condition. Blue is maximal negativity; red is maximal positivity.
A2: P2/N2 component.

FIGURE 4c

Current source densities for four-component MRA model: hard target condition. Blue is maximal negativity; red is maximal positivity.
A3: P3 component.

FIGURE 4d

Current source densities for four-component MRA model: hard target condition. Blue is maximal negativity; red is maximal positivity.
A4: late low-frequency activity.

factors, including the correctness of a model, its accuracy (given that it is correct), its computational tractability, and its sensitivity to departures from the assumptions on which it is based. With regard to these criteria, the following can be mentioned.

Principal components decomposition is unquestionably the best in terms of its numerical tractability. Not only does it require relatively few computations, but the fact that it does not necessitate a nonlinear search means that its results are exactly replicable when it is con-

ducted twice on the same data. Results of nonlinear optimization will depend on factors extraneous to the model. On the other hand, the assumptions on which principal components are based are tenuous in the biological sense. This is true not only of the rotation criteria in the model, but even the assumption of unrelated noise for different components. While this last seems

reasonable, it is in poor accord with the notion of communication between different sources. Principal components analysis has been shown (Wood and McCarthy 1984) to misallocate the signal at least to some degree. Coupled with its weak justification in the first place, this casts doubt on its usefulness.

Mocks' decomposition makes the same spatiotemporal independence

FIGURE 5a



Significance probability maps. Paired t statistic: easy target—nontarget differences.

FIGURE 5b



Significance probability maps. Paired t statistic: hard target—nontarget differences.

FIGURE 5c



Significance probability maps. Paired t statistic: hard target—easy target differences.

FIGURE 5d



Significance probability maps. Hotelling's T² statistic for three-way differences.

assumptions that our MRA model uses. Its defining criterion, that components between individuals differ primarily in their relative strengths, is hard to assess in terms of biological reasonableness. That criterion is clearly an idealization, but it would be useful if the differences in relative strengths were greater than spatial or temporal differences between subjects of their individual components. The biological reasonableness of this is hard to assess on a priori grounds; certainly, it does not follow as a consequence of any model of the brain. It might be interesting to see how the method compares with other decomposition methods when applied to a real data set.

Dipole-based decomposition methods have the advantage that there is no doubt regarding the physical model on which they are based. Evoked potentials certainly originate from charge separations at loci inside the head, and these can be modeled using classical results in electrical field theory. In addition, dipole models do not require that the temporal and spatial aspects of an evoked potential component should be unrelated, because moving and rotating dipoles can be modeled.

An additional advantage of the MRA to a dipole-based decomposition is that it may well require fewer discrete entities for an adequate model because extended dipole sheets may require multiple dipoles for an adequate modeling. An extended dipole sheet producing a coherent MRA component is

intrinsically more plausible than a highly localized source producing a dynamically diffuse signal.

In summary, MRA-based decomposition and dipole-based decomposition are the only decomposition methods among those mentioned that have a clear biological justification. Neither is clearly superior to the other in all respects, and which is the appropriate one to use may depend on the specific application. The MRA topographic analysis is more of an exploratory method than dipole modeling.

The Components

We have described the two models that were used and our reasons for believing that the appropriate number of components is either four or five. In the case of the four-component model, there is a clear need for all of the components if all of the most obvious peaks are to be fit. The second P3 component, which is where the models differ, was motivated by topographic features of the data.

An examination of the grand means ERP at all leads showed P3 to be somewhat narrower at the base for the frontal leads than for the coronal and parietal leads, indicating a faster dominant frequency at those leads. Since filtering cannot give rise to new frequencies, the possibility of two distinct components seems likely. Further, it is unlikely that the early activity can be an explanation, partly because its frequency is appreciably higher and partly because it seems to be damped too quickly to account for

an effect observed at the time of P3.

Given that the suggested activities occur cotemporally, it is hard to know how well they could be separated, on the basis of the available data. The topography of B4 shows activity both frontally and parietally but not coronally, which is hard to reconcile as the activity of a single source. A possible explanation for the parietal activity is that there is not a distinct source toward the back, but a system nonlinearity induced by the magnitude of P3. This is a possible shortcoming of the MRA, and it may be necessary to go to nonlinear systems and numerically solved differential equations in order to overcome this. If system nonlinearity is the reason for the parietal topography of B4, P3 could arise from two distinct sources, one located frontally and the other located centrally or parietally, that discharge at about the same time and differ in frequency. Confirmation of that must await further investigation based on more data.

The use of two components to fit the NI-P2-N2 activity is underfitting, at least from the biological perspective. A difficulty with the evoked potential being examined is that the peaks vary greatly in size. P3, for example, is considerably larger than P1. There are severe practical difficulties in fitting components of different scales, and we have not attempted to do so here. Adequate modeling of the early activity would probably necessitate truncating the signal after N2.

Analytical Results

The results of the analysis are supportive of the idea that MRA-based topography can be a useful means of studying evoked potentials and the effects of different brain states. Cross-validated classification levels based on component potentials were good (10 percent two-way misclassification and 30 percent three-way misclassification), and the significance levels and topographic patterns of the significance probability maps correspond reasonably to the results of other studies. Thus, for example, A3 and A1 both have well-defined topographies, but only A3 has strong significance or a well-defined significance topography.

Both the topography and the significance pattern of the A2 and B2 components suggest the involvement of more than one generator, at least for target conditions. The use of a single component under these circumstances is not the best possible solution. As we mentioned in the last subsection, it would probably be necessary to truncate the ERP prior to P3 in order to fit the early activity completely.

SUMMARY

A method of analyzing the topography of evoked potentials, together with some results of applying it to a set of data, have been presented. The results are consistent with what is known from other studies. We have shown that it is possible to distinguish between different stimulus conditions using

this method and to discuss the spatial aspects of the differences.

In recent years, EEG and ERP topographical displays have proved useful in clinical diagnosis and neurological investigations. The practical value of such exploratory methods is supported by the success of the analytically simple BEAM system of Duffy et al. (1979). Our intention is to combine a model-driven decomposition with a data-driven topographical analysis as a means of looking deeper into the data without modeling all aspects of it.

This is not to deny the value of purely modeling efforts such as dynamic dipole models. Such models will doubtless prove extremely useful in understanding the workings of the brain. They can be considered to be the confirmatory part of an analytic effort in which methods such as ours are exploratory and diagnostic. The chief advantage of a method that is partly exploratory in nature is that it depends on fewer assumptions and is more useful in spotting patterns. On the other hand, a method that is only partly exploratory is capable of revealing things that a purely exploratory method might not.

Future improvements of the method could include incorporating nonlinearities into the dynamics and taking into account the autoregressive aspects of the noise.

ACKNOWLEDGMENTS

This study was supported by National Institute on Alcohol Abuse

and Alcoholism grants AA-05524 and AA-02686 to Dr. Henri Begleiter.

REFERENCES

- Achim, A.; Richer, F.; and Saint-Hilaire, J.M. Methods for separating temporally overlapping sources of neuroelectric data. *Brain Topogr* 1:22–28, 1988.
- Cuffin, B.N., and Cohen, D. Magnetic fields of a dipole in special volume conductor shapes. *IEEE Trans Biomed Eng* 24:372–381, 1977.
- Donchin, E. A multivariate approach to the analysis of averaged evoked potentials. *IEEE Trans Biomed Eng* 13:131–139, 1966.
- Duffy, F.H.; Bartels, P.H.; and Burchfiel, J.L. Significance probability mapping: An aid in the topographic analysis of brain electrical activity. *Electroencephalogr Clin Neurophysiol* 51:455–462, 1981.
- Freeman, W.J. *Mass Action of the Nervous System*. New York: Academic Press, 1975.
- Kavanagh, R.N.; Darcey, T.M.; Lehmann, D.; and Fender, D.H. Evaluation of methods for three-dimensional localization of electrical sources in the human brain. *IEEE Trans Biomed Eng* 25:421–429, 1978.
- Maier, J.; Dagnelli, G.; Spekreijse, H.; and van Dijk, B.W. Principal components analysis for source localization of VEPs in man. *Vision Res* 22:165–177, 1987.
- Mocks, J. Topographic components model for event-related potentials and some biophysical considerations. *IEEE Trans Biomed Eng* 35:482–484, 1988.

O'Connor, S.J.; Tasman, A.; Simon, R.H.; and Hale, M.S. A model referenced method for the identification of evoked potential component waveforms. *Electroencephalogr Clin Neurophysiol* 55:233-237, 1983.

Perrin, F.; Pernier, J.; Bertrand, O.; and Echallier, J.F. Spherical splines for scalp potential and current density mapping. *Electroencephalogr Clin Neurophysiol* 72:184-187, 1989.

Scherg, M. Spatio-temporal modelling of early auditory evoked potentials. *Revue de Laryngologie* 105:103-170, 1984.

Scherg, M.; Vajasari, J.; and Picton, T.W. A source analysis of the late human auditory evoked potentials. *J Cognit Neurosci* 1:336-355, 1989.

Scherg, M., and von Cramon, D. Two bilateral sources of the late AEP as identified by a spatio-temporal dipole model. *Electroencephalogr Clin Neurophysiol* 62:32-44, 1985a.

Scherg, M., and von Cramon, D. A new interpretation of the generators of BAEP waves I-V: Results of a spatio-temporal dipole model.

Electroencephalogr Clin Neurophysiol 62:290-299, 1985b.

Sidman, R.D.; Giambalvo, V.; Allison, T.; and Bergey, P. A method for the localization of human cerebral potentials evoked by sensory stimuli. *Sensory Proc* 2:116-129, 1978.

Turetsky, B.; Raz, J.; and Fein, G. Representation of multi-channel evoked potential data using a dipole component model of intracranial generators: Application to the auditory P300. *Electroencephalogr Clin Neurophysiol* 76:540-556, 1990.

Vaughan, H.G.; Weinberg, H.; Lehmann, D.; and Okada, Y. Approaches to defining the intracranial generators of event-related electrical and magnetic fields. *Electroencephalogr Clin Neurophysiol* 38:505-544, 1986.

Wood, C.C., and McCarthy, G. Principal component analysis of event-related potentials: Simulation studies demonstrate misallocation of variance across components. *Electroencephalogr Clin Neurophysiol* 59:249-260, 1984.

Nuclear Magnetic Resonance Imaging Section

STRUCTURAL IMAGING OF THE BRAIN IN CHRONIC ALCOHOLISM

Adolf Pfefferbaum, M.D.,^{1,2} Kelvin O. Lim, M.D.,^{1,2} and Margaret Rosenbloom, M.A.²

Heavy alcohol consumption over a period of many years can lead to cognitive and neurological impairments. Presumably, these impairments are due to the direct toxic effects of alcohol on the brain, as well as the nutritional deficiency, intercurrent disease, and trauma frequently associated with alcoholism. Early studies of the brain, which could only be performed post mortem, showed that chronic alcoholics had greatly reduced brain volume. Patients with the alcohol-associated nutritional deficiency disease known as Wernicke-Korsakoff syndrome (WKS) also have characteristic lesions in subcortical brain regions.

Modern *in vivo* neuroimaging techniques enable observation and quantification of macroscopic structural brain changes related to alcohol abuse while the patient is still alive. Thus it is now possible to relate these structural brain alter-

ations to concurrent clinical characteristics and to determine whether changes progress with continued drinking or reverse during periods of abstinence. Neuroimaging techniques to be described here include both computed tomography (CT) and magnetic resonance imaging (MRI). Both provide quantifiable three-dimensional images of brain structure.

ACRONYMS

CSF	cerebrospinal fluid
CT	computed tomography
MRI	magnetic resonance imaging
NMR	nuclear magnetic resonance
RF	radiofrequency
T1 and T2	exponential time constants
TE	time after excitation at which signal is detected
TR	radiofrequency repetition rate
WKS	Wernicke-Korsakoff syndrome

¹Psychiatry and Behavioral Sciences, Stanford University School of Medicine, Stanford, CA 94305

²Psychiatry Service, Department of Veterans Affairs Medical Center, Palo Alto, CA 94394

CT studies of in vivo brain changes in chronic alcoholics first demonstrated enlarged lateral ventricles in the mid-1970s (Fox et al. 1976) and provided confirmation of earlier, in vivo reports using pneumoencephalography (Haug 1962), as well as post mortem reports (Courville 1955; Victor et al. 1971). MRI studies began to appear in the literature in the late 1980s, confirming and extending CT findings in several ways. The following brief description of these techniques comprises the information already known about the effects of chronic consumption of excessive amounts of alcohol on brain structure and some of the questions still to be addressed.

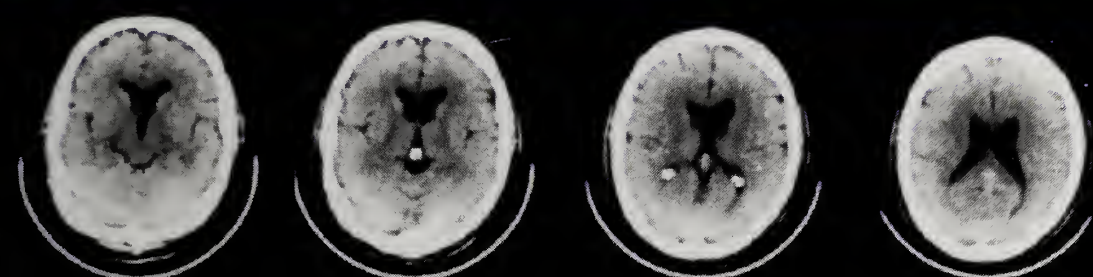
COMPUTED TOMOGRAPHY

With CT, one can image the human brain in three dimensions, using x-ray beams projected at multiple angles through axial sections of the brain (Oldendorf 1980). The x-ray beams are attenuated by different degrees as they travel through bone, brain tissue, and cerebrospinal fluid (CSF), according to these tissues' various electron densities. Back-projection reconstruction algorithms are used on the attenuation values of all the x-ray projections, producing a matrix of pixels with a value that can be visually expressed as a specific intensity on a computer console or x-ray film. Bone has a high CT number, thus appears bright, while CSF, having a low number, appears dark;

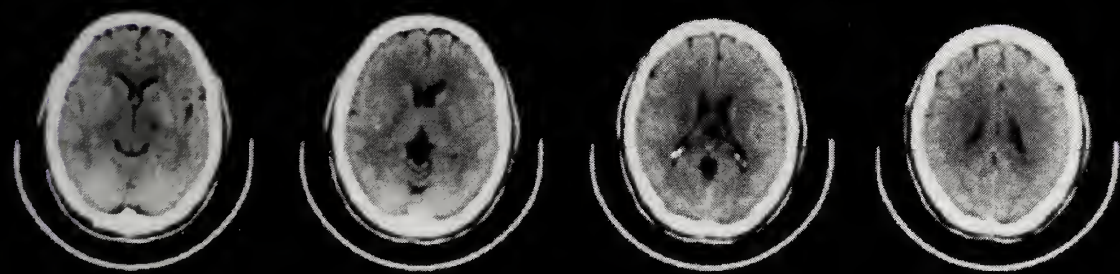
brain parenchyma numbers fall in between. The matrix of CT numbers forms an image in which skull boundaries and CSF-filled spaces are clearly visible. Some differentiation between soft tissue types is also possible.

A typical CT scan, starting rostrally and proceeding caudally, produces a series of axial images that represent adjacent slices of brain. Figure 1 illustrates two such sets of images, one from a healthy 35-year-old man and the other from a man of comparable age with a history of chronic alcohol dependence. Figure 2 presents similar data from a 60-year-old alcoholic patient and a 61-year-old control subject. Comparison of figures 1 and 2 shows that the dark medial fluid-filled spaces (ventricles) increase in size with age in the controls and that enlargement is even greater in the alcoholic patients.

The images from first-generation CT scanners were often based on small matrices of pixels (e.g., 80x80) and quite limited in resolution. Modern scanners typically produce images with up to 512x512-pixel matrices that provide more fine-grained resolution, including some differentiation of white matter from gray matter. However, even with high resolution scanners, the image is almost always less precise than it appears. Each pixel represents the average value for a voxel (the three-dimensional volume element observed) which may be as little as 1x1 mm in the imaging plane but is usually 5–10 mm thick. This

FIGURE 1

36-year-old alcoholic man
lifetime alcohol consumption=1570 kg



35-year-old healthy community male volunteer
lifetime alcohol consumption=105 kg

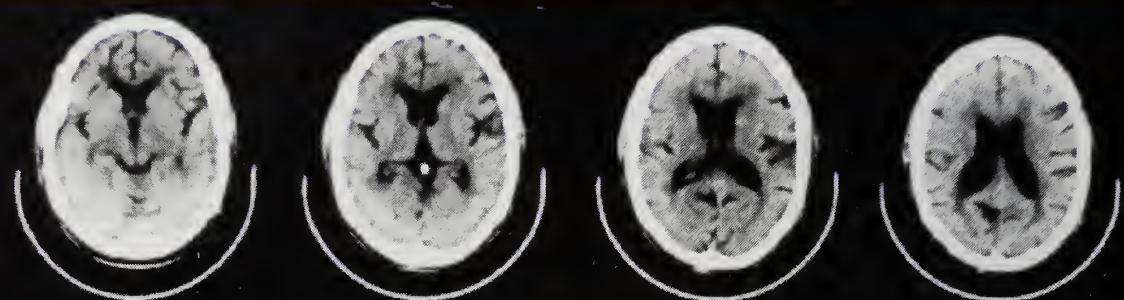
Axial CT brain sections, each 10-mm thick, from a 35-year-old healthy man and a 36-year-old man with a history of heavy alcohol consumption.

phenomenon, referred to as "volume averaging," limits the resolution of all neuroimaging modalities.

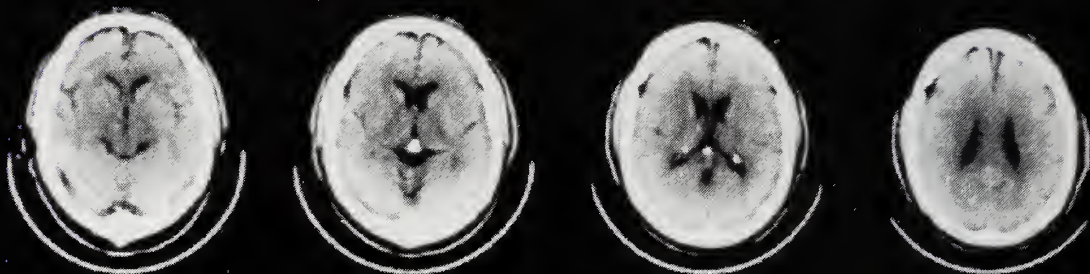
Under normal conditions, growth of the brain determines the size of the head. Brain and CSF occupy a closed space within the skull. Thus, increased amounts of CSF, in a previously healthy brain, are generally believed to result from brain tissue shrinkage. CT is useful in providing noninvasive visualization and quantification of brain tissue loss in the living subject. The ventricles and sulci (CSF-filled spaces) show up clearly on successive axial sections and have been measured in differ-

ent ways. Some investigators compare images with clinical standards based on their own experience or rank images against one another. Others measure ventricular width at various points or trace boundaries to calculate area.

Computerized techniques to measure these CSF-filled spaces more precisely have also been developed. One such technique first uses filters to remove some of the artifact at the skull boundaries and allows classification of each pixel in the image as either CSF or tissue (Pfefferbaum et al. 1986). The number of pixels classified as CSF in the

FIGURE 2

**60-year-old alcoholic man
lifetime alcohol consumption=1634 kg**



**61-year-old healthy community male volunteer
lifetime alcohol consumption=92 kg**

Axial CT brain sections, each 10-mm thick, from a 61-year-old healthy man and a 60-year-old man with a history of heavy drinking.

inner, or subcortical segment of each brain section can be summed to provide an estimate of the volume of the lateral ventricles, while the number of pixels classified as CSF in the outer, or cortical portion of each brain segment can be summed to provide an estimate of the volume of sulcal fluid. Further localization of cortical changes can be accomplished by dividing each brain section geometrically and combining subdivisions across sections in order to get approximate measures of the frontal, parietal/occipital, and temporal lobes. Because of substantial differences

in head size, and therefore brain size, across individuals, data are usually corrected for head size, either by regression analysis (Jernigan et al. 1982) or by expression as a percentage of total intracranial volume (Pfefferbaum et al. 1990b).

While CT has provided new insights into the effects of alcohol on brain morphology, this technology is limited by its resolution and by artifacts. For instance, CT images cannot distinguish whether the increased subcortical and cortical CSF spaces are at the expense of white matter, gray matter, or both. Furthermore, since CT scanning

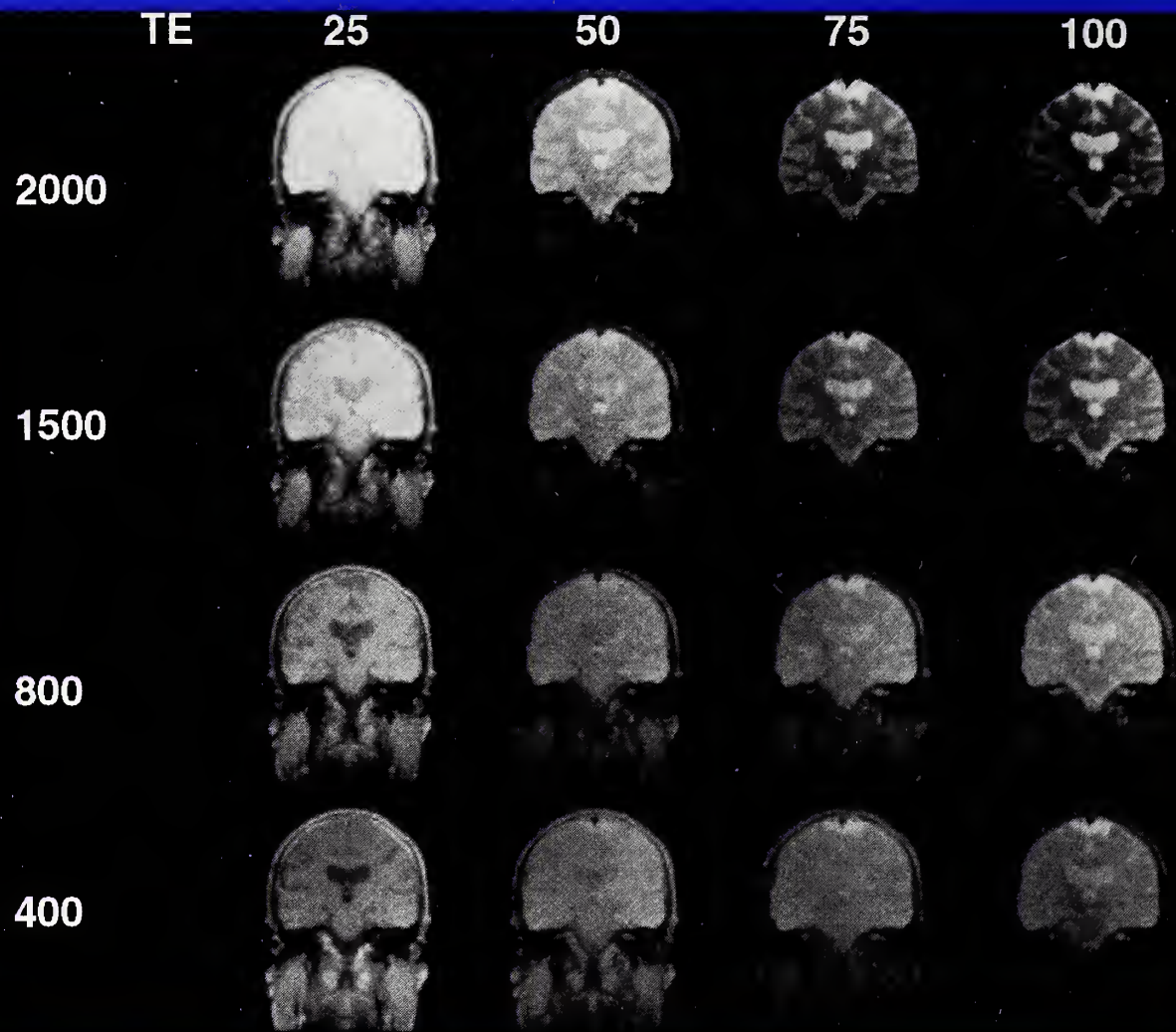
involves ionizing radiation, safety considerations limit the number and frequency of scans, especially in healthy control subjects, making it hard to evaluate test-retest reliabilities for CT data and to develop the control values essential for assessing progression or reversibility of tissue loss. In addition, some of the lesion sites, such as the cerebellum and mammillary bodies, associated with chronic alcoholism and WKS are hard to assess quantitatively on CT scans because they are obscured by artifacts from surrounding bony structures or are not optimally visualized in the axial plane. Application of the recently developed nuclear magnetic resonance (NMR)--which is free of the problem of ionizing radiation exposure, is flexible in imaging orientation, and yields excellent soft tissue contrast--promises to overcome many of these limitations.

MAGNETIC RESONANCE IMAGING (MRI)

Used instead of x-ray technology, MRI takes advantage of the fact that the nuclei of certain atoms exhibit MR and behave like small spinning magnets that align themselves when they are exposed to a strong magnetic field. When radio waves are applied perpendicular to the magnetic field at the frequency at which the atoms are spinning, the atoms absorb this energy and their alignment in the magnetic field is disturbed. When the radio waves are turned off, the nuclei realign in the magnetic field and give off en-

ergy detectable with an antenna (Oldendorf and Oldendorf 1988). Because hydrogen is the most abundant component of biological tissue, almost all clinical MRI scanners use the resonant frequency of hydrogen atoms (protons) to form images. The resulting signals arise predominantly from water, with a small contribution from lipids.

The proton MR image is primarily determined by variations in proton density, T1, and T2. Proton density reflects the number of hydrogen nuclei stimulated. T1 is an exponential time constant measuring the time required by nuclei to return to equilibrium and realign with the magnetic field after pulsation with radiofrequency (RF) waves. T2 is the exponential time constant describing signal loss due to interference between hydrogen nuclei. Proton density, T1, and T2 differ in various biological tissues, providing the subtle gradations by which details of brain structure can be seen. The relative intensities of these tissue types will vary in an MR image, depending on the time between application of the RF pulses used to elicit an MR image and the time after pulsation at which the signal is recorded. MRI acquisition protocols can be designed to emphasize differences between certain types of tissue while minimizing differences between others. For example, under certain circumstances, a "T1-weighted image" emphasizes differences between white matter and gray matter, but can render brain tissue and CSF isointense. On the other hand, a "T2-weighted

FIGURE 3**Coronal MR images of varying T1 and T2 combinations.**

"image" can be used to emphasize CSF-tissue contrast.

Figure 3 demonstrates the effects on tissue contrast achieved by varying the RF repetition rate (TR) and the time after excitation at which the signal is detected (TE) in a spin echo sequence. The TE are 25, 50, 75, and 100 milliseconds across the columns, each collected at TR of 2,000, 1,500, 800, and 400 milliseconds down the rows. The signal gets weaker as the TE increases, but the CSF fades more slowly than brain parenchyma be-

cause it has a longer T2. The longer TR, longer TE images, e.g., row 2 (TR=1,500) and column 4 (TE=100), are referred to as "T2 weighted." Tissues with a long T2 are bright. Going down the rows, one can also see that the intensity decreases as TR decreases. With declining TR, there is less time for the protons to return to equilibrium and less energy is returned after each RF pulsation. As TR decreases, the CSF decreases in intensity faster than brain parenchyma because it has a longer T1 than tissue and thus has recov-

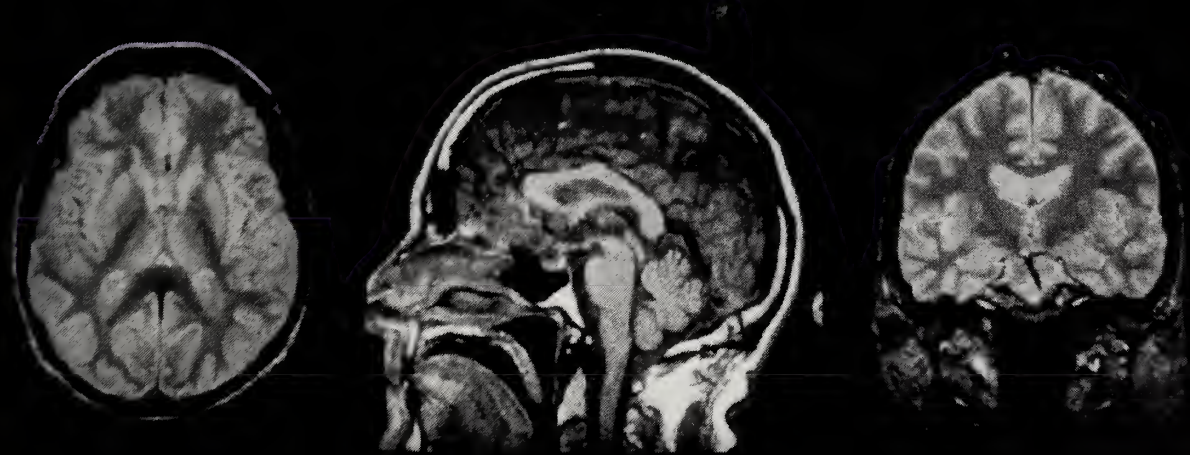
ered less since the last pulsation, producing a weaker signal. The short TR (e.g., row 4), short TE (e.g., column 1, TE=25) images are called "T1 weighted." Tissues with a short T1 are bright.

In addition to flexibility in highlighting soft tissue differences, MRI facilitates viewing the brain from different directions. During scanning, magnetic gradients can be applied in the three orthogonal directions, or planes, providing information about the spatial location of the signals in each plane. This facilitates viewing the brain and particular structures within it, not only from bottom to top (axial), as in

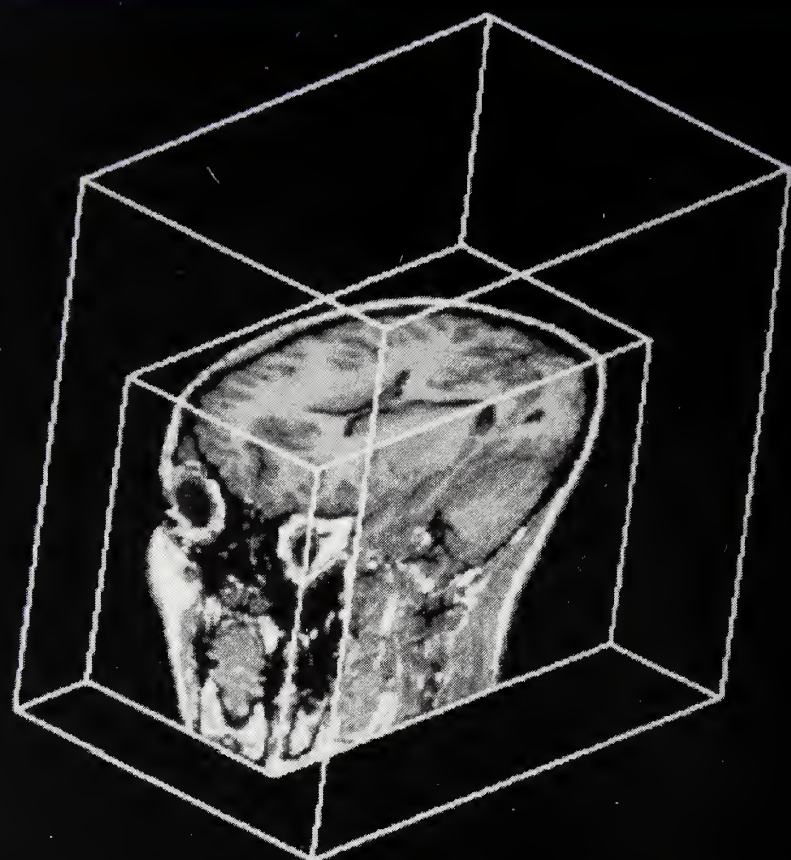
conventional CT images, but also from front to back (coronal), from left to right (sagittal), or at any oblique angle to these planes. Figure 4 presents images acquired in the axial, sagittal, and coronal planes and demonstrates the fine anatomic detail of small folia of the cerebellum on the sagittal section and the superb gray-white separation on the axial section. The bright signals outside the brain on these images are from fat in the skull bone marrow and scalp.

An advantage of MRI over CT is that bone itself produces a very small signal in most MRI acquisition sequences, eliminating this source

FIGURE 4



MR images illustrating axial, coronal, and midsagittal planes.

FIGURE 5

Three-dimensional MR image of 27-year-old healthy female's brain cut to reveal axial, sagittal, and coronal surfaces.

of artifact. Thus major sulci and surface gyri, as well as bone-encased structures at the base of the brain, can be clearly visualized and accurately measured. Although an MR image can be almost as detailed and clearly defined as a pathological brain section, it should be remembered that, like CT images, this image reflects values averaged over slices of fixed thickness, usually 3–10 mm (i.e., the image pixels represent brain voxels, with height, width, and depth).

Recent developments in MRI technology now enable the acquisition of three-dimensional MR images with almost isotropic voxels (e.g., $1.5 \times 0.9 \times 0.9$ mm). Such images may include a large proportion of the brain, and image analysis software allows this large data set to be stored and viewed from an almost infinite number of angles. In figure 5, which presents such an image set, axial, sagittal, and coronal surfaces are visible.

NEUROANATOMIC CHANGES ASSOCIATED WITH CHRONIC ALCOHOLISM

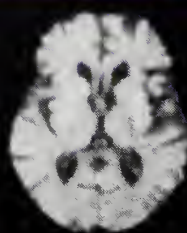
Any study of the neuroanatomic changes associated with alcoholism must take into account the normal decreases in tissue and the increase in CSF volume (i.e., brain shrinkage) that occurs in the normal aging brain (Pfefferbaum et al. 1986; Stafford et al. 1988). One approach is the statistical method of regression analysis. Data from a population of healthy community controls are regressed on age to establish age norms for each measure. Data from each alcoholic patient can then be converted into Z scores, which express the extent to which a patient differs from the norms for his or her age. Regression analysis permits assessment of the effects of disease, while controlling for the effects of normal aging. Because this method does not exclude examination of the influence of the total amount of alcohol consumed, which often covaries with age, we have implemented it in our approach to the studying of neuroanatomic variables in various patient populations (Pfefferbaum et al. 1988*a,b*, 1990*a,b*).

Several neuroimaging studies of alcoholic patients that reported increases in the size of the lateral ventricles and cortical sulci are described in reviews by Lishman (1990) and Wilkinson (1987). Figure 6 contrasts MR images from a healthy 57-year-old and an alcoholic man of the same age. The images have been computer processed to ap-

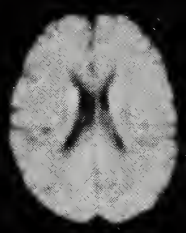
pear as slices of brain with the CSF drained away.

Increased CSF space seems to occur throughout the brain and exceeds age norms to a greater extent in alcoholic patients who are older than those who are younger (Pfefferbaum et al. 1988*a*, 1990*a*), as demonstrated in figure 7 with CT data. Recent studies using MRI have shown that it is primarily the gray matter that is reduced in alcoholic patients (Jernigan et al. 1991; Zipursky et al. 1991), with some reduction also occurring in the white matter (Pfefferbaum et al. 1990*a*). In alcoholic patients spanning the adult age range, gray matter reduction (relative to age norms) accelerates with age. These findings in alcoholic patients are in contrast to those in schizophrenia patients, for whom primarily gray matter change, but little white matter change, is seen (Zipursky et al. 1991) and for whom deviations from age norms are independent of the patient's age and length of illness.

This accelerating loss of gray matter with age in alcoholic patients could imply that the aging brain is particularly susceptible to ethanol. Alternatively, it could be due to the cumulative toxicity of a lifetime of alcohol exposure, or to some interaction of both factors. Physiological changes that accompany aging also need to be considered. For instance, Vestal et al. (1977) showed that peak blood ethanol concentration after an acute fixed dose of alcohol increases with age and attributed this effect to reduction in lean body mass and total

FIGURE 6

57-year-old male alcoholic
lifetime alcohol consumption=1866 kg



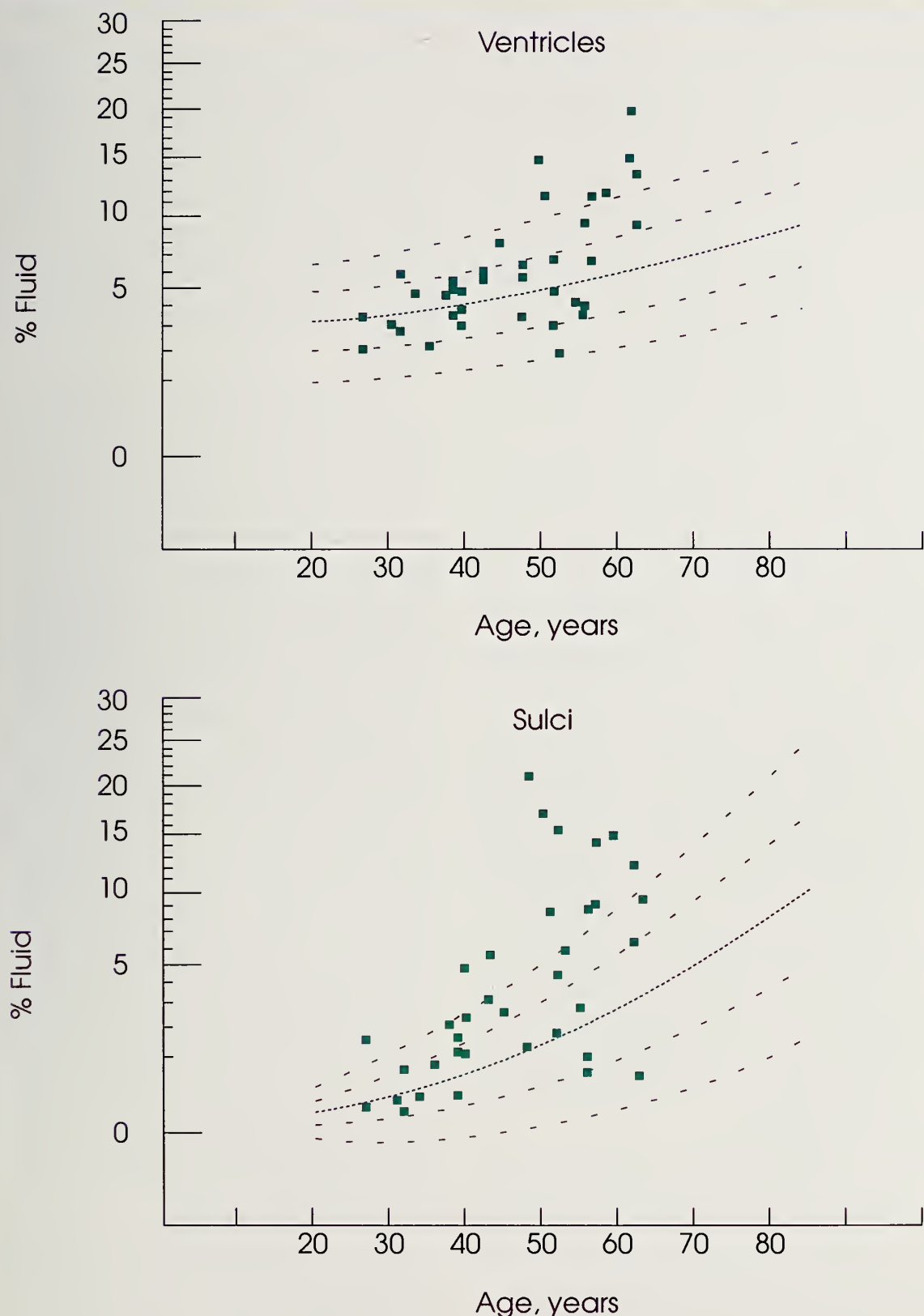
57-year-old healthy community male volunteer
lifetime alcohol consumption=60 kg

Axial MR images from a 57-year-old healthy man and a 57-year-old man with a history of heavy alcohol consumption.

body water with age. Seitz and colleagues (1990) reported significant decreases in gastric alcohol dehydrogenase activity with advancing age in men but not women, which may contribute to the blood level differences. However, Vogel-Sprott and Barrett (1984) demonstrated that even when one controls for blood alcohol level, CNS functions are more impaired by alcohol with advancing age.

The observed reduction in brain tissue in alcohol-dependent patients is the result of a multifactorial process, including the direct toxic

effects of alcohol, poor nutrition, intercurrent disease, and perhaps genetic susceptibility. In a CT study using the age-regression model to control for normal aging, we (Pfefferbaum et al. 1988a) demonstrated a relationship between lifetime alcohol consumption and ventricular enlargement beyond age norms. However, using age as a covariate, other investigators have failed to demonstrate this effect. Some investigators, such as Lishman (1990), have even remarked on a surprising lack of association between the amount of alcohol

FIGURE 7

Percentage of fluid (arcsine transformed) at ventricles and sulci, assessed from CT scans of 37 alcoholic males, plotted against control norms. Dark line, age-predicted value; light lines, 1 and 2 standard deviations from the regression (from Pfefferbaum et al. 1988a).

consumed and the amount of cortical shrinkage.

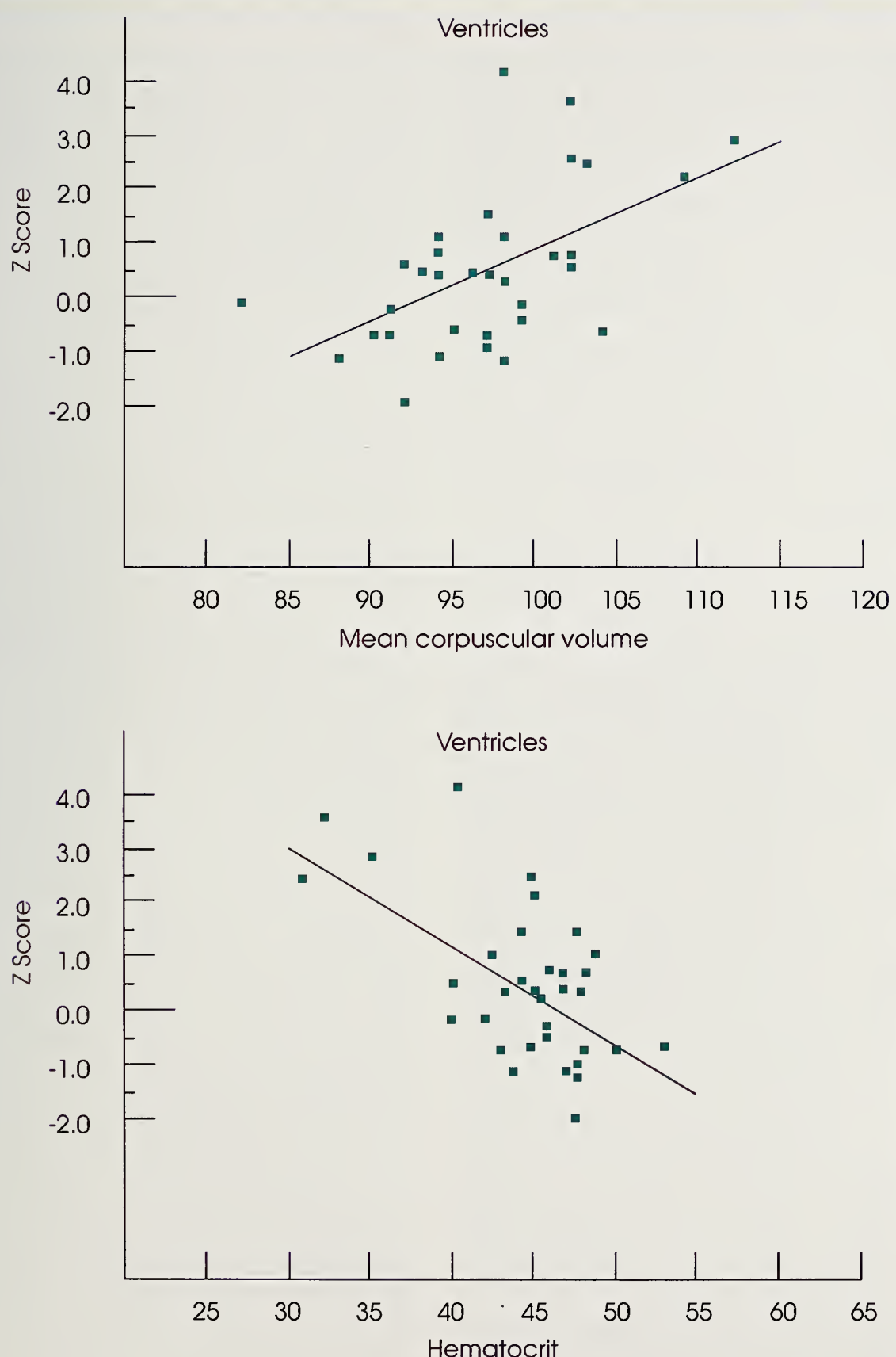
Impaired nutrition is a frequent sequela of chronic alcohol abuse and possibly interacts with alcohol exposure to produce liver disease (Lieber 1989). Extreme malnourishment, such as that which can be manifested in anorexia nervosa, is associated with brain ventricular enlargement that reverses to some extent upon treatment (Enzmann and Lane 1977; Artmann et al. 1985; Krieg et al. 1989). The level of malnourishment present in alcoholics participating in treatment programs and recruited to research protocols is considerably less than that associated with severe anorexia nervosa. In fact, in a recent body morphology study of healthy alcoholics and controls matched for socioeconomical level, age, and sex, York and Pendegast (1990) noted a lack of marked differences in body composition. Nonetheless, we find that variables reflecting nutritional status, e.g., body mass index, hemoglobin, and mean corpuscular volume, were correlated with ventricular size in a CT study (figure 8; Pfefferbaum et al. 1988a) and gray matter reduction in an MRI study (Sullivan et al. 1991).

Animal models (Davies and Smith 1981; Tavares et al. 1983; Pentney and Quigley 1987; King et al. 1988; Pentney et al. 1989; Pentney and Quackenbush 1990; for a review, see also Keane and Leonard 1989) have revealed the vulnerability of brain gray matter to chronic alcohol exposure. In addition, post mortem histopathological studies of chronic

alcoholics have shown neuronal cell body shrinkage and neuronal loss (Harper and Kril 1990). However, in contrast to our observations in living subjects, investigators who examined the volumes of gray and white matter in human neuropathological studies observed only white matter volume reduction in alcoholic brains and little or no reduction in gray matter (Harper and Kril 1985; Harper et al. 1985; de la Monte 1988).

Some of these studies can be criticized because they failed to ascertain the alcohol consumption status of the subjects at the time of death and because they often grouped subjects spanning age ranges >50 years. Nonetheless, the failure to observe at autopsy the gray matter volume changes that can be clearly seen *in vivo* is perplexing. It may be attributed to artifacts in specimen preparation and fixation that affect gray matter specifically (gray matter has a higher water content than white matter). There are also the confounding effects of normal age-related changes, which affect gray matter but not white matter over the age range of 20–60 years (Zipursky et al. 1991) and may not be adequately accounted for in these pathological studies.

Increasing attention is being paid to the possibility that the course of alcoholism among women may differ from that in men by having more intense somatic sequelae (Jones-Saumty et al. 1981; Glenn et al. 1989; Haberman and Natarajan 1989; Frezza et al. 1990; Schmidt et al.

FIGURE 8

Z scores (deviations from age norms) for ventricles of 37 alcoholic men plotted as a function of mean corpuscular volume and hematocrit (from Pfefferbaum et al. 1988a).

1990). The CT study by Jacobson (1986) is consistent with studies of liver disease (Van Thiel and Gavaler 1988) and neuropsychological functioning (Hochla and Parsons 1982), which suggest that alcoholic women are more vulnerable to the deleterious effects of alcohol. Jacobson found that the levels of ventricular enlargement in alcoholic women were similar to those in alcoholic men, but the women had consumed less alcohol and had been drinking for shorter periods of time. These findings persisted, even after the effects of different body weight and head size were taken into consideration.

There is considerable interest in the possibility of a genetic basis for susceptibility to alcohol dependence, and many biological and psychosocial variables have been considered as genetic markers for the disease (Begleiter and Porjesz 1984; Schuckit 1985; Cloninger 1987; Blum et al. 1990). To date, neuroanatomic changes do not appear to be strong candidates as genetic markers for alcoholism. Gurling et al. (1984, 1986) studied monozygotic twins showing discordance for alcoholism and reported differences in brain and ventricular volumes, as well as localized brain density measurements between the severely dependent and normal drinking co-twins. Twins discordant for less severe levels of alcoholism did not show significant differences. Ron (1983) found no difference between family history-positive and family history-negative alcoholics in the CT neuroanatomic measures.

Post mortem and in vivo studies of neuroanatomic changes in chronic alcoholics have tended to emphasize diffuse rather than specific neuroanatomic changes. Yet there are several reports that the highly localized brain lesions of the diencephalon, which are considered pathognomonic for Wernicke's encephalopathy and Korsakoff's syndrome (Victor et al. 1971), can be detected, post mortem, in a proportion of chronic alcoholics for whom the WKS has not been suspected during life (Harper 1983; Torvik 1987; Lindboe and Loberg 1988). Such lesions cannot be seen well in vivo with CT because bony artifacts impair resolution of basal brain structures, although the width of the third ventricle has been taken as an indicator (Shimamura et al. 1988). There have also been some reports of third ventricular enlargement in chronic alcoholics (Acker et al. 1987; Muuronen et al. 1989). MRI can be used to better elucidate these lesions and to measure them more directly (Charness and DeLaPaz 1987). Jernigan et al. (1991b) recently demonstrated that WKS patients also have general tissue loss plus substantial reductions in mesiotemporal and orbitofrontal cortex.

The importance of abstinence in reversing alcohol-related neuroanatomic brain changes was first highlighted by Carlen et al. (1978), using CT. Subsequent reports of larger samples from the laboratories of Carlen et al. (1984) and others (Artmann et al. 1981; Ron 1983; Muuronen et al. 1989) confirmed reversibility of brain shrinkage in a

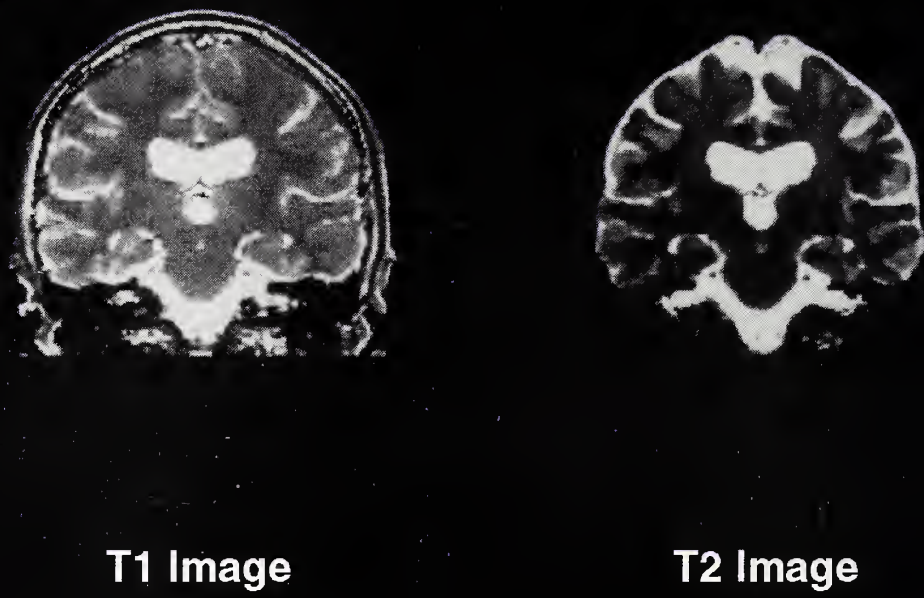
proportion of abstinent alcoholics over periods of months to years. Long-term reversibility was greater in patients who had their first scan shortly after their last drink, implying that reversibility was mainly accomplished during the initial withdrawal period (Carlen et al. 1984).

Some studies using MRI (Schroth et al. 1988; Zipursky et al. 1989) have since established that some reversibility occurs within the first few weeks of abstinence. However, in one study in which testing was performed 36 hours after the last drink and again 10 days later, no change was found in CT-measured brain shrinkage (Claus et al. 1987). Whether further reversibility occurs in the same patients over longer periods of abstinence remains to be established. The contribution of improved nutritional status during short-term treatment, a return to sobriety, and a healthier lifestyle must also be taken into account. In considering the study of reversibility, one must recognize that the effect is quite small, often requiring reliable quantitative techniques for detection. In our study (Zipursky et al. 1989), ventricular volume declined approximately 15 percent during withdrawal, an effect that may be hard to detect on visual inspection.

The fact that some of the reduction in brain tissue and the increase in CSF volume are reversible has led to the use of the term "shrinkage" rather than "atrophy" because the underlying process is not clear. One hypothesis regarding the reversibility of ventricular and sulcal

enlargement with abstinence is that there is a relative brain rehydration during withdrawal. An approach to investigating this hypothesis is to measure the relaxation time of protons from MR images of the brain. Figure 9 presents T1 and T2 images constructed from the basic images presented in figure 3. CSF has long T1 and T2 compared with tissue, and gray matter has a higher water content and thus a longer T1 than white matter. The T1 is prolonged with increases in brain tissue hydration and shortened with decreased hydration (MacDonald et al. 1986). T2 shows a similar, though slightly less precise, function (Bottomley et al. 1984; Fu et al. 1990).

Despite findings from some elegant studies with animal models and the apparent validity of relaxation time as a measure of brain hydration, the application of this technology to the study of alcohol withdrawal has produced inconsistent results. In 1981, Besson et al. reported shorter brain T1 in both the gray and white matter of intoxicated alcoholics; the T1 lengthened during withdrawal and abstinence of 1–6 weeks. Since then, a series of studies, many with limited control data and sampling at different time points, yielded conflicting results (Smith et al. 1985, 1988; Schroth et al. 1988; Besson et al. 1989a). In a more recent study on a large group of alcoholic patients and matched control subjects, T1s were longer in both gray and white matter of alcoholics measured 2 weeks post-withdrawal. The investigators interpreted their findings as indices of

FIGURE 9

Calculated T1 and T2 images from the basic data presented in figure 3.

brain hydration (Chick et al. 1989). Correlations between atrophy and T1 found in those data (Mander et al. 1989) suggest, however, that partial voluming (some CSF present in what appears to be a tissue voxel) may contribute to the increased T1 seen in alcoholics.

Adding to the confusion is the autopsy report by Harper et al. (1988) who concluded that "brain shrinkage in alcoholics is not caused by changes in hydration." Unfortunately, they failed to report the drinking status of their patients at time of death, which may have a profound bearing on the state of hydration of the alco-

holics' brains. In an interesting animal experiment, Besson et al. (1989b) demonstrated that in rats fed alcohol for 6 months, T1 increased but only at 1 month post-withdrawal. These investigators further claimed that there were no changes in T2 or water content. They concluded that the T1 effects represented alterations in the cell membrane rather than changes in hydration. Thus the data on T1 and its relationship to brain hydration are conflicting. In addition to the possible unreliability of this measure (Bottomley et al. 1987), crucial factors appear to be the time after ethanol withdrawal,

adequate tissue sampling to avoid partial voluming effects, and the need for nonalcoholic control values.

CONCLUSION

Neuroimaging studies have demonstrated that chronic alcoholism produces widespread brain shrinkage, especially in older persons. Some of this shrinkage may be reversible with abstinence, but the mechanism has yet to be elucidated. There may well be regionally specific tissue damage in addition to generalized shrinkage, which have considerable clinical importance. MRI studies are now beginning to examine the effect of excessive alcohol consumption on many brain regions of interest. Much remains to be investigated in terms of the prognostic significance of the observed brain morphologic sequelae of alcoholism, as well as the role of these changes in cognitive function. MRI, in particular, offers a unique opportunity to observe the brain as the disease progresses or remits in living alcoholic patients.

ACKNOWLEDGMENTS

This chapter was prepared with support from the National Institute on Alcohol Abuse and Alcoholism (grant AA-05965) and the Medical Service of the Department of Veterans Affairs.

REFERENCES

- Acker, C.; Jacobson, R.R.; and Lishman, W.A. Memory and ventricular size in alcoholics. *Psychol Med* 17:343-348, 1987.
- Artemann, H.; Gall, M.V.; Hacker, H.; and Herrlich, J. Reversible enlargement of cerebral spinal fluid spaces in chronic alcoholics. *Am J Neuroradiol* 2:23-27, 1981.
- Artemann, H.; Grau, H.; Adelmann, M.; and Schleiffer, R. Reversible and non-reversible enlargement of cerebrospinal fluid spaces in anorexia nervosa. *Neuroradiology* 27:304-312, 1985.
- Begleiter, H., and Porjesz, B. Event-related brain potentials in boys at risk for alcoholism. *Science* 225:1493-1496, 1984.
- Besson, J.A.O.; Crawford, J.R.; Parker, D.M.; and Smith, F.W. Magnetic resonance imaging in Alzheimer's disease, multi-infarct dementia, alcoholic dementia and Korsakoff's psychosis. *Acta Psychiatr Scand* 80:451-458, 1989a.
- Besson, J.A.O.; Glen, A.I.M.; Foreman, E.I.; Macdonald, A.; Smith, F.W.; Hutchinson, J.M.S.; Mallard, J.R.; and Ashcroft, G.W. Nuclear magnetic resonance observations in alcoholic cerebral disorder and the role of vasopressin. *Lancet* 2:923-924, 1981.
- Besson, J.A.O.; Greentree, S.G.; Foster, M.A.; and Rimmington, J.E. Effects of ethanol on the NMR characteristics of rat brain acute administration, dependency, and long-term effects. *Br J Psychiatry* 155:818-821, 1989b.
- Blum, K.; Noble, E.P.; Sheridan, P.J.; Montgomery, A.; Ritchie, T.; Jagadeeswaran, P.; Nogami, H.; Briggs, A.H.; and Cohn, J.B. Allelic association of human dopamine D2 receptor gene in alcoholism. *JAMA* 263:2055-2060, 1990.
- Bottomley, P.A.; Foster, T.H.; Argersinger, R.E.; and Pfeifer, L.M. A review of

- normal tissue hydrogen NMR relaxation times and relaxation mechanisms from 1–100 MHz: Dependence on tissue type, NMR frequency, temperature, species, excision, and age. *Med Phys* 11:425–448, 1984.
- Bottomley, P.A.; Hardy, C.J.; Argersinger, R.E.; and Allen-Moore, G. A review of IH nuclear magnetic resonance relaxation in pathology: Are T1 and T2 diagnostic? *Med Phys* 14:1–37, 1987.
- Carlen, P.L.; Wilkinson, D.A.; Wortzman, G.; and Holgate, R. Partially reversible cerebral atrophy and functional improvement in recently abstinent alcoholics. *Can J Neurol Sci* 11:441–446, 1984.
- Carlen, P.L.; Wortzman, G.; Holgate, R.C.; Wilkinson, D.A.; and Rankin, J.G. Reversible cerebral atrophy in recently abstinent chronic alcoholics measured by computed tomography scans. *Science* 200:1076–1078, 1978.
- Charness, M.E., and DeLaPaz, R.L. Mammillary body atrophy in Wernicke's encephalopathy: Antemortem identification using magnetic resonance imaging. *Ann Neurol* 22:595–600, 1987.
- Chick, J.D.; Smith, M.A.; Engleman, H.M.; Kean, D.M.; Mander, A.J.; Douglas, R.H.B.; and Best, J.J.K. Magnetic resonance imaging of the brain in alcoholics: Cerebral atrophy, lifetime alcohol consumption and cognitive deficits. *Alcohol Clin Exp Res* 13:512–518, 1989.
- Claus, D.; Wille, H.J.; Neundörfer, B.; and Gmelin, E. Is the enlargement of cerebrospinal fluid spaces reversible in abstinent alcoholics because of rehydration? *Klin Wochenschr* 65:185–193, 1987.
- Cloninger, C.R. Neurogenetic adaptive mechanisms in alcoholism. *Science* 236:410–416, 1987.
- Courville, C.B. *Effects of Alcohol on the Nervous System in Man*. Los Angeles: San Lucas Press, 1955.
- Davies, A.R., and Smith, D.E. A Golgi study of mouse hippocampal CA1 pyramidal neurons following perinatal ethanol exposure. *Neurosci Lett* 26:49–54, 1981.
- de la Monte, S.M. Disproportionate atrophy of cerebral white matter in chronic alcoholics. *Arch Neurol* 45:990–992, 1988.
- Enzmann, D.R., and Lane, B. Cranial computed tomography findings in anorexia nervosa. *J Comput Assist Tomogr* 1:410–414, 1977.
- Fox, J.H.; Ramsey, R.G.; Huckman, M.S.; and Proske, A.E. Cerebral ventricular enlargement, chronic alcoholics examined by computerized tomography. *JAMA* 236:365–368, 1976.
- Frezza, M.; di Padova, C.; Pozzato, G.; Terpin, M.; Baraona, E.; and Lieber, C.S. High blood alcohol levels in women. *N Engl J Med* 322:95–99, 1990.
- Fu, Y.; Tanaka, K.; and Nishimura, S. Evaluation of brain edema using magnetic resonance proton relaxation times. In: Long, D., ed. *Advances in Neurology, Brain Edema*. Vol. 52. New York: Raven Press, 1990. pp. 165–176.
- Glenn, S.W.; Parsons, O.A.; and Stevens, L. Effects of alcohol abuse and familial alcoholism on physical health in men and women. *Health Psychol* 8:325–341, 1989.
- Gurling, H.M.D.; Murray, R.M.; and Ron, M.A. Increased brain radiodensity in

- alcoholism: A co-twin control study. *Arch Gen Psychiatry* 43:764-767, 1986.
- Gurling, H.M.D.; Reveley, M.A.; and Murray, R.M. Increased cerebral ventricular volume in monozygotic twins discordant for alcoholism. *Lancet* i:986-987, 1984.
- Haberman, P.W., and Natarajan, G. Premature mortality and chronic alcoholism: Medical examiner cases, New Jersey. *Soc Sci Med* 29:729-732, 1989.
- Harper, C.G. The incidence of Wernicke's encephalopathy in Australia: A neuropathological study of 131 cases. *J Neurol Neurosurg Psychiatry* 46:593-598, 1983.
- Harper, C., and Kril, J.J. Brain atrophy in chronic alcoholic patients: A quantitative pathological study. *J Neurol Neurosurg Psychiatry* 48:211-217, 1985.
- Harper, C.G., and Kril, J.J. Neuropathology of alcoholism. *Alcohol Alcohol* 25:207-216, 1990.
- Harper, C.G.; Kril, J.J.; and Daly, J.M. Brain shrinkage in alcoholics is not caused by changes in hydration: A pathological study. *J Neurol Neurosurg Psychiatry* 51:124-127, 1988.
- Harper, C.G.; Kril, J.J.; and Holloway, R.L. Brain shrinkage in chronic alcoholics: A pathological study. *Br Med J* 290:501-504, 1985.
- Haug, J.O. Pneumoencephalographic studies in mental disease. *Acta Psychiatr Scand* 165:1-104, 1962.
- Hochla, N.A., and Parsons, O.A. Premature aging in female alcoholics. A neuropsychological study. *J Nerv Ment Dis* 170:241-245, 1982.
- Jacobson, R. The contributions of sex and drinking history to the CT brain scan changes in alcoholics. *Psychol Med* 16:547-549, 1986.
- Jernigan, T.L.; Butters, N.; DiTraglia, G.; Schaler, K.; Smith, T.; Irwin, M.; Grant, I.; Schuckit, M.; and Cermak, L. Reduced cerebral gray matter observed in alcoholics using magnetic resonance imaging. *Alcohol Clin Exp Res* 15:418-428, 1991a.
- Jernigan, T.L.; Schafer, K.; Butters, N.; and Cermak, L.S. Magnetic resonance imaging of alcoholic Korsakoff patients. *Neuropsychopharmacology* 4:175-186, 1991b.
- Jernigan, T.L.; Zatz, L.M.; Ahumada, A.J.; Pfefferbaum, A.; Tinklenberg, J.R.; and Moses, J.A. CT measures of cerebrospinal fluid volume in alcoholics and normal volunteers. *Psychiatry Res* 7:9-17, 1982.
- Jones-Saumty, D.J.; Fabian, M.S.; and Parsons, O.A. Medical status and cognitive functioning in alcoholic women. *Alcoholism* 5:372-377, 1981.
- Keane, B., and Leonard, B.E. Rodent models of alcoholism--A review. *Alcohol Alcohol* 24:299-309, 1989.
- King, M.A.; Hunter, B.E.; and Walker, D.W. Alterations and recovery of dendritic spine density in rat hippocampus following long-term ethanol ingestion. *Brain Res* 459:381-385, 1988.
- Krieg, J.-C.; Lauer, C.; and Pirke, K.-M. Structural brain abnormalities in patients with bulimia nervosa. *Psychiatry Res* 27:39-48, 1989.
- Lieber, C.S. Alcohol and nutrition: An overview. *Alcohol Health Res World* 13:197-205, 1989.

- Lindboe, C.F., and Loberg, E.M. The frequency of brain lesions in alcoholics. *J Neurol Sci* 88:107-113, 1988.
- Lishman, W.A. Alcohol and the brain. *Br J Psychiatry* 156:635-644, 1990.
- MacDonald, H.L.; Bell, B.A.; Smith, M.A.; Kean, D.M.; Tocher, J.L.; Douglas, R.H.B.; Miller, J.D.; and Best, J.J.K. Correlation of human NMR T1 values measured in vivo and brain water content. *Br J Radiol* 59:355-357, 1986.
- Mander, A.J.; Young, A.; Chick, J.D.; and Best, J.J.K. The relationship of cerebral atrophy and T1 in alcoholics: An MRI study. *Drug Alcohol Depend* 24:57-59, 1989.
- Muuronen, A.; Bergman, H.; Hindmarsh, T.; and Telakivi, T. Influence of improved drinking habits on brain atrophy and cognitive performance in alcoholic patients: A 5-year follow-up study. *Alcohol Clin Exp Res* 13:137-141, 1989.
- Oldendorf, W.H. *The Quest for an Image of Brain*. New York: Raven Press, 1980.
- Oldendorf, W.H., and Oldendorf, W.J. *Basics of Magnetic Resonance Imaging*. Boston: Martinus Nijhoff Publishing, 1988.
- Pentney, R., and Quackenbush, L. Nonrandom modelling of dendritic networks in old rats after long term ethanol treatment. *Alcohol Clin Exp Res* 14:326, 1990.
- Pentney, R.; Quackenbush, L.J.; and O'Neill, M. Length changes in dendritic networks of cerebellar Purkinje cells of old rats after chronic ethanol treatment. *Alcohol Clin Exp Res* 13:413-419, 1989.
- Pentney, R.J., and Quigley, P.J. Morphometric parameters of Purkinje dendritic networks after ethanol treatment during aging. *Alcohol Clin Exp Res* 11:536-540, 1987.
- Pfefferbaum, A.; Lim, K.O.; Ha, C.N.; and Zipursky, R.B. Changes in brain white and gray matter volume in alcoholism: An MRI study. *Alcohol Clin Exp Res* 14:328, 1990a.
- Pfefferbaum, A.; Rosenbloom, M.J.; Crusan, K.; and Jernigan, T.L. Brain CT changes in alcoholics. The effects of age and alcohol consumption. *Alcohol Clin Exp Res* 12:81-87, 1988a.
- Pfefferbaum, A.; Sullivan, E.V.; Jernigan, T.L.; Zipursky, R.B.; Rosenbloom, M.J.; Yesavage, J.A.; and Tinklenberg, J.R. A quantitative analysis of CT and cognitive measures in normal aging and Alzheimer's disease. *Psychiatry Res Neuroimaging* 35:115-136, 1990b.
- Pfefferbaum, A.; Zatz, L.; and Jernigan, T.L. Computer-interactive method for quantifying cerebrospinal fluid and tissue in brain CT scans: Effects of aging. *J Comput Assist Tomogr* 10:571-578, 1986.
- Pfefferbaum, A.; Zipursky, R.B.; Lim, K.O.; Zatz, L.M.; Stahl, S.M.; and Jernigan, T.L. Computed tomographic evidence for generalized sulcal and ventricular enlargement in schizophrenia. *Arch Gen Psychiatry* 45:633-640, 1988b.
- Ron, M.A. *The Alcoholic Brain: CT Scan and Psychological Findings*. Psychological Medicine Monograph Supplement 3. Cambridge: Cambridge University Press, 1983.
- Schmidt, C.; Klee, L.; and Ames, G. Review and analysis of literature on

- indicators of women's drinking problems. *Br J Addict* 85:179-192, 1990.
- Schroth, G.; Naegele, T.; Klose, U.; Mann, K.; and Petersen, D. Reversible brain shrinkage in abstinent alcoholics, measured by MRI. *Neuroradiology* 30:385-389, 1988.
- Schuckit, M.A. Genetics and the risk for alcoholism. *JAMA* 253:2614-2617, 1985.
- Seitz, H.K.; Egerer, G.; and Simanowski, U.A. High blood alcohol levels in women. *N Engl J Med* 323:58, 1990.
- Shimamura, A.P.; Jernigan, T.L.; and Squire, L.R. Korsakoff's syndrome: Radiological (CT) findings and neuropsychological correlates. *J Neurosci* 8:4400-4410, 1988.
- Smith, M.A.; Chick, J.D.; Engleman, H.M.; Kean, D.M.; Mander, A.J.; and Douglas, R.H.B. Brain hydration during alcohol withdrawal in alcoholics measured by magnetic resonance imaging. *Drug Alcohol Depend* 21:25-28, 1988.
- Smith, M.A.; Chick, J.; Kean, D.M.; Douglas, R.H.B.; Singer, A.; Kendell, R.; and Best, J.J.K. Brain water in chronic alcoholic patients measured by magnetic resonance imaging. *Lancet* 1:1273-1274, 1985.
- Stafford, J.L.; Albert, M.S.; Naeser, M.A.; Sandor, T.; and Garvey, A.J. Age-related differences in computed tomographic scan measurements. *Arch Neurol* 45:409-415, 1988.
- Sullivan, E.V.; Zipursky, R.B.; Rosenbloom, M.J.; Ha, C.N.; DeMent, S.E.; Lim, K.O.; and Pfefferbaum, A. Cerebral gray and white matter abnormalities in alcoholism: A quantitative MRI study. *J Clin Exp Neuropsychol* 13:33, 1991.
- Tavares, M.A.; Paula-Barbosa, M.M.; and Gray, E.G. A morphometric Golgi analysis of the Purkinje cell dendritic tree after long-term alcohol consumption in the adult rat. *J Neurocytol* 12:939-948, 1983.
- Torvik, A. Brain lesions in alcoholics: Neuropathological observations. *Acta Med Scand Suppl* 717:47-54, 1987.
- Van Thiel, D.H., and Gavaler, J.S. Ethanol metabolism and hepatotoxicity: Does sex make a difference? In: Galanter, M., ed. *Recent Developments in Alcoholism*. New York: Plenum Press, 1988. pp. 291-304.
- Vestal, R.E.; McGuire, E.A.; Tobin, J.D.; Andres, R.; Norris, A.H.; and Mezey, R. Aging and ethanol metabolism in man. *Clin Pharmacol Ther* 21:343-354, 1977.
- Victor, M.; Adams, R.D.; and Collins, G.H. *The Wernicke-Korsakoff Syndrome*. Philadelphia: F.A. Davis Co., 1971.
- Vogel-Sprott, M., and Barrett, P. Age, drinking habits, and the effects of alcohol. *J Stud Alcohol* 45:517-521, 1984.
- Wilkinson, D.A. CT scans and neuropsychological assessments of alcoholism. In: Parsons, O.; Butters, N.; and Nathan, P., ed. *Neuropsychology of Alcoholics: Implications for Diagnosis and Treatment*. New York: Guilford Press, 1987. pp. 76-102.
- York, J.L., and Pendergast, D.E. Body composition in detoxified alcoholics. *Alcohol Clin Exp Res* 14:180-183, 1990.
- Zipursky, R.B.; Lim, K.O.; and Pfefferbaum, A. MRI study of brain

changes with short term abstinence from alcohol. *Alcohol Clin Exp Res* 13:664-666, 1989.

Zipursky, R.B.; Lim, K.O.; Sullivan, E.V.; Brown, B.W.; and Pfefferbaum, A. Widespread cerebral gray matter volume deficits in schizophrenia. *Arch Gen Psychiatry* 1991, in press.

Zipursky, R.B.; Lim, K.O.; Sullivan, E.V.; and Pfefferbaum, A. "Contrasting Patterns of Gray and White Matter Differences in Schizophrenia and Alcoholism." Presented at the Third International Conference on Schizophrenia Research, Tucson, April 23, 1991.

7

STUDIES OF BRAIN STRUCTURE IN CHRONIC ALCOHOLISM USING MAGNETIC RESONANCE IMAGING

Terry L. Jernigan, Ph.D.^{1,2} Nelson Butters, Ph.D.^{1,2} and Laird S. Cermak, Ph.D.^{3,4}

The results described in this chapter were obtained as part of a broad research effort focusing on the causes, correlates, and consequences of long-term alcohol consumption. They reflect interest in the effects of alcohol on information processing in the nervous system and in links between these effects and brain structural changes. Of particular interest is the relationship between the relatively mild cognitive deficits observed in many chronic alcoholics and the severe, though sometimes highly circumscribed, impairments occurring in the much rarer alcoholic amnesia of Korsakoff's syndrome.

Previous neuroradiological comparisons of chronic (nonamnesic) alcoholics and nonalcoholic controls have consistently demonstrated cerebrospinal fluid (CSF) increases in the brains of the alcoholics,

especially in the subarachnoid spaces (Bergman 1987; Bergman et al. 1980; Wilkinson 1982; Wilkinson and Carlen 1980; Ron 1983; Ron et al. 1980; Carlen et al. 1981; Cala and Mastaglia 1981; Jernigan et al. 1982; Pfefferbaum et al. 1988). These changes would seem to support neuropathological reports of reduced brain weight and brain volume in alcoholics (Harper and Blumbergs 1982; Harper et al. 1985; Torvik et al. 1982) and perhaps even the general notion that ethanol is a neurotoxic agent affecting a number of brain regions important for higher cognitive functions (Neubuerger 1957; Lynch 1960;

ACRONYMS

CSF	cerebrospinal fluid
CT	computed tomography
MRI	magnetic resonance imaging

¹San Diego Veterans Affairs Medical Center, San Diego, CA 92161

²Department of Psychiatry, School of Medicine, University of California, San Diego, La Jolla, CA 92093

³Boston Veterans Affairs Medical Center, Boston, MA 02130

⁴Boston University School of Medicine, Boston, MA 02215

Miyakawa et al. 1977; Walker et al. 1981).

Interpretation of these neuroradiological findings has been challenged by reports that the increases in CSF are at least partially reversible with prolonged abstinence (Carlen et al. 1978, 1984, 1986; Artmann et al. 1981; Ron et al. 1982) and may actually reflect a transitory brain overhydration during detoxification (Besson et al. 1981, 1987; Smith et al. 1985; Chick et al. 1989). Furthermore, in some instances, these increases in CSF failed to correlate consistently and highly with neuropsychological deficits once the effect of age had been excluded, raising further doubts concerning the permanent pathological implications of the observed CSF increments (Bergman 1987; Bergman et al. 1980; Ron 1983). Thus emerges the view that while chronic alcoholism has demonstrable neurobiological effects, some of these may be relatively short lasting after patients achieve abstinence. Although mild cognitive deficits may remain, perhaps due to toxic effects of the chronic exposure to alcohol, these would appear to differ sharply from the severe, and irreversible, memory impairments of Korsakoff's syndrome.

Traditionally, the neuropathology of alcoholic amnesia has also been considered to be qualitatively dissimilar from that of typical chronic alcoholism. The syndrome is usually attributed to an acute encephalopathy caused by thiamine deficiency, which results in small hemorrhagic lesions along the diencephalic midline. Victor et al. (1989)

examined the brains of 43 Korsakoff patients and found that, in 38 cases, both the dorsomedial nucleus and the mammillary bodies were atrophied. In another five cases of Korsakoff's syndrome, none of whom had documented amnesia, only the mammillary bodies were affected. Thus, this post mortem examination implicated damage to the midline diencephalic nuclei (i.e., the dorsomedial nucleus of the thalamus and possibly the mammillary bodies) as the neurological basis of the memory disorder. However, other investigators have stressed the role played by other diencephalic structures, e.g., the paratenial nucleus (Mair et al. 1979; Mayes et al. 1988), and have raised questions about the role of structures outside the diencephalon, such as the basal forebrain structures and the hippocampus (Arendt et al. 1983; Mayes et al. 1988).

Interestingly, at autopsy, Harper (1983) found neuropathologic signs consistent with Korsakoff's disease in the brains of 131 alcoholic patients. Eighty-three percent of these cases had significant mesial diencephalic damage (including atrophy of the mammillary bodies, hemorrhagic lesions of the thalamus, dilation of the third ventricle), although only 20 percent of the cases showed signs of Wernicke's encephalopathy prior to death. In a later study (Harper et al. 1986), a review of clinical records revealed that 80 percent of pathologically diagnosed cases were not diag-

nosed with Wernicke's during life. While Harper originally interpreted these findings as an indication of the underdiagnosis of the Wernicke-Korsakoff syndrome among alcoholics, it is also possible that the severe amnesic symptoms associated with this disorder do not become clinically apparent until some damage has occurred to other structures in addition to the mesial diencephalon. That is, many long-term alcoholics may have subclinical diencephalic lesions due to their frequent bouts of malnutrition, but they may not manifest severe mental status, sensory, and motor changes until some threshold of diencephalic damage has been exceeded or until some damage to other subcortical (or cortical) structures has occurred. This issue has been discussed at length by Bowden (1990), who recently reviewed a number of other pathological studies that further demonstrate the existence of significant subcortical abnormalities in chronic alcoholics.

Using quantitative techniques to estimate the volumes of gray matter structures seen on magnetic resonance images (MRI), we attempted to determine whether damage to these structures accompanies the CSF increases observed in nonamnesic chronic alcoholics (Jernigan et al. 1991b). In addition, we compared the results in amnesic alcoholics directly with those in non-amnesic alcoholics (Jernigan et al. 1991c). The following sections, which describe our methods and present a summary of our results to date,

are based largely on two previously published reports (Jernigan et al. 1991b,c).

SUBJECTS

The nonamnesic alcoholic subjects in this study were all males. All had undergone detoxification prior to admission to the San Diego Department of Veterans Affairs Medical Center's Alcohol Treatment Program, a 28-day program for the counseling and treatment of alcoholism. The Alcohol Research Center Intake Interview (Schuckit et al. 1988) was used to obtain data on drinking and medical histories from all patients and at least one resource person each (e.g., a close friend or family member). The diagnosis of alcohol abuse or dependence was documented using DSM-III criteria (American Psychiatric Association 1980). Excluded from this study were patients who had histories of overt liver (e.g., cirrhosis, jaundice), metabolic (e.g., diabetes), vascular (e.g., coronary artery disease), or neurologic (e.g., head injury, encephalitis, epilepsy) disorders. Patients with histories of drug abuse or major psychiatric illness (e.g., schizophrenia, posttraumatic stress disorder, bipolar affective disorder) that predated the onset of alcoholism were also eliminated from the study.

The alcoholic Korsakoff patients were similar to those described by Butters and Cermak (1980). These patients had severe anterograde and retrograde amnesias associated

with 20- to 30-year histories of chronic alcoholism and probable malnutrition. Psychometric indices of their memory and general intelligence revealed severely impaired memory performance but IQ scores within normal limits. In each case, the patient's Delayed Memory Index (Wechsler Memory Scale--Revised; Wechsler 1987) was 2.0–3.5 standard deviations below the IQ scores. None of the Korsakoff patients had significant medical problems (e.g., cirrhosis, chronic obstructive pulmonary disease, cancer) at the time of this study.

Newspaper advertisements facilitated recruitment of a group of adult controls from the community. All of these control subjects were screened for history of alcohol abuse, alcoholism, drug abuse, and the medical and psychiatric disorders described for the alcoholic subjects.

IMAGING PROTOCOL

MRI was performed with a 1.5-T super-conducting magnet (General Electric, Milwaukee) at the UCSD/AMI Magnetic Resonance Institute. Two spatially registered images were obtained simultaneously for each section, using an asymmetrical, multiple-echo sequence (TR=2,000 milliseconds, TE=25, 70 milliseconds) to obtain images of the entire brain in the axial plane. Section thickness was 5 mm, with sections centered at 7.5-mm intervals.

IMAGE ANALYSIS

Detailed descriptions of the image-analytic approach used in our studies have been published elsewhere (Jernigan et al. 1990, 1991a,c,d). Image data sets were assigned random numeric codes, and all analyses were conducted blind to any subject characteristics. Briefly, each pixel location within a section of the imaged brain was classified on the basis of its signal values on both images as most resembling CSF, gray matter, white matter, or signal hyperintensity (tissue abnormality). Trained image analysts, using stylus-controlled cursors on the displayed "pixel-classified" images, then designated consistently identifiable structural landmarks and boundaries. The processed image data were then transformed spatially so that all locations within the brain images could be identified relative to a common anatomical coordinate system. Additional cerebral regions were then defined relative to this coordinate scheme (i.e., stereotactically). Thus, the boundaries of the measured structures were determined either entirely by manual designation, or in cases when boundaries could not be determined reliably, by a combination of manually and stereotactically determined boundaries.

The supratentorial cranium volume was estimated by summing supratentorial voxels (including CSF, hyperintensities, and gray and white matter) over all sections. Summing the subcortical and cortical CSF voxels over all sections

separately permitted estimation of the ventricular and cortical sulcal volumes. The gray matter voxels within each of four subcortical structures (caudate nucleus, lenticular nucleus, anterior diencephalon, and thalamus) and the cortical gray matter voxels within each of eight cerebral zones were summed separately. Eight regional volumes were also computed by summing all supratentorial voxels (including CSF, hyperintensities, and gray and white matter) within each region. Finally, construction of an index of signal alterations in the white matter involved summing voxels within the subcortical white matter regions having signal characteristics that met criteria for "gray matter" or "signal hyperintensities," i.e., they had longer T2 values.

RESULTS AND DISCUSSION

Multiple regression analyses of the control data yielded estimates of the magnitudes of normal age-related changes and effects of cranium (or cranial region) size for each measure. Because previous studies (Zatz et al. 1982; Pfefferbaum et al. 1986; Jernigan et al. 1991a) have suggested that some relationships between brain structural volumes and age or cranial volume are not linear, polynomial regressions were performed to detect significant deviations from linearity. When the simple correlation (linear component) of age with a morphologic measure was statistically significant, a quadratic term (age-squared) was added to the regression. Similarly,

when a linear term for the cranial measure contributed significantly, a quadratic term was included. When the addition of such terms significantly increased R-squared, the function was considered to be non-linear, and the function with both terms was used in the correction formula. On the basis of these analyses, new measures were computed for each normal control; they expressed the original values as deviations from the values predicted from the subjects' ages and cranium sizes. Similar analyses were then conducted to estimate any age-related change in the variance of the new deviation scores. Finally, formulae were constructed to estimate a subject's deviation from age- and cranium-predicted values in standard deviation units appropriate for the subject's age.

Subject characteristics are summarized in table 1. The values presented in table 2 represent age- and cranium size-adjusted Z scores. These values, by definition, have an expected mean of 0 and a standard deviation of 1 in the controls. In the patients, they reveal how aberrant a volume is, and, inasmuch as the deviations are expressed on a common scale, they facilitate comparisons of effects across different brain structures. They are particularly useful here, because, as we and others have pointed out in previous articles, removing age effects from samples including alcoholic patients tends to remove part of the "alcoholism" effect. The reason is that older alcoholics (with longer drinking histories) usually have

Table 1. Subject characteristics

	Control (n=80)	Alcoholic (n=34)	Korsakoff (n=11)
Mean age (S.D.)	56 (14.2)	48 (9.4)	60 (10.7)
Sex	28 F 52 M	0 F 34 M	1 F 10 M

more atrophy, which is incorrectly attributed to "aging." The approach we have used avoids this problem and provides an accurate means of removing variance associated with normal aging, even in the examination of alcoholic patients in whom age and years of alcoholism are usually confounded.

The mean Z scores and standard deviations for the structural measures are summarized in table 2. The subcortical measures reveal that mild ventricular enlargement in chronic alcoholics is accompanied by statistically significant decreases in the volumes of periventricular nuclei such as the caudate and thalamus, and by mild increases in abnormal signal within the subcortical white matter. Thus, there is evidence that ventricular CSF increases do reflect volume losses in diencephalic and other deep cerebral structures, even in nonamnesic alcoholics. Nevertheless, the degree of ventricular enlargement, and particularly the loss of volume in the anterior diencephalon (a region including hypothalamic and basal forebrain structures), clearly differentiates amnesic patients from

their nonamnesic alcoholic controls. These results are generally consistent with the neuropathological results and with the notion that Korsakoff's syndrome is accompanied by distinct pathology in diencephalic structures. However, it is somewhat surprising that the thalamic losses were not significantly more severe in the amnesic than in the nonamnesic subjects.

The cortical CSF measures confirm the often-reported dramatic increases in the subarachnoid spaces in both alcoholic groups, although the increases in the amnesic patients were statistically no greater than those in the other alcoholic patients. The cortical gray matter measures also reveal associated volume losses in the adjacent gyri in both groups, although these were generally not as striking as the CSF increases, suggesting that factors other than cortical volume losses may also contribute to these CSF increases. One quite interesting result is that although sulcal CSF did not differentiate amnesic from nonamnesic patients, volume losses in mesial temporal and orbitofrontal cortex did.

Table 2. Mean Z scores (S.D.) for brain structural measures

	Controls (n=80)	Alcoholic (n=34)	Korsakoff (n=11)
Subcortical Measures			
Ventricular fluid	0.1 (1.1)	0.8 (1.2)	2.0* (1.9)
White matter abnormality	0.1 (1.2)	0.6 (1.2)	0.3 (1.1)
Gray matter volumes			
Caudate	-0.1 (1.0)	-0.7 (0.9)	-0.8 (1.0)
Anterior diencephalon	-0.1 (1.1)	-0.4 (0.8)	-1.2† (0.7)
Thalamus	0.0 (0.9)	-0.5 (1.1)	-0.8 (1.2)
Cortical Measures			
Cortical fluid	0.1 (1.0)	1.6 (1.4)	2.3 (1.6)
Cortical gray matter	-0.1 (1.3)	-0.8 (1.2)	-1.4 (1.4)
Orbitofrontal	-0.1 (1.1)	-0.4 (1.1)	-1.6† (1.4)
Mesial-temporal	0.0 (1.1)	-0.6 (0.8)	-1.4† (0.9)
Parietal	-0.1 (1.2)	-0.9 (1.3)	-0.9 (1.4)
Dorsolateral	-0.1 (1.3)	-0.7 (1.2)	-0.8 (1.3)
Frontal operculum/ cingulate	0.0 (1.0)	0.1 (0.8)	0.3 (1.4)

Differences between Korsakoff and alcoholic: * $p < .05$; † $p < .01$.

The reduced volume of the mesial temporal gray matter found in both alcoholic groups is consistent with reported alcohol-related cell loss in limbic structures in both animals (Walker et al. 1981) and humans (Miyakawa et al. 1977). Moreover, the observed reductions in superior frontal and parietal regions are consistent with recently reported reduced number and size

of superior frontal neurons in the cortices of alcoholics' brains (Harper et al. 1987). Volume reductions in subcortical structures have not been reported in previous neuroradiological studies of chronic alcoholics although some studies have found reduced computed tomography (CT) scan density measures in the thalamus and basal ganglia (Ron

1983; Gebhardt et al. 1984; Shimamura et al. 1988).

With regard to the etiology of these cortical and subcortical volume changes, two possibilities seem worth considering. First, the losses may be directly related to the neurotoxic effects of ethanol, an interpretation supported by animal studies (Walker et al. 1981). Second, the decrements in cortical and subcortical volumes may be the consequence of the mild, but numerous, bouts of malnutrition that plague chronic alcoholics. Bowden (1990) has concluded from a review of the neuropathological literature that while such a nutritionally based Wernicke's encephalopathy (Victor et al. 1989) may be present in a large percentage of alcoholic persons, the severe neurologic (e.g., ophthalmoplegia, peripheral neuropathy) and cognitive (e.g., anterograde and retrograde amnesia) symptoms associated with this pathology may not be evident until some threshold of cerebral damage has been exceeded.

This study's finding that nonamnesic alcoholics have a pattern of subcortical and cortical changes not too dissimilar to that noted in alcoholics with Korsakoff's syndrome (Jernigan et al. 1991c) is consistent with Bowden's proposal. Further supportive evidence comes from another *in vivo* study (Pfefferbaum et al. 1988), in which weight loss and evidence for nutritional compromise were both predictors of greater ventricular enlargement within nonamnesic chronic alcoholics. However, because alcoholic

Korsakoff patients in our studies had significantly more volume loss in the anterior diencephalon (hypothalamic gray, basal forebrain), mesial temporal, and orbitofrontal regions (Jernigan et al. 1991c), the possibility that some acute event may cause damage to specific cortical-subcortical structures and be responsible for the neurological and neuropsychological differences between these two groups of alcoholics cannot be dismissed (Butters 1985).

In our ongoing longitudinal study of nonamnesic alcoholic patients, we have performed followup MRI examinations in 24 subjects who returned 3 months after their baseline evaluations (which had occurred while they were still inpatients). Preliminary regression analyses suggest that successful abstinence is significantly predictive of reduction in the amount of ventricular and sulcal CSF present at followup (relative to baseline). Surprisingly, while there was no significant increase in gray matter volumes, abstinence was associated with significant increases in white matter volume. It appears then, from this still ongoing study, that the decreases in CSF noted in abstinent alcoholics may be related to some physiological changes in the myelinization process. This finding also raises the issue of whether some of the cognitive deficits associated with alcoholism may be due to white matter rather than to gray matter changes. The cognitive consequences of white matter dysfunction have

never been addressed directly in the alcohol literature.

CONCLUSIONS

The results described here, together with those of other recent studies, allow the following conclusions:

- (1) Quantitative MRI measures of brain morphology definitely reveal differences between recently detoxified chronic alcoholics and nonalcoholic controls. The alcoholics have increased CSF in the ventricles and in the cortical sulcal spaces. These changes are associated with reduced volume of the adjacent gray matter of the diencephalon, basal ganglia, and cerebral cortex. Increased white matter abnormalities were also noted in the alcoholics. Information about the presence, degree, and regional pattern of such brain abnormalities in living patients has the potential to be very useful in our attempts to understand the effects of alcoholism.
- (2) At least some component of the CSF increase observed in recently detoxified alcoholics is reversible with abstinence over a period as short as 3 months. This decrease in CSF is accompanied by a measurable increase in white matter volume.
- (3) The pattern of cerebral changes observed in recently detoxified alcoholics with mild cognitive im-

pairment is surprisingly similar to that observed in Korsakoff patients with severe memory impairments. In particular, both amnesic and nonamnesic alcoholics have definite volume loss in cortical and subcortical structures, including the diencephalon. Nevertheless, there are significant differences between the groups: Korsakoff patients have more ventricular enlargement, less hypothalamic and septal (basal forebrain) tissue, and reduced volume of mesial-temporal and orbitofrontal cortex. Whether these differences are responsible for the Korsakoff patients' severe amnesia remains to be demonstrated.

- (4) Given recent neuropathological findings, as well as evidence from these and previous imaging studies that link nutritional deficiencies with central volume loss, it is likely that the neuropathology and some information-processing deficits of chronic alcoholics lie on a continuum with those in alcoholic amnesia and alcoholic dementia.

ACKNOWLEDGMENTS

This research was supported by funds from the Department of Veterans Affairs Medical Research Service and National Institute on Alcohol Abuse and Alcoholism grant AA-00187 to Boston University. Much of the work was done within the Alcohol Research Center at the San Diego Veterans

Affairs Medical Center. The authors are indebted to Marc Schuckit, M.D., Director of the Alcohol Research Center, and to the entire research staff of the Center.

REFERENCES

- American Psychiatric Association. *DSM-III: Diagnostic and Statistical Manual of Mental Disorders*. 3rd ed. Washington, DC: APA, 1980.
- Arendt, T.; Bigl, V.; Arendt, A.; and Tennstedt, A. Loss of neurons in the nucleus basalis of Meynert in Alzheimer's disease, paralysis agitans and Korsakoff's disease. *Acta Neuropathol* 61:101-108, 1983.
- Artemann, H.; Gall, M.V.; Hacker, H.; and Herrlich, J. Reversible enlargement of cerebral spinal fluid spaces in chronic alcoholics. *Am J Neuroradiol* 2:23-27, 1981.
- Bergman, H. Brain dysfunction related to alcoholism: Some results from the KARTAD project. In: Parson, O.A.; Butters, N.; and Nathan, P.E., eds. *Neuropsychology of Alcoholism: Implications for Diagnosis and Treatment*. New York: Guilford Press, 1987. pp. 21-45.
- Bergman, H.; Borg, S.; Hindmarsh, T.; Ideström, C.-M.; and Mützell, S. Computed tomography of the brain and neuropsychological assessment of male alcoholic patients and a random sample from the general male population. *Acta Psychiatr Scand* 62(suppl 286):77-88, 1980.
- Besson, J.A.O.; Glen, A.I.M.; Iljon Foreman, E.; MacDonald, A.; Smith, F.W.; Hutchison, J.M.S.; Mallard, J.R.; and Ashcroft, G.W. Nuclear magnetic resonance observations in alcoholic cerebral disorder and the role of vasopressin. *Lancet* 2:923-924, 1981.
- Besson, J.; Glen, E.; Glen, I.; MacDonald, L.; and Skinner, F. Essential fatty acids, mean cell volume and nuclear magnetic resonance of brains of ethanol dependent human subjects. *Alcohol Alcohol* 1(suppl):577-581, 1987.
- Bowden, S.C. Separating cognitive impairment in neurologically asymptomatic alcoholism from Wernicke-Korsakoff syndrome: Is the neuropsychological distinction justified? *Psychol Bull* 107(3):355-366, 1990.
- Butters, N. Alcoholic Korsakoff's syndrome: Some unresolved issues concerning etiology, neuropathology, and cognitive deficits. *J Clin Exp Neuropsychol* 7:181-210, 1985.
- Butters, N., and Cermak, L.S. *Alcoholic Korsakoff's Syndrome: An Information-Processing Approach to Amnesia*. New York: Academic Press, 1980.
- Cala, L.A., and Mastaglia, F.L. Computerized tomography in chronic alcoholics. *Alcohol Clin Exp Res* 5(2):283-294, 1981.
- Carlen, P.L.; Penn, R.D.; Fornazzari, L.; Bennett, J.; Wilkinson, D.A.; and Wortzman, G. Computerized tomographic scan assessment of alcoholic brain damage and its potential reversibility. *Alcohol Clin Exp Res* 10(3):226-232, 1986.
- Carlen, P.L.; Wilkinson, D.A.; Wortzman, G.; and Holgate, R. Partially reversible cerebral atrophy and functional improvement in recently abstinent alcoholics. *Can J Neurol Sci* 11:441-446, 1984.

- Carlen, P.L.; Wilkinson, D.A.; Wortzman, G.; Holgate, R.; Cordingley, J.; Lee, M.A.; Huszar, L.; Moddel, G.; Singh, R.; Kiraly, L.; and Rankin, J.G. Cerebral atrophy and functional deficits in alcoholics without clinically apparent liver disease. *Neurology* 31:377-385, 1981.
- Carlen, P.L.; Wortzman, G.; Holgate, R.C.; Wilkinson, D.A.; and Rankin, J.G. Reversible cerebral atrophy in recently abstinent chronic alcoholics measured by computed tomography scans. *Science* 200:1076-1078, 1978.
- Chick, J.D.; Smith, M.A.; Engleman, H.M.; Kean, D.M.; Mander, A.J.; Douglas, R.H.B.; and Best, J.J.K. Magnetic resonance imaging of the brain in alcoholics: Cerebral atrophy, lifetime alcohol consumption, and cognitive deficits. *Alcoholism* 13(4):512-518, 1989.
- Gebhardt, C.A.; Naeser, M.A.; and Butters, N. Computerized measures of CT scans of alcoholics: Thalamic region related to memory. *Alcohol* 1:133-140, 1984.
- Harper, C. The incidence of Wernicke's encephalopathy in Australia: A neuropathological study of 131 cases. *J Neurol Neurosurg Psychiatry* 46:593-598, 1983.
- Harper, C.G., and Blumbergs, P.C. Brain weights in alcoholics. *J Neurol Neurosurg Psychiatry* 45:838-840, 1982.
- Harper, C.G.; Giles, M.; and Finlay-Jones, R. Clinical signs in the Wernicke-Korsakoff complex: A retrospective analysis of 131 cases diagnosed at necropsy. *J Neurol Neurosurg Psychiatry* 49(4):341-345, 1986.
- Harper, C.G.; Kril, J.; and Daly, J. Are we drinking our neurones away? *Br Med J* 294:534-536, 1987.
- Harper, C.G.; Kril, J.J.; and Holloway, R. Brain shrinkage in chronic alcoholics: A pathological study. *Br Med J* 290:501-504, 1985.
- Jernigan, T.L.; Archibald, S.L.; Berhow, M.T.; Sowell, E.R.; Foster, D.S.; and Hesselink, J.R. Cerebral structure on MRI, Part I: Localization of age-related changes. *Biol Psychiatry* 29(1):55-67, 1991a.
- Jernigan, T.L.; Butters, N.; DiTraglia, G.; Schafer, K.; Smith, T.; Irwin, M.; Grant, I.; Schuckit, M.; and Cermak, L.S. Reduced cerebral grey matter observed in alcoholics using magnetic resonance imaging. *Alcohol Clin Exp Res* 15(3):418-427, 1991b.
- Jernigan, T.L.; Press, G.A.; and Hesselink, J.R. Methods for measuring brain morphologic features on magnetic resonance images: Validation and normal aging. *Arch Neurol* 47:27-32, 1990.
- Jernigan, T.L.; Schafer, K.; Butters, N.; and Cermak, L.S. Magnetic resonance imaging of alcoholic Korsakoff patients. *Neuropsychopharmacology* 4(3):175-186, 1991c.
- Jernigan, T.L.; Trauner, D.A.; Hesselink, J.R.; and Tallal, P.A. Maturation of human cerebrum observed in vivo during adolescence. *Brain* 1991d, in press.
- Jernigan, T.L.; Zatz, L.M.; Ahumada, A.J.; Pfefferbaum, A.; Moses, J.A.; and Tinklenberg, J. CT measures of cerebrospinal fluid volume in alcoholics and normal volunteers. *Psychiatry Res* 7:9-17, 1982.
- Lynch, M.J.G. Brain lesions in chronic alcoholism. *Arch Pathol* 69:342-353, 1960.
- Mair, W.P.G.; Warrington, E.K.; and Weiskrantz, L. Memory disorders in

- Korsakoff's psychosis. *Brain* 102:749–783, 1979.
- Mayes, A.R.; Meudell, P.R.; Mann, D.; and Pickering, A. Location of lesions in Korsakoff's syndrome: Neuropsychological and neuropathological data on two patients. *Cortex* 24:367–388, 1988.
- Miyakawa, T.; Hattori, E.; Shikai, I.; Shimoji, A.; Nagatoshi, K.; and Suzuki, T. Histopathological changes of chronic alcoholism. *Folia Psychiat Neurol Jpn* 31(2):253–261, 1977.
- Neubuerger, K.T. The changing neuropathologic picture of chronic alcoholism. *Arch Pathol* 63:1–6, 1957.
- Pfefferbaum, A.; Rosenbloom, M.; Crusan, K.; and Jernigan, T.L. Brain CT changes in alcoholics: Effects of age and alcohol consumption. *Alcohol Clin Exp Res* 12(1):81–87, 1988.
- Pfefferbaum, A.; Zatz, L.M.; and Jernigan, T.L. Computer-interactive method for quantifying cerebrospinal fluid and tissue in brain CT scans: Effects of aging. *J Comput Assist Tomogr* 10(4):571–578, 1986.
- Ron, M.A. The alcoholic brain: CT scan and psychological findings. *Psychol Med Monogr suppl* 3:1–33, 1983.
- Ron, M.A.; Acker, W.; and Lishman, W.A. Morphological abnormalities in the brains of chronic alcoholics: A clinical, psychological and computerized axial tomographic study. *Acta Psychiatr Scand* 62(suppl 286):31–40, 1980.
- Ron, M.A.; Acker, W.; Shaw, G.K.; and Lishman, W.A. Computerized tomography of the brain in chronic alcoholism: A survey and follow-up study. *Brain* 105:497–514, 1982.
- Schuckit, M.A.; Irwin, M.R.; Howard, T.; and Smith, T. A structured diagnostic interview for identification of primary alcoholism: A preliminary evaluation. *J Stud Alcohol* 49:93–99, 1988.
- Shimamura, A.P.; Jernigan, T.L.; and Squire, L.R. Korsakoff's syndrome: Radiological (CT) findings and neuropsychological correlates. *J Neurosci* 8(11):4400–4410, 1988.
- Smith, M.A.; Chick, J.; Kean, D.M.; Douglas, R.H.B.; Singer, A.; Kendall, R.E.; and Best, J.J.K. Brain water in chronic alcoholic patients measured by magnetic resonance imaging. *Lancet* 1:1273–1274, 1985.
- Torvik, A.; Lindboe, C.F.; and Rogde, S. Brain lesions in alcoholics. *J Neurol Sci* 56:233–248, 1982.
- Victor, M.; Adams, R.D.; and Collins, G.H. *The Wernicke-Korsakoff Syndrome and Related Neurologic Disorders Due to Alcoholism and Malnutrition*, 2nd ed. Philadelphia: F.A. Davis Company, 1989.
- Walker, D.W.; Hunter, B.; Wickliffe, C.; and Abraham, B.A. Neuroanatomical and functional deficits subsequent to chronic ethanol administration in animals. *Alcohol* 5:267–282, 1981.
- Wechsler, D. *Wechsler Memory Scale—Revised*. New York: Psychological Corporation, 1987.
- Wilkinson, D.A. Examination of alcoholics by computed tomographic (CT) scans: A critical review. *Alcohol Clin Exp Res* 6(1):31–45, 1982.
- Wilkinson, D.A., and Carlen, P.L. Relationship of neuropsychological test performance to brain morphology in amnesic and non-amnesic chronic alcoholics. *Acta Psychiatr Scand* 62(suppl 286):89–101, 1980.

Zatz, L.M.; Jernigan, T.L.; and Ahumada,
A.J. Changes on computed cranial
tomography with aging: Intracranial
fluid volume. *Am J Neuroradiol* 3:1-11, 1982.

MAGNETIC RESONANCE IMAGING AND CONTRAST AGENTS IN THE EVALUATION OF ETHANOL-DAMAGED LIVERS

S.W. Young, M.D.¹ M. Sidhu, M.D.¹ A. Jones, M.D.² H.H. Muller, M.S.¹ and J. Aggeler, M.D.³

Hepatocellular carcinoma, cirrhosis, acute alcoholic hepatitis, and other alcohol-related diseases and conditions constitute a major health care problem in the United States (Garaglano et al. 1979; Hall 1985). Ethanol-related liver diseases include acute hepatocyte toxicity, chronic hepatocyte toxicity with associated cirrhosis, and hepatocellular carcinomas. Other neoplasms associated with alcohol abuse, such as head and neck malignancies and laryngeal cancers, may occasionally produce metastatic lesions within the liver. Hepatic metastases are present in more than one-third of patients dying with cancer (Willis 1973), and although patients with primary and metastatic malignancies of the liver have a dire prognosis, early detection and treatment could improve survival rates (Foster and Lundy 1981).

Magnetic resonance imaging (MRI) scanning, in conjunction with intravenously administered MRI contrast agents, is now a clearly

ACRONYMS

ADH	alcohol dehydrogenase
CT	computed tomography
DPDP	dipyridoxal diphosphate
MEOS	microsomal ethanol oxidizing system
MRI	magnetic resonance imaging
NADH	reduced form of nicotinamide adenine dinucleotide
NMR	nuclear magnetic resonance
ROI	region of interest
SGPT	serum glutamic pyruvic transaminase
^{99m} Tc-IDA	technetium-99m iminodiacetic acid
TR/TE	pulsing sequence

¹Department of Diagnostic Radiology and Nuclear Medicine, Stanford University School of Medicine, Stanford, CA 94305

²Cell Biology and Aging Section, Department of Veterans Affairs Medical Center, San Francisco, CA 94121

³The Liver Center, University of California, San Francisco, San Francisco, CA 94121

established modality in detecting mass lesions of the liver such as hepatocellular carcinoma. It is rapidly becoming the imaging technique of choice in evaluating the liver. Preliminary evidence suggests that this approach may be useful in detecting ethanol-induced hepatocyte toxicity as well.

Recently, the overall accuracy of T1-weighted pulse sequences has been found to be superior to contrast-enhanced computed tomography (CT; Stark et al. 1987) for detecting liver malignancies. MR contrast agents have been developed in an attempt to facilitate early detection of small liver lesions and to improve MRI sensitivity and clinical efficacy (Wolf et al. 1985). Research has led to the use of water-soluble MRI contrast agents such as Gd-DTPA (Brasch et al. 1984; Engelstad and Wolf 1987), which has a distribution volume throughout the extracellular space of both normal and abnormal tissue.

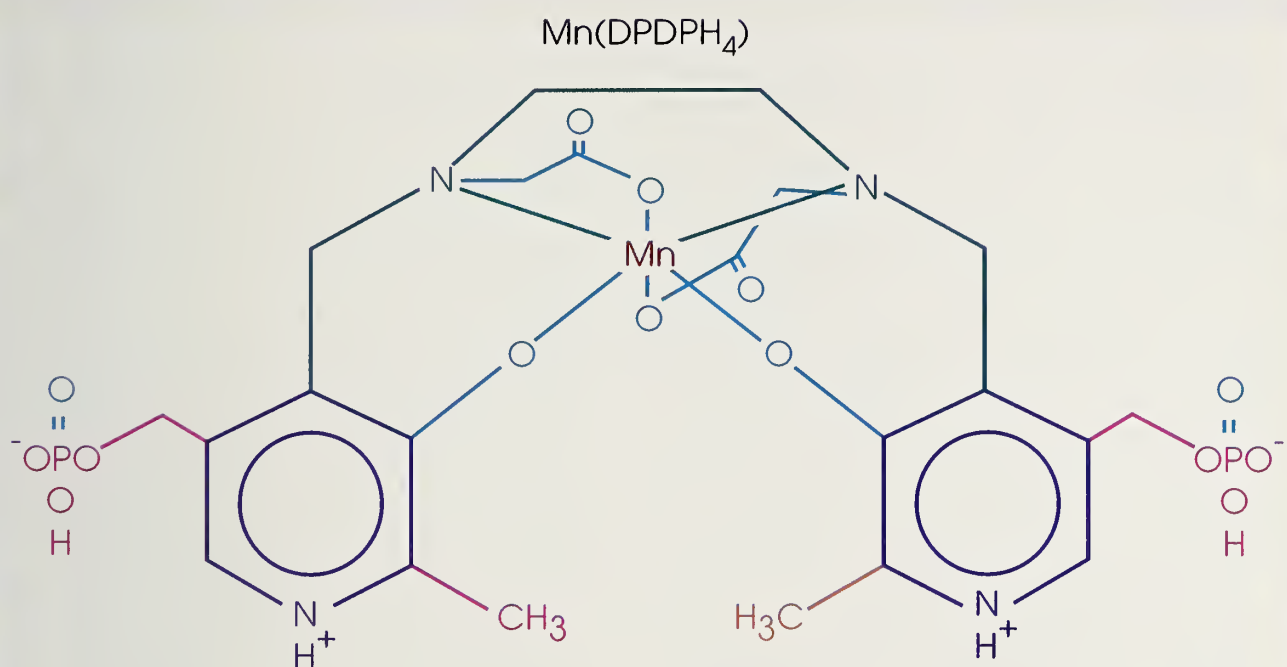
Selective enhancement of the difference between normal and abnormal liver tissue involves using particulate paramagnetic (Engelstad and Wolf 1987), superparamagnetic (Saini et al. 1985; Stark et al. 1986a; Engelstad and Wolf 1987), and fluorinated (Young 1981; Young et al. 1981; Ratner et al. 1987a; Freeman et al. 1988) emulsions to label and enhance the reticuloendothelial system within the liver. Although these methods have been successful, such agents label only a small portion of the total volume of the liver; e.g., Kupffer cells are only 2 percent of total liver volume (Jones 1982). Nevertheless, superparamag-

netic ferrite particles have been shown to enable the detection of 2- to 3-mm liver metastases in rats (Tsang et al. 1988).

New hepatocellular MR contrast agents that label hepatocyte volume (78 percent of the liver) and can be rapidly secreted in bile appear promising (Greif et al. 1985; Young et al. 1989; Lim et al. 1989). The paramagnetic contrast agent Mn-DPDP (S-O95, Salutar, Inc., Sunnyvale, CA) depicted in figure 1 is a manganese chelate derived from pyridoxal-5-phosphate, which is secreted by the liver (Lauffer et al. 1985; White et al. 1988; Rocklage et al. 1988; Elizondo et al. 1991; Lim et al. 1991). Mn-DPDP has recently been shown to produce sustained (60–90 minutes) contrast enhancement of the liver *in vivo* on both long and short TR/TE pulsing sequences and to be useful in measuring hepatocyte function (Young et al. 1989; Young and Bradley 1990). Such a hepatobiliary MR contrast agent may be capable of detecting liver metastases not detected by agents confined to the extracellular space or Kupffer cells.

ETHANOL LIVER TOXICITY

Within the hepatocyte, there are three main pathways for ethanol metabolism to acetaldehyde: (1) the microsomal ethanol oxidizing system (MEOS) located in the endoplasmic reticulum; (2) the alcohol dehydrogenase (ADH) pathway of the cytosol; and (3) catalase located in the peroxisomes (Lieber 1984). The discovery that ethanol in-

FIGURE 1

Schematic drawing of Mn-DPDP, a manganese/pyridoxal-5-phosphate hexadentate chelate.

creases proliferation of the endoplasmic reticulum led to the discovery of the inducible cytochrome P₄₅₀-dependent ethanol oxidation pathway within liver microsomes (Koop et al. 1982). The existence of this cytochrome P₄₅₀-dependent pathway has explained many ethanol-drug interactions as well as alterations in ethanol metabolism and toxicity by other compounds (Morgan et al. 1982; Lieber 1982). Some of the toxic effects of ethanol have been linked to the generation of the reduced form of nicotinamide adenine dinucleotide (NADH) by the oxidation of ethanol via the ADH pathway, to the interactions of ethanol with membranes, and to hypermetabolic hypoxia (Salaspuro

and Lieber 1978; Lieber 1982, 1984; Hall 1985).

Acetaldehyde is a toxic product of ethanol metabolism in the liver. It covalently binds proteins, causing lipid peroxidation and hepatic protein and water retention. The result is hepatocyte swelling and increased portal pressure. Abnormal morphology (e.g., enlarged and abnormal christa, paracrystalline inclusions, and disrupted membranes) and function of mitochondria are characteristic of early-stage alcohol-induced liver injury in animals and in man (Lieber 1982).

In normal animals, manganese is secreted by the liver, and vitamin B₆ (pyridoxal-5-phosphate) and its metabolites are metabolized in the

mitochondria (Lui et al. 1981). The levels of pyridoxal-5-phosphate, which partially protects hepatocytes from acetaldehyde toxicity (Lumeng 1978; Kakuma et al. 1981), are depressed in ethanol-fed animals (Shane 1982). The MR contrast agent Mn-DPDP, a manganese/pyridoxal-5-phosphate chelate, is transported into the hepatocyte and secreted in bile. Although the exact metabolic steps are not known, we have shown by MRI scanning that liver processing of Mn-DPDP is altered in hepatotoxic rodents. Whereas alcohol toxicity affects many hepatocyte subunits, it is likely that impairment of these subunits contributes to the changes in many regions of the liver (i.e., zones I, II, III) observed on MRI/Mn-DPDP scans.

LIVER IMAGING WITH MAGNETIC RESONANCE

The first reports on proton (¹H) MRI indicated that MRI techniques used to screen the liver for focal lesions were not as sensitive or specific as CT scanning (Moss et al. 1984; Wittenberg et al. 1986; Glazer et al. 1986). To improve MRI sensitivity and clinical efficacy, researchers designing pharmacologically acceptable relaxation agents (Harder and Chaberek 1959; Whidby et al. 1970; Desreux et al. 1980) have emphasized efficacy (measured by molar relaxometry) and safety (measured by toxicity experiments). Their efforts have led to the use of such well-known MRI relaxation agents as Gd-DTPA or Gd-DOTA (Brasch et al. 1984; Gadian et al. 1985).

Previously, the development of MR contrast agents concentrated on water-soluble agents, which have a distribution volume throughout the extracellular space (Wolf et al. 1986; Hamm et al. 1987). While these provide excellent enhancement of the extracellular water, they lack specific pharmacokinetic tissue interactions and thus accumulate in the extracellular space of both normal and abnormal tissue. Pulsing sequences designed to detect abnormal T1 and T2 relaxation rates (Stark et al. 1986b; Edelman et al. 1986; Bottomley et al. 1987) have led to some improvement, but until recently the specificity of these contrast agents for lesions and normal tissue has been unimpressive.

Particulate paramagnetic, superparamagnetic, and fluorinated emulsions label the reticuloendothelial system within the liver; however, these types of MRI contrast agents label only a small portion of the total volume of the liver. They reveal nothing about the functional status of hepatocytes, which predominate in the liver volume (Jones 1990). Furthermore, these agents often have unacceptably long dwelling times within body tissues.

HEPATOBILIARY MR CONTRAST AGENTS

Five-substituted iron-EHPG derivatives that mimic the technetium-^{99m} iminodiacetic acid (^{99m}Tc-IDA) complexes currently used for cholescintigraphy (Chervu et al. 1984) have been used to evaluate biliary

Table 1. Comparison of pre-Mn-DPDP ROI values among the study groups of normal and ethanol- and D-galactosamine-treated rabbits

TR/TE	Normal	ETOH	D-Gal
330/30	141 ± 39	154 ± 14	130 ± 36
330/75	114 ± 15	125 ± 15	97 ± 29

Means ± S.D.

excretion in normal animals (Nunn et al. 1983; Greif et al. 1985; Lauffer et al. 1985, 1987). Although the process of biliary excretion has not been defined, it appears to be determined by lipophilicity and protein-binding affinity (e.g., of albumin or cytosolic proteins; Nunn et al. 1983; Chervu et al. 1984; Greif et al. 1985; Lauffer et al. 1985, 1987; Engelstad et al. 1987).

Mn-DPDP (figure 1; Young et al. 1981) represents the biomimetic approach to studying liver disease. As opposed to the development of diagnostic MRI contrast agents, therapeutic drug development has been superbly successful in applying the principle of biomimetic drug design. The novel chemical entities

created mimic natural molecules to such an extent that they can interact directly with them in crucial biological processes. As a derivative of pyridoxal-5-phosphate, an essential coenzyme for a number of important biochemical reactions, especially transamination in cardiac tissue and hepatocytes, Mn-DPDP is the first *in vivo* MR contrast agent designed to estimate the functional status of the hepatocyte (Stark et al. 1987).

In the synthesis of Mn-DPDP, the ligand dipyridoxal diphosphate (DPDP) was prepared from pyridoxal-5-phosphate and ethylenediamine to give a Schiff base intermediate that is reduced *in situ*

Table 2. Comparisons between normal and ethanol- and D-galactosamine-treated groups of rabbits

TR/TE	ETOH vs. Normal (minutes)	D-Gal vs. Normal (minutes)
330/30	10-60	20-60
330/75	10,40-60	3-60

Time intervals indicated are the intervals for which $p < 0.05$.

Table 3. MRI enhancement of acute ethanol-induced liver changes

	Enhancement	
	T1W	T2W
High dosage		
Ethanol	56.5	-45.4
Control	79.5	-35.7
Significance	<i>p</i> = 0.017	NS
Low dosage*		
Ethanol	66.5	-18.2
Control	83.6	-25.1
Significance	<i>p</i> = 0.013	NS

NS=not significant.

*Precontrast T2 signal intensity significantly different between the groups.

to the desired N,N'-bis-(pyridoxal-5-phosphate) ethylenediamine (Elizondo et al. 1991). The resulting diamine, alkylated with bromoacetic acid, yields the novel ligand N,N'-bis-(pyridoxal-5-phosphate) ethylenediamine-N,N'-diacetic acid.

DPDP has been completely characterized by high-resolution NMR, elemental analysis, potentiometry, and mass spectroscopy. DPDP forms 1:1 chelates with manganese(II) that are extremely water soluble (500-mM solutions) and have acceptable molar relaxivity (about 3.5 mM/seconds at 10 MHz in plasma). X-ray quality crystals were obtained from concentrated aqueous solutions at pH 7. The crystal structure shows the Mn(II) chelate consists of discrete Mn(II)DPDP molecules which form, together with water molecules, an indefinite, hydrogen-bonded, polymeric network. Mn(II) resides in the center of a distorted octahedron made up of two aromatic hydroxyl oxygen atoms, two carboxylic oxygen atoms,

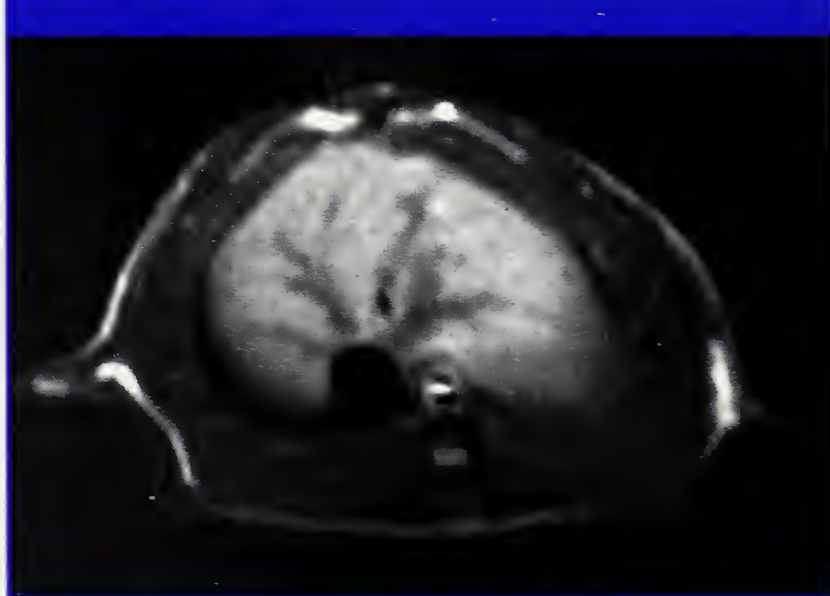
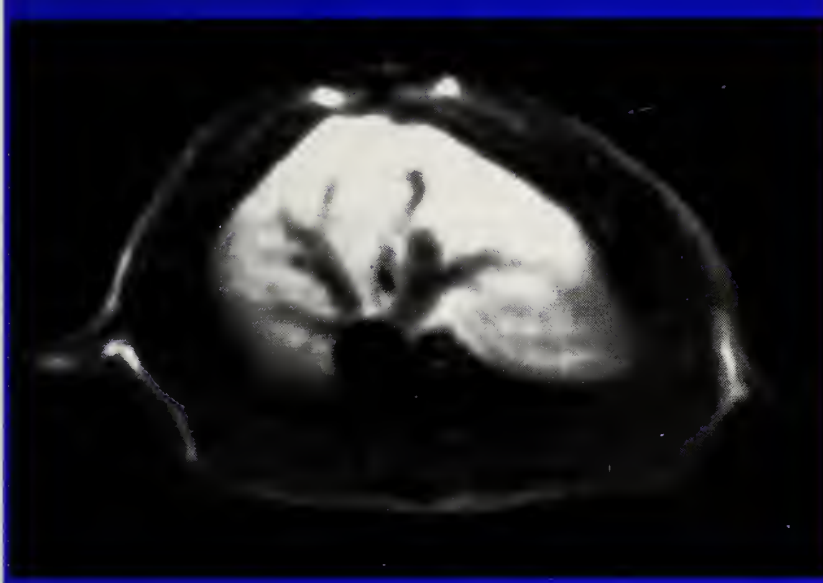
FIGURE 2a**Axial MRI scans of rat livers before the administration of Mn-DPDP in normal animals.**

FIGURE 2b

Axial MRI scans of rat livers after the administration of Mn-DPDP in normal animals.

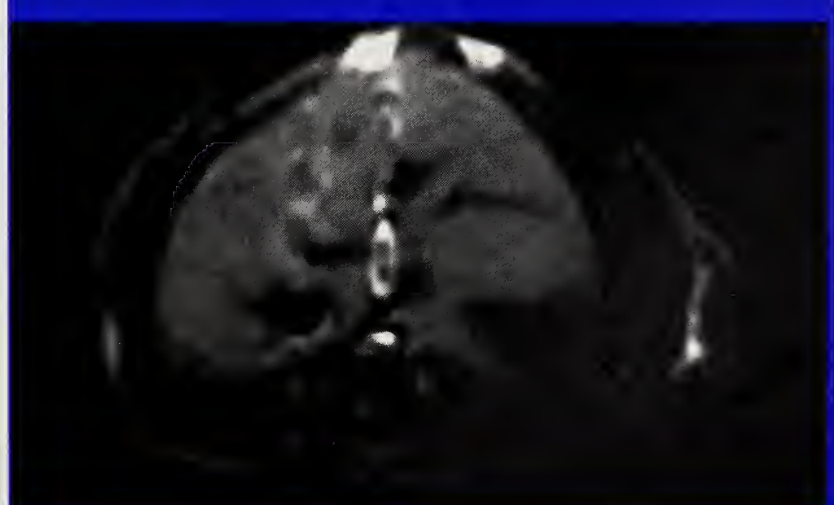
and two tertiary nitrogen atoms, as shown in figure 1.

The nuclear magnetic resonance (NMR) signals ^1H , T1, T2, flow, and chemical shift of MRI reflect the biochemical and physiological status of the tissue being evaluated (Bottomley et al. 1987). Clinical applications of hepatic MRI have successfully used the anatomic information provided by MRI scans. Although gross liver deformity due to alcoholic cirrhosis and fatty liver replacement has been observed with MRI, this technique has not been used to detect early ethanol-induced hepatocyte damage in patients. Animal (rat) studies, however, have demonstrated correlations between steatosis and increased T2 relaxation following ethanol ingestion and between lengthened T1 and

hepatocyte necrosis following the ingestion of carbon tetrachloride and D-galactosamine. Significant lengthening of both T1 and T2 was noted in animals with significant steatosis and necrosis (Camara et al. 1983; Ratner et al. 1986), even though these relaxation rates are known to be field dependent (Brown 1985; Koenig et al. 1985).

BIODISTRIBUTION STUDIES USING MRI

Pharmacokinetics research on rodents has included analysis of Mn-DPDP and tissues containing Mn-DPDP using a high-resolution NMR Bruker MSL-400 spectrometer (^1H , ^{13}C , and ^{31}P). Relaxivity measurements were made on a RADX 530 NMR Proton Spin Analyzer at 10 MHz. Analyses following intravenous administration of Mn-DPDP

FIGURE 2c

Axial MRI scans of rat livers in animals administered ethanol.

(100 μmol) revealed a >60 percent decrease in T1 of the liver at a dose of only 0.05 mM/kg body weight. Maximum uptake of Mn-DPDP by the liver was recorded at approximately 1 hour, with approximately 85 percent clearance by 6 hours. The kidneys had maximum uptake within 30 minutes but cleared more slowly. Thirty minutes after injection, 13 percent of the Mn-DPDP was present in the liver, 9 percent in the small intestine, 3 percent in the blood, 1.3 percent in the kidneys, and <1 percent in other organs (Elizondo et al. 1991).

Whole-body clearance studies revealed that 43 percent of injected Mn-DPDP is cleared by renal excretion and 47 percent by fecal excretion after 6 hours. There is 6 percent body retention 7 days after administration. Mn-DPDP relaxivity

in tissues increased substantially over that with aqueous solutions (i.e., Mn-DPDP relaxivity within the hepatocytes is greater in Mn-DPDP in normal saline). The aqueous versus liver R_1 values were 2.8 and 21.7 mM/second, respectively, and the R_2 values were 3.7 and 62.7 mM/second, respectively.

The LD₅₀ of the Mn-DPDP is 5.4 mM/kg. The safety factor, expressed as the ratio of LD₅₀ to the dose used for imaging, is 544 for Mn-DPDP, indicating it is comparatively safer than Gd-DTPA, which has a safety factor in the range of 62–100 (Elizondo et al. 1991).

MRI STUDIES

Over the past 15 years, we have imaged rodents (mice, rats, hamsters) and rabbits, using scanners operating between 0.38 and 4.7 T, and we have been working with animal models of human disease (Ballerio et al. 1987; Ratner et al. 1987a,b, 1988a,b; Freeman et al. 1988; Young et al. 1989; Young and Bradley 1990). During preliminary Mn-DPDP pharmacokinetics research in rabbits (Young et al. 1989; Young and Bradley 1990), MRI at 0.38 and 1.5 T revealed significant increases in hepatic image intensity (region of interest, ROI), with pulsing sequences designed to increase the T1 contribution (i.e., short TR/TE). Biphasic (early increase and subsequent stable decrease)

FIGURE 2d



Axial MRI scans of rat livers in animals administered ethanol. Note the decreased contrast enhancement in the livers of the ethanol-treated animals compared with the livers of saline-treated controls (figure 2b).

image intensity changes were noted on pulsing sequences designed to increase the T2 contribution at 0.38 T. Although changes in Mn-DPDP concentration could account for the increased image intensity, the studies also suggest the possibility that Mn-DPDP relaxivity is changed within the hepatocyte. This change in relaxivity could occur during the transport, protein-binding, and/or metabolism of the agent because of changes in coordinate sites, correlation time, or access of cellular water to the paramagnetic atoms.

MRI images confirmed that damaged livers can be detected during the MRI/Mn-DPDP studies. Rabbits treated with D-galactosamine to induce hepatocyte necrosis could not be differentiated from untreated controls on MRI scans prior to the administration of Mn-DPDP.

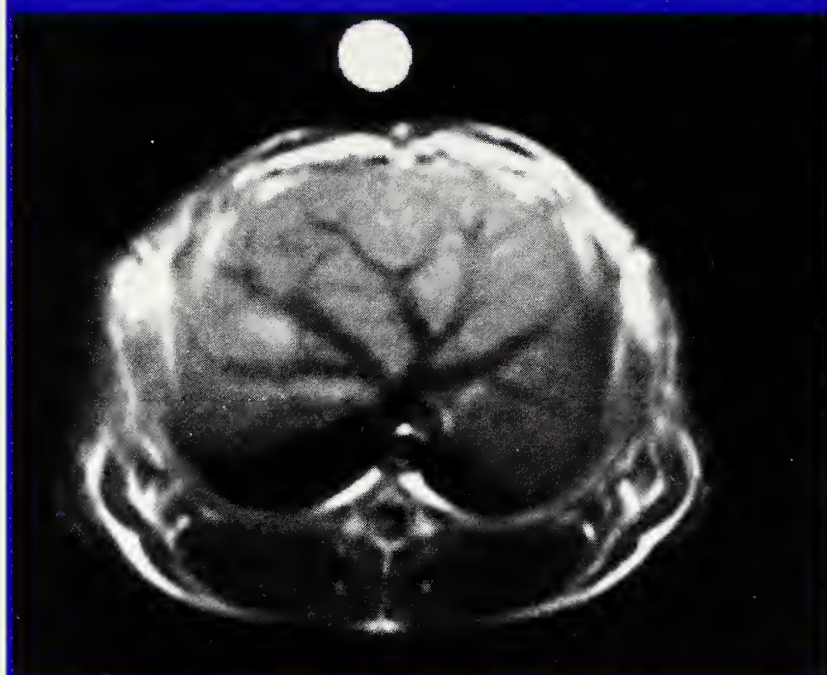
However, MRI scans obtained following Mn-DPDP injection revealed no uptake of Mn-DPDP by the liver, thus indicating severe hepatocyte damage. Rabbits treated with ethanol had a reduced Mn-DPDP uptake, but the difference between these and control rabbits was less significant than that for the D-galactosamine-treated animals, suggesting intermediate hepatocyte damage (Young et al. 1989).

Hepatotoxicity in Rabbits

New Zealand white rabbits weighing from 1.6 to 2.5 kg were anesthetized via initial intramuscular injection of ketamine (35 mg/kg) and rompun (5 mg/kg). Butterfly catheters were then inserted into ear veins for future intravenous injections. The rabbits were placed in the head coil of a 0.38 T resistive magnet. The following parameters describe the preinjection control

Table 4. MRI enhancement of chronic ethanol-induced liver changes

	Enhancement		
	T1W	T2W(TR2000)	T2W(TR2500)
1 Week			
Ethanol	86.2	-27.3	
Control	93.9	-41.8	
2 Weeks			
Ethanol	92.1	-4.9	-25.3
Control	99.5	-44.8	-34.8
3 Weeks			
Ethanol	82.2	-45.4	-2.2
Control	109.4	-35.7	-20.3
4 Weeks			
Ethanol	95	-26.6	
Control	93	-32.2	

FIGURE 3a

Axial MRI scans of a rabbit liver containing an implanted carcinoma before intravenous administration of 50 mM Mn-DPDP. The scans were obtained at 1.5 T using a 200/20 (TR/TE) pulsing sequence. The carcinoma in the right medial lobule measures 3 mm diameter x 17 mm length. Note the increased conspicuity of the neoplasm in the postcontrast studies on the T1 weighted scan. Carcinoma/liver intensity difference was 0.

scans: TR, 330 milliseconds; TE, 30 and 75 milliseconds; excitations, four; thickness, 9 mm; gap, 10 percent; matrix, 128x128; slices in transaxial orientation, three.

ROI in the liver and gallbladder were measured, and all images were photographed. ROI obtained from the liver in all animals before and for 60 minutes following Mn-DPDP administration were evaluated by slice and echo and corrected for changes in scaling factors as a result of changes in tuning of receiver gains from scan to scan. Background corrections were then made and percent differ-

ences were calculated on the basis of the calculation (Precontrast ROI - postcontrast ROI) \times 100/precontrast ROI. Mean and standard deviation values at each time point were evaluated and plotted for each group. Serum glutamic pyruvic transaminase (SGPT) samples were obtained from all animals. Tests for significance between groups were performed using a standard unpaired Student's t test (Young et al. 1989).

SGPT levels measured both pre- and post-Mn-DPDP administration revealed significant hepatocyte necrosis in ethanol-treated rabbits (93 ± 20.8 , pre; 329.3 ± 90.0 , post) as well as D-galactosamine-treated rabbits (89.0 ± 49.9 , pre; 1517.2 ± 1776.8 , post), although, as expected, considerably more hepatocyte damage was induced by D-galactosamine. Despite significant hepatocyte necrosis, however, normal and ethanol- and D-galactosamine-treated animals could not be differentiated from each other (all $p > 0.14$) on the basis of pre-Mn-DPDP ROI values (table I).

During the 60-minute observation period, the intensity readings recorded from the liver in normal control animals not receiving Mn-DPDP did not change significantly, indicating stability in the scanner and no progressive effect from the anesthesia. However, significant

differences were noted between the normal, ethanol, and D-galactosamine groups following Mn-DPDP administration. Comparison between normal animals and normal animals receiving Mn-DPDP revealed visible paramagnetic contrast enhancement.

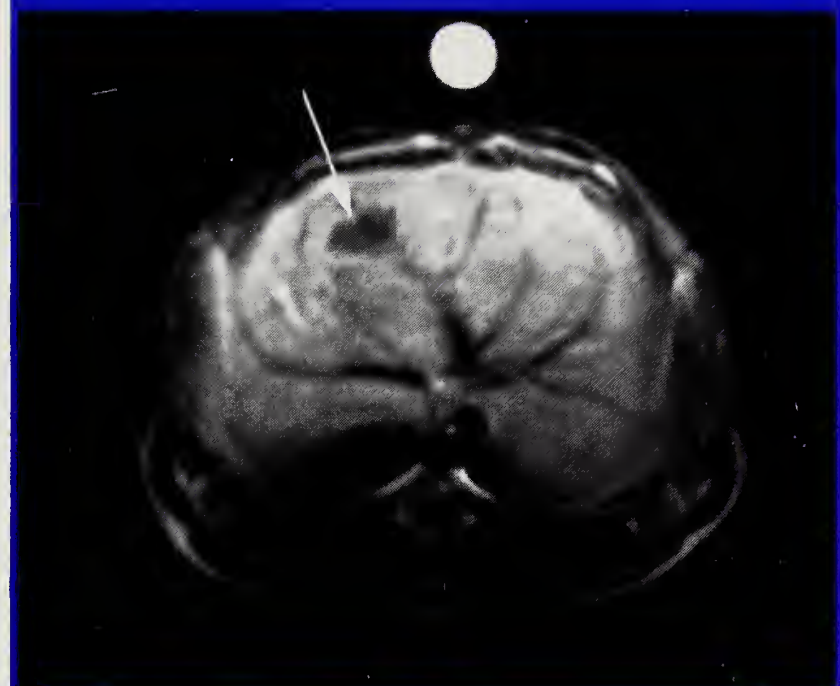
Student's t test comparisons of normal and ethanol-treated groups and normal and D-galactosamine-treated groups revealed significant differences between toxin-damaged and normal livers as early as 3 minutes post-Mn-DPDP administration (table 2).

Hepatocyte Toxicity in Rats

We have recently undertaken the study of acute and chronic ethanol toxicity in rats, employing MRI/Mn-DPDP and electron microscopy of ethanol-treated livers. Statistically significant differences in contrast enhancement between control rats and rats receiving acute ethanol treatment (9.3 or 3 g/kg by intraperitoneal injection) were observed following Mn-DPDP (table 3). Contrast enhancement (figure 2) in the control group was 83.6 percent ($n=4$) and 66.5 percent in ethanol-treated animals ($n=8$) ($p=0.013$).

Chronically treated animals received a diet with 36 percent of calories provided by ethanol over a period of 1-4 weeks; in the early

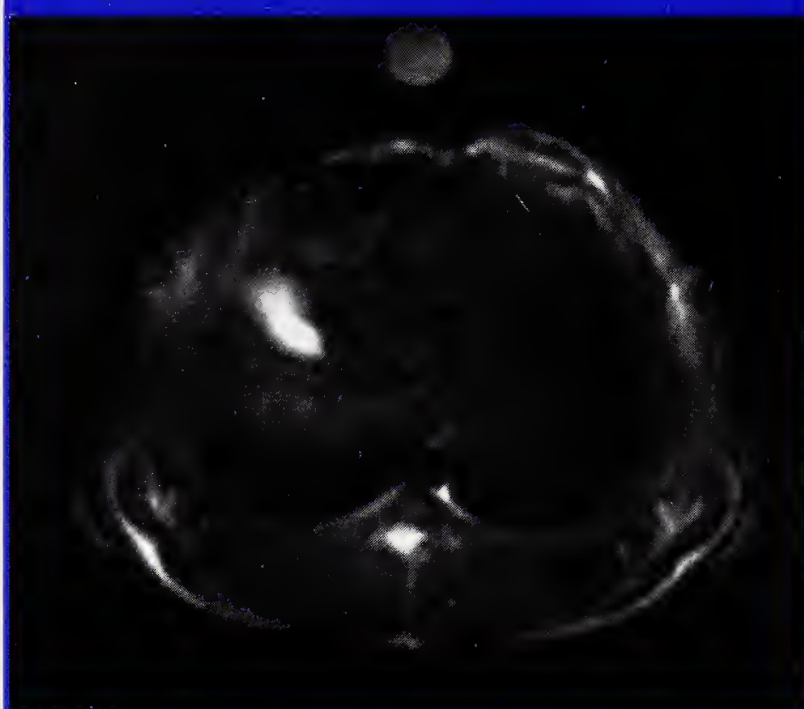
FIGURE 3b



Axial MRI scans of a rabbit liver containing an implanted carcinoma after intravenous administration of 50 mM Mn-DPDP. The scans were obtained at 1.5 T using a 200/20 (TR/TE) pulsing sequence. The carcinoma in the right medial lobule (arrow) measures 3 mm diameter x 17 mm length. Note the increased conspicuity of the neoplasm in the postcontrast studies on the T1 weighted scan. Carcinoma/liver intensity difference was 81.

stages of the study, only the 2-week animals had reached a statistically significant difference in contrast enhancement: control, 99.5 percent ($n=3$) and chronic ethanol-fed rats, 92.1 percent ($n=4$; $p=0.049$; table 4).

Electron micrographs of the livers of animals that received either 9.3 or 3 g/kg ethanol intraperitoneal revealed extensive damage, including abnormal nuclei, swollen endoplasmic reticulum, and abnormal bile canaliculi. Acute intragastric ethanol administration did not result in such extensive damage as intraperitoneal administration; the

FIGURE 3c

Axial MRI scans of a rabbit liver containing an implanted carcinoma before intravenous administration of 50 mM Mn-DPDP. The scans were obtained at 1.5 T using a 1200/60 sequence. The carcinoma in the right media lobule measures 3 mm diameter x 17 mm length. Note the increased conspicuity of the neoplasm in the postcontrast studies on the T2 weighted scan. Carcinoma/liver intensity difference was 6.

liver damage may be related in part to inflammatory peritoneal effects. Electron micrographs of livers obtained from the rats following chronic ethanol ingestion revealed characteristic liver damage, including increased smooth endoplasmic reticulum, swollen mitochondria, and gradual accumulation of fat within the hepatocytes. These changes (especially hypertrophy of the smooth endoplasmic reticulum) were initially noted in the 1-week livers. Over the next 4 weeks, these changes became progressively worse, so that by 4 weeks of ethanol ingestion, damage is seen

throughout the liver. Overall, the increase in fat accumulation by 4 weeks was not as striking as might have been expected, but some cells clearly have large amounts of lipid and show large droplets that would not be expected in control cells.

Liver Cancers in Animals

MRI/Mn-DPDP studies have been performed at 1.5 T using normal and liver cancer rabbits (figure 3) administered 5- to 50- μ M/kg Mn-DPDP intravenously (Young and Bradley 1990). Pulsing sequences (TR/TE) of 300/25 and 200/25 were used to increase the T1 influence, and Mn-DPDP provided excellent contrast enhancement even at 13 μ M/kg. Image ROI intensity readings increased between 63 and 100 percent, depending upon the conditions of the experiment.

In rabbits with implanted V2 carcinomas, neoplasms as small as 2–3 mm were detected. Contrast enhancement and lesion detectability increased substantially on both short TR/TE and long TR/TE sequences; however, some neoplasms were only detectable on the long TR/TE sequences.

Liver Cancers in Humans

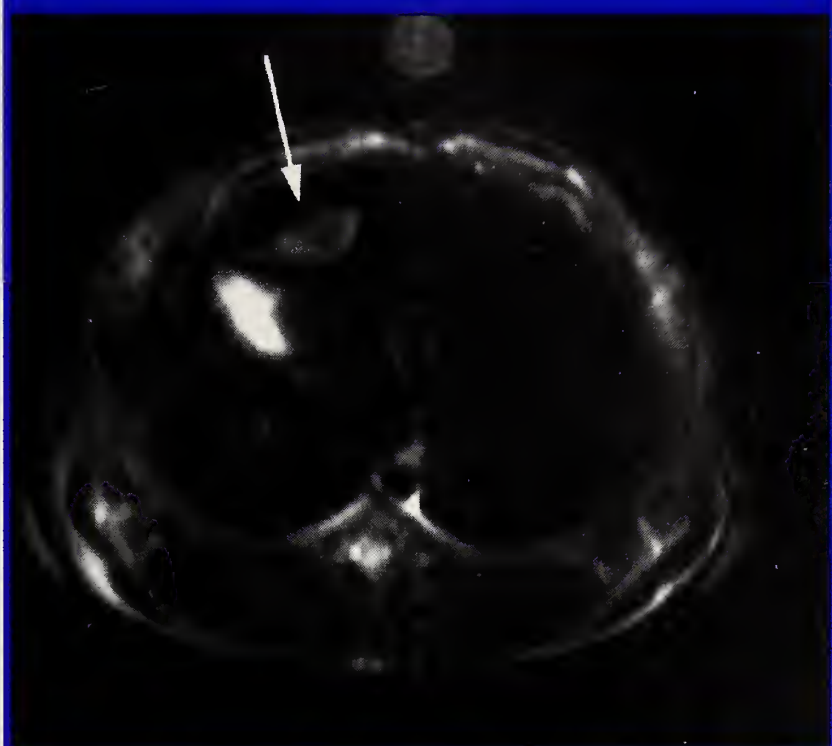
The recently completed 96-patient phase II clinical trial of Mn-DPDP included several patients with hepatocellular carcinoma or regenerating nodules. In that study, Mn-DPDP improved the contrast resolution

of hepatocellular tumors. Occasionally, regenerating nodules in cirrhotic patients could be differentiated from hepatocellular carcinomas because of the increased uptake of Mn-DPDP in the regenerating nodules. Presumably, the increased contrast enhancement in regenerating liver nodules is related to the increased protein synthesis, possibly also to an increased accumulation of the contrast agent.

CONCLUSIONS

MRI is now clearly established as a modality in the noninvasive evaluation of liver disease. In conjunction with contrast media such as Mn-DPDP that are accumulated selectively in the hepatocytes, MRI can improve in the detection of space-occupying lesions such as metastases or hepatocellular carcinomas related to cirrhosis and chronic ethanol ingestion. Since Mn-DPDP requires normally functioning hepatocytes to produce contrast enhancement, preliminary studies indicate that contrast enhancement as seen on MRI scans can be used to estimate the amount of hepatocyte damage related to toxins such as D-galactosamine or ethanol. These observations offer the attractive possibility of using contrast-enhanced MRI scans to indicate hepa-

FIGURE 3d



Axial MRI scans of a rabbit liver containing an implanted carcinoma after intravenous administration of 50 mM Mn-DPDP. The scans were obtained at 1.5 T using a 1200/60 sequence. The carcinoma in the right medial lobule (arrow) measures 3 mm diameter x 17 mm length. Note the increased conspicuity of the neoplasm in the postcontrast studies on the T2 weighted scan. The liver darkening is due to the large R₂ characteristic of Mn-DPDP in liver tissue. Carcinoma/liver intensity difference was 71.

tocyte damage and liver metabolic status *in vivo*.

A long plateau of contrast enhancement has been seen in both human and animal studies between 20 and 90 minutes postadministration of MR contrast agent Mn-DPDP. This enhanced image may result from saturation of membrane transport and/or carrier protein systems within the cell, or perhaps from prolonged intracellular binding to cytosol proteins. Regardless of the specific explanation, patient

evaluation can be facilitated by the long stable plateau period. Once reliable protocols have been established, a single scan between 25 and 90 minutes presumably would be sufficient to determine whether hepatocytes were normal or not following Mn-DPDP administration.

REFERENCES

- Ballerio, C.; Bradley, B.R.; Muller, H.H.; and Young, S.W. Microsphere distribution in normal and tumor-bearing (DMBA induced carcinogenesis) hamster cheek pouch. *Invest Radiol* 22:456-461, 1987.
- Bottomley, P.A.; Hardy, C.J.; Argersinger, R.E.; and Allen-Moore, G. A review of ¹H nuclear magnetic resonance relaxation in pathology: Are T1 and T2 diagnostic? *Med Phys* 14(1):1-37, 1987.
- Brasch, R.C.; Weinmann, H.J.; and Wesbey, G.E. Contrast-enhanced NMR imaging: Animal studies using gadolinium-DTPA complex. *Am J Roent* 142:625-630, 1984.
- Brown, M.A. Effects of operating magnetic field on potential NMR contrast agents. *Magn Reson Imaging* 3(1):3-10, 1985.
- Camara, D.S.; Caruana Jr., J.A.; Schwartz, K.A.; Montes, M.; and Nolan, J.P. D-Galactosamine liver injury: Absorption of endotoxin and protective effect of small bowel and colon resection in rabbits (41555). *Proc Soc Exp Biol Med* 172:255-259, 1983.
- Chervu, L.R.; Nunn, A.D.; and Loberg, M.D. Radiopharmaceuticals for hepatobiliary imaging. *Semin Nucl Med* 12:5-17, 1984.
- Desreux, J.F. Nuclear magnetic reso-
- nance spectroscopy of lanthanide complexes with a tetraacetic tetraaza macrocycle. Unusual conformational properties. *Inorg Chem* 19:1319-1324, 1980.
- Edelman, R.R.; Hahn, P.F.; Buxton, R.; Wittenberg, J.; Ferrucci, J.T.; Saini, S.; and Brady, T.J. Rapid MR imaging with suspended respiration: Clinical application in the liver. *Radiology* 161:125-131, 1986.
- Elizondo, G.; Fretz, C.J.; Start, D.D.; Rocklage, S.M.; Quay, S.C.; Worah, D.; Tsang, Y.M.; Chen, C.M.M.; and Ferrucci, J.T. Preclinical evaluation of MnDPDP: New paramagnetic hepatobiliary contrast agent for MR imaging. *Radiology* 178:73-78, 1991.
- Engelstad, B.L.; White, D.L.; Huberty, J.P.; Wynne, C.S.; Ramos, E.C.; McNamara, M.T.; and Goldberg, H.I. Hepatobiliary magnetic resonance contrast agents assessed by gadolinium-153 scintigraphy. *Invest Radiol* 22:232-238, 1987.
- Engelstad, B.L., and Wolf, G. Contrast agents. In: Bradley, M., and Stark, D.D., eds. *Magnetic Resonance Imaging*. St. Louis: C.V. Mosby, 1987. pp. 161-181.
- Foster, J.H., and Lundy, J. Liver metastases. *Curr Probl Surg* 18:160-282, 1981.
- Freeman, D.M.; Muller, H.H.; Hurd, R.E.; and Young, S.W. Rapid ¹⁹F magnetic resonance imaging of perfluorooctylbromide in vivo. *Magn Reson Imaging* 5:61-64, 1988.
- Gadian, D.G.; Payne, J.A.; Bryant, D.J.; Young, I.R.; Carr, D.H.; and Bydder, G.M. Gadolinium-DTPA as a contrast agent in MR imaging: Theoretical projections and practical observations. *J Comput Assist Tomogr* 9:242-251, 1985.
- Garagliano, C.F.; Lilienfeld, A.M.; and

- Mendeloff, A.I. Incidence rates of liver cirrhosis and related disease in Baltimore and selected areas of the United States. *J Chronic Dis* 32:543-554, 1979.
- Glazer, G.M.; Aisen, A.M.; Francis, I.R.; Gross, B.H.; Gyves, J.W.; and Ensminger, W.D. Evaluation of focal hepatic masses: A comparative study of MRI and CT. *Gastrointest Radiol* 11:263-268, 1986.
- Greif, L.W.; Bustom, R.B.; Lauffer, R.B.; Saini, S.; Stark, D.D.; Wedeen, V.J.; Rosen, B.R.; and Brady, T.J. Pulse sequence optimization for MR imaging using a paramagnetic hepatobiliary contrast agent. *Radiology* 157:461-466, 1985.
- Hall, P. *Alcoholic Liver Disease: Pathobiology, Epidemiology and Clinical Aspects*. New York: Wiley-Medical, 1985. pp. 1-40, 230-249.
- Hamm, B.; Wolf, J.J.; and Felix, R. Conventional and rapid MR imaging of the liver with Gd-DTPA. *Radiology* 164:313-320, 1987.
- Harder, R., and Chaberek, S. The interaction of rare earth ions with diet by unitriaminepentaacetic acid. *Inorg Nucl Chem* 11(3):197-209, 1959.
- Jones, A.L. Anatomy of the normal liver. In: Zakim, D., and Boyer, T.D., eds. *Hepatology: A Textbook of Liver Disease*. Philadelphia: W.B. Saunders, 1982. pp. 3-31.
- Jones, A.L. Anatomy of the normal liver. In: Zakim, D., and Boyer, T.D., eds. *Hepatology: A Textbook of Liver Disease*. 2nd ed. Philadelphia: W.B. Saunders, 1990. pp. 3-30.
- Kakuma, S.; Leevy, C.M.; Frank, O.; and Baker, H. Protection of pyridoxal 5'-phosphate against toxicity of acetaldehyde to hepatocytes. *Proc Soc Exp Biol Med* 168(3):325-329, 1981.
- Koenig, S.H.; Brown III, R.D.; Goldstein, E.J.; Burnett, K.R.; and Wolf, G.L. Magnetic field dependence of proton relaxation rates in tissue with added Mn²⁺: Rabbit liver and kidney. *Magn Reson Med* 2(2):159-168, 1985.
- Koop, D.R.; Morgan, E.T.; Tarr, G.E.; and Coon, M.J. Purification and characterization of a unique isozyme of cytochrome P-450 from liver microsomes of ethanol-treated rabbits. *J Biol Chem* 257:8472-8480, 1982.
- Lauffer, R.B.; Greif, W.L.; Stark, D.D.; Vincent, A.C.; Saini, S.; Wedeen, V.J.; and Brady, T.J. Pulse sequence optimization for MR imaging using a paramagnetic hepatobiliary contrast agent: Initial imaging and biodistribution studies. *J Comput Assist Tomogr* 9(3):431-438, 1985.
- Lauffer, R.B.; Vincent, A.C.; Padmanabhan, S.; Villringer, A.; Saini, S.; Elmaleh, D.R.; and Brady, T.J. Hepatobiliary MR contrast agents: 5-Substituted iron-EHPG derivatives. *Magn Reson Med* 4:582-590, 1987.
- Lieber, C.S. *Medical Disorders of Alcoholism: Pathogenesis and Treatment*. Philadelphia: W.B. Saunders, 1982.
- Lieber, C.S. Alcohol and the liver: 1984 update. *Hepatology* 4(6):1243-1260, 1984.
- Lim, K.O.; Worah, D.; O'Toole, M.; Van Wagoner, M.; Leese, P.; Pfefferbaum, A.; and Quay, S. "MR Hepatobiliary Imaging: First Human Experience with Mn(DPDP)." Presented at the 75th Scientific Assembly and Annual Meeting of the Radiological Society of North America, November 1989.

America, Chicago, IL, November 26–December 1, 1989.

Lim, K.O.; Stark, D.D.; Leese, P.T.; Pfefferbaum, A.; Rocklage, S.M.; and Quay, S.C. Hepatobiliary MR imaging: First human experience with MnDPDP. *Radiology* 178:79–82, 1991.

Lui, A.; Lumeng, L.; and Li, T.K. Metabolism of vitamin B6 in rat liver mitochondria. *J Biol Chem* 256(12):6041–6046, 1981.

Lumeng, L. The role of acetaldehyde in mediating the deleterious effect of ethanol on pyridoxal 5'-phosphate metabolism. *J Clin Invest* 62(2):286–293, 1978.

Morgan, E.T.; Koop, D.R.; and Coon, M.J. Catalytic activity of cytochrome P-450 isozyme 3a isolated from liver microsomes of ethanol-treated rabbits. *J Biol Chem* 257(23):13951–13957, 1982.

Moss, A.A.; Goldberg, H.I.; Stark, D.D.; Davis, P.L.; Margulia, A.R.; Kaufman, L.; and Crooks, L.E. Hepatic tumors: Magnetic resonance and CT appearance. *Radiology* 150:141–147, 1984.

Nunn, A.D.; Loberg, M.D.; and Conley, R.A. A structure-distribution-relationship approach leading to the development of Tc-99m mebrofenin: An improved cholescintigraphic agent. *J Nucl Med* (24):423–430, 1983.

Ratner, A.; Hurd, R.; Muller, H.H.; Bradley-Simpson, B.; Pitts, W.; Shibata, D.; Sotak, C.; and Young, S.W. ¹⁹F Magnetic resonance imaging of the reticuloendothelial system. *Magn Reson Med* 5(6):548–554, 1987a.

Ratner, A.V.; Carter, E.A.; Pohost, G.M.; and Wands, J.R. Nuclear magnetic resonance spectroscopy and imaging in the study of experimental liver diseases. *Alcohol Clin Exp Res* 10(3):241–245, 1986.

Ratner, A.V.; McCann, V.; Bradley-Simpson, B.; Muller, H.H.; Sotak, C.; Hurd, R.; Barchas, J.; and Young, S.W. In vivo detection and imaging of neuroleptic drugs using ¹⁹F nuclear magnetic resonance. *Magn Reson Med* 2:592, 1987b.

Ratner, A.V.; Muller, H.H.; Bradley-Simpson, B.; Hirst, D.; Pitts, W.; and Young, S.W. Detection of acute radiation damage to the spleen using ¹⁹F magnetic resonance imaging. *Am J Roent* 151:477–480, 1988a.

Ratner, A.V.; Muller, H.H.; Bradley-Simpson, B.; Pitts, W.; Shibata, D.; Sotak, C.; and Young, S.W. Detection of tumors with ¹⁹F magnetic resonance imaging. *Invest Radiol* 23(5):361–364, 1988b.

Rocklage, S.M.; Quay, S.C.; and Worah, D. Manganese (dipyridoxal diphosphate): A paramagnetic contrast agent for hepatobiliary and blood brain barrier defect imaging. *Diagn Imaging Intl Suppl*:78–99, 1988.

Saini, S.; Widder, D.; and Stark, D.D. "Reticuloendothelial Contrast Agents for Enhanced MRI Detection of Liver Tumors." Presented at the 4th Annual Meeting of the Society of Magnetic Resonance in Medicine, London, August 19–23, 1985.

Salaspuro, M., and Lieber, C.S. Concentration dependency of ethanol

elimination: Its exaggeration after chronic consumption. *Ann Clin Res* 10:294-297, 1978.

Shane, B. Vitamin B₆ metabolism and turnover in the ethanol-fed rat. *J Nutr* 112(4):610-618, 1982.

Stark, D.D.; Groman, E.V.; and Saini, S. "Ferrite: A Superparamagnetic Contrast Agent for MR Imaging." Presented at the 5th Annual Meeting of the Society of Magnetic Resonance in Medicine, Montreal, August 19-22, 1986a.

Stark, D.D.; Wittenberg, J.; Butch, R.J.; and Ferucci, J.T. Hepatic metastases: Randomized, controlled comparison of detection with MR imaging and CT. *Radiology* 165:399-406, 1987.

Stark, D.D.; Wittenberg, J.; Edelman, R.R.; Middleton, M.S.; Saini, S.; Butch, R.J.; Brady, T.J.; and Ferrucci Jr., J.T. Detection of hepatic metastases: Analysis of pulse sequence performance in MR imaging. *Radiology* 159:365-370, 1986b.

Tsang, Y.M.; Stark, D.D.; Chen, M.C.M.; Weissleder, R.; Wittenberg, J.; and Ferrucci, J.T. Hepatic micrometastases in the rat: Ferrite-enhanced MR imaging. *Radiology* 167:21-24, 1988.

Whidby, J.F., and Leyden, D.E. pH dependence of the N.M.R. line broadening of water by paramagnetic EDTA chelates. *Anal Chim Acta* 51:25-30, 1970.

White, D.L.; Tongol, J.M.; Roco, C.L.; Muettterties, K.A.; Englestad, B.L.; Rocklage, S.M.; Cacheries, W.P.; and Quay, S.C. Clearance, excretion, and organ distribution of Mn from the MRI contrast agent manganese dipyridoxal-diphosphate (Mn-DPDP). *Soc Magn Reson Med Abstr* 1:531, 1988.

Willis, R.A. Secondary tumours of the liver. In: *The Spread of Tumours in the*

Human Body. London: Butterworths, 1973. pp. 175-192.

Wittenberg, J.; Stark, D.D.; Butch, R.J.; and Ferucci Jr., J.T. "Comparative Accuracy of MRI and CT for Liver Metastases." Presented at the 5th Annual Meeting of the Society of Magnetic Resonance in Medicine, Montreal, August 19-22, 1986.

Wolf, G.L.; Burnett, K.R.; Goldstein, E.J.; and Joseph, P.M. Contrast agents for magnetic resonance imaging. In: Cressell, H.Y., ed. *Magnetic Resonance Annual*. New York: Raven Press, 1985. pp. 231-266.

Wolf, G.L.; Joseph, P.M.; and Goldstein, E.J. Optimal pulsing sequences for MR contrast agents. *Am J Roent* 147:367, 1986.

Young, S.W., and Bradley, B. Detection of hepatic malignancies using Mn-DPDP (manganese dipyridoxal diphosphate) hepatobiliary MRI contrast agent. *J Magn Reson Imaging* 8(3):267-272, 1990.

Young, S.W. Development and evaluation of future contrast media: Macromolecules and perfluorinated compounds. *Contrast Media in Computed Tomography*. Excerpta Medica International Congress Series 561:101-106, 1981.

Young, S.W.; Enzmann, D.R.; Lon D.; and Muller, H.H. Perfluoro-octylbromide contrast enhancement of malignant tumors: Preliminary observations. *Am J Roent* 137:141-146, 1981.

Young, S.W.; Simpson, B.B.; Ratner, A.V.; Matkin, C.; and Carter, E. MRI measurement of hepatocyte toxicity using a new MRI contrast agent Mn-DPDP (manganese dipyridoxal diphosphate, a manganese/pyridoxal-5-phosphate chelate). *Magn Reson Med* 10(1):1-13; 1989.

³¹P NMR AS A TOOL TO INVESTIGATE THE TESTICULAR TOXICITY OF ETHANOL IN VIVO

D.H. Van Thiel, M.D.,¹ H. Farghali, Ph.D.,¹ J.S. Gavalier, Ph.D.,² and C. Ho, Ph.D.³

Ethanol has been recognized as a testicular toxin for many years. The toxic effect of ethanol upon the testes has been demonstrated in vivo in chronic alcoholics and in normal men, rats, and mice after alcohol administration; in vitro models include isolated perfused testes and isolated Leydig cells maintained in tissue culture (Van Thiel et al. 1974, 1975, 1979; Cobb et al. 1980; Van Thiel 1983). In each of the in vivo models, acute ethanol exposure has been associated with a long-lasting reduction in testosterone production and secretion (Van Thiel et al. 1974, 1979; Van Thiel 1983) while chronic ethanol exposure is associated with germ cell injury that eventually is manifested as testicular atrophy and infertility (Van Thiel et al. 1974).

With in vitro model systems, the toxic effects of ethanol can be observed rather quickly, i.e., within 1–2 hours of initiation of exposure (Cobb et al. 1980). These toxic ef-

fects occur at rather low concentrations of ethanol (25 mg/dL), well below both the legal limit of intoxication (100 mg/dL) and the limit associated with overt neurotoxicity manifested by lethargy and eventually coma (250–500 mg/dL).

Despite the obvious and universally observed adverse effects of

ACRONYMS

ALT	alanine aminotransferase
AST	aspartate aminotransferase
ATP	adenosine triphosphate
BTB	blood-testis barrier
CD	cytochalasin D
DMSO	dimethyl sulfoxide
Gd-DTPA	gadolinium diethylenetri-aminepentaacetic acid
Gd-PTDM	gadopentate dimeglumine
NMR	nuclear magnetic resonance
PCr	phosphocreatine
PD	phosphodiesters
P _i	inorganic phosphate
PME	phosphomonoesters

Departments of Surgery¹ and Medicine², University of Pittsburgh School of Medicine, Pittsburgh, PA 15213

³NMR Institute, Carnegie Mellon University, Pittsburgh, PA 15213

ethanol exposure on germ cells, the precise mechanisms responsible for these effects have not been determined. A major reason for this lack in our knowledge is that few if any systems exist for the *in vivo* assessment of germ cell maturation and function.

The Sertoli cells of the testes make up <2–3 percent of the testicular volume, yet they define the abluminal and adluminal compartments of the seminiferous tubules. They are responsible for “nursing” germ cells as they differentiate from spermatogonia to mature spermatozoa. Thus, Sertoli cells are critical in the maintenance of testicular integrity and function. Recently developed methods for Sertoli cell isolation and culture provide an opportunity to study Sertoli cell function *in vitro* (Steinberger et al. 1975; Skinner and Griswold 1980). In this chapter, we will discuss the use of nuclear magnetic resonance (NMR) imaging and spectroscopy to study Sertoli cell function as defined by the integrity of the blood-testis barrier (BTB) *in vivo*.

MATERIALS AND METHODS

Materials

Cytochalasin D (CD) was purchased in 1-mg vials from Sigma (St. Louis, MO). Gadopentate dimeglumine (Gd-PTDM; trade name, Magnevist), a derivative of gadolinium diethylenetriaminepentaacetic acid (Gd-DTPA), was provided by Berlex Laboratories, Inc. (Wayne, NJ). Pentobarbital (Nembutal) was ob-

tained from Abbott Laboratories (North Chicago, IL); polyethylene tubing, PE 50, from Clay Adams (Parsippany, NJ). All other chemicals, including dimethyl sulfoxide (DMSO) and ethyl alcohol, were reagent grade, obtained from standard commercial sources.

Feasibility Experiments

Adult male Sprague-Dawley rats weighing 260–330 g were used for the initial feasibility studies. Prior to the testicular injections, an intravenous line of polyethylene tubing was inserted into the femoral vein and secured. This line served as an access line for the intravenous administration of Gd-PTDM and for the maintenance of deep anesthesia.

After anesthetization with an intraperitoneal injection of pentobarbital (50 mg/kg), each rat received two 50- μ L intratesticular injections of CD (1 mM in normal saline), one each into the caudal and cranial poles of the testis (Russell et al. 1987). In the feasibility studies, each rat’s right testis was CD-treated; each left testis was sham-injected using saline without CD to serve as a control. A 26-gauge needle was used for all injections.

Fourteen rats were used to determine the effect of CD on the BTB. The feasibility procedure was repeated, substituting for the CD solution two 50- μ L doses of 2, 5, 25, 50, or 100 percent ethanol, administered intratesticular to the right testis. The left testis of each animal, sham-injected with an equal volume of normal saline, served as the control.

The variation in image intensity between the two testes as a function of time after Gd-PTDM injection was examined every 5 minutes for up to 35 minutes. Thereafter, serial 30-minute images were assessed through 7 hours to determine the time at which the effect of CD and ethanol, acting as a BTB-disrupting agent, was maximal.

Proton NMR imaging was carried out using a Bruker Biospec NMR system with a 4.7-tesla, 40-cm diameter magnet equipped with a 15-cm diameter gradient insert capable of maximum strength of 12 Gauss/cm. A spin-echo sequence with TE=34 milliseconds and TR=500 milliseconds was used for all experiments. Two transaxial proton images each of four slices (thickness=2 mm; field of view=3 cm; number of averages=2 [total time=4.5 minutes]) were obtained before and at various times after an intravenous injection of Gd-PTDM (0.4 mM/kg). Integrated images over a 0.5-cm diameter circular region of interest were obtained using the image analysis program available in the Bruker software package.

The increases in image intensity following Gd-PTDM injection were expressed as percentages, relative to the pre-gadolinium image intensity. The number of integrated image intensities estimated from each testis was four, covering a length of 8 mm of each testis. The mean image intensity for each group was calculated, and differences between means were evaluated using the Student's t test; a *p* value of <0.05

was considered to be statistically significant.

In Vivo Short-Term Ethanol Ingestion Experiments

Eighteen male Lewis rats (3 weeks old) obtained from Zivic Miller Laboratories (Zelienople, PA) were paired for weight and housed in individual cages. The rats were isocalorically pair-fed for 10 weeks. In experimental rats' liquid diet, ethanol accounted for 36 percent of the total calories (Van Thiel et al. 1975, 1979; Gavaler et al. 1980). Dextrimaltose was the isocaloric substitute for ethanol in the control liquid diet. Body weight was monitored weekly throughout the experimental period.

NMR spectroscopy and image measurements were performed within a 3-day period. Each set of ethanol and pair-fed isocaloric control animals were studied on the same day.

As in the feasibility studies, the NMR measurements were made on a Bruker Biospec 4.7/40 spectrometer equipped with a 15-cm diameter gradient insert. ^{31}P NMR spectra at 81 MHz were obtained using a 2.5-cm diameter saddle coil designed to cover both testes of the rat. The rat tail was placed away from the coil to minimize the signal obtained from the tail. A total of 128 scans were obtained over a period of 256 seconds (2 seconds/scan).

The relative concentrations of phosphorus-containing metabolites were obtained by integration of the peak areas of the phosphomonoesters,

inorganic phosphate, phosphodiesters, and β -adenosine triphosphate (β -ATP) resonances. Intratesticular pH was determined by measuring the position of the intracellular inorganic phosphate signal with respect to the phosphocreatine signal, using the equation

$$\text{pH} = 6.75 + \log [(\sigma - 3.27)/(5.69 - \sigma)]$$

where σ is the chemical shift difference between inorganic phosphate and the phosphocreatine resonance.

^1H NMR imaging involved the use of a spin echo sequence before and 5 minutes after the intravenous injection of a bolus of Gd-PTDM (0.4 mM/kg). Imaging was followed by a flush of 0.5 ml normal saline. In each case, the four transverse slices obtained had these image parameters: slice thickness=2 mm; field of view=3 cm; TR=500 milliseconds; TE=34 milliseconds; matrix size=128x128. The image intensity was determined using the Bruker image processing software for two slices each from the left and right testes; these four values were then used in the statistical analysis.

Immediately after ^{31}P NMR spectroscopy and ^1H imaging, the rat's right testis and right hepatic lobe were freeze-clamped in liquid nitrogen. The frozen tissue, ground in liquid nitrogen, and a 4 percent (w/v) precooled perchloric acid solution (1x5 w/v) was thoroughly homogenized in a precooled Polytron homogenizer. The samples were

centrifuged at 4 °C at 3,000 rpm for 10 minutes. The supernatant was brought to pH 7.0 using 6 M K_2CO_3 , and respun at 4 °C at 3,000 rpm for 5 minutes. The resulting supernatants were maintained at -70 °C until assay for ATP content (Gruber et al. 1974). ATP was quantified enzymatically by ultraviolet spectrophotometry using commercially available kits (Sigma, St. Louis). The ATP content of the testes and livers was expressed as micromoles per gram of each organ.

Immediately before sacrifice, the rats were anesthetized with pentobarbital, and blood was collected from the inferior vena cava. The serum was separated and maintained at 4 °C until analysis. Serum levels of alanine aminotransferase (ALT) and aspartate aminotransferase (AST) were determined colorimetrically using Sigma kits. Serum testosterone levels were determined by radioimmunoassay using kits obtained from Diagnostic Products Corporation (Los Angeles). Serum ethanol level determination in the alcohol-treated rats used an alcohol dehydrogenase method and Sigma kits.

The statistical differences between the results for ethanol-fed and the pair-fed control animals were assessed using the paired t test. Reported values are the mean plus or minus the standard error of the mean (S.E.M.). A p value <0.05 was considered statistically significant.

RESULTS

In the pilot feasibility experiments, testicular image intensity, assessed every 5 minutes through 35 minutes after Gd-PTDM injection and intra-testicular administration of CD, the known disrupter of the BTB, peaked at 30 minutes.

Following Gd-PTDM injection, the image intensity of both sham-treated and CD-treated testes increased, but the increased intensity of the CD-treated testes was significantly greater than that of the sham-treated ones, suggesting increased retention of the contrast agent. Furthermore, the image intensity of the CD-treated testis appeared to increase at each 5-minute interval through 30 minutes, whereas there was little or no change in the image intensity of the sham-treated testis beyond the initial 5-minute image. The difference in intensity between the two testes of a given animal at 30 minutes was significant ($p<0.005$).

The slight increase in intensity of the sham-treated testis at 5 minutes was a result of the presence of the Gd-PTDM within the extracellular space. In the CD-treated testis, the continuing increase in image intensity resulted from the slow diffusion of the Gd-PTDM into the seminiferous tubules following disruption of the BTB. Thus the near-constant contrast effects observed in sham-treated testes reflect a steady-state concentration of gadopentetate in extracellular testicular tissues during the imaging studies. In contrast, testes injected with CD and 100 per-

cent ethanol increased as a function of time throughout the study, concomitant with progressive BTB disruption. Figure 1 shows the percentage of change in image intensity at 5 and 30 minutes after Gd-PTDM injection in CD-treated (R) and control (L) testes.

The data in table 1 demonstrate the effect of intratesticular injection of various concentrations of alcohol on the image intensity of the right testes following intravenous injection of Gd-PTDM. Alcohol concentrations of 2, 5, 25, and 50 percent did not alter image intensity, as shown by the percent image intensity values averaged over four determinations each for all animals in each group. However, 100 percent alcohol increased the image intensity significantly ($p<0.005$), from a value of 130 percent in the saline-treated left testes to 157 percent in the alcohol-treated right testes.

Short-term ethanol feeding studies conducted after the completion of the feasibility experiments demonstrated the effect of orally ingested ethanol on the integrity of the Sertoli cell-determined BTB and the energy status of the testes. The body weight gain of both ethanol-fed and pair-fed control rats through 10 weeks is shown in figure 2.

At the age of 5 weeks (i.e., after 2 weeks on the liquid diet), throughout the remainder of the experiment, the alcohol-fed rats exhibited significantly ($p<0.05$) less body weight gain than the dextrimaltose-fed control rats. After 10 weeks on the liquid diets, the average body

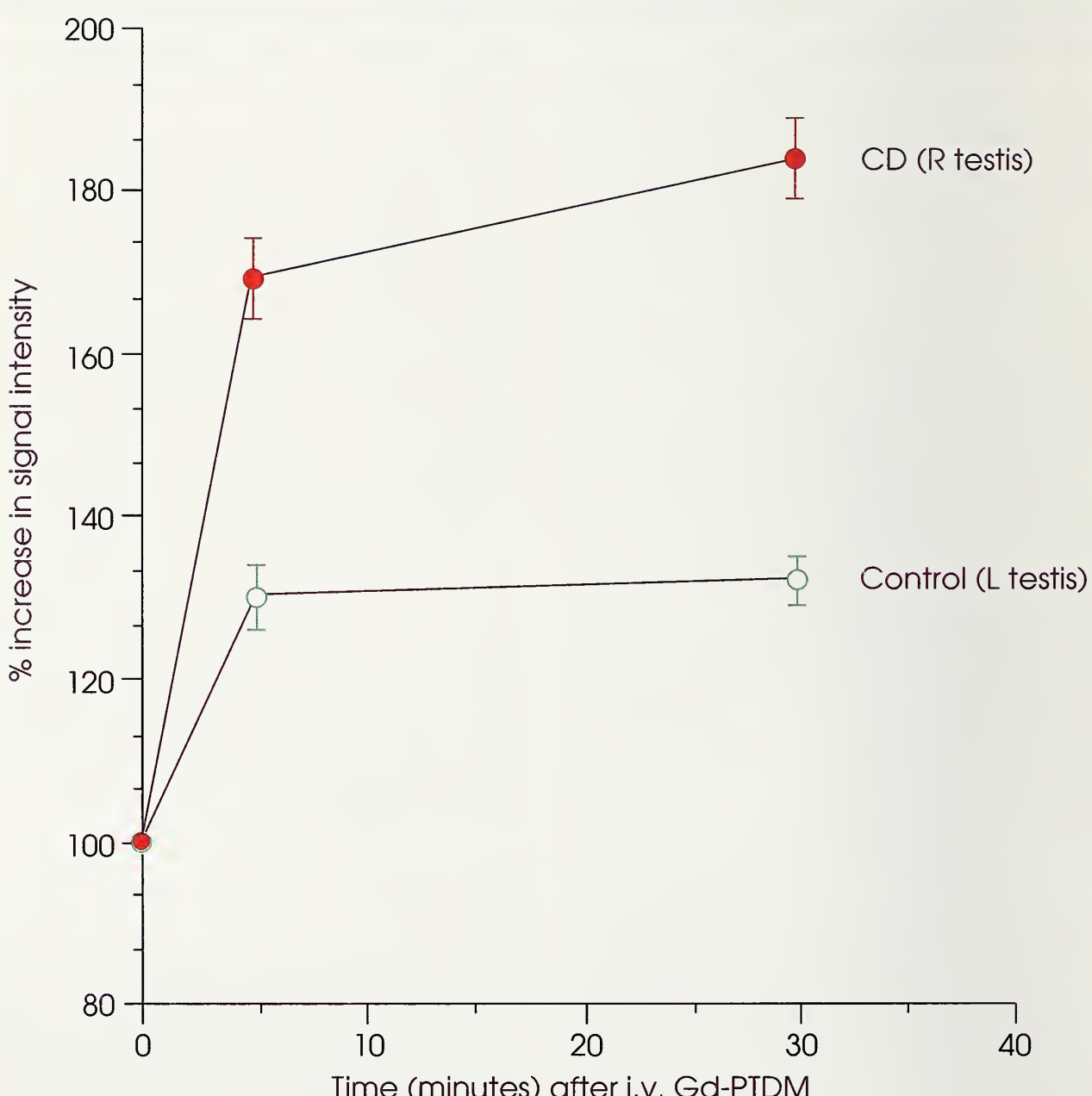
weights were 375.3 ± 9.9 and 342 ± 10.6 g for control and ethanol-fed rats, respectively.

Representative *in vivo* ^{31}P NMR spectra recorded from the testes of ethanol-fed and pair-fed control rats are shown in figure 3. The signals recorded were identified by

numbers: 1, phosphomonoesters (PME); 2, inorganic phosphate (P_i); 3, phosphodiesters (PD); 4, a trace of phosphocreatine (PCr); and 5, γ , 6, α , and 7, β ATP resonances, respectively, as shown in figure 3.

A reduction of the PD signal in the ethanol-treated animals, com-

FIGURE 1



Percent increase in image intensity of the right cytochalasin-treated testis and the left saline-injected testis following gadopentetate infusion. Each point is the mean value for four animals. The brackets represent the S.E.M.

pared with that of controls, is shown in figure 4. The calculated ratios of PD/ β -ATP, PME/ β -ATP, and P_i/ β -ATP for all pairs were all lower in the alcohol-fed animals than in the isocaloric controls. However, only the PD/ β -ATP ratio was statistically lower for the alcohol-treated group ($p<0.05$). The calculated intracellular pH of the testes was similar for the two groups: 7.23 ± 0.01 and 7.20 ± 0.02 for the control and ethanol-fed rats, respectively.

Figure 5 demonstrates the effect of Gd-PTDM on the difference in absolute image intensity between the post- and pre-Gd-PTDM images ($I_{post} - I_{pre}$) of both testes of the alcohol-treated rats, compared with that of the pair-fed controls. Five minutes after the Gd-PTDM injection, the image intensity of the testes of both the alcohol-treated and control rats increased; but the increase was statistically greater in the testes of alcohol-treated rats

than in those of the controls ($p<0.05$). The average image intensity difference for the alcohol-treated rats was 131 percent of the intensity difference for the isocalorically fed controls. However, the net change in the image intensity ($I_{post} - I_{pre}$) following Gd-PTDM injection showed a less marked difference between the two groups.

Ten weeks' ethanol feeding resulted in a 20 percent lower testicular ATP. The ATP content of the testes was 3.00 ± 0.20 and 3.70 ± 0.15 $\mu\text{mol/g}$ for the alcohol-fed and control rats, respectively ($p<0.05$). Likewise, liver ATP was 24 percent lower in alcohol-fed animals than in controls: 2.4 ± 0.3 and 3.0 ± 0.3 $\mu\text{mol/g}$, respectively, although this difference was not statistically significant.

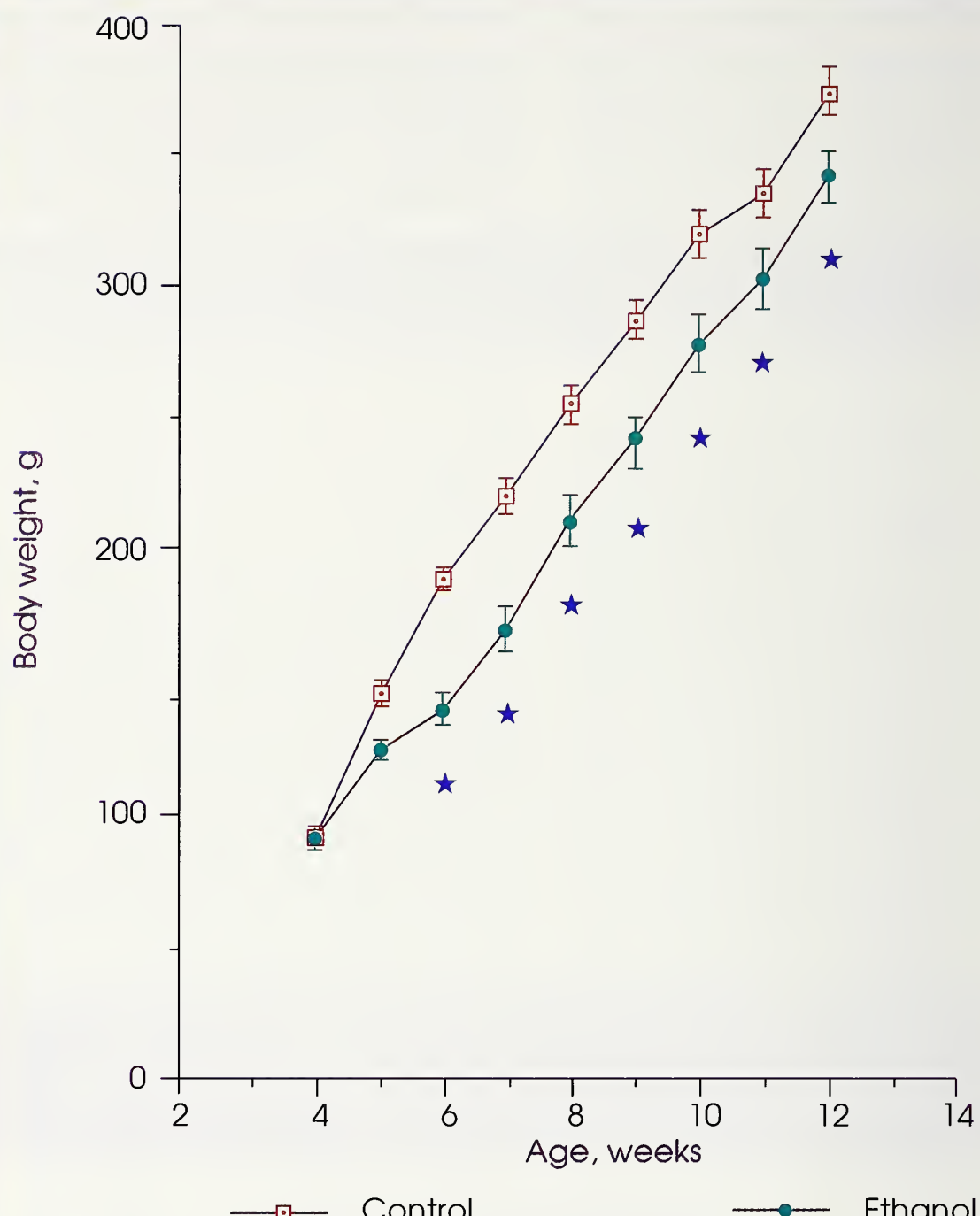
Ten weeks of ethanol feeding also caused a significantly ($p<0.05$) higher serum ALT level in alcohol-fed animals (93 ± 17 U/mL) than in

Table 1. Effect of intratesticular alcohol (2x50 μL) on the increase in image intensity of rat testes following intravenous injection of Gd-PTDM

Percent alcohol concentration	n	Percent increase in image intensity*		Statistically significant
		Saline treated	Alcohol treated	
2	8	118 ± 11	120 ± 18	NS
5	8	101 ± 10	104 ± 15	NS
25	8	125 ± 20	126 ± 22	NS
50	8	116 ± 6	128 ± 21	NS
100	24	130 ± 15	157 ± 21	$p<0.005$

n=number of determinations; NS=not significant.

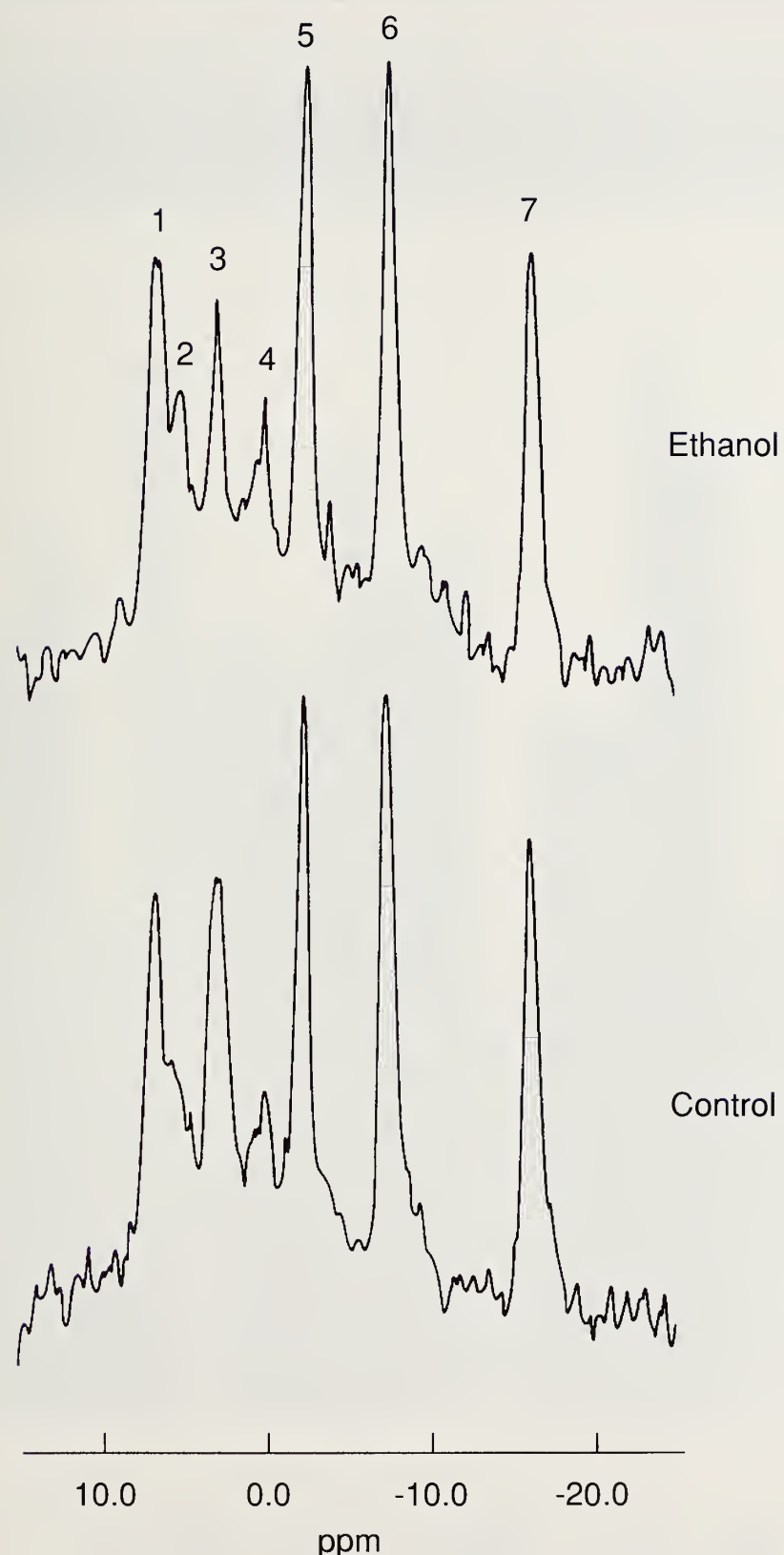
*Means \pm S.D.

FIGURE 2

Increase in body weight of alcohol-fed and isocaloric-fed control animals. Each point represents the mean value at each time point. The brackets represent the S.E.M. The asterisks represent values that are significantly different from the controls ($p < 0.05$).

control rats (38 ± 14 U/mL). The serum AST level of 328 ± 43 U/mL was also significantly ($p < 0.05$) greater than the 162 ± 20 U/mL in controls. Serum testosterone lev-

els did not differ between the two groups. The serum alcohol levels at the time of sacrifice were <10 mg percent in all alcohol-fed animals.

FIGURE 3

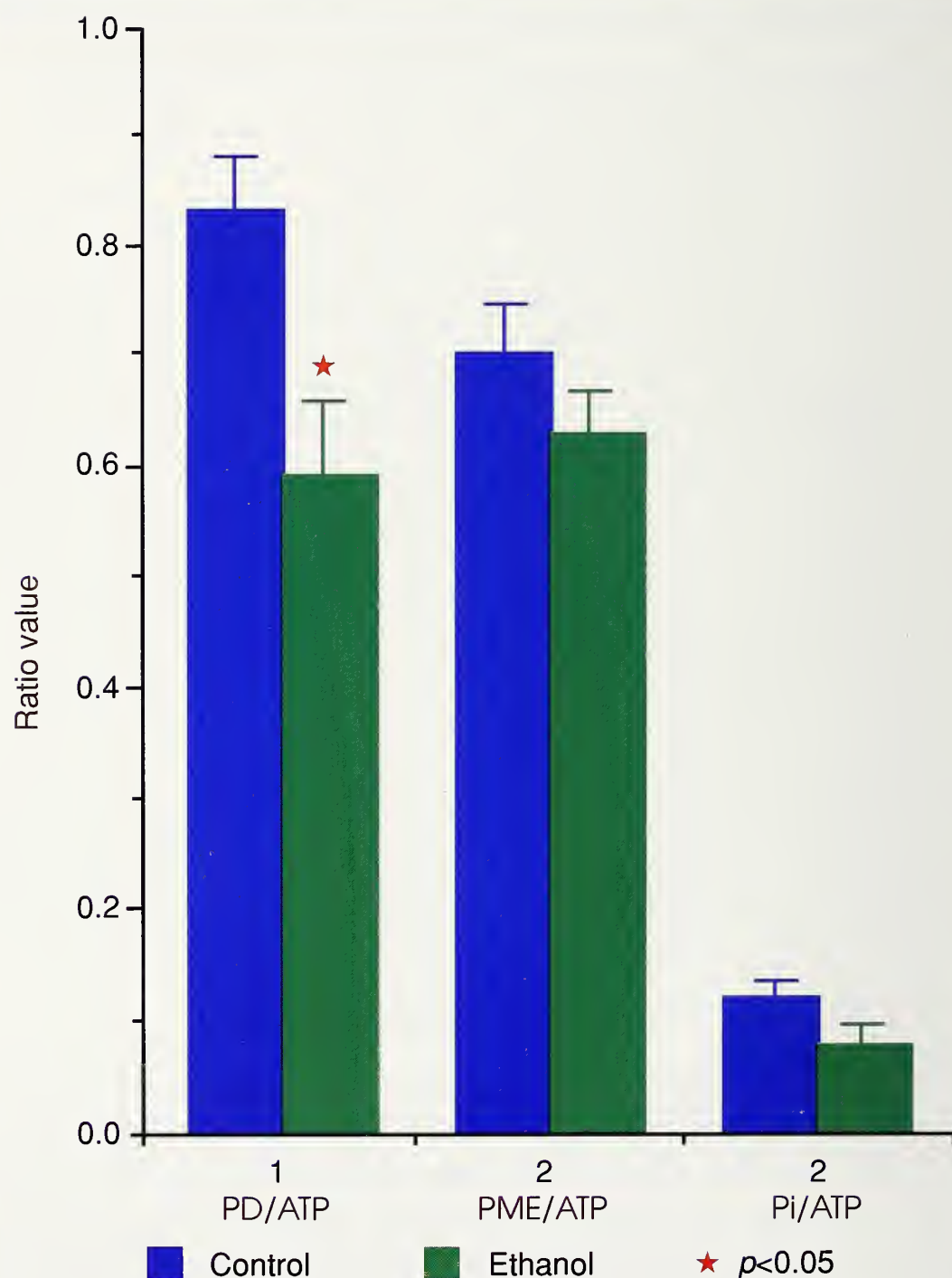
Representative ^{31}P NMR spectra of rat testes of isocaloric control and ethanol-fed animals. The identified peaks in the figure are as follows: (1) phosphomonoesters; (2) inorganic phosphate; (3) phosphodiesters; (4) phosphocreatine; (5) γ -ATP; (6) α -ATP; and (7) β -ATP.

DISCUSSION

Magnetic resonance images of the rat testes demonstrated a difference between the left and right

testis of any given animal in which the right testis was successively injected with CD (intratesticular) and Gd-PTDM (intravenous). Because Gd-PTDM does not normally pene-

FIGURE 4



Ratios of PD/β-ATP, PME/β-ATP, and Pi/β-ATP in the testes of the alcohol-fed and isocalorically fed animals. The bars represent mean values; the brackets represent S.E.M.

trate the blood-organ barrier (Kabalka et al. 1988), it has been used to identify agents that disrupt this physiologic barrier (Runge et al. 1985). The relatively small percent-

age of increase in image intensity seen following Gd-PTDM injection in the control DMSO-injected left testis in the feasibility studies clearly demonstrates that normally

FIGURE 5

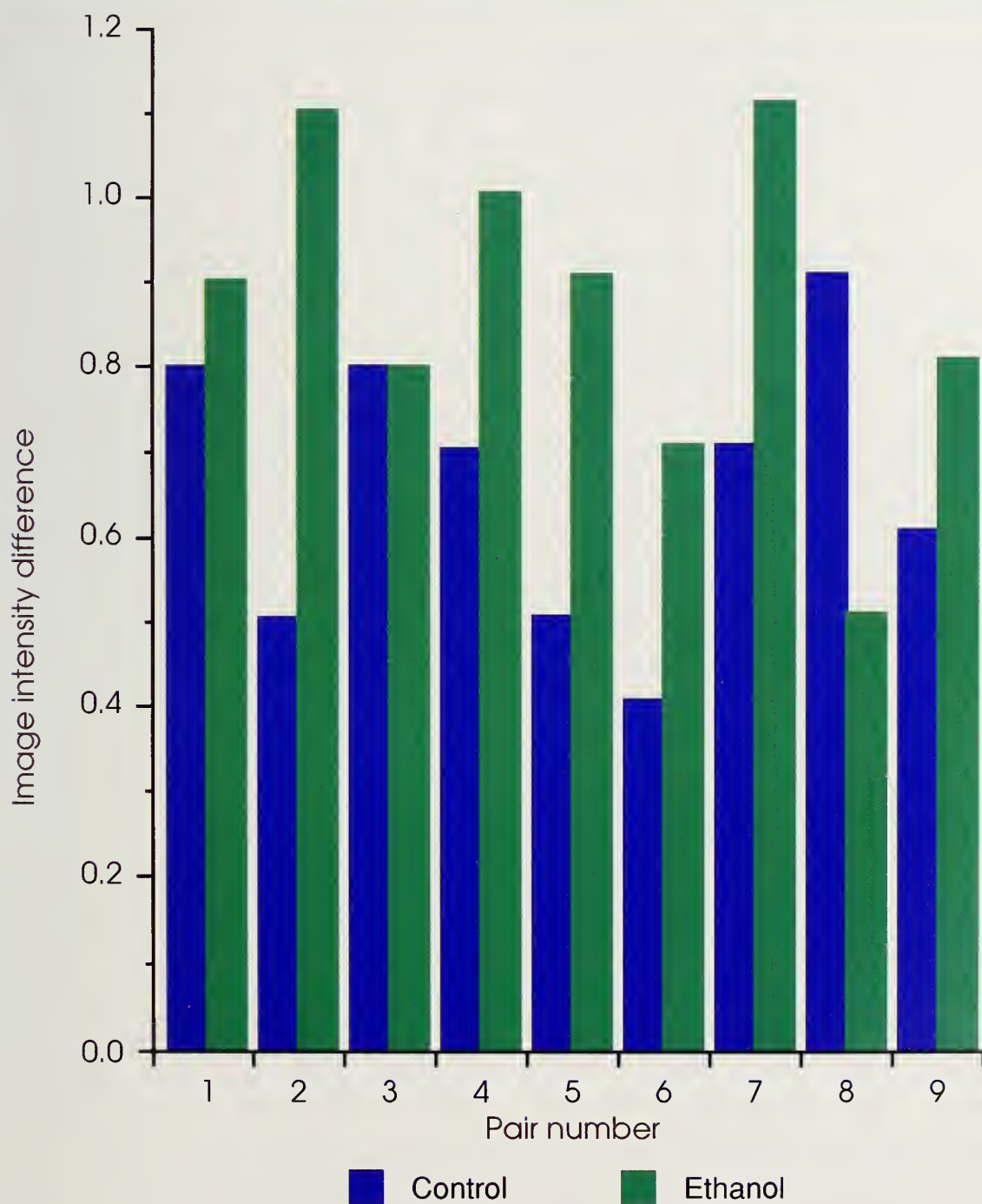


Image intensity differences for the testes of control and alcohol-fed animals following infusion of gadopentetate. The data for nine pair of animals are shown.

the BTB is impermeable to gadopentate. On the other hand, CD is known to disrupt the BTB to a degree that varies with the time the testis is exposed to CD. The effect of CD as a BTB disrupter has been shown to last up to 7 hours, but achieves a maximal level of barrier injury at 30 minutes (Russell et al. 1987).

The use of the intravascular contrast agent Gd-PTDM facilitated detection of a disruption of BTB integrity produced by intratesticular CD. A similar effect was noted following an intratesticular injection of 100 percent ethanol. The disruption of the BTB by CD reported herein confirms the data reported by Weber et al. (1988).

Because Russell et al. (1987) reported that an intratesticular injection of alcohol at low concentrations causes extensive damage to regions adjacent to the site of injection, it cannot be assumed categorically that the increased signal intensity noted after the injection of 100 percent alcohol in this study resulted from disruption of the BTB rather than local tissue injury.

To investigate this problem of interpreting the initial feasibility studies, a short-term ethanol feeding study was designed to avoid the confounds of ethanol injection into the testes. It allowed determination of the sequence of ethanol-induced testicular injury in alcohol abuse. This study demonstrated quite clearly that a disruption of the BTB precedes the reduction in serum testosterone levels and the development of gonadal injury known to

occur with alcohol feeding. It suggested that an ethanol-induced Sertoli cell injury occurs before any identifiable Leydig cell or germ cell injury is apparent.

In the short-term ethanol-feeding experiment, NMR spectroscopy facilitated identification of an ethanol-induced reduction in the PD/ATP ratio. It is well known that intracellular phosphomonoesters and phosphodiesters are intermediary metabolites of membrane phospholipids. Information relative to the levels of these compounds within a cell can thus provide indirect information concerning the turnover of membrane phospholipids and possibly overall cell integrity (Hachisuka et al. 1990). Data from the present study demonstrate a clear reduction in the PD/ATP ratio in the testes of rats fed ethanol. The PD/ATP ratio of the testes of 13-week-old rats has been reported to be about 0.8 (van der Grond et al. 1990), which is similar to the value found for the isocalorically fed control rats in this study.

It has been suggested that ^{31}P NMR-detected alterations of phosphorus metabolites can either antedate or occur in the absence of changes in morphology or structure (Pettegrew et al. 1987), which is precisely what was noted in the experiments reported here. These findings are particularly surprising, however, because ethanol administration is known to produce diffuse membrane effects at the level of the intact cell (Franks and Lieb 1987; Wood and Schroeder 1988).

Moreover, the reduction of the testicular PD/ β -ATP ratio following short-term ethanol administration in the present study was accompanied by a reduction in the absolute amount of ATP in the testes of alcohol-fed rats.

Both acute and chronic ethanol administration have been reported to reduce the total phosphate pool in the liver (Desmolin et al. 1987; Helzberg et al. 1987; Takahashi et al. 1990). The effect of chronic ethanol on the PD/ATP ratio and ATP in the testes may reflect a similar alcohol-induced injury and may contribute to the observed loss of integrity of the BTB. In this regard, it is particularly important to note that the identifiable changes in the testicular phosphate pool and the disruption in the BTB in response to short-term ethanol feeding in this study were observed in the absence of altered plasma testosterone levels. This suggests that the membrane changes precede the reduction in serum testosterone levels (Leydig cell injury) known to occur with chronic ethanol administration (Van Thiel et al. 1975; Russell et al. 1987).

Through the use of ^{31}P NMR spectroscopy and ^1H imaging, this study demonstrates that short-term feeding of ethanol to rats reduces both the PD/ β -ATP ratio and the ATP contents of the testes, while increasing the influx of Gd-PTDM across the BTB prior to producing a reduction in the serum testosterone level.

ACKNOWLEDGMENTS

This work was supported in part by National Institute on Alcohol Abuse and Alcoholism grant AA04425.

REFERENCES

- Cobb, C.F.; Ennis, M.F.; Van Thiel, D.H.; Gavaler, J.S.; and Lester, R. Isolated testes perfusion: A method using a cell- and protein-free perfusate useful for the evaluation of potential drug and/or metabolic injury. *Metabolism* 29:71–79, 1980.
- Desmolin, F.; Canioni, P.; Crotte, C.; Gerolami, A.; and Cozzone, P.J. Hepatic metabolism during acute ethanol administration, a phosphorus-31 nuclear magnetic resonance study on the perfused rat liver under normoxic and hypoxic conditions. *Hepatology* 7:315–323, 1987.
- Franks, N.P., and Lieb, W.R. Are the biological effects of ethanol due to primary interactions with lipids or with proteins? *Alcohol Alcohol* 1 (suppl) :139–145, 1987.
- Gavaler, J.S.; Van Thiel, D.H.; and Lester, R. Ethanol, a gonadal toxin in the mature rat of both sexes: Similarities and differences. *Alcohol Clin Exp Res* 4:271–276, 1980.
- Gruber, W.; Mollering, H.; and Bergmeyer, H.U. Determination of ADP, ATP and sum of GTP + ITP in biological materials. In: Bergmeyer, H.U., ed. *Methods of Enzymatic Analysis*. 2nd ed. New York: Academic Press, 1974.
- Hachisuka, T.; Nakayama, S.; Tomita, T.; and Takagi, H. ^{31}P nuclear magnetic resonance study of phospholipid metabolites in hypothermic preserved liver. *Transplant Proc* 22:485–487, 1990.

Helzberg, J.H.; Brown, M.S.; Smith, D.J.; and Gordon, E.R. Metabolic state of the rat liver with ethanol: Comparison of in vivo ^{31}P -phosphorus nuclear magnetic resonance spectroscopy with freeze clamp assessment. *Hepatology* 7:83-88, 1987.

Kabalka, G.W.; Buonocore, E.; Hubner, K.; Davis, M.; and Huang, L. Gadolinium-labeled liposomes containing paramagnetic amphipathic agents: Targeted MRI contrast agents for the liver. *Magn Reson Med* 8:89-95, 1988.

Pettegrew, J.W.; Kopp, J.J.; Minshew, N.J.; Glonek, T.; Feliksik, J.M.; Tow, J.P.; and Cohen, M.M. ^{31}P nuclear magnetic resonance studies of phosphoglyceride metabolism in developing and degenerating brain: Preliminary observations. *J Neuropathol Exp Neurol* 46:419-430, 1987.

Runge, V.M.; Clanton, J.A.; Price, A.C.; Wehr, C.J.; Herzer, W.A.; Partain, C.L.; and James Jr., A.E. The use of Gd-DTPA as a perfusion agent and marker of blood-brain barrier disruption. *Magn Reson Imaging* 3:43-55, 1985.

Russell, L.D.; Saxena, N.K.; and Weber, J.E. Intratesticular injection as a method to assess the potential toxicity of various agents and to study mechanisms of normal spermatogenesis. *Gamete Res* 17:43-56, 1987.

Skinner, M.K., and Griswold, M.D. Sertoli cells synthesize and secrete a transferrin-like protein. *J Biol Chem* 255:9523-9528, 1980.

Steinberger, A.; Heindel, J.J.; Lindsey, J.N.; Elkington, J.S.H.; Sanborn, B.M.; and Steinberger, E. Isolation and culture of FSH responsive Sertoli cells. *Endocrinol Rev Commun* 2:261-266, 1975.

Takahashi, H.; Geoffrim, Y.; Butler, K.W.; and French, S.W. In vivo hepatic-energy metabolism during the progression of alcoholic liver disease: A noninvasive ^{31}P nuclear magnetic resonance study in rats. *Hepatology* 11:65-73, 1990.

van der Grond, J.; van Echteld, C.J.E.; and Mali, W.P.Th.M. In vivo ^{31}P MRS of the testis of the rat during maturation. Program of the Congress of NMR in Medicine and Biology, Strasbourg, France, May 2-5, 1990, p. 63.

Van Thiel, D.H. Ethanol: Its adverse effects upon the hypothalamic-pituitary-gonadal axis. *J Lab Clin Med* 101:21-33, 1983.

Van Thiel, D.H.; Gavaler, J.S.; Cobb, C.F.; Sherins, R.J.; and Lester, R. Alcohol-induced testicular atrophy in the adult male rat. *Endocrinology* 105:888-895, 1979.

Van Thiel, D.H.; Gavaler, J.S.; Lester, R.; and Goodman, M.D. Alcohol-induced testicular atrophy: An experimental model for hypogonadism occurring in chronic alcoholic men. *Gastroenterology* 69:326-332, 1975.

Van Thiel, D.H.; Lester, R.; and Sherins, R.J. Hypogonadism in alcoholic liver disease: Evidence for a double defect. *Gastroenterology* 67:1188-1199, 1974.

Weber, J.E.; Turner, T.T.; Tung, K.S.K.; and Russell, L.D. Effects of cytochalasin D on the integrity of the Sertoli cell (blood-testis) barrier. *Am J Anat* 182:130-147, 1988.

Wood, W.G., and Schroeder, F. Membrane effects of ethanol: Bulk lipid versus lipid domains. *Life Sci* 43:467-475, 1988.

Nuclear Magnetic Resonance Spectroscopy Section

10

OVERVIEW OF NONINVASIVE APPROACHES TO METABOLIC AND ADDICTIVE DISEASE

Britton Chance, Ph.D., D.Sc.¹

As the prime target of alcohol toxicity and aberrant metabolism, the liver is the organ that succumbs initially to chronic alcoholism. It is susceptible to alcohol because it contains the pathway from alcohol to acetaldehyde, the recognized toxic product of alcohol metabolism. Much research has been done to identify the consequences of alcohol and aldehyde metabolism in the liver. Unfortunately, most of the significant data have been obtained from animal models, which, though meritorious in that they do not involve human subjects, are as imperfect as animal models can be for a human disease.

Alcohol primarily affects the redox state of the liver: Very active nicotinamide adenine dinucleotide (NAD) reduction triggered by alcohol and aldehyde dehydrogenase creates a state of pathological reduction in the liver. Recognition of this pathology has been enhanced by the work of Ozawa (1981), a pioneer in the use of the mitochondrial redox ratio (in terms of acetoac-

etate/hydroxybutyrate) to indicate overreduction of the human liver during and following transplantation. Such studies have shown that perturbation of the redox state is characteristic of the fragile state of the recently transplanted organ.

ACRONYMS

CAC	<i>citric acid cycle</i>
DG	<i>deoxyglucose</i>
MRI	<i>magnetic resonance imaging</i>
MRS	<i>magnetic resonance spectroscopy</i>
NAD	<i>nicotinamide adenine dinucleotide</i>
NAD/NADH	<i>redox ratio of NAD to its reduced form NADH</i>
PET	<i>positron emission tomography</i>
NMR	<i>nuclear magnetic resonance</i>
SQUID	<i>superconducting quantum interference device</i>
TRS	<i>time-resolved spectroscopy</i>

¹Institute for Structural and Functional Studies, University of Pennsylvania School of Medicine, Philadelphia, PA 19104

The bellwether of the redox state of mitochondria is the redox ratio of NAD to its reduced form NADH (NAD/NADH). This ratio can be correctly inferred from the extent of reduction of NAD, observed fluorometrically from the surface of either perfused or *in situ* liver (Quistorff and Chance 1986). Whether this measurement is made *in vitro* or *in vivo*, it correlates quantitatively with the value obtained by analytical biochemistry. Recent developments in NADH fluorometry allow consideration of its use *in vivo*, both intraoperatively and postoperatively (Chance et al. 1991).

The purpose of this overview is to compare five methods of noninvasively measuring the redox state of the liver--magnetic resonance imaging (MRI), magnetic resonance spectroscopy (MRS), positron emission tomography (PET), superconducting quantum interference device (SQUID), and time-resolved spectroscopy (TRS)--and to explain how they can best be used in alcoholism research. These methods can be compared from the standpoint of relevance to the problems of metabolism, drug addiction, and tissue pathology.

Whereas the special goal of the experimental method is to localize chemicals functionally, the structural data provided by MRI are less important than the data provided by MRS and PET. MRS and SQUID are probably the most important; however, TRS itself can contribute significantly to localized studies of the liver.

In determining what instrumentation is necessary for studying metabolic and addictive disease in alcoholism, the first and most important question is: What degree of localization is necessary to study these two phenomena? Investigation of molecular effects requires resolution at the cell organelle level for optimum understanding of the biomedical problem. Given that no modality will yet operate at the molecular level, one must ask how to study the receptor level in addiction and the enzyme level in metabolism.

POSITRON EMISSION TOMOGRAPHY

Sensitivity is the characteristic advantage of PET scanning. A few nanomoles of intense radioactive label will give coincident counts against zero background. Although intended simply to identify the receptor, PET labels receptor proportional to its amount. This measurement of proportion is of great advantage in following the course of addiction from adaptation to habituation. Furthermore, the antibody tag can be highly specific. The drawback of PET is that the amount of radioactivity that must be administered is a significant fraction of the annual permissible dose.

Metabolism can often be followed by PET, but to a limited extent because the methods to calculate tracer amounts and tracer assimilation velocities are restricted. The most popular of these--glucose

uptake measured by deoxyglucose (DG) labeling--still is controversial with respect to both reversibility of the mechanism and the method of calculating absolute rates. Nevertheless, proportionalities between glucose metabolism and DG labeling are indisputable. The problem with glucose labeling is that it is not clear whether this method measures oxidative or glycolytic responses, whereas independent evidence concerning the aerobic or anaerobic state of the tissue is desired. Although oxygen reduction to water has been proposed for such a measurement, PET does not, in fact, measure oxygen concentration, but rather, the rate of water production. PET is, however, an instrument of neuroscience that could be used effectively in animal model studies.

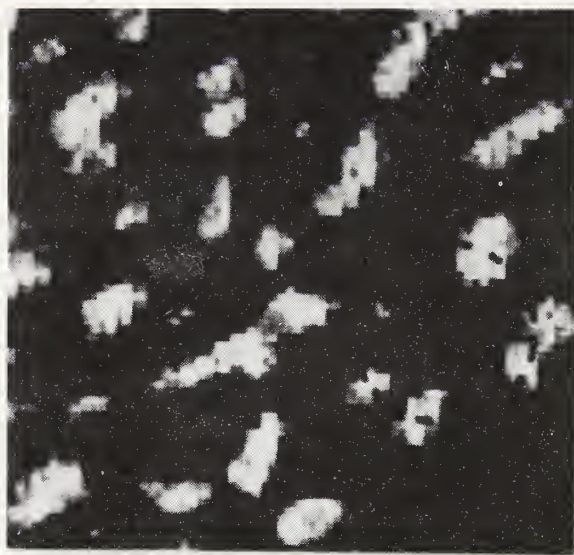
Monitoring the addictive process via radioactive labels on antibodies appropriate for the alcohol receptors can give adequate detectability and localization with PET scanning. The resolution available with MRI, or with MRS, is inadequate to deal with receptors, thus PET remains advantageous. There is some question regarding which is preferable--direct determination of the number of receptors or of the intensity of the addictive process, as judged by alcohol intake. It is moot for the present, but certainly, if compounds were developed to block the receptor, monitoring the decrease in number of available receptor sites would be of great importance.

NUCLEAR MAGNETIC RESONANCE (NMR)

NMR is best applied in "discovering" unnatural compounds and following their function in metabolic pathways. The possibility that NMR could be used to explore liver metabolism was pioneered by Alan McLaughlin (McLaughlin et al. 1978). He not only showed the quality of data that could be obtained with the existing equipment, but recognized the short T₂ of adenosine triphosphate in the alcoholic liver and verified noninvasively the lack of the creatine kinase system. This deficit results in a higher inorganic phosphate peak in the metabolizing liver than is characteristic of resting skeletal muscle. Further, as shown in figure 1 (a spectrum of animal liver), it was recognized that other peaks, particularly those of phosphomonesters and phosphodiesters, are readily observable in the metabolizing liver. The cycle of high-energy and low-energy phosphate compounds, so well studied by NMR, reflects the impact of deenergization in alcoholism. Indeed, when alcohol uptake is large, alcohol itself is detectable by ¹H NMR. Its impact on citric acid cycle (CAC) metabolism can be detected by using glutamate as a probe of CAC function. Undoubtedly, NMR is ideal for the study of metabolic biochemistry.

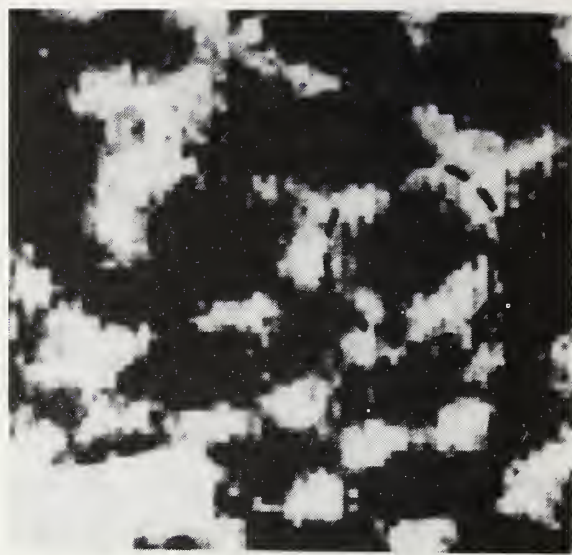
PHOTON MIGRATION IN TISSUES

None of the methods described effectively measures oxygen delivery

FIGURE 1

PL 16.4 Ethanol
CR, 0.40-0.21

Scan 3.6 x 3.6 mm



PL 17.4 Control
CR, 0.45-0.28

Television display of redox ratio scans of control and ethanol-perfused (6 mM) rat liver. The scan was taken at the depth of 350 μm in both livers. Each scan represents 5,041 single-point measurements of FP/PN ratio. White is oxidized (high ratio); black is reduced (low ratio). The range of the grey scale (the CR value given below the pictures) is slightly different for the two pictures in order to resolve the pattern.

to tissue and oxygen metabolism, which requires optical spectroscopy in the red region of the spectrum. Photon migration in tissues has well-defined patterns. Being three-dimensional, it affords methods of scanning for tissue volumes that are hypoxic or whose oxygen metabolism is otherwise affected by alcohol metabolism (Cui et al. 1991).

MAGNETIC FIELDS

Detection of small magnetic fields (SQUID) is an innovative technique that is particularly sensitive to the

field developed by columnar structures of the acoustic, visual, and sensory motor regions of the brain. This highly selective method works in real time without the need for isotopes, making it very attractive. However, it is not clear whether the columnar structures so well portrayed by these methods are altered in the addictive process.

REAL-TIME THERMOGRAPHY

Restricted to use in animal models, real-time thermography of metabolic heat in the brain promises to be as important in animal models as

electron encephalography. Metabolic heat is measured in real time in the superficial layers of the cerebral cortex of animal models. Thermal measurement of the patterns of metabolic activity, together with modifications of these patterns by alcohol, appears to be a unique opportunity to visualize the mechanism of action of metabolic and drug-like effects of alcohol *in vivo*.

FREEZE-TRAP REDOX SCAN METABOLIC IMAGING

The "gold standard" of three-dimensional measurement of metabolism, the freeze-trap redox scanning method, is restricted to animal models (Quistorff et al. 1978, 1985). This "one shot" method is comparable to isotopic deoxyglucose labeling of brain function using radioautography. The metabolic imprints of brain function and of the effects of drugs and hypoxia, for example, are preserved by rapid freeze-trapping and identified by the ratio of flavoprotein to pyridine nucleotide fluorescence. Its resolution is comparable to or exceeds that of isotopic labeling. This method is a great deal more convenient than isotopic labeling because of the rapidity at which the scans can be accomplished.

The general goals of our research on freeze-trap redox scanning are to enhance the success of liver transplants in the case of acute liver disease, to monitor precisely chemiluminescence events associated with these transplants, and finally, to monitor the health of the liver before and after transplant, using the special modalities available.

To make two- and three-dimensional redox scans possible, this laboratory, in collaboration with Bjorn Quistorff, constructed a redox scanning device. This unique device captures in three dimensions the redox state of freeze-trapped tissue. Such images may be taken in a time series of different lobes of the same liver.

An example of the appropriate use of freeze-trap redox scanning is the demonstration of alcohol's effect on the redox structure of the liver where periportal, pericentral, and perivenous regions alter in their response to alcohol, as shown in figure 1 (Quistorff et al. 1978). In these regions, relatively high oxidized ellipsoidal structures perpendicular to the surface have been identified with the essential functions of the acinus. The resolution required for such studies is on the order of 50–100 μm , the approximate size of single cells or groups of cells. The target dimension of the imaging technology described here is representative of metabolic function.

THE ROLE OF IMAGING IN ASSESSMENT OF TRANSPLANT PROBLEMS

Some research initiatives of practical importance in the study of alcoholism are associated with liver transplantation. One of these--the investigation of possible free radical damage in post-transfusion reflow--involves online chemiluminescence measurements (Okuda et al. 1991). Because the effectiveness or validity of reflow in a transplanted liver is crucial, the measurement of the

differential response of all the lobes to the perfusate is particularly important.

Obviously, MRS examination of the liver after transplantation can be advantageous. However, the management of a post-transplant patient in the MRI or MRS in the first few hours following surgery is not feasible because of the requirements of patient care and transport. Online monitoring of liver oxygenation and redox state prior to closure is more practical.

Assuming that liver transplantation in patients with alcoholic cirrhosis is possible, a proposal for postoperative monitoring of the liver would involve gluing to each of the four lobes of the liver a small-diameter fluorescence probe, which could be brought out through the surgical drain. Use of these probes to monitor the redox state would replace the procedure now used--sampling the blood to determine the acetoacetate/ β -hydroxybutyrate ratio, which requires a 10-minute assay interval and inevitable delays unacceptable in proper patient care. Thus, monitoring the state of the post-transplant liver can now be considered in view of new and important modalities for online assay of its function.

COMPARISON OF METHODS

To determine the extent to which ultimate resolution is possible for the various methods described in this chapter, one must take into account that they each represent different quantities. For example, when even the distinction between mitochondria and cytosol might be

desired, MRS would be appropriate because it measures intracellular parameters and thus would be expected to have the highest resolution. PET, on the other hand, is better for dealing with extracellular markers where antibody reactions are evoked to label receptor sites, which while small themselves, would be representative of a portion of the cell surface. This method, which yields measurements for groups of cells, would not be expected to show the intracellular detail provided by MRS. The optical measurement of tissue oxygenation, as viewed from the capillary bed, or more properly, from the sinusoids of the liver, is a more global response. Thus its resolution would ultimately correspond to the acinus, while, on the other hand, a lobular distribution of oxygen might also be valuable in the case of liver transplant.

ACKNOWLEDGMENTS

This work was supported in part by National Institute on Alcohol Abuse and Alcoholism grant AA-07186.

REFERENCES

Chance, B.; Ikai, I.; Tanaka, A.; and Okuda, M. Tissue kinetics: Metabolic control as studied by the kinetics of ATP formation and degradation in liver. In: Grunnet, N., and Quistorff, B., eds. *Regulation of Hepatic Function*. Alfred Benzon Symposium 30. Copenhagen: Munksgaard, 1991. pp. 141-157.

Cui, W.; Kumar, C.; and Chance, B. Experimental study of migration depth for the photons measured at sample

- surface. In: Chance, B., ed. *Proceedings of Time-Resolved Spectroscopy and Imaging of Tissues*. Bellingham, WA: SPIE, 1991. pp. 180-191.
- McLaughlin, A.C.; Takeda, H.; and Chance, B. ^{31}P NMR studies on perfused mouse liver. In: Dutton, P.L.; Leigh, J.S., Jr.; and Scarpa, A., eds. *Frontiers of Biological Energetics*. Vol. 2. New York: Academic Press, 1978. pp. 1351-1356.
- Okuda, M.; Ikai, I.; Chance, B.; and Kumar, C. Oxygen radical production during ischemia reperfusion in the isolated perfused rat liver as monitored by luminol-enhanced chemiluminescence. *Biochem Biophys Res Commun* 1991, in press.
- Ozawa, K. Biological significance of mitochondrial redox potential in shock and multiple organ failure--redox theory. In: Lefer, A.M., and Schumer, M., eds. *Molecular and Cellular Aspects of Shock and Trauma*. New York: Alan R. Liss, 1981. pp. 39-66.
- Quistorff, B., and Chance, B. Redox scanning in the study of metabolic zonation of liver. In: Thurman, R.G.; Kauffman, F.C.; and Jungerman, K., eds. *Regulation of Hepatic Metabolism*. New York: Plenum Publishing Corp., 1986. pp. 185-207.
- Quistorff, B.; Chance, B.; and Takeda, H. Two- and three-dimensional redox heterogeneity of rat liver. Effects of anoxia and alcohol on the lobular redox pattern. In: Dutton, P.L.; Leigh, J.S., Jr.; and Scarpa, A., eds. *Frontiers of Biological Energetics*. Vol. 2. New York: Academic Press, 1978. pp. 1487-1497.
- Quistorff, B.; Haselgrove, J.C.; and Chance, B. High spatial resolution readout of 3-D metabolic organ structure: An automated, low-temperature redox ratio-scanning instrument. *Anal Biochem* 148:389-400, 1985.

MAGNETIC RESONANCE SPECTROSCOPY AND SPECTROSCOPIC IMAGING OF HUMAN LIVER, HEART, KIDNEY, AND BRAIN

Dieter J. Meyerhoff, Ph.D., Hoby P. Hetherington, Ph.D., James W. Hugg, Ph.D., Gerald B. Matson, Ph.D., George Fein, Ph.D., Andrew A. Maudsley, Ph.D., and Michael W. Weiner, M.D.¹

Magnetic resonance spectroscopy (MRS) detects a number of compounds that participate in tissue energy metabolism and phospholipid metabolism. ^{31}P MRS detects adenosine triphosphate (ATP), phosphocreatine (PCr), inorganic phosphate (P_i), phosphomonoesters (PMEs, largely phosphorylcholine and phosphorylethanolamine), and phosphodiesters (PDEs, most likely glycero-3-phosphorylcholine and glycero-3-phosphorylethanolamine). Tissue pH and free magnesium concentration can be determined from chemical shift differences between ^{31}P metabolite resonances. ^1H MRS detects N-acetylaspartate (NAA, an amino acid reported to be located exclusively in neurons), choline, total creatine and PCr (Cr+PCr), and lactate.

ACRONYMS

ATP	adenosine triphosphate
Cr+PCr	total creatine and phosphocreatine
HIV	human immunodeficiency virus
ISIS	image-selected <i>in vivo</i> spectroscopy
MCA	middle cerebral artery
MRS	magnetic resonance spectroscopy
MRSI	magnetic resonance spectroscopic imaging
NAA	N-acetylaspartate
PCr	phosphocreatine
PDE	phosphodiester
P_i	inorganic phosphate
PME	phosphomonoester
TI	spin lattice relaxation time
VOI	volume of interest
WMSH	white matter signal hyperintensities

¹ Magnetic Resonance Unit, Department of Veterans Affairs Medical Center and University of California, San Francisco, San Francisco, CA 94121

During the initial development of localized MRS, most investigators used so-called "single volume" techniques that used slice-selecting gradients. Early studies in this laboratory used primarily the image-selected *in vivo* spectroscopy (ISIS) technique (Matson et al. 1988; Roth et al. 1988; Schaefer et al. 1988; Hubesch et al. 1989a; Lawry et al. 1989). Subsequently, magnetic resonance spectroscopic imaging (MRSI) techniques developed and implemented for clinical use (Twieg et al. 1989; Maudsley et al. 1990) allowed biochemical information to be obtained simultaneously from multiple volumes within the imaged region. These techniques use time-varying magnetic field gradients to encode spatially spectral information on the imaged object.

This review briefly summarizes work in this laboratory using ^{31}P and ^1H MRS and MRSI for the investigation of liver, heart, kidney, and brain. Specifically related to alcohol and its pathological effects, quantitative studies have been performed on acute alcoholic hepatitis and cirrhosis of the liver. Furthermore, the rate of ethanol uptake into human brain has been directly measured and compared with the rate of rise in blood ethanol. The results of these studies demonstrate the use of MRS to measure tissue ethanol levels and to detect the effects of ethanol on tissue metabolism.

METHODS

All studies reported here have been performed on a Philips 2.0 tesla (T) Gyroscan SI5 MRI/MRS system using techniques developed by Philips Medical Systems and by this laboratory. Initial ^{31}P studies used the ISIS technique modified with a postacquisition saturation pulse (Matson et al. 1988) for better localization with rapid signal averaging. While studies on the brain used an "earphone" coil, studies on the liver, kidney, and heart used surface coils for transmission and reception.

Early ^{31}P spectroscopic imaging studies of the brain and studies with surface coils used a simple free induction decay data acquisition (Twieg et al. 1989) whereas recent brain studies have used spin echo data acquisition (Maudsley et al. 1990). For measurement of ethanol levels in human brain, ^1H MRS was performed using a modified ISIS technique (Hetherington et al. 1989). Recently, ^1H MRSI has been performed on human brain using a localization technique with double echo transverse slice selection and phase encoding in two dimensions over the transverse slice (Luyten et al. 1990). All spectra were analyzed and curve-fitted for signal integration using NMRI software. Molar concentrations of phosphorus-containing tissue metabolites were obtained using a quantitation method de-

veloped in this laboratory (Roth et al. 1988). All data are expressed as mean \pm standard error.

RESULTS

Human Liver

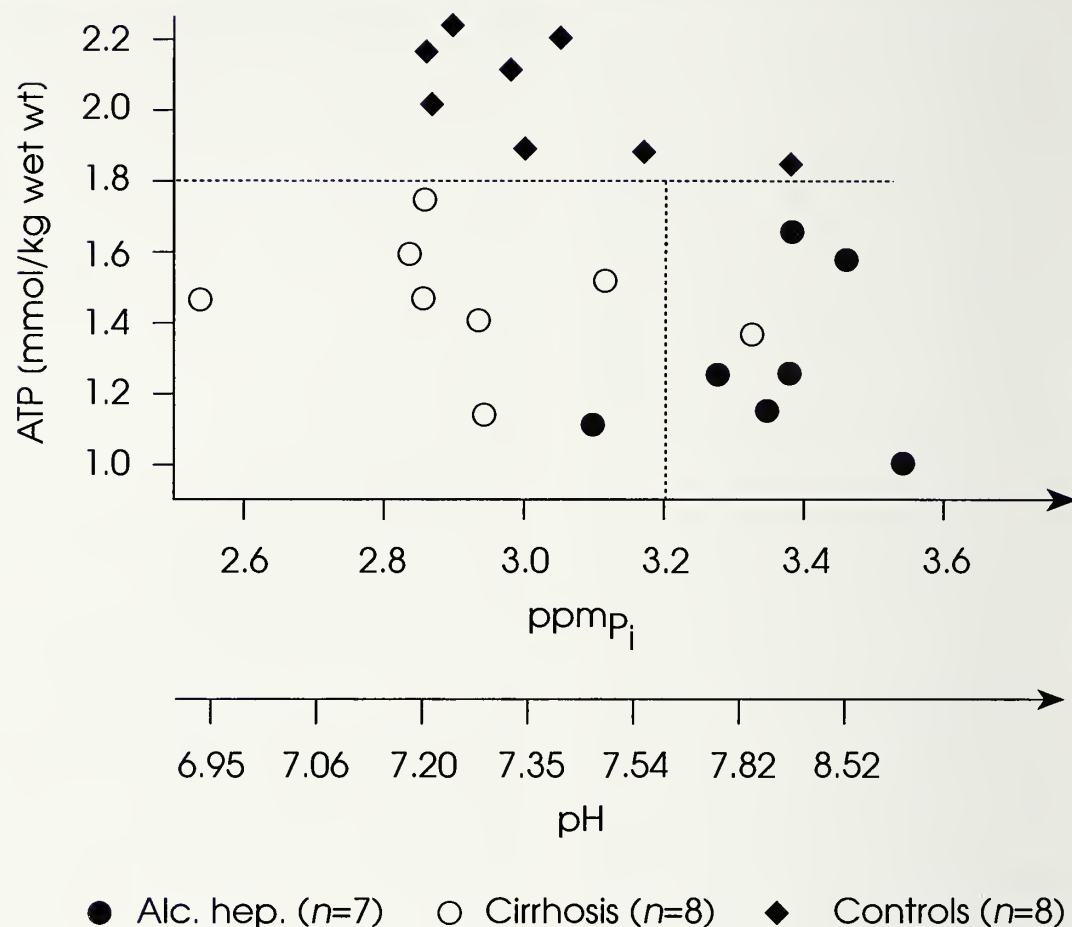
Phosphorus-containing metabolites in normal human liver have been quantitated noninvasively with localized ^{31}P MRS using surface coils (Meyerhoff et al. 1989a, 1990). The location of the volume of interest (VOI) in the posterior segment of the right lobe of the liver was defined by standard ^1H MRI. Subsequently, ISIS was used to acquire ^{31}P MR spectra from the VOI. To account for partial signal saturation produced by rapid signal averaging, the spin lattice relaxation times (T_1) of all MR-visible hepatic phosphorus nuclei were measured (Meyerhoff et al. 1990). The corrected resonance integrals were used to derive molar concentrations for the following hepatic metabolites in eight healthy subjects (mmol/kg wet weight): ATP, 2.0 ± 0.1 ; P_i , 2.2 ± 0.1 ; PDE, 5.3 ± 0.6 ; and PME, 0.8 ± 0.1 (Meyerhoff et al. 1991). These values provide a basis for comparison with studies of hepatic disease in this laboratory (Meyerhoff et al. 1989a).

In addition to ISIS studies on healthy control subjects ($n=21$), localized ^{31}P MRS was also performed on the liver of patients with alcoholic hepatitis ($n=10$), alcoholic cirrhosis ($n=9$), and viral hepatitis B ($n=3$) (Meyerhoff et al. 1989a). The investi-

gation demonstrated that (1) relative signal intensities of hepatic metabolites in alcoholic liver disease were not significantly different from those in healthy subjects (except for P_i/ATP , which was reduced in alcoholic cirrhosis relative to normal controls), (2) absolute hepatic phosphorus metabolite concentrations were decreased by 25–46 percent in alcoholic hepatitis and 13–50 percent in alcoholic cirrhosis, relative to healthy subjects, and (3) hepatic intracellular pH was 7.4 in healthy subjects, more acidic in alcoholic cirrhosis, and more alkaline in alcoholic hepatitis.

Figure 1 is a plot of absolute hepatic ATP concentration versus P_i chemical shift/intracellular pH for alcoholic liver disease patients and normal controls. The plot can be divided into three sectors, as shown: The upper sector contains only measured values for controls, the lower left sector contains 7 of 8 alcoholic cirrhosis cases, and the lower right sector contains 6 of 7 alcoholic hepatitis cases. These preliminary findings indicate that hepatic metabolite ratios are not a sensitive measure of alcoholic liver disease, that quantitative ^{31}P MRS is a means of noninvasively showing metabolic changes associated with alcoholic liver disease, and that alcoholic hepatitis and cirrhosis may be distinguished by hepatic intracellular pH measured by ^{31}P MRS (Meyerhoff et al. 1989a).

Measurements on three patients with viral hepatitis B showed nor-

FIGURE 1

Calculated hepatic ATP concentrations plotted against chemical shift of hepatic P_i (in ppm) and intracellular pH for control subjects and alcoholic hepatitis and alcoholic cirrhosis patients. The dashed lines indicate the sector limits, as explained in the text (from Meyerhoff et al. 1989a).

mal pH and no reduction in metabolite concentrations relative to normal controls (while PMEs were increased more than twofold), indicating that the high pH and low ATP concentration are typical for only the alcoholic form of hepatitis. The most likely explanation for the measured reduction in metabolite concentrations in alcoholic liver

disease is a loss of viable liver cells due to necrosis or fibrosis, for example, rather than a reduction of metabolite concentrations in the hepatocytes. The increased hepatic pH in alcoholic hepatitis may indicate the ability of the liver to regenerate, while the low pH in alcoholic cirrhosis reflects severe damage to the liver.

Human Heart

Localized ^{31}P MRS used to investigate heart metabolism in normal volunteers (Schaefer et al. 1988) and in patients with dilated cardiomyopathy and left ventricular hypertrophy (Schaefer et al. 1990) demonstrated the feasibility of performing these studies on patients with myocardial disease. Seventeen patients and fourteen control subjects were studied. Spectra were obtained from the human heart at rest using MRSI with phase-encoding in all three dimensions as a localization technique. The PCr/ATP ratio was 0.89 ± 0.08 in normal subjects under resting conditions and did not differ significantly in patients with dilated cardiomyopathy or left ventricular hypertrophy. A prominent peak in the PDE region of the ^{31}P MR spectra was seen much more frequently in patients with dilated cardiomyopathy, possibly signifying abnormal phospholipid metabolism in this condition. This finding resulted in significantly higher ratios of PDE/PCr (1.28 ± 0.35) and PDE/ATP (0.79 ± 0.18) in this group, compared with normal subjects (0.33 ± 0.08 and 0.29 ± 0.08 , respectively). However, the various patient groups could not be reliably distinguished from each other on the basis of spectral patterns. Preliminary ^{31}P metabolite maps of transverse slices through the heart and chest of normal volunteers were recently obtained by surface coil ^{31}P MRSI (Meyerhoff et al. 1991).

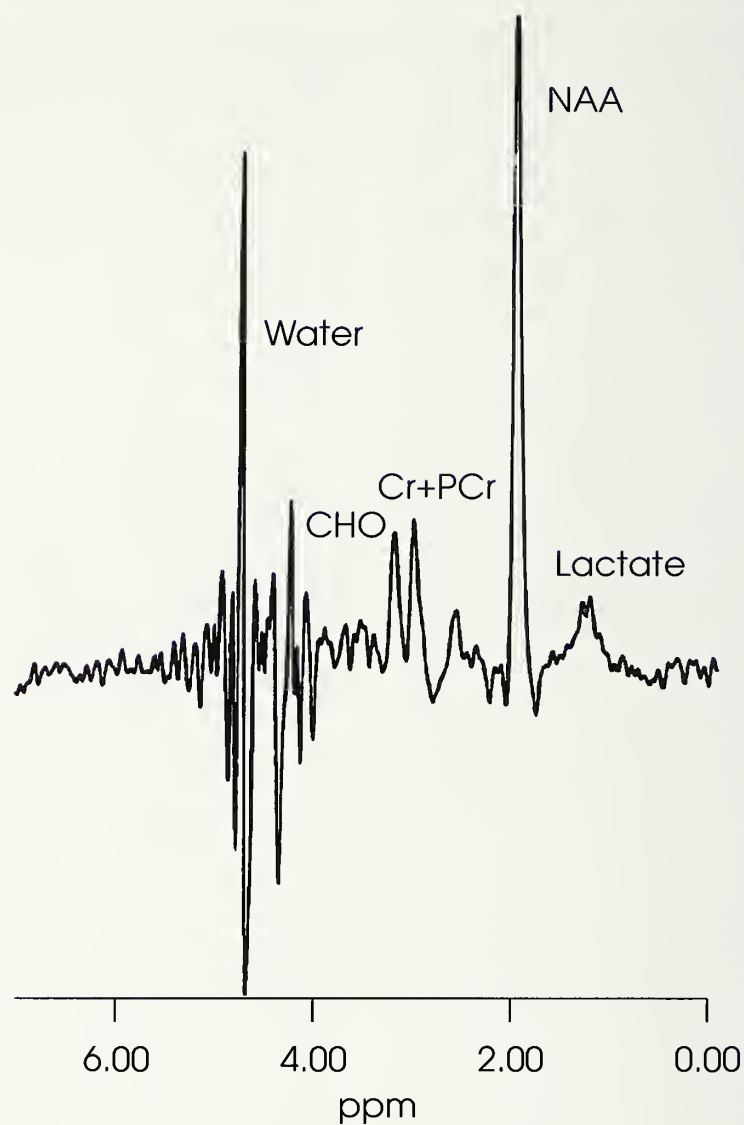
Human Kidney

Image-guided ^{31}P MRS (ISIS) was used to obtain spatially localized ^{31}P spectra of good quality from healthy, normal human kidneys and, to determine the effects of kidney transplantation on renal metabolism, from well functioning renal allografts (Boska et al. 1990). A surface coil of 14-cm diameter was used for acquiring phosphorus signals from a VOI located within the kidney. Little or no PCr in all spectra verified the absence of muscle contamination and was consistent with proper volume localization. The intensity ratio of PME/ATP in the transplanted kidneys ($\text{PME}/\text{ATP} = 1.1 \pm 0.2$) was insignificantly elevated ($p=0.24$) compared with that of healthy normal kidneys ($\text{PME}/\text{ATP} = 0.8 \pm 0.1$). The P_i/ATP ratio was similar in the two groups ($\text{P}_i/\text{ATP} = 1.1 \pm 0.1$ in transplanted kidneys versus 1.2 ± 0.2 in normal kidneys). Intracellular tissue pH, as shown by the chemical shift of inorganic phosphate, was the same in both normal and transplanted kidneys. Despite the practical problems presented by organ depth, respiratory movement, and tissue heterogeneity, these results demonstrate that image-guided ^{31}P MR spectra can reliably be obtained from human kidneys (Boska et al. 1990).

Human Brain

Kinetics of Ethanol Uptake

The goal of this work was to measure and compare the kinetics of ethanol uptake in human brain and

FIGURE 2

Water-suppressed ^1H ISIS spectrum of normal human brain (parietal lobe) at rest. Resonances are from residual water, choline (CHO), creatine and phosphocreatine (Cr + PCr), N-acetylaspartate (NAA), and lactate.

blood using water-suppressed localized ^1H ISIS (Hetherington et al. 1989). Subjects with signs of alcoholism and liver disease were excluded from this study. Ethanol (1 mL/kg) in the form of vodka in a fruit juice mixer (total volume: 0.5 L) was consumed orally within the magnet in 1.5–7.0 minutes. ^1H MR spectra, acquired before, during,

and after consumption of alcohol, were localized to a 100 mL volume of white matter in the parietal lobe. Venous blood was sampled continuously via a forearm catheter, before and after conclusion of ethanol consumption. The blood ethanol level was determined enzymatically.

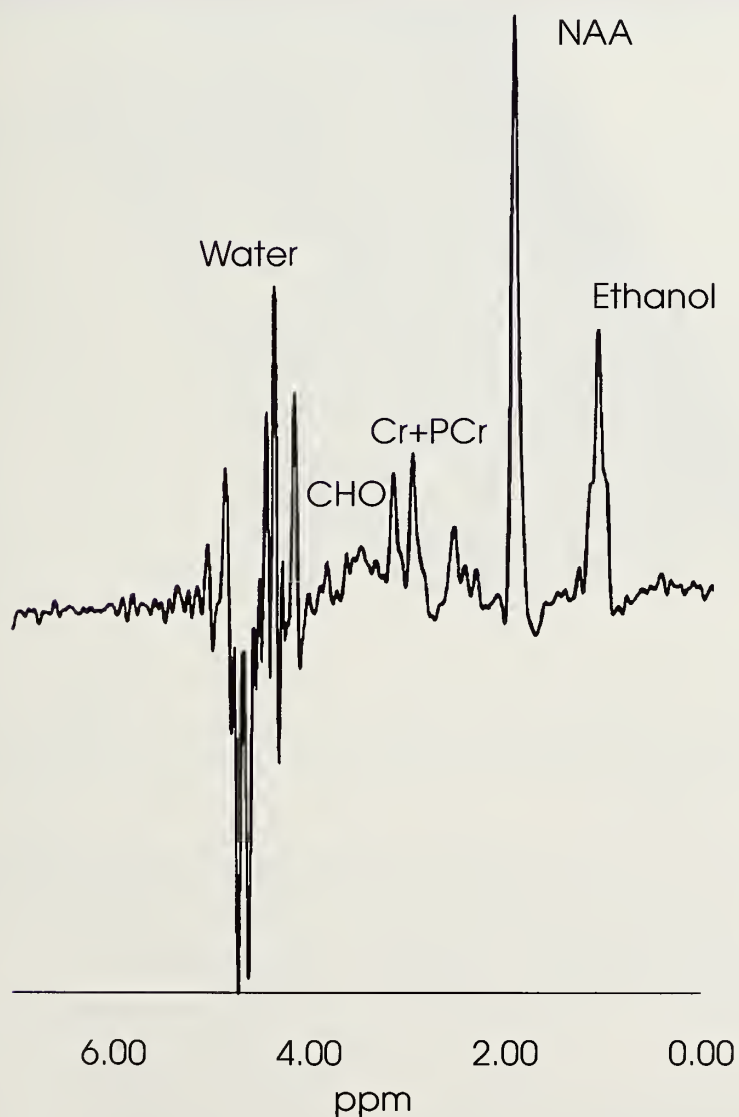
Figures 2 and 3 show spectra acquired before and 60 minutes after

ethanol loading. Resonances from residual water due to incomplete water suppression, choline, Cr+PCr, and NAA are visible in both spectra. The spectrum in figure 2 has a resonance at 1.33 ppm from resting levels of lactate, the end product of anaerobic glycolysis, while the spectrum in figure 3 shows a strong

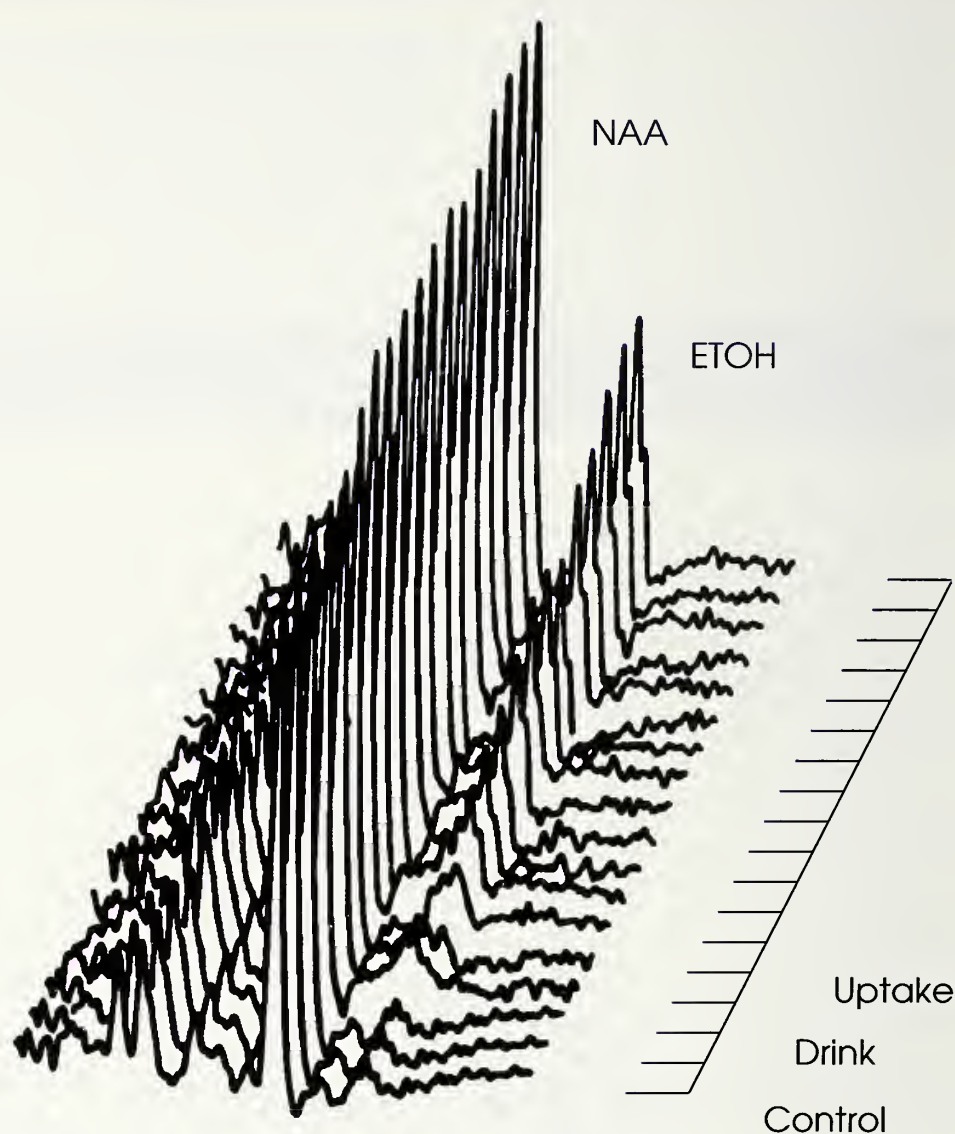
resonance at 1.2 ppm due to the methyl group in ethanol.

Figure 4 displays a typical set of spectra acquired with a 3-minute time resolution before (control), during (drinking), and after consumption of alcohol. Ethanol (EtOH) was easily identified by the chemical shift and triplet structure of its methyl resonance. The first 60 min-

FIGURE 3



Water-suppressed ^1H ISIS spectrum of normal human brain (parietal lobe) 60 minutes after conclusion of oral ethanol administration. Resonances are from residual water, choline (CHO), creatine and phosphocreatine (Cr + PCr), N-acetylaspartate (NAA), and ethanol.

FIGURE 4

Time course of ethanol uptake in the brain: Water-suppressed ^1H ISIS spectra of normal human brain (parietal lobe) before, during, and after oral consumption of alcohol.
Time resolution: 3 minutes.

utes of brain and blood ethanol uptake was modeled using an exponential of the form:

$$\text{EtOH}(t) = \text{EtOH}_0 [1 - \exp(k(t - t_0))]$$

where t is time in minutes and EtOH_0 , k , and t_0 (t_0 , a time offset to account for consumption and mix-

ing time of the ethanol) are fitted variables.

Figure 5 shows experimental values for the rise of ethanol in brain and blood and calculated curves for a single subject. Although the exponential turnover rates, k , were varied (0.031 ± 0.014 for brain and 0.043 ± 0.027 for venous blood in all

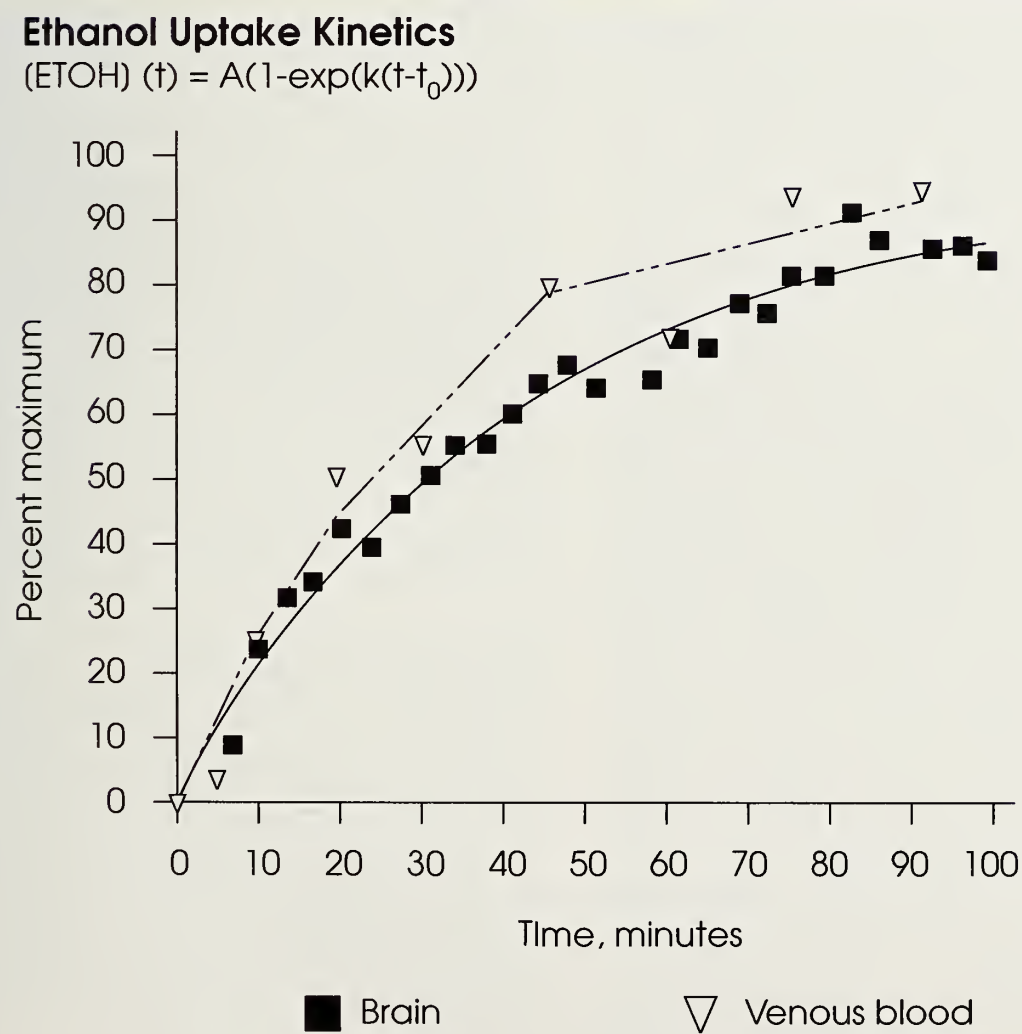
five cases), the ratio of the venous blood to brain ethanol rates was greater than 1.0, having a mean of 1.44 ± 0.36 . These uptake kinetics suggest that brain ethanol levels lag venous blood ethanol levels (Hetherington et al. 1989).

AIDS Dementia Complex

Human immunodeficiency virus (HIV)-infected individuals often demonstrate neuropsychiatric im-

pairment; however, it is unclear how brain metabolism may be altered in such patients. Localized ^{31}P MRS (ISIS) was used to assess noninvasively brain energy and phospholipid metabolism and intracellular pH (Deicken et al. 1991). Initially, the study comprised 17 HIV-seropositive men with various degrees of neuropsychiatric impairment and 6 control subjects. The ^{31}P MR spectra were obtained from a heteroge-

FIGURE 5



Ethanol uptake as percent maximum vs. time in brain (filled squares) and in venous blood (open triangles). The lines connecting these points are calculated curves to an exponential fit through the experimental points.

neous 5 cm × 5 cm × 5 cm VOI in the center of the brain. The patients with HIV infection had a significantly lower ATP/P_i ratio (suggesting a compromised bioenergetic tissue status) and a trend for a lower PCr/P_i ratio than did the control group. In addition, the ATP/P_i and PCr/P_i ratios both had significant negative correlations with the overall severity of neuropsychiatric impairment.

In an additional study, 3 HIV-seropositive men with neuropsychiatric impairment were compared with 11 HIV-seronegative men. In this study, localized ³¹P MR spectra were obtained from two relatively homogeneous VOIs: a predominantly white matter VOI and a predominantly subcortical gray matter VOI. The three HIV-infected patients demonstrated significantly decreased ATP and PCr concentrations in the white matter VOI. These results suggest that HIV infection of the brain may impair brain cellular oxidative metabolism and that the degree of metabolic compromise may be related to the severity of neuropsychiatric impairment (Deicken et al. 1991).

White matter ATP concentrations in HIV-negative alcoholics, examined in a third study, were not significantly different from HIV-positive nonalcoholics, while HIV-positive alcoholics had significantly decreased white matter ATP concentrations. Therefore, these MR results, and the recent evoked-response finding of increased latency of the frontal P3A component in HIV-positive alcoholics relative to

HIV-positive nonalcoholics, suggest that alcohol abuse potentiates the adverse effects of HIV infection on white matter energy metabolism.

Temporal Lobe Epilepsy

To investigate alterations of brain metabolism associated with temporal lobe epilepsy, ³¹P MRS (ISIS) studies were performed on the anterior temporal lobes of patients with medically refractory complex partial seizures (Hubesch et al. 1989b). Interictally, the pH was significantly more alkaline in the temporal lobe ipsilateral to the seizure focus (7.22 versus 7.06, $p<0.05$), and the P_i concentration was greater on the side of the epileptogenic focus (1.9 versus 1.1 mM, $p<0.05$). These changes of pH and P_i may represent metabolic alterations secondary to seizures. Alternatively, since alkalosis enhances neural excitability and may enhance seizure activity, the elevated pH of the seizure focus may provide insight into the pathophysiological mechanism of epileptic seizures (Hubesch et al. 1989b).

Cerebral Infarction

Previous ³¹P MRS studies of human chronic brain infarctions showed no alterations of phosphorus metabolite ratios and a general decrease of signal intensity. The goal of these experiments was to determine quantitatively the alterations of phosphorus metabolites in regions of human brain damaged by chronic stroke (Sappey-Marinier et al. 1991b). Image-guided ³¹P MRS (ISIS) was performed on the brain of

normal subjects ($n=8$) and of patients ($n=6$) with cerebral infarction older than 3 months (chronic stroke). The most important finding was that the reductions in phosphorus metabolite concentrations of infarcted regions ranged from 8 to 67 percent, relative to those levels in normal subjects. Significant decreases were 67 percent in PME (0.9 ± 0.2 versus 2.7 ± 0.3 , $p < 0.01$), 51 percent in PDE (4.0 ± 0.4 versus 8.1 ± 0.5 , $p < 0.01$), and 39 percent in ATP (1.4 ± 0.3 versus 2.3 ± 0.3 , $p < 0.05$). In contrast, P_i and PCr showed a small and nonsignificant decrease (<18 percent).

Metabolite ratios were also altered in chronic stroke: The ATP/PCr and the ATP/ P_i ratio were reduced in infarcted regions, reflecting the poor bioenergetic status of infarcted tissue. The pH measured in the infarcted region (7.25 ± 0.07) was significantly more alkaline than that in normal brain (7.03 ± 0.04 , $p < 0.05$). Therefore, chronic stroke is associated with significant changes of brain metabolites and pH that are different from those reported for other brain diseases. 1H MR studies with ISIS showed marked reductions of choline and creatine and a greater reduction of NAA, consistent with the view that NAA is a marker of viable neurons. In the majority of the patients with chronic infarctions, elevated lactate levels were measured.

Recently, both ^{31}P and 1H MRSI were performed on 11 patients with cerebral infarcts (Hugg et al. 1990). The results show reduced ^{31}P

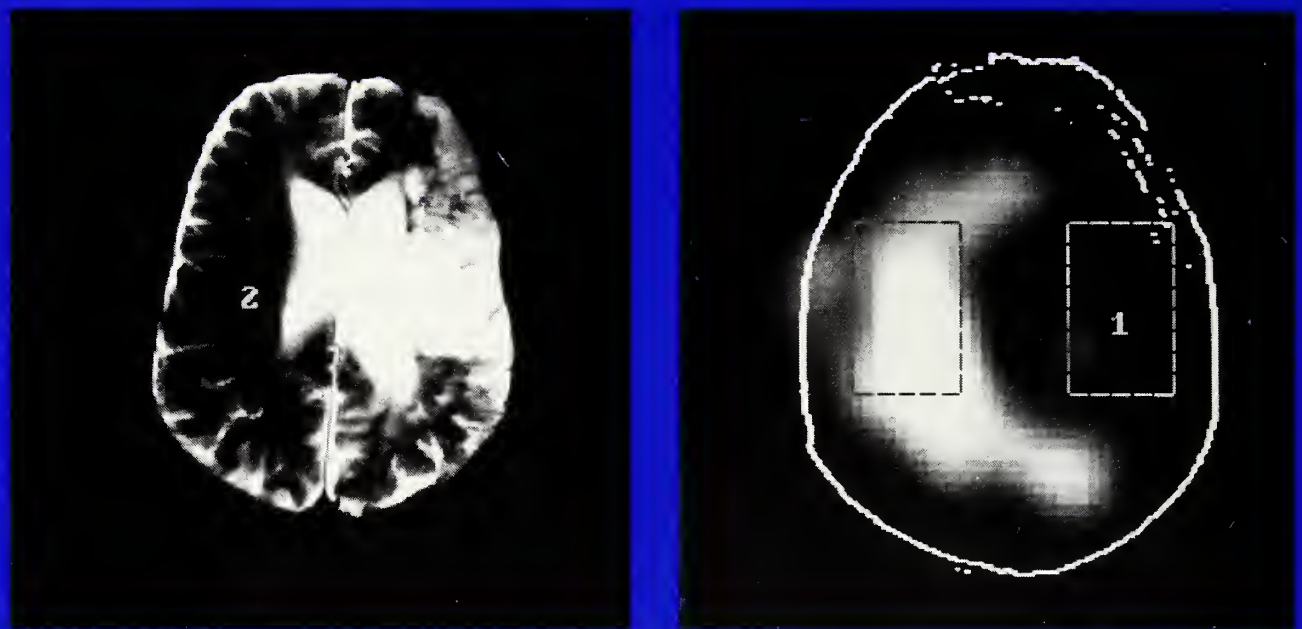
metabolite levels, reduced choline and creatine with greater reduction of NAA, elevated lactate in large middle cerebral artery (MCA) infarcts, and alkaline pH. The finding of persistent elevated lactate with tissue alkalosis suggests the possibility that "luxury perfusion," which causes tissue alkalosis, may be responsible for increased lactate by selectively stimulating anaerobic glycolysis (Hugg et al. 1990).

Figure 6 shows a transverse 1H MR image through the brain of a patient with a chronic MCA infarct and the spatially corresponding ^{31}P MR spectroscopic image of the same infarct, reconstructed from the total phosphate contents in the slice. The region of the chronic infarct is characterized by a hyperintensity on the 1H MR image and a signal void on the ^{31}P spectroscopic image that also includes the area of the ventricles.

^{31}P spectra reconstructed from the stroke region (region 1 as indicated on the images) and the corresponding contralateral region (region 2 as indicated on the images) are depicted in figure 7. They demonstrate high signal intensity in region 2 (upper spectrum), all resonances typical for human brain, and almost no signal intensity in region 1 (lower spectrum), indicating near total loss of viable cells in this chronic stroke.

Elderly Brain

Signal hyperintensities in the white matter are identified on brain MRI studies of 25–50 percent of elderly subjects. Although the prevalence

FIGURE 6

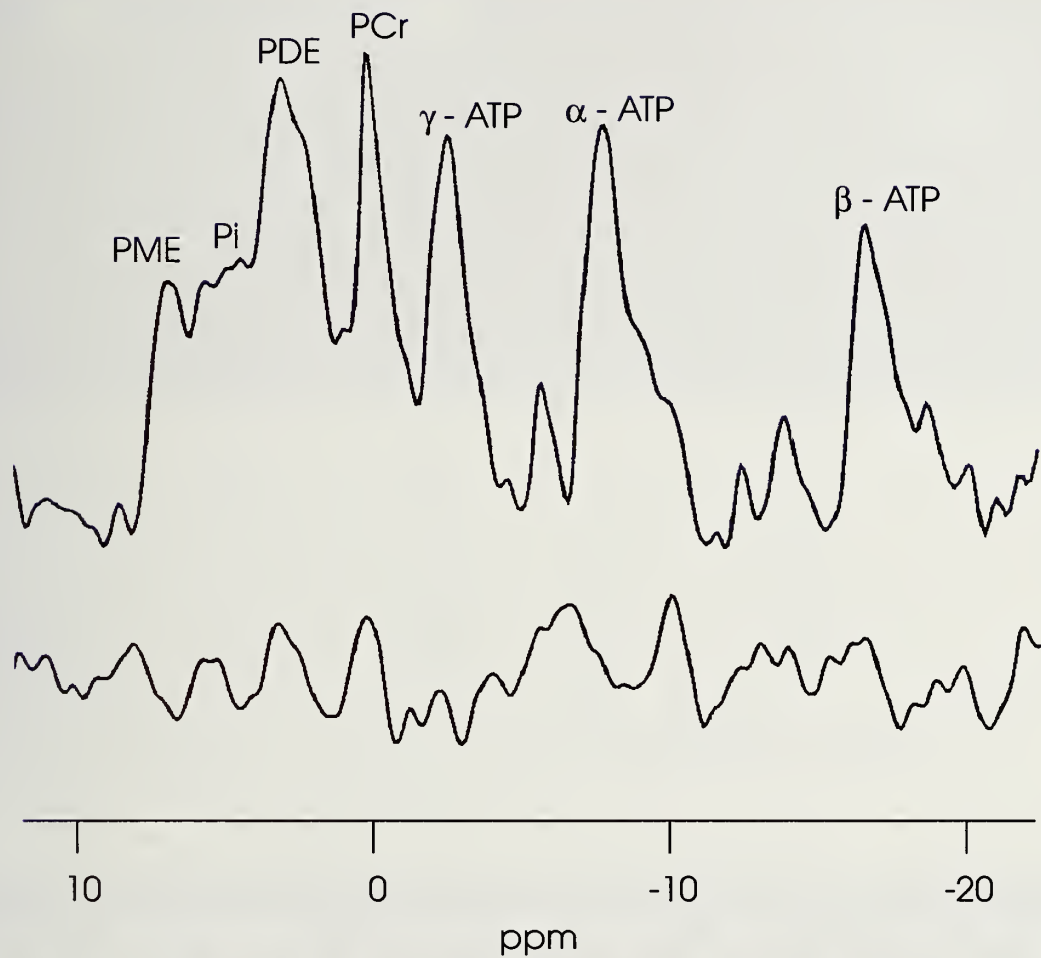
Transverse ^1H MR (left) and ^{31}P MRS (right) image of the brain of a patient with a chronic MCA infarct.

and extent of these phenomena are increased with aging, cerebrovascular disease, and dementia, the findings are still of unknown etiology and clinical significance. We used localized ^{31}P MRS (ISIS) to characterize the metabolic status and intracellular pH of hemispheric white matter brain volumes in 30 elderly patients whose MRI white matter signal hyperintensities (WMSH) ranged from absent to extensive (Sappey-Marinier et al. 1989, 1991a).

In patients with extensive WMSH on MRI, ^{31}P MRS signals were obtained from a standard white matter volume in the hemisphere with the more extensive MRI hyperintensities. In patients with minimal or absent WMSH on MRI, MRS signals were obtained from comparable hemispheric white matter volumes. We found that white matter volumes with extensive WMSH

evidenced a 25 percent decreased ATP/ P_i metabolite concentration ratio (1.49 ± 0.15 , $n=12$) compared with white matter volumes having absent or minimal WMSH (2.00 ± 0.19 , $n=12$, $p=0.04$). These findings suggest that extensive WMSH indicate a process that affects cellular white matter energy metabolism.

Similar studies in 13 of these subjects revealed a trend toward a lowered ATP/ P_i metabolite concentration ratio in a superior bilateral white matter volume without WMSH in subjects with extensive WMSH on inferior MRI volumes, suggesting that the metabolic changes may affect white matter beyond the areas of focal WMSH (Sappey-Marinier et al., 1991a). Preliminary ^{31}P and ^1H metabolite maps obtained from the brain of patients with WMSH reveal reduced ^{31}P metabolite and NAA concentra-

FIGURE 7

^{31}P MR spectra reconstructed from region 2 (top) and region 1 (bottom) of the chronic infarct depicted in figure 6.

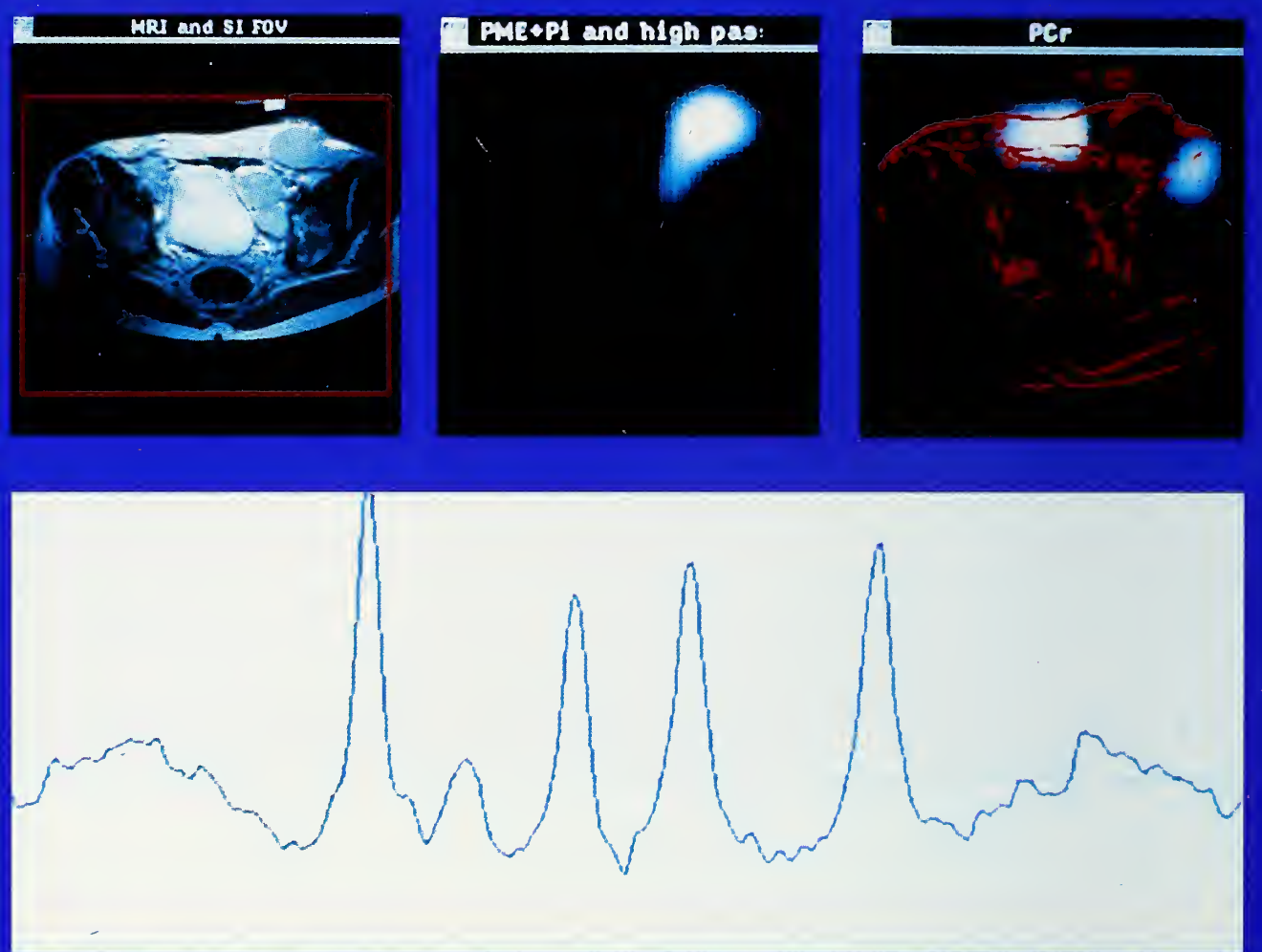
tions in areas of WMSH, probably indicating general loss of neuronal cells.

Spectroscopic Imaging of Organs Other Than the Brain

The feasibility of metabolite mapping with three-dimensional ^{31}P MRSI of human organs outside of the brain was investigated (Meyerhoff et al. 1991). A nonselective excitation pulse was used with a single large circular surface coil to transmit and receive. Individual

phosphorus metabolite distribution maps were obtained from the livers of healthy volunteers and a colon cancer patient, from the hearts and chests of healthy volunteers, from the lower leg of a patient with a hematoma in the calf, and from the groin area of a patient with a lymphoma (see discussion of figure 8).

The metabolite images revealed anatomical detail and allowed differentiation of body organs and lesions from surrounding tissue. Three-dimensional localized ^{31}P

FIGURE 8

Results of a combined ^1H MRI and ^{31}P MRSI examination of a patient with a lymphoma in the groin.

spectra could be reconstructed from these data sets with nominal volumes of 4–15 cm³, corresponding to real volume sizes of approximately 10–30 cm³. The spectra showed characteristic resonances and metabolite intensity ratios for the tissue of origin demonstrating good three-dimensional localization (Meyerhoff et al. 1991).

Figure 8 demonstrates that the information can be obtained from a combined ^1H MRI and ^{31}P MRSI study on a patient with a lymphoma in the groin. The standard ^1H MRI shown on the left has a su-

perimposed rectangle indicating the field of view for the MRSI examination. For ^{31}P MRSI data acquisition, a surface coil was positioned over the lymphoma, as indicated by a reference standard in the center of the surface coil plane, visible as a little white rectangle on the ^1H MRI.

The two ^{31}P metabolite maps on the right side in figure 8 were reconstructed from the integrated signal intensities of the PME plus P_i resonances (left) and the PCr resonance (right) in the sensitive area of the surface coil. The high-

pass filtered ^1H MR image superimposed on the PCr image helps to correlate both images and indicates that PCr is not present in the lymphoma but only in adjacent muscle tissue.

The region of the PME plus P_i signal intensity shown in the left ^{31}P MRS image is restricted to the region of the focal lesions and shows highest intensities in areas close to the surface coil. The ^{31}P spectrum in figure 8 was obtained from about 20 cm^3 of tissue in the center of the tumor. It demonstrates high PME and low PDE (indicative of rapidly proliferating cells) and no PCr in the lymphoma.

^1H MRSI to obtain metabolite distribution maps with surface coils similar to those obtained in the brain has not been successful to date. Tissue heterogeneity and the use of surface coils with inhomogeneous B1 fields currently preclude sufficient suppression of the strong water and fat resonances in organs other than the brain.

CONCLUSION

MRS techniques are unique among noninvasive imaging techniques. They can provide both biochemical and anatomical information in repeated examinations without causing known harm to the subject. The tissue can be observed in its original state without perturbing its bioenergetic status. Since these techniques use basically the same instrumentation as MRI, spectroscopy can be performed in a clinical setting by sim-

ply adding on to the existing high-field MRI instruments.

While existing MRS techniques and necessary hardware and software are continuously being refined for special applications, there seems to be a need for considerable improvement in the sensitivity of detection of the MR signal from metabolites present only at low concentrations. Spectroscopy techniques have shown their capability of providing information not obtainable by other noninvasive methods. MRS will, therefore, prove useful as an independent tool and as a technique that is complementary to other imaging modalities.

ACKNOWLEDGMENTS

This manuscript summarizes work performed in collaboration with Drs. Dominique Sappey-Marinier, Jeff Duijn, Saul Schaefer, Barry Massie, Raymond Deicken, Shane MacKay, Giovanna Calabrese, and Michael Boska. This work would not be possible without National Institutes of Health grant R01 DK33293, Veterans Administration Medical Research Service, and support from Philips Medical Systems.

REFERENCES

- Boska, M.D.; Meyerhoff, D.J.; Twieg, D.B.; Karczmar, G.S.; Matson, G.B.; and Weiner, M.W. Image-guided ^{31}P magnetic resonance spectroscopy of orthotopic and transplanted human kidneys. *Kidney Int* 38:294-300, 1990.

Deicken, R.; Hubesch, B.; Jensen, P.; Sappey-Marinier, D.; Krell, P.; Wisniewski, A.; Vanderburg, D.; Parks, R.; Fein, G.; and Weiner, M.W. Alterations in brain phosphate metabolite concentrations in patients with HIV infection. *Arch Neurol* 48:203-209, 1991.

Hetherington, H.; Matson, G.B.; and Weiner, M.W. Measurement of lactate and ethanol in human brain with use of ¹H ISIS MR spectroscopy. *Radiology* 173(P):121, 1989.

Hubesch, B.; Sappey-Marinier, D.; Hetherington, H.; Twieg, D.; and Weiner, M.W. ³¹P MRS studies of human brain. *Invest Radiol* 24:1039-1042, 1989a.

Hubesch, B.; Sappey-Marinier, D.; Laxer, K.; and Weiner, M.W. Alterations of pH and P_i in seizure foci of temporal lobe epilepsy. *Radiology* 173(P):234, 1989b.

Hugg, J.W.; Duijn, J.H.; Matson, G.B.; Maudsley, A.A.; Tsuruda, J.; and Weiner, M.W. " ³¹P and ¹H Spectroscopic Imaging of Brain Infarcts." Abstract presented at the American Society of Neuroradiology 29th Annual Meeting, Washington, DC, 1990.

Lawry, T.J.; Karczmar, G.S.; Weiner, M.W.; and Matson, G.B. Computer simulation of MRS localization techniques: An analysis of ISIS. *Magn Reson Med* 9:299-314, 1989.

Luyten, P.R.; Marien, A.J.H.; Heindel, W.; van Gerwen, P.H.J.; Herholz, K.; den Hollander, J.; Friedmann, G.; and Heiss, W.-D. Metabolic imaging of patients with intracranial tumors: ³¹P MR spectroscopic imaging and PET. *Radiology* 176:791-799, 1990.

Matson, G.B.; Twieg, D.B.; Karczmar, G.S.; Lawry, T.J.; Gober, J.R.; Valenza, M.;

Boska, M.D.; and Weiner, M.W. Image-guided surface coil ³¹P MRS of human liver, heart, and kidney. *Radiology* 169:541-547, 1988.

Maudsley, A.A.; Twieg, D.B.; Sappey-Marinier, D.S.; Hubesch, B.; Hugg, J.W.; Matson, G.B.; and Weiner, M.W. Spin echo ³¹P spectroscopic imaging in the human brain. *Magn Reson Med* 14:415-422, 1990.

Meyerhoff, D.J.; Boska, M.D.; Thomas, M.A.; and Weiner, M.W. Alcoholic liver disease: Quantitative image-guided ³¹P magnetic resonance spectroscopy. *Radiology* 173:393-400, 1989a.

Meyerhoff, D.J.; Karczmar, G.S.; Matson, G.B.; Boska, M.D.; and Weiner, M.W. Non-invasive quantitation of human liver metabolites using image-guided ³¹P magnetic resonance spectroscopy. *NMR Biomed* 3:17-22, 1990.

Meyerhoff, D.J.; Karczmar, G.S.; and Weiner, M.W. Abnormalities of the liver evaluated by ³¹P MRS. *Invest Radiol* 24:980-984, 1989b.

Meyerhoff, D.J.; Maudsley, A.A.; Schaefer, S.; and Weiner, M.W. Phosphorus-31 magnetic resonance metabolite imaging in the human body. *Magn Reson Imaging* 1991, in press.

Roth, K.; Hubesch, B.; Meyerhoff, D.J.; Naruse, S.; Gober, J.; Lawry, T.; Boska, M.D.; Matson, G.B.; and Weiner, M.W. Non-invasive quantitation of phosphorous metabolites in human tissue by NMR spectroscopy. *J Magn Reson* 81:299-311, 1988.

Sappey-Marinier, D.; Deicken, R.F.; Fein, G.; Calabrese, G.; Hubesch, B.; Van Dyke, C.; Dillon, W.; Davenport, L.; Meyerhoff, D.J.; and Weiner, M.W. Alterations of

brain phosphorus metabolites associated with MRI white matter signal hyperintensities. *Radiology* 1991a, in press.

Sappey-Marinier, D.; Hubesch, B.; Deicken, R.; Fein, G.; Matson, G.B.; and Weiner, M.W. ^{31}P metabolites in chronic stroke and deep white matter lesions. *Soc Magn Reson Med Abs* 3:I070, 1989.

Sappey-Marinier, D.; Hubesch, B.; Matson, G.B.; and Weiner, M.W. Decreased phosphorus metabolites and alkalosis in chronic cerebral infarction. *Radiology* 1991b, in press.

Schaefer, S.; Gober, J.; Valenza, M.; Karczmar, G.; Matson, G.B.; Camacho, A.; Botvinick, E.; Massie, B.M.; and Weiner, M.W. Nuclear magnetic resonance

imaging guided $^{31}\text{phosphorus}$ spectroscopy of the human heart. *J Am Coll Cardiol* 12:1444-1455, 1988.

Schaefer, S.; Gober, J.R.; Schwartz, G.S.; Twieg, D.B.; Weiner, M.W.; and Massie, B. In vivo phosphorus-31 spectroscopic imaging in patients with global myocardial disease. *Am J Cardiol* 65:II54-II61, 1990.

Twieg, D.B.; Meyerhoff, D.J.; Hubesch, B.; Roth, K.; Sappey-Marinier, D.; Boska, M.D.; Gober, J.; Schaefer, S.; and Weiner, M.W. Localized phosphorus-31 MRS in humans by spectroscopic imaging. *Magn Reson Med* 12:291-305, 1989.

12

NMR STUDIES OF CEREBRAL METABOLISM

Robert G. Shulman, Ph.D.¹ Kevin L. Behar, Ph.D.² Douglas L. Rothman, Ph.D.³
and Graeme F. Mason, Ph.D.¹

Nuclear magnetic resonance (NMR) spectroscopy experiments performed on humans and animals can be divided into two general classifications. The first, "tissue characterization," is really the phenomenology of normal conditions and various pathologies, including stroke, tumors, multiple sclerosis, and epilepsy. It is probably the most common kind of NMR study of humans. Localization is very important for tissue characterization, and NMR provides a means to localize and study the pathology.

The second classification of NMR experiments is the measurement of rates of metabolic pathways, the steps of which are generally well known. The objective is to refine our knowledge of these pathways and their control and to provide quantitative information about rates of isotopic turnover.

An example of isotopic turnover measurement is an experiment that

actually measures the rate at which metabolites such as lactate or glutamate are isotopically labeled following an infusion of ¹³C-labeled glucose. The label is not radioactive, and the experiment is performed under steady-state chemical conditions; consequently, the experiment does not perturb the subject significantly. These isotopic turnover measurements can be interpreted to obtain values of the cerebral metabolic rate for oxygen (CMRO₂) and the cerebral metabolic rate for glucose (CMRglc), as discussed in this chapter.

ACRONYMS

CMRglc	cerebral metabolic rate for glucose
CMRO ₂	cerebral metabolic rate for oxygen
NMR	nuclear magnetic resonance
TCA	tricarboxylic acid

¹Department of Molecular Biophysics and Biochemistry, Yale University, New Haven, CT 06511

²Department of Neurology, Yale Medical School, New Haven, CT 06511

³Department of Internal Medicine, Yale Medical School, New Haven, CT 06511

LOCALIZATION VIA PROTON NMR SPECTRA OF THE HUMAN BRAIN

The first observations of brain spectra by proton (^1H) NMR showed the wealth of information that was available (Behar et al. 1983). Subsequent animal studies refined water suppression and improved the spectral resolution (Rothman et al. 1984; Hetherington et al. 1985). When large human-sized magnets became available for spectroscopy, it was possible to obtain ^1H NMR spectra from the human brain (Bottomley et al. 1985; Luyten et al. 1986; Hanstock et al. 1988). The brain was the easiest organ in which to develop *in vivo* ^1H NMR spectroscopy because of the absence of large lipid resonances and the lack of motion.

Meanwhile, methods of spectral localization became available in which magnetic field gradients and frequency selective pulses were used to select volumes of interest. More recently, both ^{31}P NMR and ^1H NMR of the brain have been combined with chemical shift imaging, in which, instead of localizing the data acquisition from a selected volume of interest, the data are acquired from the entire volume, usually the whole head. The spectra from all the volume elements are then processed and displayed (Segebarth et al. 1990).

It was shown by den Hollander and subsequently in our laboratory that lactate can be observed in the stroke region in humans. Subsequent chemical shift imaging of the brain showed that the lactate is localized

in the region of the infarct (Berkelbach van der Sprenkel et al. 1988).

DETERMINATION OF METABOLIC RATES

Figure 1 is a schematic representation of glucose metabolism, beginning with glucose transport from the blood into the brain via a reversible transporter and down the glycolytic pathway at the rate V_{gly} . In the muscle, glucose transport is rate limiting, and the intracellular glucose concentration is very low. In the brain, there is very rapid glucose transport back and forth across the blood-brain barrier, followed by phosphorylation by hexokinase and metabolism by the glycolytic pathway (Siesjö 1978).

The labeled carbon in the six-carbon compound representing glucose in figure 1 goes down the pathway to the methyl group of lactate. It enters the Krebs cycle and on the first pass labels C4 of glutamate. Because there are large pools of glutamate (and sometimes large pools of lactate), the turnover times of ^{13}C in the lactate or in the glutamate pools in the brain can be long enough (approximately 10–20 minutes) that these time courses can be measured by detection of ^{13}C labeling using NMR.

Measurement of the rate of isotopic flow into lactate yields the glycolytic rate, and the flow into glutamate yields the tricarboxylic acid (TCA) cycle rate. As a point of technique, we do not observe the ^{13}C nucleus directly with ^{13}C NMR. Instead, we look at the protons that

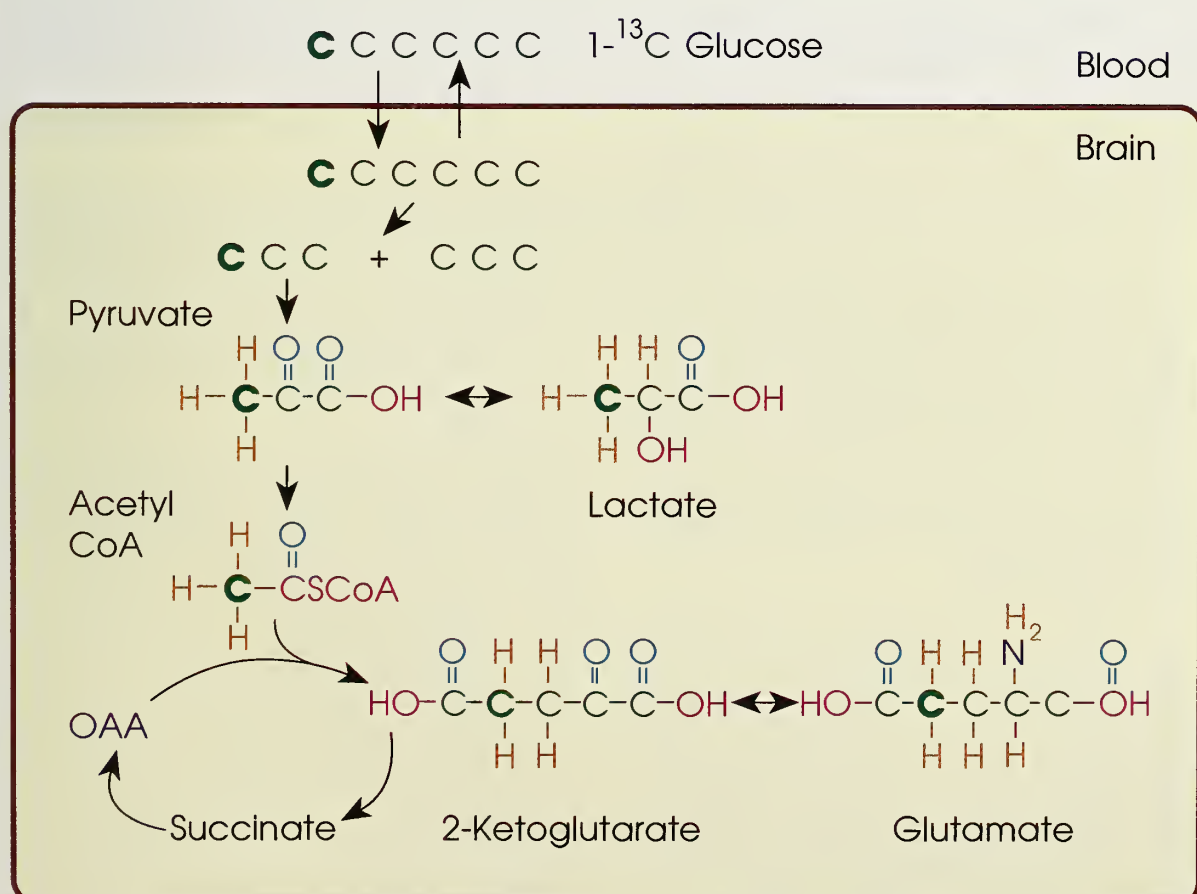
are coupled to the ^{13}C and consequently obtain much greater sensitivity of the protons. Because the proton is the most sensitive nucleus, proton NMR yields high enough signal-to-noise ratios to measure the time course of the ^{13}C labeling.

EXPERIMENTAL DEMONSTRATION OF ISOTOPIC TURNOVER

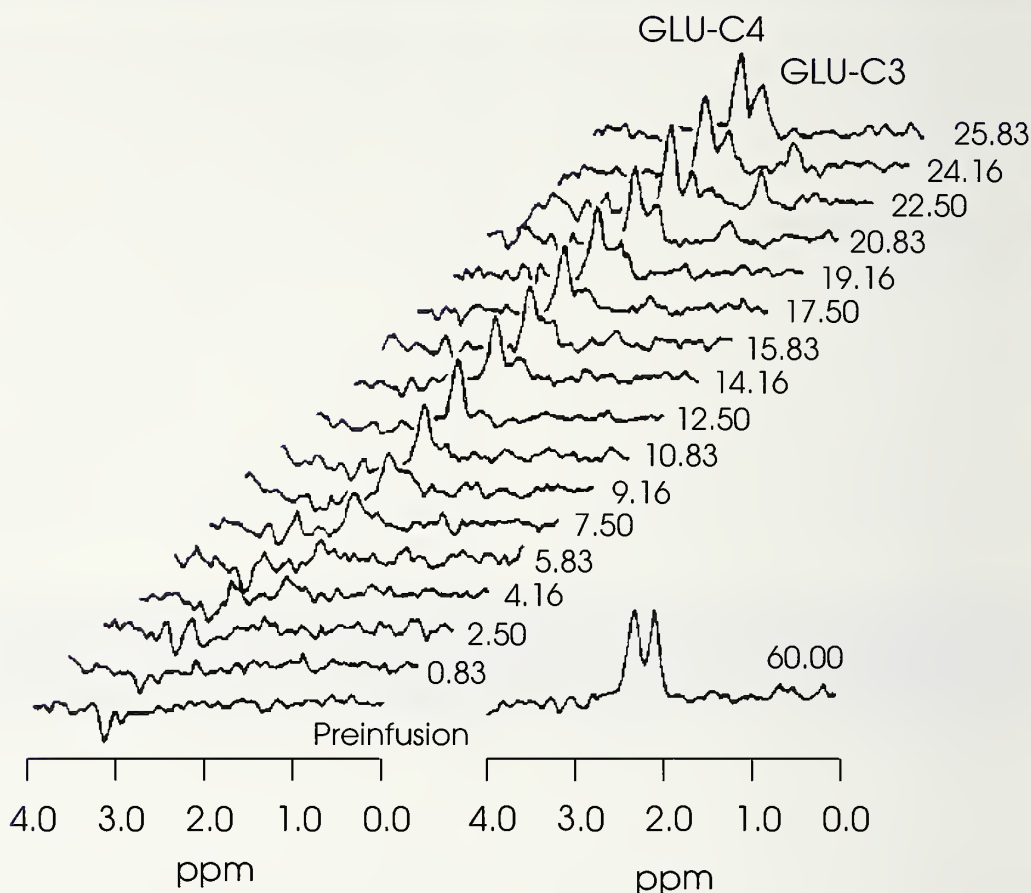
The isotopic turnover experiment consists of the following: The $[^{13}\text{C}]$ glucose is raised as rapidly as possible, and the plasma glucose ^{13}C enrichment and concentration are

measured from blood samples. In animals, we achieved the desired concentration in 1–3 minutes (Fitzpatrick et al. 1990). In humans, the $[^{13}\text{C}]$ glucose was increased over a period of approximately 20 minutes (Rothman et al. 1990). After infusion, the ^{13}C in glutamate C4 is measured every 1.5 minutes in the rat and every 6 or 7 minutes in the human. Detailed accounts have been published concerning experiments in rats (Fitzpatrick et al. 1990) and the changes observed after portacaval shunting (Fitzpatrick et al. 1989).

FIGURE 1



Schematic representation of ^{13}C flow from $(1-^{13}\text{C})$ glucose to $(4-^{13}\text{C})$ glutamate.

FIGURE 2

Stacked plot of ^1H -observed, ^{13}C -edited difference spectra obtained from a rat brain *in vivo*. Spectra were acquired during an infusion of ($1-^{13}\text{C}$)glucose. The midpoint time (in minutes) is indicated to the right of each spectrum. The resonances in each spectrum represent predominantly the ($4-^{13}\text{CH}_2$) of glutamate (GLU-C4) at 2.35 ppm and the ($3-^{13}\text{CH}_2$) of glutamate (GLU-C3) at 2.09 ppm. After death, the ($3-^{13}\text{CH}_3$) of lactate was observed at 1.33 ppm (data not shown). Data adapted from Fitzpatrick et al. 1990.

INTERPRETATION OF NMR DATA VIA MODELING

To calculate CMRO₂ and CMR_{glc} from these turnover experiments, we developed a simple model of the pathway and evaluated the errors caused by the simplifications in this model; these errors proved to be negligible (Mason et al. 1991).

The spectral acquisitions in a rat are shown in figure 2. These differ-

ence spectra show the resonances of protons that are next to ^{13}C atoms at positions C4 and C3. The rate of incorporation of the label from [$1-^{13}\text{C}$]glucose into [$4-^{13}\text{C}$]glutamate and [$3-^{13}\text{C}$]glutamate can be derived from the increasing intensities of these peaks. The simplest chemical reaction is one in which the glucose flows down a pathway to label a pool of glutamate and

the fraction of glutamate that is labeled with ^{13}C is given by

$$\frac{G^*}{G} = \frac{f}{2} (1 - e^{-kt})$$

where f is the fractional ^{13}C enrichment of glucose, k is the rate constant (equal to V_{TCA}/G , where V_{TCA} is the TCA cycle flux), and G and G^* are the total and labeled concentrations of glutamate, respectively.

The glutamate C4 labeling data from five rats were fit to this equation by a computer model, and a value of $1.58 \pm 0.37 \mu\text{mol}/\text{minute/g}$ was calculated for V_{TCA} . The uncertainty arises not from NMR signal-to-noise ratios or from uncertainties in the model but from interanimal variations.

CONCLUSIONS

The importance of the computer modeling is that it allowed monitoring of the sensitivity of the fit to potential deviations from the assumptions of the model. Such sensitivities were assessed by using values of parameters reported in the extensive literature on rat brains as input for the model. At the extremes of these ranges, the values determined by fitting the model to the NMR data lay well within the uncertainties of ± 10 percent introduced by the noise in the NMR experiment, hence the simplifications did not introduce significant errors into the calculated values of V_{TCA} (Mason et al. 1991).

One advantage of rat measurements over human studies is that this kind of quantitative analysis of the results is possible in the animal. With such results, the animal studies provide a substantial basis for using the simple model to analyze human data and to obtain brain metabolic rates in the human from ^{13}C turnover of the glutamate pool.

REFERENCES

- Behar, K.L.; den Hollander, J.A.; Stromski, M.E.; Ogino, T.; Shulman, R.G.; Petroff, O.A.C.; and Prichard, J.W. High resolution ^1H NMR study of cerebral hypoxia in vivo. *Proc Natl Acad Sci USA* 80:4945–4948, 1983.
- Berkelbach van der Sprenkel, J.W.; Luyten, P.R.; van Rijen, P.C.; Tulleken, C.A.F.; and den Hollander, J.A. Cerebral lactate detected by regional proton magnetic resonance spectroscopy in a patient with cerebral infarction. *Stroke* 19:1556–1560, 1988.
- Bottomley, P.A.; Edelstein, W.A.; Foster, T.H.; and Adams, W.A. In vivo solvent-hydrogen nuclear magnetic resonance spectroscopy: A window to metabolism? *Proc Natl Acad Sci USA* 82:2148–2152, 1985.
- Fitzpatrick, S.M.; Behar, K.L.; and Shulman, R.G. In vivo NMR spectroscopy studies of cerebral metabolism in rats after portal-caval shunting. In: Butterworth, R.F., and Layrargues, G.P., ed(s). *Hepatic Encephalopathy*. Clifton, NJ: Humana Press, Inc., 1989. pp. 177–187.
- Fitzpatrick, S.M.; Hetherington, H.P.; Behar, K.L.; and Shulman, R.G. The flux from glucose to glutamate in the rat

brain in vivo as determined by ^1H -observed, ^{13}C -edited NMR spectroscopy. *J Cereb Blood Flow Metab* 10:170–179, 1990.

Hanstok, C.C.; Rothman, D.L.; Jue, T.; and Shulman, R.G. Volume-selected proton spectroscopy in the human brain. *J Magn Reson* 77:583–588, 1988.

Hetherington, H.P.; Avison, M.J.; and Shulman, R.G. ^1H homonuclear editing of rat brain using semi-selective pulses. *Proc Natl Acad Sci USA* 82:3115–3118, 1985.

Luyten, P.R.; Marien, A.J.H.; Sijtsma, B.; and den Hollander, J.A. Solvent-suppressed spatially resolved spectroscopy. An approach to high-resolution NMR on a whole-body MR system. *J Magn Reson* 67:148–155, 1986.

Mason, G.F.; Behar, K.L.; Rothman, D.L.; and Shulman, R.G. NMR determination of TCA cycle rate and alpha-ketoglutarate/gluta-

mate exchange flux in rat brain. *J Cereb Blood Flow Metab* 1991, in press.

Rothman, D.L.; Behar, K.L.; Hetherington, H.P.; and Shulman, R.G. Homonuclear ^1H double-resonance difference spectroscopy of the rat brain in vivo. *Proc Natl Acad Sci USA* 81:6330–6334, 1984.

Rothman, D.L.; Novotny, E.J.; Shulman, G.I.; Howseman, A.M.; Mason, G.F.; Petroff, O.A.C.; Nixon, T.W.; Hanstock, C.C.; Prichard, J.W.; and Shulman, R.G. Determination of human glutamate turnover times by ^1H NMR. *Magn Reson Med Abstr* 2:986, 1990.

Segebarth, C.M.; Baleriaux, D.F.; Luyten, P.R.; and den Hollander, J.A. Detection of metabolic heterogeneity of human intracranial tumors in vivo by ^1H NMR spectroscopic imaging. *J Magn Reson Med* 13:62–76, 1990.

Siesjo, B.K. *Brain Energy Metabolism*. New York: John Wiley & Sons, 1978.

13

ALTERATIONS IN MEMBRANE METABOLISM AND PHYSIOLOGY IN ALZHEIMER'S DISEASE: IMPLICATIONS FOR ETIOLOGY

Jay W. Pettegrew, M.D., William E. Klunk, M.D., Ph.D., and Richard J. McClure, Ph.D.¹

Alzheimer's disease (AD) impairs the brain's fundamental capacity to store, manipulate, and retrieve information. Information processing is mediated by a plethora of neuronal systems and neurotransmitters but at the most basic level results from processes occurring at the neuronal membrane, the communication center of the cell. By definition, the dysfunction in AD involves more than one neuronal system (McKhann et al. 1984) and by later stages typically affects all systems. It seems probable that a disorder such as AD should have demonstrable, widespread abnormalities in membrane structure and/or function. It also is possible that these abnormalities play an important role in the pathogenesis of the disorder. Energy metabolism is another area that is vitally impor-

ACRONYMS

AD	<i>Alzheimer's disease</i>
ATP	<i>adenosine triphosphate</i>
EPSP	<i>excitatory postsynaptic potential</i>
GABA	<i>gamma-amino-butyric acid</i>
HPLC	<i>high-pressure liquid chromatography</i>
IC ₅₀	<i>concentration which inhibits 50 percent of the basal response</i>
NFT	<i>neurofibrillary tangles</i>
NMR	<i>nuclear magnetic resonance</i>
PDE	<i>phosphodiester</i>
PME	<i>phosphomonoester</i>
PtdA	<i>phosphatidic acid</i>
PtdC	<i>phosphatidylcholine</i>
PtdE	<i>phosphatidylethanolamine</i>
PtdI	<i>phosphatidylinositol</i>
PtdS	<i>phosphatidylserine</i>
SP	<i>senile plaque</i>

¹Department of Psychiatry, Western Psychiatric Institute and Clinic, University of Pittsburgh School of Medicine, Pittsburgh, PA 15213

tant to normal brain function. A recent study suggests that AD may be associated with alterations in energy metabolism in elderly females (Aronson et al. 1990). Therefore, this laboratory has been exploring membrane and energy metabolism of AD. This chapter briefly reviews several areas of interest and discusses possible implications for the etiology and pathogenesis of AD.

MEMBRANE METABOLITES

Recent studies in vitro from this laboratory reveal alterations in membrane phospholipid metabolism in AD patients (Pettegrew et al. 1984, 1985, 1987*a,b*, 1988*a,b*, 1989). These findings have now been supported by in vivo studies of AD brain (Brown et al. 1989; Gdowski et al. 1988; Panchalingam et al. 1991). Both in vitro and in vivo studies have shown that a class of molecules called phosphomonoesters (PMEs) is elevated in AD brain. PMEs are precursors of membrane phospholipids and products of phospholipase C and glycerol phosphodiesterase activity (Pettegrew 1989). The PMEs (phosphoethanolamine, L-phosphoserine, and phosphocholine) are normally found in abundance (1–2 mM) in the brain in contrast to other organs (McIlwain and Bachelard 1985). Brain PMEs are normally elevated (5–7 mM) in the period of neuritic proliferation during brain development (Pettegrew et al. 1990*a*). This also coincides with the occurrence of normal programmed cell death and synaptic pruning in developing

brain (Pittman and Oppenheim 1979; Cowen et al. 1984; Oppenheim 1985; Clarke 1985). The abnormal elevation (5–7 mM) of PME levels in Alzheimer brain is similar to those observed in developing brain (Pettegrew et al. 1990*a*). This elevation appears to occur early in the course of the disease because the PME levels inversely correlate with the numbers of senile plaques (SPs) (Pettegrew et al. 1988*b*).

MOLECULAR STRUCTURE OF PMES

L-phosphoserine and phosphoethanolamine are structurally similar to the amino acid neurotransmitters L-glutamate and gamma-amino-butyric acid (GABA), respectively. The acidic phosphate ester group of L-phosphoserine and phosphoethanolamine corresponds functionally to the -CH₂-carboxylic acid group of L-glutamate and GABA. All of these molecules are conformationally mobile; thus each of the molecules can exist in a number of different conformations. This is best illustrated by the existence of three receptor subtypes for L-glutamate and the two stable conformations found in the crystal structures of L-glutamate (Bernal 1931; Hirokawa 1955). In a molecular mechanics study (McClure and Pettegrew 1989), the crystal structures of L-glutamate, L-phosphoserine, GABA, and phosphoethanolamine (obtained from the Cambridge Structural Database System; Allen et al. 1979) were the starting point for energy minimization using the MacroModel

(Version 2.5, Copyright Columbia University) suite of programs. The molecular shape of the energy-minimized structure of L-phosphoserine is similar to L-glutamate (Pettegrew 1989), as is that of phosphoethanolamine to GABA. The functional groups of the minimized conformers of L-glutamate and L-phosphoserine were superimposed on each other in three-dimensional space by a least-squares procedure and found to overlap with <0.2 Å average deviation per atom. Similarly, the overlap of the minimized structures of GABA and phosphoethanolamine was excellent. The predominant energy term affecting the above minimizations is the interaction of the charged amino and acidic groups. These interactions may be overestimated, because they were performed in gas phase without the dampening of solvation effects. However, the similarity of both the crystal structures and minimized structures indicate that L-phosphoserine and phosphoethanolamine can adopt conformations that have a shape and charge topology comparable to those of L-glutamate and GABA, respectively.

RECEPTOR BINDING AND ELECTROPHYSIOLOGY OF PMES

Guided by the structural similarities of PMEs to amino acid neurotransmitters described above, we have investigated the ability of PMEs to compete for binding with markers of several specific amino acid receptor subtypes. There are at least

three L-glutamate receptor subtypes, commonly referred to as the AMPA/Quis, kainic acid, and NMDA receptors, since these ligands preferentially label the respective receptor subtypes (Watkins et al. 1990; Lodge and Johnson 1990). PMEs have specific interactions with these receptor subtypes, depending on the PME tested and the receptor subtype studied (Klunk et al. 1991). None of the PMEs, at concentrations up to 10 mM, are able to compete for binding with [³H]AMPA, which labels the AMPA/Quis site. L-phosphoserine is able to compete for binding sites with [³H]kainic acid with an IC₅₀ (concentration which inhibits 50 percent of the basal response) of approximately 1 mM. Phosphoethanolamine showed no significant inhibition of [³H]kainic acid binding at concentrations up to 10 mM. Phosphocholine could not be tested in this assay since it is only available as the calcium salt, and calcium alone inhibits [³H]kainic acid binding (Braitman and Coyle 1987). L-phosphoserine also proved to be unique among the PMEs in its ability to inhibit the binding of [³H]CGS-19755, a selective NMDA competitive antagonist (Murphy et al. 1988). L-phosphoserine inhibited [³H]CGS-19755 binding with an IC₅₀ of 0.7 mM; phosphoethanolamine and phosphocholine showed no inhibition at 10 mM. Although this suggests activity at the NMDA receptor site, it does not differentiate between agonist and antagonist activity. This differentiation can be made by studying the effects of L-phosphoserine on the

binding of the noncompetitive NMDA antagonist [^3H]MK-801 (Reynolds and Miller 1988). Basal levels of [^3H]MK-801 binding are stimulated by NMDA (or L-glutamate) and glycine agonists and inhibited by NMDA antagonists. Glycine-stimulated [^3H]MK-801 binding is further augmented by NMDA agonists and inhibited by NMDA antagonists. The effects of L-phosphoserine on both basal and glycine-stimulated [^3H]MK-801 binding are consistent with its role as an NMDA antagonist. Competition experiments with NMDA suggest that L-phosphoserine has both competitive and noncompetitive antagonist properties. The competitive actions are prominent, and the noncompetitive effects may be mediated through the glycine regulatory site of the NMDA receptor complex (Reynolds and Miller 1988).

These binding studies support the hypothesis that L-phosphoserine can assume a shape and charge topology similar to L-glutamate. However, the replacement of the carboxylic acid function with phosphate has changed the action at this site to that of an antagonist. This may be due to the increased negative charge of the phosphate group (Fagg et al. 1982) or the addition of two more potential hydrogen bond acceptors in the oxygens of the phosphate group (Freund et al. 1984).

L-phosphoserine also has been reported to have relatively potent effects on the ibotenic acid-stimulated hydrolysis of inositol phospholipids (Nicoletti et al. 1986a;

Schoepp and Johnson 1989). Hydrolysis of membrane inositol phospholipids may serve as a transduction mechanism for several neurotransmitters, including the excitatory amino acid system stimulated by ibotenic acid and inhibited by L-AP4 (Nicoletti et al. 1986a,b; Schoepp and Johnson 1989). The study by Schoepp and Johnson (1989) also implies that the actions of L-phosphoserine may be mediated through binding to a calcium/chloride- and L-AP4-sensitive uptake site for L-glutamate; this is presently under investigation. Also under investigation is the elucidation of the action of phosphoethanolamine at GABA receptors.

In hippocampal slice preparations, the two abundant PMEs, phosphoethanolamine and L-phosphoserine, reliably alter properties of synaptic transmission at the Schaffer collateral/commissural-CA1 cell synapse. Phosphoethanolamine (1–5 mM) reversibly decreases in a concentration-dependent fashion the population excitatory postsynaptic potential (EPSP) amplitude of CA1 pyramidal cells. There is no effect on slice levels of phosphocreatine or adenosine triphosphate (ATP). L-phosphoserine initially decreases, then after a 30-minute incubation increases the EPSP in the same preparation; these effects are not reversible. The increase in EPSP is mirrored by a decrease in both phosphocreatine and ATP (Bradler et al. 1991).

These neuropharmacological activities of L-phosphoserine have important implications for AD. The

direct NMDA receptor antagonism of L-phosphoserine could play a role in the memory difficulties, because the NMDA receptor has been implicated in basic mechanisms of memory and learning, such as long-term potentiation (Brown et al. 1988). However, if L-phosphoserine has more prominent effects on the uptake of L-glutamate, its predominant action could be as an indirect L-glutamate agonist and thereby a potential neurotoxin.

MEMBRANE BIOPHYSICS

L-phosphoserine, phosphoethanolamine, and phosphocholine increase molecular motion in the hydrocarbon core of normal human erythrocytes after brief incubation (30 minute) at concentrations (1–5 mM) observed in AD brain (Pettegrew et al. 1990b). Erythrocytes obtained from probable AD patients (Alzheimer's Disease and Related Disorders Association-National Institute of Neurological and Communicative Disorders and Stroke criteria; McKhann et al. 1984) have similar increased molecular motion in the hydrocarbon core, as is observed in normal erythrocytes incubated with the PME. Age-matched control erythrocytes do not have this increased motion (Pettegrew et al. 1990b). These results suggest that the PME can cross the brain-blood barrier and enter the plasma membrane of circulating erythrocytes. After entering the erythrocyte membrane, the molecular dynamics of the hydrocarbon core are altered. Similar

membrane changes have been observed in platelets from AD patients (Zubenko et al. 1987). These results suggest that circulating erythrocytes and platelets might be "reporter cells" for molecular changes occurring in the brains of AD patients.

The PMEs also have structural effects on membranes. Both L-phosphoserine and phosphoethanolamine significantly alter the phase and structure of model membranes made from phosphatidylserine (PtdS) and phosphatidylethanolamine (PtdE) but not phosphatidylcholine (PtdC). The changes induced in the model membranes are those that underlie the formation of vesicles (micellar phase) and the fusion of vesicles to membrane bilayers (hexagonal II phase), i.e., exocytosis of vesicle content as observed in neurotransmitter release. Therefore, the PMEs could enhance their own delivery into the extracellular space where they could be active against receptors such as the L-glutamate receptor (Pettegrew 1989; Pettegrew and Panchalingham 1989).

MEMBRANE PHOSPHOLIPIDS

Phosphodiesters (PDEs), breakdown products of membrane phospholipids (Pettegrew 1989), are elevated in AD brain (Pettegrew et al. 1988a). Because levels of the building blocks (PME) and breakdown products (PDE) of membrane phospholipids are altered during the course of AD, studies were initiated to determine if the levels of the mem-

brane phospholipids themselves were altered in AD, and if so, how the phospholipid levels might correlate with the numbers of SPs and neurofibrillary tangles (NFTs). The mole ratios of bilayer/nonbilayer membrane phospholipids are normally tightly controlled (Storch and Kleinfeld 1985). Phospholipid composition is an important determinant of the structure, dynamics, and function of cellular membranes and of many proteins which reside in these membranes (Cullis and DeKruijff 1979; Prives et al. 1982; Cohen 1983; Benga and Holmes 1984; Carruthers and Melchior 1984, 1986; Connolly et al. 1985; Farmer et al. 1985; Peng and Froehner 1985; Peng and Poo 1986; Delisle and Williams 1986; Fong and McNamee 1986; Froehner 1986; Hirokawa 1986; DeKruijff 1987; Maksymiw et al. 1987; Nelson and Veshnock 1987). Therefore, alterations in the phospholipid composition of brain cellular membranes could have important consequences for neuronal function. For example, a recent study suggests that altered membranes could account for the altered binding affinity of D₁ dopamine receptors in AD brain (Keyser et al. 1990).

Ongoing work in our laboratory demonstrates a reduction in AD brain phospholipids measured by high-pressure liquid chromatography (HPLC) and expressed as micromoles of phospholipid per gram wet weight of brain. As compared to non-AD controls (60 samples, 9 brains), AD brain (131 samples, 17 brains) has decreased levels of PtdC

($p=0.001$), PtdE ($p=0.003$), PtdS ($p=0.04$), and cholesterol ($p=0.01$). To equate phospholipid levels with a measure of disease severity, the levels of PtdC, PtdE, PtdS, and cholesterol were compared with the number of SPs per $\times 200$ magnification between cortical layers II and IV in the same brain regions. This comparison revealed a nonlinear correlation for PtdC that peaked at approximately 10 SPs per $\times 200$ magnification and declined with increasing SP numbers ($r=0.9$, $p=0.0001$). Linear negative correlations were observed for PtdE ($r=0.6$, $p=0.02$) and PtdS ($r=0.8$, $p=0.003$); there was no correlation for cholesterol ($r=0.08$, $p=0.5$).

These results demonstrate altered levels of PtdC, PtdE, PtdS, and cholesterol in AD brain as compared to age-matched, non-AD diseased (demented and nondemented) controls. From this perspective, there is a fundamental degeneration of brain membranes in AD that is not observed in the other, non-AD diseases studied.

High-resolution ³¹P nuclear magnetic resonance (NMR) spectra were obtained for brain phospholipids using the methods of Meneses and Glonek (1988). The quantitation of the phospholipids by ³¹P NMR provides important independent verification of results obtained by HPLC analysis and also provides quantitation of some phospholipids not separated by HPLC analysis. Twenty-two samples from 10 AD brains and 22 samples from 9 non-AD neurological control brains were analyzed. High-resolution ³¹P NMR spectra allowed quantitation

of the phospholipids lyso-PtdE, cardiolipin, an unknown resonance, PtdE-plasmalogen, PtdE, PtdS+sphingomyelin, phosphatidylinositol (PtdI), PtdC-plasmalogen, PtdC, and phosphatidic acid (PtdA). Expressed as the mole percentage of the Folch extractable phosphorus, the mean levels of PtdC, PtdC-plasmalogen, PtdI, PtdS, sphingomyelin, PtdE-plasmalogen, cardiolipin, or PtdA did not differ significantly in AD brain compared to non-AD controls. There was, however, a decrease in the mean levels of PtdE in AD brain ($p<0.03$). When the levels of the individual phospholipids were compared to the numbers of SPs and NFTs, the only significant correlations were between the levels of PtdC and cardiolipin and the numbers of SPs. Again there was a nonlinear correlation between the levels of PtdC and SPs which peaked at approximately 15–20 SPs per $\times 200$ magnification and then decreased ($r=0.65$, $p=0.007$). These results are quite similar to those obtained by HPLC. The cardiolipin levels have a nonlinear correlation with SPs; the levels of cardiolipin increase with the numbers of SPs ($r=0.75$, $p=0.0006$).

The levels of phospholipids in AD and non-AD controls, as determined by HPLC or ^{31}P NMR, showed no correlation between the levels of PtdS, PtdE, PtdC, or cholesterol and the postmortem interval.

Several other significant correlations were found between various metabolites or between metabolites and measures of disease severity. In the same tissue sam-

ples, there were significant correlations between the levels of PtdC-plasmalogen and the levels of both PME ($r=0.81$, $p=0.01$) and PDE ($r=0.81$, $p=0.01$). The levels of PtdA and Blessed scores correlated significantly ($r=0.63$, $p=0.05$) as did the levels of cardiolipin and the Mini-Mental scores ($r=0.74$, $p=0.01$).

However, by both HPLC and ^{31}P NMR analyses, the levels of PtdC initially increase then decrease with increasing numbers of SPs. These findings suggest an increase in PtdC synthesis early in the pathogenesis of AD at a time when PME levels are high. In theory, the augmented synthesis of PtdC could shunt available choline from acetylcholine synthesis (Pettegrew 1989), producing a functional cholinergic deficit which is clinically observed (Bartus et al. 1982).

The alterations in the mole ratios of the membrane phospholipids also could alter the normal insertion and maintenance of proteins into the cellular membrane. This could potentially contribute to an exaggerated release and processing of the amyloid precursor protein from neuronal cells in AD brain. From this perspective, the accumulation of β -amyloid in AD brain could be secondary to a fundamental alteration in the cellular membrane.

INTERACTIONS BETWEEN MEMBRANE AND ENERGY METABOLISM

^{31}P NMR studies show that the levels of cardiolipin appear to increase

rapidly with increasing numbers of SPs. Cardiolipin is found predominantly in the inner mitochondrial membrane of the cell (Daum 1985). In the inner mitochondrial membrane, complex IV (cytochrome c oxidase) has a predilection for phospholipids in general (Knowles et al. 1979; Marsh et al. 1982; Griffith et al. 1986) and cardiolipin in particular (Powell et al. 1985). Cardiolipin is thought to be an important modulator of complex IV activity (Seelig and Seelig 1985), but this has been disputed (Powell et al. 1985). The increase in cardiolipin levels with increasing numbers of SPs could reflect a compensatory mechanism to maintain normal electron transport chain function and ATP production. Positron emission tomography findings reveal decreased glucose uptake in areas of association cortex of AD brain (Haxby et al. 1986); these areas characteristically also have the greatest numbers of SPs (Brun and Gustafson 1976; Pearson et al. 1985).

Studies in the Fischer 344 rat demonstrate that brief anoxia produces decreased levels of phosphocreatine and increased levels of the PME without changes in the levels of ATP. These results suggest a metabolic linkage between high-energy phosphate and membrane phospholipid metabolism (Pettegrew et al. unpublished observations). This is of considerable interest because a recent in vivo ^{31}P NMR spectroscopy study demonstrates a linear correlation between the levels of brain ATP and Mattis scores ($r=0.7$, $p=0.009$) (Panchalingham et al.

1991). The recent report of increased incidence of AD in elderly females with a history of myocardial infarction supports this suggested association between AD and compromised energy metabolism (Aronson et al. 1990).

CONCLUSION

AD is a progressive degenerative neurological disease in which initial loss of memory functions is followed by loss of all cognitive abilities. Information storage, retrieval, and transfer depend on functional membranes. Recent in vitro and in vivo studies demonstrate an elevation in brain PMEs early in the course of AD. PMEs (phosphoethanolamine, L-phosphoserine, and phosphocholine), the building blocks of membrane phospholipids, are normally found in abundance (1–2 mM) in the brain in contrast to other organs. In the brain the PMEs are normally elevated (5–7 mM) during the period of dendritic proliferation, which coincides with the occurrence of normal programmed cell death and synaptic pruning. PMEs are abnormally elevated in the AD brain (5–7 mM), and this elevation appears to occur early in the course of the disease (PME levels inversely correlate with the numbers of SPs). Phosphoethanolamine and L-phosphoserine have striking structural similarities to the known neurotransmitters GABA and L-glutamate, respectively. Binding and electrophysiological studies reveal L-phosphoserine to be active at the

L-glutamate site of the NMDA receptor. These findings provide a possible explanation for the prominent early memory loss in AD and the later loss of pyramidal cells which contain these receptors. The PMEs also alter the dynamics, phase, and structure of model and cellular membranes. The induced changes in phase and structure provide a mechanism for the packaging and release of the PMEs into the extracellular space. In addition, erythrocytes from AD patients show strikingly similar changes in membrane dynamics as observed in normal erythrocytes incubated with the PMEs. This suggests erythrocytes might provide a "cellular reporter" on molecular changes occurring in the brains of AD patients. AD brain also shows abnormalities in phospholipid composition as compared to normal and diseased controls. This abnormality also could lead to membrane dysfunction. Furthermore, early elevations in PtdC may cause choline to be shunted away from acetylcholine synthesis. Changes in membrane metabolism appear to be coupled to changes in energy metabolism which, in turn, correlate with disease severity in *in vivo* studies.

ACKNOWLEDGMENTS

This work was supported by National Institute on Aging grants AG05657, AG08371, AG09017, AG05133, and AG08974 to Jay W. Pettegrew, M.D.

REFERENCES

- Allen, F.H.; Bellard, S.A.; Brice, M.D.; Cartwright, B.A.; Doubleday, A.; Higgs, H.; Hummelink, T.; Hummelink Peters, B.G.; Kennard, O.; Motherwell, W.D.S.; Rodgers, J.R.; and Watson, D.G. The Cambridge crystallographic data centre: Computer-based search, retrieval, analysis and display of information. *Acta Crystallogr B* 35:2331–2339, 1979.
- Aronson, M.K.I.; Ooi, W.L.; Morgenstern, H.; Hafner, M.S.; Masur, D.; Crystal, H.; Frishman, W.H.; Fisher, D.; and Katzman, R. Women, myocardial infarction, and dementia in the very old. *Neurology* 40:1102–1106, 1990.
- Bartus, R.T.; Dean, R.L.; Beer, B.; and Lippa, A.S. The cholinergic hypothesis of geriatric memory dysfunction. *Science* 217:408–417, 1982.
- Benga, G., and Holmes, R.P. Interactions between components in biological membranes and their implications for membrane function. *Prog Biophys Mol Biol* 43:195–257, 1984.
- Bernal, J.D. The crystal structure of the natural amino acids and related compounds. *Z Kristallogr* 78:363–365, 1931.
- Bradler, J.E.; Barrionuevo, G.; Panchalingam, K.; McKeag, D.; and Pettegrew, J.W. Intermediates of phospholipid metabolism elevated in Alzheimer's disease have neurophysiological and metabolic actions in hippocampus. *Synapse* 1991, in press.
- Braitman, D.J., and Coyle, J.T. Inhibition of [β H]kainic acid receptor binding by divalent cations correlates with ion affinity for the channel. *Neuropharmacology* 26:1247–1251, 1987.

- Brown, G.G.; Levine, S.R.; Gorell, J.M.; Pettegrew, J.W.; Gdowski, J.W.; Bueri, J.A.; Helpern, J.A.; and Welch, K.M.A. In vivo ^{31}P NMR profiles of Alzheimer's disease and multiple subcortical infarct dementia. *Neurology* 39:1423–1427, 1989.
- Brown, T.H.; Chapman, P.F.; Kairiss, E.W.; and Keenan, C.L. Long-term synaptic potentiation. *Science* 242:724–728, 1988.
- Brun, A., and Gustafson, L. Distribution of cerebral degeneration in Alzheimer's disease. A clinico-pathological study. *Arch Psychiatr Nervenkr* 223:15–33, 1976.
- Carruthers, A., and Melchior, D. A rapid method of reconstituting human erythrocyte sugar transport proteins. *Biochemistry* 23:2712–2718, 1984.
- Carruthers, A., and Melchior, D. How bilayer lipids affect membrane volume protein activity. *Trends Biochem Sci* 11:331–335, 1986.
- Clarke, P.G. Neuronal death in the development of the vertebrate nervous system. *Trends Neurosci* 8:345–349, 1985.
- Cohen, C.M. The molecular organization of the red cell membrane skeleton. *Semin Hematol* 20:141–158, 1983.
- Connolly, T.; Carruthers, A.; and Melchior, D. Effects of bilayer cholesterol of human erythrocyte hexose transport protein activity in synthetic lecithin bilayers. *Biochemistry* 24:2865–2873, 1985.
- Cowen, W.M.; Fawcett, J.W.; O'Leary, D.D.M.; and Stanfield, B.B. Regressive events in neurogenesis. *Science* 225:1258–1265, 1984.
- Cullis, P.R., and DeKruifff, B. Lipid polymorphism and the functional roles of lipids in biological membranes. *Biochim Biophys Acta* 559:399–420, 1979.
- Daum, G. Lipids of mitochondria. *Biochim Biophys Acta* 822:1–42, 1985.
- DeKruifff, B. Polymorphic regulation of membrane lipid composition. *Nature* 329:587–588, 1987.
- Delisle, R., and Williams, J. Regulation of membrane fusion in secretory exocytosis. *Annu Rev Physiol* 48:225–238, 1986.
- Fagg, G.E.; Foster, A.C.; Harris, E.W.; Lanthorn, T.H.; and Cotman, C.W. Structure-activity relationships of L-glutamate receptor ligands: Role of the ω -acidic terminal. *Neurosci Lett* 31:59–64, 1982.
- Farmer, B.; Harmon, M.; and Butterfield, D. ESR study of the erythrocyte membrane skeletal protein: Influence of the state of aggregation of spectrin on the physical state of membrane protein, bilayer lipid, and cell surface carbohydrates. *Biochim Biophys Acta* 821:420, 1985.
- Fong, T.M., and McNamee, M.G. Correlation between acetylcholine receptor function and structural properties of membranes. *Biochemistry* 25:830–840, 1986.
- Freund, R.K.; Crooks, S.L.; Koerner, J.F.; and Johnson, R.L. Antagonist activity of phosphorus-containing glutamate analogs in the perforant path. *Brain Res* 291:150–153, 1984.
- Froehner, S. The role of the postsynaptic cytoskeleton in AChR organization. *Trends Neurosci* 9:37–41, 1986.
- Gdowski, J.W.; Brown, G.G.; Levine, S.R.; Smith, M.; Helpern, J.; Bueri, J.; Gorell, J.

- and Welch, K.M.A. Patterns of phospholipid metabolism differ between Alzheimer and multi-infarct dementia (Abstract). *Neurology* 38(suppl 1):268, 1988.
- Griffith, O.H.; McMillen, D.A.; Keana, J.F.W.; and Jost, P.C. Lipid-protein interactions in cytochrome c oxidase. A comparison of covalently attached phospholipid photo-spin-label with label free to diffuse in the bilayer. *Biochemistry* 25:574–584, 1986.
- Haxby, J.V.; Grady, C.L.; Duara, R.; Schlageter, N.; Berg, C.; and Rapoport, S.I. Neocortical metabolic abnormalities precede non-memory cognitive deficits in early-type dementia. *Arch Neurol* 43:882–885, 1986.
- Hirokawa, N. Quick-freeze, deep-etch visualization of the axonal cytoskeleton. *Trends Neurosci* 9:67–71, 1986.
- Hirokawa, S. A new modification of L-glutamic acid and its crystal structure. *Acta Crystallogr* 8:637–641, 1955.
- Keyser, J.D.; Ebinger, G.; and Vauquelin, G. Dl-dopamine receptor abnormality in frontal cortex points to a functional alteration of cortical cell membranes in diseases. *Arch Neurol* 47:761–763 1990.
- Klunk, W.E.; McClure, R.J.; and Pettegrew, J.W. L-Phosphoserine, a metabolite elevated in Alzheimer's disease, interacts with specific L-glutamate receptor subtypes. *J Neurochem* 56:1997–2003, 1991.
- Knowles, P.F.; Watts, A.; and Marsh, D. Spin-label studies of lipid immobilization in dimyristoylphosphatidylcholine-substituted cytochrome oxidase. *Biochemistry* 18:4480–4487, 1979.
- Lodge, D., and Johnson, K.M. Noncompetitive excitatory amino acid receptor antagonists. *Trends Pharmacol Sci* 11:81–86, 1990.
- Maksymiw, R.; Sui, S.F.; Gaub, H.; and Sackmann, E. Electrostatic coupling of spectrin dimers to phosphatidylserine containing lipid lamellae. *Biochemistry* 26:2983–2990, 1987.
- Marsh, D.A.; Watts, A.; Pates, R.D.; Uhl, R.; Knowles, P.F.; and Esmann, M. ESR spin-label studies of lipid-protein interactions in membranes. *Biophys J* 37:265–274, 1982.
- McClure, R.J., and Pettegrew, J.W. Computer molecular modeling of L-glutamate agonists and antagonists (Abstract). *Neurology* 39(suppl 1):398, 1989.
- McIlwain, H., and Bachelard, H.S. *Biochemistry and the Central Nervous System*. New York: Churchill Livingstone, 1985. pp. 41–43.
- McKhann, G.; Drachman, D.; Folstein, M.; Katzman, R.; Price, D.; and Stadlan, E.M. Clinical diagnosis of Alzheimer's disease: Report of the NINCDS-ADRDA work group under the auspices of the Department of Health and Human Services Task Force on Alzheimer's disease. *Neurology* 34:939–944, 1984.
- Meneses, P., and Glonek, T. High resolution ^{31}P NMR of extracted phospholipids. *J Lipid Res* 29:679–689, 1988.
- Murphy, D.E.; Hutchison, A.J.; Hurt, S.D.; Williams, M.; and Sills, M.A. Characterization of the binding of [$\text{H}-3$]-CGS-19755: A novel N-methyl-D-aspartate antagonist with nanomolar affinity in rat brain. *Br J Pharmacol* 95:932–938, 1988.

Nelson, W., and Veshnock, P.J. Ankyrin binding to ($\text{Na}^{+}\text{K}^{+}$) ATPase and implications for the organization of membrane domains in polarized cells. *Nature* 328:533–536, 1987.

Nicoletti, F.; Meek, J.L.; Iadarola, M.J.; Chuang, D.M.; Roth, B.L.; and Costa, E. Coupling of inositol phospholipid metabolism with excitatory amino acid recognition sites in rat hippocampus. *J Neurochem* 46:40–46, 1986a.

Nicoletti, F.; Wroblewski, J.T.; Iadarola, M.J.; and Costa, E. Serine-O-phosphate, an endogenous metabolite, inhibits the stimulation of inositol phospholipid hydrolysis elicited by ibotenic acid in rat hippocampal slices. *Neuropharmacology* 25:335–338, 1986b.

Oppenheim, R.W. Naturally occurring cell death during neural development. *Trends Neurosci* 8:487–493, 1985.

Panchalingam, K.; Strychor, S.; Tretta, M.; and Pettegrew, J.W. In vivo ^{31}P NMR shows decreased brain ATP utilization is correlated with severity of dementia in Alzheimer's disease (Abstract). *Neurology* 41(suppl 1):269, 1991.

Pearson, R.C.A.; Esiri, M.M.; Hiorns, R.W.; Wilcock, G.K.; and Powell, T.P.S. Anatomical correlates of the distribution of the pathological changes in the neocortex in Alzheimer's disease. *Proc Natl Acad Sci USA* 82:4531–4534, 1985.

Peng, H., and Froehner, S. Association of the postsynaptic 43K protein with newly formed acetylcholine receptor clusters in cultured muscle cells. *J Cell Biol* 100:1698–1705, 1985.

Peng, H., and Poo, M. Formation and dispersal of acetylcholine receptor

clusters in muscle cells. *Trends Neurosci* 9:125–129, 1986.

Pettegrew, J.W. Molecular insights into Alzheimer's disease. In: Khachaturian, Z.; Cotman C.; and Pettegrew, J.W., eds. *Calcium, Membranes, Aging and Alzheimer's Disease*. Vol. 568. New York: New York Academy of Sciences, 1989. pp. 5–28.

Pettegrew, J.W.; Kopp, S.J.; Minshew, N.J.; Glonek, T.; Feliksik, J.M.; Tow, J.P.; and Cohen, M.M. ^{31}P NMR studies of phospholipid metabolism in developing and degenerating brain (Abstract). *Neurology* 35(Suppl 1):257, 1985.

Pettegrew, J.W.; Kopp, S.J.; Minshew, N.J.; Glonek, T.; Feliksik, J.M.; Tow, J.P.; and Cohen, M.M. ^{31}P nuclear magnetic resonance studies of phosphoglyceride metabolism in developing and degenerating brain: Preliminary observations. *J Neuropathol Exp Neurol* 46:419–430, 1987a.

Pettegrew, J.W.; McKeag, D.; and Strychor, S. "Metabolites Elevated in Brain Alter Membrane Properties." Society of Neurosciences Nineteenth Annual Meeting, Phoenix, AZ, November 2, 1989. Abstract 443.l.

Pettegrew, J.W.; Minshew, N.J.; Cohen, M.M.; Kopp, S.J.; and Glonek, T. ^{31}P NMR changes in Alzheimer's and Huntington's disease brain (Abstract). *Neurology* 34(suppl 1):281, 1984.

Pettegrew, J.W.; Moossy, J.; Withers, G.; McKeag, D.; and Panchalingam, K. ^{31}P nuclear magnetic resonance study of the brain in Alzheimer's disease. *J Neuropathol Exp Neurol* 47:235–248, 1988a.

Pettegrew, J.W., and Panchalingham, K. Solid state ^{31}P and ^{27}Al NMR studies of model membranes and mammalian

brain: Possible implications for Alzheimer's disease. In: Pettegrew, J.W., ed. *Nuclear Magnetic Resonance: The Principles and Applications of NMR Spectroscopy and Imaging to Biomedical Research*. New York: Springer-Verlag, 1989. pp. 310-354.

Pettegrew, J.W.; Panchalingam, K.; Moossy, J.; Martinez, J.; Rao, G.; and Boller, F. Correlation of phosphorus-31 magnetic resonance spectroscopy and morphologic findings in Alzheimer's disease. *Arch Neurol* 45:1093-1096, 1988b.

Pettegrew, J.W.; Panchalingam, K.; Withers, G.; McKeag, D.; and Strychor, S. Changes in brain energy and phospholipid metabolism during development and aging in the Fischer 344 rat. *J Neuropathol Exp Neurol* 49:237-249, 1990a.

Pettegrew, J.W.; Strychor, S.; Tretta, M.; and McKeag, D. Membrane molecular alterations in Alzheimer's erythrocytes *Neurology (Cleveland)* Abstract 40(suppl 1):404, 1990b.

Pettegrew, J.W.; Withers, G.; Panchalingam, K.; and Post, J.F. ³¹P nuclear magnetic resonance spectroscopy of brain in aging and Alzheimer's disease. *J Neural Transm Suppl* 24:261-268, 1987b.

Pittman, R., and Oppenheim, R.W. Cell death of motoneurons in the chick embryo spinal cord. IV. Evidence that a functional neuromuscular interaction is involved in the regulation of naturally occurring cell death and the stabilization of synapses. *J Comp Neurol* 187:425-436, 1979.

Powell, G.L.; Knowles, P.F.; and Marsh, D. Association of spin-labelled cardiolipin with dimyristoylphosphatidylcholine-substituted bovine heart cytochrome c oxidase. A generalized specificity

increase rather than highly specific binding sites. *Biochim Biophys Acta* 816:191-194, 1985.

Prives, H.; Fulton, A.; Penman, S.; Daniels, M.P.; and Christian, C.N. Interaction of the cytoskeleton framework with acetylcholine receptors on the surface of embryonic muscle cells in culture. *J Cell Biol* 92:231-236, 1982.

Reynolds, I.J., and Miller, R.J. Multiple sites for the regulation of the N-methyl-D-aspartate receptor. *Mol Pharmacol* 33:581-584, 1988.

Schoepp, D.D., and Johnson, B.G. Comparison of excitatory amino acid-stimulated phosphoinositide hydrolysis and N-[³H]-acetylaspartylglutamate binding in rat brain: Selective inhibition of phosphoinositide hydrolysis by 2-amino-3-phosphonopropionate. *J Neurochem* 53:273-278, 1989.

Seelig, A., and Seelig, J. Phospholipid composition and organization of cytochrome c oxidase preparations as determined by ³¹P-nuclear magnetic resonance. *Biochim Biophys Acta* 815:153-158, 1985.

Storch, J., and Kleinfeld, A. The lipid structure of biological membranes. *Trends Biochem Sci* 10:418-421, 1985.

Watkins, J.C.; Krosgaard-Larsen, P.; and Honore, T. Structure-activity relationships in the development of excitatory amino acid receptor agonists and competitive antagonists. *Trends Pharmacol Sci* 11:25-33, 1990.

Zubenko, G.S.; Cohen, B.M.; Reynolds, C.F.; Boller, F.; Malinakova, I.; and Keefe, M.A. Platelet membrane fluidity in Alzheimer's disease and major depression. *Am J Psychiatry* 144:860-868, 1987.

14

MOLECULAR INSIGHTS INTO SCHIZOPHRENIA

Jay W. Pettegrew, M.D., and Nancy J. Minshew, M.D.¹

INTRODUCTION

Evidence for Impaired Frontal Lobe Function in Schizophrenia

Several lines of evidence indicate impaired frontal lobe function ("hypofrontality") in some schizophrenic patients. (Buchsbaum et al. 1982; Weinberger et al. 1986). Cerebral blood flow studies using xenon-133 demonstrate a reduced ratio of frontal lobe to whole surface blood flow in schizophrenic patients under resting conditions (Ingvar and Franzen 1974) and during cortical activation with the Wisconsin Card Sort (Berman et al. 1988). Reduced frontal to occipital metabolic rate also is observed in some schizophrenics (Buchsbaum 1987). These studies suggest that further metabolic studies of the frontal lobe might enhance our understanding of the pathophysiology of schizophrenia. Since normal brain function is dependent on normal high-energy phosphate and membrane phospholipid metabolism, either or both of these aspects of

ACRONYMS

ADP	adenosine diphosphate
ATP	adenosine triphosphate
ATPase	adenosine triphosphatase
α -GP	α -glycerol phosphate
GPC	glycerol 3-phosphocholine
GPE	glycerol 3-phosphoethanolamine
Ins(1,4,5)P ₃	inositol 1,4,5-triphosphate
NAD	nicotinamide adenine dinucleotide
NMR	nuclear magnetic resonance
PC	phosphocholine
PCr	phosphocreatine
PDE	phosphodiester
PE	phosphoethanolamine
PET	positron emission tomography
P _i	inorganic orthophosphate
PME	phosphomonoester
PS	phosphoserine
PtdC	phosphatidylcholine
PtdE	phosphatidylethanolamine
PtdI	phosphatidylinositol
PtdS	phosphatidylserine
TR	time to pulse repetition

¹Department of Psychiatry, Western Psychiatric Institute and Clinic, Pittsburgh, PA 15213

brain metabolism might be altered in schizophrenia.

Evidence for Membrane Alterations in Schizophrenia

Other evidence links possible membrane-related abnormalities to the pathophysiology of major psychoses. Several studies examining erythrocyte membrane phospholipids have shown phosphatidylcholine (PtdC) to be reduced in some patients with schizophrenia (Stevens 1972; Henn 1980; Hitzemann et al. 1984). Increases in phosphatidylserine (PtdS) and smaller decreases in phosphatidylethanolamine (PtdE) also have been noted but less consistently replicated (Rotrosen and Wolkin 1987). Such abnormalities appear to be independent of previous drug treatment (Stevens 1972). Phospholipase A₂ activity, which alters phospholipid fatty acid composition through the deacylation-reacylation cycle, has been found to be increased in some schizophrenics (Gattaz 1987). In addition, Kaiya and colleagues (1985) have described abnormalities in the phosphatidylinositol (PtdI) cycle in a subgroup of schizophrenic patients. There are therefore reasons to suspect alterations in brain membrane phospholipid metabolism in some patients with schizophrenia. However, to date, these parameters have only been examined in peripheral tissues. Support for drawing analogies between peripheral blood elements and brain tissue is derived from observed membrane abnormalities in

peripheral cells in Huntington's chorea, myotonic dystrophy, affective illness, and Alzheimer's disease (Butterfield et al. 1977, 1978, 1985; Pettegrew et al. 1979a,b,c, 1981, 1982, 1983b; Butterfield and Markesberry 1980; Markesberry et al. 1980; Diamond et al. 1983; Blass et al. 1985; Sherman et al. 1986; Zubenko et al. 1987; Miller et al. 1989).

³¹P NMR ASSESSMENT OF BRAIN HIGH-ENERGY PHOSPHATE AND MEMBRANE PHOSPHOLIPID METABOLISM

Significance of In Vitro ³¹P NMR Studies

Phosphorus-31 nuclear magnetic resonance (³¹P NMR) spectroscopy has proven to be a powerful analytical method for investigating phosphorus metabolism in neural and extraneural tissues (Barany and Glonek 1984). Studies on neural tissues have utilized tissue extracts (Pettegrew et al. 1979a; Glonek et al. 1982), in vitro brain slices (Cohen et al. 1984), and in vivo studies of animals and humans (Chance et al. 1978; Ackerman et al. 1980; Cady et al. 1983; Petroff et al. 1985; Maris et al. 1985).

The in vitro analytical studies provide chemical conditions that are more favorable for ³¹P NMR analysis than those occurring in the living brain and therefore achieve greater sensitivity and resolution than in vivo studies. The enhanced sensitivity and resolution of in vitro extract studies allow the characterization and quantitation of many different phosphorus-containing

compounds. Results from the *in vitro* studies are very important to properly interpret *in vivo* findings in which the resolution and peak dispersion are reduced. Data from previous *in vitro* ^{31}P NMR studies demonstrated a remarkable correlation with those obtained from more classical assay procedures. In addition, these data revealed previously uncharacterized metabolites and unrecognized metabolic relationships (Glonek et al. 1982; Cohen et al. 1984). The details of brain tissue, harvesting, perchloric acid extraction, and ^{31}P NMR analyses have been previously published (Pettegrew et al. 1987*a*, 1988*c*, 1990*b*).

To interpret ^{31}P NMR spectra correctly, the identities of the individual resonance signals must be carefully verified through the use of appropriate biochemical and spectroscopic procedures. The importance of this verification was recently demonstrated for a prominent ^{31}P NMR resonance at 3.84 ppm (3.84 δ) in mammalian brain, which was identified as phosphoethanolamine (PE) (Pettegrew et al. 1986). The identification was based on ^1H and ^{31}P NMR findings (including pH titrations) at 4.7 and 14.1 T, as well as thin-layer chromatographic analysis. In addition, L-phosphoserine is a significant contributor to the phosphomonoester resonance region in mammalian brain, including that of humans (Pettegrew et al. 1990*b*).

In a representative high-resolution ^{31}P NMR spectrum of a brain perchloric acid extract, the easily identifiable resonances and their

chemical shifts (δ) include the phosphomonoesters (PMEs): α -glycerol phosphate (α -GP, 4.29 δ), PE (3.84 δ), phosphoserine (PS, 3.89 δ), and phosphocholine (PC, 3.33 δ); inorganic orthophosphate (P_i , 2.63 δ); the phosphodiesters (PDEs): glycerol 3-phosphoethanolamine (GPE, 0.81 δ) and glycerol 3-phosphocholine (GPC, -0.13 δ); phosphocreatine (PCr, -3.12 δ); the nucleotide triphosphates, especially adenosine triphosphate (ATP, γ -5.80 δ , α -10.92 δ , β -21.48); the nucleotide diphosphates, especially adenosine diphosphate (ADP, β -6.11 δ , α -10.61 δ); dinucleotides such as nicotinamide adenine dinucleotide (NAD, -11.37 δ); and a complex resonance band centered around -12.89 δ which is composed of nucleoside diphospho- derivatives (e.g., uridine diphosphosugars) and cytidine diphospho- derivatives (e.g., cytidine diphosphocholine and cytidine diphosphoethanolamine).

The PMEs PC, PE, and L-PS are normally found in abundance in mammalian brain, including human, and are important constituents in the metabolism of their respective phospholipids. The brain concentrations (mM) are PE=1.5, PC=0.5, and L-PS=0.3. The levels of the PMEs are increased approximately 3-fold in the developing brain during nutritive proliferation (Pettegrew et al. 1990*b*). Similar high levels of PMEs have been found in newborn human brain by ^{31}P NMR (Cady et al. 1983). In addition, inositol 1,4,5-triphosphate [$\text{Ins}(1,4,5)\text{P}_3$] is a PME and an important second messenger involved in the regulation of in-

extracellular calcium levels (Berridge and Irvine 1984). Ins(1,4,5)P₃ is derived from PtdI(4,5)P₂, which comprises approximately 1–10 percent of the total PtdI (Majerus et al. 1986). Since the PtdI concentration in mammalian brain is approximately 1.9 mM (McIlwain and Bachelard 1985), the normal concentration of PtdI(4,5)P₂ is approximately 0.01–0.1 mM. Therefore, the levels of Ins(1,4,5)P₃, normally found in brain tissue would be below the limits of detection by *in vivo* ³¹P NMR. The PMEs are produced by (1) phosphorylation of their respective bases by kinases, (2) phospholipase C cleavage of their respective phospholipids, or (3) phosphodiesterase cleavage of their respective PDEs such as GPC and GPE. The PMEs are broken down by phospholipase D to release P_i and the constituent base.

The PDEs GPC and GPE also are in high abundance in human brain. These PDEs are products of phospholipase A₁+A₂ activity and are converted to their respective PMEs by PDE phosphodiesterase activity. Despite their high abundance in the brain, the physiological function of the PDEs remains unknown.

Periods of Brain Development

Brain maturation and development can be arbitrarily divided into four periods (McIlwain and Bachelard 1985). Period I is the stage of cellular division, extending up to birth in the rat. The rat brain at birth has approximately 15 percent of its

adult weight and no recordable electrical activity. Period II in the rat extends from birth to 10 days of age. In Period II, there is growth in the size of individual cells, rapid outgrowth of axons, and rapid development of dendritic connections. During this period there is also a rapid increase in brain lipid content, which peaks at approximately 10 days. During Period III (10–20 days of age in the rat), synaptic densities and the number of nerve terminals rapidly increase and electroencephalographic activity develops. During this period there are increases in cell volume and the associated K⁺ space, with decreases in the extracellular Na⁺ and Cl⁻ spaces. The rates of glucose uptake, glycolysis, and oxidative phosphorylation all steadily increase from birth and reach their adult levels during Period III. Naturally occurring cell death has been demonstrated during the period of synaptogenesis, which would correspond to Periods II and III in the rat (Pittman and Oppenheim 1979; Cowan et al. 1984; Oppenheim 1985; Clarke 1985). Adenosine triphosphatase (ATPase) activity, including activity requiring added Na⁺ and K⁺, increases during Periods II and III. Period IV in the rat extends from 20 days and is associated with active myelination but little further brain growth. During this period creatine phosphokinase activity reaches maximal levels. Senescence in rats is thought to develop after 12 months of age and certainly by 24 months of age.

Animal Studies of Brain Development and Aging

There are striking effects of animal development and aging on the brain levels of α -GP, PE, PC, GPE, GPC, PCr, and Pi (Pettegrew et al. 1990b). The PMEs (α -GP, PE, and PC) are high in the immature brain and rapidly decrease from the newborn period to 3 months of age ($p=0.0001$). The levels of α -GP and PC then remain relatively constant until 12 months of age, but the levels of PE increase slightly ($0.01 < p < 0.05$). From 12 to 24 months, the levels of PC decrease ($0.0001 < p < 0.001$). In contrast, the PDEs (GPE and GPC) are very low or undetectable in the newborn period and then rise rapidly up to 3 months of age ($p=0.0001$) after which the levels rise at a slower rate up to 24 months of age. The PME/PDE ratio, which is an estimate of membrane phospholipid anabolic/catabolic activity (Pettegrew et al. 1987a), is high in the newborn period, rapidly decreases up to 3 months of age ($p=0.0001$), and then remains relatively constant up to 12 months of age. After 12 months of age the PME/PDE ratio decreases slightly ($0.01 < p < 0.05$), suggesting that membrane phospholipid breakdown is proceeding slightly faster than membrane phospholipid synthesis.

Possible enzymatic causes for the high PME levels during brain development are (1) increased choline, ethanolamine, or serine kinase activity; (2) increased phospholipase C activity; (3) increased glycerophosphodiesterase activity; (4) decreased cytidine diphosphate-choline phosphotransferase activity;

(5) decreased PME phosphatase activity; or (6) decreased phospholipase D activity. Possible enzymatic causes for the low PDE levels during brain development are decreased phospholipase A₁ and A₂ activity or decreased glycerophosphodiesterase activity.

These ³¹P NMR results tentatively suggest very high phospholipid anabolic activity without appreciable catabolic activity from 12 hours to 10 days of age. This would coincide with an increase in the size of neuronal cells, the rapid outgrowth of axons, and the rapid development of dendritic connections reported to occur in Period II. After 10 days of age, there is a rather rapid increase in PDEs which are catabolic breakdown products of membrane phospholipids. The PME levels start to decrease at 10 days of age, but the PME/PDE ratio remains high (>10). The increasing PDEs observed from 10 to 30 days of age could represent the metabolic correlates of naturally occurring cell death and the remodeling of neuritic connections. Cell death has been demonstrated to occur naturally during neural development and, in particular, occurs at about the time of rapid synaptogenesis, which is from birth to 20 days of age in the rat (Pittman and Oppenheim 1979; Cowan et al. 1984; Oppenheim 1985; Clarke 1985). From 1 to 3 months of age the PMEs continue to decrease and the PDEs continue to increase, although not as rapidly as before. The PME/PDE ratio falls from 10 to 2, indicating that the rate of phospholipid synthesis is decreasing.

The changes in PMEs and PDEs occurring from 1 to 3 months of age could reflect active myelination, which is known to occur during this time in the rat. After 3 months of age, the turnover rate for phospholipids (PME/PDE) remains relatively constant until 12 months of age. From 12 to 24 months of age, the PME/PDE ratio decreases further ($0.01 < p < 0.05$), suggesting that membrane catabolism is proceeding slightly faster than anabolism.

PCr is the most metabolically labile of the brain high-energy phosphates. Levels of PCr are quite low in the newborn period and appear to decrease even further up to 5 days of age. After 5 days of age, the PCr levels rapidly increase up to 1 month of age, with less rapid increases between 1 and 3 months of age (12 hours versus 3 months, $p=0.0001$). After 3 months of age, the PCr levels undergo less dramatic but steady increases up to 24 months of age. In contrast, the levels of P_i are relatively high in the newborn, decrease up to 5 days of age, followed by increases up to 10 days of age. After 10 days of age, the P_i levels drop rapidly until 3 months of age ($0.01 < p < 0.05$). From 3 months of age until 12 months of age, the P_i levels appear to increase slightly, with more rapid increases from 12 to 24 months of age.

The PCr/ P_i ratio is the ratio of the most labile form of high-energy phosphate (PCr) to the ultimate breakdown product of all high-energy phosphates (P_i) and thus provides a convenient measure of the energy status of the brain. The

PCr/ P_i ratio is quite low in the newborn period until 5 days of age, after which time the PCr/ P_i ratio rapidly increases up to 3 months of age ($p=0.0001$). After 3 months of age, the PCr/ P_i ratio remains relatively constant up to 24 months of age. The rapid increase in the PCr/ P_i ratio up to 1 month of age correlates with the development of the glycolytic and oxidative pathways, the increase in Na^+-K^+ ATPase activity, and the onset of electroencephalographic activity. The PCr/ P_i ratio appears to increase slightly after 12 months of age, suggesting decreased utilization of PCr. The brain levels of ATP do not undergo similar changes; there are no significant differences in brain ATP content comparing animals of 12 hours versus 3 months, 3 months versus 12 months, or 12 months versus 24 months of age.

In Vivo ^{31}P NMR Studies

Brain chemistry also can be assessed in vivo using ^{31}P NMR spectroscopy. ^{31}P has a nuclear magnetic moment and is present in 100 percent natural abundance, thus no isotope has to be given to the subject. ^{31}P NMR spectroscopy provides a direct in vivo assessment of the brain membrane phospholipid and high-energy phosphate metabolism. The PME and PDE resonances in mammalian brain originate predominantly from the precursors and breakdown products, respectively, of membrane phospholipids (Pettegrew et al. 1986, 1987b). The PCr, ATP, ADP, and P_i

levels reflect the state of energy metabolism (Pettegrew et al. 1987b). In addition, the intracellular pH can be directly assessed (Petroff et al. 1985; Pettegrew et al. 1988c). Because NMR spectroscopy is safe and noninvasive, repeated measurements can be carried out in the same individual over a period of time, enabling longitudinal studies.

In vivo ^{31}P NMR spectra on human subjects have been obtained using a General Electric Signa System with the spectroscopy research accessory. The field strength is 1.5 T, yielding a proton frequency of 63.970 MHz and a phosphorus frequency of 25.895 MHz. The subject is placed supine on the NMR magnet transport table, and the head is positioned inside a plexiglass head holder containing a support bracket for securing a surface coil. The surface coil is positioned over the head to sample signals from the dorsal prefrontal cortex.

All subjects have routine T1 weighted ^1H magnetic resonance imaging (MRI) scans in the sagittal, coronal, and axial planes immediately preceding or following the ^{31}P NMR spectroscopy studies. ^1H images, which are used to identify the location and volume of brain sampled by spectroscopy as well as the ^{31}P NMR spectra, are acquired with the same probe containing an 8-in ^{31}P surface coil and a 3-in surface coil dual tuned at both the ^{31}P and ^1H frequencies. ^1H images for spectral localization are obtained by transmitting with a Helmholtz body coil and receiving with the

3-in surface coil. The localized ^1H images and the ^{31}P NMR spectra are from approximately 15–20 cm³ of the dorsal prefrontal cortex. The B_0 field is then shimmed on the $\text{H}_2\text{O}/^1\text{H}$ signal to a line width of approximately 0.1 ppm.

^{31}P NMR spectra are obtained using a B_1 field gradient and a pulse-acquire sequence. A pulse width of 800 microseconds produces a spectrum with PCr/P_i and PME/PDE ratios typical of mammalian brain. The importance of these considerations has previously been pointed out (Pettegrew et al. 1983a). Other acquisition parameters are as follows: time to pulse repetition (TR), 2 seconds; sweep width, 2 kHz; receiver filter, 1 kHz; and number of complex data points, 2,048. The integrated spectral areas are the same for TR values of 2, 4, and 6 seconds. Therefore, a TR of 2 seconds is used to allow a greater signal-to-noise ratio to be obtained for a fixed total acquisition time without signal saturation.

All spectra are processed on a Nicolet data station with 5 Hz exponential multiplication, first and second order phase correction to bring all peaks into absorption mode, and baseline correction by means of a series of linear tilts between known baseline points. Integrated areas are then calculated using the GENCAP program which fits the spectrum with a series of Lorentzian lines. Known doublets, such as the ionized ends region, are fitted with two Lorentzians, and known triplets, such as the middle region, are fitted with three

Lorentzians. The PME and PDE peaks are fitted with one, two, or three Lorentzian lines to obtain the most accurate fit. For each spectrum, the integrated areas of the PME, P_i , PDE, PCr, ionized ends (γ -ATP and β -ADP), esterified ends (α -ATP and α -ADP), and middle (β -ATP) regions are determined. From these integrated areas, the mole percentage of PME, P_i , PDE, PCr, ATP, and ADP are calculated as the integrated area under the resonance peak divided by the total spectral integrated area. The intracellular pH is determined by the chemical shift difference between the PCr and P_i peaks (Petroff et al. 1985) or between the γ and α peaks of ATP (Pettegrew et al. 1988c). Our in vivo results compare quite favorably with previously published in vitro results (Glonek et al. 1982; Cohen et al. 1984; Pettegrew et al. 1987b, 1990b), verifying the validity of the in vivo method used in the present study. Test-retest and inter-rater reliability results give standard deviations of <5 percent of the mean for each parameter ($n=10$).

Comparison of In Vitro and In Vivo ^{31}P NMR Findings

The PME, P_i , PDE, and PCr resonances of brain are not completely resolved in the unprocessed in vivo ^{31}P NMR spectrum obtained at 1.5 T. This is probably due to a combination of at least four factors: (1) The NMR natural line widths for these in vivo brain chemical species are probably broader than for the same chemical species in solution,

indicating longer correlation times (τ_c) for the species in vivo. (2) Some of these chemical species could be in chemical exchange with divalent cations such as Ca^{2+} and Mg^{2+} . If the chemical exchange rate is intermediate with respect to the observed frequency (ω_0), this could lead to line broadening (Pettegrew et al. 1988c). The PME, PDE, and P_i have been shown to chelate divalent and trivalent cations in solution (Panchalingam et al. 1987) so this possibility also could exist in vivo. (3) There is decreased chemical shift dispersion at 1.5 T compared to B_0 fields of 4.7 T or higher. (4) The B_0 field homogeneity across the human head is not as good as that attainable across smaller samples (5–20 mm diameters) with better dielectric homogeneity.

Normal Brain Development and Aging

To properly interpret the findings in the schizophrenics, it is important to know how high-energy phosphate and membrane phospholipid metabolism change in normal human brain development and aging. In vivo ^{31}P NMR of the dorsal prefrontal cortex was performed on 29 normal volunteers ages 12–81 years. All subjects had normal medical and neurological examinations, no subjects met *Diagnostic and Statistical Manual of Mental Disorders, Third Edition, Revised* (DSM-III-R; APA 1987) criteria for any psychiatric disorder, and no subjects had a positive family history for neuropsychiatric disorders. There was a significant decrease in the levels of PME with

age ($p=0.01$; $r=0.52$) and a significant increase in the levels of PDE ($p=0.01$; $r=0.52$). There were no age-related changes in the levels of PCr, P_i or ATP.

The studies in normal human volunteers show effects of brain development and aging similar to those demonstrated in the Fischer 344 rat. The PMEs increase between the ages of 10 and 20 years, remain relatively stable up to 40–50 years, and then slowly decline after 50 years of age. The PDEs decrease between the ages of 10 and 20 years, remain relatively stable up to 40–50 years, and then slowly increase over the age of 50 years. The changes in brain levels of PME and PDE in individuals between 10 and 20 years of age probably reflect increasing membrane anabolic activity and decreasing membrane catabolic activity between these ages. The decreasing PMEs and increasing PDEs that occur over the age of 50 years presumably reflect the loss of dendritic spines and the processes that occur with aging.

Schizophrenics and Controls

Brain high-energy phosphate and membrane phospholipid metabolism were investigated under resting conditions in the dorsal prefrontal cortex of neuroleptic naive, first episode schizophrenic patients and healthy controls matched for age, sex, race, education, and parental education. Neuroleptic naive patients were chosen because of the known lasting effects of neuroleptics on membrane phospholipids (Essali et al. 1989). Patients at an early stage of the illness were cho-

sen to exclude the possible effects of length of illness and hospitalization. Eleven schizophrenic patients (7 males, 4 females; 24.4 ± 1.4 years; mean \pm standard error of the mean; 7 white, 4 black; 11.7 ± 0.8 years education) and 10 matched healthy controls (6 males, 4 females; 24.1 ± 1.8 years; 7 white, 2 black, 1 oriental; 12.7 ± 0.3 years education) were studied. Patients were assessed by the Schedule for Affective Disorders and Schizophrenia (SADS) (Endicott and Spitzer 1978) and met both DSM-III-R (APA 1987) and Research Diagnostic Criteria (RDC) for schizophrenia (Spitzer et al. 1990). The DSM-III-R subclassification for the patients was six undifferentiated and five paranoid. None was previously treated with neuroleptics as reported by the patients' families or the referring physicians. The mean illness duration was 19.1 ± 5.9 months. None had a history of or met DSM-III-R criteria for persistent substance abuse. Physical examination did not reveal abnormalities in any patient. The patients also were assessed using the Brief Psychiatric Rating Scale (BPRS) (Overall and Gorham 1962). All the patients were followed for at least 6 months after entry into the study to ensure diagnostic stability. The control subjects were selected from among students and hospital staff. Psychiatric, medical, and family history information were obtained using a structured form. All patients and controls signed an informed consent. There are no significant group differences between the patients and controls for age, sex,

race, education, or parental education. MRI results are normal in the schizophrenics and controls as reported by experienced neuroradiologists. The following metabolic alterations were observed in the dorsal prefrontal cortex of the schizophrenic patients: (1) decreased levels of PMEs (schizophrenics, 15.5 ± 0.9 ; controls, 20.3 ± 0.9 ; $p=0.002$); (2) increased levels of PDEs (schizophrenics, 36.4 ± 1.5 ; controls, 32.2 ± 0.6 ; $p=0.02$); (3) increased levels of ATP (schizophrenics, 9.6 ± 0.5 ; controls, 7.4 ± 0.4 ; $p=0.02$); and (4) decreased levels of P_i (schizophrenics, 7.9 ± 0.5 ; controls, 9.9 ± 0.5 ; $p=0.01$). There were no group differences in the levels of PCr, ADP, or intracellular pH.

Possible causes for decreased observable levels of PME in schizophrenic brain are (1) decreased kinase activity; (2) decreased phospholipase C activity; (3) decreased PDE phosphodiesterase activity; (4) increased phospholipase D activity; (5) increased chemical exchange with divalent cations leading to decreased NMR observability; or (6) increased τ_c with resulting decreased NMR observability.

Possible causes for increased PDEs in schizophrenic brain include decreased PDE phosphodiesterase activity and increased phospholipase A_1+A_2 activity. Gattaz (1987) has reported increased activity of phospholipase A_2 in schizophrenia. Other possible causes of the increased observable PDEs are decreased τ_c with increased NMR observability or decreased chemical exchange with divalent cations re-

sulting in increased NMR observability. Decreased PDE phosphodiesterase activity could account for both the decreased PME and increased PDE levels observed in the schizophrenic patients studied.

The present findings of decreased PME and increased PDE levels also could suggest decreased synthesis and increased breakdown of membrane phospholipids in schizophrenia. Similar results are observed in normal aging in animals by in vitro ^{31}P NMR (Cady et al. 1983) and humans by in vivo ^{31}P NMR spectroscopy (Pettegrew et al. 1990a). Demisch and coworkers (1987) have reported a significantly decreased incorporation of ^{14}C -labeled arachidonic acid in PtdC, PtdE, and PtdI in patients with schizoaffective and schizophrenia-form disorders, which could suggest decreased membrane phospholipid synthesis. As previously mentioned, decreased levels of membrane PtdC have been observed in erythrocytes in some schizophrenics (Stevens 1972; Henn 1980; Hitzemann et al. 1984). All the schizophrenic patients in the present study had normal MRI findings (as reported by neuroradiologists) at the time of their ^{31}P NMR studies. It is possible, therefore, that the PME and PDE alterations could represent metabolic alterations which antedate the onset of anatomical changes.

The increased ATP and decreased P_i observed in the present study suggest decreased ATP utilization with decreased production of P_i . These findings are consistent

with hypoactivity of the dorsal prefrontal cortex as suggested by decreased cerebral blood flow and decreased uptake of 2-deoxyglucose (Ingvar and Franzen 1974; Buchsbaum et al. 1982; Weinberger et al. 1986). Both cerebral blood flow and 2-deoxyglucose uptake are indirect measures of cerebral energy metabolism. The uptake of glucose and presumably 2-deoxyglucose is dependent upon normal membrane properties (Carruthers et al. 1989), and the decreased uptake of 2-deoxyglucose observed in some schizophrenics also could reflect altered membrane phospholipids.

Schizophrenics and Autistics

Normal intelligence quotient (IQ), adult autistic patients, who are similar in age to the schizophrenic patients and share some of the negative symptoms, were studied by *in vivo* ^{31}P NMR spectroscopy using the identical protocol used for the schizophrenic patients. Adult autistic patients, who are similar in age to the schizophrenic patients in this study and share the negative symptoms of schizophrenia, do not have altered levels of brain PME or PDE by *in vivo* ^{31}P NMR (Pettegrew et al. 1989; Minshew et al. 1990, 1991). However, the autistic patients have decreased levels of ATP, the opposite of that observed in the schizophrenic patients. The decreased levels of ATP suggest increased ATP utilization in the autistics. This is consistent with a positron emission tomography (PET) study of 12 young adult autism-

tic men, in which an increase was reported in metabolic rate for glucose in frontal, parietal, temporal, and occipital cortex; hippocampus; thalamus; and basal ganglia (Rumsey et al. 1985).

Schizophrenia, Normal Aging, and Alzheimer's Disease

It is of interest that the changes in PMEs and PDEs observed in schizophrenics are distinct and in opposition of those observed with Alzheimer's disease, which is associated with increases in brain PMEs early in the course of the disease. Elevated brain levels of PDEs occur later in the course of Alzheimer's disease and probably reflect the onset of membrane degenerative changes (Pettegrew et al. 1984, 1987b, 1988a,b, 1990b; Brown et al. 1989). As previously mentioned, the changes observed in schizophrenia are quite similar to those observed in normal aging in which the brain levels of PMEs are decreased and the PDEs are increased (Pettegrew 1987b). From this perspective, schizophrenia could be considered a form of premature brain aging, perhaps involving only certain neural systems. This formulation would be consistent with the concept of dementia praecox expounded many years ago (Morel 1860; Kraepelin 1971). All the schizophrenic patients in the present study had normal MRI findings, as reported by neuroradiologists, at the time of their ^{31}P NMR studies. It is possible, therefore, that the PME and PDE alterations could represent metabolic alter-

ations which antedate the onset of anatomical changes. This could provide a possible metabolic explanation for the development of cerebral atrophy observed in some schizophrenics (Andreasen et al. 1986; Andreasen 1988), including the affected twin of monozygotic twins discordant for schizophrenia (Suddath et al. 1990).

Schizophrenia and Programmed Synaptic Pruning

The findings of decreased PMEs and increased PDEs in first-episode, drug-naïve schizophrenic patients also could be due to abnormal brain development (Feinberg 1982; Weinberger 1987). There is now substantial evidence for programmed neuronal cell loss, callosal axon loss, and synaptic elimination in normal animal and human brain development (Huttenlocher 1979; Purves and Lichtman 1980; Huttenlocher et al. 1982; Rakic and Riley 1983; Cowan et al. 1984). The present *in vivo* ^{31}P NMR findings indicate that the cell bodies, processes, and terminals in the sampled area of the dorsal prefrontal cortex of the schizophrenic patients contain depressed levels of PMEs and elevated levels of PDEs compared with the control subjects. *In vivo* ^{31}P NMR studies of normal volunteers between the ages of 12 and 85 years also reveal a transient decrease in the levels of PMEs and an increase in the levels of PDE during adolescence (10–20 years) (Panchalingam et al. 1990). However, the decreased PMEs and increased PDEs observed in the schizophrenic

patients appear to be more pronounced than in the normal volunteers of comparable age. This suggests decreased synthesis and enhanced breakdown of membranes occurring in the schizophrenic patients. This could be due to altered timing or abnormal enhancement of normal programmed synaptic pruning during adolescence, as initially suggested by Feinberg (1982), which occurs in the prefrontal cortex of humans during adolescence as demonstrated by Huttenlocher (1979). An exaggeration of these regressive synaptic events involving apical and basal dendrites could produce brain structural changes similar to those observed in schizophrenia in which the predominant reduction is in gray but not white matter. An exaggeration of normal neuronal cell death should produce decreased numbers of neurons and their projection axons and, therefore, reduce the volume of both gray and white matter.

Schizophrenia and Prefrontal Glutamatergic Pathways

The descending prefrontal glutamatergic pathway is a major input to both the striatum and the limbic cortex. Exaggerated synaptic pruning of prefrontal-limbic glutamatergic axonal terminals could produce a reduced neurophil volume, resulting in what might appear as an enhanced clustering of cells as observed for pre- α -cells in the parahippocampal gyrus (Falkai et al. 1988). Excessive pruning of prefrontal-striatal glutamatergic axonal

terminals ending on striatal dopaminergic terminals could decrease the tonic release of dopamine from the dopaminergic terminals, resulting in secondary upregulation of the postsynaptic dopaminergic receptors. A number of postmortem studies have demonstrated increased numbers of D₂ receptors in the caudate and putamen of patients with schizophrenia (Seeman et al. 1984; Jaskiw and Kleinman 1988), but a recent study suggests this is secondary to neuroleptic treatment within 3 months of death (Kornhuber et al. 1989). Two *in vivo* PET studies of brain D₂ receptors in schizophrenic patients have appeared. One study reported increased numbers of D₂ receptors in the striatum of drug-naïve schizophrenic patients (Wong et al. 1986), but the other study could not replicate this finding (Farde et al. 1987). The phasic release of dopamine is thought to be responsive to stress. With upregulation of postsynaptic dopaminergic receptors, stress could result in exaggerated mesolimbic activity, producing positive symptoms. Neuroleptics which block postsynaptic D₂ receptors could modulate the mesolimbic activity back to normal. This formulation has been suggested recently by Grace (1991).

Potential Therapeutic Effect of Neurotrophic Agents

As discussed above, the PME and PDE findings observed in schizophrenia are consistent with two separate hypotheses. First, it is possible that premature aging of the

prefrontal cortex occurs in schizophrenia since the ³¹P NMR findings in this disorder resemble the changes observed in normal aging in humans (Pettegrew et al. 1987a, 1990a) and animals (Pettegrew et al. 1990b). Second, there may be an exaggeration or altered timing of the normal programmed synaptic pruning during adolescence as suggested by Feinberg (1982) and as demonstrated to occur in the prefrontal cortex of humans during this age period (Huttenlocher 1979). Should decreased brain PMEs and increased PDEs be found in a much larger sample of schizophrenic patients, then consideration should be given to the possible use of brain trophic factors early in the course of schizophrenia. The goal would be to identify by ³¹P NMR those individuals who demonstrate the PME and PDE changes early in the course of the illness, or even better, prior to the onset of symptoms. These individuals would then be candidates for neurotrophic therapy to slow, stop, or ideally, reverse the membrane alterations. This is obviously highly speculative, and even if this approach should prove beneficial, it is still far into the future. However, by starting to plan for the future now, perhaps we can make the future less far off.

The ability of ³¹P NMR to monitor high-energy phosphates as well as membrane phospholipid metabolites could provide new insights not previously available with other techniques. ³¹P NMR spectroscopy also appears to be a practicable procedure for longitudinal studies

which may provide new information on the possible evolution of regional biochemical changes in schizophrenia.

REFERENCES

- Ackerman, J.H.; Grove, T.H.; Wong, G.G.; Gadian, D.G.; and Radda, G.K. Mapping of metabolites in whole animals by ^{31}P NMR using surface coils. *Nature* 283:167-170, 1980.
- American Psychiatric Association (APA). Workgroup to revise DSM-III. *Diagnostic and Statistical Manual of Mental Disorders* (DSM-III-R). 3rd ed., revised. Washington, DC: APA, 1987.
- Andreasen, N.; Nasrallah, H.A.; Dunn, V.; Olson, S.C.; Grove, W.M.; Ehrhardt, J.C.; Coffman, J.A.; and Crossett, J.H.W. Structural abnormalities in the frontal system in schizophrenia. *Arch Gen Psychiatry* 43:136-144 1986.
- Andreasen, N.C. Brain imaging: Applications in psychiatry. *Science* 239:1381-1388, 1988.
- Barany, M., and Glonek, T. Identification of diseased states by phosphorus-31 NMR. In: Gorenstein, D.G., ed. *Phosphorus-31 NMR, Principles and Applications*. New York: Academic Press, 1984. pp. 511-515.
- Berman, K.F.; Illowsky, B.P.; and Weinberger, D.R. Physiological dysfunction of dorsolateral prefrontal cortex in schizophrenia. *Arch Gen Psychiatry* 45:616-622, 1988.
- Berridge, M.J., and Irvine, R.F. Inositol triphosphate, a novel second messenger in cellular signal transduction. *Nature* 312:315-321, 1984.
- Blass, J.P.; Hanin, I.; Barclay, L.; Kopp, U.; and Reding, M.J. Red blood cell abnormalities in Alzheimer's disease. *J Am Geriatr Soc* 33:401-405, 1985.
- Brown, G.G.; Levine, S.R.; Gorell, J.M.; Pettegrew, J.W.; Gdowski, J.W.; Bueri, J.A.; Helpern, J.A.; and Welch, K.M.A. In vivo ^{31}P NMR profiles of Alzheimer's disease and multiple subcortical infarct dementia. *Neurology* 39:1423-1427, 1989.
- Buchsbaum, M.S. Positron emission tomography in schizophrenia. In: Meltzer, H.Y., ed. *Psychopharmacology: The Third Generation of Progress*. New York: Raven Press, 1987. pp. 783-792.
- Buchsbaum, M.S.; Ingvar, D.H.; Kessler, R.; Waters, R.N.; Cappelette, J.; van Kammen, D.P.; King, C.; Johnson, J.L.; Manning, R.B.; Flynn, R.W.; Mann, L.S.; Bunney, W.E.; and Sokoloff, L. Cerebral glucography with positron tomography. *Arch Gen Psychiatry* 39:251-259, 1982.
- Butterfield, D.A., and Markesberry, W.R. Specificity of biophysical and biochemical alterations in erythrocyte membranes with neurological disorders. *J Neurol Sci* 97:261-271, 1980.
- Butterfield, D.A.; Nicholas, M.M.; and Markesberry, W.R. Evidence for an increased rate of choline efflux across erythrocyte membranes in Alzheimer's disease. *Neurochem Res* 10:909-918, 1985.
- Butterfield, D.A.; Oeswein, J.W.; and Markesberry, W.R. Electron spin resonance study of membrane protein alterations in erythrocytes in Huntington's disease (Letter). *Nature* 267:453-455, 1977.
- Butterfield, D.A.; Oeswein, J.W.; Prunty, M.E.; Hisle, K.C.; and Markesberry, W.R. Increased sodium plus potassium

- adenosine triphosphatase activity in erythrocyte membranes in Huntington's disease. *Ann Neurol* 4:60–62, 1978.
- Cady, E.B.; Dawson, M.J.; Hope, P.L.; Tofts, P.S.; Costello, A.M.; Delpy, D.T.; Reynolds, E.O.R.; and Wilkes, D.R. Non-invasive investigations of cerebral metabolism in newborn infants by phosphorus nuclear magnetic resonance spectroscopy. *Lancet* i:1059–1062, 1983.
- Carruthers, A.; Helgerson, A.L.; Herbert, D.N.; Tefft Jr., R.E.; Naderi, S.; and Melchior, D.L. Effects of calcium ATP and lipids on human erythrocyte sugar transport. *Ann NY Acad Sci* 568:52–67, 1989.
- Chance, B.; Nakase Y.; Bond, M.; Leigh Jr., J.S.; and McDonald, G. Detection of ^{31}P nuclear magnetic resonance signals in brain by in vivo and freeze trapped assays. *Proc Natl Acad Sci USA* 75:4925–4929, 1978.
- Clarke, P.G. Neuronal death in the development of the vertebrate nervous system. *Trends Neurosci* 8:345–349, 1985.
- Cohen, M.M.; Pettegrew, J.W.; Kopp, S.J.; Minshew, N.; and Glonek, T. P-31 nuclear magnetic resonance analysis of brain: Normoxic and anoxic brain slices. *Neurochem Res* 9(6):785–801, 1984.
- Cowan, W.M.; Fawcett, J.W.; O'Leary, D.D.; and Stanfield, B.B. Regressive events in neurogenesis. *Science* 225:1258–1265, 1984.
- Demisch, L.; Gerbaldo, H.; Heinz, K.; and Kirsten, R. Transmembranal signalling in schizophrenic and affective disorders: Studies on arachidonic acid and phospholipids. *Schizophr Res* 22:275–282, 1987.
- Diamond, J.M.; Matsuyama, S.S.; Meier, K.; and Jarvik, L.F. Elevation of erythrocyte countertransport rates in Alzheimer's dementia (Letter). *N Engl J Med* 309:1061–1062, 1983.
- Endicott, J., and Spitzer, R.L. A diagnostic interview: The schedule for affective disorders and schizophrenia. *Arch Gen Psychiatry* 35:837, 1978.
- Essali, M.A.; Das, I.; deBelleroche, J.; and Hirsch, S.R. The platelets polyphosphoinositide system in schizophrenia: Pathological and pharmacological implications. *Schizophr Res* 2:148, 1989.
- Falkai, P.; Bogerts, B.; and Rozumek, M. Cell loss and volume reduction in the entorhinal cortex of schizophrenics. *Eur Arch Psychiatry Neurol Sci* 24:515–521, 1988.
- Farde, L.; Wiesel, F.A.; Hall, H.; Halldin, C.; Stone-Elander, S.; and Sedvall, G. No D2 receptor increase in PET study of schizophrenia (Letter). *Arch Gen Psychiatry* 44:671–672, 1987.
- Feinberg, I. Schizophrenia: Caused by a fault in programmed synaptic elimination during adolescence? *J Psychiatr Res* 17: 319–334, 1982.
- Gattaz, W. Increased plasma phospholipase A2 activity in schizophrenic patients: Reduction after neuroleptic therapy. *Biol Psychiatry* 22:421, 1987.
- Glonek, T.; Kopp, S.J.; Kot, E.; Pettegrew, J.W.; Harrison, W.H.; and Cohen, M.M. P-31 nuclear magnetic resonance analysis of brain. The perchloric acid extract spectrum. *J Neurochem* 39:1210–1219, 1982.
- Grace, A.A. Phasic versus tonic dopamine release and the modulation of dopamine system responsibility: A

- hypothesis for the etiology of schizophrenia. *Neuroscience* 1991, in press.
- Henn, F. Biological concepts of schizophrenia. In: Baxter, C., and Melnechuk, T., eds. *Perspectives in Schizophrenia Research*. New York: Raven Press, 1980. pp. 209-225.
- Hitzemann, R.; Hirschowitz, D.; and Garver, D. Membrane abnormalities in the psychoses and affective disorders. *J Psychiatr Res* 18:319, 1984.
- Huttenlocher, P.R. Synaptic density in human frontal cortex. Developmental changes and effects of aging. *Brain Res* 163:195-205, 1979.
- Huttenlocher, P.R.; deCourten, C.; Garey, L.J.; and Van Der Loos, H. Synaptogenesis in human visual cortex--evidence for synapse elimination during normal development. *Neurosci Lett* 33:247-252, 1982.
- Ingvar, D.H., and Franzen, G. Abnormalities of cerebral blood flow distribution in patients with chronic schizophrenia. *Acta Psychiatr Scand* 50:425-462, 1974.
- Jaskiw, G., and Kleinman, J. Postmortem neurochemistry studies in schizophrenia. In: Schulz, S.C., and Tamminga, C.A., eds. *Schizophrenia: A Scientific Focus*. New York: Oxford University Press, 1988.
- Kaiya, H.; Takeuchi, K.; Namba, M.; Imai, A.; Nakashima, S.; and Nozawa, Y. Abnormal phosphatidylinositol-cycle of platelet membrane in schizophrenia--A preliminary study. *Fol Psychiatr Neurol Jpn* 38(4):437, 1985.
- Kornhuber, J.; Riederer, P.; Reynolds, G.P.; Beckmann, H.; Jellinger, K.; and Gabriel, E. ³H-spiperone binding sites in post-mortem brains from schizophrenic patients: Relationship to neuroleptic drug treatment, abnormal movements, and positive symptoms. *J Neural Transm* 75:1-10, 1989.
- Kraepelin, E. *Dementia Praecox and Paraphrenia*. Edinburgh: Churchill Livingstone. Translated by Barclay, R.M., and Robertson, G.M., 1971. New York: Krieger RE, 1919.
- Majerus, P.W.; Connolly, T.M.; Deckmyn, H.; Ross, T.S.; Bross, T.E.; Ishii, H.; Bansal, V.S.; and Wilson, D.B. The metabolism of phosphoinositide-derived messenger molecules. *Science* 234:1519-1526, 1986.
- Maris, J.M.; Evans, A.E.; McLaughlin, A.C.; D'Angio, G.J.; Bolinger, L.; Manos, H.; and Chance, B. ³¹P nuclear magnetic resonance in situ. *N Engl J Med* 312:1500-1505, 1985.
- Markesberry, W.R.; Leung, P.K.; and Butterfield, D.A. Spin label and biochemical studies of erythrocyte membranes in Alzheimer's disease. *J Neurol Sci* 45:323-330, 1980.
- McIlwain, H., and Bachelard, H.S. *Biochemistry and the Central Nervous System*. 5th ed. Edinburgh: Churchill Livingstone, 1985. pp. 291.
- Miller, B.L.; Jenden, D.; Tang, C.; and Read, S. Choline and choline-bound phospholipids in aging and Alzheimer's disease. *Neurology* 39(suppl 1):254, 1989.
- Minshew, N.J.; Panchalingam, K.; Phillips, N.E.; Strychor, S.; and Pettegrew, J.W. Membrane phospholipid and energy metabolism in Down's syndrome are different than in Alzheimer's disease (Abstract). *Neurology* 41(suppl 1):117, 1991.
- Minshew, N.J.; Pettegrew, J.W.; and Panchalingam, K. Membrane phospholipid alterations observed in Alzheimer's disease are not present in Down's

- syndrome (Abstract). *Biol Psychiatry* 27(9A):123A–124A, 1990.
- Morel, B.A. *Traitemen des Maladies Mentales*. Paris: Victor Masson, 1860.
- Oppenheim, R.W. Naturally occurring cell death during neural development. *Trends Neurosci* 8:487–493, 1985.
- Overall, J.E., and Gorham, D.R. The brief psychiatric rating scale. *Psychol Rep* 10:799–812, 1962.
- Panchalingam, K.; Pettegrew, J.W.; Strychor, S.; and Tretta, M. Effect of normal aging on membrane phospholipid metabolism by ^{31}P NMR spectroscopy (Abstract). *Soc Neurosci* 16:843, 1990.
- Panchalingam, K.; Post, J.F.M.; and Pettegrew, J.W. Evidence for increased aluminum binding ligands in Alzheimer's disease. A ^{31}P NMR study. *Neurology* 37(suppl 1):331, 1987.
- Petroff, O.A.C.; Prichard, J.W.; Behar, K.L.; Alger, J.R.; den Hollander, J.A.; and Shulman, R.G. Cerebral intracellular pH by ^{31}P nuclear magnetic resonance spectroscopy. *Neurology* 35:781–788, 1985.
- Pettegrew, J.W.; Glonek, T.; Baskin, F.; and Rosenberg, R.N. Phosphorus-31 NMR of neuroblastoma clonal lines: Effect of cell confluence state and dibutyryl cyclic AMP. *Neurochem Res* 4:795–801, 1979a.
- Pettegrew, J.W.; Kopp, S.J.; Dadok, J.; Minshew, S.J.; Feliksik, J.M.; Glonek, T.; and Cohen, M.M. Chemical characterization of a prominent phosphomonoester resonance from mammalian brain: ^{31}P and ^1H NMR analysis at 4.7 and 14.1 Tesla. *J Magn Reson* 67:443–450, 1986.
- Pettegrew, J.W.; Kopp, S.J.; Minshew, N.J.; Glonek, T.; Feliksik, J.M.; Tow, J.P.; and Cohen, M.M. ^{31}P nuclear magnetic resonance studies of phosphoglyceride metabolism in developing and degenerating brain: Preliminary observations. *J Neuropathol Exp Neurol* 46:419–430, 1987a.
- Pettegrew, J.W.; Minshew, N.J.; Cohen, M.M.; Kopp, S.J.; and Glonek, T. ^{31}P NMR changes in Alzheimer's and Huntington's disease brain (Abstract). *Neurology* 34(suppl 1):281, 1984.
- Pettegrew, J.W.; Minshew, N.J.; Diehl, J.; Smith, T.; Kopp, S.J.; and Glonek, T. Anatomical considerations for interpreting topical ^{31}P -NMR. *Lancet* ii:913, 1983a.
- Pettegrew, J.W.; Minshew, N.J.; and Payton, J.B. ^{31}P NMR in normal IQ adult autistics. *Biol Psychiatry* 25:182, 1989.
- Pettegrew, J.W.; Minshew, N.J.; and Stewart, R.M. Dynamic membrane studies in individuals at risk for Huntington's disease. *Life Sci* 32:1207–1212, 1983b.
- Pettegrew, J.W.; Moossey, J.; Withers, G.; McKeag, D.; and Panchalingam, K. ^{31}P NMR nuclear magnetic resonance study of the brain in Alzheimer's disease. *J Neuropathol Exp Neurol* 47:235–248, 1988a.
- Pettegrew, J.W.; Nichols, J.S.; Minshew, N.J.; Rush, A.J.; and Stewart, R.M. Membrane biophysical studies of lymphocytes and erythrocytes in manic-depressive illness. *J Affective Disord* 4:237–247, 1982.
- Pettegrew, J.W.; Nichols, J.S.; and Stewart, R.M. Membrane studies in Huntington's disease: Steady-state and time-dependent fluorescence spectroscopy

- of intact lymphocytes. *J Neurochem* 36:1966–1976, 1981.
- Pettegrew, J.W.; Nichols, J.S.; and Stewart, R.M. Fluorescence spectroscopy on Huntington's fibroblasts. *J Neurochem* 33:905–911, 1979b.
- Pettegrew, J.W.; Nichols, J.S.; and Stewart, R.M. Studies of the fluorescence of fibroblasts from Huntington's disease: Evidence of a membrane abnormality. *N Engl J Med* 300:678, 1979c.
- Pettegrew, J.W.; Panchalingam, K.; Moossy, J.; Martinez, J.; Rao, G.; and Boller, F. Correlation of phosphorus-31 magnetic resonance spectroscopy and morphological findings in Alzheimer's disease. *Arch Neurol* 45:1093–1096, 1988b.
- Pettegrew, J.W.; Panchalingam, K.; Strychor, S.; and Branthover, G. Analysis of membrane phospholipids in Alzheimer's disease brain by ^{31}P NMR (Abstract). *Soc Neurosci* 16:498, 1990a.
- Pettegrew, J.W.; Panchalingam, K.; Withers, G.; McKeag, D.; and Strychor, S. Changes in brain energy and phospholipid metabolism during development and aging in the Fischer 344 rat. *J Neuropathol Exp Neurol* 49(3):237–249, 1990b.
- Pettegrew, J.W.; Withers, G.; Panchalingam, K.; and Post, J.F. ^{31}P nuclear magnetic resonance (NMR) spectroscopy of brain in aging and Alzheimer's disease. *J Neural Transm Suppl* 24:261–268, 1987b.
- Pettegrew, J.W.; Withers, G.; Panchalingam, K.; and Post, J.F.M. Considerations for brain pH assessment by ^{31}P NMR. *Mag Reson Imaging* 6:135–142, 1988c.
- Pittman, R., and Oppenheim, R.W. Cell death of motoneurons in the chick embryo spinal cord. IV. Evidence that a functional neuromuscular interaction is involved in the regulation of naturally occurring cell death and the stabilization of synapses. *J Comp Neurol* 187:425–436, 1979.
- Purves, D., and Lichtman, J.W. Elimination of synapses in the developing nervous system. *Science* 210:153–157, 1980.
- Rakic, P., and Riley, K.P. Overproduction and elimination of retinal axons in the fetal rhesus monkey. *Science* 219:1441–1444, 1983.
- Rotrosen, J., and Wolkin, A. Phospholipid and prostaglandin hypothesis in schizophrenia. In: Meltzer, H.Y., ed. *Psychopharmacology: The Third Generation of Progress*. New York: Raven Press, 1987.
- Rumsey, J.M.; Duara, R.; Grady, C.; Rapoport, J.L.; Margolin, R.A.; Rapoport, S.I.; and Cutler, N.R. Brain metabolism in autism. Resting cerebral glucose utilization rates as measured with positron emission tomography. *Arch Gen Psychiatry* 42:448–455, 1985.
- Seeman, P.; Ulpian, C.; Bergeron, C.; Riederer, P.; Jellinger, K.; Gabriel, E.; Reynolds, G.P.; and Tourelotte, W.W. Bimodal distribution of dopamine receptor densities in brains of schizophrenics. *Science* 225:728, 1984.
- Sherman, K.A.; Gibson, G.E.; and Blass, J.P. Human red blood cell choline uptake with age and Alzheimer's disease. *Neurobiol Aging* 7:205–209, 1986.
- Spitzer, R.L.; Endicott, J.; and Robins, E. *Research Diagnostic Criteria (RDC) for a Selected Group of Function Disorders*. 3rd

ed. New York: New York State Psychiatric Institute, 1990.

Stevens, J.D. The distribution of phospholipid fractions in the red cell membrane of schizophrenics. *Schizophr Bull* 6:60, 1972.

Suddath, R.L.; Christison, G.W.; Torrey, E.F.; Casanova, M.F.; and Weinberger, D.R. Anatomical abnormalities in the brains of monozygotic twins discordant for schizophrenia. *N Engl J Med* 322:789-794, 1990.

Weinberger, D.R. Implications of normal brain development for the pathogenesis of schizophrenia. *Arch Gen Psychiatry* 44:660-669, 1987.

Weinberger, D.R.; Berman, K.F.; and Zec, D.F. Psychological dysfunction of the

dorsolateral prefrontal cortex in schizophrenia. *Arch Gen Psychiatry* 43:114-124, 1986.

Wong, D.F.; Wagner Jr., H.N.; Tune, L.E.; Dannals, R.F.; Pearlson, G.D.; Links, J.M.; Tamminga, C.A.; Broussolle, E.P.; Ravert, H.T.; Wilson, A.A.; Toung, J.K.T.; Malat, J.; Williams, J.A.; Lorcan, A.; O'Tuama, O.; Snyder, S.H.; Kuhar, M.J.; and Gjedde, A. Positron emission tomography reveals elevated D2 dopamine receptors in drug-naive schizophrenics [published erratum appears in *Science* 235:623, 1987]. *Science* 234:1558-1563, 1986.

Zubenko, G.S.; Cohen, B.M.; Reynolds, C.F.; Boller, F.; Malinakova, I.; and Keefe, M.A. Platelet membrane fluidity in Alzheimer's disease and major depression. *Am J Psychiatry* 144:860-868, 1987.

INFLUENCE OF MG²⁺ ON DISTRIBUTION OF IONIZED CA²⁺ IN VASCULAR MUSCLE AND ON CELLULAR BIOENERGETICS AND INTRACELLULAR FREE MG²⁺ AND PH IN PERFUSED HEARTS PROBED BY DIGITAL IMAGING MICROSCOPY, ³¹P NMR, AND REFLECTANCE SPECTROSCOPY¹

Burton M. Altura, Ph.D.,² Randall L. Barbour, Ph.D.,³ Seth D. Reiner, M.D.,⁴ Amin Zhang, M.D.,² T.P. Cheng, Ph.D.,⁵ Terry L. Dowd, Ph.D.,⁶ Raj K. Gupta, Ph.D.,⁶ Fann Wu, M.D.,² and Bella T. Altura, Ph.D.²

Data have accumulated to indicate that the level of extracellular Mg ($[Mg^{2+}]_o$) can modulate basal tone, myogenic tone, and contractile responsiveness of vascular smooth muscle cells (VSMC) in response to various physiological and pharmacological stimuli by affecting Ca content, binding, and transport across VSMC membranes (Altura

and Altura 1981, 1984, 1985b, 1990a,b). However, it is unclear whether $[Mg^{2+}]_o$ affects intracellular free Ca²⁺ ($[Ca^{2+}]_i$) in VSMC. Studies were therefore designed to determine the effects of variations in $[Mg^{2+}]_o$ on the distribution of $[Ca^{2+}]_i$ using digital imaging fluorescence microscopy of fura-2 fluorescence of single VSMC cultured from rat aortas.

¹Some of this work was presented in abstract form before the Federation of American Societies for Experimental Biology (Fed Proc 46:I305, 1987; FASEB J 2:A702, 1988; FASEB J 2:A774, 1988). Departments of Physiology,² Pathology,³ Radiology,⁴ and Anatomy and Cell Biology,⁵ State University of New York, Health Science Center, 450 Clarkson Avenue, Brooklyn, NY 11203

⁶Department of Physiology and Biophysics, Albert Einstein College of Medicine, Bronx, NY 10461

ACRONYMS

ADP	<i>adenosine diphosphate</i>
ATP	<i>adenosine triphosphate</i>
$[Ca^{2+}]_i$	<i>intracellular free Ca²⁺</i>
cAMP	<i>cyclic 3'5'-adenosine monophosphate</i>
Cr	<i>creatinine</i>
CrP	<i>creatine phosphate</i>
$[Mg^{2+}]_i$	<i>intracellular free Mg²⁺</i>
$[Mg^{2+}]_o$	<i>extracellular Mg</i>
NMR	<i>nuclear magnetic resonance</i>
PCr	<i>phosphocreatine</i>
pH _i	<i>intracellular pH</i>
P _i	<i>inorganic orthophosphate</i>
SR	<i>sarcoplasmic reticulum</i>
VSMC	<i>vascular smooth muscle cells</i>

Understanding the effects that variations in the level of $[Mg^{2+}]_o$ have on blood vessels and the myocardium is becoming increasingly important. Elevation in the plasma level of this divalent cation is used clinically to aid cardioplegia for cardiopulmonary bypass procedures (Hearse et al. 1978; Sunamori et al. 1980), to treat acute myocardial infarction (Rasmussen et al. 1986; Altura and Altura 1985a, 1990b), and to attenuate and abort different types of cardiac arrhythmias (Iseri et al. 1984; Altura and Altura 1984, 1990b; Ramee et al. 1985). A high incidence of cardiac arrhythmias, atrial fibrillation, and hypertension appears to be associated with hypomagnesemia in hospitalized and alcoholic patients (Altura and Altura 1984, 1985a; Ryzen et al. 1985; Whang et al. 1985). Recently, it has been demonstrated in experimental animals that dietary Mg can prevent

atherosclerosis (Altura et al. 1990), a forerunner of ischemic heart disease.

Two prominent physiological effects of $[Mg^{2+}]_o$ are alteration of coronary vascular tone and of heart rate (Altura and Altura 1985b, 1990b). Low levels of $[Mg^{2+}]_o$ can cause coronary vasospasm (Turlapaty and Altura 1980; Altura and Altura 1981, 1985b; Bloom 1985) and hypertension (Altura and Altura 1984, 1985b, 1990a; Altura et al. 1984), whereas elevated levels cause vasodilation (Mordes and Wacker 1978; Altura and Altura 1984, 1985b; Friedman et al. 1987) and bradycardia (Mordes and Wacker 1978; Altura and Altura 1984, 1985b; Friedman et al. 1987). Studies by Altura and Turlapaty (1982; Turlapaty and Altura 1980) have shown that $[Mg^{2+}]_o$ can affect the sensitivity of isolated canine coronary arteries to a variety of vasoactive agents. Low levels of $[Mg^{2+}]_o$ caused enhanced contractility while high levels attenuated the contractile effects of these agents. The pronounced and varied effects of $[Mg^{2+}]_o$ suggest that this divalent cation may affect cardiac contractility either by modulating the autoregulatory mechanisms controlling the delivery of essential nutrients to the heart, by directly affecting key reactions controlling the production and utilization of metabolic energy, or both.

Cardioplegic solutions used to arrest the heart commonly employ $[Mg^{2+}]_o$ in concentrations of 6–16 mM (Hearse et al. 1978; Sunamori et al. 1980; Altura and Altura 1985b). In addition, since 1918 preeclamptic

and eclamptic pregnant women have been treated with magnesium sulfate to prevent convulsions, edema, hypertension, strokes, loss of the fetus, and maternal death (see references in Altura et al. 1983). Such therapeutic regimens often result in plasma [Mg] levels in excess of 3.0 mM (Mordes and Wacker 1978). Despite these data and clinical studies, as well as a number of experimental studies (Altura and Altura 1984, 1985*a,b*, 1990*b*), it is not clear what elevated $[Mg^{2+}]_o$ does to the hemodynamics of the myocardium, divorced from nervous innervation and circulating neurohumors.

Hess et al. (1982) suggested that adult myocardial muscle cells exhibit intracellular free Mg^{2+} ($[Mg^{2+}]_i$) levels in the range of 2.5–3.1 mM. However, these values have recently been questioned (Blatter and McGuigan 1986; Garfinkel et al. 1986). It should be emphasized that no data exist on what effect elevated $[Mg^{2+}]_o$, such as that found in cardioplegia and Mg-treated preeclamptic women, has on myocardial $[Mg^{2+}]_i$ levels. Although there is some information on the effects of $[Mg^{2+}]_o$ on cardiac dynamics (Shine 1979; Altura and Altura 1985*b*, 1990*b*; Friedman et al. 1987), as well as on cellular metabolism (Shine 1979; Altura and Altura 1985*b*, 1990*b*), it is not clear what myocardial bioenergetic reactions are linked to the action(s) of $[Mg^{2+}]_o$ on cardiac hemodynamics per se.

In the study of such relationships, the ability to monitor cellular energy metabolism without dis-

rupting normal physiological function is important. Accordingly, this study was designed to examine the effects of elevated levels of $[Mg^{2+}]_o$ on the hemodynamic performance and cellular bioenergetics of the isolated, perfused working rat heart via the noninvasive techniques of ^{31}P nuclear magnetic resonance (^{31}P NMR) spectroscopy and reflectance spectrophotometry. Use of these techniques facilitates comparison of the hemodynamic performance of the heart to simultaneous measurements of steady-state intracellular oxygen tension, the redox state of cytochrome aa₃, cellular energy levels, intracellular pH (pH_i), and $[Mg^{2+}]_i$.

METHODS

Digital Image Analysis of $(Ca^{2+})_i$ in Vascular Muscle

Aortic smooth muscle cells from adult Wistar rats were cultured at 37 °C in a humidified atmosphere composed of 95 percent air and 5 percent CO₂. Cells for image analysis experiments were plated onto glass cover slips at a density of 1.0×10^6 cells/mL. All images were performed on a digital fluorescence microscope (TN8500 Image Analysis System) using fura-2 as a fluorescent Ca²⁺ indicator. Each cover slip containing a monolayer of cells was loaded with fura-2 (Molecular Probes, Eugene, OR) by incubation with 2-μM fura-2/AM in the culture media for 60 minutes under the conditions described. The cover slips were washed in buffer solution (pH 7.4) containing 0, 0.3, 1.2, and 4.8

mM MgSO_4 , respectively. In addition to MgSO_4 , the buffer solution contained NaCl (118 mM), KCl (4.8 mM), CaCl_2 (2.5 mM), KH_2PO_4 (1.2 mM), HEPES (5 mM), and glucose (10 mM).

The cover slips containing fura-2-loaded cells were affixed to holders (glass slides) that were placed on the temperature-controlled stage of the fluorescence microscope. The fluorescence signal was monitored by a silicon-intensified target camera and image processor at 510 nm using, alternatively, 340- or 380-nm excitation wavelengths. $[\text{Ca}^{2+}]$ values were calculated in vitro for a K_d of 224-nM fura-2/ Ca^{2+} complex by using maximum and minimum fluorescence ratios as the ratios of the fluorescence of chemically generated fura-2 with Ca^{2+} -EGTA buffers of known Ca^{2+} concentration at 340 and 380 nm ultraviolet light. The signals were detected at 510 nm, the spatial distribution of the fluorescence signal emitted by preloaded intracellular fura-2 (F340 and F380, respectively) (Cobbold and Rink 1987).

Perfused Rat Heart Preparation

^{31}P NMR and optical measurements were performed on isolated rat hearts in the Langendorff and working modes (Neely and Rovetto 1975). Perfusion in the Langendorff mode was also used in the initial cannulation of the heart and during transfer into the NMR magnet.

Perfusion Apparatus and Medium

The configuration of the perfusion apparatus used for the NMR and optical studies is similar to that de-

scribed by Barbour et al. (1984). The system consists of a Langendorff perfusion apparatus operating in conjunction with two working heart setups functioning in parallel, one with perfusate containing 1.2 mM MgSO_4 and the other, 4.8 mM MgSO_4 . For the optical studies, a 3-ft-long water-jacketed polyethylene tube containing the perfusion lines was used to facilitate positioning of the heart adjacent to the integrating sphere yet to avoid cooling the medium.

A similar apparatus was used for the NMR studies. The approximately 10-ft-long polyethylene tube used contained a vacuum line to draw off the coronary effluent. The cannula assembly used for the NMR studies was identical to that described by Barbour et al. (1984), except that the assembly was designed to fit into a 16-mm NMR tube. The perfusion medium, a modified Krebs-Henseleit buffer solution (Krebs and Henseleit 1932), had the following composition: NaCl (118 mM), KCl (4.7 mM), CaCl_2 (2.5 mM), MgSO_4 (1.2 or 4.8 mM), KH_2PO_4 (1.2 mM), NaHCO_3 (24 mM), and glucose (10 mM). The pH of the buffer was maintained at 7.4 by gassing the solution with a 95 percent O_2 and 5 percent CO_2 mixture.

Preparation of Rat Heart

Male Wistar rats weighing between 250 and 350 g were anesthetized with ether and injected with sodium-heparin (1,500 units/kg) 10 minutes before use. Animals were then reanesthetized, and after thoracotomy, their hearts, with the

attached lungs, were quickly removed and immersed into a frozen slush of perfusion medium to induce arrest.

Cannulation of the Heart

Prior to cannulation, the heart was trimmed of excess tissue, and lung tissue was carefully removed from the point at which the pulmonary vein joins the left atrium. When the aorta was secured to its cannula, retrograde perfusion was begun immediately by opening the aortic line. Hearts typically resumed sinus rhythm within 10–15 seconds. The perfusion pressure was 90 cm H₂O.

Working Mode

Those experiments involving working hearts employed cannulation in the Langendorff model, in which the left atrium was cannulated via one of the four pulmonary veins and secured with surgical thread. The left atrial line, which contained 1.2 mM MgSO₄, was then opened, simultaneous with closing the line from the Langendorff reservoir and diverting aortic output to a line that ended with a 22-gauge needle positioned 90 cm above the heart. Pressure development and heart rate were measured with a Statham model P23db pressure transducer connected to the aortic line and recorded on a Beckman R-511 four-channel physiologic recorder. Coronary outflow and aortic output were measured simultaneously by collecting the effluents.

Optical Measurements and Instrumentation

Optical measurements of the epicardial layer of the heart were obtained with an external integrating sphere interfaced with a Perkin-Elmer Lambda 5 spectrophotometer and to a 3600 data station operating PECUV software, which served for instrument setup and data acquisition, storage, retrieval, and processing of the spectral data files. Sample and reference light from the spectrophotometer were directed to the integrating sphere via two 4-ft-long fiber optical cables. Sample light entering the sphere passed through the device and exited a 1-cm diameter opening located on the opposite side. A glass cover slip, secured by a watertight seal, was placed over the opening of the sample port to prevent contamination of the sphere by the coronary effluent. The inner aspect of the sphere was coated with a layer of barium sulfate, which serves to diffuse scattered reference and back-scattered sample light entering the sphere prior to detection by a Hamamatsu R1463 photomultiplier tube housed in the sphere.

Before each measurement, the instrument was calibrated to the 656.1-nm emission line of deuterium and background-corrected by scanning a barium sulfate planchet placed in front of the sample port. Wavelength scans were performed in the transmission mode by scanning from 650 to 500 nm in steps of

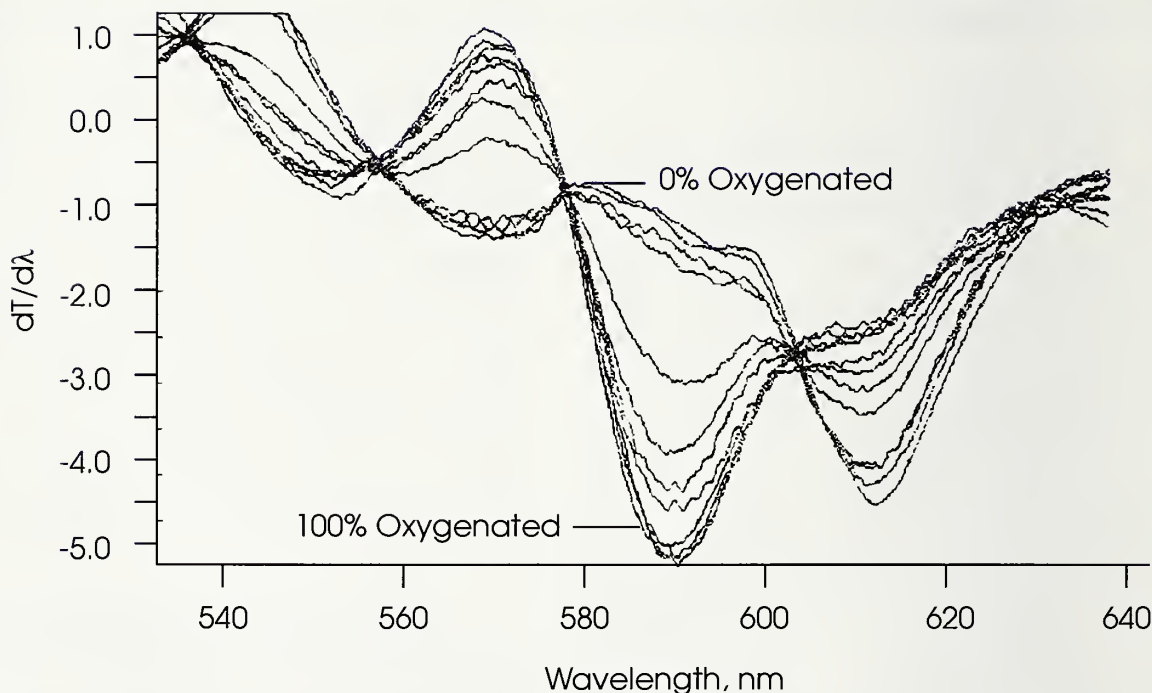
0.5 nm at a rate of 240 nm/minute. The slit width was 4 nm and response time, 0.2 seconds. Reflectance measurements were performed by placing the sphere in a horizontal position sufficiently close to the heart such that the coronary effluent came in contact with the glass cover slip, thereby forming an optical guide and avoiding an air interface. In this configuration, the heart, attached to the cannulae, was

allowed to beat freely without interference from the sphere.

Spectral Analysis

The level of oxymyoglobin and the redox state of cytochrome oxidase were determined by evaluating the first derivative of the spectra. The oxymyoglobin level was determined by measuring the difference in slope at the inflection points along the myoglobin peak that, in

FIGURE 1



First derivative, smoothed reflectance spectra of perfused rat heart. Isolated rat hearts perfused in the Langendorff mode with elevated $(Mg^{2+})_o$. Diffuse surface reflectance measurements performed using an external integrating sphere interfaced to a Perkin-Elmer Lambda 5 spectrophotometer at the indicated frequencies on the epicardial layer of the left ventricle. Resultant spectra were processed using a smoothing procedure and the derivative spectra determined. Spectra shown identify response of tissue to graded hypoxia. Values denote the O_2 tension in the perfusate in KPa. Difference in the maximal and minimal values at approximately 572 and 592 nm, respectively, correspond to the decline in the levels of oxymyoglobin upon increased hypoxia. Similarly, the difference between the reflectance intensity at 605 nm and the minimal at 614-616 nm increases upon increased hypoxia, indicating higher levels of reduced cytochrome aa₃.

the derivative spectra, corresponds to maximum and minimum points at approximately 572 and 592 nm, respectively. Similarly, the redox state of cytochrome oxidase was determined by measuring the difference in slope at an inflection point between 614 and 616 nm and at the absorption maximum of 605 nm. This approach was chosen over analysis of primary spectra because derivative analysis is known to have enhanced sensitivity in the evaluation of overlapping multicomponent spectra (Butler 1972). A Kubelka-Munk analysis (1931) was also found unsuitable because it lacks the capability to align the sphere with each heart in an identical fashion. This alignment problem causes proportional changes in the reflectance intensities of comparable hearts, thus rendering it difficult to differentiate true changes in primary spectra absorbance coefficients from the effects of different alignment.

Preliminary analysis of the spectrum showed that although a motion artifact was clearly evident, its effect could largely be eliminated by applying a smoothing function (Savitsky and Golay 1964). The success of this operation indicates that the motion artifact superimposes on the spectrum a signal with stable amplitude and frequency and small peak width relative to the peak width of the spectral components. The result-

ing spectra had a signal-to-noise ratio of at least 20:1. Figure 1 illustrates a typical series of spectra obtained after performing these operations.

A 100 percent oxidized state was arbitrarily defined as the signal intensity obtained from a heart in the Langendorff mode in the presence of 4.8 mM MgSO₄. This state was selected for comparison because it represented the best oxygenation state seen in these preparations. A zero percent oxidized state was defined as the signal intensity obtained in hearts after perfusion with 95 percent N₂ and 5 percent CO₂ (anoxic media) for 20 minutes. Calculation of the relative oxygenation state was performed by a linear interpolation between these two states.⁷

³¹P NMR Measurements and Instrumentation

All perfused heart spectra were obtained on a Varian XL200 spectrometer operating at the ³¹P resonance frequency of 81 MHz in a 16-mm broad band probe maintained at 37 °C by equilibration with preheated air. ³¹P spectra were accumulated within a spectral width of 5,000 Hz, an acquisition time of 0.8 seconds, and a recycle time of 1.6 seconds. A 90° pulse was applied, and each spectrum was the result of the accumulation of 400 transients processed with a 30-Hz line-broadening function to

⁷Tamura et al. (1978) determined that approximately 15 percent of the signal at 605 nm is due to the contribution of myoglobin. Thus, to the extent that the relative oxygenation state of myoglobin differs significantly from that of cytochrome aa₃, it will introduce some error in the determination of its true redox state by this method. This problem, however, is common to all dual-wavelength methods.

improve the signal-to-noise ratio. Each spectrum was run unlocked and referenced to the phosphocreatine (PCr) resonance at ~3.2 ppm.

pH_i and [Mg²⁺]_i Measurements

pH_i was determined by measuring the difference between the inorganic orthophosphate (P_i) and the PCr resonances. To convert the chemical shift difference (δ_{obs} in Hz) and pH_i, we used a titration relationship (Jacobus et al. 1978) derived from a least-squares fit to titration data:

$$\text{pH}_i = 6.73 + \log \frac{(\delta_{\text{obs}} - 2.90 \text{ Vp})}{(5.70 \text{ Vp} - \delta_{\text{obs}})} \quad (1)$$

where Vp is the ³¹P Larmor frequency in megaHertz (81 MHz in this study). This relationship is valid at pH values in the range of 6–8 (Gadian et al. 1982).

[Mg²⁺]_i was determined by the method of chemical shift difference between the α- and β-phosphoryl group resonances of adenosine triphosphate (ATP) in the ³¹P spectrum (Gupta and Moore 1980). The difference in the chemical shift between the α-P and β-P resonances of ATP depends on the extent of Mg complexation by ATP. [Mg²⁺]_i can be calculated with an accurate knowledge of the dissociation constant of MgATP measured under intracellular ionic conditions through the following equations:

$$\phi = \frac{[\text{ATP}]_{\text{free}}}{[\text{ATP}]_{\text{total}}} \left(\frac{\delta_{\alpha\beta}^{\text{cell}} - \delta_{\alpha\beta}^{\text{MgATP}}}{\delta_{\alpha\beta}^{\text{ATP}} - \delta_{\alpha\beta}^{\text{MgATP}}} \right) \quad (2)$$

$$[\text{Mg}^{2+}]_i = K_d^{\text{MgATP}} \left\{ \frac{1}{\phi} - 1 \right\} \quad (3)$$

where the K_d^{MgATP} used equaled 50 μM. δ_{αβ}^{cell} is the chemical shift difference between the α-P and β-P resonances of intracellular ATP. δ_{αβ}^{ATP} and δ_{αβ}^{MgATP} are the values of this separation for noncellular ATP and MgATP, controls being 876 and 674 Hz, respectively, under our spectrometer conditions. φ is the fraction of ATP uncomplexed to Mg²⁺. [ATP]_{free} is the uncomplexed ATP concentration, and [ATP]_{total} is the concentration of total NMR-observable ATP.

All hemodynamic, optical, and ³¹P NMR measurements were ascertained temporally when the hearts demonstrated distinct, observable physiologic changes (e.g. heart rate changes upon switching from 1.2 to 4.8 mM [Mg²⁺]_o or from 4.8 to 1.2 mM [Mg²⁺]_o). Measurements were obtained within 3–5 minutes after equilibration of the heart in the new [Mg²⁺]_o environment.

Calculation of Metabolite Concentrations

Cytosolic metabolic concentrations were calculated assuming the cytosolic volume was 60 percent of the net weight (Giesen and Kammermeier 1980). Creatine phosphate (CrP), P_i, and ATP levels were determined directly from the NMR spectra and corrected for partial saturation using T₁ values of 2.06, 0.81, and 0.75 seconds, respectively (Bittl and Ingwall 1985). ATP levels were determined by averaging the

corrected integrated intensities of the α - and β -phosphate resonances. Correction for the presence of P_i in the medium was made by subtracting the resonance intensity observed with medium alone and accounting for the displacement of the heart. P_i was included in the perfusate because it had been demonstrated that hearts perform better when it is included in the medium (Starnes et al. 1985). Creatine (Cr) concentration was calculated on the basis of changes in $[CrP]$ assuming total $[CrP]+[Cr]$ was 17 mM (Clarke and Willis 1987). Free cytosolic $[MgADP]$ levels were calculated on the basis of the creatine kinase reaction, assuming conditions of equilibrium:

$$[MgADP] = \frac{[MgATP][Cr]K_{eq}^{CK}}{[CrP][H^+]} \quad (4)$$

$MgATP$ was calculated using a dissociation constant of 50 μM (Gupta et al. 1984), and a value of $3.08 \times 10^{-10} M$ was used for K_{eq}^{CK} (Watts 1973).

Cytosolic Phosphorylation Potential

The cytosolic phosphorylation potential $[ATP]/\{[ADP]x[P_i]\}$ was calculated on the basis of the amount of Mg nucleotide plus free nucleotide. A K_d for $MgADP$ of 0.43 mM (Gupta and Benovic 1978) was used to calculate the concentration of free ADP.

Free Energy of ATP Hydrolysis

The change in the free energy of ATP hydrolysis ($-\delta G/\delta E$, where E is

the degree of advancement of hydrolysis) was calculated from the

$$-\frac{\delta G}{\delta E} = \Delta G_{obs}^o + RT \ln \frac{[ADP][P_i]}{[ATP]} \quad (5)$$

equation described by Gibbs (1985): where ΔG_{obs}^o will vary in accordance with the concentration of Mg and pH (Rosing and Slater 1972); the gas constant (R) is 8.31 J/ $^{\circ}K/mol$, and the temperature (T) is 310 $^{\circ}K$. For this study, a ΔG_{obs}^o value of -29.3 kJ/mol was determined for hearts perfused in the presence of 1.2 and 4.8 mM $MgSO_4$ (Rosing and Slater 1972).

Statistical Evaluation

Where appropriate, a Student's t or paired t test or ANOVA was used to compare mean values \pm S.E.M. for biological significance. A p value <0.05 was considered significant.

RESULTS

Digital Image Analysis of $(Ca^{2+})_i$ and Cell Geometry in Cultured Rat Aortic Smooth Muscle Cells

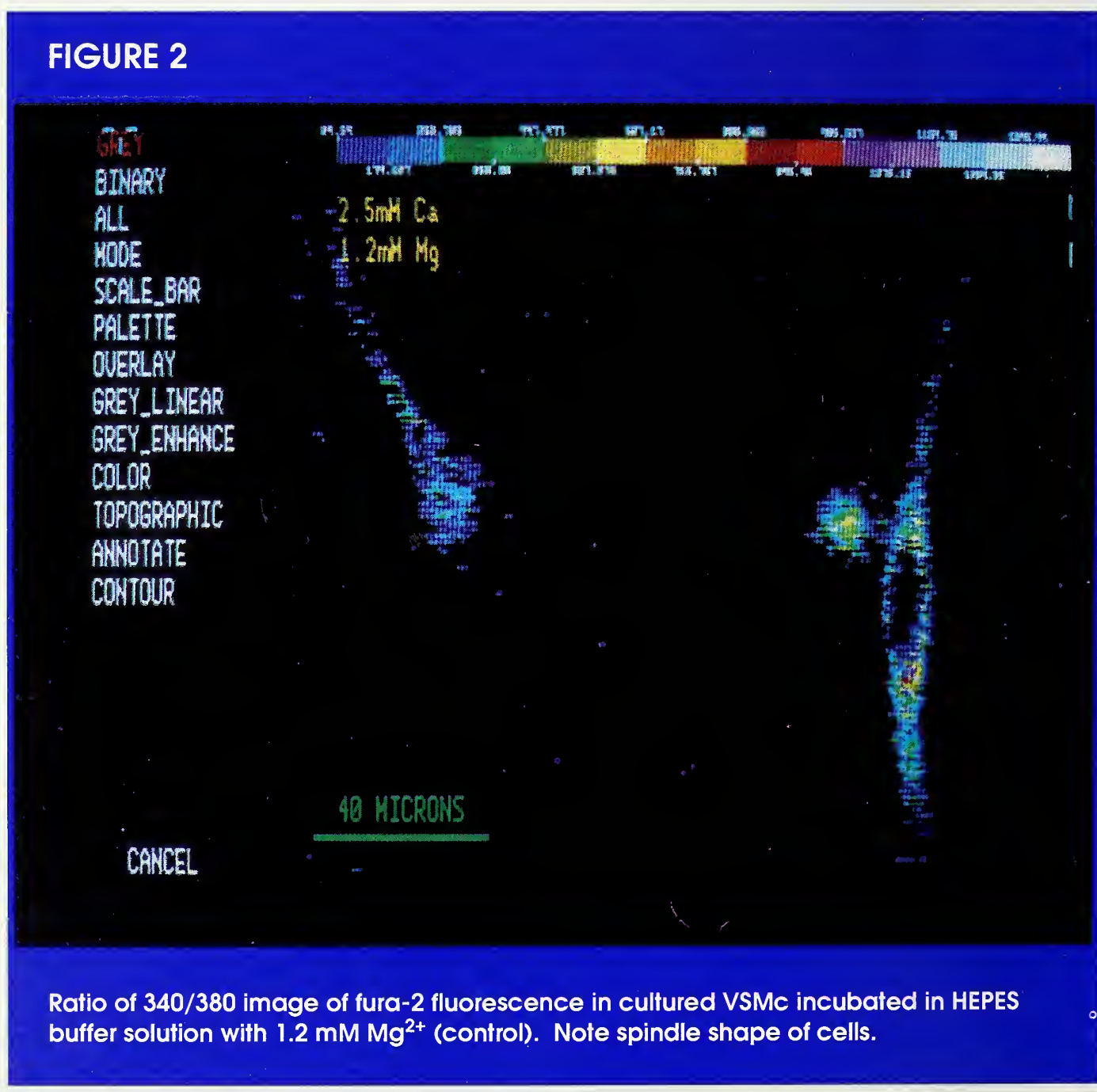
When incubated with buffer solution containing 1.2 mM $[Mg^{2+}]_o$, the myocytes were spindle-shaped, and the basal level of $[Ca^{2+}]_i$ estimated from the ratio (F340/F380) was 96.6 ± 7.9 nM with a heterogeneous distribution (figure 2). $[Mg^{2+}]_o$ withdrawal from the incubation medium consistently induced a dramatic increment of $[Ca^{2+}]_i$ up to 579.6 ± 39.3 nM, or about a 5.8-fold elevation, compared with that in control experiments (figure 3). In addition, most of the cells rounded up. Similarly, lowering $[Mg^{2+}]_o$ to 0.3 mM

(the lowest physiological range) elevated $[Ca^{2+}]_i$ to the intermediate level of 348.0 ± 31.5 nM (table 1). However, the heterogeneous distribution of $[Ca^{2+}]_i$ was still evident when $[Mg^{2+}]_o$ was lowered. When exposed to 0.3 mM $[Mg^{2+}]_o$ some of the cells rounded up, but the numbers were far fewer than with 0 mM $[Mg^{2+}]_o$. In contrast, elevation of $[Mg^{2+}]_o$ to 4.8 mM decreased $[Ca^{2+}]_i$ to 72.0 ± 4.6 nM (table 1). Removal of $[Ca^{2+}]_o$ abolished the increments of $[Ca^{2+}]_i$ induced by $[Mg^{2+}]_o$ withdrawal.

Hemodynamic Responses of Perfused Rat Heart

The hemodynamic response of rat hearts perfused in the working mode with normal (1.2 mM) and elevated (4.8 mM) $[Mg^{2+}]_o$ is shown in table 2. Rat hearts perfused with 1.2 mM MgSO₄ exhibited a rate-pressure product of 2.36×10^4 mmHg/minute and a cardiac output of 21 mL/minute/g. Elevation of $[Mg^{2+}]_o$ to 4.8 mM caused a significant increase in coronary flow (38 percent) while heart rate was decreased by

FIGURE 2



35 percent. Despite the pronounced bradycardia, the rate-pressure product was only slightly reduced (2.08×10^4 mmHg/minute) due to a significant increase in systolic pressure (36 percent). At a level of 2.4 mM $[Mg^{2+}]_o$, systolic pressure increased by 16 percent, while heart rate was reduced by 23 percent, yielding a 10 percent decline in the rate-pressure product (results not shown). In the presence of 4.8 mM $[Mg^{2+}]_o$, total cardiac output actually

increased by 23 percent, owing to a >100 percent increase in stroke volume.

Aortic output amounted to less than one-third of the total output and was unaffected by variations in $[Mg^{2+}]_o$. This relatively low aortic output, which stems from the high afterload (90 cm H₂O) imposed on the heart, serves to maintain a high diastolic pressure (Neely et al. 1976). This procedure thus avoids an initial ischemic insult, which can occur in

FIGURE 3

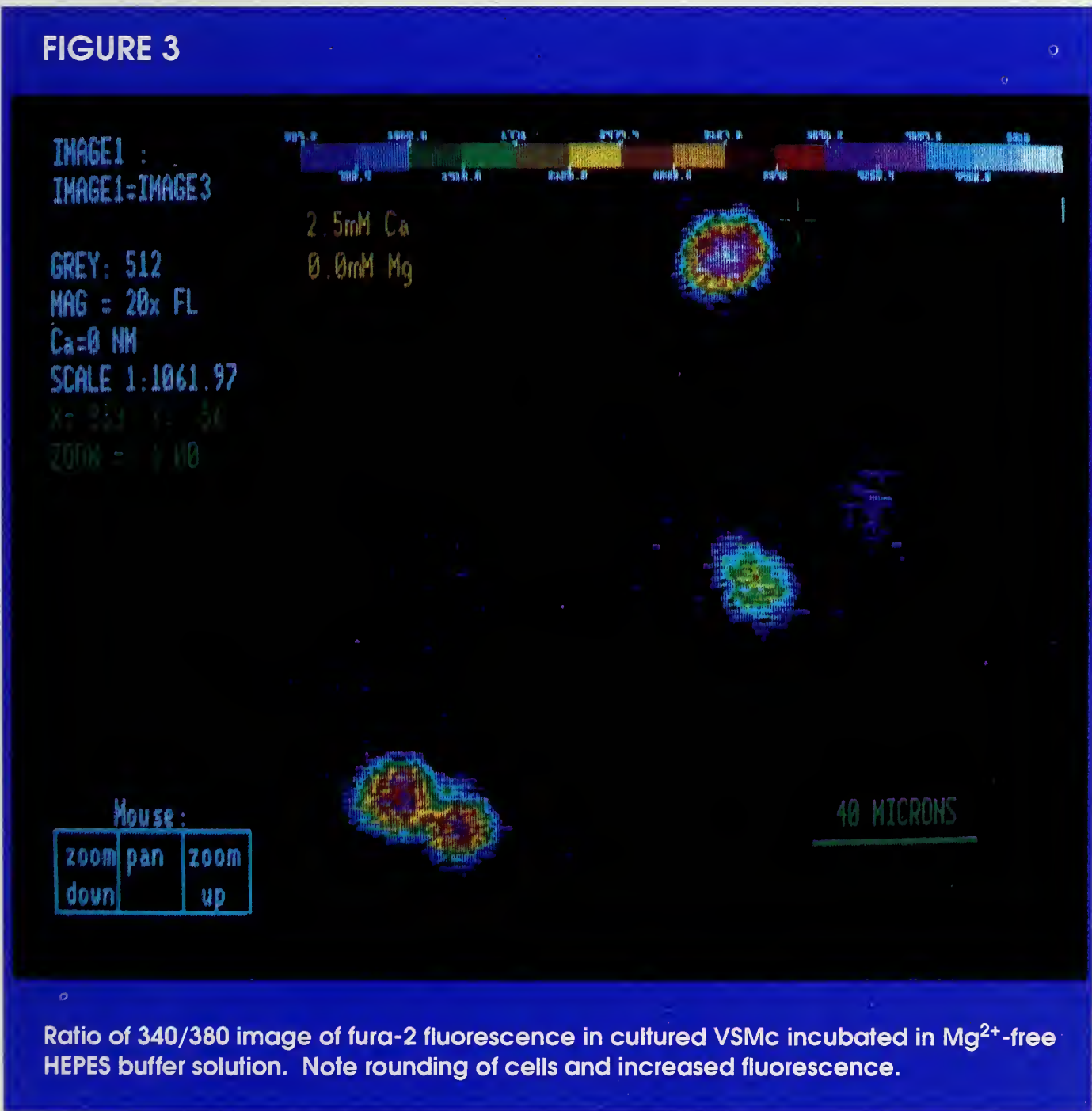


Table 1. Effects of $(Mg^{2+})_o$ on the regulation of $(Ca^{2+})_i$ in cultured vascular smooth muscle from rats

$(Mg^{2+})_o$ (mM)	$(Ca^{2+})_o$ (mM)	n	$(Ca^{2+})_i$ (nM)
1.2	2.5	48	93.6 ± 7.93
0	2.5	91	$579.5 \pm 39.3^*$
0.3	2.5	116	$348.0 \pm 31.5^*$
4.8	2.5	126	$72.0 \pm 4.55^*$
0	0	21	$3.6 \pm 0.51^*$

Means \pm S.E.M.; n, the number of cells.*Significantly different from 1.2 mM Mg^{2+} and all other values ($p < 0.02$).

hearts with low diastolic pressure upon transition from the Langendorff to the working mode. Our results indicate that in the isolated working

heart, elevated $[Mg^{2+}]_o$ has coronary vasodilatory, negative chronotropic, and positive inotropic-like effects on the heart. The reintroduction of

Table 2. Effects of elevated $(Mg^{2+})_o$ on cardiac function in hearts perfused by working mode (90 cm H_2O)

Parameters	1.2 mM $(Mg^{2+})_o$ (initial)	4.8 mM $(Mg^{2+})_o$	1.2 mM $(Mg^{2+})_o$ (readmittance)
Heart rate (beats/minute)	211 ± 9	$137 \pm 16^*$	207 ± 15
Coronary flow (mL/minute/g)	14.5 ± 2.0	$20.0 \pm 2.9^\dagger$	14.6 ± 1.5
Aortic output (mL/minute)	7.6 ± 0.9	7.2 ± 0.08	7.3 ± 0.7
Stroke volume (mL/minute)	0.10 ± 0.01	$0.22 \pm 0.04^\ddagger$	0.10 ± 0.01
Cardiac output (mL/minute)	22.2 ± 2.4	$27.2 \pm 3.3^\$$	21.8 ± 1.8
Systolic pressure (mmHg)	112 ± 6.8	$152 \pm 7.7^\$$	107 ± 8.50
Rate-pressure product (mmHg/minute)	$2.36 \pm 0.16 \times 10^4$	$2.08 \pm 0.16 \times 10^4\$$	$2.21 \pm 0.17 \times 10^4$

Means \pm S.E.M.* $p < 0.005$; $^\dagger p < 0.03$; $^\ddagger p < 0.015$; $^\$ p < 0.05$; paired t tests.

Table 3. Effects of elevated (Mg^{2+})_o on cellular oxygenation state

$(Mg^{2+})_o$ (mM)	Oxymyoglobin (%)	Oxidized cytochrome aa ₃ (%)
1.2	52.7 ± 5.5	74.0 ± 2.4
4.8	68.0 ± 5.8*	85.1 ± 3.0*

Means ± S.E.M.; n=8.
*p<0.1.

1.2 mM [Mg²⁺]_o resulted in a return to baseline levels of all hemodynamic parameters (table 2).

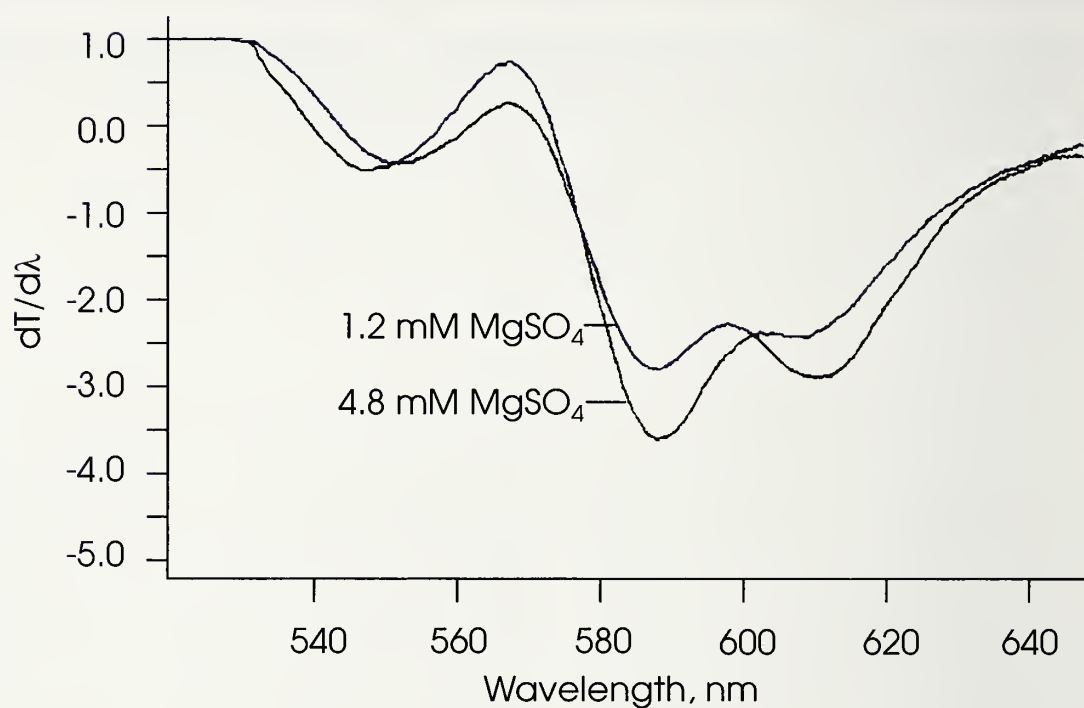
Optical Measurements

Simultaneous with the hemodynamic measurements, the use of an integrating sphere interfaced to a Perkin-Elmer Lambda 5 spectrophotometer yielded diffuse surface reflectance measurements of hearts perfused in the Langendorff and working modes. These optical measurements were obtained approximately 3–10 minutes after cannulation, when the hearts had achieved a stable hemodynamic performance. Steady-state levels of oxymyoglobin and oxidized cytochrome aa₃ resulted from evaluation of the first derivative of the resultant spectra (as described in the Methods section).

The results in table 3 demonstrate the effects of elevated [Mg²⁺]_o on the steady-state levels of oxymyoglobin and the redox state of cytochrome aa₃. Hearts perfused in the working mode with 1.2 mM MgSO₄ had steady-state oxymyoglobin levels of 53 percent while the

levels of oxidized cytochrome aa₃, were 74 percent, compared with levels of 72 and 81 percent, respectively, for hearts perfused with 1.2 mM [Mg²⁺]_o in the Langendorff mode (results not shown). The extent of oxidized cytochrome aa₃ is comparable to the 78 percent level measured under similar conditions by Hassinen and Hiltunen (1975). Perfusion of working hearts with 4.8 mM [Mg²⁺]_o significantly (15 and 11 percent, respectively) increased steady-state levels of oxymyoglobin and oxidized cytochrome aa₃.⁸

Further investigation of this observation included perfusing the hearts over a wide range of O₂ tensions (anoxic to 650 Torr) and measurement of the levels of oxymyoglobin and extent of oxidized cytochrome aa₃. Figures 4 and 5 demonstrate that oxymyoglobin levels vary in a nonlinear fashion with change in the redox state of cytochrome aa₃, caused by progressive hypoxia, results that corroborate a report by Caspary et al. (1985).

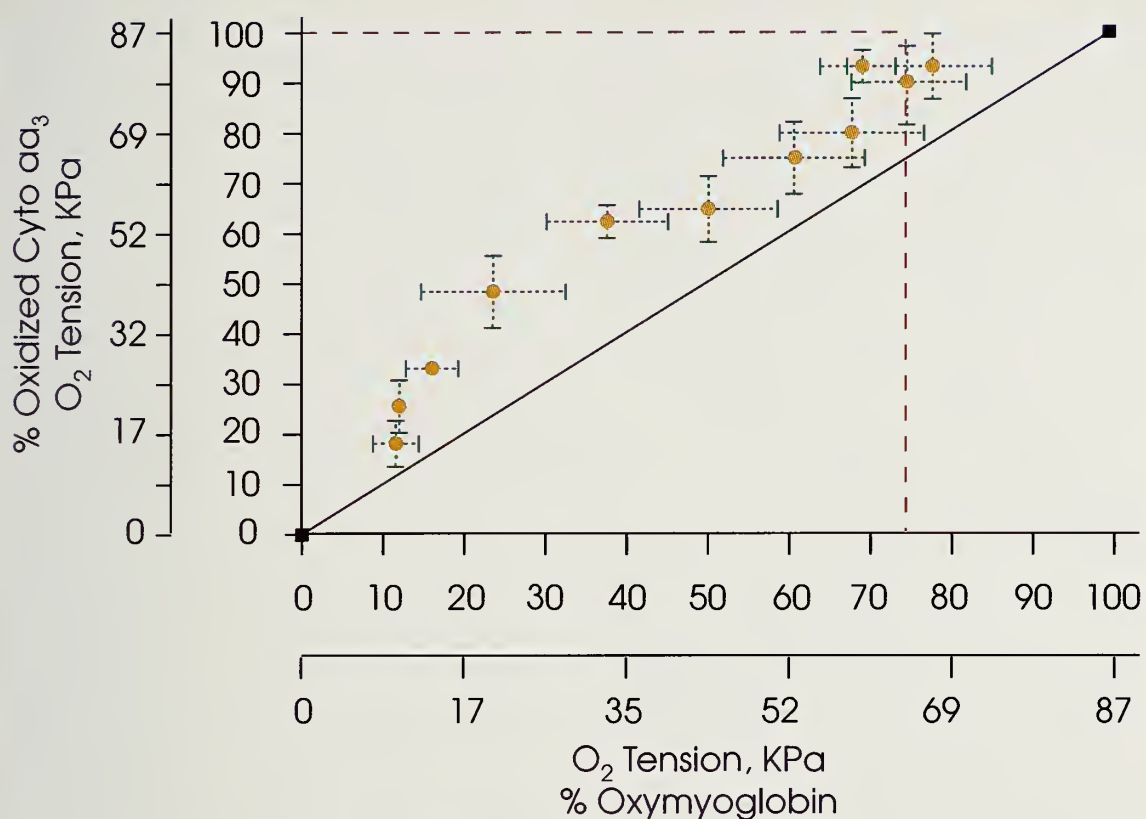
FIGURE 4

Effects of elevated (Mg^{2+})_o on the first derivative, smoothed reflectance spectra of isolated working rat heart. Reflectance measurements were performed on hearts perfused with Krebs-Henseleit buffer containing 1.2 or 4.8 mM $MgSO_4$. Optical spectra were obtained within 2-5 minutes after the onset of hemodynamic changes shown in table 2.

The new finding that the prevailing workload affects the difference between oxymyoglobin level and extent of oxidized cytochrome aa_3 may represent a

means of noninvasively assessing the "adequacy of the response" (i.e., change in coronary flow) to varying metabolic demands. The significance of this concept is

⁸Previous studies by Tamura et al. (1978) have shown a 1:1 relationship between the level of oxymyoglobin and degree of oxidized cytochrome aa_3 in perfused hearts over a wide range of values, indicating the presence of steep O_2 gradients over a wide range of values between the cytosol and mitochondria. In apparent contrast to these findings, the results reported here show a much lower level of oxymyoglobin compared with the level of oxidized cytochrome aa_3 in working hearts. This observation is consistent with the known higher affinity that cytochrome aa_3 has for O_2 than myoglobin (Oshino et al. 1974), signifying that a much smaller O_2 gradient exists in these preparations. Notably, the difference between the level of oxymyoglobin and degree of oxidized cytochrome aa_3 was greatly reduced for hearts perfused in the Langendorff mode, indicating that the observed difference is sensitive to the prevailing workload. In fact, we interpret the results of Tamura et al. (1978) to be consistent with this observation because their measurements were performed on hearts using a workload similar to that in our Langendorff preparations, yet they were perfused at a much lower temperature (25 °C). Thus, relative to our studies, their measurements were performed on hearts having greatly reduced metabolic demand.

FIGURE 5

Dependence of level of oxymyoglobin on extent of oxidized cytochrome aa₃. Rat hearts perfused at the indicated level of O₂ tension in the Langendorff mode in the presence of elevated (Mg²⁺)_o. Surface reflectance measurements performed as described in figure 1. Solid line denotes line of identity depicting a 1:1 relationship between the extent of oxidized cytochrome aa₃ and level of oxymyoglobin. Dotted line indicates the O₂ tension below which the extent of oxidized cytochrome aa₃ declines. Values shown are means \pm S.D. for three to four hearts per data point.

explored in the section entitled Discussion.

Although myocardial O₂ consumption was not directly measured, these results suggest that O₂ consumption is reduced in the presence of elevated [Mg²⁺]_o. This suggestion is reasonable because the rate-pressure product, which is decreased in the presence of elevated [Mg²⁺]_o, is linearly correlated with O₂ consumption (Kobayashi and Neely 1979). Moreover, Friedman et al. (1987) had demonstrated that

Mg²⁺ infusion reduced O₂ consumption in the neurally intact, open-chest dog heart preparation. The increased oxygenation state of the heart may also result from enhanced coronary flow, which increases the rate of O₂ delivery to the tissue.

Demonstrating that steady-state levels of oxymyoglobin and the extent of oxidized cytochrome aa₃ are increased in hearts perfused with elevated [Mg²⁺]_o, the results shown

in table 3 indicate that either a decrease in metabolic demand or an increase in O_2 supply, or both, have occurred. The decline in rate-pressure product and increase in coronary flow show that, in fact, both mechanisms are responsible for the improved oxygenation state of the heart. This finding, together with evidence that the inotropic state of the heart has improved, demonstrates that elevated $[Mg^{2+}]_o$ increases efficiency of the heart.

^{31}P NMR Measurements

The effects of elevated $[Mg^{2+}]_o$ on cytosolic phosphate levels in hearts perfused in the Langendorff and working mode are shown in table 4 and figures 6 and 7. Perfusioning hearts with elevated $[Mg^{2+}]_o$ in the Langendorff mode significantly increased CrP levels (22 percent), while P_i levels declined correspondingly. Because of a large variance, the change in P_i level was of borderline significance ($p=0.07$). However, in

view of the well-defined biochemical relationships, the observed change in P_i level is likely to be significant biologically. In the working mode, increased extracellular $[Mg^{2+}]_o$ caused the level of CrP to increase by 40 percent, while ATP levels declined by 17 percent. The loss of ATP was indicated by a decline in intensity of all three resonances, suggesting that ATP was being metabolized beyond ADP, thereby liberating additional phosphate to participate in other reactions.

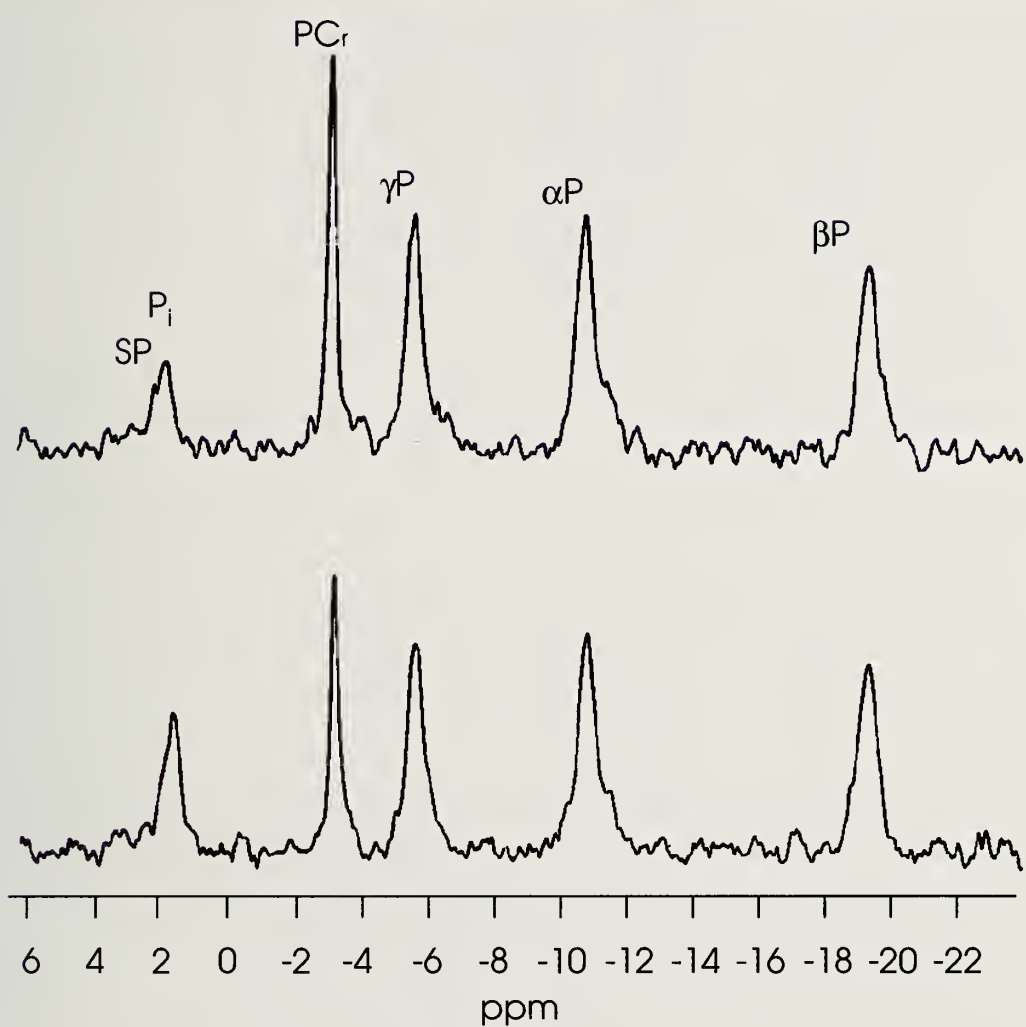
This suggestion may explain why CrP levels increased more than would be anticipated on the basis of the change of ATP level. In fact, unlike hearts perfused in the Langendorff mode, hearts perfused in the working mode with elevated $[Mg^{2+}]_o$ had increased levels of total observable inorganic phosphorus plus sugar-phosphate (table 4). Because sugar-phosphates in this preparation have a relatively low signal-to-noise ratio and its

Table 4. Effects of elevated $(Mg^{2+})_o$ on cellular energy levels

Perfusion mode	$(Mg^{2+})_o$ (mM)	(P_i) (mM)	(CrP) (mM)	(ATP) (mM)
Langendorff (control)	1.2	4.7 ± 1.2	9.2 ± 0.5	6.8 ± 0.1
Langendorff	4.8	$2.2 \pm 0.6^*$	$11.3 \pm 0.5^\dagger$	6.7 ± 0.1
Working (control)	1.2	(22.6 ± 1.8)	6.3 ± 0.7	7.5 ± 0.1
Working	4.8	$(27.2 \pm 2.6)^\ddagger$	$9.0 \pm 1.0^\ddagger$	$6.2 \pm 0.4^\ddagger$

Means \pm S.E.M.; $n=5$. Values shown in parentheses for P_i are percentage of total observable phosphorus.

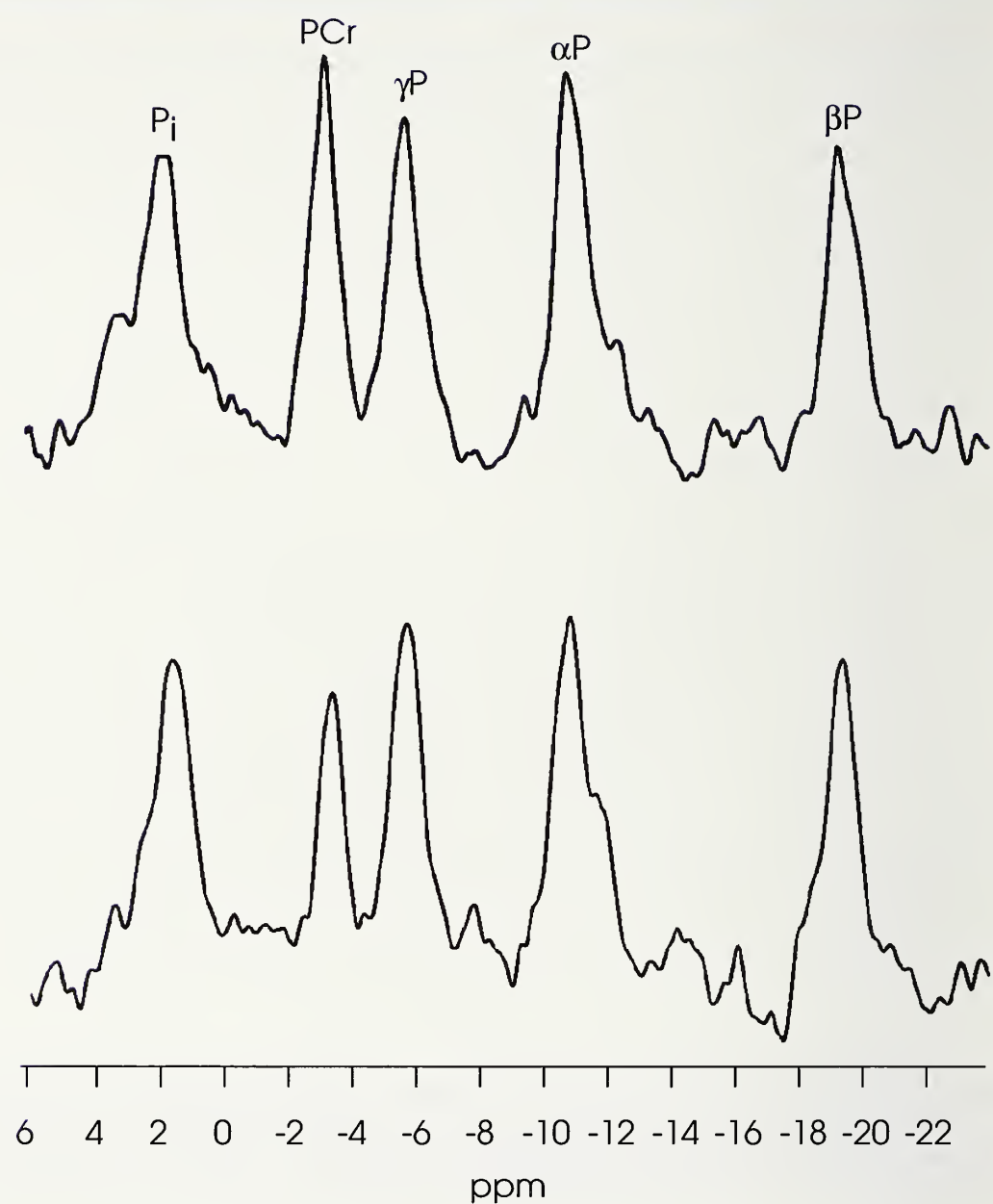
* $p=0.07$; $^\dagger p<0.01$; $^\ddagger p=0.09$; $^\ddagger p=0.02$.

FIGURE 6

^{31}P NMR spectra, at 81 MHz, of isolated Langendorff-perfused rat heart at 37 °C, show the resonances of PCr , ATP (αP , βP , and γP), Pi , and sugar-phosphates (SP) obtained with 1.2 mM Mg^{2+} in the perfusion medium (lower trace) and 20 minutes after perfusion with medium containing 4.8 mM Mg^{2+} (upper trace). Each spectrum was acquired in 10.7 minutes after time-averaging 400 free induction decay transients with a pulse recycle time of 1.6 seconds. A line-broadening function of 30 Hz was used to improve the spectral signal-to-noise ratio. Note readily apparent increase in the amplitude of the PCr resonance and a decrease in Pi upon transfer to 4.8 mM Mg^{2+} perfusate.

resonance overlaps with that of P_i , the levels of inorganic phosphate and sugar-phosphate were not quantitated separately. Hence, we report only the combined level of these constituents as a percentage of total observable phosphorus,

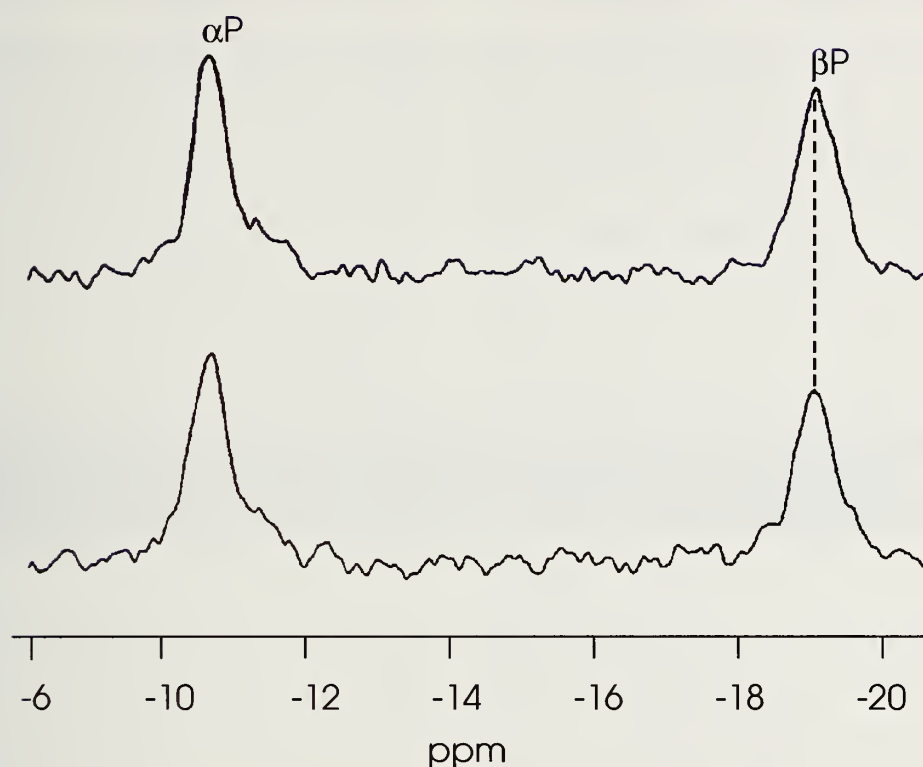
instead of the millimolar concentration. In working hearts perfused with normal $[\text{Mg}^{2+}]_o$, sugar-phosphate levels were very low. However, these levels rose in hearts perfused with elevated $[\text{Mg}^{2+}]_o$ (figure 7).

FIGURE 7

^{31}P NMR spectra, at 81 MHz, of isolated perfused working rat heart at 37 °C, show the resonances of PCr , ATP (αP , βP , and γP), and P_i obtained with 1.2 mM Mg^{2+} (lower trace) and 4.8 mM Mg^{2+} (upper trace) in the perfusion medium, 20 minutes after the onset of perfusion. Other conditions and spectral acquisition parameters were the same as in figure 6. Note sizable increase in the PCr resonance upon transfer of the heart to 4.8 mM Mg^{2+} -containing perfusate and P_i resonance in 4.8 mM Mg^{2+} , which has undergone an alkaline shift in pH_i .

Typical ^{31}P NMR spectra illustrating the effects of increased $[\text{Mg}^{2+}]_o$ on the phosphometabolites of hearts perfused in the Langendorff and working modes are shown

in figures 6 and 7, respectively. Expanded regions of the NMR spectra illustrating the observed changes in pH and $[\text{Mg}^{2+}]_i$ levels are shown in figure 8.

FIGURE 8a

Section of ^{31}P NMR spectra showing the effects of elevated Mg^{2+} (4.8 mM) perfusate on $(\text{Mg}^{2+})_i$, measured from the separation between the αP and βP resonances of intracellular ATP, along with appropriate (1.2 mM Mg^{2+}) perfusate controls. Other conditions and spectral acquisition parameters were the same as in figure 6. The decreased separation between the αP and βP resonances upon transfer to 4.8 mM Mg^{2+} demonstrates increased free $(\text{Mg}^{2+})_i$ compared with controls (1.2 mM Mg^{2+}).

Table 5 shows that associated with variations in intracellular phosphate levels, perfusing hearts with elevated $[\text{Mg}^{2+}]_o$ increased pH_i by 0.12–0.13 units and nearly doubled $[\text{Mg}^{2+}]_i$. This observation contrasts with the longstanding assumption often quoted in physiology textbooks (West 1985) that unlike Ca^{2+} , intracellular Mg^{2+} is unable to change acutely in response to a variation in its extracellular level. In view of the multitude of intracellular reactions requiring Mg^{2+} as an essential cofactor (Garfinkel and Garfinkel 1985; Garfinkel et al. 1986),

we believe that our observation is extremely significant. It may require reconsideration of the possible roles of varying the level of extracellular Mg^{2+} , i.e., influencing the flux through various metabolic reactions and serving as an effective antagonist to intracellular Ca^{2+} .

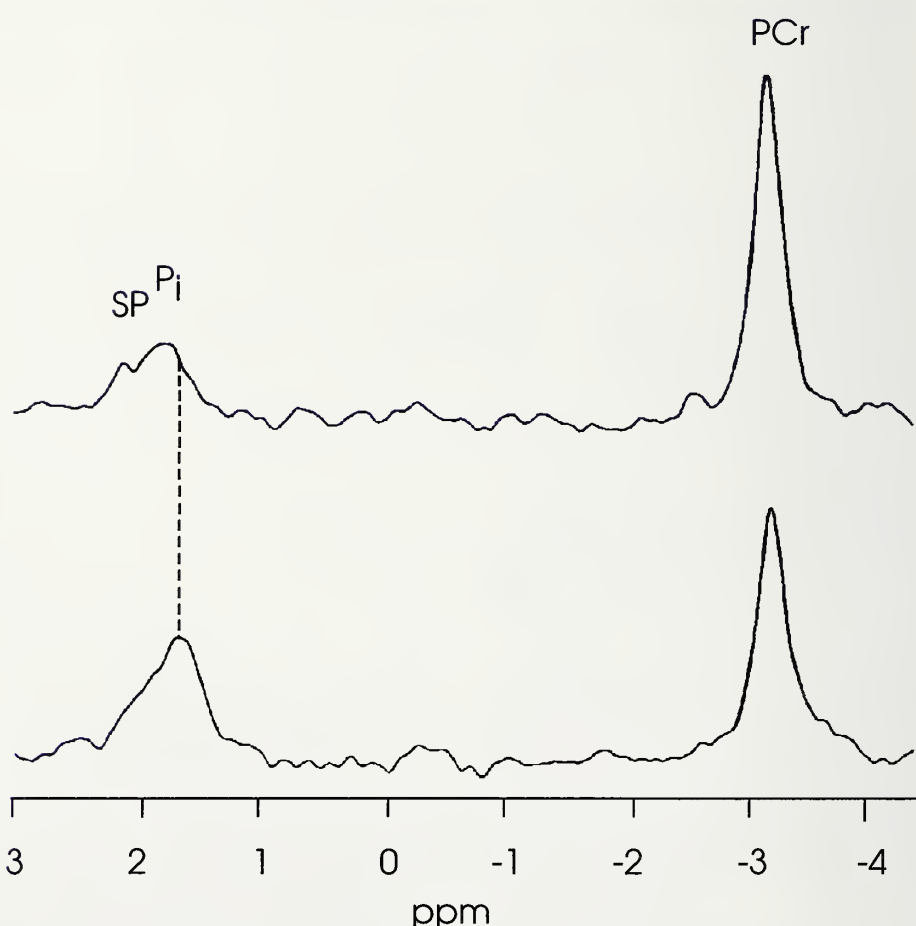
Figure 9 illustrates a typical time course of the variation of intracellular pH and Mg^{2+} . Within 10 minutes of exposure to elevated $[\text{Mg}^{2+}]_o$, $[\text{Mg}^{2+}]_i$ increased from 524 to 1,008 μM , while pH_i increased from 7.13 to 7.19. Continued exposure to elevated $[\text{Mg}^{2+}]_o$ further increased pH_i

to 7.26, while $[Mg^{2+}]_i$ increased to 1,164 μM . Reperfusing hearts with 1.2 mM $[Mg^{2+}]_o$ caused intracellular free Mg^{2+} and pH to return to control levels.

Table 6 demonstrates that perfusing hearts in the working mode with elevated $[Mg^{2+}]_o$ decreased the level of MgADP from 43 to 27 μM and reduced total ADP concentration from 73 to 38 μM . These decreases correspond to 37 and 48 percent declines in the levels of

MgADP and total ADP, respectively. MgADP concentration was calculated using equation 4 and assuming equilibrium of the creatinine kinase reaction. Total ADP levels were calculated using a K_d value for MgADP of 0.43 mM (Watts 1973) and the measured level of $[Mg^{2+}]_i$. A similar, but smaller, reduction in the levels of MgADP and total ADP was observed in hearts perfused in the Langendorff mode. In both prepa-

FIGURE 8b



Sections of ^{31}P NMR spectra showing the effects of elevated Mg^{2+} (4.8 mM) perfusate on pH_i , measured from the chemical shift difference between intracellular P_i and PCr resonances, along with appropriate (1.2 mM Mg^{2+}) perfusate controls. Other conditions and spectral acquisition parameters were the same as in figure 6. The increased separation between PCr and P_i resonances upon transfer to 4.8 mM Mg^{2+} demonstrate increased pH_i compared with controls (1.2 mM Mg^{2+}).

Table 5. Effects of elevated (Mg^{2+})_o on pH_i and (Mg^{2+})_i

Perfusion mode	(Mg^{2+}) _o (mM)	n	(Mg^{2+}) _i (mM)	(pH) _i
Langendorff (control)	1.2	9	0.65 ± 0.04	7.11 ± 0.01
Langendorff	4.8	7	1.21 ± 0.12*	7.24 ± 0.03*
Working (control)	1.2	5	0.60 ± 0.04	7.09 ± 0.02
Working	4.8	5	1.09 ± 0.5*	7.21 ± 0.04†

Means ± S.E.M.
*p<0.001; †p<0.02.

rations, the observed rise in CrP (table 4) and decline in ADP likely resulted from the rise in cytosolic pH (table 5), thereby pulling the reaction in favor of CrP synthesis.

The mechanism for [Mg^{2+}]_o-induced alkalinization of the cytosol is unclear; however, as mentioned previously, enhanced coronary flow

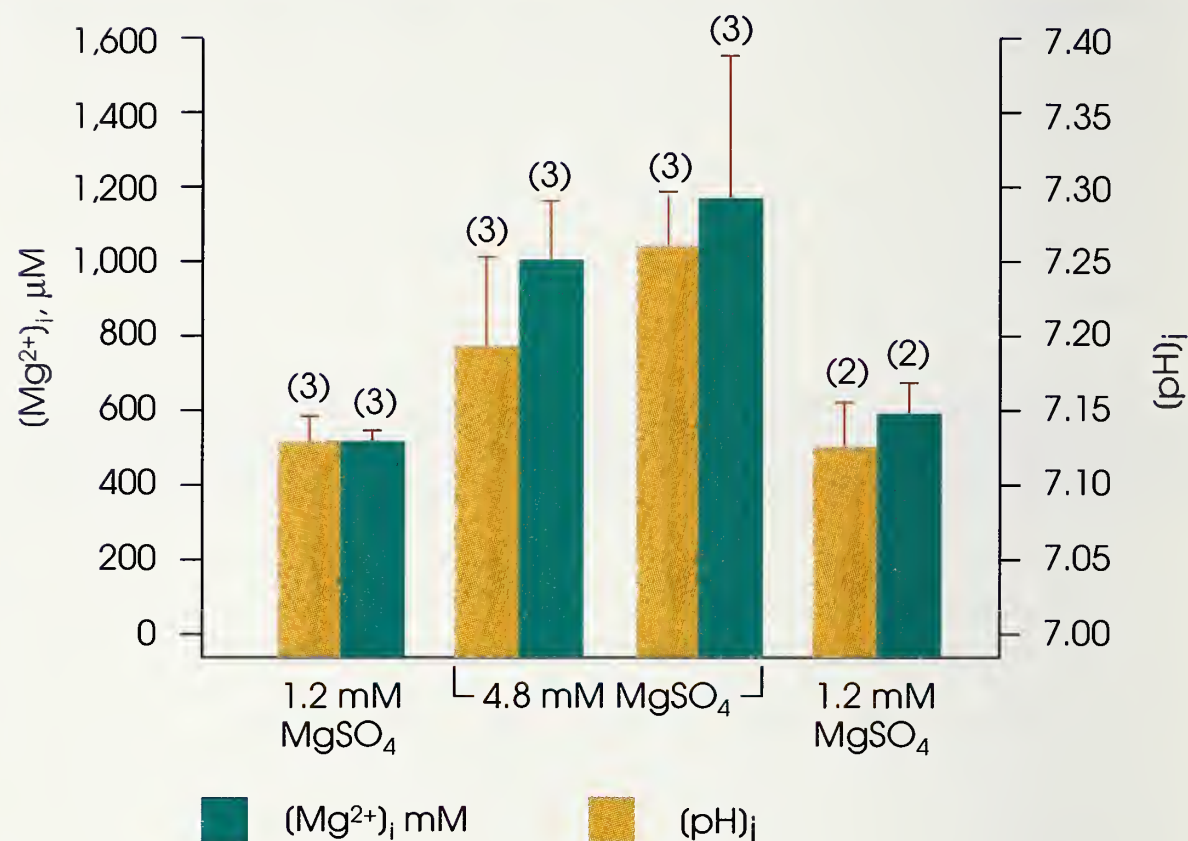
(table 2) may have contributed to the removal of metabolic acids. In the Langendorff preparation, the rise in the levels of CrP was also accompanied by a corresponding decline in the levels of cytosolic P_i, while ATP levels remained unchanged (table 4). Under these conditions, the combined effect of

Table 6. Effects of elevated (Mg^{2+})_o on calculated levels of ADP, free energy available from ATP hydrolysis, and the cytosolic phosphorylation potential

Perfusion mode	(Mg^{2+}) _o (mM)	(MgADP) (μ M)	(ADP) _i (μ M)	(ATP) (ADP)(P _i)	-ΔG/ΔE (kJ/mol)
Langendorff (Control)	1.2	22 ± 2.0	36 ± 3.5	40.2 ± 13	56.7 ± 0.61
Langendorff	4.8	17 ± 1.6	24 ± 2.0†	112 ± 24*	59.3 ± 0.72†
Working (Control)	1.2	43 ± 6.0	73 ± 8	(102 ± 11)	
Working	4.8	27 ± 5.0*	38 ± 7†	(165 ± 29)	

Paired t tests. Values in parentheses for working hearts correspond to the calculated ATP/ADP ratio.

*p<0.05; †p<0.01.

FIGURE 9

Effects of elevated $(\text{Mg}^{2+})_o$ on $(\text{pH})_i$ and $(\text{Mg}^{2+})_i$. ^{31}P NMR spectra were obtained on isolated rat hearts perfused in the presence of 1.2 or 4.8 mM MgSO_4 . The level of intracellular free Mg^{2+} and pH were calculated using equations 3 and 1, respectively. Results presented from left to right represent consecutive spectra obtained under the indicated conditions with essentially no delay between acquiring the respective spectra. Values are means \pm S.E.M. Values in parentheses indicate number of determinations.

decreased levels of P_i and ADP increased the cytosolic phosphorylation potential from 41 to 112 mM^{-1} and the free energy change of ATP hydrolysis from ~ 56.7 to 59.3 kJ/mol (table 6).

Similar analysis of working hearts was precluded by inability to distinguish quantitatively the resonances of P_i and sugar-phosphates. Nevertheless, the ATP/ADP ratio was determined. It increased by approximately 60 percent in response

to perfusion of hearts with elevated $[Mg^{2+}]_o$. Interestingly, working heart sugar-phosphate levels, which are undetectable in hearts perfused in the Langendorff mode, rose upon transfer to 4.8 mM $[Mg^{2+}]_o$. This change was accompanied by a 17 percent decline in the levels of ATP. At this time, it is unclear whether the rising sugar-phosphate level and decreasing ATP indicate an effect of $[Mg^{2+}]_i$ on ATP synthesis or utilization, or whether they simply

indicate cardiac distress at the higher workload.

DISCUSSION

Effects of $(Mg^{2+})_o$ on $(Ca^{2+})_i$ and Cell Geometry in Cultured VSMC Assessed by Image Analysis

Several lines of investigation have clearly shown that the level of $[Mg^{2+}]_o$ can modulate basal tone, myogenic tone, and contractile responsiveness of peripheral and cerebral VSMC *in vivo* and *in vitro* (Altura and Altura 1981, 1984, 1985b, 1990a,b; Nagai et al. 1988; Nishio et al. 1988, 1989). Previous studies have shown, too, that $[Mg^{2+}]_o$ can modulate Ca content, binding, and transport across VSMC membranes (Altura and Altura 1971, 1981, 1990b; Turlapaty and Altura, 1978; Sjögren et al. 1990). However, until the present digital image analysis studies, it was unclear whether $[Mg^{2+}]_o$ could either alter true $[Ca^{2+}]_i$ levels in VSMC or exert effects on cell geometry. For the first time, the studies reported here clearly demonstrate—at least for cultured rat aortic smooth muscle cells—that $[Mg^{2+}]_o$ can control both the distribution of $[Ca^{2+}]_i$ and the shape of VSMC.

In light of earlier results with vascular muscle, it is probably safe to assume that $[Mg^{2+}]_o$ exerts these actions on $[Ca^{2+}]_i$ and cell geometry by controlling plasma membrane permeability to external and internal Ca^{2+} and by modulating sarcoplasmic reticulum release of Ca^{2+} . The new data support the suggestion that Mg deficiency may play an important role in the pathogenesis of

such cardiovascular diseases as cardiac and cerebral ischemia, hypertension, atherosclerosis, and stroke as a consequence of its control of cellular and subcellular levels of Ca^{2+} as well as its ability to modulate cell geometry.

Effects of $(Mg^{2+})_o$ on Cardiac Hemodynamics

This study has employed ^{31}P NMR and reflectance spectrophotometry as noninvasive probes to characterize the cellular bioenergetic responses of isolated perfused hearts to alterations in the hemodynamic function caused by acute exposure to elevated levels of $[Mg^{2+}]_o$. The results of these hemodynamic studies (table 2) confirm previously reported negative chronotropic (Mordes and Wacker 1978; Altura and Altura 1985b; Nagai et al. 1988) and vasodilatory (Mordes and Wacker 1978; Altura and Altura 1984, 1985b, 1990b; Nagai et al. 1988; Nishio et al. 1989) effects of increased $[Mg^{2+}]_o$. The negative chronotropic effect is likely due to direct action on the sinoatrial node, causing a decreased rate of diastolic depolarization and production of pacemaker shifts (Seifen 1968). $[Mg^{2+}]_o$ -induced relaxation of coronary vascular smooth muscle has been reported to result from a direct relaxant action on vascular smooth muscle cells (Turlapaty and Altura 1980; Altura and Turlapaty 1982), interference with the action of various vasoconstrictive agents (Altura and Turlapaty 1982), and possible blockage of some sympa-

thetic ganglia (Stanbury 1948; Mordes and Wacker 1978).

While the observed effects of $[Mg^{2+}]_o$ on heart rate and coronary flow probably do not directly involve the myocyte, they appear to influence myocyte activity indirectly, e.g., enhancing coronary flow, thus increasing the delivery of O_2 and essential nutrients and improving the removal of metabolic waste products. It is important to point out, however, that even though $[Mg^{2+}]_o$ -induced vasodilation may indirectly affect myocyte function, this effect by itself cannot fully account for the effects of $[Mg^{2+}]_o$ on cardiac bioenergetics (see further discussion). Nuutinen et al. (1982) clearly showed, in isolated perfused rat hearts, that quite unlike Mg^{2+} induced vasodilation, vasodilation induced by adenosine concentrations up to 12 μM had no effect on tissue content of adenine nucleotides, creatine phosphate, creatine, or their ratios.

Elevated $[Mg^{2+}]_o$ had a positive inotropic effect, as shown by increased systolic pressure and cardiac output (due to increased coronary flow), despite pronounced bradycardia. These observations agree with results recently reported by James et al. (1987), who showed that intravenous infusion of $MgSO_4$ in intact baboons caused a serum Mg^{2+} increase of 3–4 mM and significantly increased cardiac output and stroke volume, while lowering heart rate. In addition, they observed that Mg^{2+} administration increased stroke work, indicating an

improvement in myocardial contractility.

A reduction in heart rate caused by exposure to elevated $[Mg^{2+}]_o$ would not by itself account for this improved cardiac output and systolic pressure. The observation of increased stroke work is new. When considered together with the NMR results and other findings, as discussed later, it strongly indicates an intracellular effect of Mg^{2+} on the myocyte.

Although some drugs such as calcium antagonists (Ca^{2+} entry blockers) can cause coronary vasodilation and a fall in heart rate (Schwartz et al. 1981; Fleckenstein 1983), these types of molecules do not exert the inotropic-like actions of Mg^{2+} , nor do they improve cardiac output and systolic pressure. On the other hand, classical inotropic agents, such as catecholamines, glucagon, and cardiac glycosides, do not produce direct coronary vasodilation or a fall in heart rate like Mg^{2+} . Thus, Mg^{2+} appears to be unique in its effects on cardiac hemodynamics at least in the isolated rat heart.

Because Mg^{2+} has generally been regarded as a negative inotropic agent, the results in this chapter and those of James et al. (1987) are initially surprising. While convincing evidence exists for the cardiodepressive effects of high concentrations (>8 mM) of $[Mg^{2+}]_o$, the evidence for such effects at lower levels (2–5 mM) is less clear (Mordes and Wacker 1978; Altura and Altura 1985b). Shine and Douglas (1974) reported that increasing $[Mg^{2+}]_o$ from 3

to 20 mM decreased the inotropic state of rat ventricular strips, independent of the level of Ca^{2+} in the perfusate. The experimental conditions of those studies, however, were far removed from those of our preparations. Ventricular strips were perfused at 24 °C with a flow rate (per gram of tissue) and heart rate equivalent to only 10 and 25 percent, respectively, of those reported here. Shine and Douglas (1975) subsequently reported little effect on the isolated rabbit ventricular strips when Mg^{2+} levels were <20 mM.

One possible explanation regarding our observation of a positive inotropic-like effect of $[\text{Mg}^{2+}]_o$ is offered by the earlier observation by Altura and Altura (1974) that adding 1.2 mM $[\text{Mg}^{2+}]_o$ to rat aortic strips in the presence of titrating amounts of Ca^{2+} caused a large increase in isometric contractile force, compared with that obtained when strips were perfused without additional Mg^{2+} . They suggested that Mg^{2+} may displace Ca^{2+} bound to intracellular sites (e.g., sarcoplasmic reticulum [SR], contractile proteins), thereby rendering it available for contraction. Our new findings, through image analysis of $[\text{Ca}^{2+}]_i$, support this notion.

The displacement of Ca^{2+} by Mg^{2+} may account for the effects of $[\text{Mg}^{2+}]_o$ on stroke volume. An increase in stroke volume strongly indicates a relaxation in wall tension, perhaps as a result of Mg^{2+} inducing Ca^{2+} release from troponin-binding sites during diastole. This relaxation would cause a rise in cytosolic

free Ca^{2+} that could then be translocated into the SR via membrane-bound Ca-ATPase, thereby increasing intracellular stores available for release during the next contractile event. The observation that Mg^{2+} can mediate Ca^{2+} - Ca^{2+} release in cardiac muscle (Rüegg 1987) is consistent with this suggestion.

Whereas elevated levels of $[\text{Mg}^{2+}]_o$ have been demonstrated to block efflux of ^{45}Ca in vascular smooth muscle (Altura and Altura 1981), which increases the level of cytosolic Ca^{2+} , it is distinctly possible that the inotropic effects of Mg^{2+} observed in the present study are due in part to such a phenomenon. Furthermore, it is well known that Mg^{2+} activates adenylate cyclase to form cyclic 3'5'-adenosine monophosphate (cAMP) in all cells, including cardiac muscle (Rüegg 1987). The activation of adenylate cyclase by elevations in the Mg:Ca ratio in mammalian cardiac muscle regulates the slow Ca^{2+} channels: The more cAMP formation, the more Ca^{2+} influx (Rüegg 1987). Although cAMP also tends to aid in the rebinding of Ca^{2+} to the SR, which might tend to cause relaxation, such a series of Mg^{2+} -mediated events could result in a greater amount of Ca^{2+} stored in the SR, primed and ready for release during late systole.

Added to these possibilities is the probability that an elevation in cytosolic free Mg^{2+} would result in more cross-bridges, hence greater tension development. A role for Mg^{2+} as a cofactor for enzyme activities involved in cross-bridging is

generally accepted, despite some controversy concerning the precise quantitative effects and interactions (Garfinkel and Garfinkel 1985; Garfinkel et al. 1986; Rüegg 1987).

Another possible explanation for the observed positive inotropic-like effects of $[Mg^{2+}]_o$ comes from results of the NMR studies shown in tables 5 and 6, which demonstrate a Mg^{2+} -induced alkalinization of the cytosol linked to an increased free energy change of ATP hydrolysis. Jacobus et al. (1982) examined the effect of respiratory and ischemia-induced acidosis on ventricular pressure development. They showed that a 50 percent reduction in developed pressure occurred when cytosolic pH declined from 7.22 to 7.00 and 7.13 for respiratory and ischemia-induced acidosis, respectively. These values are comparable to a 36 percent increase in systolic pressure observed in our working hearts perfused with elevated $[Mg^{2+}]_o$, coincident with an increase in cytosolic pH from 7.09 to 7.21 in our experiments.

Because Mg^{2+} is an essential co-factor for myosin ATPase, an increase in its concentration, together with a rise in cytosolic pH, may directly affect function of the contractile apparatus, as discussed. This suggestion is supported by results obtained by Poole-Wilson and Langer (1979), who showed that variations in cytosolic pH cause alterations in Ca^{2+} fluxes across the sarcolemmal membrane. In addition, it is known that Ca^{2+} responsiveness of the contractile proteins is modulated by pH_i (see Rüegg 1987 for review): Elevation in pH_i would

result in increased Ca^{2+} sensitivity; i.e., the length-tension curves would be shifted to the left as the pH_i goes up. Alternatively, the improved coronary flow observed in hearts perfused with elevated $[Mg^{2+}]_o$ may aid in the removal of metabolic acids.

More than likely, several of these suggested pathways and mechanisms act in concert as $[Mg^{2+}]_i$ rises to enhance myocardial function. By depleting cellular $[Mg^{2+}]$, alcohol would reverse these beneficial effects of Mg^{2+} on the heart.

Steady-State Levels of Oxymyoglobin and Oxidized Cytochrome aa₃ in Perfused Hearts

There is good evidence of heterogeneity in most tissues regarding perfusion and cellular metabolism (Chance et al. 1978; Steenbergen et al. 1978); therefore, optical measurements to determine the extent of oxidized cytochrome aa₃ integrated over a relatively wide area fail to detect a critical pO_2 level. Below this pO_2 , oxidative metabolism is rapidly inhibited, in contrast to that of isolated mitochondria. Steenbergen et al. (1978) showed that as a consequence of this heterogeneity, zones of severely hypoxic tissue occur with progressive hypoxia. Their observations explain the proportional decline in the extent of oxidized cytochrome aa₃ upon increasing hypoxia shown in figure 5. This heterogeneity is undetected simply because of the range covered by the optical measurement, an explanation that makes it unnec-

essary to postulate that cytochrome aa₃ may have a low affinity for O₂ in situ compared with that of isolated mitochondria (Tamura et al. 1986).

For hearts perfused in the Langendorff and working modes, 18 and 26 percent, respectively, of the epicardial layer was anoxic (table 4). The extent of this anoxia may indicate that the O₂-carrying capacity of blood-free media is insufficient to meet the oxidative demand of the heart. While this may occur at higher workloads, it seems unlikely that this occurs to a significant degree under the experimental conditions in this study. Neely and coworkers (1976) clearly showed that in isolated working hearts the rate-pressure product varies in a linear manner with O₂ consumption for workloads as high as 53×10^3 mmHg/minute. If O₂ availability were limiting, this relationship might well have been expected to be nonlinear.

Some groups have reported that a moderate extent of anoxia exists in excised and in situ tissues perfused with aqueous, perfluorocarbon, or blood-based media. For example, Tamura et al. (1986) recently reported observing approximately 20 percent reduced cytochrome aa₃ in isolated perfused rat hearts. They noted that this level increased at higher levels of O₂ consumption. In an earlier report, Hassinen and Hiltunen (1975) had observed that reduced cytochrome aa₃ was 22 percent in rat hearts perfused under conditions similar to those described in this

report. In agreement with these findings is a report by Figulla et al. (1984), who observed a range of approximately 15–22 percent reduced cytochrome aa₃ in isolated guinea pig hearts, depending on the method of analysis employed.

Studies on in situ brain have also reported a moderate level of reduced cytochrome aa₃. Heinrich et al. (1984) reported resting levels of 16 and 40 percent reduced cytochrome aa₃ in guinea pig brain perfused in situ with blood-free medium in the presence and absence of glucose, respectively. The 16 percent level is close to the 13–14 percent reduced cytochrome aa₃ in rat brain perfused with a perfluorocarbon medium reported by Piantadosi and Jobsis-Vandervliet (1984). Earlier, Jobsis et al. (1977) had reported that a resting level of 9–30 percent reduced cytochrome aa₃ in in situ blood-perfused cat brain was based on oxidative shifts caused by spreading depression or direct cortical stimulation. Oxidative shifts of brain in situ were also observed in response to hyperoxia (Peretsman and Rosenthal 1977) and during recovery from hypoxic or ischemic episodes (Palladino et al. 1983; Kariman et al. 1983; Wienspergen and Gygaz 1983).

The observation by Tamura et al. (1978) of a 1:1 relationship between the levels of oxymyoglobin and extent of oxidized cytochrome aa₃ in response to progressive hypoxia has been interpreted to indicate the presence of steep O₂ gradients within the tissue. This interpretation is reasonable, since the much

greater affinity of cytochrome aa₃ for O₂ than for myoglobin would ensure a lower steady-state level of oxymyoglobin for a given level of oxidized cytochrome aa₃, if, in fact, no gradient existed. In apparent contrast to these findings, our results (figure 5) illustrate a nonlinear relationship between the extent of oxidized cytochrome aa₃ and the level of oxymyoglobin. This observation agrees remarkably well with findings reported by Caspary et al. (1985) and Tamura et al. (1986).

Careful inspection of figure 5 reveals that cytochrome aa₃ remains almost fully oxidized until the level of oxymyoglobin drops below 75 percent; by a level of 50 percent oxidized cytochrome aa₃, oxymyoglobin levels have declined to 25 percent. These findings, which indicate that with progressive hypoxia, the magnitude of intracellular O₂ gradients decline, are consistent with the evidence that perfusion of tissues is regulated so as to maintain them on the "brink of anoxia" (Steenbergen et al. 1978).

An important observation made here was that the difference between the extent of oxidized cytochrome aa₃ and oxymyoglobin increased with increasing workload. We emphasize this point because we believe it represents a means of noninvasively identifying the "adequacy of response" of a change in coronary flow to a change in workload. Monitoring changes in this difference, together with changes in coronary flow, contractility, and O₂ consumption, would enable determination of whether an observed

change in coronary flow was minimally adequate to meet tissue oxygenation requirements without compromising contractility. An increase in this difference would indicate that coronary flow had not increased by the minimal amount needed to meet the increased oxidative demand of the heart. Conversely, a decrease in this difference would indicate that coronary flow had improved by an amount more than that required to meet increased demand.

This interpretation is likely oversimplified and would depend to some degree upon the physiological significance of maintaining a portion of the tissue anoxic. For example, the observation of increasing difference in the extent of oxidized cytochrome aa₃ and oxymyoglobin with increased workload may be indicative of reserve oxidative capacity of the tissue. If this were true, then the observation by Tamura et al. (1986) that the extent of reduced cytochrome aa₃ increased with increasing O₂ consumption would indicate that, under their experimental conditions and in the context of the present discussion, the response of coronary flow to increased workload was grossly inadequate. The fact that, in this case, O₂ consumption was able to increase with increased workload indicates that, at a given workload, the heart is capable of sustaining function over a wide range of coronary flows.

The primary means of enhancing the delivery of O₂ and other essential nutrients to the heart upon in-

creased metabolic demand is augmenting coronary flow rather than by increasing the degree of O₂ extraction (Olsson and Steinhart 1982). From an evolutionary perspective, it would appear desirable to have a range of responses of coronary flow to increased workload, rather than a precise 1:1 relationship, thereby permitting adaptation to the need to modulate delivery to the heart of other essential nutrients synthesized in the peripheral circulation (e.g., creatine, hormones), independent of the need for O₂ delivery. The lower limit of this range would correspond to the minimum flow needed to maintain the tissue on the brink of anoxia. Accordingly, our observation that [Mg²⁺]_o can increase coronary flow, independent of the O₂ needs of the tissue, is evidence for the existence of physiological mechanisms capable of responding to the proposed needs.

Effects of Elevated (Mg²⁺)_o on (Mg²⁺)_i in Perfused Rat Hearts

An important finding made here is that acute exposure of the heart to elevated levels of [Mg²⁺]_o can cause a significant and rapid rise in the level of [Mg²⁺]_i (figure 9, table 5). However, studies of rat heart by Polimeni and Page (1973) demonstrated a slow exchange of [Mg²⁺]_i with [Mg²⁺]_o; the single rate of exchange at 37 °C having a $t_{1/2}$ of 182 minutes. At this rate of exchange, and based on a Mg content in rat heart of 17.3±0.2 mM/kg cell water (Polimeni and Page 1973), the increase in [Mg²⁺]_i observed here (table 5) would require 10–12 min-

utes. While this value might be within the range of time obtained by the NMR measurements, the hemodynamic effects of elevated [Mg²⁺]_o were observed to occur within just 1–3 minutes after exposure to this medium.

The steep rise in [Mg²⁺]_i in response to elevated [Mg²⁺]_o would indicate that (a) the increase observed in [Mg²⁺]_i resulted primarily from a redistribution of Mg²⁺ within intracellular stores (i.e., from mitochondria and SR to cytoplasm) rather than as a result of a net increase in tissue levels, (b) the effects of elevated [Mg²⁺]_o on cardiac function result from its action at extracellular sites (e.g., atrioventricular node), thus are independent of a secondary rise in [Mg²⁺]_i levels, or (c) the increase in [Mg²⁺]_i is a consequence of an increase in Mg²⁺ influx. As noted, while the action of elevated [Mg²⁺]_o on coronary flow and heart rate probably does not directly involve the myocyte, the positive inotropic-like effects observed are not readily explained by the effects of Mg²⁺ on these parameters.

The reported basal values of [Mg²⁺]_i in myocardial tissue vary widely, from 0.4 to 4 mM (see Garfinkel et al. 1986 for review). Ion-selective electrode measurements of [Mg²⁺]_i in cardiac tissue vary from 0.4 to 3.5 mM (for review, see Altura and Altura 1990b), apparently due to significant interference from Na⁺ and K⁺, which results in calibration problems. Blatter and McGuigan (1986) recently concluded that cardiac [Mg²⁺]_i detected by ion-selective microelectrodes must lie within

the range of 0.4–0.9 mM. More recently, Wittenberg et al. (1988) obtained a free Mg²⁺ level of 0.5 mM in isolated rat cardiac myocytes. The basal values of free Mg²⁺ measured in isolated Langendorff and working hearts in the study reported here are comparable to those obtained by Gupta and Gupta (1987) in other tissues.

The observed increase in [Mg²⁺]_i with an increase in [Mg²⁺]_o directly shows that [Mg²⁺]_i in cardiac cells can rapidly respond to acute changes in the external environment. The mechanism of these changes--whether it involves influx of Mg²⁺ across the sarcolemma or a mere redistribution of [Mg²⁺]_i--remains to be investigated. The mechanism for regulation of [Mg²⁺]_i is unknown, although an electroneutral 2Na⁺:1Mg²⁺ exchange in muscle cells has been postulated (Gupta and Moore 1980). Our observation of simultaneous increases in cardiac free Mg²⁺ and phosphorylation potential is the first of its kind; it supports a role for [Mg²⁺]_i in the management of cardiac phosphorylation potential (see further discussion). It also demonstrates the influence of external Mg²⁺ ion on cellular bioenergetics via the intermediary of internal free Mg²⁺, and possibly also via pH_i.

Also worthy of mention is an increase in [Mg²⁺]_i observed during ischemia in some of our preliminary experiments, in which the pH_i was lower and not elevated, in contrast to the elevated response to 4.8 mM Mg²⁺ in this study. The increase in free Mg²⁺ with acute ischemia was

reversible upon reperfusion in some experiments, as it was with increases due to a change in [Mg²⁺]_o, suggesting that irreversible ischemic injury occurs only after a delay of several minutes.

Effects of Mg²⁺ on Cardiac Energetics

Elevated [Mg²⁺]_o significantly modifies the response of cellular energetics and coronary flow to a given workload. Our results indicate that associated with an improved inotropic state and increased coronary flow (table 2), perfusing hearts with elevated [Mg²⁺]_o improved their oxygenation state (table 4), simultaneously increasing the cytosolic phosphorylation potential and free energy change of ATP hydrolysis (table 6). As noted, the observed increase in cytosolic pH and [Mg²⁺]_i levels may be significant. The observed rise in CrP levels concomitant with increased pH_i is consistent with evidence that the creatine kinase reaction is near equilibrium (Bittl and Ingwall 1985).

The molecular mechanisms linking the generation of metabolic energy, nutrient delivery, and efficiency of contractility to changes in workload remain ill defined. Nishiki et al. (1978) proposed that the phosphorylation state of cytosolic adenine nucleotides are in near equilibrium with sites I and II of the respiratory chain. Nuutinen et al. (1982) also showed that coronary flow and O₂ consumption varied inversely and in a linear fashion with the log of the phosphorylation potential in response to an increase

in workload, a change in Ca^{2+} level, or the presence of a metabolic inhibitor.

More recently, investigators using NMR have observed a poor relationship or lack of relationship between respiratory rates and phosphorylation state of cytosolic adenine nucleotides (Matthews et al. 1982; Balaban et al. 1986; Katz et al. 1987, 1988). In another NMR study such a relationship was seen only under conditions of limited O_2 availability (Clarke and Willis 1987). For example, using the work-jump technique to vary workload, Katz et al. (1987, 1988) observed no changes in the levels of CrP, ATP, or P_i and only a small increase in the CrP/ATP ratio in rat hearts perfused with glucose. In contrast, NAD(P)H surface fluorescence increased, suggesting that increases in the mitochondrial NADH redox state regulated respiration at higher workloads (Katz et al. 1987).

Further evidence inconsistent with the near-equilibrium hypothesis was reported by Matthews et al. (1982), who observed that perfusion of rat hearts with various metabolic substrates produced large differences in phosphorylation potential at comparable levels of mechanical activity. An increase in mechanical activity by infusion of positive inotropic agents had little effect on the phosphorylation potential. From et al. (1986) also observed that at a fixed workload the phosphorylation potential could vary widely, depending on the substrate being metabolized.

Although the experimental design employed here was not in-

tended to explore the control of respiration, a comparison of results with those reported by Starnes et al. (1985) is useful. That group observed substrate-dependent differences in the cytosolic phosphorylation potential at a given workload. Higher levels were observed when hearts were perfused with acetate or palmitate than when perfused with glucose. However, when the workload was varied, an inverse linear relationship was observed between the rate of O_2 consumption and the log of the phosphorylation potential, thereby yielding two sets of nearly parallel lines. These results were interpreted to indicate that at different metabolic set points, i.e., different levels of phosphorylation potentials, the heart may exhibit similar degrees of mechanical performance and rates of respiration, depending on the substrate being metabolized. In this regard, the effect of $[\text{Mg}^{2+}]_o$ on the phosphorylation potential, as observed in this study, appears similar to the effects of oxidizing acetate or palmitate. In both cases, increases in the phosphorylation potential were significant, suggesting that $[\text{Mg}^{2+}]_i$ may also alter the set point at which rates of respiration and contractility are linked. In contrast to those reported by Starnes et al. (1985), our results clearly demonstrate that with a rise in the phosphorylation potential, the inotropic state of the heart and its efficiency appear to be improved.

It is apparent from the results presented here that $[\text{Mg}^{2+}]_o$ exerts a

strong modulating effect not only on coronary flow, but on cellular energy levels, utilization of O₂, and efficiency of contractility. An important observation of this study is that the combination of effects that Mg²⁺ has on the myocardium is unlike that of any other known agent.

At present, the cardiotonic drugs in clinical use increase contractile force at a given sarcomere length either by increasing free myoplasmic [Ca²⁺]_i or by increasing the Ca²⁺ sensitivity of the myofilaments (Rüegg 1987). An ideal cardiac drug would unload the heart and increase force development in the ischemic or failing heart by increasing Ca²⁺ sensitivity, *not by raising* [Ca²⁺]_i. The elevation of [Ca²⁺]_i as is accomplished by catecholamines, glucagon, phosphodiesterase inhibitors, and cardiac glycosides puts already compromised patients at risk because Ca²⁺ overload often results in cardiac cell death. Unlike other drugs, Mg²⁺ increases stroke volume (table 2; Friedman et al. 1987; James et al. 1987), reduces wall tension (table 2), lowers myocardial O₂ consumption (table 2; Friedman et al. 1987), lowers heart rate (table 2; Iseri et al. 1984; Altura and Altura 1985b; Friedman et al. 1987), increases coronary blood flow (table 2), lowers peripheral vascular resistance (Altura and Altura 1985b, 1990b; Nagai et al. 1988; Nishio et al. 1989), dilates the arterioles in the microcirculation (Nagai et al. 1988; Nishio et al. 1989), attenuates the contractile activity of constrictor agents (Altura and Altura 1981, 1984, 1990b), and modulates Ca²⁺ re-

lease and influx at the sarcolemma (table 1; Turlapati and Altura 1978; Altura and Altura 1971, 1981, 1985b, 1990b).

ACKNOWLEDGMENTS

The work reported in this article was supported in part by National Institutes of Health grants HL 29600 (to Burton Altura) and DK 32030 (to Raj Gupta) and by National Institute on Alcohol Abuse and Alcoholism grant AA 08674 (to Burton Altura).

REFERENCES

- Altura, B.M., and Altura, B.T. Influence of magnesium on drug-induced contractions and ion content in rabbit aorta. *Am J Physiol* 220:938–944, 1971.
- Altura, B.M., and Altura, B.T. Magnesium and contraction of arterial smooth muscle. *Microvasc Res* 7:145–155, 1974.
- Altura, B.M., and Altura, B.T. Magnesium ions and contraction of vascular smooth muscles: Relationship to some vascular diseases. *Fed Proc* 40:2672–2679, 1981.
- Altura, B.M., and Altura, B.T. Magnesium, electrolyte transport and coronary vascular tone. *Drugs* 28(suppl 1):120–142, 1984.
- Altura, B.M., and Altura, B.T. New perspectives on the role of magnesium in the pathophysiology of the cardiovascular system. I. Clinical aspects. *Magnesium* 2:226–244, 1985a.
- Altura, B.M., and Altura, B.T. New perspectives on the role of magnesium in the pathophysiology of the cardiovascular system. II. Experimental aspects. *Magnesium* 4:245–271, 1985b.

- Altura, B.M., and Altura, B.T. Role of magnesium in pathogenesis of high blood pressure: Relationship to its actions on cardiac and vascular smooth muscle. In: Laragh, J.H., and Brenner, B.M., eds. *Hypertension: Pathophysiology, Diagnosis and Management*. Vol. I. New York: Raven Press, 1990a. pp. 1003–1025.
- Altura, B.M., and Altura, B.T. Magnesium and the cardiovascular system: Experimental and clinical aspects updated. In: Sigel, H., and Sigel, A., eds. *Metal Ions in Biological Systems: Compendium on Magnesium and its Role in Biology, Nutrition, and Physiology*. Vol. 26. New York: Marcel Dekker, Inc., 1990b. pp. 359–416.
- Altura, B.M.; Altura, B.T.; and Carella, A. Magnesium deficiency-induced spasms of umbilical vessels: Relation to preeclampsia, hypertension, growth retardation. *Science* 221:376–378, 1983.
- Altura, B.M.; Altura, B.T.; Gebrewold, A.; Ising, H.; and Günther, T. Magnesium deficiency and hypertension: Correlation between magnesium-deficient diets and microcirculatory changes in situ. *Science* 223:1315–1317, 1984.
- Altura, B.M., and Turlapaty, P.D.M.V. Withdrawal of magnesium enhances coronary arterial spasms produced by vasoactive agents. *Br J Pharmacol* 77:649–659, 1982.
- Altura, B.T.; Brust, M.; Bloom, S.; Barbour, R.L.; Stempak, J.G.; and Altura, B.M. Magnesium dietary intake modulates blood lipid levels and atherogenesis. *Proc Natl Acad Sci USA* 87:1840–1844, 1990.
- Balaban, R.S.; Kantor, H.L.; Katz, L.A.; and Briggs, R.W. Relation between work and phosphate metabolites in the in vivo paced mammalian heart. *Science* 232:1121–1123, 1986.
- Barbour, R.L.; Sotak, C.H.; Levy, G.C.; and Chan, S.H.P. Use of gated perfusion to study early effects of anoxia on energy metabolism: A new ^{31}P NMR method. *Biochemistry* 23:6053–6062, 1984.
- Bittl, J.A., and Ingwall, J.S. Reaction rates of creatine kinase and ATP synthesis in the isolated rat heart. *J Biol Chem* 260:3512–3517, 1985.
- Blatter, L.A., and McGuigan, J.A.S. Free intracellular magnesium concentration in ferret ventricular muscle measured with ion selective microelectrodes. *Q J Exp Physiol* 71:467–473, 1986.
- Bloom, S. Coronary arterial lesions in magnesium deficient hamsters. *Magnesium* 4:82–95, 1985.
- Butler, W.L. Absorption spectroscopy of biological materials. *Methods Enzymol* 24b:3–25, 1972.
- Caspary, L.; Hoffman, J.; Ahmad, H.R.; and Lubbers, D.W. Multicomponent analysis of reflection spectra from the guinea pig heart for measuring tissue oxygenation by quantitative determination of oxygen saturation of myoglobin and of the redox state of cytochrome aa₃, c, and b. In: Kruezer, F.; Cain, S.M.; Turek, Z.; and Goldstick, T.K. *Oxygen Transport to Tissue*. Vol. 7. New York: Plenum Press, 1985. pp. 263–270.
- Chance, B.; Barlow, C.; Nakase, Y.; Takeda, H.; Mayevsky, A.; Fischetti, R.; Grahan, N.; and Sorge, J. Heterogeneity of oxygen delivery in normoxic and hypoxic states: A fluorometer study. *Am J Physiol* 235:H809–H820, 1978.
- Clarke, K., and Willis, R.J. Energy metabolism and contractile function in rat heart during graded, isovolumic perfusion using ^{31}P nuclear magnetic

resonance spectroscopy. *J Mol Cell Cardiol* 19:1153–1160, 1987.

Cobbold, P.H., and Rink, T.J. Fluorescence and bioluminescence measurements of cytoplasmic free calcium. *Biochem J* 248: 313–328, 1987.

Figulla, H.R.; Hoffmann, J.; and Lubbers, D.W. Evaluation of reflection spectra of the isolated heart by multi-component spectra analysis in comparison to other evaluating methods. In: Lubbers, D.W.; Acker, H.; Leniger-Follet, E.; and Goldstick, T.K., eds. *Oxygen Transport to Tissue*. Vol. 5. New York: Plenum Press, 1984. pp. 821–830.

Fleckenstein, A. *Calcium Antagonism in Heart and Smooth Muscle*. New York: Wiley, 1983.

Friedman, H.S.; Nguyen, T.N.; Mokroau, A.M.; Barbour, R.L.; Murakawa, T.; and Altura, B.M. Effects of magnesium chloride on cardiovascular hemodynamics in the neurally-intact dog. *J Pharmacol Exp Ther* 243:126–130, 1987.

From, A.H.L.; Petein, M.A.; Michurski, S.P.; Zimmer, S.D.; and Ugurbil, K. ³¹P NMR studies of respiratory regulation in the intact myocardium. *FEBS Lett* 206:257–261, 1986.

Gadian, D.G.; Radda, G.K.; Dawson, J.; and Wilkie, D.R. pH_i measurements of cardiac and skeletal muscle using ³¹P NMR. In: *Intracellular pH: Its Measurement, Regulation and Utilization in Cellular Functions*. New York: Alan R. Liss, Inc., 1982. pp. 61–67.

Garfinkel, L.; Altschuld, R.A.; and Garfinkel, D. Magnesium in cardiac energy metabolism. *J Mol Cell Cardiol* 18:1003–1013, 1986.

Garfinkel, L., and Garfinkel, D. Magnesium regulation of the glycolytic

pathway and the enzymes involved. *Magnesium* 4:60–72, 1985.

Gibbs, C. The cytoplasmic phosphorylation potential. *J Mol Cell Cardiol* 17:727–731, 1985.

Giesen, J., and Kammermeir, H. Relationship of phosphorylation potential and oxygen consumption in isolated perfused rat hearts. *J Mol Cell Cardiol* 12:891–907, 1980.

Gupta, R.K., and Benovic, J.L. Magnetic resonance studies of the interaction of divalent cations with 2,3-biophosphoglycerate. *Biochem Biophys Res Commun* 84:130–137, 1978.

Gupta, R.K., and Gupta, P. ³¹P NMR measurement of intracellular free magnesium in cells and organisms. In: Gupta, R.K., ed. *NMR Spectroscopy of Cells and Organisms*. Vol. II. Boca Raton: CRC Press, 1987. pp. 33–43.

Gupta, R.K.; Gupta, P.; and Moore, R.D. NMR studies of intracellular metal ions in intact cells and tissues. *Ann Rev Biophys Bioeng* 13:221–246, 1984.

Gupta, R.K., and Moore, R.D. ³¹P NMR studies of the interaction of intracellular free Mg²⁺ in intact frog skeletal muscle. *J Biol Chem* 255:3987–3993, 1980.

Hassinen, I.E., and Hiltunen, K. Respiratory control in isolated perfused rat heart. Role of the equilibrium relations between the mitochondrial electron carriers and the adenylate system. *Biochim Biophys Acta* 408:319–330, 1975.

Hearse, D.J.; Stewart, D.A.; and Braimbridge, M.V. Myocardial protection during ischemic cardiac arrest. The importance of magnesium in cardio-plegic infusates. *J Thoracic Cardiovasc Surg* 75:877–885, 1978.

Heinrich, U.; Yu, B.; Hoffmann, J.; and Lubbers, D.W. The effect of glucose on the oxygen supply of the blood-free perfused guinea pig brain as measured by reflection spectra and PO₂ histograms. In: Lubbers, D.W.; Acker, H.; Leninger-Follet, E.; and Goldstick, T.K., eds. *Oxygen Transport to Tissue*. Vol. 5. New York: Plenum Press, 1984. pp. 261–271.

Hess, P.; Metzger, P.; and Weingart, R. Free magnesium in sheep, ferret and frog striated muscle at rest measured with ion-selective micro-electrodes. *J Physiol Lond* 33:173–188, 1982.

Iseri, L.T.; Chung, P.; and Tobsis, J. Magnesium therapy for intractable ventricular tachyarrhythmias in normomagnesemic patients. *West J Med* 138:823–828, 1984.

Jacobus, W.E.; Pores, I.H.; Lucas, S.K.; Weisfeldt, M.L.; and Flaherty, J.T. Tight coupling of intracellular pH and ventricular performance. *J Mol Cell Cardiol* 10:39, 1978.

Jacobus, W.E.; Pores, I.H.; Lucas, S.K.; Weisfeldt, M.L.; and Flaherty, J.T. Intracellular acidosis and contractility in the normal and ischemic heart examined by ³¹P NMR. *J Mol Cell Cardiol* 14(suppl. 3):13–20, 1982.

James, M.F.M.; Cork, R.C.; and Dennett, J.E. Cardiovascular effects of magnesium sulphate in the baboon. *Magnesium* 6:314–324, 1987.

Jobsis, F.F.; Keizer, J.H.; LaManna, J.C.; and Rosenthal, M. Reflectance spectrophotometry of cytochrome aa₃ in vivo. *J Appl Physiol* 43:858–872, 1977.

Kariman, K.; Jobsis, F.F.; and Saltzman, H.A. Cytochrome a, a₃ reoxidation.

Early indicator of metabolic recovery from hemorrhagic shock in rats. *J Clin Invest* 72:180–191, 1983.

Katz, L.A.; Koretsky, A.P.; and Balaban, R.S. A mechanism of respiratory control in the heart: A ³¹P NMR and NADH fluorescence study. *FEBS Lett* 221:270–276, 1987.

Katz, L.A.; Koretsky, A.P.; and Balaban, R.S. Activation of dehydrogenase activity and cardiac respiration: A ³¹P NMR study. *Am J Physiol* 255:H185–H188, 1988.

Kobayashi, K., and Neely, J.R. Control of maximum rates of glycolysis in rat cardiac muscle. *Circ Res* 44:166–175, 1979.

Krebs, H.A., and Henseleit, K. Untersuchungen über die Harnstoffbildung in Tierkörper. *Hoppe-Seyler's Z Physiol Chem* 210:33–36, 1932.

Kubelka, P., and Munk, F. Ein Beitrag Zur Optik der Farbanstriche. *Z Tech Physik* 12:593–601, 1931.

Matthews, P.M.; Williams, S.R.; Seymour, A.M.; Schwartz, A.; Dube, G.; Gadian, D.G.; and Radda, G.K. A ³¹P NMR study of some metabolic and functional effects of the inotropic agents epinephrine and ouabain, and the ionophore R022985 (x537A) in the isolated, perfused rat heart. *Biochim Biophys Acta* 720:163–171, 1982.

Mordes, J.P., and Wacker, W.E.C. Excess magnesium. *Pharmacol Rev* 29:273–300, 1978.

Nagai, I.; Gebrewold, A.; Altura, B.T.; and Altura, B.M. Magnesium salts exert direct vasodilator effects on rat cremaster muscle microcirculation. *Arch Intern Pharmacodyn* 294:194–214, 1988.

- Neely, J.R., and Rovetto, M.J. Techniques for perfusing rat hearts. *Method Enzymol* 39:43–60, 1975.
- Neely, J.R.; Whitmer, K.M.; and Mochizaki, S. Effects of mechanical activity and hormones on myocardial glucose and fatty acid utilization. *Circ Res* 38(suppl 1):I22–I30, 1976.
- Nishiki, K.; Erecinska, M.; and Wilson, D.F. Energy relationships between cytosolic metabolism and mitochondrial respiration in rat hearts. *Am J Physiol* 234:C73–C81, 1978.
- Nishio, A.; Gebrewold, A.; Altura, B.T.; and Altura, B.M. Comparative effects of magnesium salts on reactivity of arterioles and venules to constrictor agents. An insitu study on microcirculation. *J Pharmacol Exp Ther* 246:859–865, 1988.
- Nishio, A.; Gebrewold, A.; Altura, B.M.; and Altura, B.T. Comparative vasodilator effects of magnesium salts on mesenteric arterioles and venules. *Arch Intern Pharmacodyn* 298:139–163, 1989.
- Nuutinen, E.M.; Nishiki, K.; Erecinska, M.; and Wilson, D.F. Role of mitochondrial oxidative phosphorylation in regulation of coronary blood flow. *Am J Physiol* 243:H159–H169, 1982.
- Olsson, R.A., and Steinhart, C.K. Metabolic regulation of coronary blood flow. *Physiologist* 25:51–55, 1982.
- Oshino, N.; Sugano, T.; Oshino, R.; and Chance, B. Mitochondrial function under hypoxic conditions: The steady states of cytochrome a + a₃ and their relation to mitochondrial energy states. *Biochim Biophys Acta* 368:298–310, 1974.
- Palladino, W.G.; Proctor, H.J.; and Jobsis, F.F. Effect of hypothermia during hypoxic hypotension on cerebral metabolism. *J Surg Res* 34:388–393, 1983.
- Peretsman, S.J., and Rosenthal, M. Brain cytochrome a, a³ redox states measured in situ in chronic cat preparations: Effects of hyperoxia and direct cortical stimulation. *Brain Res* 128:553–558, 1977.
- Piantadosi, C.A., and Jobsis-Vandervliet, F.F. Spectrophotometry of cerebral cytochrome a, a₃ in bloodless rats. *Brain Res* 305:89–94, 1984.
- Polimeni, P.I., and Page, E. Magnesium in heart muscle. *Circ Res* 33:367–374, 1973.
- Poole-Wilson, P.A., and Langer, G.A. Effects of acidosis on mechanical function and Ca⁺⁺ exchange in rabbit myocardium. *Am J Physiol* 236:H525–H533, 1979.
- Ramee, S.R.; While, C.J.; Svinaric, J.T.; Watson, T.D.; and Fox, R.F. Torsades de points and magnesium deficiency. *Am Heart J* 109:164–167, 1985.
- Rasmussen, H.S.; Norregard, P.; Lindeneg, O.; McNair, P.; Backer, V.; and Balslev, S. Intravenous magnesium in acute myocardial infarction. *Lancet* 1:234–236, 1986.
- Rosing, J., and Slater, E.C. The value of ΔG for the hydrolysis of ATP. *Biochim Biophys Acta* 267:275–290, 1972.
- Rüegg, J.C. *Calcium in Muscle Activation*. New York: Springer Verlag, 1987.
- Ryzen, E.; Wagner, P.W.; Singer, F.R.; and Rude, R.K. Magnesium deficiency in a medical ICU population. *Critical Care Med* 13:19–21, 1985.
- Savisky, A.B., and Golay, M. Smoothing and differentiation of data by simplified least squares procedures. *Anal Chem* 36:1627–1639, 1964.

- Schwartz, A.; Grupp, G.; Millard, R.W.; Grupp, I.L.; Lathrop, D.A.; Matlib, M.A.; Vaghy, P.L.; and Alle, J.R. Calcium-channel blockers: Possible mechanisms of protective effects on the ischemic myocardium. In: Weiss, G.B., ed. *New Perspectives on Calcium Antagonists*. Washington, DC: American Physiological Society, 1981. pp. 191-210.
- Seifen, E. Dependency on Mg and Ca concentration of cycle length in spontaneously beating guinea-pig atria. *Pflügers Arch Eur J Physiol* 303:46-56, 1968.
- Shine, K.I., and Douglas, A.M. Magnesium effect on ionic exchange and mechanical function in rat ventricle. *Am J Physiol* 227:317-324, 1974.
- Shine, K.I., and Douglas, A.M. Magnesium effects in rabbit ventricle. *Am J Physiol* 228:1545-1554, 1975.
- Shine, K.I. Myocardial effects of magnesium. *Am J Physiol* 237:H413-H423, 1979.
- Sjogren, A.; Edvinsson, L.; and Fallgren, B. Magnesium deficiency in coronary artery disease and cardiac arrhythmias. *J Intern Med* 226(4):213-222, 1989.
- Snow, T.R.; Kleinmann, L.H.; LaManna, J.C.; Wechsler, A.S.; and Jobsis, F.F. Responses of cyt aa₃ in the in situ canine heart to transient ischemia episodes. *Bas Res Cardiol* 76:289-304, 1981.
- Stanbury, J.B. The blocking action of magnesium ion on sympathetic ganglia. *J Pharmacol Exp Ther* 93:52-62, 1948.
- Starnes, J.W.; Wilson, D.F.; and Erecinska, M. Substrate dependence of metabolic state and coronary flow in perfused rat heart. *Am J Physiol* 249:H799-H806, 1985.
- Steenbergen, C.; Delleeuw, G.; and Williamson, J.R. Analysis of control of glycolysis in ischemic hearts during heterogeneous zones of anoxia. *J Mol Cell Cardiol* 10:617-639, 1978.
- Sunamori, M.; Suzuki, A.; and Harrison Jr., C.E. Effect of magnesium in cardioplegic solution upon hypothermic ischemic myocardial mitochondria. *Jpn Circ J* 44:81-86, 1980.
- Tamura, M.; Oshino, N.; Chance, B.; and Silver, I.A. Optical measurements of intracellular oxygen concentration of rat heart in-vitro. *Arch Biochem Biophys* 191:8-22, 1978.
- Tamura, M.; Sieyarua, A.; and Huzeki, O. Spectroscopic characteristics of rat skeletal and cardiac tissues in the visible and near-infrared region. In: Silver, I.A., and Silver, A., eds. *Oxygen Transport to Tissue*. Vol. IX. New York: Plenum Press, 1986. pp. 297-300.
- Turlapaty, P.D.M.V., and Altura, B.M. Extracellular magnesium ions control calcium exchange and content of vascular smooth muscle. *Eur J Pharmacol* 53:421-423, 1978.
- Turlapaty, P.D.M.V., and Altura, B.M. Magnesium deficiency produces spasms of coronary arteries: Relationship to etiology of sudden death ischemic heart disease. *Science* 208:198-200, 1980.
- Watts, D.C. Creatine kinase (adenosine 5'-triphosphate-creatine phosphotransferase. In: Boyer, P.D., ed. *The Enzymes*. Vol. VIII, Part A. New York: Academic Press, 1973. pp. 383-455.
- West, J.B., ed. *Best and Taylor's Physiological Basis of Medical Practice*. 11th ed. Baltimore: Williams and Wilkins, 1985.
- Whang, R.; Oei, T.O.; and Watanabe, A. Frequency of hypomagnesemia in hos-

pitalized patients receiving digitalis. *Arch Intern Med* 145:655-656, 1985.

Wienspergen, N., and Gygaz, P. Incomplete cerebral ischemia in the rat: Vascular and metabolic changes as measured by infrared transillumination in vivo. In: Bicher, H., and Bruley, D.F., eds. *Oxygen Transport to Tissue*. Vol. IV. New York: Plenum Press, 1983. pp. 5-15.

Wittenberg, B.A.; Doeller, J.E.; Gupta, R.K.; and White, R.L. Measurement of sarcolemmal permeability and intracellular pH, free magnesium, and high-energy phosphates of isolated heart cells. In: Clark, W.A.; Decker, R.S.; and Borg, T.K., eds. *Biology of Isolated Adult Cardiac Myocytes*. New York: Elsevier Science Publishing Co., 1988. pp. 118-130.

IN VIVO MEASUREMENT OF CEREBRAL BLOOD FLOW AND OXYGEN CONSUMPTION USING ^{17}O MAGNETIC RESONANCE IMAGING

Alan C. McLaughlin, Ph.D.¹ James Pekar, Ph.D.² Laszlo Ligeti, M.D.^{1,3} Zoltan Ruttnar, M.D.¹ Robbe Lyon, Ph.D.¹ Teresa Sinnwell, B.A.¹ Peter van Gelderen, M.Sc.² Daniel Fiat, Ph.D.^{1,4} and Chrit T.W. Moonen, Ph.D.²

Most of the metabolic energy of the brain is derived from the oxidation of glucose (Siesjo 1978). The cerebral rate of oxygen consumption (CMRO_2) is usually calculated from the product of the cerebral flow and the arterial/venous difference for oxygen (Sokoloff 1989). This indirect approach requires simultaneous determination of the cerebral blood flow and the arterial/venous difference for oxygen in the same region of the brain, which is usually difficult to achieve.

Arai et al. (1990) recently reported ^{17}O nuclear magnetic resonance (NMR) spectra from excised

rat brain in vitro and showed that the ^{17}O NMR signal from water in excised rat brain tissue was larger when the rat had previously inhaled specifically enriched $^{17}\text{O}_2$ gas. Since water is the predominant end

ACRONYMS

CHF_3	trifluoromethane
CMR_{glc}	cerebral metabolic rate of glucose
CMRO_2	cerebral rate of oxygen consumption
MRI	magnetic resonance imaging
NMR	nuclear magnetic resonance

¹Laboratory of Metabolism and Molecular Biology, Division of Intramural Clinical and Biological Research, National Institute on Alcohol Abuse and Alcoholism, Rockville, MD 20852

²Biomedical Engineering and Instrumentation Branch, National Center for Research Resources, National Institutes of Health, Bethesda, MD 20892

³Permanent Address: Experimental Research Department, Second Institute of Physiology, Semmelweis Medical University, Budapest, HUNGARY

⁴Permanent Address: Department of Physiology and Biophysics, University of Illinois, Chicago, IL 60612

product of oxygen metabolism in the brain (Sokoloff 1989). Arai et al. (1990) suggested using this approach to measure the CMRO₂.

There are, however, a number of problems with this approach. First, as Arai et al. (1990) point out, H₂¹⁷O produced in other organs will recirculate into the brain. Second, standard *in vivo* NMR techniques cannot localize NMR signals acquired from an intact head to specific regions of the brain. We circumvented the first problem by measuring both the recirculation of H₂¹⁷O into arterial blood and the cerebral blood flow; this information was used to calculate the increase of H₂¹⁷O in the brain due to recirculation. We circumvented the second problem by using NMR imaging techniques to measure the ¹⁷O NMR signal in a well-defined region of the brain. The results demonstrate that ¹⁷O NMR techniques can be used to measure cerebral blood flow and oxygen consumption in an 0.8 cm³ voxel in the cat brain.

THEORY

Calculation of Cerebral Rate of Oxygen Consumption

We assume that each molecule of ¹⁷O₂ consumed in the brain produces two molecules of H₂¹⁷O. If C_b(t), C_a(t), and C_v(t) are the "excess" concentrations of H₂¹⁷O in brain tissue, arterial blood, and venous blood, respectively (i.e., concentrations above the natural abundance level), and Q is the cerebral blood flow, the mass balance of H₂¹⁷O dur-

ing inhalation of ¹⁷O₂ gas is given by the equation

$$\frac{dC_b(t)}{dt} = 2\alpha \text{CMRO}_2 + Q(C_a(t) - C_v(t)) \quad (1)$$

where α is the specific enrichment of the inhaled ¹⁷O₂ gas.

If water in brain tissue is in equilibrium with water in venous blood, C_b(t) = λ C_v(t), where λ is the brain/blood partition coefficient, and equation 1 becomes

$$\begin{aligned} \frac{dC_b(t)}{dt} + (Q/\lambda) C_b(t) \\ = 2\alpha \text{CMRO}_2 + Q C_a(t) \end{aligned} \quad (2)$$

Equation 2 can be integrated to obtain the result

$$\begin{aligned} C_b(T) = 2\alpha \text{CMRO}_2 (\lambda/Q) (1 - \exp[-(Q/\lambda)T]) \\ + Q \int_0^T C_a(t) \exp[(Q/\lambda)(t-T)] dt \end{aligned} \quad (3)$$

The first term on the right-hand side of equation 3 accounts for production of H₂¹⁷O in the brain. The second term accounts for "wash-in" of H₂¹⁷O from arterial blood into the brain; it is identical to the expression derived originally by Kety (1951) to analyze tissue concentrations of an inert tracer in terms of blood flow (see equation 4).

Calculation of Cerebral Blood Flow

Cerebral blood flow values can be calculated from the "washout" of an inert diffusible tracer from the brain. If the arterial concentration of the inert tracer, C_a(t), is known, the cerebral blood flow, Q, can be calculated from the cerebral con-

centration of the tracer, $C_b(t)$, using the equation (Kety 1951)

$$C_b(T) = Q \int_0^T C_a(t) \exp[-(Q/\lambda)(t-T)] dt \quad (4)$$

If the tracer is given as a bolus injection, equation 4 reduces to the expression

$$C_b(T) = C_b(0) \exp[-(Q/\lambda)T] \quad (5)$$

where $C_b(0)$ is the concentration of tracer in the brain immediately after bolus injection.

Comparison of Units for Q and CMRO_2 with Conventional Units

The units of the terms in equation 3 are chosen so that the concentrations of $C_b(t)$ and $C_a(t)$ can be normalized using the natural abundance concentration of $H_2^{17}\text{O}$ (20.3 mmol/L water). The units of $C_b(t)$ are millimoles of $H_2^{17}\text{O}$ per liter of brain water, and the units of $C_a(t)$ and $C_v(t)$ are millimoles $H_2^{17}\text{O}$ per liter of blood water. The units of CMRO_2 are millimoles of O_2 per liter of brain water per minute and the units of Q are milliliters of blood water per milliliter of brain water per minute; λ is dimensionless.

The units of Q , CMRO_2 , and λ used for most conventional tracer methods are milliliters of blood per gram of brain per minute, millimoles of O_2 per kilogram of brain per minute, and milliliters per gram, respectively. If we define Q_o , CMRO_{2o} , and λ_o as the values of the parameters in conventional units,

the conversion between the units used in this study and conventional units is given by the following equations:

$$Q = \beta_{\text{blood}} \rho_{\text{blood}} / \beta_{\text{brain}} Q_o \quad (6)$$

$$\text{CMRO}_2 = 1/\beta_{\text{brain}} \text{CMRO}_{2o} \quad (7)$$

$$\lambda = \beta_{\text{blood}} \rho_{\text{blood}} / \beta_{\text{brain}} \lambda_o \quad (8)$$

where

β_{blood} = weight blood water/weight blood

β_{brain} = weight brain water/weight brain tissue

ρ_{blood} = weight blood/volume blood

We assume β_{blood} and β_{brain} for cat are the same as the values determined for humans, i.e., $\beta_{\text{blood}} = 0.81$ and $\beta_{\text{brain}} = 0.80$ (Ter-Pogossian et al. 1970), and that $\rho_{\text{blood}} = 1.05 \text{ g/mL}$ (Altman 1961). Using these values, $Q = 1.06 Q_o$, $\text{CMRO}_2 = 1.25 \text{ CMRO}_{2o}$, and $\lambda = 1.06 \lambda_o$, we assume $\lambda_o = 0.90$ (Herscovitsch and Raichle 1985).

Comparison of equations 6 and 8 shows that $Q/\lambda = Q_o/\lambda_o$. The bolus washout experiment (see figure 4) can thus be used to calculate Q in conventional units simply by using λ in conventional units.

MATERIALS AND METHODS

Animal Preparation

Cats were anesthetized with an initial dose of pentobarbital (40 mg/kg) and maintained with a supplemental dose (4 mg/kg) every 40 minutes. Catheters were inserted into the femoral artery and vein, and into the lingual arteries. The animal was intubated, artificially

ventilated with room air and paralyzed with succinyl choline (4 µg/minute in a venous drip). Blood pressure was monitored, and blood gas samples were taken periodically. The respiratory rate was adjusted to maintain arterial carbon dioxide pressure in the range 35–42 mmHg. The average arterial oxygen pressure was 100±5 mmHg. The average mean arterial blood pressure was 111±5 mmHg during the control period, but dropped during arterial sampling. The animal was maintained at 37 °C during surgery and NMR measurements with a water-jacketed blanket.

Magnetic Resonance Imaging

All magnetic resonance images (MRI) were acquired with a General Electric 4.7 tesla CSI system equipped with self-shielded gradients. Two-dimensional ¹H MRI were obtained using 5 mm slices in the axial, sagittal, and coronal planes. A stimulated echo sequence was used: The echo time was 80 milliseconds, the mixing time was 20 milliseconds, and the repetition delay was 1 second.

The ¹H MRI were used to choose the 0.8 cm slice used for acquisition of 8x8 two-dimensional ¹⁷O or ¹⁹F images from a defined region in the cat brain. The slice was selected using a sinc function radiofrequency pulse. Two-dimensional ¹⁷O or ¹⁹F magnetic resonance images were obtained using spectroscopic imaging techniques (Brown et al. 1982) with limited (i.e., 6x6) sampling in k space. The pulse width was 1.0 millisecond, and phase encoding was

performed with half-sinusoidal gradient pulses of 2 millisecond duration. The sweep width was 2 kHz; acquisition time, 8 milliseconds. The field of view was 8 cm × 8 cm, and the nominal voxel size was 0.8 cm³, for both the ¹⁷O and ¹⁹F images.

The ¹⁷O NMR studies used a 3.5 cm diameter single-turn surface coil, double-tuned for ¹⁷O and ¹H according to the approach of Schnall et al. (1985). The ¹⁹F studies used a 3.0 cm diameter single-turn surface coil, tuned to ¹H for shimming and collection of ¹H images, and then retuned to ¹⁹F. Both coils were placed on the surface of the skin directly over the calvarium; no invasive surgical procedures were performed.

The specific enrichment of H₂¹⁷O used for the arterial bolus injections was either 30 percent or 35 percent, and sodium chloride was added to a final concentration to 0.1 M. The specific enrichment of ¹⁷O₂ gas used for inhalation was 37.5 percent or 29 percent. Following H₂¹⁷O bolus injection, ¹⁷O images were obtained with a 22 second time resolution; following ¹⁷O₂ inhalation, ¹⁷O images were obtained with a 59 second time resolution; following inhalation of CHF₃, ¹⁹F images were obtained with a 29 second time resolution.

The in vivo H₂¹⁷O signals from each voxel were normalized using the signal from natural abundance H₂¹⁷O (20.3 mmol).

Measurement of Arterial H₂¹⁷O Curves

Three arterial blood samples (0.6 mL) were withdrawn prior to injec-

tion of enriched H_2^{17}O . Ten arterial blood samples were withdrawn (one every 60 seconds) during the control period after injection of enriched H_2^{17}O , but before inhalation of enriched $^{17}\text{O}_2$. Twenty arterial blood samples were withdrawn (one every 30 seconds) during inhalation of enriched $^{17}\text{O}_2$. The samples were treated with 20 μL 0.5 M EDTA and transferred to 10 mm NMR tubes. ^{17}O NMR spectra of the blood samples were acquired using a Bruker MSL 300 spectrometer. The amplitude of the H_2^{17}O signal from each sample was normalized using the natural abundance signal from H_2^{17}O .

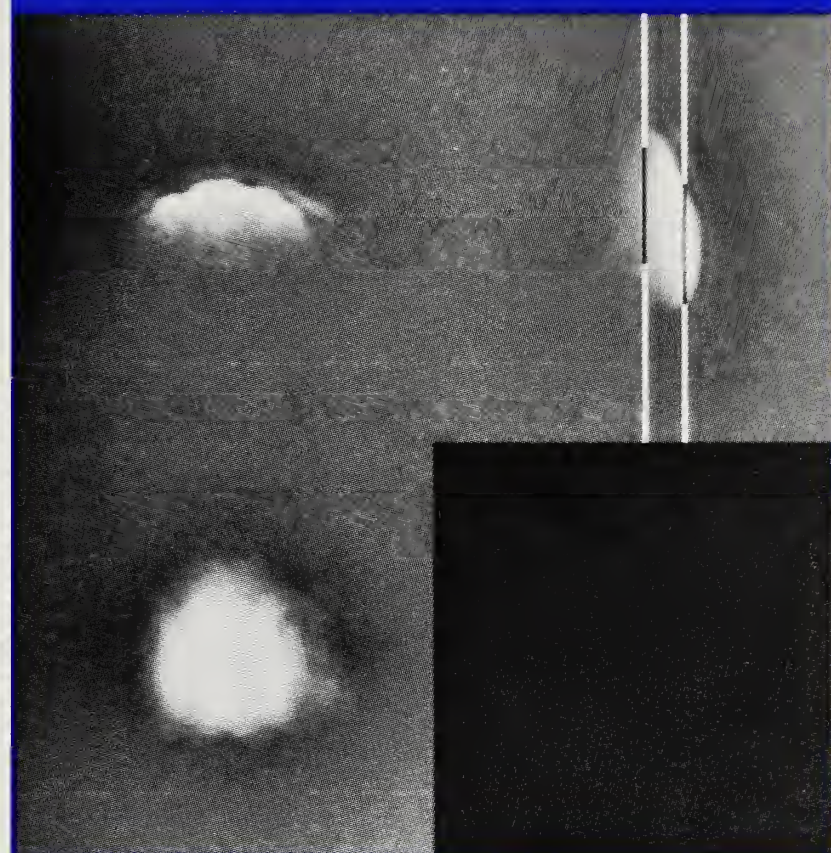
The mean arterial blood pressure decreased during the withdrawal of arterial blood samples. At the end of the sampling procedure, the average mean arterial pressure was 74 ± 5 mmHg.

RESULTS

^1H Magnetic Resonance Imaging

Figure 1 shows axial, sagittal, and coronal ^1H images of a cat head, taken with a surface coil. The axial and sagittal images display the expected fall-off in sensitivity as a function of distance from the coil (Ackerman et al. 1980). The 0.8 cm slice used for the ^{17}O imaging experiments is outlined on the axial image.

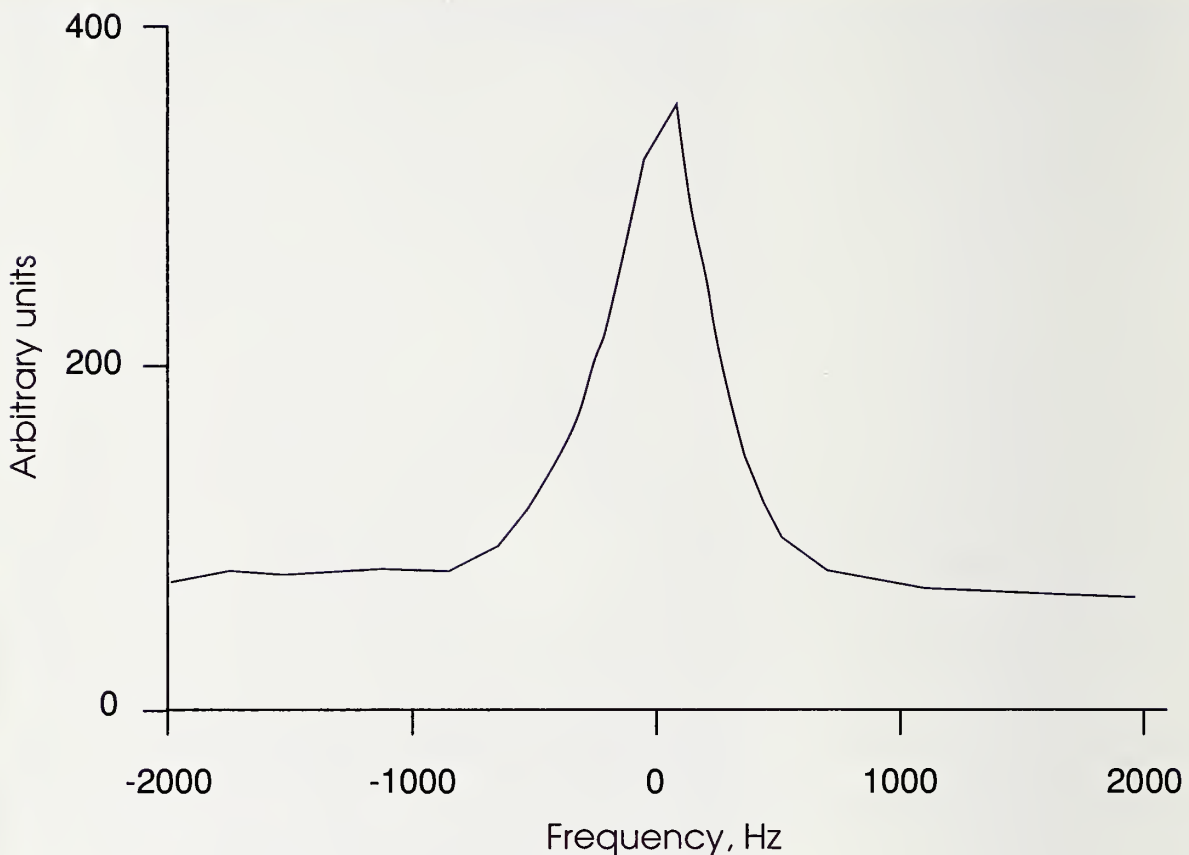
FIGURE 1



^1H magnetic resonance images of a cat brain taken with a surface coil. Right, axial scan; top left, sagittal scan; bottom left, coronal scan. The axial scan is oriented so that the surface coil is on the right; the sagittal scan, so that the surface coil is on the top. The two lines on the axial scan delineate the 0.8 cm slice selected for acquisition of two-dimensional ^{17}O NMR images.

^{17}O NMR Imaging During Bolus Injection and Washout of H_2^{17}O

Figure 2 shows the ^{17}O spectrum from the "central" 0.8 cm^3 voxel (i.e., the voxel with the highest H_2^{17}O signal) in the slice shown in figure 1. The spectrum, taken from an image that was collected in 59 seconds, contains only the signal from natural abundance (20.3 mmol/L) H_2^{17}O in the brain. Figure 3 shows the 8x8 two-dimensional ^{17}O NMR image (collected in 59 seconds) of natural abundance H_2^{17}O in the slice shown in figure 1.

FIGURE 2

^{17}O NMR spectrum from the central 0.8 cm^3 voxel in the slice delineated in figure 1. The signal arises from natural abundance (20.3 mmol) H_2^{17}O . The spectrum was taken from an image that was acquired in 59 seconds. The free-induction decay was apodized with a 180 Hz line width.

Figure 4 shows the time dependence of the H_2^{17}O concentration in the central 0.8 cm^3 voxel in the slice shown in figure 1. After a 6 minute control period, a 0.15 mL bolus of enriched H_2^{17}O was injected, via the lingual artery, into each carotid artery. The concentration of H_2^{17}O in the central voxel increased approximately 2-fold immediately after the injection, then decreased exponentially to a level approximately 10 percent above the initial level. The immediate increase in H_2^{17}O concentration in the

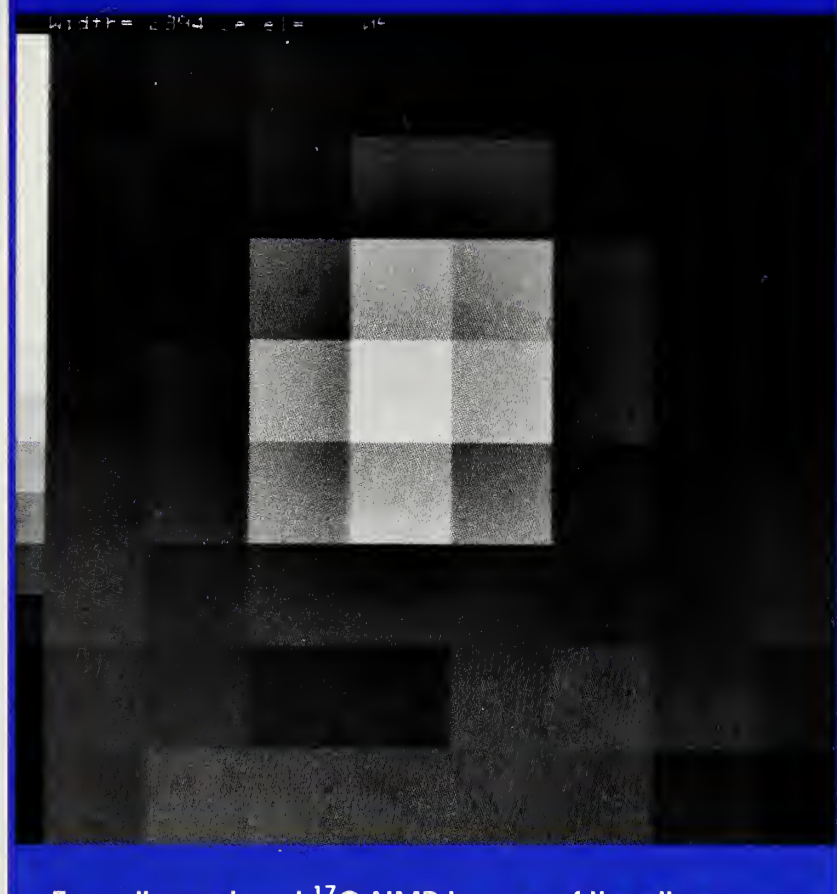
brain can be attributed to diffusion of H_2^{17}O from the arterial bolus into the brain, while the subsequent decrease in the H_2^{17}O concentration can be attributed to washout of H_2^{17}O from the brain. The data shown in figure 4 were fit to a single exponential decay, with a rate constant of 0.36 min^{-1} . Assuming that λ is 0.90 mL/g (Herscovitch and Raichle 1985), equation 5 can be used to calculate the cerebral blood flow, Q . For the data shown in figure 4, Q is calculated to be 0.32 mL/g/minute .

¹⁷O NMR Imaging During Inhalation of ¹⁷O₂

Inhalation of enriched ¹⁷O₂ gas was started approximately 30 minutes after the bolus injection of enriched H₂¹⁷O. Figure 5 shows the time dependence of the H₂¹⁷O concentration in the central 0.8 cm³ voxel of the slice shown in figure 1, before and during inhalation of enriched ¹⁷O₂.

Figure 6 shows the concentration of H₂¹⁷O in arterial blood before and during inhalation of enriched ¹⁷O₂. The arterial curve, i.e., the concentration of excess H₂¹⁷O produced by metabolism of enriched ¹⁷O₂, was calculated by subtracting the initial H₂¹⁷O concentration in the blood from the instantaneous H₂¹⁷O concentration in the blood. The arterial curve, Ca(t), and the calculated value of the cerebral blood flow, Q, were used to analyze the data shown in figure 5, using equation 3. The calculated value for the CMRO₂ from the fit of the data shown in figure 5 was 1.84 μmol O₂/mL brain water/minute. The units of CMRO₂ calculated by most radioactive tracer methods are millimoles of O₂ per kilogram of brain tissue per minute. When the units used in this study are converted to conventional units (see earlier section entitled Theory), the CMRO₂ calculated from the data shown in figure 5 is 1.47 mmol/kg/minute.

FIGURE 3

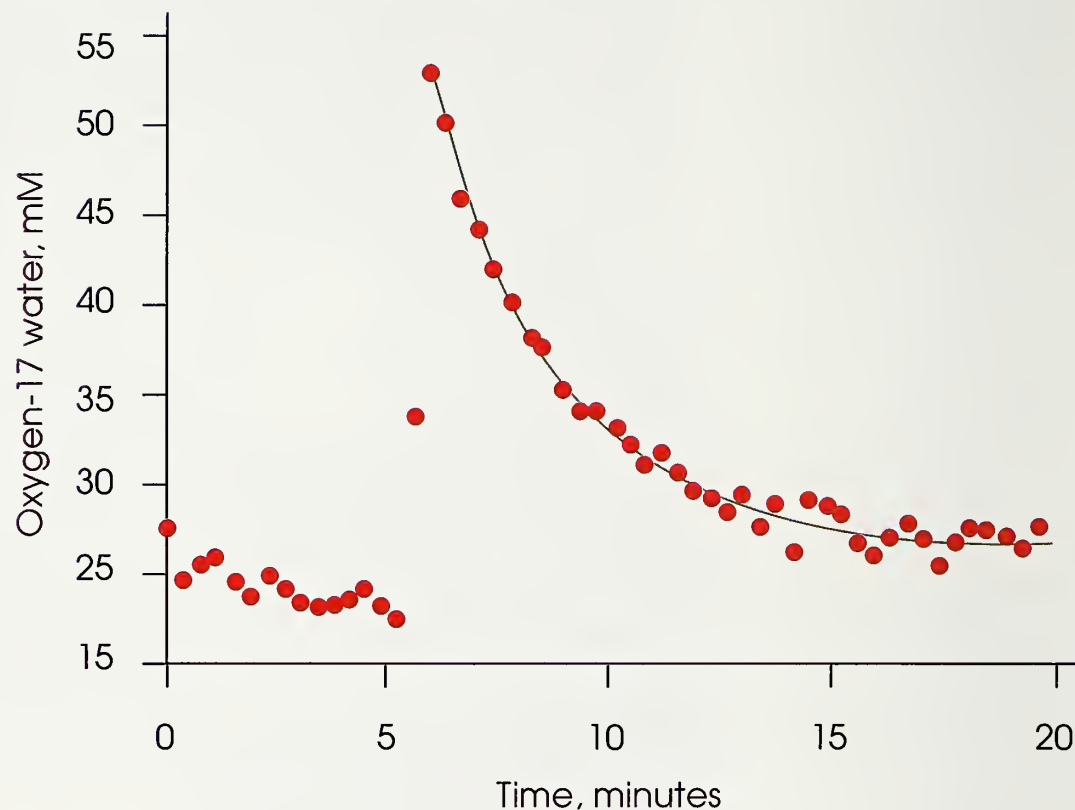


Two-dimensional ¹⁷O NMR image of the slice delineated in figure 1. The field of view is 8x8 cm, and the voxel size is 1x1 cm. The brightness is proportional to the intensity of the signal from natural-abundance H₂¹⁷O.

The experimental protocol was repeated on five different animals. In each animal, ¹H MRI was used to define a 0.8 cm slice in the region of the cat brain similar to that illustrated in figure 1. The average cerebral blood flow for the central 0.8 cm³ voxel in the slice was 0.39±0.12 mL/g/minute, and the average cerebral oxygen consumption for the central 0.8 cm³ voxel in the slice was 0.90±0.42 mmol O₂/kg/minute.

¹⁹F NMR Imaging During Inhalation and Washout of CHF₃

¹H MRI was used to define an 0.8 cm slice in the region of the cat brain

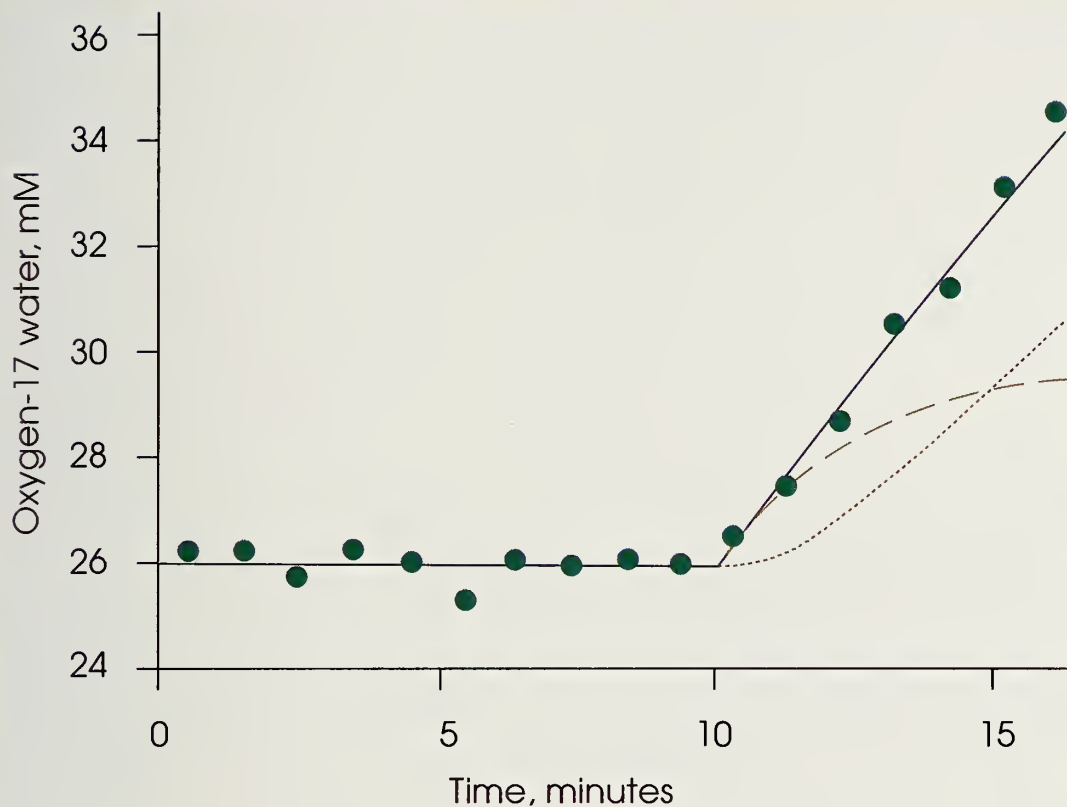
FIGURE 4

Time dependence of the intensity of the H_2^{17}O signal from the central voxel of the slice delineated in figure 1 after injection of an arterial bolus of enriched H_2^{17}O . The bolus was injected at 6 minutes. The solid curve is the exponential fit to the washout curve.

similar to that illustrated in figure 1. Figure 7 shows the ^{19}F spectrum from the central 0.8 cm^3 voxel of this slice after 15 minute inhalation of a mixture containing 20 percent oxygen, 15 percent nitrogen, and 65 percent trifluoromethane (CHF_3). The ^{19}F NMR signal, which arises from CHF_3 in the brain, is split into a doublet due to hyperfine coupling between the fluorine atoms and the proton bound to the same carbon atom. The spectrum was acquired in 29 seconds.

Figure 8 shows the amplitude of the ^{19}F NMR signal from the central

0.8 cm^3 voxel as a function of time before, during, and after inhalation of CHF_3 . During inhalation of CHF_3 , the amplitude of the ^{19}F signal from CHF_3 increased in intensity and reached a steady state. The decrease in amplitude of the ^{19}F NMR signal when the inhalation of CHF_3 was discontinued can be attributed to washout of CHF_3 from the brain. An arterial washout curve, measured in cats under similar experimental conditions (Barranco et al. 1989), was used to analyze the washout of CHF_3 from the brain using equation 4. The value of the

FIGURE 5

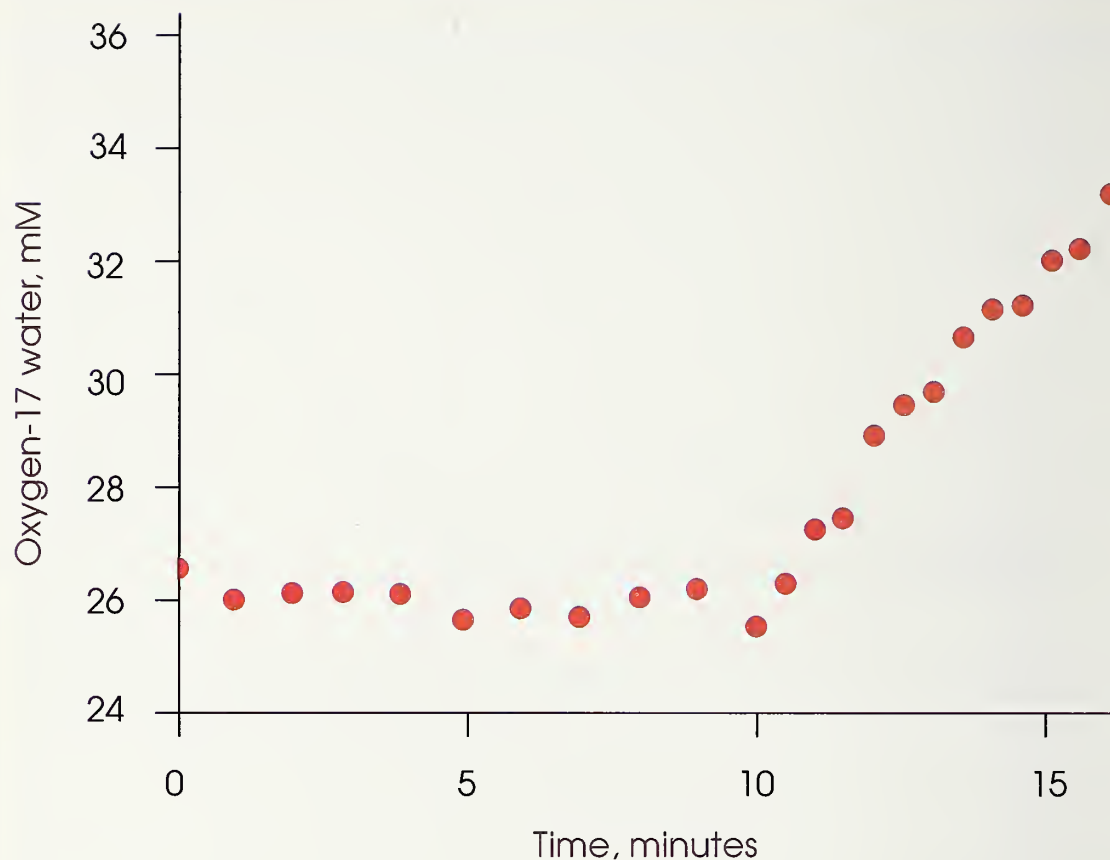
Time dependence of the intensity of the H_2^{17}O signal from the central voxel in the slice delineated in figure 1 after inhalation of enriched $^{17}\text{O}_2$. Inhalation of $^{17}\text{O}_2$ started at 10 minutes. The solid curve is the best fit of the data to equation 3. The dotted curve is the calculated increase of H_2^{17}O in the brain due to recirculation; the dashed curve is the calculated increase of H_2^{17}O in the brain due to metabolism.

cerebral blood flow calculated from the data shown in figure 8 was 0.54 mL/g/minute.

DISCUSSION

The average value of cerebral blood flow in the central 0.8 cm^3 voxel is $0.39 \pm 0.12 \text{ mL/g/minute}$. This value can be compared with the cerebral blood flow calculated from autoradiographic measurements in the brain of a cat under pentobarbital anesthesia (Schuier et al. 1987). The average blood flow

for cortical gray matter is approximately 0.54 mL/g/minute , while the average blood flow for white matter is approximately 0.15 mL/g/minute (Schuier et al. 1987). Assuming approximately equal volumes of white and gray matter, the expected average blood flow is 0.34 mL/g/minute . The agreement between cerebral blood flow values calculated with ^{17}O NMR techniques and cerebral blood flow values estimated from autoradiological data (Schuier et al. 1987) is reasonable.

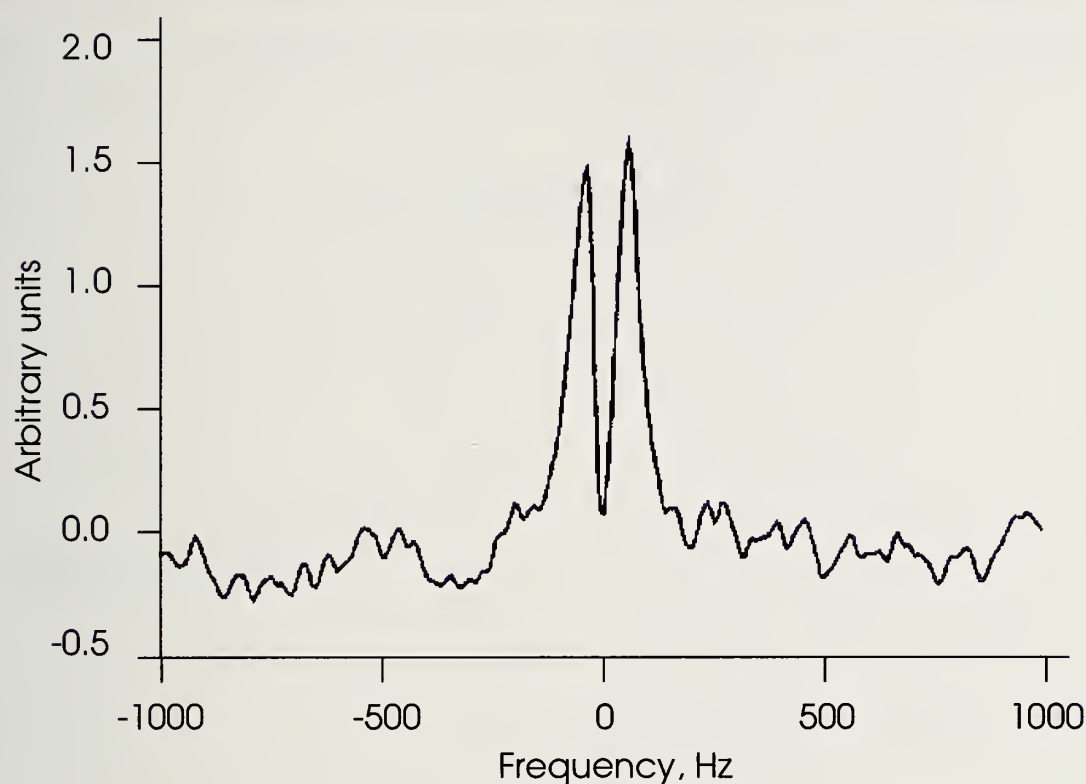
FIGURE 6

Time dependence of the intensity of the H_2^{17}O signal from arterial blood after inhalation of enriched $^{17}\text{O}_2$. Inhalation of $^{17}\text{O}_2$ started at 10 minutes.

Since the 0.8 cm^3 voxels used in this study contain both gray and white matter, the value of Q calculated by the bolus injection technique is an average of the cerebral blood flows in the two compartments. However, the average value will be weighted toward the fast cerebral blood flow value for gray matter (Hoedt-Rasmussen et al. 1966). Using the blood flow values for gray and white matter calculated from autoradiological measurements (Schuier et al. 1987), and assuming approximately equal volumes of gray and white matter in a typical region of the brain, the av-

erage value of blood flow calculated from the bolus washout curve could overestimate the true average value by approximately 30 percent.

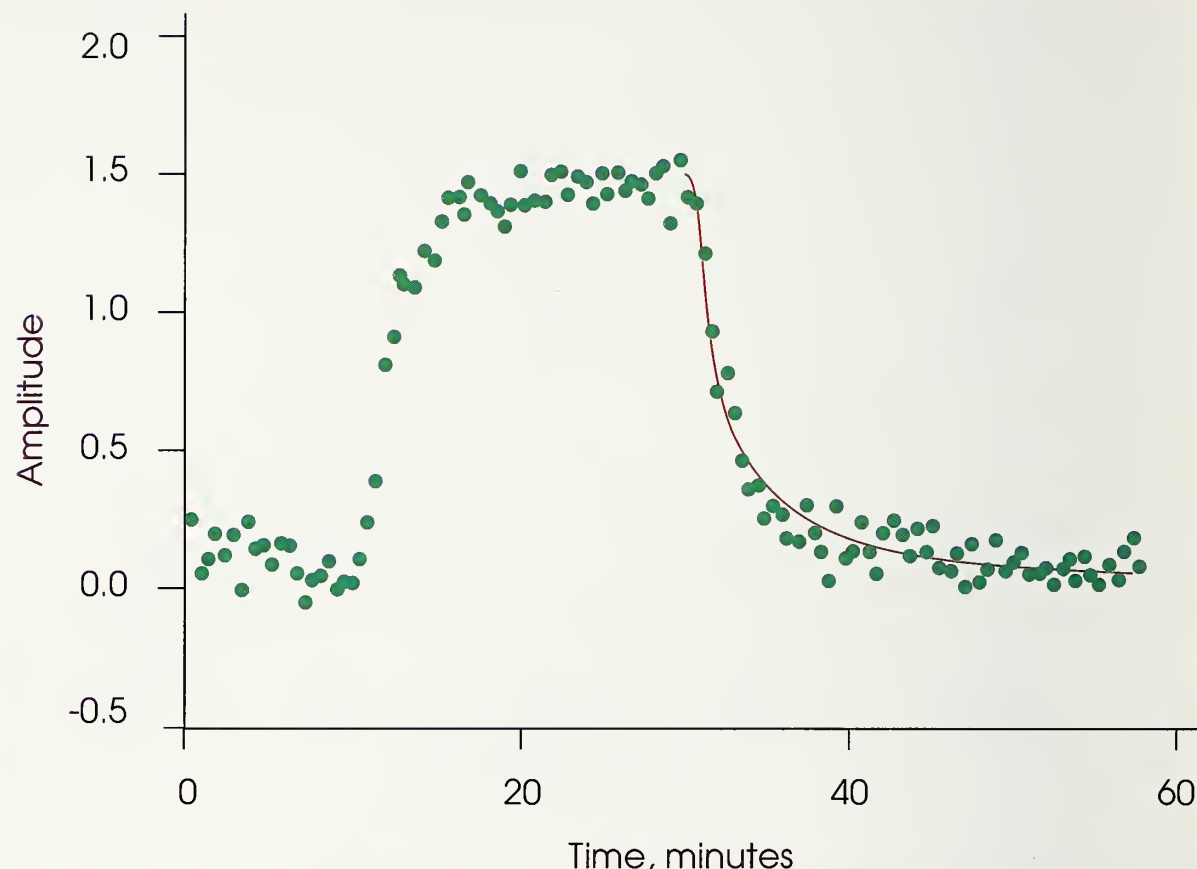
The average CMRO_2 in the central 0.8 cm^3 voxel is $0.90 \pm 0.42 \text{ mmol/kg/minute}$. This value can be compared with the CMRO_2 estimated from autoradiographic measurements of cerebral metabolic rate of glucose (CMRglc) in the cat brain. The average value of CMRglc in the anterior lateral gyrus, the middle suprasylvian gyrus, and the middle ectosylvian gyrus in a cat under pentobarbital anesthesia is

FIGURE 7

^{19}F NMR spectrum from the central 0.8 cm^3 voxel of a slice similar to the one shown in figure 1 after 15-minute inhalation of CHF_3 . The spectrum was taken from an image that was acquired in 29 seconds. The free-induction decay was apodized with a line width of 20 Hz.

0.25 mmol/kg/minute (Tanaka et al. 1985). Assuming the $\text{CMRO}_2/\text{CMRglc}$ ratio is 5.5 (Siesjo 1978), the CMRO_2 in this region is calculated to be 1.37 mmol/kg/minute. The average value for cerebral oxygen consumption calculated using ^{17}O NMR is approximately 66 percent of the value estimated from autoradiological measurements of CMRglc . Given the differences between the two techniques, the agreement between the different values of CMRO_2 for the cat brain is reasonable.

Overestimation of the average cerebral blood flow using a bolus washout technique does not significantly affect the calculation of CMRO_2 . When the data sets for the five animals are processed with values of Q reduced by 30 percent from the values calculated using equation 5, the individual values of CMRO_2 are changed by an average of 2 percent. A similar result is observed when Q is increased by 30 percent. The calculation of CMRO_2 is thus relatively insensitive to errors in the calculated value of Q .

FIGURE 8

Time dependence of the intensity (arbitrary units) of the ^{19}F NMR signal from the central voxel during wash-in and wash-out of CHF_3 . Inhalation of CHF_3 started at 10 minutes and ended at 30 minutes. The solid curve is the biexponential fit to the wash-out curve.

In this study, we used sequential samples taken from a femoral artery catheter to obtain the arterial H_2^{17}O curve during inhalation of enriched $^{17}\text{O}_2$. A problem with the sampling approach is that the volume of blood withdrawn may cause a decrease in the mean arterial blood pressure. In this study, the mean arterial blood pressure dropped to approximately 74 mmHg during the sampling procedure. Because the blood pressure remained within the autoregulatory range, this pressure drop should not substantially affect the cerebral

blood flow or the CMRO_2 measured in this study. In the future, however, the blood pressure drop during sampling could be minimized by using larger animals.

The ^{17}O imaging data in the present work were obtained with a surface coil placed on the top of the head. While this provided high NMR sensitivity for the region of brain immediately under the coil, the NMR sensitivity for other regions of the brain was reduced (see figure 1). This approach is useful for studying regions of the brain close to the surface. It should be possi-

ble to obtain CMRO_2 images of the entire brain with an imaging coil that surrounds the entire head. However, since the imaging coil reduces the NMR sensitivity, the voxel size may have to be increased.

Can the ^{17}O NMR approach outlined in this study be used to obtain CMRO_2 images in clinical situations? NMR imaging is a non-invasive technique now used routinely in clinical practice. $^{17}\text{O}_2$ and H_2^{17}O are nonradioactive, stable compounds that can be administered to humans with little or no side effects. However, three other aspects of the experiment would be difficult to carry over to clinical situations.

First, arterial bolus injection techniques are difficult to use in routine clinical studies. This problem can be circumvented using inhaled tracers that can be detected using NMR. CHF_3 is a suitable tracer for cerebral blood flow studies because it can be detected by ^{19}F NMR (Barranco et al. 1989; Ewing et al. 1990). Figure 8 shows that ^{19}F NMR can be used to monitor the washout of inhaled CHF_3 from an 0.8 cm^3 voxel in the cat brain. The ^{19}F NMR approach, which does not require invasive arterial cannulation, can thus be used instead of the bolus injection approach to measure cerebral blood flow. Because CHF_3 appears to have few side effects (Branch et al. 1989), the ^{19}F NMR imaging approach should be suitable for clinical measurements of cerebral blood flow.

The second problem is the use of continued arterial sampling to measure recirculation of H_2^{17}O . This problem might be avoided by using mass spectrometric analysis of expired air to estimate arterial concentrations of H_2^{17}O .

The third problem is related to the fact that the current experiments were performed at 4.7 tesla, whereas most clinical imaging is performed at 1.5 tesla. Since the sensitivity of the NMR technique decreases as the magnetic field strength decreases, the ^{17}O NMR approach for imaging CMRO_2 is probably not practical at 1.5 tesla. However, this method should be feasible with the new "high-field" (circa 4 tesla) clinical magnets now in operation.

In summary, ^{17}O NMR techniques have been used to calculate cerebral blood flow and oxygen consumption in an 0.8 cm^3 voxel in the cat brain. Although a number of problems remain to be solved, the technique has the potential to image cerebral blood flow and oxygen consumption in humans.

ACKNOWLEDGMENTS

This work was performed at the In Vivo NMR Research Center, National Institutes of Health, Bethesda, MD.

REFERENCES

- Ackerman, J.J.H.; Grove, T.H.; Wong, G.G.; Gadian, D.G.; and Radda, G.K. Mapping of metabolites in whole animals by ^{31}P NMR using surface coils. *Nature* 283:167–170, 1980.

- Altman, P.L. *Blood and Other Body Fluids* (Biological Handbook Series). Washington, DC: Federation of American Societies for Experimental Biology, 1961. p. 14.
- Arai, T.; Nakao, S.; Mori, K.; Ishimori, K.; Morishima, I.; Miyazawa, T; and Fritz-Zieroth, B. Cerebral oxygen utilization analyzed by the use of oxygen-17 and its nuclear magnetic resonance. *Biochem Biophys Res Commun* 169:153–158, 1990.
- Barranco, D.; Sutton, L.N.; Florin, S.; Greenberg, J.; Sinnwell, T.; Ligeti, L.; and McLaughlin, A.C. Use of ¹⁹F NMR spectroscopy for measurement of cerebral blood flow: A comparative study using microspheres. *J Cereb Blood Flow Metab* 9:886–891, 1989.
- Branch, C.A.; Ewing, J.R.; Fagan, S.C.; Butt, S.; Simkins, R.; and Welch, K.M.A. Toxicity of potential fluorinated indicators for NMR measurements of CBF. *J Cereb Blood Flow Metab* 9(suppl 1):SI02, 1989.
- Brown, T.R.; Kincaid, B.M.; and Ugurbil, K. NMR chemical shift imaging in three dimensions. *Proc Natl Acad Sci USA* 79:3523–3526, 1982.
- Ewing, J.R.; Branch, C.A.; Fagan, S.C.; Helpern, J.A.; Simkins, R.T.; Butt, S.M.; and Welch, K.M.A. Fluorocarbon-23 measure of cat cerebral blood flow by nuclear magnetic resonance. *Stroke* 21:100–106, 1990.
- Herscovitch, P., and Raichle, M.E. What is the correct value for the brain-blood partition coefficient for water? *J Cereb Blood Flow Metab* 5:65–69, 1985.
- Hoedt-Rasmussen, K.; Sveinsdottir, E.; and Lassen, N.A. Regional cerebral blood flow in man determined by intraarterial injection of radioactive inert gas. *Circ Res* 18:237–247, 1966.
- Kety, S. The theory and applications of the exchange of inert gas at the lungs and tissues. *Pharmacol Rev* 3:1–41, 1951.
- Schnall, M.D.; Subramanian, V.H.; Leigh, J.S.; and Chance, B. A new double-tuned probe for concurrent ¹H and ³¹P NMR. *J Magn Reson* 65:122–129, 1985.
- Schuier, F.J.; Jones, S.C.; Fedora, T.; and Reivich, M. ¹⁴Cjidoantipyrine and microsphere blood flow estimates in cat brain. *Am J Physiol* 253:H1289–H1297, 1987.
- Siesjo, B.K. *Brain Energy Metabolism*. New York: John Wiley and Sons, 1978. pp. 101–130.
- Sokoloff, L. Circulation and energy metabolism of the brain. In: Seigel, G.J.; Agranoff, B.; Albers, R.W.; and Molinoff, P., eds. *Basic Neurochemistry*. 4th ed. New York: Raven Press, 1989. pp. 565–590.
- Tanaka, K.; Welsh, F.A.; Greenberg, J.H.; O'Flynn, R.; Harris, V.A.; and Reivich, M. Regional alterations in glucose consumption and metabolite levels during postischemic recovery in cat brain. *J Cereb Blood Flow Metab* 5:502–511, 1985.
- Ter-Pogossian, M.M.; Eichling, J.O.; Davis, D.O.; and Welch, M.J. The measure in vivo of regional cerebral oxygen utilization by means of oxyhemoglobin labeled with radioactive oxygen-15. *J Clin Invest* 49:381–391, 1970.

17

DETECTION OF ETHANOL TOLERANCE IN HUMAN BRAIN WITH IN VIVO PROTON MAGNETIC RESONANCE SPECTROSCOPY

Jack H. Mendelson, M.D., Tak-Ming Chiu, Ph.D., Leslie Amass, Ph.D., Nancy K. Mello, Ph.D., Siew Koon Teoh, M.D., Bryan Woods, M.D., and Erin Rhoades¹

There is considerable evidence that the effects of ethanol on the central nervous system are not analogous to opiate receptor binding (Pert and Snyder 1973) or cocaine-mediated effects at the dopamine transporter (Ritz et al. 1987). In contrast, ethanol has a more diffuse effect on cell membranes, subsequently modifying neurotransmitter function, ion channel activity, and secondary and tertiary messenger system processes. In 1977, Chin and Goldstein described the acute effects of ethanol on in vitro brain synaptosome preparations as membrane lipid disordering or "fluidization." However, synaptosomes obtained from animals chronically exposed to ethanol had significantly less disordering of membrane lipids following acute ethanol exposure (Chin and Goldstein 1977). Harris and Shroeder (1981)

confirmed and extended these observations.

Subsequent studies with liver cell membranes (Rottenberg et al. 1981; Waring et al. 1981; Schuller et al. 1984; Polokoff et al. 1985; Taraschi et al. 1985; Taraschi et al. 1986a,b) and erythrocytes (Taraschi et al. 1986a) yielded similar data on the presence of ethanol-induced membrane tolerance. Such tolerance is characterized by a reduction in the partition coefficient of ethanol in the membrane without any significant changes in lipid order (Rottenberg et al. 1981; Kelly-Murphy et al. 1984). Nie and his associates (1989) postulated that the basis for ethanol-

ACRONYM

MRS	magnetic resonance spectroscopy
-----	---------------------------------

¹The Alcohol and Drug Abuse Research Center and the Brain Imaging Center, McLean Hospital-Harvard Medical School, Belmont, MA 02178

induced membrane tolerance may be "an alteration in the phospholipids which leads to a structural modification of the lipid bilayer."

Until recently, no techniques have been available for assessing covariance of ethanol-induced membrane tolerance with behavioral tolerance for ethanol in humans. We now report *in vivo* application of *in vitro* proton magnetic resonance spectroscopy (MRS) for assessment of ethanol interactions in brain and behavioral tolerance in humans.

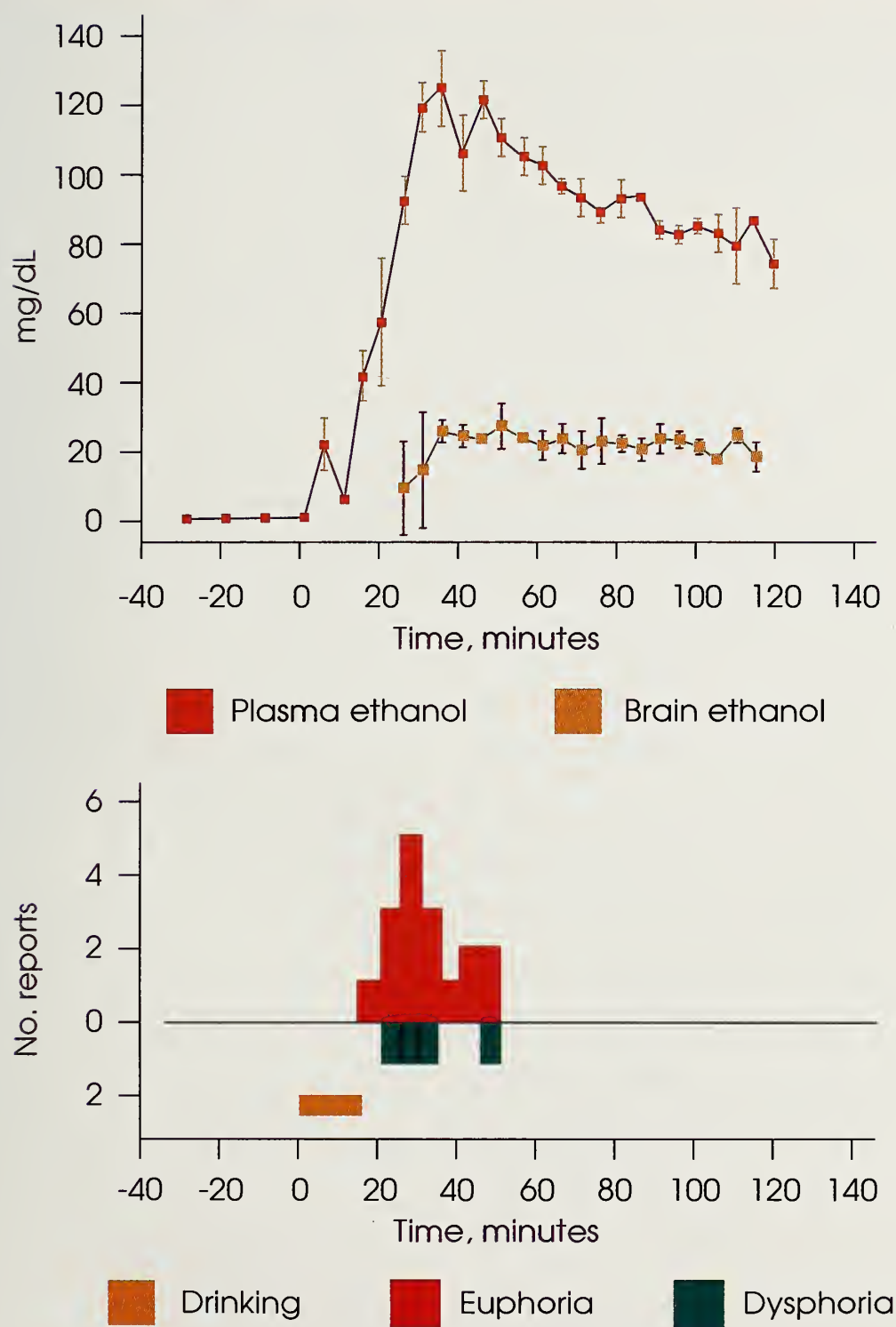
DETERMINATION OF ETHANOL CONCENTRATION IN BRAIN WITH *IN VIVO* PROTON MAGNETIC RESONANCE SPECTROSCOPY

Hanstöck and coworkers first described procedures for determination of ethanol concentration in the human brain with *in vivo* proton MRS (Hanstöck et al. 1988, 1990). However, other investigators (Hetherington et al. 1989; Moxon et al. 1989) found poor concordance between brain ethanol concentrations determined by *in vivo* proton MRS and blood ethanol levels measured by conventional analytic techniques.

In 1990, we reported our initial studies on determination of ethanol concentration in regional areas of human brain with *in vivo* proton MRS (Mendelson et al. 1990). The subjects who participated in this study were healthy adult males who reported occasional social alcohol use (2–6 drinks per week) and no past history of alcohol or drug

dependence. *In vivo* proton magnetic resonance spectra were obtained from each subject prior to ingestion of alcohol (ethanol, 0.7 g/kg body weight) and during a subsequent time course corresponding to the ascending, peak, and descending phases of the blood ethanol curve. Blood ethanol levels were determined from plasma samples collected via intravenous catheter, and using a special nonferrous instrumental device, the subjects recorded changes in their mood states prior to and following ethanol intake (Mendelson et al. 1990).

Figure 1 shows mean (\pm S.D.) plasma and brain ethanol levels following ethanol intake. Brain ethanol levels were computed by utilizing the spectral measurement of N-acetyl aspartate as an internal standard. Figure 1 also displays mood state (euphoria or dysphoria) as a function of time following drinking. Euphoria was most frequently reported during the ascending phase of the blood ethanol curve or when plasma ethanol levels had reached peak values. This finding is consistent with previous reports of alcohol-induced mood state changes during the ascending blood ethanol curve (Lukas and Mendelson 1988). However, brain ethanol levels determined by *in vivo* proton MRS were significantly lower (4- to 6-fold) than blood ethanol levels (Mendelson et al. 1990).

FIGURE 1

Plasma ethanol levels, brain ethanol levels, and mood state changes prior to and following alcohol intake (ethanol, 0.7 g/kg p.o.) by five subjects. Euphoria and dysphoria data represent the summed number of reports (by instrumental "joy stick" device responses) for each mood state change from all five subjects during sequential 5-minute time blocks (from Mendelson et al. 1990).

DETECTION OF ETHANOL IN BRAIN WITH IN VIVO MRS AND THE PARTITION COEFFICIENT OF ETHANOL IN NEURAL MEMBRANES

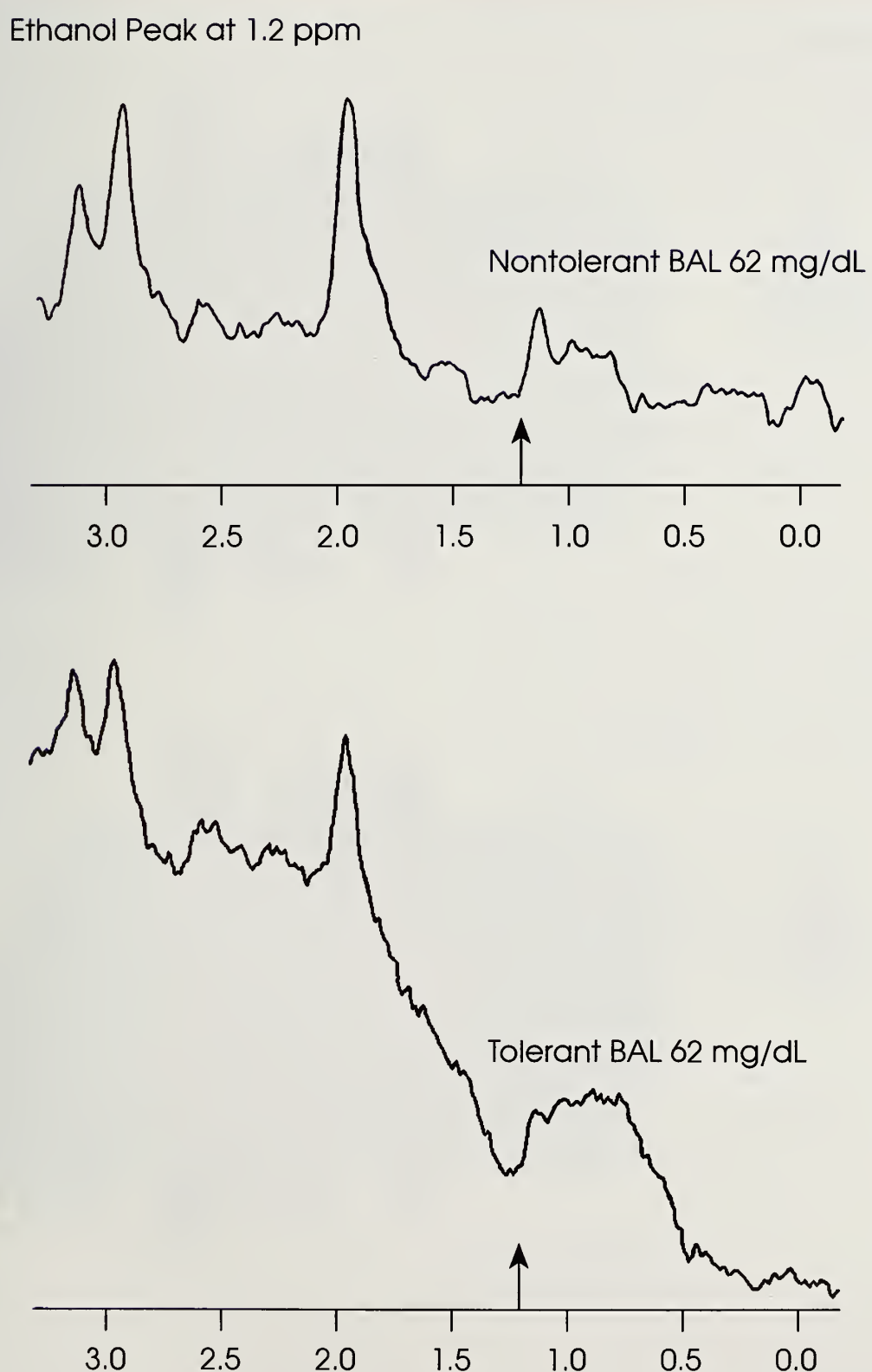
We observed (Mendelson et al. 1990) that following acute alcohol intake, the anticipated concentration of ethanol in brain is not detectable by blood ethanol level. This observation was consistent with reports of other investigators that low and moderate concentrations of ethanol in the brain were invisible when measured with in vivo proton MRS (Hetherington et al. 1989; Moxon et al. 1989). Rose and associates (1990) have obtained data in studies of in vivo ethanol T₂ relaxation time which suggest that lack of detection of ethanol in the brain by MRS is associated with restriction of ethanol mobility during partitioning into cell membranes. We were able to detect a small concentration of ethanol in brain from five subjects when their blood alcohol levels were 50 mg/dL or higher (figure 1) (Mendelson et al. 1990). However, MRS could detect no brain ethanol in one subject (a healthy adult male, age 34, who had a past history of heavy drinking and behavioral tolerance) when this subject's blood ethanol levels exceeded 50 mg/dL.

At present, we are assessing the effects of acute ethanol intake on blood and brain ethanol concentration in cohorts of healthy adult males without past history of heavy ethanol intake but with behavioral tolerance to ethanol. We have completed assessments of six occa-

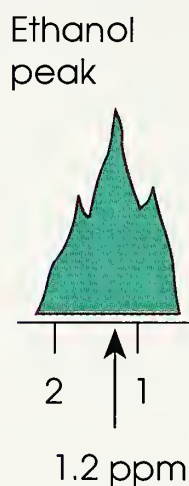
sional social drinkers who reported low tolerance for ethanol and four heavy drinkers who reported considerable ethanol tolerance. With in vivo MRS, we detected ethanol in the brains of all of the nontolerant men when their blood alcohol levels exceeded 50 mg/dL. In contrast, we were unable to detect ethanol in the brains of tolerant men when their blood ethanol levels exceeded 50 mg/dL.

Figure 2 shows ethanol spectra (1.2 ppm) from a tolerant and non-tolerant subject. These spectra were obtained at virtually identical times following completion of acute ethanol intake and when the subjects' blood alcohol levels were also identical (62 mg/dL). The ethanol spectra from the nontolerant individual is clearly discernible at 1.2 ppm whereas the spectral peak for ethanol of the tolerant subject is very low and barely discernible.

Figure 3 is a schematic description of our hypothesis concerning the relationship between ethanol effects on the cell membrane and the detection of ethanol concentration in brain with in vivo proton MRS. At left is depicted the partition coefficient of ethanol in a "nontolerant" membrane after acute ethanol intake. We postulate that proton MRS could be used for detection of an ethanol spectrum of significant magnitude (1.2 ppm) under these conditions. Depicted at right is a reduced partition coefficient for ethanol, which occurs after development of membrane tolerance. Visibility of ethanol by

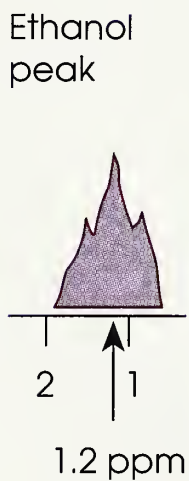
FIGURE 2

Magnetic resonance spectra of an ethanol peak at 1.2 ppm for a nontolerant subject (top panel) and absence of the ethanol peak at 1.2 ppm for a tolerant subject (bottom panel). Blood alcohol level (BAL, 62 mg/dL) was identical for both subjects.

FIGURE 3**Nontolerant**

Lipid membrane

Ethanol

**Tolerant**

Lipid membrane

Ethanol



Reduced partition coefficient of ethanol

Schematic representation of reduced partition coefficient for ethanol in lipid membrane of tolerant (bottom panel) versus nontolerant (top panel) membrane. Ethanol peak at 1.2 ppm determined by *in vivo* proton MRS would be smaller for tolerance (bottom panel) than for nontolerance (top panel).

in vivo proton MRS would be significantly lower under these conditions compared with the detection of ethanol by MRS in the nontolerant membrane.

The observation of lower visibility of ethanol in brain from tolerant than from nontolerant persons with MRS procedures is consistent with the hypothesis that membrane tolerance induced by chronic alcohol intake is associated with a decrement in the partitioning of alcohol into the membrane lipid bilayer. Although the basic mechanisms underlying this process remain to be determined, studies conducted by Nie and his associates (1989) suggest that changes in lipid order in the central region of the membrane lipid bilayer do not account for the reduced partition coefficient of ethanol in the tolerant membrane. These investigators have also noted that membrane tolerance is associated with changes in membrane phospholipids and that these changes regress following reduction in ethanol tolerance. If in vivo MRS can identify individuals with and without ethanol tolerance, such studies should facilitate a more precise understanding of the relationships between patterns of ethanol consumption and the development of behavioral tolerance in humans. Because of the important pharmacologic relationship of ethanol tolerance to the development of ethanol dependence, in vivo MRS studies may also contribute to a better understanding of the neural basis of ethanol dependence in humans.

ACKNOWLEDGMENTS

This research was supported in part by grant AA 06252 from the National Institute on Alcohol Abuse and Alcoholism; grants DA 00101, DA 00064, and DA 00115 from the National Institute on Drug Abuse; and a grant to McLean Hospital from General Electric Medical Systems.

REFERENCES

- Chin, J.H., and Goldstein, D.B. Drug tolerance in biomembranes: A spin label study of the effects of ethanol. *Science* 196:684-685, 1977.
- Hanstok, C.C.; Rothman, D.L.; Shulman, R.G.; Novotny, E.J.; Petroff, O.A.C.; and Prichard, J.W. Alcohol observed in human brain by proton magnetic resonance spectroscopy. *Soc Magn Reson Med Abstr* 2:1071, 1988.
- Hanstok, C.C.; Rothman, D.L.; Shulman, R.G.; Novotny, E.J.; Petroff, O.A.C.; and Prichard, J.W. Measurement of ethanol in the human brain using NMR spectroscopy. *J Stud Alcohol* 51:104-107, 1990.
- Harris, R.A., and Shroeder, F. Ethanol and the physical properties of brain membranes: Fluorescence studies. *Mol Pharmacol* 20:128-137, 1981.
- Hetherington, H.P.; Rowley, H.; Peterson, K.; Boska, M.; Diamond, I.; and Weiner, M.W. The kinetics of alcohol uptake in human brain and blood by volume selective 1H MRS. *Soc Magn Reson Med Abstr* 3:370, 1989.
- Kelly-Murphy, S.; Waring, A.J.; Rottenberg, H.; and Rubin, E. Effects of

chronic ethanol consumption on the partition of lipophilic compounds into erythrocyte membranes. *Lab Invest* 50:174–183, 1984.

Lukas, S.E., and Mendelson, J.H. Electroencephalographic activity and plasma ACTH during alcohol-induced euphoria. *Biol Psychiatry* 23:141–148, 1988.

Mendelson, J.H.; Woods, B.T.; Chiu, T.-M.; Mello, N.K.; Lukas, S.E.; Teoh, S.K.; Sintavanarong, P.; Cochin, J.; Hopkins, M.A.; and Dobrosielski, M. In vivo proton magnetic resonance spectroscopy of alcohol in human brain. *Alcohol* 7:443–447, 1990.

Moxon, L.N.; Rose, S.E.; Galloway, G.J.; Haseler, L.J.; Brereton, I.M.; Marshman, M.F.; Field, J.; Crozier, S.; Bore, P.J.; and Doddrell, D.M. Non-detection of alcohol in the brain by ¹H magnetic resonance spectroscopy. *Soc Magn Reson Med Abstr* 3:595, 1989.

Nie, Y.; Stubbs, C.D.; Williams, B.W.; and Rubin, E. Ethanol causes decreased partitioning into biological membranes without changes in lipid order. *Arch Biochem Biophys* 268:349–359, 1989.

Pert, C.B., and Snyder, S.H. Opiate receptor: Demonstration in nervous tissue. *Science* 179:1011–1014, 1973.

Polokoff, M.A.; Simon, T.J.; Harris, R.A.; Simon, F.R.; and Iwahashi, M. Chronic ethanol increases liver plasma membrane fluidity. *Biochemistry* 24:3114–3120, 1985.

Ritz, M.C.; Lamb, R.J.; Goldberg, S.R.; and Kuhar, M.J. Cocaine receptors on dopamine transporters are related to self-administration of cocaine. *Science* 237:1219–1223, 1987.

Rose, S.E.; Moxon, L.N.; Galloway, G.J.; Brereton, I.M.; Crozier, S.; Field, J.; Marshman, M.F.; Bore, P.J.; and Doddrell, D.M. Measurement of the T_2 relaxation time of cerebral ethanol, *in vivo*. *Soc Magn Reson Med Abstr* 4:1259, 1990.

Rottenberg, H.; Waring, A.; and Rubin, E. Tolerance and cross-tolerance in chronic alcoholics: Reduced membrane binding of ethanol and other drugs. *Science* 213:583–585, 1981.

Schuller, A.; Moscat, J.; Diez, E.; Fernandez-Checa, C.; Gavilanes, F.G.; and Municio, A.M. The fluidity of plasma membranes from ethanol-treated rat liver. *Mol Cell Biochem* 64:89–95, 1984.

Taraschi, T.F.; Ellingson, J.S.; Wu, A.; Zimmerman, R.; and Rubin, E. Membrane tolerance to ethanol is rapidly lost after withdrawal: A model for studies of membrane adaptation. *Proc Natl Acad Sci USA* 83(11):3669–3673, 1986a.

Taraschi, T.F.; Ellingson, J.S.; Wu, A.; Zimmerman, R.F.; and Rubin, E. Phosphatidylinositol from ethanol-fed rats confers membrane tolerance to ethanol. *Proc Natl Acad Sci USA* 83(24):9398–9402, 1986b.

Taraschi, T.F.; Wu, A.; and Rubin, E. Phospholipid spin probes measure the effects of ethanol on the molecular order of liver microsomes. *Biochemistry* 24:7096–7101, 1985.

Waring, A.J.; Rottenberg, H.; Ohnishi, T.; and Rubin, E. Membranes and phospholipids of liver mitochondria from chronic alcoholic rats are resistant to membrane disordering by alcohol. *Proc Natl Acad Sci USA* 78(4):2582–2586, 1981.

Positron Emission Tomography and Single Photon Emission Computed Tomography Section

18

ADVANCES IN SPECT IMAGING FOR NEUROPSYCHIATRY

Richard Coppola, D.Sc.¹

The past few years have seen a surge of interest in single photon emission computed tomography (SPECT) spurred by newly developed imaging agents and improvements in scanner technology. At two recent Society for Nuclear Medicine meetings, Dr. Henry Wagner chose SPECT brain scans as "Picture of the Year" (Wagner 1989, 1990).

This chapter concerns advances in SPECT, as reflected in the recent work of the National Institute of Mental Health (NIMH) Clinical Brain Disorders Branch (CBDB). It is not intended to be a comprehensive review.

REGIONAL CEREBRAL BLOOD FLOW

Our interest in SPECT arose from the early studies of Weinberger et al. (1986), who used the inert tracer, radioactive xenon-133, and a helmet-type radiation detector system. During that procedure, the

subject inhales a mixture of radioactive xenon and air for a specified period of time, usually 1 minute. After that, while the subject breathes fresh air, xenon clears from the tissue in proportion to blood flow. Through measurement of the clearance curve, blood flow can be quantified in absolute terms

ACRONYMS

DLPFC	<i>dorsolateral prefrontal cortex</i>
ECD	<i>ethyl cysteinate dimer</i>
HM-PAO	<i>hexamethyl propylene amine oxime</i>
IMP	<i>iodoamphetamine</i>
rCBF	<i>regional cerebral blood flow</i>
PET	<i>positron emission tomography</i>
QNB	<i>3-quinuclidinyl-4-iodobenzilate</i>
ROI	<i>regions of interest</i>
SPECT	<i>single photon emission computed tomography</i>
WCS	<i>Wisconsin Card Sort</i>

¹Clinical Brain Disorders Branch, National Institute of Mental Health Neuroscience Center, St. Elizabeths, Washington, DC 20032

(Obrist et al. 1975). The clearance curve is measured regionally by the set of detectors that surround the head, and blood flow is then calculated for each detector location.

Clinical studies have compared regional cerebral blood flow (rCBF) changes in schizophrenic patients and normal controls during resting conditions and during performance of a cognitive task (Weinberger et al. 1986). There were no differences in blood flow during rest. However, under cognitive activation conditions, such as using the Wisconsin Card Sort (WCS) task, compared with a number-matching task, rCBF differences were observed between the clinical groups.

Several points are important in such comparisons. One is that resting conditions may fail to distinguish any differences in rCBF. Another is that a cognitive task is necessary to reveal patient differences, and an active comparison task is required to control for the neural activation that is not specific to the task. Isolation of the cognitive component of interest in this manner enables study of the pattern of regional activation associated with it. The activation due to visual stimuli and motor responses is common to both tasks, thus any differences in the resulting pattern of rCBF should be attributable to the cognitive components differing between the tasks.

Although in these early studies (Weinberger et al. 1986) schizophrenic patients did not differ from normal subjects at rest, a statistically significant difference between

the groups was found by comparison of the rCBF during the WCS with that during the number-matching task. Thus, while normal subjects revealed activation for a detector located over dorsolateral prefrontal cortex, the schizophrenic patients failed to show this activation.

DYNAMIC SPECT

The helmet-type detector system has certain advantages in terms of straightforward interpretation and quantification but is limited in terms of both spatial resolution and localization to areas of the cortical mantle. Because of these limitations, it would be very desirable to follow the earlier studies using a technique that would allow more detailed examination of functional neurophysiology.

Tomographic techniques facilitate computation of brain measures from two-dimensional slices that include both cortical and subcortical structures. Tomography requires a set of "pictures" or projections from all angles surrounding the object to be reconstructed. In positron emission tomography (PET), data are accumulated from various projections, according to coincidence detection. The positron emitter used as the radioactive marker for the process of interest decays by producing a positron. This particle travels only a very short distance before annihilating with a free electron, producing two photons that travel in different directions, 180° apart. By surrounding the object of interest--

in this case, the brain--with a set of detectors and searching for the simultaneous movement of the two photons, one can determine the ray line along which the original event occurred. It is the straight line drawn between the two detectors that "sees" the two photons.

In contrast, with SPECT agents, only a single photon is available for detection. Determination of the ray line or projection requires collimation, in which, essentially, the detectors see activity only along a line of sight determined by the lead "tubes" in front of them. Because of this collimation, only those photons that pass through the lead are detected; most are lost. Thus, SPECT recovers a much smaller percentage of the available radioactivity than PET.

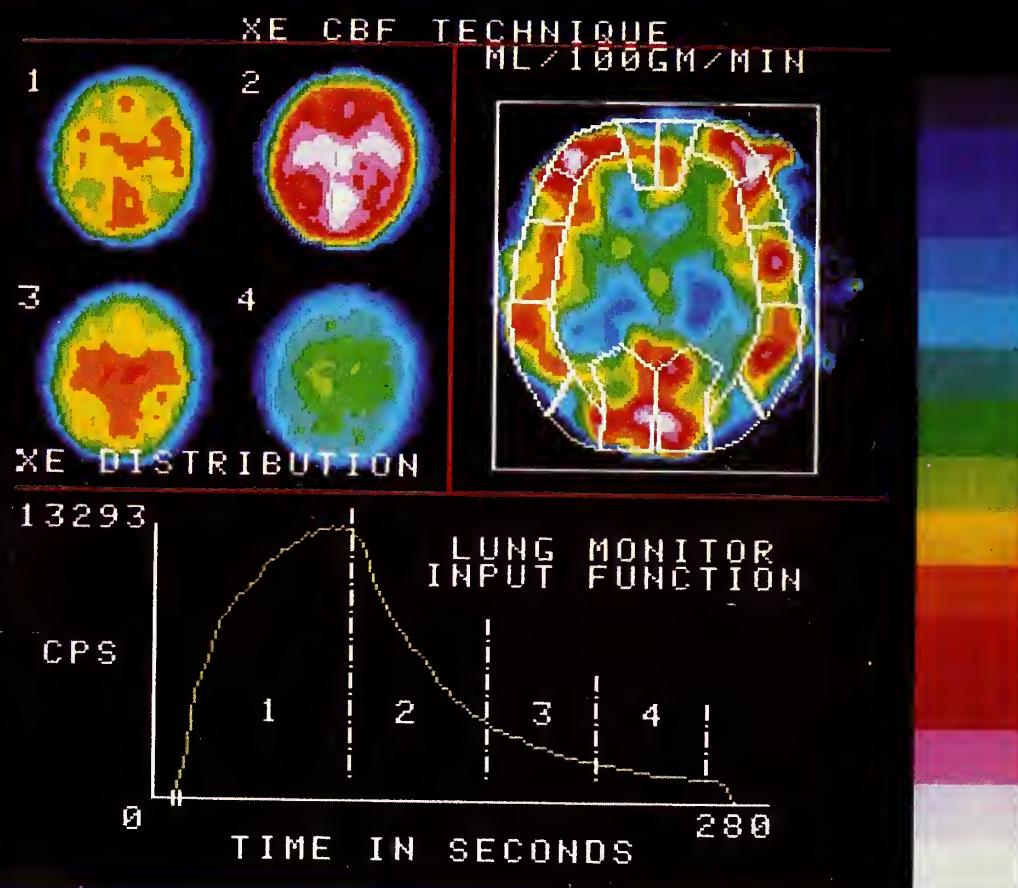
The degree of sensitivity possible for SPECT is a direct tradeoff with spatial resolution. Finer spatial resolution requires smaller "holes" in the collimators, thus decreasing the number of photons detected. SPECT is still capable of quite respectable resolution compared with that of PET, as our 3-quinuclidinyl-4-iodobenzilate (QNB) scans will demonstrate.

Another tradeoff that benefits SPECT is the availability of the single-photon-emitting isotopes generally in use. Positron emitters are short-lived, i.e., their half-lives are on the order of minutes, and they must be produced in a nearby cyclotron. SPECT isotopes have relatively longer half-lives and are available for purchase by mail.

The ^{133}Xe inhalation technique can be applied to dynamic SPECT. A rapidly rotating SPECT camera (Stokely et al. 1980) has enough dynamic sensitivity to collect counts sufficient to reconstruct the distribution of activity within a very short period of time. Four "pictures" are reconstructed to yield four time points to be used for flow calculation. Four collection periods correspond to the first 90 seconds that radioactive Xe is rebreathed and three 60-second collections during washout, when room air is inhaled and exhaled air is trapped to contain the radioactive exhaust. Following the dynamics in the sequence of pictures made from the four collections enables calculation of the blood flow.

Figure 1 illustrates the overall procedure, showing the four collections, the lung curve used as the input function, and the final flow picture. This final picture is then overlaid with a size-adjusted template in order to measure CBF in particular regions of interest (ROI). When a cognitive task is performed during this time period, the measured CBF corresponds to the distribution of task-related neural activity. A special feature of the scanner used in our laboratory is that the gantry operates at a tilt, allowing the subject to be seated in a relatively upright position during task performance and data collection.

SPECT studies can be conducted in close temporal proximity: The dosimetry allows as many repeat measurements as needed for drug

FIGURE 1

Xenon blood flow, measured by dynamic SPECT. At the upper left are the four static pictures obtained during the 4.5-minute procedure. At the bottom is the lung curve used as an approximation of the input function. The upper right-hand flow picture was computed from the dynamic information, then overlaid with the measurement template.

investigations. Our laboratory (Daniel et al. 1991) compared CBF in a group of schizophrenic patients performing the WCS task and a bar-matching control task on two occasions 1 week apart. The subjects received either placebo or acute amphetamine administration in counterbalanced order on these two occasions. The task order was the same on each of the two study days but counterbalanced across subjects. The global effect of amphetamine was a reduction in CBF; however, the regional effect was

enhanced signal-to-noise ratios in relevant cortical areas. That is, following placebo administration, there was no difference in rCBF during WCS and bar-matching tasks, in any of the ROIs. After amphetamine administration, however, there was a significant difference, especially for the ROI that would correspond to the dorsolateral pre-frontal cortex (DLPFC).

A comparison of schizophrenic patients and normal controls was made using essentially the same methods, i.e., dynamic SPECT and

^{133}Xe (Marenco et al. 1991). ROIs on three slices measured for all conditions constituted the data base. Because global blood flow changes that might be task- or group-related can obscure regional differences, this examination comprised several methods of analysis. Significant task activation seen in the normal control group for a set of ROIs that included DLPFC was not seen in the patient group. This absence of activation in schizophrenic patients translated into a significant patient-versus-normal group difference in the activation scores (i.e., WCS minus bar-matching task, region by region).

Dynamic SPECT with ^{133}Xe suffers from severe count limitations. The collimation required even for 16-mm nominal resolution (20-mm axial slice thickness) reduces the available counts and consequently limits image quality and quantification. Another isotope of xenon, ^{127}Xe , has superior qualities for SPECT; it offers five times the number of photons available in a similar patient dose of ^{133}Xe . We have shown that ^{127}Xe is a viable isotope for use in SPECT and that 9-mm in-plane resolution can be achieved for absolute blood flow measurement. The problem remains that ^{127}Xe is very expensive and scarcely available. We are investigating a reactor production scheme and development of a reuse system that could lower the cost and provide year-round availability.

Several other imaging agents that are taken up in brain in proportion to blood flow have been

seen in the current surge of imaging applications (Ring et al. 1991). Iodoamphetamine (^{123}I -IMP) has problems of redistribution; i.e., a stable pattern in brain is maintained only for a very short period of time and its half-life is such that the radioactivity is not cleared for several days. The use of IMP is thus limited to a single investigation at a time, consequently an activation task and its control would have to be performed several days apart. Furthermore IMP is not a "pure" flow agent and may interact with other substrates that could differ across clinical groups.

Technetium-labeled hexamethyl propylene amine oxime ($^{99\text{m}}\text{Tc}$ -HM-PAO), which has a more stable distribution and a "better" relationship to blood flow, has been recently used more as a task-related agent.

Our group and several others have demonstrated the possibility of split-dose methods for performing back-to-back examinations allowing two task-related studies to be conducted at a single sitting. Because the distribution of $^{99\text{m}}\text{Tc}$ -HM-PAO is stable for some time, the activity recorded in the first of a pair of investigations can be considered background and subtracted from the second data set once appropriate dose and decay corrections have been made. Nonetheless, problems in quantification remain. The resulting activity is proportional to flow but does not provide an absolute measurement, thus some form of normalization is required before statistical comparisons can be made. Moreover, the

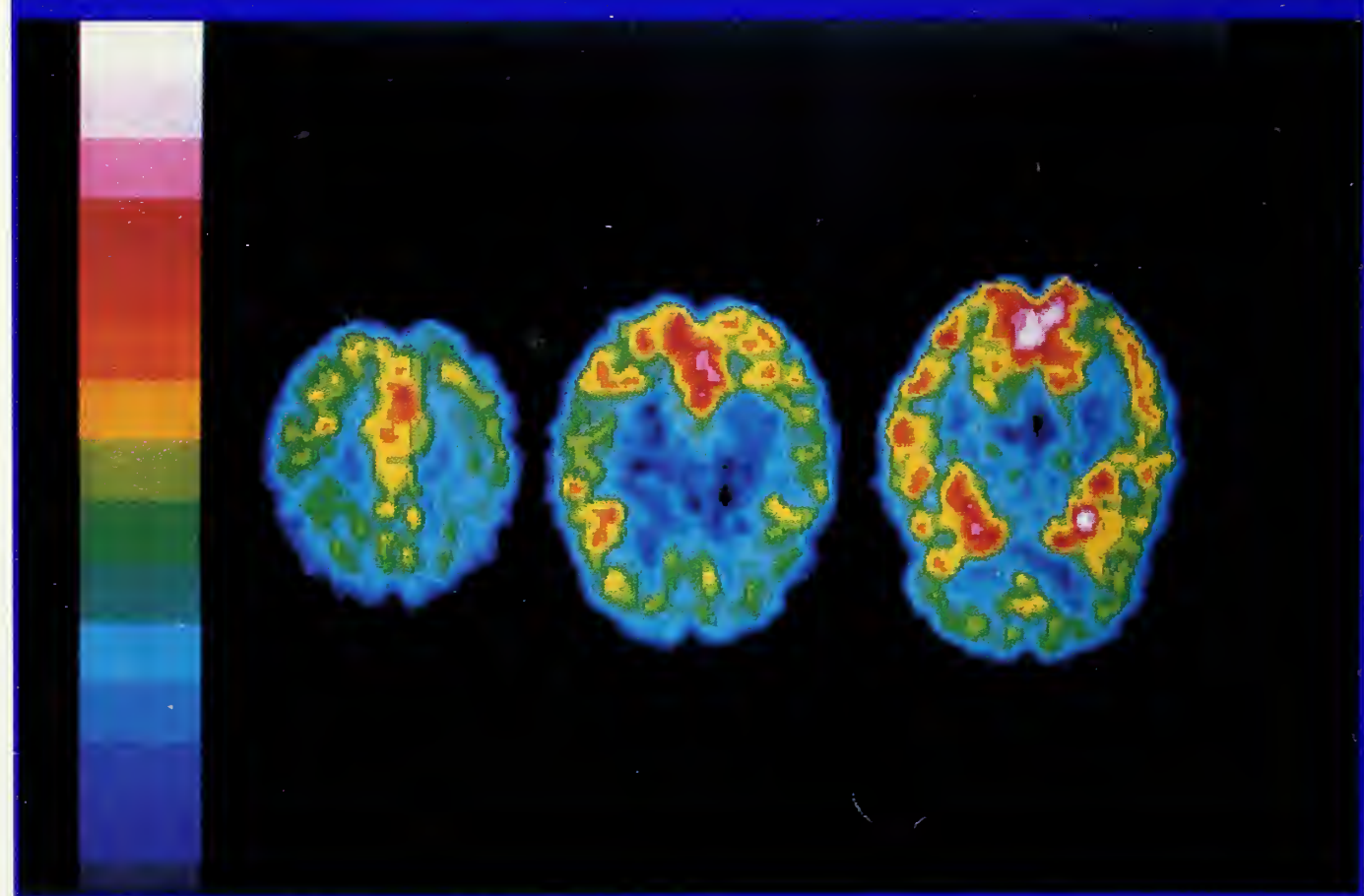
uptake with flow appears to be nonlinear; therefore, some correction should be made, especially for high-flow regions.

SPECT NEUROCHEMISTRY

Perhaps the most exciting advances in SPECT are in the area of brain neurochemistry. The CBDB first pursued this line of research with ^{123}I -labeled QNB (I-QNB), a cholinergic receptor ligand, a compound that is taken up and binds to the muscarinic receptors in brain. The rate of uptake is such that, when a suitable period of time elapses before imaging, the resulting activity

distribution appears to become essentially independent of blood flow. At that point in time, the distribution is stable, thus one can compensate for the low sensitivity and low level of radioactivity by increasing scan time. Using this method, our laboratory (Weinberger et al. 1991) has obtained 9-mm and even 6-mm image resolution (nominal in-plane resolution of the collimators that were employed). Figure 2 shows frontal defects in a patient scanned with the 6-mm collimator. Comparison of regional variations in activity showed a high degree of agreement with receptor density, as

FIGURE 2



^{123}I -QNB SPECT scan, showing frontal defects. These three slices were obtained using a 6-mm collimator (from Weinberger et al. 1991).

measured by post mortem tissue techniques.

SPECT data from a group of severely demented patients revealed severely compromised cortical receptor distribution. Furthermore, there was a high degree of correspondence between the region of diminished uptake and impaired function in the cortical area predicted by neuropsychological examination. Interpretation of these results is problematic. Magnetic resonance imaging showed that these patients had a degree of tissue loss in these regions, as well as reduced function on PET-glucose scans. Nonetheless, QNB distribution, which relates to the integrity of the cholinergic system, may be sensitive to changes that predate functional or tissue losses.

Dynamic SPECT has the ability to track the uptake of such compounds, thus it may be possible to model the kinetics in such a way as to facilitate more explicit quantification. Jones et al. (1990) have developed methods for dynamic data collection at resolutions that allow imaging studies in animals. They compared ^{99m}Tc ethyl cysteinate dimer (ECD) and QNB in cynomolgus monkeys using these methods. ECD is a rapid first-pass uptake compound with characteristics that make it a good flow agent. Comparison of the kinetics of this compound and of QNB demonstrates clearly that at 20 hours postadministration, QNB uptake is diffusion-limited and independent of flow, whereas the ECD distribu-

tion stabilizes after a few minutes, accurately reflecting blood flow.

Further improvements in collimation allow even better resolution for animal imaging. By reducing the field of view, Jones et al. (1990) have shown that dual-focus fan beam collimation with nominal 4-mm resolution can be achieved.

CONCLUSION

SPECT has considerable potential for neuropsychiatric research, as well as for clinical applications in brain imaging. Once the initial radiochemistry questions have been answered, the availability of SPECT agents will render it considerably more advantageous than PET. An onsite cyclotron is not needed, and, in many cases, the imaging agent can be produced from a kit by a nuclear medicine technician. The scanner itself is less expensive and more easily maintained than a PET scanner.

Issues of statistical analysis and registration with anatomical information remain, regardless of the specific imaging modality employed. Advances in these areas will enhance the research capability of all the neuroimaging methods over the next several years.

REFERENCES

- Daniel, D.G.; Weinberger, D.R.; Jones, D.W.; Zigan, J.R.; Coppola, R.; Handel, S.; Bigelow, L.F.; Goldberg, T.E.; Berman, K.F.; and Kleinman, J.E. The effect of amphetamine on regional cerebral blood flow during cognitive activation

- in schizophrenia. *J Neurosci* 1991, in press.
- Jones, D.W.; Saunders, R.C.; Gorey, J.G.; Hosain, R.; Coppola, R.; Reba, R.C.; and Weinberger, D.R. "Dynamic SPECT Comparison of I-123-QNB Kinetics and Blood Flow (Tc-99m-ECD) in Monkey." Presented at the Society for Nuclear Medicine Annual Meeting, 1990.
- Marenco, S.; Coppola, R.; Daniel, D.G.; Ziegler, J.R.; Gorey, J.G.; Jones, D.W.; Berman, K.F.; and Weinberger, D.R. rCBF activation with the Wisconsin card sort test in normal and schizophrenic subjects measured by dynamic SPECT. *J Cereb Blood Flow Metab* 11(suppl 2):S822, 1991.
- Obrist, W.D.; Thompson, H.K.; Wang, H.S.; and Wilkinson, W.E. Regional cerebral blood flow estimated by Xe-133 inhalation. *Stroke* 6:245-256, 1975.
- Ring, H.A.; George, M.; Costa, D.C.; and Ell, P.J. The use of cerebral activation procedures with single photon emission tomography. *Eur J Nucl Med* 18:133-141, 1991.
- Stokely, E.M.; Sveinsdottir, E.; Lassen, N.A.; and Rommer, P. A single photon dynamic computer assisted tomograph (DCAT) for imaging brain function in multiple cross-section. *J Comput Assist Tomogr* 4:230-240, 1980.
- Wagner, H.N. SNM highlights, 1989: "Why not?" *J Nucl Med* 30:1283-1295, 1989.
- Wagner, H.N. Scientific highlights, 1990: The universe within. *J Nucl Med* 31:17A-26A, 1990.
- Weinberger, D.R.; Berman, K.F.; and Zec, R.F. Physiological dysfunction of dorsolateral prefrontal cortex in schizophrenia: I. Regional cerebral blood flow evidence. *Arch Gen Psychiatry* 43:114-124, 1986.
- Weinberger, D.R.; Gibson, R.; Coppola, R.; Jones, D.W.; Molchan, S.; Sunderland, T.; Berman, K.F.; and Reba, R.C. The distribution of cerebral muscarinic acetylcholine receptors in vivo in patients with dementia. *Arch Neurol* 48:169-176, 1991.

SPECT IMAGING OF THE BENZODIAZEPINE RECEPTOR

Marc Laruelle, M.D., Elzbieta Sybirska, M.D., Ph.D., Mohammed Al-Tikriti, Ph.D., Ronald M. Baldwin, Ph.D., and Robert B. Innis, M.D., Ph.D.¹

In recent years, the ability of single photon emission computed tomography (SPECT) to visualize neurotransmitter receptors in living subjects has gained considerable attention. SPECT may offer a viable alternative to the heavier and more expensive positron emission tomography (PET) technology. Positron-emitting isotopes are short lived (e.g., $T_{1/2}$ of 2–110 minutes) and must, therefore, be produced near the imaging facility. In contrast, gamma-emitting isotopes have longer half-lives (e.g., 13 hours for ^{123}I) and may be shipped to a hospital from distant commercial sites. For these reasons, SPECT is a more affordable and available tool than PET for the medical community. To illustrate the capabilities of SPECT neuroreceptor imaging, we report our SPECT studies of the benzodiazepine (BZ) receptor in nonhuman primates using ^{123}I -labeled Ro 16-0154 (ethyl 7-iodo-5,6-

dihydro-5-methyl-6-oxo-4H-imidazo[1,5-a][1,4]benzodiazepine-3-carboxylate).

The BZ drugs are widely used for their anxiolytic, sedative, and anticonvulsant properties. These drugs exert their pharmacological effect by agonistic interaction with specific receptors in the central nervous system (Möhler and Okada 1978; Squires and Braestrup 1977; Braestrup et al. 1977). Central BZ receptors and GABA_A receptors are part of the same supramolecular complex and BZ agonist binding enhances the affinity of GABA for

ACRONYMS

BZ	<i>benzodiazepine</i>
CM	<i>canthomeatal</i>
HPLC	<i>high-pressure liquid chromatography</i>
PET	<i>positron emission tomography</i>
ROI	<i>regions of interest</i>
SPECT	<i>single photon emission computed tomography</i>

¹Departments of Psychiatry, Yale University and Department of Veterans Affairs Medical Center, 950 Campbell Avenue, West Haven, CT 06516

its receptor via allosteric interactions (Polc et al. 1982; Tallman and Gallagher 1985). BZ antagonists like flumazenil (Ro 15-1788) do not induce an intrinsic pharmacological effect on their own, rather they compete with BZ agonists (Hunkeler et al. 1981) and are used in the treatment of BZ intoxication. BZ receptors have been implicated in a wide variety of neuropsychiatric illnesses, including anxiety (Tallman et al. 1980; Wood et al. 1988), ethanol dependence (Davis and Ticku et al. 1981; Suzdak et al. 1986), Huntington's disease (Penney and Young 1982; Walker et al. 1984; Whitehouse et al. 1985), Alzheimer's disease (Owen et al. 1983), Parkinson's disease (Maloteaux et al. 1988), and epilepsy (Savic et al. 1988; Johnson et al. 1990a).

The BZ receptors have been visualized in human and non-human primate brain with several PET radioligands: [¹¹C]flunitrazepam (Comar et al. 1979), [¹¹C]suriclon (Frost et al. 1986); and [¹¹C]Ro 15-1788 (Hantraye et al. 1984; Samson et al. 1985; Persson et al. 1985; Shinotoh et al. 1986). Quantification of the BZ receptors has been reported with [¹¹C]Ro 15-1788 (Pappata et al. 1988; Savic et al. 1988). Successful imaging of the BZ receptors with [¹¹C]Ro 15-1788 led Beer et al. (1990) to use the iodine-containing analogue Ro 16-0154 as an imaging agent for SPECT (see chemical structures, figure 1).

Our evaluation of Ro 16-0154 as a BZ receptor probe for SPECT imaging has progressed from in vitro to

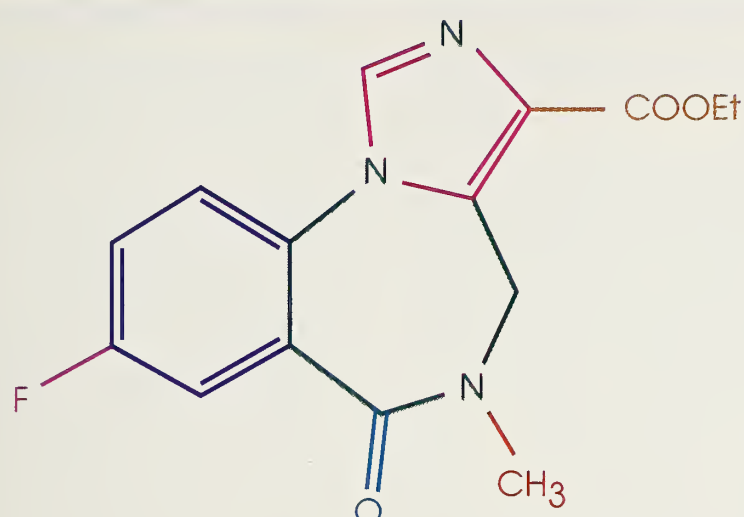
in vivo experimentation in roughly the following order:

- (1) In vitro study of the pharmacological selectivity of binding of the ¹²⁵I-labeled probe to tissue homogenates prepared from monkey brain (Johnson et al. 1990b);
- (2) In vivo study of the time course of brain uptake of the ¹²³I-labeled probe with SPECT in monkeys (Innis et al. 1991a);
- (3) Assessment of the in vivo pharmacological selectivity of [¹²³I]Ro 16-0154 brain uptake with displacement studies using BZ-related agents (Innis et al. 1991b);
- (4) Ex vivo study of the anatomic localization of intravenously administered [¹²³I]Ro 16-0154, and comparison in the same tissue sections with the distribution of BZ receptors measured with in vitro receptor autoradiography using [¹²⁵I]Ro 16-0154 (Sybriska et al. 1990);
- (5) Measurement of the metabolism of the radioligand in plasma and identification of the radioactivity that enters brain; and
- (6) Measurement of the intra-cerebral concentration of free radioligand using the technique of in vivo microdialysis.

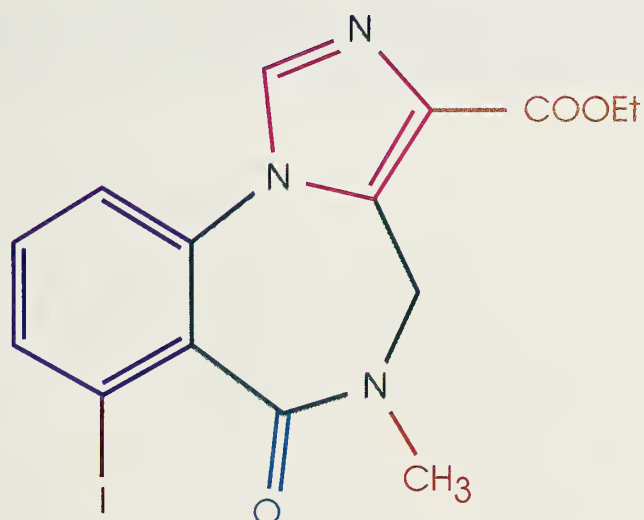
METHODS

Radiolabeling

Radiolabeled Ro 16-0154 was prepared by oxidative radioiodination of the tributyltin precursor (ethyl 7-tributyltin-5,6-dihydro-5-methylmethoxy-6-oxo-4H-imidazo[1,5-a][1,4]

FIGURE 1

Ro 15-1788



Ro 16-0154

Chemical structures of Ro 16-0154 and Ro 15-1788.

benzodiazepine-3-carboxylate), following a no-carrier-added method of iodination (McBride et al. 1991). Tracer was separated from the precursor on an isocratic high-pressure liquid chromatography (HPLC) system with a C-18 reverse phase column and a mobile phase of 55

percent methanol/water. The specific activity was estimated to be 1,700 Ci/mmol for [¹²⁵I]Ro 16-0154 and over 180,000 Ci/mol for [¹²³I]Ro 16-0154. Radiochemical purity was >98 percent. For in vivo studies, the product was reformulated in 6-mL sterile saline with 3 percent ethanol.

In Vitro Homogenate Binding

Homogenate binding studies were performed as described by Johnson et al. (1990b): Frozen rhesus and human occipital and cerebellar cortices were homogenized at 4 °C with a Brinkmann Polytron (setting 6 for 30 seconds) at a dilution of 1:20 (weight/volume) in 25-mM potassium phosphate assay buffer, pH 7.4, then centrifuged (50,000 $\times g \times 10$ minutes) and resuspended 3 times. The final pellet was stored at -80 °C until use. The day of the assay, the tissue was resuspended to a final concentration of 1:1,200. Nonspecific binding was defined by coincubation with 1 μM clonazepam. Saturation studies involved incubation with either increasing concentrations of the radiolabeled compound (0.1–10 nM) or increasing concentrations of the nonradiolabeled analogue (10^{-11} to 10^{-5} M) in the presence of constant concentration of the radioligand. The ligand concentration for displacement studies was 6–8 pM. Association and dissociation experiments were performed at 0, 21, and 37 °C. Dissociation was precipitated by the addition of 1 μM clonazepam. Binding of [^{125}I]Ro 16-0154 was compared with the binding of other BZ ligands ([^3H]flunitrazepam and [^3H]Ro 15-1788). Because BZ have been subtyped as "central" (neuronal) and "peripheral" (present on glial cells and in the kidneys) types, we also compared the binding of [^{125}I]Ro 16-0154 with a selective "peripheral" BZ receptor ligand, [^3H]PK 11195. Data were analyzed with the nonlinear regression analysis program LIG-

AND (Munson and Rodbard 1980), adapted by McPherson (1985).

SPECT Imaging

SPECT scanning experiments were performed with baboons (*Papio anubis*) and rhesus monkeys (*Macaca mulatta*). Animals were anesthetized with pentobarbital intravenously and aligned with a laser light for imaging in planes parallel to the canthomeatal (CM) line. The head was immobilized with a "bean bag" that was molded around the head and hardened on evacuation (Olympic Medical, Seattle, WA). [^{123}I]Ro 16-0154 was injected intravenously at a dose of 9.8 ± 1 mCi (expressed as mean \pm S.E.M.), and brain uptake was monitored in serial 2-minute acquisitions with the 810X Brain Imager (Strichman Medical Equipment, Medfield, MA). This imaging device obtained single slices with an in-plane resolution of approximately 8 mm and a z-axis resolution of 13 mm. Images were attenuation-corrected, assuming uniform attenuation equal to that of water in an ellipse drawn around the brain.

Images were reconstructed in planes parallel to the CM line. Because the highest concentration of radioactivity was consistently localized in the occipital area, the plane through this region (approximately 15 mm rostral to the CM line) was selected for detailed kinetic analyses. The regions of interest (ROI) outlined corresponded roughly to right and left occipital, parietal, striatal, and frontal regions (figure 2). The ROI template was

then applied to all slices from that study. Data were analyzed as the average regional radioactivity, expressed as "counts/2 minutes/pixel." Radioactivity measurements were decay-corrected to time of injection.

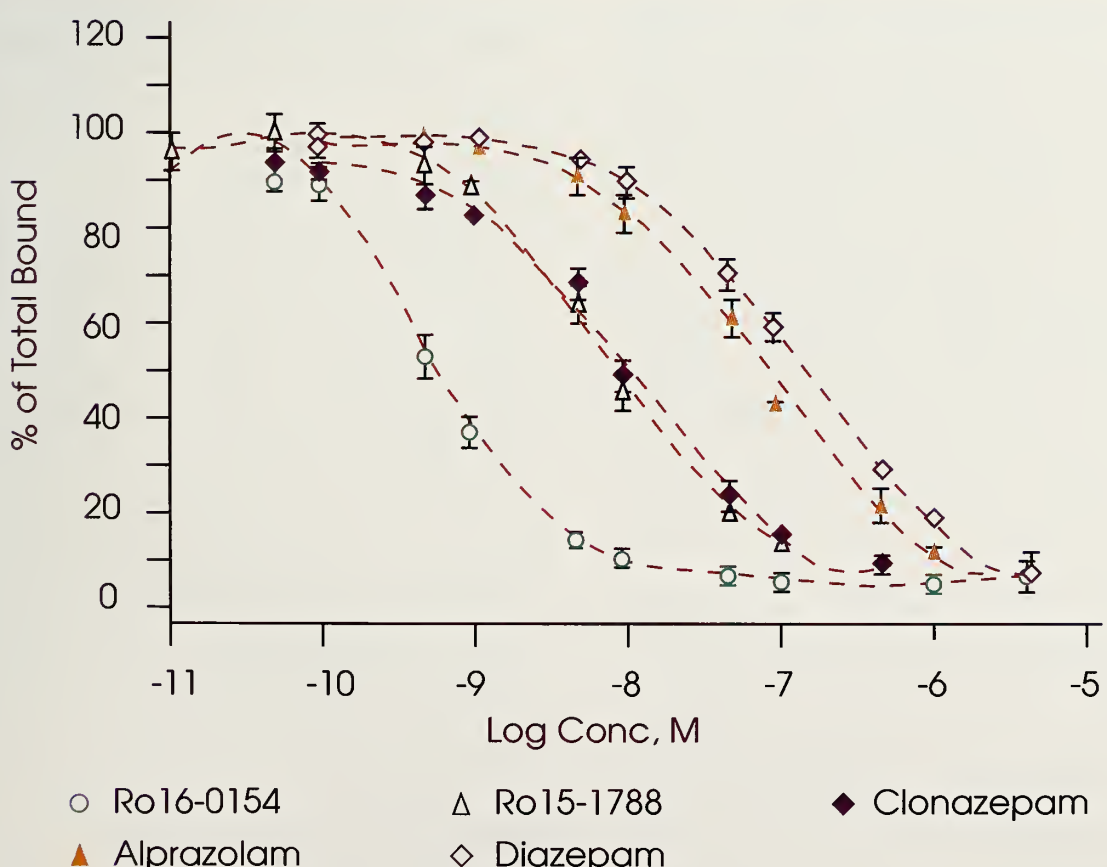
In displacement studies, the animals' core body temperature was maintained at 32–34 °C to ensure a more stable baseline. At this temperature, the washout rate of [^{123}I]Ro 16-0154 after the peak of activity was only 3.3 percent/hour. Complete displacement experiments were performed with one in-

jection of 0.2 mg/kg Ro 15-1788 at 6 hours postinjection of radioligand. Stepwise displacements were obtained by injecting increasing doses of BZ agents at 50- to 60-minute intervals.

Ex Vivo Autoradiography

Six monkeys were studied with ex vivo autoradiography. Under pentobarbital anesthesia, animals were placed in stereotaxic apparatus. Two 19-gauge needles were inserted into the lateral skull along the canthomeatal line. The animal was then moved to the SPECT

FIGURE 2



Displacement of (^{125}I)Ro 16-0154 binding to human cortical membranes measured at 37 °C (K_i values listed in table 1; from Johnson et al. 1990b).

table, and the head positioned so that the transaxial laser light passed directly over the two needles and the midline laser light was centrally located on the facial features. Following injection of the radio-tracer [^{123}I]Ro 16-0154 (mean dose, 8 mCi), the animal was scanned in the Strichman 810X until a plateau of brain uptake was reached (approximately 100 minutes). The animal was then sacrificed with pentobarbital overdose, and serial SPECT scans (2-minute acquisitions) were obtained through the entire brain every 5 mm.

A dye spot was marked on the surface of the brain with a 26-gauge needle passing through the 19-gauge needle in the skull. The calvarium was removed, and the brain was bisected in the midsagittal line. The medial surface of the hemisphere was placed on the bottom of a specially designed brain mold in which the dye spots were aligned on 1 of 11 razor blades, whereupon the mold functioned like an "egg slicer," simultaneously providing up to 10 slabs of brain, each 5-mm thick. These thick slabs were frozen on dry ice between glass slides. Cryostat sections (20- μm thick) were apposed to ^3H Hyperfilm (Amersham) for various time intervals (8–24 hours). For an average injected dose of 8 mCi [^{123}I]Ro 16-0154, the optimal film exposure of the film was obtained at about 12 hours.

^{123}I autoradiographic standards were prepared as ^{123}I -embedded brain paste 20- μm -thick sections. These standards were apposed for

various periods with commercially available ^3H standards in plastic sections, so that the optical density generated by the ^3H standards could be calibrated to activity concentration of ^{123}I . Brain sections were apposed to films together with the ^3H standards. After exposure, the film was developed and the autoradiograms were digitized (Loats Associates, Westminster, MD). Optical densities of the ROI were transformed in activity concentration by the use of the ^3H standards. After decay of ^{123}I radioactivity in tissue (7–10 days), serial sections were used for in vitro receptor autoradiography with [^{125}I]Ro 16-0154, as described in the next section. This procedure allowed comparison on the same tissue slice of the results of ex vivo autoradiography with in vivo receptor autoradiography.

In Vitro Receptor Autoradiography

Slide-mounted tissue sections (20- μm thick) of monkey brains (two adult male rhesus and four adult male vervets) were incubated with 10 pM [^{125}I]Ro 16-0154 in buffer (25 mM potassium phosphate, 150 mM NaCl, pH 7.4) for 60 minutes at 4 °C. Nonspecific binding was defined by coincubation with 1 μM clonazepam. After incubation, sections were washed 3 times for 5 minutes in buffer at 4 °C and quickly dried under a stream of cold air. Slide-mounted sections were apposed to film (Hyperfilm, Amersham) for 3–18 hours together with commercially available ^{125}I standards (Amersham ^{125}I Microscales). After exposure and

development, autoradiograms were digitized and ROI were analyzed with computerized densitometry (Loats). Following film exposure, tissue sections were stained with cresyl violet or neutral red for histological identification of neuroanatomic regions.

Metabolites Analyses in Plasma and Cerebral Tissue

Metabolic analyses of five animals involved serial arterial plasma sampling. Blood samples were taken in heparin-treated syringes and stored at 0–4 °C until analysis. The plasma was separated by centrifugation, and a 200- μ L aliquot was counted in a calibrated gamma counter to provide the total ^{123}I radioactivity. For determination of protein binding, a 200- μ L aliquot was subjected to centrifugal ultrafiltration with a membrane having a 30,000 molecular weight cutoff. The free (i.e., non-protein bound) fraction for each animal was calculated as the product of plasma-free fraction and total filtrate radioactivity.

For metabolite analysis, the plasma was extracted 3 times with equal volumes of ethyl acetate; the organic solvent was evaporated, and the residue was taken up in 55 percent MeOH/H₂O and analyzed by HPLC on a C-18 reverse-phase column, eluting with the same solvent at a flow rate of 0.8 mL/minute. Control samples were analyzed in the same way each time: An aliquot of ^{123}I product was added to a sample of whole blood at the time of administration and to another sample at the time of anal-

ysis (15–18 hours later). These measurements confirmed the stability of the compound, provided actual protein-binding data in each subject, and served to calibrate the HPLC system.

The chemical identity of the radioactivity in brain was measured in two separate experiments in which two African green monkeys (one per experiment) were sacrificed 120 minutes postinjection of radioligand. Activity was extracted with ethyl acetate, and metabolite analyses were performed by the same method as that used for plasma.

Microdialysis Measurements

Four microdialysis probes with exposed tips of 3-mm length (Bradberry and Roth 1989) were inserted in frontal and occipital gray matter and right and left parietal lobe white matter of a 6-kg pentobarbital-anesthetized male vervet monkey whose head was fixed in a stereotaxic apparatus. The flow rate for the physiological perfusion buffer dialysate was 0.5 μ L/minute (Bradberry and Roth 1989). The probes were allowed to equilibrate in tissue for 1 hour before intravenous injection of 12 mCi [^{123}I]Ro 16-0154. From each probe, dialysate fluid (5- μ L samples) was collected for serial 10-minute intervals for 120 minutes. Recovery from the dialysate probes was estimated *in vitro* by placing them in perfusion fluid with [^{123}I]Ro 16-0154 (1 μ Ci/mL, a concentration approximating that in monkey brain at time of maximal uptake). The average recovery (calculated as the concentration of

radioactivity in the dialysate compared to that in the external fluid) for the four probes at a flow rate of 0.5 μ L/minute was 19 percent, measured immediately before and after the experiment.

RESULTS

In Vitro Homogenate Binding

Kinetic Studies

The kinetics of [125 I]Ro 16-0154 binding to brain membranes were studied at 0, 21, and 37 °C. As expected, the association of the radioligand reached equilibrium faster at higher temperatures. Equilibration required approximately 90–120 minutes at 0 °C; 30 minutes at 21 °C; and 12 minutes at 37 °C.

Detailed dissociation studies at 0, 21, and 37 °C were conducted after binding had reached apparent equilibrium. Dissociation was precipitated by the addition of 1 μ M clonazepam. The dissociation $T_{1/2}$ was approximately 2 minutes at 37 °C; 20 minutes at 21 °C, and >45 minutes at 0 °C.

Saturation Studies

Regression analyses of the Scatchard transformation of the saturation data were linear, consistent with the binding to a single class of saturable sites. The K_D was 0.28±0.1 nM at 0 °C; 0.27±0.1 nM at 21 °C; and 0.52±0.1 nM at 37 °C (data expressed as mean ± S.E.M. of three experiments). We thus observed a 2-fold decrease of affinity with increasing temperatures. In comparison, [3 H]Ro 15-1788 showed a 5-fold decrease of

affinity between the K_D at 0 °C (1.1±0.1 nM) and 37 °C (5.8±1.1 nM). Unaffected by temperature, B_{max} was similar for the three ligands used (45±4 fmol/mg protein). Nonspecific binding of [125 I]Ro 16-0154 measured in the presence of 1 μ M clonazepam was >10 percent of the total binding at radioligand concentration less than the K_D value. To evaluate this ligand for in vivo studies, we examined the effect of adding a physiological concentration of NaCl (150 mM) on binding. The presence of NaCl induced a 15 percent increase in affinity, while the B_{max} was unaffected. Thus, Ro 16-0154 appeared to be a potentially valuable ligand for in vivo studies, demonstrating a saturable binding with high affinity to a single class of sites and low nonspecific binding in conditions approximating the in vivo environment.

Displacement Studies

BZ agonists (clonazepam, midazolam, flunitrazepam, alprazolam, and diazepam), antagonists (Ro 16-0154 and Ro 15-1788), and the inverse agonist methyl 6,7-dimethoxy-4-ethyl- β -carboline-3-carboxylate (DMCM) were tested for their potencies to displace [125 I]Ro 16-0154, [3 H]Ro 15-1788, and [3 H]flunitrazepam binding at 0, 21, and 37 °C. BZ agents displaced [125 I]Ro 16-0154 in a monophasic manner; their potencies were similar to those previously reported for displacing other BZ radioligands. The order of potency of the various BZ agents for displacing [125 I]Ro 16-0154, [3 H]Ro 15-1788, and [3 H]flunitrazepam was

Table 1. Displacement of (¹²⁵I)Ro 16-0154 to human occipital cortex at 37 °C

Agents	K_i (nM)*
Agonists	
Clonazepam	10.6 ± 0.9
Midazolam	22.4 ± 0.9
Flunitrazepam	34.3 ± 2.4
Alprazolam	61.0 ± 2.6
Diazepam	128 ± 3
Antagonists	
Ro 16-0154	0.5 ± 0.1
Ro 15-1788	7.7 ± 0.9
Inverse Agonist	
DMCM	2.3 ± 0.3

Displacement studies were performed at 37 °C at (¹²⁵I)Ro 16-0154 concentrations of 6-8 pM with increasing doses of unlabeled drugs (10⁻¹¹ to 10⁻⁵ M) and analyzed with the program LIGAND. Other compounds tested--butaclamol, ketanserin, raclopride, scopolamine, prazosin, clonidine, GABA, and bicuculline--showed no significant displacement at a concentration of 10 µM.

*Means ± S.E.M.; n=3.

the same. The K_i of the agonist increased by 10- to 20-fold at 37 °C compared with their K_i values at 0 °C. The K_i values of the antagonists showed a less robust dependence on temperature: The increase of the K_i of [¹²³I]Ro 16-0154 was 2-fold while that of K_i for [³H]Ro 15-1788 was 4-fold at 37 °C versus 0 °C.

In vitro displacements of [¹²⁵I]Ro 16-0154 by various BZ agents at 37 °C are presented in figure 2; the corresponding K_i values are given in table I. A variety of non-BZ agents (butaclamol, ketanserin, raclopride, scopolamine, prazosin, clonidine, GABA, and bicuculline) failed to show any significant displacement of [¹²⁵I]Ro 16-0154 at concentrations up to 10 µM. Thus, binding of [¹²⁵I]Ro

16-0154 in human cortex appears to be selective for the BZ receptor.

“Central” Versus “Peripheral” BZ Receptor Binding

In human cortex, the binding of the selective peripheral BZ receptor ligand [³H]PK 11195 was about 50 percent of that for either [¹²⁵I]Ro 16-0154 or [³H]Ro 15-1788. Neither Ro 16-0154 nor Ro 15-1788 showed any potency for displacing [³H]PK 11195, while PK 11195 showed little potency to displace [¹²⁵I]Ro 16-0154 and [³H]Ro 15-1788 binding. In rat kidney homogenate, where only the peripheral subtype of BZ receptors is reported, no specific binding of [¹²⁵I]Ro 16-0154 and [³H]Ro 15-1788 was detectable, and both Ro 16-0154 and Ro 15-1788 failed to displace

$[^3\text{H}]PK 11195$ binding. These experiments support the notion that $[^{125}\text{I}]Ro 16-0154$ is specific for the central subtype of BZ receptors.

SPECT Measurement of Brain Uptake

Following intravenous injection of $[^{123}\text{I}]Ro 16-0154$, brain uptake increased rapidly to a peak that occurred at 70 ± 10 minutes (mean \pm S.E.M., $n=8$). The uptake was consistently higher in the occipital area. At the time of maximal uptake, the relative count densities in brain regions were occipital (100 percent), temporoparietal (66 ± 4 percent), frontal (66 ± 4 percent), striatal (46 ± 2 percent), and cerebellar (65 ± 4 percent), expressed as mean \pm S.E.M. for the first eight animals studied (figure 3). Because of the limited spatial resolution of the camera and the "blurring" of the activity distribution that it induced, a region devoid of receptors (which means consisting only of white matter) could not be properly analyzed. Nevertheless, the regional distribution of the activity was in accordance with the known distribution of BZ receptors in primate brain.

After peak uptake, brain activity showed a relatively slow washout period for at least the next 240 minutes. Washout of radioactivity was dependent upon body temperature of the animal: 14 ± 0.8 percent/hour at 37°C and 3.3 ± 1.1 percent/hour at $32-34^\circ\text{C}$, measured as the percent change of peak occipital activity per hour.

FIGURE 3a



Transaxial slice through the baboon brain at the level of the occipital cortex and striatum approximately 70 minutes postinjection of 16 mCi ($[^{123}\text{I}]Ro 16-0154$). This image was reconstructed from data acquired by the Strichman 810x over 2 minutes from a plane parallel and approximately 15 mm superior to the canthomeatal line (from Innis et al. 1991b).

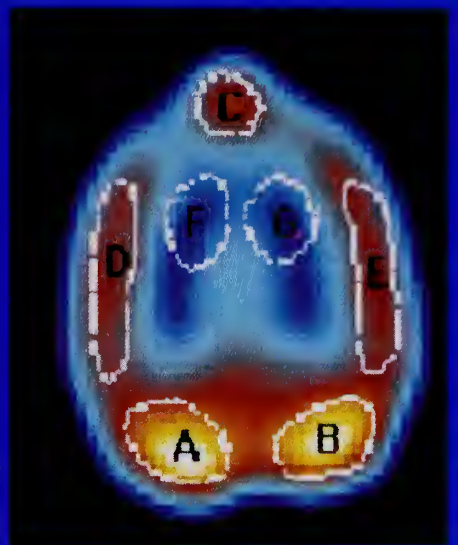
In Vivo Displacement Studies

Stepwise Displacement Studies

Approximately 90 percent of brain radioactivity was displaced by the intravenous administration of the structurally related BZ antagonist Ro 15-1788 (0.2 mg/kg; figures 3c and 4c). Thus, even up to 6 hours postinjection of radioligand, the vast majority of brain radioactivity appeared to be associated with the BZ receptor, therefore dis-

FIGURE 3b

Region Information			
NAME	AREA	COUNTS	DENSITY
A) R OCCIP	62	199567	3218
B) L OCCIP	61	195207	3200
C) FRONTAL	34	91265	2684
D) R PARIET	65	172030	2646
E) L PARIET	69	181606	2631
F) R STRIA	43	71961	1673
G) L STRIA	44	74026	1682



Typical regions of interest drawn on the computer screen to determine concentration of radioactivity. The area of the region is expressed in pixels, and the density in counts/2 minutes/pixel: Each pixel corresponds to approximately 1.6x1.6 mm (from Innis et al. 1991b).

placeable by BZ agents. This long period of relatively stable brain uptake of [^{123}I]Ro 16-0154 was used as a baseline against which to compare the effects of increasing doses of five BZ receptor drugs (figures 4a, 4b, and 5).

These stepwise curves were analyzed using the residual activity after the final dose of displacer as a measure of nondisplaceable radioligand (typically 5–10 percent of peak levels). The nondisplaceable level was subtracted from each point to provide a measure of specifically bound radioligand. The percent decrease of specific uptake following each dose of displacer was measured at the plateau level in the 5- to 10-minute period prior to the next displacing dose. The dose of displacer required to inhibit 50 percent of specific uptake (ED_{50}) was determined from a straight-line fit

of the log-probit plot of percent displacement versus log of cumulative dose.

Stepwise displacement studies were performed 2–3 times for each of five BZ agents: two antagonists (Ro 16-0154 and Ro 15-1788) and three agonists (diazepam, alprazolam, and clonazepam). The reproducibility of ED_{50} measurements studied in different animals varied by <3-fold (table 2). The relative order of in vivo potency of the five agents was: Ro 16-0154 > Ro 15-1788 >> clonazepam \approx alprazolam > diazepam.

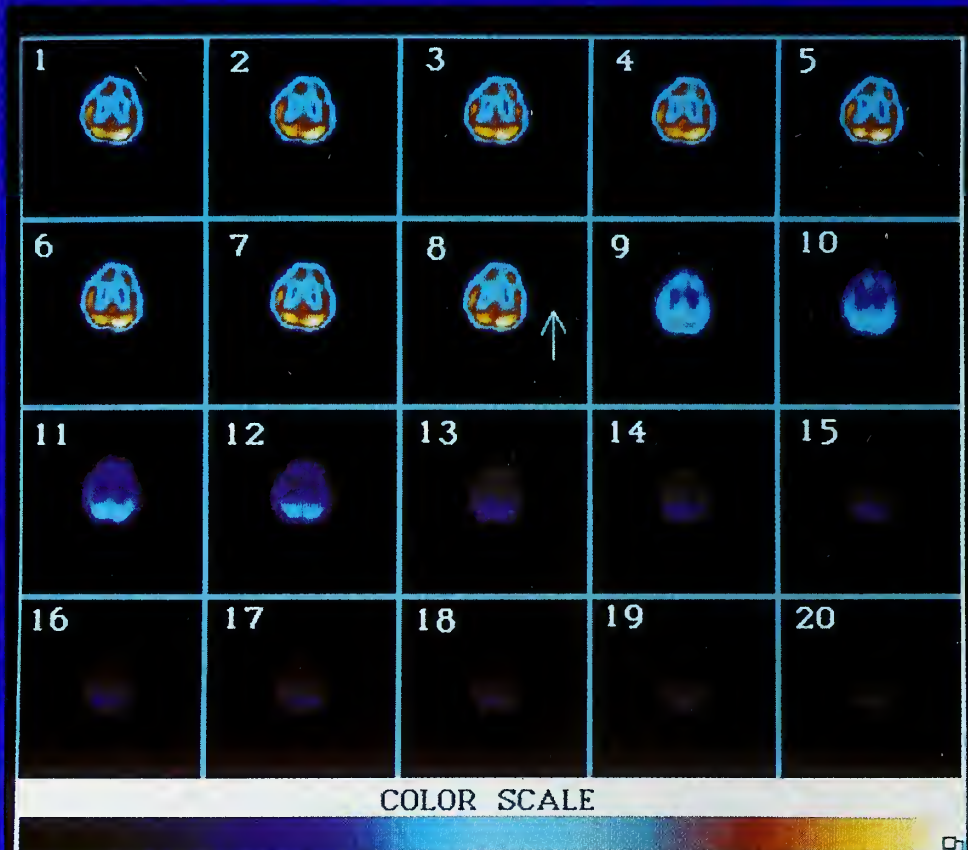
In addition to providing a measure of in vivo potency, the stepwise displacement curves provided pharmacokinetic information on the time required by the displacing agent to reach the brain's BZ receptor. For example, the displacement curves of Ro 16-0154

were more shallow than those of Ro 15-1788 (figures 4a and b), indicating that Ro 16-0154 was relatively slow in gaining access to the BZ receptor. To gain a measure of this pharmacokinetic parameter, the individual displacement curves were fit to exponential curves and the $T_{1/2}$ values were calculated (table 2). The speed of drug access to the BZ receptor was *not* correlated with *in vivo* potency. For example, Ro 15-1788 caused a more rapid displacement but was 4-fold less potent than Ro 16-0154.

Correlation of In Vivo Drug Potency with In Vitro Receptor Affinity

The inhibition constant K_i , which is inversely related to affinity, was determined using primate brain and incubation temperature of 37 °C. As the *in vivo* measure of potency, ED_{50} was highly correlated with the *in vitro* measure of receptor affinity (K_i), when displayed as either a linear-linear ($r=0.98$) or the more stringent log-log plot ($r=0.94$; figure 6).

FIGURE 3c



Repeat pictures from serial 2-minute acquisitions through the same area of baboon brain, with slice 1 starting approximately 60 minutes postinjection of 15 mCi (^{123}I)Ro 16-0154. Between slices 8 and 9, the administration of nonradioactive Ro 15-1788 (0.1 mg/kg, i.v.) caused a rapid decrease of almost 90 percent of radioactivity from the brain. This washout of radioactivity is consistent with displacement of radioligand bound to the benzodiazepine receptor (from Innis et al. 1991b).

Single Dose Displacement

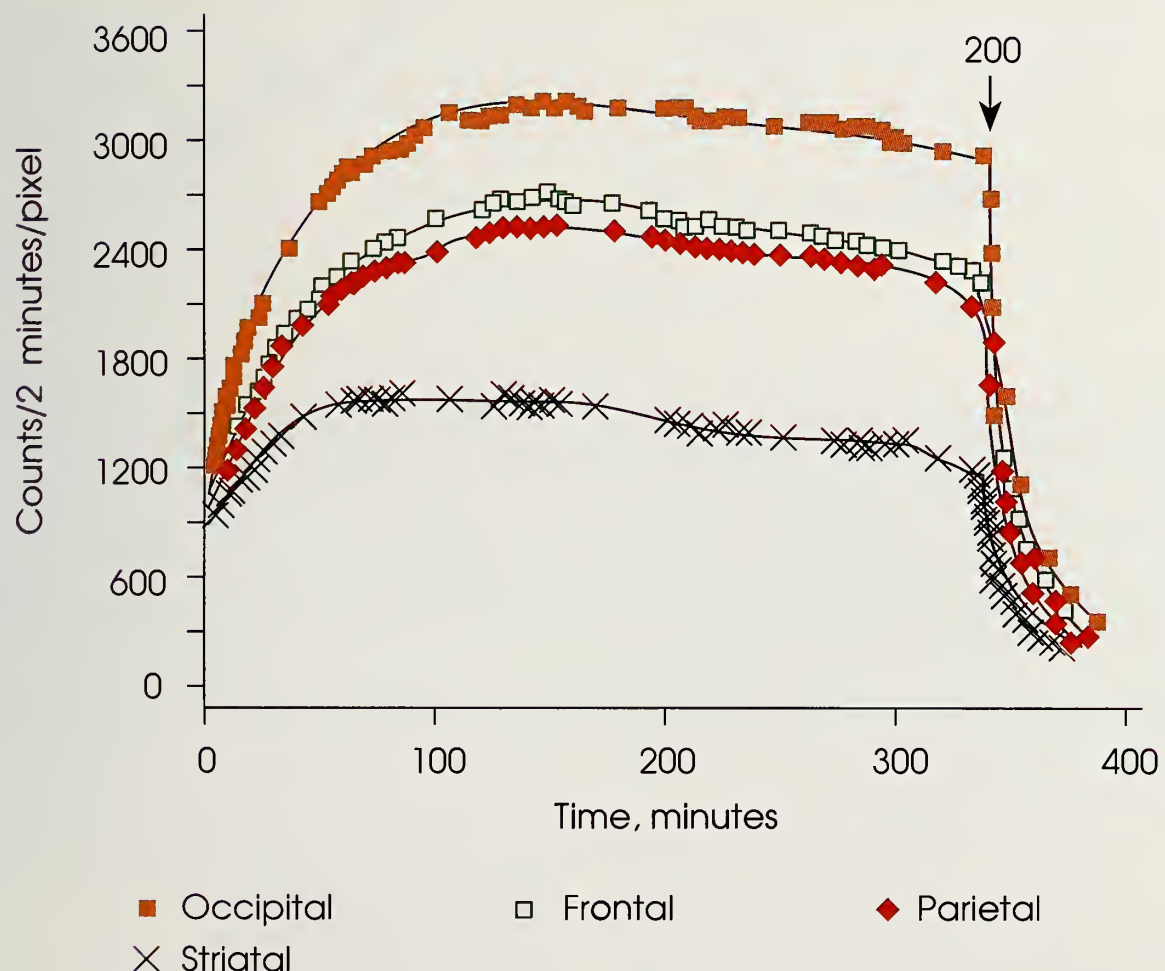
The analysis of the stepwise displacement curves uses the *cumulative* dose. The accuracy of this cumulative dose analysis depends upon the assumption that an insignificant amount of previous doses of displacer has been removed from the brain. To test the accuracy of this method for the displacing agent Ro 15-1788, we compared the displacement caused by a single intravenous injection of

20 µg/kg to the result determined by stepwise displacement above, which was the average of three separate experimental measurements. Since stepwise curves typically used two initial doses of 10 µg/kg Ro 15-1788, separated by 40–60 minutes, the experimental question was: Does a single dose of 20 µg/kg Ro

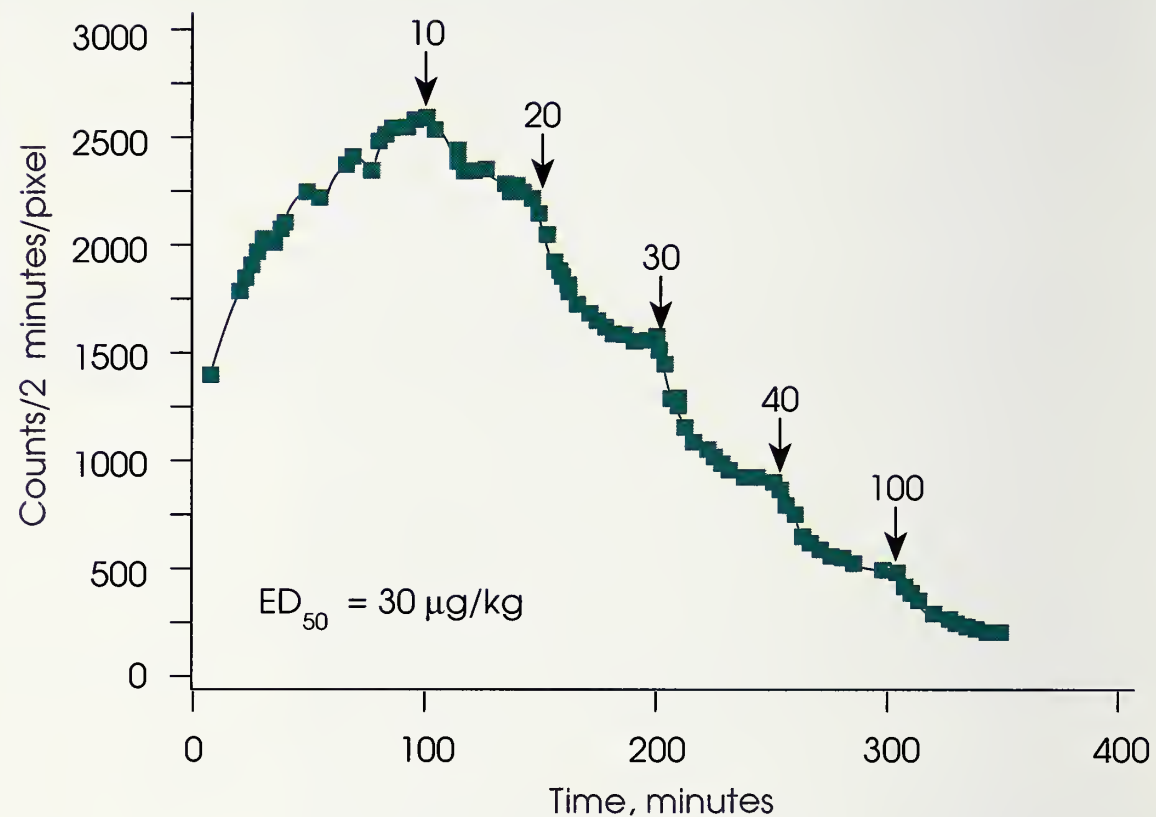
15-1788 equal that of two doses of 10 µg/kg administered at different times?

The administration of 20 µg/kg Ro 15-1788 caused displacement of 41 percent (mean value of two separate measurements of 39 and 42 percent). This value was similar to the average displacement value of stepwise

FIGURE 4a



Time course of brain radioactive densities in monkeys following intravenous injection of (¹²³I)Ro 16-0154 at time 0 (from Innis et al. 1991b). Late displacement with Ro 15-1788. Animal was injected with 15 mCi (¹²³I)Ro 16-0154, and serial 1- to 2-minute scans were obtained from the transaxial slice approximately 15 mm rostral to the canthomeatal line. Listed from highest to lowest, regional activities were: occipital (■); frontal (□); parietal (◆); and striatal (X). Ro 15-1788 (200 µg/kg, i.v.) caused a rapid decrease of almost 90 percent of brain radioactivity.

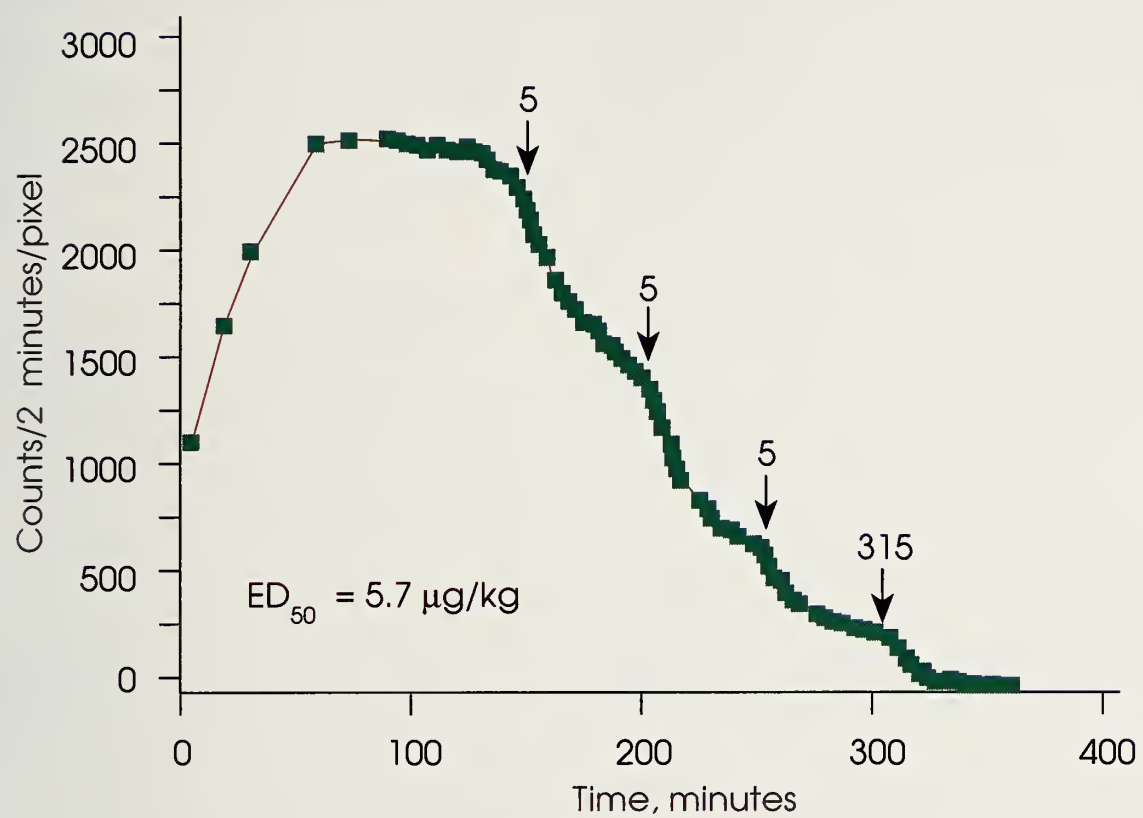
FIGURE 4b

Time course of brain radioactive densities in monkeys following intravenous injection of $[^{123}\text{I}]$ Ro 16-0154 at time 0 (from Innis et al. 1991b). Stepwise displacement with Ro 15-1788. Following injection of 14.9 mCi $[^{123}\text{I}]$ Ro 16-0154, nonradioactive Ro 15-1788 was injected intravenously with the individual doses indicated in microgram per kilogram units. "Specific" uptake was defined as the difference between "total" uptake (graphed above) and "nondisplaceable" uptake remaining after the last dose of Ro 15-1788. The ED_{50} of the displacing agent (i.e., Ro 15-1788) was defined as the cumulative dose required to displace 50 percent of the "specific" uptake and was determined from a log-probit plot to be 30 $\mu\text{g}/\text{kg}$. The ED_{50} 's determined from three other regions (parietal, frontal, and striatal) were virtually identical to that shown above for the occipital area.

curves in three experiments (62 percent). If previous doses of Ro 15-1788 had been cleared from brain, the stepwise displacement should, in fact, have been less than that from a single dose. This study suggests that, within the accuracy of the measurements and for time intervals of 40–60 minutes, cumulative dose analysis is acceptable for stepwise displacement curves for Ro 15-1788.

Ex Vivo and In Vitro Autoradiography

The ex vivo distribution of intravenously administered $[^{123}\text{I}]$ Ro 16-1054 and the in vitro autoradiographic distribution of BZ receptors of the same tissue section are displayed in figure 7. The general profile of ex vivo distribution was similar to that from in vitro autoradiography performed 1 week later on the same

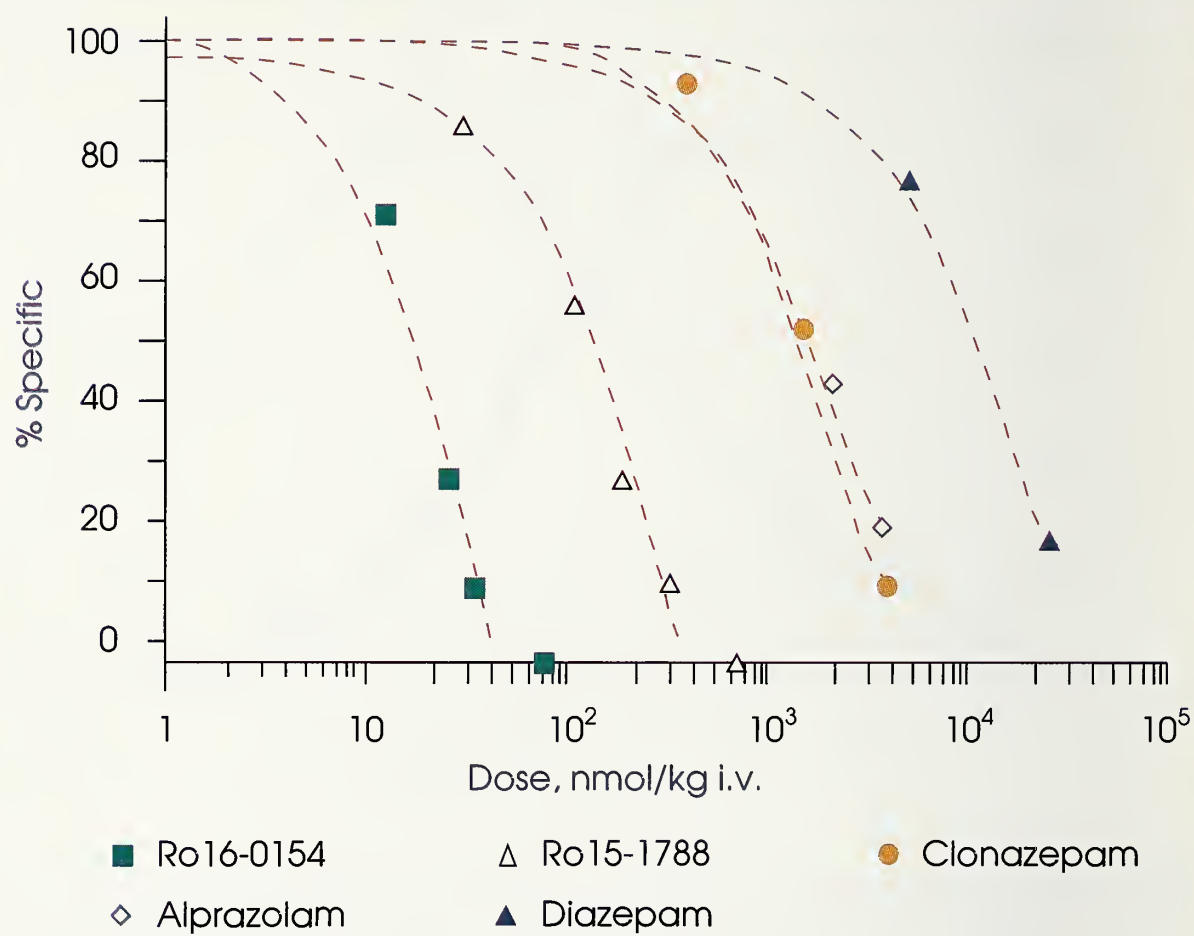
FIGURE 4c

Time course of brain radioactive densities in monkeys following intravenous injection of $[^{123}\text{I}]$ Ro 16-0154 at time 0 (from Innis et al. 1991b). Stepwise displacement with Ro 16-0154. Following injection of 12.4 mCi $[^{123}\text{I}]$ Ro 16-0154, nonradioactive Ro 16-0154 was injected intravenously with the individual doses indicated in microgram per kilogram units. The ED_{50} calculated for the occipital area described above was 7 $\mu\text{g}/\text{kg}$. Comparison of figures 4b and c shows that *in vivo* displacement of the benzodiazepine radioligand caused by Ro 15-1788 is more rapid but less potent than that with Ro 16-0154.

slices. Results from *ex vivo* and *in vivo* autoradiography of 15 brain structures were highly correlated (table 3; $r=0.8$). However, some areas showed consistent binding discrepancies between the *in vitro* and *ex vivo* autoradiograms. For example, the lateral geniculate nucleus showed higher *ex vivo* than *in vitro* binding values. The putamen was higher than the globus pallidus *in vitro* and lower *ex vivo*.

Following maximal brain uptake of $[^{123}\text{I}]$ Ro 16-0154 in one animal, non-

radioactive Ro 16-0154 was injected at a dose thought to occupy >90 percent of BZ receptors (0.03 mg/kg, intravenous). *Ex vivo* autoradiographic data from this displacement study were compared with that from a control animal of the same species (i.e., *vervet*) by expressing radioactivity levels as a percentage of white matter values in each animal. These regional gray to white matter ratios were reduced by about 90 percent following injection of nonradioactive

FIGURE 5

The *in vivo* displacement of $(^{123}\text{I})\text{Ro}$ 16-0154 by five benzodiazepine receptor agents is plotted as the percentage of specific uptake in the occipital area versus cumulative dose of displacer. Each curve was determined from one scanning session in which stepwise increasing doses of the displacer were administered (as in figures 4b and c). The relative *in vivo* potencies of these agents were: Ro 16-0154 > Ro 15-788 > clonazepam \approx alprazolam > diazepam (from Innis et al. 1991b).

Ro 16-0154. The remaining radioactivity would represent residual specific binding and nondisplaceable brain uptake (which itself is both nonspecific binding and free radioligand in brain extracellular space).

In vitro autoradiography revealed a widespread distribution of $[^{125}\text{I}]$ Ro 16-0154 specific binding in all gray matter areas. Cortical regions showed the highest density of binding. Binding was highest in the

occipital cortex, especially at the level of Brodmann's area 17. The lateral geniculate nucleus, as well as the limbic structures (amygdala and hippocampus), also displayed high-density binding while the striatal structures showed a lower density. The optical density overlying white matter was almost identical to the background density, indicating an absence of specific binding at this level. Slices coincubated with 1 μM

clonazepam also exhibited a general density not significantly different from background, which indicated nonspecific binding so low that it could not be distinguished from background activity with this method. Nonspecific binding was estimated to be around 1.5 percent of the specific binding.

Metabolites Analysis in Plasma and Cerebral Tissue

Within minutes after intravenous administration of [^{123}I]Ro 16-0154, HPLC revealed a more polar metabolite--probably the carboxylic acid derived from hydrolysis of the ester function (Halldin et al. 1988; Beer et al. 1990)--in the plasma (figure 8a). Plasma protein binding of [^{123}I]Ro 16-0154 was such that the free (unbound) activity was 26.1 percent in nonhuman primate blood. After intravenous administration of [^{123}I]Ro 16-0154, the concentration of free parent compound in

arterial plasma dropped rapidly in the first few minutes after intravenous administration, followed by a 2-hour period of slow clearance, paralleling the pattern of activity in occipital cortex, a region of high receptor density (figure 8b). Over 90 percent of brain activity could be extracted in ethyl acetate and over 99 percent of extracted radioactivity comigrated with parent compound on the HPLC. This demonstrated that the *in vivo* metabolism of [^{123}I]Ro 16-0154 in the brain during the scanning procedure is negligible and that the metabolites present in the plasma apparently do not cross the blood-brain barrier in primates.

Microdialysis Measurement

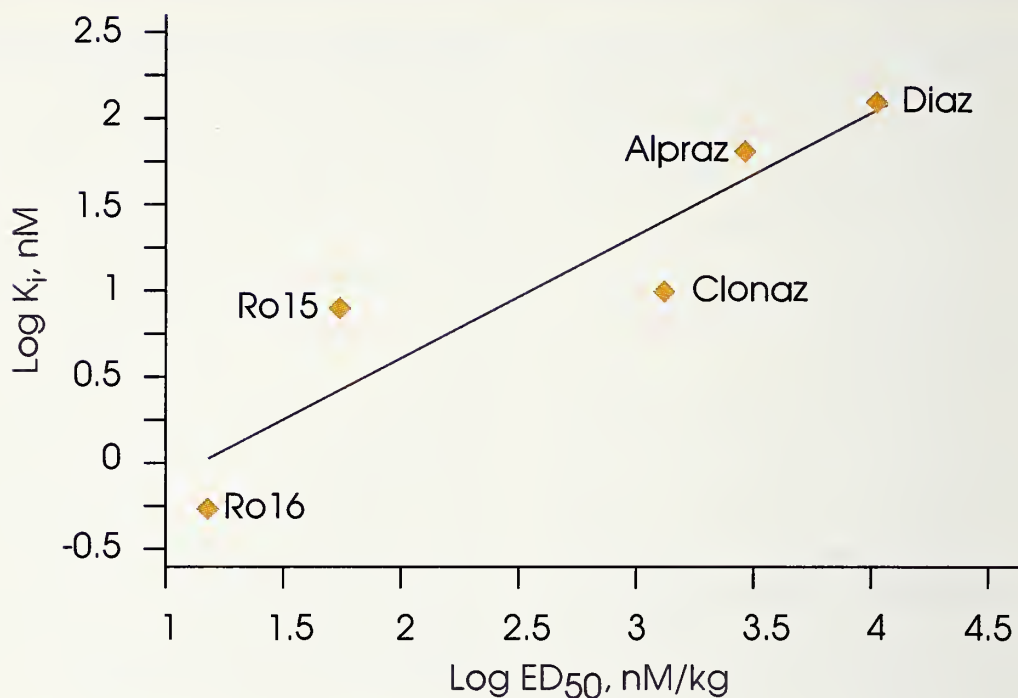
The concentration of radioactivity in the dialysate increased over the first 40 minutes to a plateau and remained relatively stable until the end of the experiment, 120 minutes

Table 2. Displacement of (^{123}I)Ro 16-0154 in nonhuman primate brain

Displacer	ED_{50} (nM/kg)		Exponential fit	
	Mean	(Individual values)	$T_{1/2}$	r Value
Ro 16-0154	15.4	(13.9; 17.0)	15.1 ± 2.2	0.992 ± 0.002
Ro 15-1788	52.8	(33.0; 59.3; 98.9)	11.2 ± 0.5	0.994 ± 0.002
Clonazepam	1,330	(950; 1,710)	11.3 ± 0.2	0.995 ± 0.001
Alprazolam	2,800	(1,720; 3,890)	12.5 ± 2.0	0.989 ± 0.002
Diazepam	10,700	(10,200; 11,200)	13.0 ± 1.2	0.994 ± 0.001

Stepwise increasing doses of displacer were administered intravenously, and the ED_{50} was calculated from a log-probit plot using the cumulative dose as described in the section entitled Methods.

Displacement curves from individual doses were fit to exponential curves, and $T_{1/2}$ and r values were calculated (from Innis et al. 1991b).

FIGURE 6

Correlation of the in vivo ED₅₀ doses and in vitro K_i concentrations of five BZ agents. The ED₅₀ of each agent was determined from stepwise displacement of (¹²³I)Ro 16-0154 in monkey brain. The K_i values were determined from homogenate binding studies of (¹²⁵I)Ro 16-0154 binding to membranes prepared from human and monkey cerebral cortex, which gave virtually identical results. The K_i value represents the mean of three separate determinations; the ED₅₀ value, the mean of two to three separate experiments. A linear fit determined with least squares analysis method had a correlation coefficient r = 0.92. The displacing agents were: Ro16 = Ro 16-0154; Ro15 = Ro 15-1788; Clonaz = clonazepam; Alpraz = alprazolam; and Diaz = diazepam (from Innis et al. 1991b).

(figure 9). Assuming a recovery of 19 percent, the average dialysate concentrations from all four probes during the plateau period were approximately 9×10⁻⁴ percent of the injected dose per milliliter, a concentration approximately twice that of the free parent compound in the plasma (4×10⁻⁴ percent). These data suggest that a relatively long period of pseudoequilibrium is established during the washout phase (30–120 minutes), with a constant ratio of the concentration of radioligand in the

brain's extracellular space to the free parent radioligand in plasma. Furthermore, the higher brain levels presumably provide a concentration gradient that underlies the washout of radioactivity from the brain.

DISCUSSION

[¹²³I]Ro 16-0154 appears to be an excellent radioligand to visualize and quantify central BZ receptors with SPECT:

(1) [^{125}I]Ro 16-0154 binds in vitro to a saturable homogeneous class of binding sites. Measured at 37 °C, the affinity of Ro 16-0154 is 10-fold greater than that of Ro 15-1788. Nonspecific binding of [^{125}I]Ro 16-0154 was <10 percent of total binding. Pharmacological characterization of the in vitro data suggested that [^{125}I]Ro 16-0154

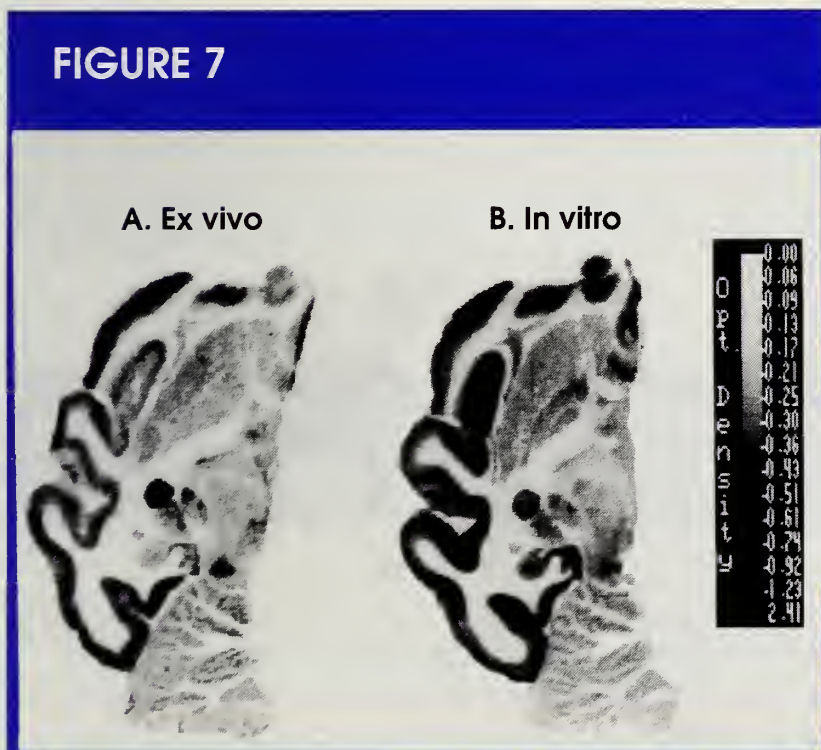
bound selectively to the central BZ receptors thought to be located on neurons.

(2) SPECT imaging with [^{123}I]Ro 16-0154 in nonhuman primates showed that peak activity was reached about 70 minutes postinjection and was followed by a relatively slow rate of washout. The regional brain activity demonstrated by SPECT was consistent with the known distribution of BZ receptors.

(3) Pharmacological characterization of the in vivo uptake was feasible because of the slow rate of washout, especially in hypothermic animals maintained at 32–34 °C. The in vivo ED₅₀ of various BZ agents correlated well with their in vitro receptor affinities. The nondisplaceable activity (corresponding to free and the nonspecifically bound ligand) was <10 percent of the total activity.

(4) Ex vivo autoradiographic studies demonstrated at the level of the light microscope the distribution of radioactivity in brain at the time of death. The results of ex vivo autoradiography closely matched the distribution of BZ receptors measured by in vitro autoradiography.

FIGURE 7



BZ receptor labeling. A. Ex vivo autoradiogram of a transaxial section obtained from 7-kg rhesus monkey following injection of 4.9 mCi (^{123}I)Ro 16-0154 scanning in Strichman 810x for 90 minutes, and euthanasia via overdose of pentobarbital. Digitized autoradiogram represents 12-hour exposure time. High concentration ^3H autoradiographic standards were simultaneously apposed to the film and separately calibrated for ^{123}I equivalents. These standards were used to convert optical densities to absolute radioactive densities measured as density per meter per milligram (dpm/mg) of tissue. B. In vitro receptor autoradiogram obtained with (^{125}I)Ro 16-0154 in a tissue section adjacent to the one shown in A after the ^{123}I radioactivity had decayed. A shows the distribution of total ^{123}I radioactivity in monkey brain at the time of death. B shows the distribution of BZ receptors in an adjacent tissue section.

- (5) Almost all radioactivity in primate brain represented parent compound, suggesting that the more polar plasma metabolites do not cross the blood-brain barrier, consistent with studies in rodent brain by Beer et al. (1990).
- (6) In vivo microdialysis confirmed that a state of pseudoequilibrium was achieved after peak brain levels and that free brain activity and free plasma parent compound are relatively stable from 30 to 120 minutes postinjection.

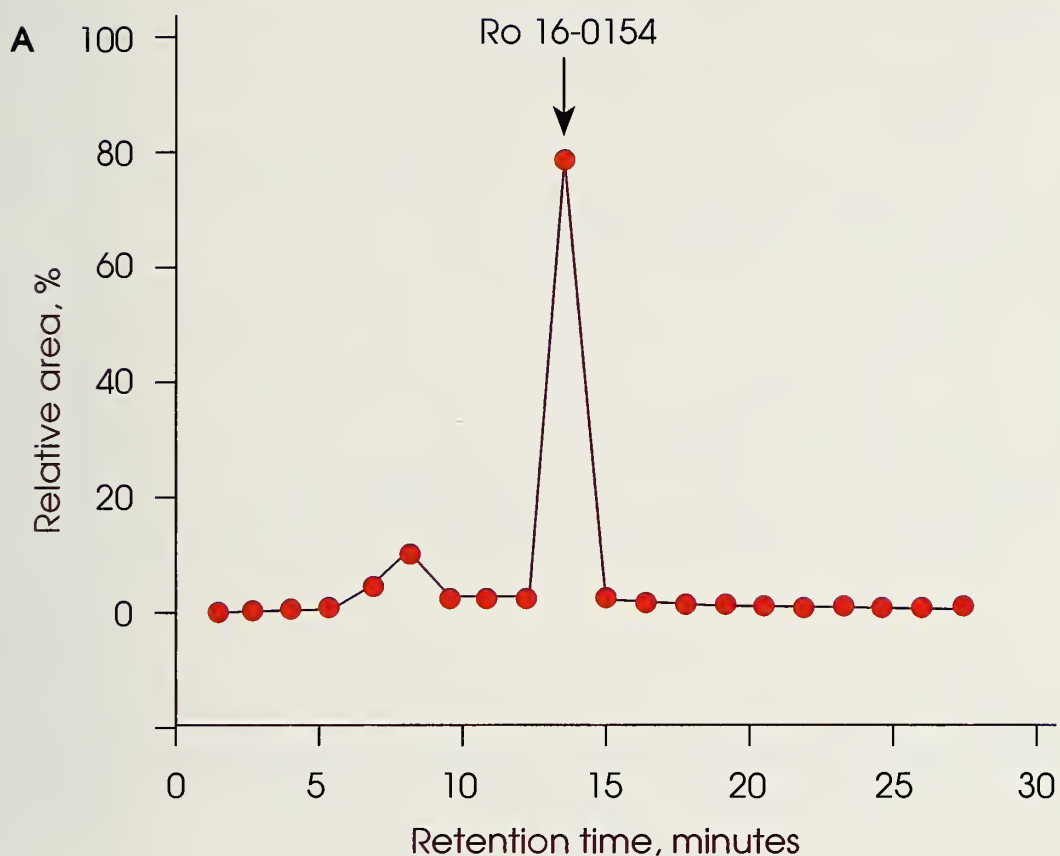
Comparison with Other Radiotracers

Various tracers were previously tested for their ability to measure BZ receptors in vivo. The agonists [¹¹C]flunitrazepam and [¹¹C]clonazepam have several disadvantages, including relatively low affinity at 37 °C and high levels of nonspecific binding (Sadzot and Frost 1990). [¹¹C]Ro 15-1788 has been successfully used in PET studies for visualization and quantification of BZ receptors (Hantraye et al. 1984; Samson et al. 1985; Persson et al. 1985; Shinotoh et al. 1986; Pappata et al. 1988; Savic et al. 1988). Ro 15-1788

Table 3. In vitro and ex vivo autoradiography of (¹²⁵I)Ro 16-0154 and (¹²³I)Ro 16-0154 binding in monkey brain

Region	In Vitro (10 ³ dpm/mg)	Ex Vivo (10 ³ dpm/mg)
Occipital cortex, area 17	34.3 ± 1.4	33.1 ± 0.8
Occipital cortex, area 17	32.7 ± 1.1	17.8 ± 1.4
Occipital cortex, total	22.4 ± 1.6	15.4 ± 1.5
Temporal cortex	22.5 ± 1.9	14.7 ± 0.8
Insula	29.0 ± 2.9	13.9 ± 0.1
Prefrontal cortex	26.4 ± 1.9	14.5 ± 2.0
Caudate nucleus	8.4 ± 0.7	8.2 ± 1.6
Globus pallidus	12.0 ± 0.1	7.3 ± 0.1
Putamen	8.6 ± 0.9	9.1 ± 0.4
Clastrum	9.5 ± 3.9	7.9 ± 0.6
Lateral geniculate nucleus	17.5 ± 0.9	23.5 ± 3.5
Amygdala	7.7 ± 0.2	10.0 ± 1.1
Hippocampus	17.4 ± 3.2	11.1 ± 0.3
Cerebellum	12.5 ± 1.7	10.4 ± 0.9
White matter	0.5 ± 0.1	0.8 ± 0.2

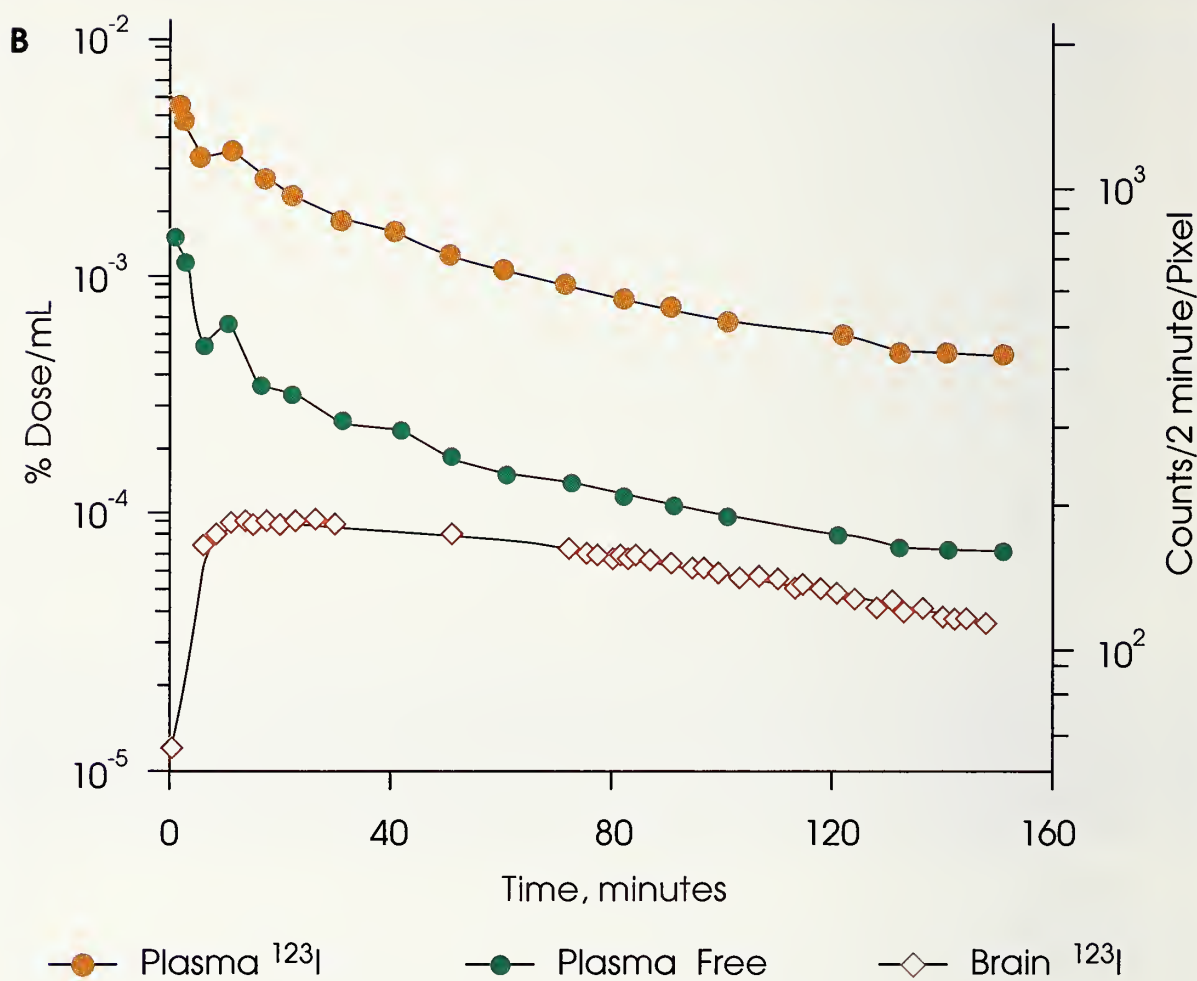
Comparison of in vitro and ex vivo binding performed with autoradiography on the same slices of brain from a representative animal. Values represent mean ± S.E.M. of all sections in which the brain structure was located, typically 3-10 tissue sections per structure. Results of ex vivo and in vitro autoradiography were highly correlated in these 15 brain structures ($r=0.8$).

FIGURE 8a

Metabolites of (¹²³I)Ro 16-0154 in human plasma. HPLC composition of ethyl acetate extract of arterial plasma 60 minutes after intravenous administration of 4.6 mCi (¹²³I)Ro 16-0154 to a human volunteer. Parent Ro 16-0154 retention time, 14 minutes; metabolite, 8 minutes.

($K_D = 5 \text{ nM}$) has a 10-fold lower affinity at 37 °C than Ro 16-0154 ($K_D = 0.5 \text{ nM}$). [¹¹C]Ro 15-1788 activity in the brain reached a peak 5–10 minutes after intravenous injection (Persson et al. 1989), while Ro 16-0154 activity peaked at 70 minutes. Ro 15-1788 had a more rapid rate of brain washout--about 50 percent/hour, as estimated from Samson et al. (1985)--than Ro 16-0154 (15 percent/hour), consistent with the rapid plasma clearance of Ro 15-1788 (Geller and Thompson 1988).

Sadzot and Frost (1990) noted that this might raise significant problems in the application of the equilibrium method with Ro 15-1788. In humans, the percentage of injected dose in the brain at peak time is 7 percent for [¹¹C]Ro 15-1788 versus 11.7 ± 1.5 percent (mean \pm S.D.) for [¹²³I]Ro 16-0154, as measured by whole-body scanning with conjugate counting ($n=4$, our unpublished results). Thus, Ro 16-0154 offers several advantages over Ro 15-1788 for *in vivo* imaging.

FIGURE 8b

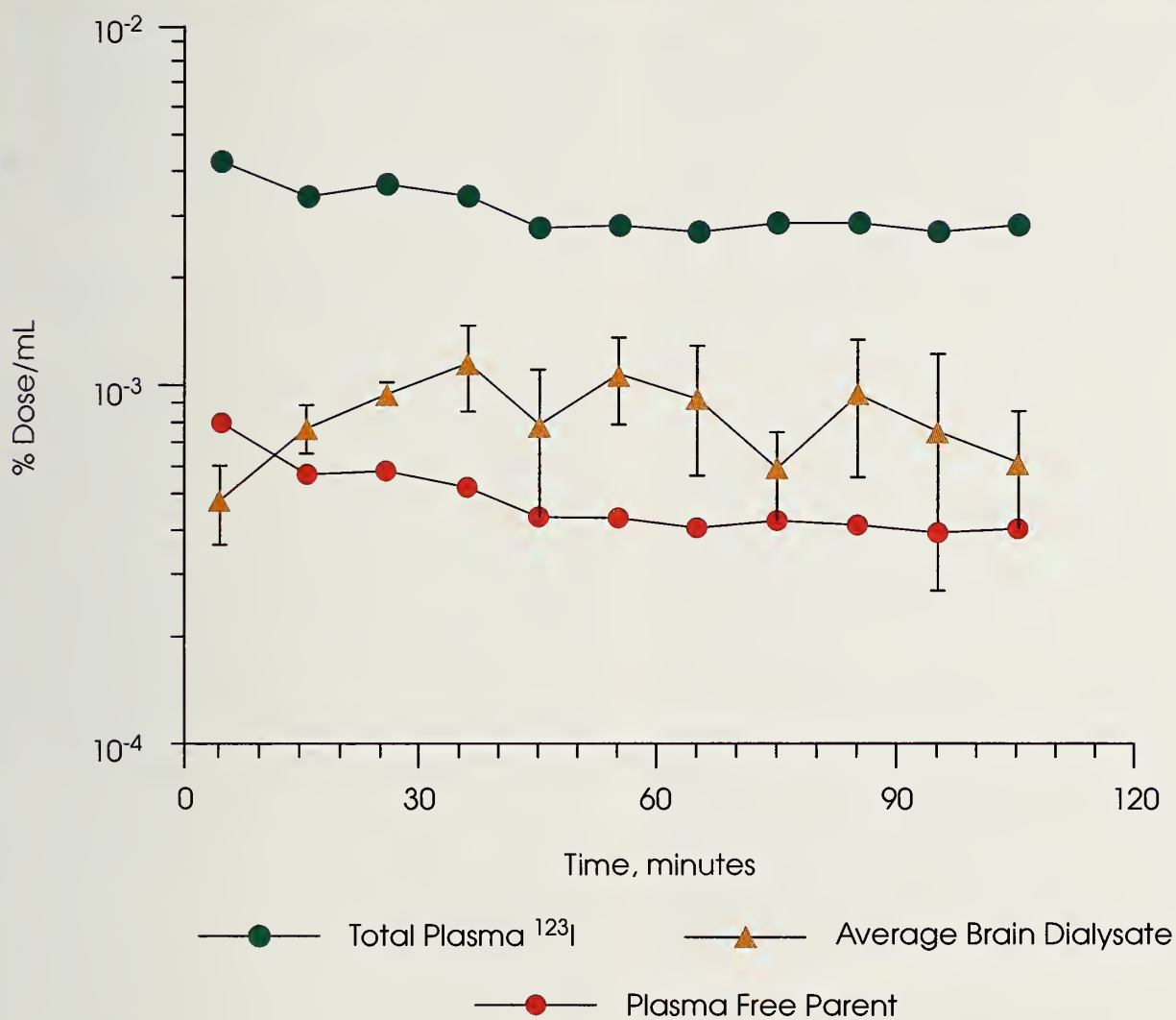
Metabolites of $(^{123}\text{I})\text{Ro} 16-0154$ in human plasma. Time course of free (non-protein bound) parent compound in same subject compared with total plasma ^{123}I (left axis) and uptake of radioactivity in occipital cortex, a representative receptor-specific brain region (right axis).

Receptor Reserve

These in vivo displacement studies confirm previous reports of a major receptor reserve for the BZ binding site (Haefely and Polc 1986). This conclusion derives from the expected receptor occupancy required for effects induced by both agonists and antagonists. For example, maximal sedative and anti-convulsant effects of the agonist diazepam occur at doses of

300–1,000 nM/kg intravenous (Rall and Schleifer 1980).

The in vivo displacement studies with $[^{123}\text{I}]$ Ro 16-0154 suggest that these doses would correspond to only 10–30 percent receptor occupancy (figure 5). The remaining 70–90 percent of the binding sites are referred to as "spare receptors" that make up the "receptor reserve." The rationale for this terminology is that the entire reserve could theoretically be inactivated without

FIGURE 9

Concentration of total ^{123}I radioactivity in arterial plasma (●); free parent (^{123}I)Ro 16-0154 in plasma (●); and concentration of free radioligand in brain (▲). The latter was measured using in vivo microdialysis, assuming 19 percent recovery from the dialysis probes, following intravenous injection of 10 mCi (^{123}I)Ro 16-0154. Data decay-corrected to time 0.

diminishing the efficacy (or peak response) of agonist drugs. In the case of significant receptor reserve, in vivo potency estimations (like ED₅₀ measurements described here) will suggest that agonists are unusually weak relative to clinically or behaviorally effective doses.

The situation is reversed for antagonists. For example, the ED₅₀ of

the antagonist Ro 15-1788 required to block agonist-induced anticonvulsant effects is 2.8 mg/kg intravenous (Hunkeler et al. 1981), which would correspond to approximately 90 percent receptor occupancy (figure 5). The antagonist must block nearly the entire receptor reserve before it can effectively diminish the action of the agonists.

Thus, in vivo potency estimations (e.g., ED₅₀ measurements) may suggest that antagonists are unusually strong, relative to clinically or behaviorally effective doses.

A major reserve for the BZ receptor has significant implications for brain imaging studies, whether performed with PET or SPECT. For example, saturation studies (for determination of B_{max} and K_D) require significant receptor occupancy (certainly >50 percent) by the radioligand. If the tracer is an agonist, then supramaximal doses of sedating agents should be administered, and such studies may be impossible in human subjects. Comparable saturation studies with an antagonist radioligand would be expected to have minimal pharmacological side effects because the highest dose of the antagonist would barely occupy the full receptor reserve.

For the studies reported here, the radioligand itself occupies only a small percentage of receptors. The radionuclide ([¹²³I]NaI) is provided on a no-carrier-added basis, and the use of a tributyltin precursor (in contrast to iodine isotope exchange) produces a product with very high specific activity (>180,000 Ci/mmol). A dose of 10 mCi [¹²³I]Ro 16-0154 is estimated to occupy <0.2 percent of the BZ receptors in monkey brain (Innis et al. 1991a). Thus, the radiotracer doses used in these studies would be expected to have no pharmacological effects.

Comparison with PET Imaging

The in vivo potency of drugs for the BZ receptor has been examined with PET, using [¹¹C]Ro 15-1788 (Pappata et al. 1988; Shinotoh et al. 1989; Brouillet et al. 1990); however, SPECT offers several advantages over PET in making such potency measurements. First, the brain uptake of [¹²³I]Ro 16-0154 is more stable for a longer period of time than the PET radioligand [¹¹C]Ro 15-1788. As mentioned previously, clearance of [¹²³I]Ro 16-0154 from brain at normothermic temperatures occurs at approximately 14 percent/hour once peak values have been reached. Although data have not been reported in similar fashion for comparable PET studies, estimation from the reported graphic data suggests a washout rate of almost 60 percent/hour (Pappata et al. 1988). The stable period of brain uptake of the SPECT radioligand may derive in part from the 10-fold higher affinity of Ro 16-0154 over Ro 15-1788 (Johnson et al. 1990b). The use of [¹²³I]Ro 16-0154 provides a longer and more stable baseline against which to measure the effects of displacing agents.

Second, the longer T_{1/2} of ¹²³I (13 hours) compared with that of ¹¹C (20 minutes) allows longer individual experiments, thus multiple injections of displacing agents. For example, our studies with [¹²³I]Ro 16-0154 frequently lasted 6 hours, during which a comparable ¹¹C-labeled compound would have decayed by 18 half-lives.

Therefore, because of the long-lived biological and physical prop-

erties of [¹²³I]Ro 16-0154, the determination of ED₅₀ from three to five displacing doses could be accomplished in one experiment with a single animal using SPECT. Comparable PET studies with [¹¹C]Ro 15-1788 require separate experiments for each dose of the displacing agent (Pappata et al. 1988).

ACKNOWLEDGMENTS

This chapter was prepared with support from the Veterans Administration (Merit Review Award to Robert Innis and the National Center for the Study of Post-Traumatic Stress Disorder) and the Public Health Service (grants MH 44866, NS 06208, and MH 25642).

REFERENCES

- Beer, H.-F.; Bläuenstein, P.A.; Hasler, P.H.; Delaloye, B.; Riccabona, G.; Bangerl, I.; Hunkeler, W.; Bonetti, E.P.; Pieri, L.; and Richards, J.G. In vitro and in vivo evaluation of iodine-123-Ro 16-0154: A new imaging agent for SPECT investigations of benzodiazepine receptors. *J Nucl Med* 31:1007-1014, 1990.
- Bradberry, C.W., and Roth, R.H. Cocaine increases extracellular dopamine in rat nucleus accumbens and ventral tegmental area as shown by in vivo microdialysis. *Neurosci Lett* 103:97-102, 1989.
- Braestrup, C.; Albrechten, R.; and Squires, R.F. High densities of benzodiazepine receptors in human cortical areas. *Nature* 269:702-704, 1977.
- Brouillet, E.; Chavoix, C.; Hantraye, P.; Kunimoto, M.; Khalili-Varasteh, M.; Chevalier, P.; Frydman, A.; Gaillot, J.; Prenant, C.; Crouzel, M.; Mazière, B.; and Mazière, M. Interaction of suriclonine with central type benzodiazepine receptors in living baboons. *Eur J Pharmacol* 175:49-55, 1990.
- Comar, D.; Mazière, M.; Godot, J.M.; Berger, G.; Soussaline, E.; Menini, C.; Arfel, G.; and Naquet R. Visualization of ¹¹C-flunitrazepam in the brain of the live baboon. *Nature* 280:329-331, 1979.
- Davis, W.C., and Ticku, M.J. Ethanol enhances [³H]diazepam binding at the benzodiazepine- γ -aminobutyric acid receptor-ionophore complex. *Mol Pharmacol* 20:287-294, 1981.
- Frost, J.J.; Wagner, H.N., Jr.; Dannals, R.F.; Ravert, H.T.; Wilson, A.A.; Links, J.M.; Rosenbaum, A.E.; Trifiletti, R.R.; and Snyder, S.H. Imaging benzodiazepine receptors in man with [¹¹C]suriclonine by positron emission tomography. *Eur J Pharmacol* 122:381-383, 1986.
- Geller, E., and Thompson, D. Proceedings of the International Symposium of Flumazenil--the first benzodiazepine antagonist. *Eur J Anesthesiol* 2(suppl.):332, 1988.
- Haefely, W., and Polc, P. Physiology of GABA enhancement by benzodiazepines and barbiturates. In: Olsen, R.W., and Venter, J.C., eds. *Benzodiazepine/GABA Receptors and Chloride Channels: Structural and Functional Properties*. New York: Alan R. Liss, Inc., 1986. pp. 97-133.
- Halldin, C.; Stone-Elander, S.; Thorell, J.; Persson, A.; and Sedvall, G. ¹¹C-labelling of Ro 15-1788 in two different positions, and also ¹¹C-labelling of its main

- metabolite Ro 15-3890, for PET studies of benzodiazepine receptors. *Appl Radiat Isot* 39:993–997, 1988.
- Hantraye, P.; Kaijima, M.; Prenant, C.; Guibert, B.; Sastre, J.; Crouzel, M.; Naquet, R.; Comar, D.; and Mazière, M. Central type benzodiazepine binding sites: A positron emission tomography study in the baboon's brain. *Neurosci Lett* 48:115–120, 1984.
- Hunkeler, W.; Möhler, H.; Pieri, L.; Pole, P.; Boneti, E.P.; Cumin, R.; Schaffner, R.; and Haefely, W. Selective antagonists of benzodiazepines. *Nature* 290(5806):514–516, 1981.
- Innis, R.B.; Zoghbi, S.S.; Johnson, E.W.; Woods, S.; Al-Tikriti, M.; Baldwin, R.; Seibyl, J.; Malison, R.; Zubal, G.; Charney, D.; Heninger, G.; and Hoffer, P. SPECT imaging of the benzodiazepine receptor in non-human primate brain with [^{123}I]Ro 16-0154. *Eur J Pharmacol* 193:249–252, 1991a.
- Innis, R.B.; Al-Tikriti, M.S.; Zoghbi, S.S.; Baldwin, R.M.; Sybirnska, E.H.; Laruelle, M.A.; Malison, R.T.; Seibyl, J.P.; Zimmermann, R.C.; Johnson, E.W.; Smith, E.O.; Charney, D.S.; Heninger, G.R.; Woods, S.W.; and Hoffer, P.B. SPECT imaging of the benzodiazepine receptor: Feasibility of in vivo potency measurements from stepwise displacement curves. *J Nucl Med* 1991b, in press.
- Johnson, E.W.; de Lanerolle, N.C.; Kim, J.H.; Sundaresan, S.; Spencer, D.D.; and Innis, R.B. Autoradiographic quantitation of central and peripheral benzodiazepine receptors in human epileptogenic tissue. *Soc Neurosci Abstr* 16(Part 1):308, 1990a.
- Johnson, E.W.; Woods, S.W.; Zoghbi, S.S.; McBride, B.J.; Baldwin, R.M.; and Innis, R.B. Receptor binding characterization of the benzodiazepine radioligand [^{125}I]Ro 16-0154: Potential probe for SPECT brain imaging. *Life Sci* 47:1535–1546, 1990b.
- Luabeya, M.K.; Maloteaux, J.M.; and Laduron, P.M. Regional and cortical distribution of serotonin S2, benzodiazepine, muscarinic and dopamine D2 receptors in human brain. *J Neurochem* 43:1068–1071, 1984.
- Maloteaux, J.M.; Luabeya, M.A.K.; Vanisberg, M.A.; Laterre, E.C.; Laduron, P.M.; Javoy-Agid, F.; and Agid, Y. Benzodiazepine receptors in normal human brain, in Parkinson's disease, and in progressive supranuclear palsy. *Brain Res* 446:321–332, 1988.
- McBride, B.J.; Baldwin, R.M.; Kerr, J.M.; and Wu, J.L. A simple method for the preparation of ^{123}I - and ^{125}I -labeled iodobenzodiazepines. *Appl Radiat Isot* 42:173–175, 1991.
- McPherson, G.A. Analysis of radiobinding experiments. A collection of computer programs for the IBM PC. *J Pharmacol Methods* 14:213–228, 1985.
- Möhler, H., and Okada, T. The benzodiazepine receptor in normal and pathological human brain. *Br J Psychiatry* 133:261–268, 1978.
- Munson, P., and Rodbard, D. LIGAND: A versatile computerized approach for characterization of ligand binding systems. *Ann Biochem* 107:220–239, 1980.
- Owen, F.; Poulter, M.; Waddington, J.L.; Marshal, R.D.; and Crow, T.J. [^3H]Ro5-4864 and [^3H]flunitrazepam binding in kainate-lesioned rat striatum and in temporal cortex of brains from patients with senile dementia of the Alzheimer type. *Brain Res* 278:373–375, 1983.

- Pappata, S.; Samson, Y.; Chavoix, C.; Prenant, C.; Mazière, M.; and Baron, J.C. Regional specific binding of ^{11}C -Ro 15-1788 to central type benzodiazepine receptors in human brain: quantitative evaluation by PET. *J Cereb Blood Flow Metab* 8:304-313, 1988.
- Penney, J.B., Jr., and Young, A.B. Quantitative autoradiography of neurotransmitter receptors in Huntington disease. *Neurology* 32:1391-1395, 1982.
- Persson, A.; Ehling, E.; Erikson, L.; Farde, L.; Hedstrom, C-G.; Litton, J-E.; Mindus, P.; and Sedvall, G. Imaging of ^{11}C -labeled Ro 15-1788 to benzodiazepine receptors in the human brain by positron emission tomography. *J Psychiatr Res* 19:609-622, 1985.
- Persson, A.; Pauli, S.; Swahn, C.G.; Halldin, C.; and Sedvall, G. Cerebral uptake of ^{11}C Ro 15-1788 and its acid metabolite ^{11}C Ro 15-3890. PET study in healthy volunteers. *Human Psychopharmacol* 4:215-220, 1989.
- Polc, P.; Bonetti, E.P.; Schaffner, R.; and Haefely, W. A three-state model of the benzodiazepine receptor explains the interactions between the benzodiazepine antagonist Ro 15-1788, benzodiazepine tranquilizers, β -carbolines, and phenobarbitone. *Naunyn Schmiedebergs Arch Pharmacol* 321:260-264, 1982.
- Rall, T.W., and Schleifer, L.S. Drugs effective in the therapy of the epilepsies. In: Gilman, A.F.; Goodman, L.S.; Rall, T.W.; and Murad, F., eds. *The Pharmacological Basis of Therapeutics*, 7th ed. New York: Macmillan, 1980. pp. 446-472.
- Sadzot, B., and Frost, J.J. Benzodiazepine receptors. In: Frost, J.J., and Wagner, H.N., Jr., eds. *Quantitative Imaging: Neuroreceptors, Neurotransmitters, and Enzymes*. New York: Raven Press, 1990. pp. 81-95.
- Samson, Y.; Hantraye, P.; Baron, J.C.; Soussaline, F.; Comar, D.; and Mazière, M. Kinetic and displacement of $[^{11}\text{C}]$ Ro 15-1788, a benzodiazepine antagonist, studied in human brain *in vivo* by positron tomography. *Eur J Pharmacol* 110:247-251, 1985.
- Savic, I.; Roland, P.; Sedvall, G.; Persson, A.; Pauli, S.; and Widen, L. In vivo demonstration of reduced benzodiazepine receptor binding in human epileptic foci. *Lancet* 2(8616):863-866, 1988.
- Shinotoh, H.; Ioyo, M.; Yamada, T.; Inoue, O.; Suzuki, K.; Itoh, T.; Fukuda, H.; Yamasaki, T.; Tateno, Y.; and Hirayama, K. Detection of benzodiazepine receptor occupancy in the human brain by positron emission tomography. *Psychopharmacology* 99:202-207, 1989.
- Shinotoh, H.; Yamasaki, T.; Inoue, O.; Itoh, T.; Suzuki, K.; Hashimoto, K.; Tateno Y.; and Ikehira H. Visualization of specific binding sites of benzodiazepine in human brain. *J Nud Med* 27:1593-1599, 1986.
- Squires, R.F., and Braestrup, C. Benzodiazepine receptors in rat brain. *Nature* 266:732-734, 1977.
- Suzdak, P.D.; Glowa, J.R.; Crawley, J.N.; Schwartz, R.D.; Skolnick, P.; and Paul, S.M. A selective imidazobenzodiazepine antagonist of ethanol in the rat. *Science* 234:1243-1247, 1986.
- Sybirska, E.; Al-Tikriti, M.; Johnson, E.W.; Zoghbi, S.; and Innis, R.B. SPECT imaging of the benzodiazepine receptor: Autoradiographic comparison of receptor density and radioligand

distribution. *Soc Neurosci Abstr* 16(Part 1):693, 1990.

Tallman, J.F.; Paul, S.M.; Skolnick, P.; Gallager, D.W. Receptors for the age of anxiety: Pharmacology of the benzodiazepines. *Science* 207:274–281, 1980.

Tallman, J.F., and Gallager, D.W. The GABA-ergic system: A locus of benzodiazepine action. *Ann Rev Neurosci* 8:21–44, 1985.

Walker, F.O.; Young, A.B.; Penney, J.B.; Dovorini-Zis, K.; and Shoulson, I. Benzodiazepine and GABA receptors in early Huntington's disease. *Neurology* 34:1237–1240, 1984.

Wood, S.W.; Charney, D.S.; Silver, J.M.; and Heninger, G.R. Effects of a benzodiazepine receptor antagonist in patients with panic disorder. *Am Psychiatry New Res Abstr* NR262:129, 1988.

PET AND SPECT IMAGING IN COGNITIVE DISORDERS OF AGING AND ALCOHOLISM

William J. Jagust, M.D.¹

Functional imaging techniques for clinical neuroscience applications permit the visualization of brain function with high spatial resolution and quantitative accuracy. Imaging studies of humans with a variety of diseases and pathological conditions utilize modalities that reveal anatomy. Although such studies provide important insights into the neural substrates of normal and abnormal behavior, they are limited because they cannot evaluate biochemical, neuropharmacologic, and neurophysiologic changes. Many conditions may be associated with minimal or nonspecific structural changes, accompanied by severe biochemical derangements. Until the advent of functional brain imaging, the primary method of studying these biochemical changes was post mortem neurochemistry.

Within the past decade, new techniques for the imaging of brain function have been developed. These techniques, positron emission tomography (PET) and single photon emission computed

ACRONYMS

AD	<i>Alzheimer's disease</i>
FDG	[2- ¹⁸ F]deoxyglucose
FDOPA	[6- ¹⁸ F]dihydroxyphenylalanine
HM-PAO	[^{99m} Tc-hexamethyl-propylamine oxime
IMP	[¹²³ I]N-isopropyl-p-iodoamphetamine
KS	Korsakoff's syndrome
MID	multi-infarct dementia
MMSE	mini-mental status examination
OER	oxygen extraction ratio
PD	Parkinson's disease
PET	positron emission tomography
PSP	progressive supranuclear palsy
rCBF	regional cerebral blood flow
rCMR _{glc}	regional cerebral metabolic rate for glucose
rCMRO ₂	regional cerebral metabolic rate for oxygen
SPECT	single photon emission computed tomography

¹Lawrence Berkeley Laboratory, Berkeley, CA 94720 and University of California at Davis, CA 95616

tomography (SPECT), utilize radiation-detecting instruments (tomographs) to provide three-dimensional images of the distribution of injected radiotracers. Labeling a variety of molecules with radionuclides facilitates the study of a host of different physiological processes.

This chapter will review recent developments in functional brain imaging. A review of the use of SPECT and PET in the study of cognitive disorders associated with aging, specifically Alzheimer's disease and other neurodegenerative illnesses, will demonstrate how the identification of brain regions with abnormal function but normal structure can improve diagnosis and the understanding of pathophysiology. A discussion of early results and potential applications of these techniques to cognitive disturbances associated with alcohol use will conclude the chapter.

PRINCIPLES OF EMISSION TOMOGRAPHY

In all emission tomographic techniques, an injected radioactive tracer is detected by a tomograph. The tracer consists of a molecule of interest--e.g., a metabolic substrate such as deoxyglucose--labeled with a radioactive isotope such as ^{11}C or ^{18}F that can be detected by tomography. Depending upon the nature of the emitted radiation, different principles may apply to accurate mapping of the distribution of the tracer by tomography. The final result is a series of tomographic

brain "slices" that provide three-dimensional information.

The ultimate goal of PET and SPECT is not simply the production of the image, but the quantitation of physiological processes. Models that rely on a priori information about the behavior of the tracer *in vivo*, in conjunction with time-varying measurements of the tracer in the circulation and the brain, are necessary for quantitative measurement of physiological processes such as the transport and metabolism of the molecule. Once such biochemical information is available, the mathematics of the modeling is relatively straightforward, although assumptions about the behavior of the tracer must be carefully evaluated in each experimental situation.

The essential difference between PET and SPECT is in the types of radioactive isotopes used to label the molecules of interest. PET uses isotopes whose decay process results in two high-energy photons oriented so that they are always 180° opposite each other. SPECT uses isotopes that decay by emitting single photons in random directions. Most of the PET isotopes have shorter half-lives than those of the SPECT isotopes. These differences have profound consequences for the radiochemical synthesis methods, as well as the nature of the tomographs and measurements that can be made.

PET tomographs consist of a radial array of crystal detectors, electronically coupled to detect the simultaneous excitation of two

opposing crystals by the simultaneously emitted high-energy photons. Thus, the positron emission can be localized to a line, and the reconstruction of an image from these multiple projection lines results in a map of the distribution of the tracer. The intrinsic property of electronic collimation leads to a high sensitivity (generally defined as counts per millicurie of activity per second) for detection of radionuclides. The result is more data describing tracer location, compared with SPECT, which permits the higher resolution with PET (on the order of several millimeters). The high sensitivity of PET also translates into the ability to acquire many counts in a short time period, thus allowing dynamic, time-varying measurements to be made quickly.

In SPECT imaging, the tracer map is ascertained by using collimation to localize the line along which a decay event occurred. Collimation results in a restriction of the field of view of each detector element, which in turn results in a decrease in sensitivity, relative to PET, when the collimation is done electronically. The decrease in sensitivity of SPECT scanners is greater as resolution is improved, with practical limitations at resolutions less than about 8–10 mm. In addition, the problems of radiation scatter and attenuation by brain and skull are more difficult to solve with SPECT imaging than with PET, resulting in somewhat less accurate measurements of brain radioactivity. A detailed analysis of the physics and instrumentation of these two tech-

niques has been published elsewhere (Budinger 1987).

The isotopes used in SPECT and PET obviously differ as well. These isotopes, and some of the compounds of interest which have been labeled with them, are shown in tables 1 and 2. The commonly used PET isotopes, particularly carbon and oxygen, are natural constituents of organic molecules. Therefore, utilization of these isotopes in the synthesis of tracers frequently will preserve the biological behavior of the molecule of interest. The use of ^{18}F is also advantageous because of its relatively longer half-life.

The breadth of possibilities for chemical synthesis of SPECT tracers is not as great as for PET tracers because the radionuclides used generally are not natural constituents of the biological molecules (e.g., iodine and technetium as opposed to carbon and oxygen). Consequently, SPECT tracers for human brain studies have been widely used only for measurements of regional cerebral blood flow (rCBF). Many potential SPECT tracers for the study of the acetylcholine, dopamine, serotonin, and adrenergic systems are in various stages of development. Development of new tracers for both PET and SPECT is ongoing in many laboratories, representing an important but time-consuming enterprise inasmuch as the *in vivo* behavior of a tracer must be entirely understood in order to model mathematically and quantitate the physiological process of interest.

Table 1. Some PET tracers used to study the human brain, radionuclides used to label them, and the physiological processes they quantitate

Isotope	Tracer	Physiological process
¹⁸ F	FDG	Glucose metabolism
	Fluoromethane	Blood flow
	N-Methyl spiperone	D-2 Dopamine receptors
	Fluoro-DOPA	Dopamine uptake and metabolism
	Haloperidol	D-2 Dopamine receptors
¹⁵ O	O ₂	Oxygen metabolism
	H ₂ O	Blood flow
	CO ₂	Blood flow
¹¹ C	CO	Blood volume
	Deoxyglucose	Glucose metabolism
	DMO	Tissue pH
	N-Methyl spiperone	D-2 Dopamine receptors
	Carfentanil	Mu opiate receptors
	Diprenorphine	Mu, delta, and kappa opiate receptors
	Leucine, methionine	Protein synthesis
	Methyl-bromo-LSD	S-2 Serotonin receptors
	N-Methyl nicotine	Nicotinic receptors
⁶⁸ Ga	EDTA	Blood-brain barrier permeability

DMO, dimethyloxazolidinedione.

PET and SPECT consequently are considerably different in applicability to neuroscience research questions. The short half-lives of many PET isotopes make their use for repeated measurements simpler, allowing sequential studies in the same patient. Whereas the variability of PET data appears to increase with the test-retest time period, studying the same subject at one sitting minimizes problems inherent in differences between the subject's physiological states at different test times and decreases errors of repositioning the patient in

the scanner. SPECT isotopes, which have longer half-lives, generally require that test-retest paradigms be performed on different days.

Although many PET studies can be done using the longer lived tracer ¹⁸F, which can be generated by a regional cyclotron for delivery to several local PET centers, the use of PET tracers with shorter half-lives such as ¹⁵O and ¹¹C necessitates a cyclotron in close proximity to the PET scanner, resulting in additional expense and the need for additional technical support. Improvements in the technology of

compact cyclotrons specifically designed to produce radionuclides for PET studies will lessen the technical support and space requirements for PET in the future.

Because of the nature of the quantitative studies usually conducted by PET centers, only small numbers of subjects can be practically studied in a particular investigative protocol. SPECT is less technically demanding than PET, consequently facilitating the study of larger patient series. Measurements of tissue radioactivity can be performed more accurately with PET than with SPECT, mainly because the actual radioactivity concentration measurement in brain structures requires an instrument resolution less than the size of the structures of interest. PET resolution is close to that needed for the investigation of most small cerebral structures. A second advantage of PET is the ease with

which dynamic studies can be performed because of its high sensitivity.

PET IMAGING IN DEMENTIA

The study of dementing illnesses illustrates several reasons for the use of PET. First, dementia has been well studied, so that considerable experience in a number of laboratories around the world has confirmed key findings. Second, dementing illnesses are often associated with minimal or nonspecific structural change, whereas functional changes may be severe and relatively specific. Finally, relationships between cognitive function, measured neuropsychologically, and regional brain biochemistry in this group of disorders have been intensively investigated, thus providing a potential model for the study of alcohol-related cognitive impairment.

Table 2. Some SPECT tracers used to study the human brain, radionuclides to label them, and the physiological processes they quantitate

Isotope	Tracer	Physiological process
¹²³ I	IMP	Blood flow
	HIPDM	Blood flow
	QNB	Muscarinic cholinergic receptors
	IBZM	D-2 Dopamine receptors
^{99m} Tc	HM-PAO	Blood flow
	ECD	Blood flow

IMP, N-isopropyl-p-iodoamphetamine; HIPDM, N,N,N',N'-(2-hydroxy-3-methyl-5-iodobenzyl)-1,3-propanediamine; QNB, quinuclidinyl-4-iodobenzilate; IBZM, iodobenzamide; HM-PAO, hexamethyl-propylamine oxime; ECD, ethyl cysteinate dimer.

While it is well known that cerebral atrophy is a concomitant of dementia, it is also clear that atrophy occurs in normal aging to such an extent that it is difficult to identify an older patient as demented on the basis of structural imaging studies alone (DeCarli et al. 1990; Jernigan et al. 1990). Such studies have traditionally aided the clinician in excluding reversible or curable dementias, but provided little assistance in positively diagnosing the most common cause of dementia in the elderly, Alzheimer's disease (AD).

Initial studies of AD using PET applied the $^{15}\text{O}-\text{O}_2$ and $^{15}\text{O}-\text{H}_2\text{O}$ methods to measure regional cerebral metabolic rates for oxygen (rCMRO_2) and rCBF, respectively (Frackowiak et al. 1981). These studies showed deficits in both of these variables in temporal and parietal cortex in AD. Furthermore, simultaneous measurement of rCBF and rCMRO_2 permitted the calculation of the regional oxygen extraction ratio (OER). The normal OER in AD suggests that tissue is not ischemic, but rather that flow is reduced consequent to reduced metabolic needs. Further study of regional cerebral metabolic rates for glucose (rCMRglc) using the [$2-\text{F}^18$]deoxyglucose (FDG) method (Friedland et al. 1983; Benson et al. 1983; Foster et al. 1984) showed predominantly decreased glucose metabolism in temporal and parietal cortex of AD patients. Figure 1 shows the pattern of temporal and parietal hypometabolism that has been seen using PET with FDG and

compares results obtained with two tomographs of different resolutions.

These findings have been confirmed in numerous laboratories, with the additional information that as AD progresses, the frontal lobes become progressively more hypometabolic (Duara et al. 1986; Jagust et al. 1987b). In addition, the abnormalities have been found at very early disease stages, when memory loss is the only significant clinical finding (Cutler et al. 1985; Haxby et al. 1986; Kuhl et al. 1987).

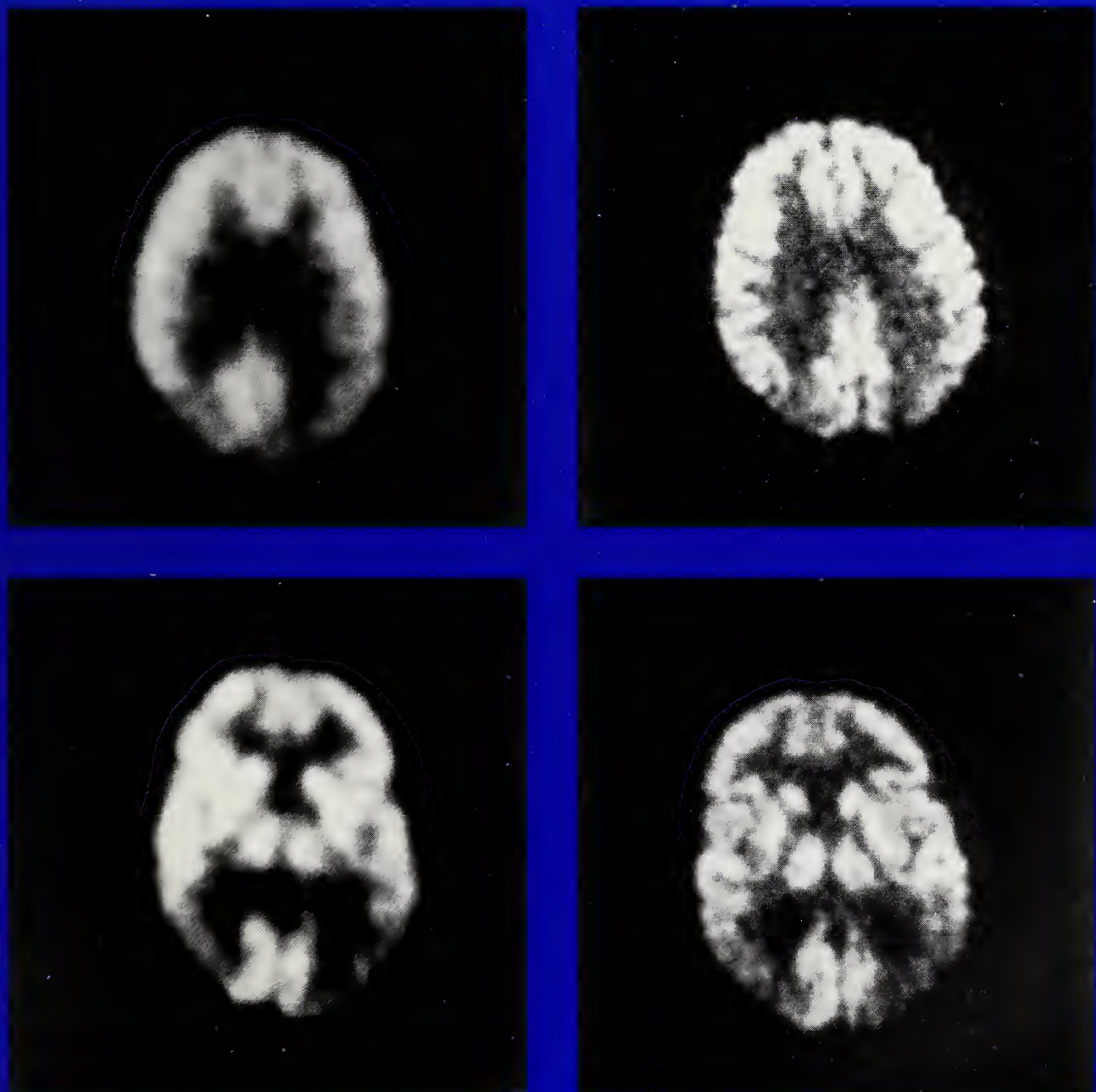
Extensive studies have related neuropsychological abnormalities to these metabolic changes. AD patients manifesting specific neurobehavioral syndromes (such as aphasias or profound visuospatial disturbances) show reduced rCMRglc in the brain regions classically associated with such functions (Foster et al. 1983). Evaluation of left-right differences in AD patients has also demonstrated considerable asymmetry of rCMRglc between the two hemispheres, compared with that in age-matched control subjects. These asymmetries parallel asymmetries of cognitive function, such that patients with poorer visuospatial performance than language ability show relatively reduced right hemisphere glucose metabolism, and vice versa (Koss et al. 1985; Haxby et al. 1985). Using a variety of neuropsychological instruments, our laboratory has found relationships between cognitive ability and rCMRglc (Friedland et al. 1987).

DYNAMIC PET STUDIES

Because PET has high sensitivity, it is capable of relatively good temporal resolution, evident in such paradigms as the $^{15}\text{O}-\text{H}_2\text{O}$ bolus injection autoradiographic technique,

which permits acquisition of quantitative rCBF data after only 40 seconds of imaging. The uses and potential of such studies have been well documented in activation paradigms, e.g., repeated blood flow studies, performed in one subject at

FIGURE 1



PET-FDG images taken in the same patient on two separate tomographs. The top images represent a slice 7 cm above and parallel to the orbitomeatal line; the bottom images, a slice 5 cm above and parallel to this line. The left images were taken on the PET280, an instrument with 8 mm in-plane resolution, and the right images were taken on the PET600, an instrument with 2.6 mm in-plane resolution. The images demonstrate reduced glucose metabolism in parietal cortex and temporal cortex bilaterally.

the same sitting, used to investigate the patterns of regional activation during cerebral activity (Petersen et al. 1988). Such studies allow the subtraction of sequential PET scans, performed during different cognitive activities, in order to tease apart the contributions of different brain regions to different cognitive functions.

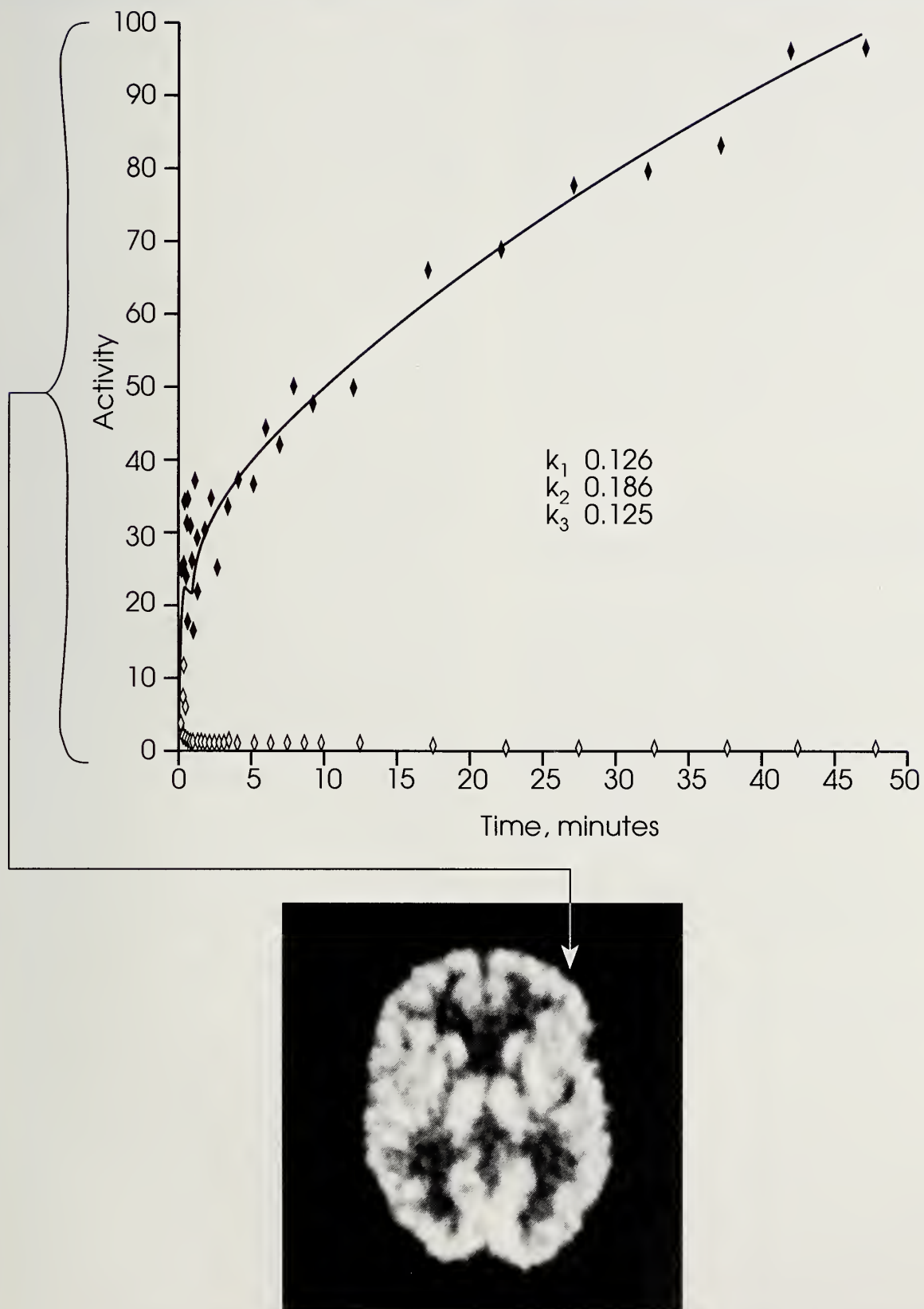
PET temporal resolution capabilities also permit dynamic studies in which multiple measurements of tracer uptake provide considerably more detail than could be obtained in a single image. Dynamic PET requires what is essentially sequential PET scanning over the time course of tracer uptake; it produces a time-activity curve for tracer uptake in the brain. This time-activity curve, in combination with a time-activity curve of plasma tracer activity, may be used with a model to describe the uptake, transport, and metabolism of the tracer. Figure 2 is an example of dynamic PET data.

Such compartmental models are very important for deriving quantitative data from PET studies of neurotransmitter receptors, in which the contribution of tracer in the vascular space and in bound and unbound tissue compartments must be separated. In addition, dynamic PET studies using FDG can be used to investigate the mechanisms of altered glucose metabolism. By using Sokoloff's (1977) three-compartment model with dynamic PET data describing brain uptake and plasma activity, we can derive the rate constants describing forward and reverse glu-

cose transport from blood to brain (k_1^* and k_2^* , respectively) and glucose phosphorylation by the enzyme hexokinase (k_3).

Our laboratory employed dynamic PET with FDG to estimate the kinetic parameters k_1^* , k_2^* , and k_3^* that describe glucose transport and phosphorylation in order to investigate whether reduced transport or phosphorylation was the mechanism underlying the frequently seen hypometabolism in AD (Jagust et al. 1991b). The subjects were six patients with AD and seven healthy age-matched control subjects. A recently completed high-resolution tomograph (PET600, with 2.6 mm in-plane resolution) was used to acquire brain uptake data in one tomographic plane, and a radial artery catheter connected to a plastic scintillator was used to acquire arterial input data. A non-linear iterative least-squares fitting procedure, which included terms for the vascular fraction and time delay to the peripheral sampling site, was used to fit a three-compartment model to the brain data. Regions studied included frontal, temporal, occipital, the entire cortex, and subcortical white matter.

A significant ($p < 0.05$) decrease was found in k_1^* in frontal and temporal cortex in the AD patients, compared with that in controls. The values for control subjects were 0.157 and 0.161 mL/g/minute in frontal and temporal cortex, respectively; the AD patient values were 0.127 mL/g/minute in frontal and 0.126 mL/g/minute in temporal cortex. Regional CMR_{glc} was also

FIGURE 2

Dynamic PET data taken from the frontal lobe region of a control subject. The solid diamonds represent the time course of brain uptake of tracer, measured with the PET600 tomograph; the open diamonds represent the time course of blood tracer activity. Results of a three-compartment model fit to the metabolic parameters k_1-k_3 are shown.

significantly ($p<0.02$) lower in all cortical brain regions of the AD patients than in those of the controls. Lower k_3^* values found in all brain regions in the AD patients were not statistically significant. These findings provide evidence of an *in vivo* abnormality of forward glucose transport in AD; however, this transport defect is probably not the cause of the diminution in glucose metabolism widely found in AD patients. A diminution of this magnitude should not lower intracerebral glucose content enough to alter rCMRglc.

PET IMAGING IN OTHER NEURODEGENERATIVE DISEASES

In addition to its use in studies of the common dementia of AD, PET has been applied to the study of other neurodegenerative diseases associated with aging. These studies have provided information useful to the clinician in the differentiation of a variety of neurological illnesses from each other and from AD. PET studies have also helped to explain pathophysiologic mechanisms in a number of poorly understood illnesses.

Patients with Pick's disease experience cognitive decline that has often been said to be indistinguishable from AD, yet careful cognitive examination may provide evidence of dysfunction related to frontal and anterior temporal systems, as well as structural imaging evidence of frontotemporal atrophy (Cummings and Duchen 1981; Knopman et al. 1989). Imaging

with PET provides quite striking evidence of a pattern of glucose metabolism that differs from that seen in AD. In two patients whose autopsies subsequently confirmed the diagnosis of Pick's disease, PET imaging with FDG has shown hypometabolism involving the frontal lobes, in contrast to the more posterior involvement of temporal and parietal cortex seen in AD (Friedland et al. 1986; Kamo et al. 1987). These findings, which may have clinical utility, illustrate how PET can detect physiological changes that correspond to behavioral abnormalities accompanying minimal structural changes.

Movement disorders, particularly Parkinson's disease (PD) and progressive supranuclear palsy (PSP), have also been studied with PET. These illnesses are of interest because of the frequent association of cognitive changes that may have physiological correlates and because using specific tracers to evaluate the dopaminergic systems of both may lead to important insights concerning pathophysiology and treatment.

PET studies of Parkinson's disease have examined the relationships between cerebral energy metabolism and cognition and between subcortical energy metabolism and dopamine metabolism and movement. Although many investigators have found increased blood flow and glucose metabolism in the basal ganglia of PD patients (Rougemont et al. 1984; Wolfson et al. 1985), findings in the cerebral cortex have

been more variable. Some authors have reported diminished global cerebral blood flow, detected by the inhaled ^{133}Xe technique (Lavy et al. 1979), while others, using this technique as well as PET with $^{15}\text{O}-\text{H}_2\text{O}$, have noted diminished frontal lobe blood flow (Wolfson et al. 1985; Perlmutter and Raichle 1985). Although these studies did not explore the relationship between the altered perfusion patterns and cognitive function, other PET studies indicate that demented PD patients may have diminished temporal and parietal blood flow and glucose metabolism similar to that seen in AD (Kuhl et al. 1984). These findings are of particular interest because of the frequent neuropathological occurrence of AD simultaneously with that of Parkinson's disease (Boller et al. 1980). In addition, a recent report has shown that depressed PD patients demonstrate diminished glucose metabolism in the inferior frontal lobes (Mayberg et al. 1990).

Patients with PSP experience a dementia characterized by cognitive slowing. PSP is often called "subcortical dementia" because of contrasts with AD. AD patients are more likely to suffer from disorders of language and from visuospatial relationships, reflecting prominent involvement of association neocortex in addition to memory loss. PET-FDG studies have made an important contribution to the understanding of PSP by demonstrating prominent frontal lobe hypometabolism (D'Antona et al. 1985; Foster et al. 1988). Thus, the cognitive changes associated with PSP

have been postulated to result from subcortical disruption of frontal system afferents.

The PET tracer [$6-^{18}\text{F}$]dihydroxyphenylalanine (FDOPA) has been used to evaluate dopamine metabolism in these diseases as well. FDOPA is taken up by the nigral neuron, decarboxylated to fluorodopamine, and stored in the dopaminergic storage vesicle in a manner similar to that of the unlabeled dopamine precursor levodopa; therefore, its behavior studied with PET provides useful information about the integrity and function of the dopamine system. Patients with hemiparkinsonism have shown reduced tracer accumulation in the striatum contralateral to the affected extremity. This reduced tracer accumulation is more severe in the putamen than in the caudate (Garnett et al. 1984). PD and PSP patients have been shown to exhibit lower ratios of radioactivity in striatum to surrounding brain than controls following FDOPA injection (Leenders et al. 1986, 1988).

SPECT IMAGING IN DEMENTIA

PET studies of cerebral physiology served as the groundwork for other physiological imaging studies, and SPECT imaging has now become a popular method for studying cognitively impaired individuals. Because of the wider availability of SPECT technology, its use as a clinical tool has grown, and clinical research using this modality is also becoming increasingly important. Despite

SPECT limitations for quantitative recovery of radionuclide distribution data, its advantages--ease of use and technical accessibility--may permit the study of larger numbers of patients representing many different disease states.

A number of laboratories have carefully used SPECT in the diagnosis of demented subjects. Studies employing tracers for cerebral perfusion have yielded findings similar to those obtained via metabolic tracers in studies of AD, probably because PET studies of OER showed that flow and metabolism are normally coupled. With the most commonly used tracers, [¹²³I]N-isopropyl-p-iodoamphetamine (IMP) and [^{99m}Tc-hexamethyl-propylamine oxime (HM-PAO), a number of laboratories (Cohen et al. 1986; Johnson et al. 1987; Jagust et al. 1987a; Gemmell et al. 1987) have demonstrated diminished temporoparietal perfusion, which has been related to clinical features of illness, e.g., severity of dementia and type of cognitive dysfunction (Perani et al. 1988).

The earliest stages of dementia, when diagnosis is most difficult, have received special attention in the Lawrence Berkeley Laboratory, which recruited patients in the earliest stages of AD in order to evaluate the sensitivity of SPECT and IMP in elucidating the cause of dementia (Reed et al. 1989). Of 21 patients, all of whom underwent SPECT scans and neuropsychological testing, 9 were very mildly demented. Even though all complained of memory loss and

were believed to have AD, their scores on the mini-mental status examination (MMSE) (Folstein et al. 1975) were in the normal range (mean, 26.6; S.D., 1.7). These mildly demented subjects probably represented the earliest stage of AD which is now clinically detectable. The other 12 patients were moderately demented (MMSE mean score, 15.0; S.D., 5.4). Thirty-six healthy, age-matched control subjects were also studied; 14 received SPECT scans, and 22 underwent neuropsychological testing, but no control subject received both. These SPECT data were quantitated by calculating an rCBF ratio, defined as the ratio of regional radioactivity normalized to occipital cortical radioactivity.

Studies of four cortical rCBF ratios--orbitofrontal and dorsolateral frontal cortex and temporal and parietal cortex--revealed considerable overlap between the patients (both mildly and moderately demented) and the control subjects for all brain regions. When SPECT and neuropsychological abnormalities were defined as scores outside the 95 percent confidence intervals for the control group means, 100 percent of the AD patients showed memory abnormalities revealed on neuropsychological tests, while only 55 percent of the mildly demented and 83 percent of the moderately demented patients showed temporal or parietal perfusion deficits. On the other hand, only 7 percent of control subjects had temporal or parietal SPECT abnormalities, suggesting that CBF abnormality may

be a more reliable indicator of dementia than abnormal memory function, which was seen in 27 percent of control subjects. Although other methods of SPECT data analysis might be more sensitive for the diagnosis of AD (e.g. visual inspection by a trained observer), it is clear that a normal SPECT scan does not rule out the presence of AD. Nevertheless, a high proportion of extremely mildly demented patients show temporal and parietal perfusion deficits.

Like PET images, SPECT images of patients with AD frequently demonstrate asymmetric functional involvement. While we have noted a greater preponderance of left hemisphere involvement in younger patients with AD (Jagust et al. 1990), it is notable that asymmetric scans may occur in patients of any age. At times, this may lead to the incorrect diagnosis of vascular dementia, although structural imaging studies should easily differentiate the two.

SPECT IMAGING IN OTHER DEMENTIAS

A variety of other dementing illnesses studied with SPECT and perfusion tracers generally show patterns of rCBF different from that seen in AD. Patients with the AIDS dementia complex show focal and multifocal perfusion deficits, with no predilection for any particular brain region (Pohl et al. 1988). Multi-infarct dementia (MID) patients similarly show focal and multifocal deficits, although some have demonstrated temporal and pari-

etal perfusion deficits (Gemmell et al. 1987), a finding that may result from temporal and parietal cortex infarcts easily identified by computed tomography or magnetic resonance imaging. There are also suggestions of frontal lobe hypoperfusion in patients with MID (Cohen et al. 1986; Jagust et al. 1987a). This deficit may be the imaging correlate of the clinical and neuropsychological frontal lobe deficits displayed by many of these patients (Ishii et al. 1986; Wolfe et al. 1990).

SPECT studies of patients with frontal lobe dementias parallel the work described earlier using PET with FDG to study Pick's disease. Our studies of a group of patients with clinical evidence of frontal lobe dysfunction (e.g., behavioral disinhibition, apathy, aphasia, and mutism) using SPECT and IMP show physiological dysfunction (i.e., diminished tracer uptake) in the frontal lobes in contrast to the temporoparietal abnormalities of AD (Jagust et al. 1989). While such frontal lobe glucose metabolic abnormalities may reflect Pick's disease, all dementias with frontal lobe symptoms and perfusion abnormalities cannot be diagnosed as Pick's disease without autopsy confirmation; some such syndromes are associated with nonspecific pathology (Neary et al. 1986). It also is possible that some of these patients have frontally predominant AD. Nevertheless, SPECT imaging in these cases may be clinically useful in documenting abnormalities of regional function that can explain the

clinical symptoms and support the diagnosis of a frontal lobe dementia syndrome.

SPECT IMAGING IN OTHER DEGENERATIVE DISEASES

SPECT is applicable to the study of Parkinson's disease. Using SPECT with ^{99m}Tc -HM-PAO, Pizzolato et al. (1988) found diminished temporal and parietal perfusion in PD patients with dementia. The work is similar to that reported by Kuhl et al. (1984), who used PET and FDG. We recently used SPECT with IMP to study the relationship between cognitive function and regional physiology and found that patients with generalized cognitive decline show reduced temporal lobe perfusion, perhaps predicting the subsequent development of AD. However, patients with frontal lobe cognitive disturbances showed reduced frontal perfusion. These results suggest that cognitive disturbances in PD are not unitary, and they reflect abnormalities in a variety of different cortical systems (Jagust et al. 1991a). We have found that patients with PSP also show diminished frontal lobe perfusion, thus confirming PET and glucose metabolic tracer findings.

Not surprisingly, SPECT and PET findings for patients with Huntington's disease are similar: Symptomatic patients have diminished perfusion in the caudate nuclei (Reid et al. 1988; Smith et al. 1988). Although PET studies suggest that imaging the caudate nuclei with FDG can be helpful in predict-

ing which of these patients will later develop the disease (Mazziotta et al. 1987), the utility of SPECT in assessing at-risk individuals has not been adequately studied.

RECENT PET DEVELOPMENTS AND APPLICATIONS TO ALCOHOL RESEARCH

Both PET and SPECT have considerable potential for investigations related to the effects of alcohol on the brain. A number of recent technical advances will improve quantitative measurement of a variety of physiological processes.

One of the more important developments in PET technology is the improvement of instrument resolution that has occurred over the past 5 years. While initial scanners had spatial resolution on the order of 1–2 cm, newer scanners provide resolution in the range of several millimeters. In our laboratory, the recently designed PET600 has an in-plane resolution of 2.6 mm, with an axial resolution of 6 mm. Clinical studies using this tomograph are under way, and quantitative data are routinely obtained (Valk et al. 1990). Similarly, commercial instruments with resolutions on the order of 5–6 mm are routinely used. Figure 1 shows the contrast in resolutions obtained with two different instruments.

This degree of resolution has direct implications for quantitation of physiological function in structures of interest. System resolution must be at least one-half the size of a region of interest in order to fully

recover activity (Hoffman et al. 1979), thus a 4-mm cortical region requires resolution on the order of 2 mm for full recovery (in three dimensions, full recovery requires even better resolution). These requirements have limited our ability to quantitate radiotracer uptake accurately in small structures such as the hippocampus and the brain-stem. However, improved resolution now permits more accurate studies of such regions.

We used the PET600 tomograph to quantitate rCMR_{glc} in small cerebral structures that were previously inaccessible for study in patients with AD, in particular, the mesial temporal lobes, primarily the hippocampus and the amygdala, in 13 patients with AD and 6 control subjects, matched for age and education. The AD patients met current research criteria for probable AD; they had extensive evaluations including CT or magnetic resonance imaging scans, as well as a 4-hour battery of cognitive testing. The same battery was administered to the control subjects to ascertain normal cognition. Notably, the AD patients as a group were very mildly demented; the majority were in early stages of the disease, their deficits confined to memory loss.

Each subject (or patient) was seated in a chair in a dimly lit room during a 30-minute uptake phase, and then moved to the PET600 scanner, which was tilted in a plane -20° to the orbitomeatal line to image the long axis of the temporal lobes. Three contiguous slices, each 5 mm thick, were imaged through

the temporal lobes, and a fourth slice was imaged 2.0 cm higher, passing through the thalamus and frontal lobes. Each slice was imaged for 10 minutes, and generally contained 1×10^6 to 2×10^6 coincident events. Transmission data were acquired immediately prior to the emission scans and were used to correct for attenuation. Arterial blood samples were taken intermittently until the end of the study, which was generally about 70 minutes following injection. The PET data were used with the arterial input function along with the previously obtained rate constants in the operational equation to determine rCMR_{glc}. Values for rCMR_{glc} were averaged across tomographic slices for the structures present at multiple levels.

The differences between the AD and control groups were profound for virtually all brain regions. The reductions in rCMR_{glc} were at least 20–30 percent in almost all cortical regions, including association neocortex such as temporal lobes and visual association cortex, as well as primary visual cortex and mesial temporal cortex. Subcortical regions (e.g., thalamus, striatum, and midbrain) did not show significant differences. These findings contradict previous PET studies, which suggested that primary sensory cortex is not affected in AD. In addition, these data suggest that neocortical regions of the temporal lobe are as severely affected as the mesial temporal lobes--a surprising finding, for it casts doubt on the generally held view that the disease

begins in the mesial temporal cortex. Indeed, these results suggest that AD is a disease of the entire temporal lobe, not just the temporal allocortex.

In preliminary explorations of the relationship between cognitive function and these metabolic rates, we constructed scales by combining a number of measures from several different neuropsychological tests. These measures were grouped on an a priori basis because they represented good measures of a given cognitive function. The scores were Z-transformed using the mean and standard deviation of the AD patients' scores, and scales were built for constructional and language abilities. Because there were preliminary data from a relatively small number of subjects, we correlated rCMR_{glc} with the scores using Pearson correlation coefficient. The patterns that emerged are consistent with our knowledge of cognition: The highest correlations were between constructional ability and right midtemporal and posttemporal rCMR_{glc} and between language ability and left anterior and midtemporal rCMR_{glc}. This effect is not nonspecific; e.g., correlations between left posterior temporal rCMR_{glc} and the constructional scale were not significant. Figure 3 demonstrates these relationships.

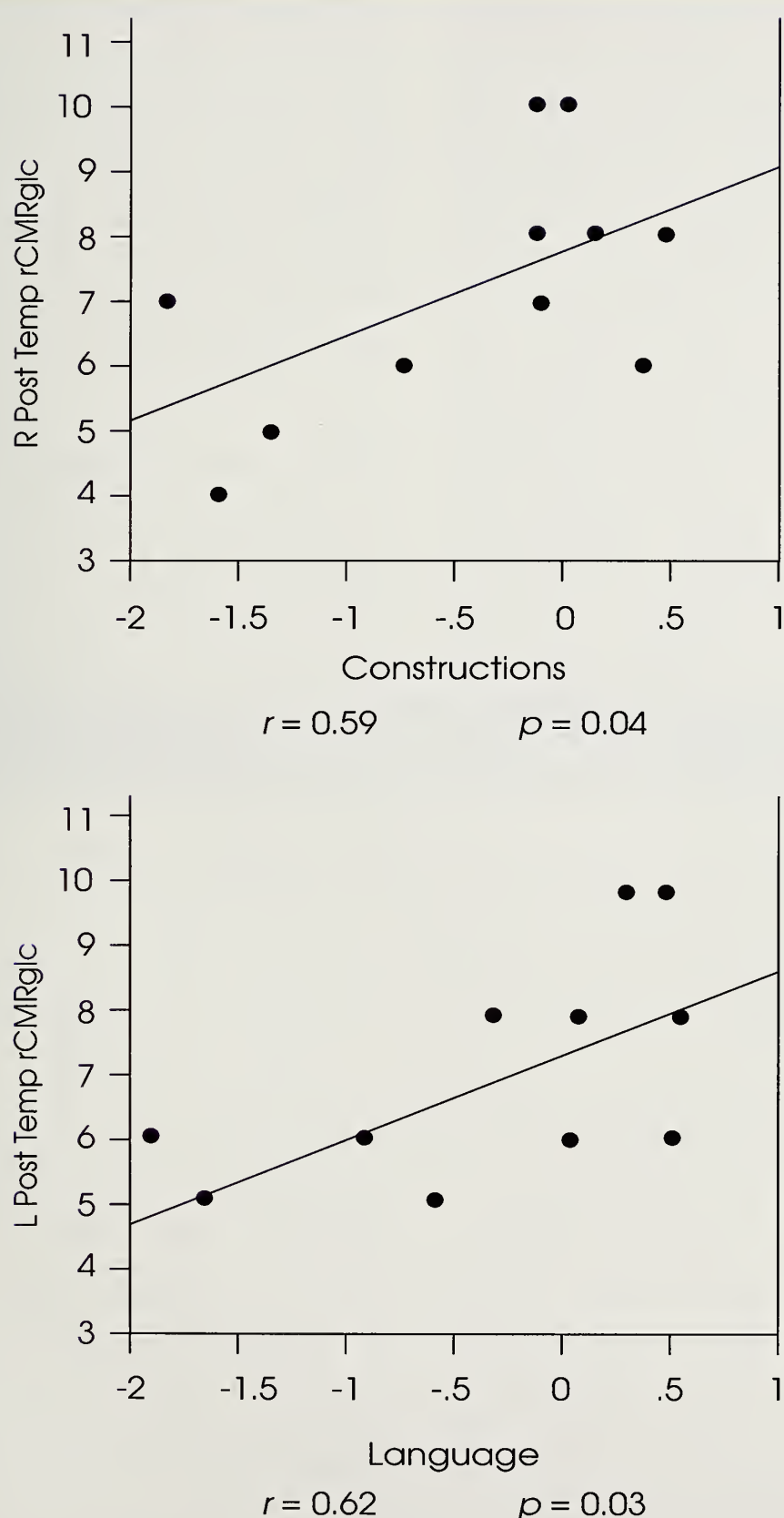
Alcohol Studies

The well-known acute and chronic effects of alcohol upon cognitive function have been studied with a variety of cognitive testing

paradigms, and structural neuroimaging has documented changes in anatomy consequent to prolonged alcohol use. Many of these abnormalities reflect dysfunction in both frontal and limbic-diencephalic systems. PET-FDG is potentially very sensitive to the early and subtle changes that may be induced by alcohol. In particular, PET-FDG may help relate neuropsychological deficits to regional brain changes in order to explain the effects of alcohol on cognitive and neural systems. Such an approach could also help to elucidate the neural basis of normal cognition.

Few studies have used these techniques to evaluate alcoholic neurobehavioral syndromes, and there are no studies investigating the full spectrum of the disorder. Samson et al. (1986) studied six abstinent chronic alcoholics who were specifically without cognitive dysfunction. While the metabolic rates in these patients were no lower than those of a matched control group, a 9 percent relative decline in mesial frontal lobe glucose metabolism was significant. Thus, the PET-FDG sensitive technique is capable of showing that even unimpaired alcoholics have frontal lobe dysfunction.

Wik and colleagues (1988) found rCMR_{glc} to be diminished in almost all brain regions in a group of nine alcoholics, compared with controls. That study was flawed, however, because the mental status of the patients was not described and the tracer used, $[^{11}\text{C}]$ glucose, had not been adequately modeled to

FIGURE 3

Correlations between neuropsychological measures of constructional ability (top) and language ability (bottom) and right and left posterior temporal lobe rCMRglc in a group of AD patients.

extract quantitative data. Sachs et al. (1987), using the well-validated [^{11}C]deoxyglucose technique with PET, found that 10 alcoholics generally showed lower rCMR_{glc} measurements compared with non-alcoholic controls. As in the study by Wik et al., these patients were not clearly characterized neuropsychologically; however, they did not have Korsakoff's syndrome (KS). Using PET with FDG, Kessler et al. (1984) found that essentially every brain region studied in six patients with KS showed lower rCMR_{glc} than in controls; their data also suggested the possible existence of two separate subgroups, one with low frontal metabolism and high basal ganglia and thalamic metabolism and the other with the opposite findings. These patients were not compared with other, non-KS, chronic alcoholics, so it is not known whether some of their brain regions might have been more affected than might be expected secondary to chronic alcoholism alone.

To investigate memory function and the relationship between cognitive function and rCMR_{glc} in patients with alcohol-induced neurobehavioral syndromes, we conducted an identical high-resolution PET-FDG study of one patient. This 59-year-old male alcoholic with KS was admitted to a Veterans Administration medical center in an acute state of confusion (Wernicke's encephalopathy), which after treatment with thiamine, cleared, leaving him with a severe amnestic syndrome. A CT scan showed only

cerebellar atrophy, and a lumbar puncture and routine laboratory tests were unremarkable. The results of cognitive testing performed within 3 days of the PET scan demonstrated severely impaired memory: The revised Wechsler Memory Scale verbal memory score was 56 (mean=100), the visual score was <50, and delayed recall was <50. The patient was unable to learn paired word associates and was confabulatory in his responses to recall for paragraphs. Although he had mild deficits in verbal and constructional abilities, his memory function impairment was disproportionate to that of his other functions; the clinical diagnosis was Korsakoff's syndrome. His PET data, in comparison with data from the group of AD and control subjects shown in figure 3 are shown graphically in figure 4; the PET image is shown in figure 5.

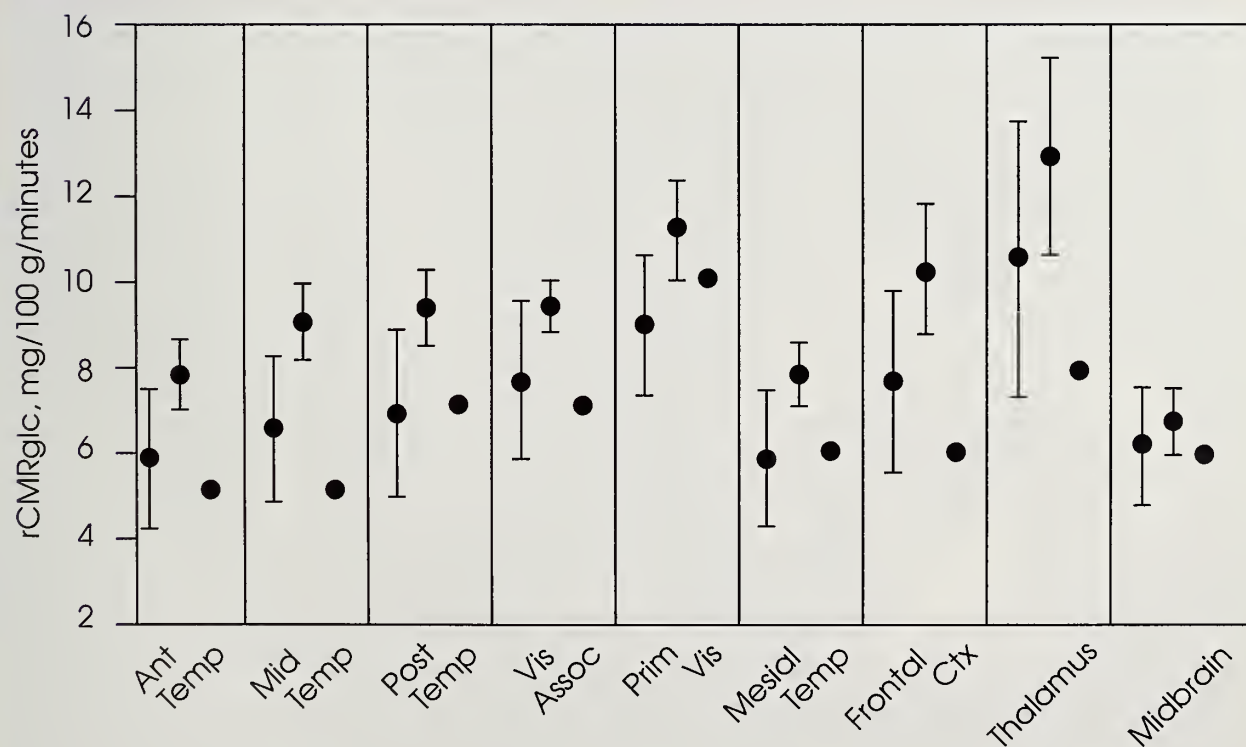
While data from this single Korsakoff's patient does not permit drawing meaningful, statistical conclusions, his rCMR_{glc} values were generally in the same range as those of the AD patients (interestingly, the patient showed mild generalized cognitive dysfunction). However, the lowest values were seen in the mid-temporal neocortex, as well as the frontal cortex and thalamus. The PET image clearly shows frontal hypometabolism. These findings support the contention that KS is associated with global metabolic dysfunction (in which cortical components are diminished because of the effect of alcohol on

neocortex), accompanied by a more profound and specific metabolic dysfunction in the frontal lobes and thalamus. Obviously, study of a larger group of patients will be necessary to investigate this relationship more thoroughly, but careful neuropsychological evaluation with high-resolution PET data offers promise in unraveling the relationships between chronic alcohol abuse and regional brain dysfunction.

Studies of glucose utilization are not the only potential application of PET with relationship to alcohol abuse. As table 1 shows, numerous PET tracers are available. The use of the $[^{15}\text{O}]$ water paradigm for

measurement of rCBF will facilitate investigation of patterns of regional cerebral activation in response to cognitive tasks, permitting a mechanistic evaluation of alterations in cognition in acute and chronic alcohol syndromes. In addition, the availability of neurotransmitter receptor ligands and presynaptic markers will permit the study of alterations of neurotransmitter systems associated with alcohol use and abuse. The PET capability of studying living patients with these disorders permits clinical correlations, so that the functional consequences of these disturbances will become apparent.

FIGURE 4



rCMRglc for brain regions from AD patients (left data point), control subjects (center data point), and a single patient (right data point) with Korsakoff's syndrome. The error bars represent 1 standard deviation (S.D.).

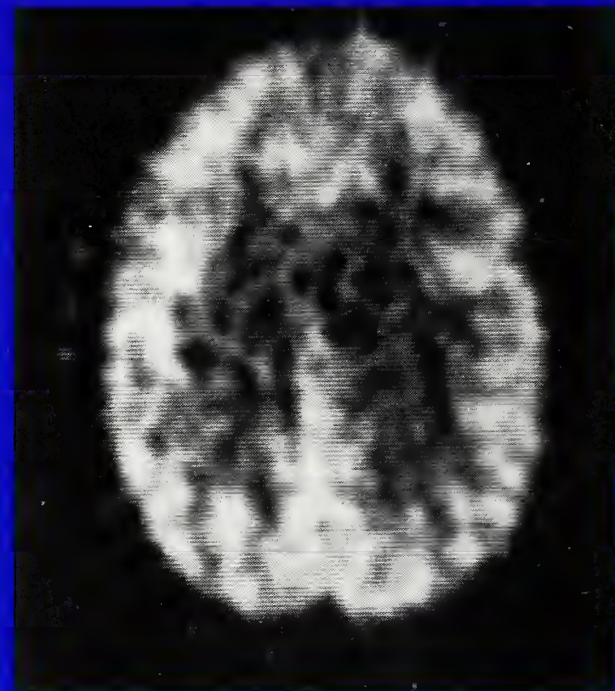
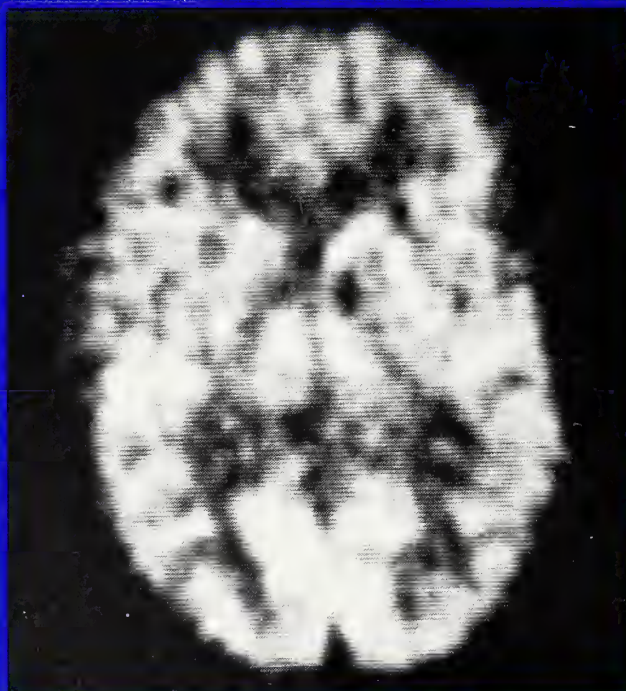
RECENT SPECT DEVELOPMENTS AND APPLICATIONS TO ALCOHOL RESEARCH

Improvements in SPECT technology are similar to those described for PET. Most important is improved instrument resolution, which is being accomplished without great loss of sensitivity by the use of additional crystal detectors placed around the field of view. Thus, although collimation reduces sensitivity, increased detector material minimizes the effect. Despite physical factors that limit the ultimate SPECT resolution attainable, instruments with in-plane resolution on the order of 8 mm are now available. With reasonable solutions to the problems of attenuation and

scatter, truly quantitative SPECT imaging is feasible. Even without quantitative imaging, SPECT can provide considerable information. Another advantage of SPECT may be the direct clinical benefit of being able to study patients in many nontertiary care settings.

One potential use of SPECT is in characterizing the regional disturbances consequent to chronic alcohol abuse in a method similar to PET with FDG. Several caveats apply: (1) Most routine SPECT functional imaging studies use regional perfusion tracers, which differ from metabolic tracers. Inferences about metabolism and flow coupling cannot be drawn from studies of degenerative dementias, in which quantitative experimental evidence

FIGURE 5



PET-FDG images of a patient with Korsakoff's syndrome at two tomographic levels, 5 cm (left) and 7 cm (right) above and parallel to the orbitomeatal line, taken with the PET600. Images demonstrate reduced tracer uptake that is visually apparent in the frontal lobes.

supports hypotheses concerning the maintenance of normal coupling of flow and metabolism. Such assumptions must be reexamined with respect to each new disease. For example, an obvious exception to this assumption is in stroke, where changes in flow and metabolism are not necessarily related. Thus, SPECT perfusion changes seen in alcohol use could result from vascular changes and not necessarily neuronal metabolic changes. (2) When SPECT data are analyzed nonquantitatively, regional ratios are often used to differentiate patient groups. Such ratios rely upon numerous implicit assumptions, e.g., that the denominator of the ratio is not affected differentially in two different groups. (3) Regional ratio methods cannot detect global differences between patient groups. SPECT perfusion studies must have quantitative data, obtained either with SPECT or through separate experiments with PET, to satisfy assumptions in data analysis and interpretation. Subject to these restrictions, large-scale SPECT perfusion studies of patients with alcohol-related brain injury can proceed on a scientific footing.

SPECT has other potential uses similar to those described for PET, e.g., the use of neurotransmitter receptor ligands to evaluate regional *in vivo* neurochemistry. The application of available SPECT tracers for use in studying the dopaminergic and cholinergic systems, as well as the development of new tracers for other systems, will further

advance the evaluation of alcohol-related brain injury.

ACKNOWLEDGMENTS

This work was supported by National Institute on Aging grants AG07793 and AG05890 and by the Director, Office of Energy Research, Office of Health and Environmental Research, U.S. Department of Energy, under contract DE-AC03-76SF00098.

REFERENCES

- Benson, D.F.; Kuhl, D.E.; Hawkins, R.A.; Phelps, M.E.; Cummings, J.L.; and Tsai, S.Y. The fluorodeoxyglucose ^{18}F scan in Alzheimer's disease and multi-infarct dementia. *Arch Neurol* 40:711-714, 1983.
- Boller, F.; Mizutani, T.; Roessmann, U.; and Gambetti, P. Parkinson disease, dementia, and Alzheimer disease: Clinicopathological correlations. *Ann Neurol* 7:329-335, 1980.
- Budinger, T.F. New technologies for noninvasive imaging in aging and dementia. In: Glenner, G.G., and Wurtman, R.J., eds. *Advancing Frontiers in Alzheimer's Disease*. Austin: University of Texas Press, 1987. pp. 175-199.
- Cohen, M.B.; Graham, L.S.; Lake, R.; Metter, E.J.; Fitten, J.; Kulkarni, M.K.; Sevrin, R.; Yamada, L.; Chang, C.C.; Woodruff, N.; and Kling, A.S. Diagnosis of Alzheimer's disease and multiple infarct dementia by tomographic imaging of iodine-123 IMP. *J Nucl Med* 27:769-774, 1986.
- Cummings, J.L., and Duchen, L.W. Kluver-Bucy syndrome in Pick disease:

Clinical and pathological correlations. *Neurology* 31:1415–1422, 1981.

Cutler, N.R.; Haxby, J.V.; Duara, R.; Grady, C.L.; Moore, A.M.; Parisi, J.E.; White, J.; Heston, L.; Margolin, R.M.; and Rapoport, S.I. Brain metabolism as measured with positron emission tomography: Serial assessment in a patient with familial Alzheimer's disease. *Neurology* 35:1556–1561, 1985.

D'Antona, R.; Baron, J.C.; Samson, S.Y.; Serdaru, M.; Viader, F.; Agid, Y.; and Cambier, J. Subcortical dementia: Frontal cortex hypometabolism detected by positron emission tomography in patients with progressive supranuclear palsy. *Brain* 108:785–799, 1985.

DeCarli, C.; Kaye, J.A.; Horwitz, B.; and Rapoport, S.I. Critical analysis of the use of computer-assisted transverse axial tomography to study human brain in aging and dementia of the Alzheimer type. *Neurology* 40:872–883, 1990.

Duara, R.; Grady, C.; Haxby, J.; Sundaram, M.; Cutler, N.R.; Heston, L.; Moore, A.; Schlageter, N.; Larson, S.; and Rapoport, S.I. Positron emission tomography in Alzheimer's disease. *Neurology* 36:879–887, 1986.

Folstein, M.F.; Folstein, S.E.; and McHugh, P.R. Mini Mental State: A practical method for grading the cognitive state of patients for the clinician. *J Psychiatr Res* 12:189–198, 1975.

Foster, N.L.; Chase, T.N.; Fedio, P.; Patronas, N.J.; Brooks, R.A.; and DiChiro, G. Alzheimer's disease: Focal cortical changes shown by positron emission tomography. *Neurology* 33:961–965, 1983.

Foster, N.L.; Chase, T.N.; Mansi, L.; Brooks, R.; Fedio, P.; Patronas, N.J.; and DiChiro, G. Cortical abnormalities in Alzheimer's disease. *Ann Neurol* 16:649–654, 1984.

Foster, N.L.; Gilman, S.; Berent, S.; Morin, E.M.; Brown, M.B.; and Koeppe, R.A. Cerebral hypometabolism in progressive supranuclear palsy studied with positron emission tomography. *Ann Neurol* 24:399–406, 1988.

Frackowiak, R.S.J.; Pozzilli, G.; Legg, N.J.; DuBoulay, G.H.; Marshall, J.; Lenzi, G.L.; and Jones, T. Regional cerebral oxygen supply and utilization in dementia. *Brain* 104:753–778, 1981.

Friedland, R.P.; Budinger, T.F.; Ganz, E.; Yano, Y.; Mathis, C.A.; Koss, B.; Ober, B.A.; Huesman, R.H.; and Derenzo, S.E. Regional cerebral metabolic alterations in dementia of the Alzheimer type: Positron emission tomography with [¹⁸F]fluorodeoxyglucose. *J Comput Assist Tomogr* 7:590–598, 1983.

Friedland, R.P.; Jagust, W.J.; Budinger, T.F.; Koss, E.; and Ober, B.A. Consistency of temporal-parietal cortex hypometabolism in probable Alzheimer's disease (AD): Relationships to cognitive decline. *Neurology* 37(suppl 1):224, 1987.

Friedland, R.P.; Jagust, W.J.; Ober, B.A.; Dronkers, N.F.; Koss, E.; Simpson, G.V.; Ellis, W.G.; and Budinger, T.F. The pathophysiology of Pick's disease: A comprehensive case study. *Neurology* 36(suppl 1):268, 1986.

Garnett, E.S.; Nahmias, C.; and Firnau, G. Central dopaminergic pathways in hemiparkinsonism examined by positron emission tomography. *Can J Neurol Sci* 11:174–179, 1984.

- Gemmell, H.G.; Sharp, P.F.; Besson, J.A.O.; Crawford, J.R.; Ebmeier, K.P.; Davidson, J.; and Smith, F.W. Differential diagnosis in dementia using the cerebral blood flow agent ^{99m}Tc HM-PAO: A SPECT study. *J Comput Assist Tomogr* 11:398–402, 1987.
- Haxby, J.V.; Duara, R.; Grady, C.L.; Cutler, N.R.; and Rapoport, S.I. Relations between neuropsychological and cerebral metabolic asymmetries in early Alzheimer's disease. *J Cereb Blood Flow Metab* 5:193–200, 1985.
- Haxby, J.V.; Grady, C.L.; Duara, R.; Schlageter, N.; Berg, G.; and Rapoport, S.I. Neocortical metabolic abnormalities precede nonmemory cognitive defects in early Alzheimer's-type dementia. *Arch Neurol* 43:882–885, 1986.
- Hoffman, E.J.; Huang, S.C.; and Phelps, M.E. Quantitation in positron emission tomography. I. Effect of object size. *J Comput Assist Tomogr* 3:299–308, 1979.
- Ishii, N.; Nishihara, Y.; and Imamura, T. Why do frontal lobe symptoms predominate in vascular dementia with lacunes? *Neurology* 36:340–345, 1986.
- Jagust, W.J.; Budinger, T.F.; and Reed, B.R. The diagnosis of dementia with single photon emission computed tomography. *Arch Neurol* 44:258–262, 1987a.
- Jagust, W.J.; Friedland, R.P.; Koss, E.; Ober, B.A.; Mathis, C.A.; Huesman, R.H.; and Budinger, T.F. Progression of regional cerebral glucose metabolic abnormalities in Alzheimer's disease. *Neurology* 37(suppl 1):156, 1987b.
- Jagust, W.J.; Reed, B.R.; Eberling, J.L.; Martin, E.M.; and Nelson-Abbott, R.A. Cognitive function and cerebral blood flow in Parkinson's disease. *Neurology* 41(suppl 1):357, 1991a.
- Jagust, W.J.; Reed, B.R.; Seab, J.P.; and Budinger, T.F. Alzheimer's disease: Age at onset and SPECT patterns of regional cerebral blood flow. *Arch Neurol* 47:628–633, 1990.
- Jagust, W.J.; Reed, B.R.; Seab, J.P.; Kramer, J.H.; and Budinger, T.F. Clinical-physiologic correlates of Alzheimer's disease and frontal lobe dementia. *Am J Physiol Imaging* 4:89–96, 1989.
- Jagust, W.J.; Seab, J.P.; Huesman, R.H.; Valk, P.E.; Mathis, C.A.; Reed, B.R.; and Budinger, T.F. Diminished glucose transport in Alzheimer's disease: Dynamic PET studies. *J Cereb Blood Flow Metab* 11:323–330, 1991b.
- Jernigan, T.L.; Press, G.A.; and Hesselink, J.R. Methods for measuring brain morphologic features on magnetic resonance images: Validation and normal aging. *Arch Neurol* 47:27–32, 1990.
- Johnson, K.A.; Mueller, S.T.; Walshe, T.M.; English, R.J.; and Holman, B.L. Cerebral perfusion imaging in Alzheimer's disease: Use of single photon emission computed tomography and iofetamine hydrochloride I-123. *Arch Neurol* 44:165–168, 1987.
- Kamo, H.; McGeer, P.L.; Harrop, R.; McGeer, E.G.; Calne, D.B.; Martin, W.R.W.; and Pate, B.D. Positron emission tomography and histopathology in Pick's disease. *Neurology* 37:439–445, 1987.
- Kessler, R.M.; Parker, E.S.; Clark, C.S.; Martin, P.R.; George, D.T.; Weingartner, H.; Sokoloff, L.; Eberg, M.H.; and Mishkin, M. Regional cerebral glucose metabolism in patients with alcoholic Korsakoff syndrome. *Soc Neurosci Abstr* 10:541, 1984.

Knopman, D.S.; Christensen, K.J.; Schut, L.J.; Harbaugh, R.E.; Reeder, T.; Ngo, T.; and Frey, W. The spectrum of imaging and neuropsychological findings in Pick's disease. *Neurology* 39:362-368, 1989.

Koss, E.; Friedland, R.P.; Ober, B.A.; and Jagust, W.J. Differences in lateral hemispheric asymmetries of glucose utilization between early- and late-onset Alzheimer-type dementia. *Am J Psychiatry* 142:638-640, 1985.

Kuhl, D.E.; Metter, E.J.; and Riege, W.H. Patterns of local cerebral glucose utilization determined in Parkinson's disease by the [¹⁸F]fluorodeoxyglucose method. *Ann Neurol* 15:419-424, 1984.

Kuhl, D.E.; Small, G.W.; Riege, W.H.; Fujikawa, D.G.; Metter, E.J.; Benson, D.F.; Ashford, J.W.; Mazziotta, J.C.; Maltese, A.; and Dorsey, D.A. Cerebral metabolic patterns before the diagnosis of probable Alzheimer's disease. *J Cereb Blood Flow Metab* 7(suppl 1):S406, 1987.

Lavy, S.; Melamed, E.; Cooper, G.; Bentin, S.; and Rinot, Y. Regional cerebral blood flow in patients with Parkinson's disease. *Arch Neurol* 36:344-348, 1979.

Leenders, K.L.; Frackowiak, R.S.J.; and Lees, A.J. Steele-Richardson-Olszewski syndrome: Brain energy metabolism, blood flow and fluorodopa uptake measured by positron emission tomography. *Brain* 111:615-630, 1988.

Leenders, K.L.; Palmer, A.J.; Quinn, N.; Clark, J.C.; Firnau, G.; Garnett, E.S.; Nahmias, C.; Jones, T.; and Marsden, C.D. Brain dopamine metabolism in patients with Parkinson's disease measured with positron emission tomography. *J Neurol Neurosurg Psychiatry* 49:853-860, 1986.

Mayberg, H.S.; Starkstein, S.E.; Sadzot, B.; Preziosi, T.; Andrezejewski, P.L.; Dannals, R.F.; Wagner, H.N.; and Robinson, R.G. Selective hypometabolism in the inferior frontal lobe in depressed patients with Parkinson's disease. *Ann Neurol* 28:57-64, 1990.

Mazziotta, J.C.; Phelps, M.E.; Pahl, J.J.; Huang, S.C.; Baxter, L.R.; Riege, W.H.; Hoffman, J.M.; Kuhl, D.E.; Lanto, A.B.; and Wapenski, J.A. Reduced cerebral glucose metabolism in asymptomatic subjects at risk for Huntington's disease. *N Engl J Med* 316:357-362, 1987.

Neary, D.; Snowden, J.S.; Mann, D.M.A.; Bowen, D.M.; Sims, N.R.; Benton, J.S.; Northern, B.; Yates, P.O.; and Davison, A.N. Neuropsychological syndromes in presenile dementia due to cerebral atrophy. *J Neurol Neurosurg Psychiatry* 49:163-174, 1986.

Perani, D.; DiPiero, V.; Vallar, G.; Cappa, S.; Messa, C.; Bottini, G.; Berti, A.; Passafiume, D.; Scarlato, G.; Gerundini, P.; Lenzi, G.L.; and Fazio, F. Technetium-99m HM-PAO-SPECT study of regional cerebral perfusion in early Alzheimer's disease. *J Nucl Med* 29:1507-1514, 1988.

Perlmutter, J.S., and Raichle, M.E. Regional blood flow in hemiparkinsonism. *Neurology* 35:1127-1134, 1985.

Petersen, S.E.; Fox, P.T.; Posner, M.I.; Mintun, M.; and Raichle, M.E. Positron emission tomographic studies of the cortical anatomy of single-word processing. *Nature* 331:585-589, 1988.

Pizzolato, G.; Dam, M.; Borsato, N.; Saitta, B.; Da Col, D.; Perlotto, N.; Zanco, P.; Ferlin, G.; and Battistin, L. ^{99m}Tc-HM-PAO SPECT in Parkinson's disease. *J Cereb Blood Flow Metab* 8:S101-S108, 1988.

Pohl, P.; Vogl, G.; Fill, H.; Rossler, H.; Zangerle, R.; and Gerstenbrand, F. Single photon emission computed tomography in AIDS dementia complex. *J Nucl Med* 29:1382–1386, 1988.

Reed, B.R.; Jagust, W.J.; Seab, J.P.; and Ober, B.A. Memory and regional cerebral blood flow in mildly symptomatic Alzheimer's disease. *Neurology* 39:1537–1539, 1989.

Reid, I.C.; Besson, J.A.O.; Best, P.V.; Sharp, P.F.; Gemmell, H.G.; and Smith, F.W. Imaging of cerebral blood flow markers in Huntington's disease using single photon emission computed tomography. *J Neurol Neurosurg Psychiatry* 51:1264–1268, 1988.

Rougemont, D.; Baron, J.C.; Collard, P.; Bustany, P.; Comar, D.; and Agid, Y. Local cerebral glucose utilisation in treated and untreated patients with Parkinson's disease. *J Neurol Neurosurg Psychiatry* 47:824–830, 1984.

Sachs, H.; Russell, J.A.G.; Christman, D.R.; and Cook, B. Alteration of regional cerebral glucose metabolic rate in non-Korsakoff chronic alcoholism. *Arch Neurol* 44:1242–1251, 1987.

Samson, Y.; Baron, J.C.; Feline, A.; Bories, J.; and Crouzel, C. Local cerebral glucose utilization in chronic alcoholics: A positron tomographic study. *J Neurol Neurosurg Psychiatry* 49:1165–1170, 1986.

Smith, F.W.; Besson, J.A.; Gemmell, H.G.; and Sharp, P.F. The use of technetium-

99m-HM-PAO in the assessment of patients with dementia and other neuropsychiatric conditions. *J Cereb Blood Flow Metab* 8:S116–S122, 1988.

Sokoloff, L.; Reivich, M.; Kennedy, C.; DesRosiers, M.H.; Patlak, C.S.; Pettigrew, K.D.; Sakurada, O.; and Shinohara, M. The (14C)deoxyglucose method for the measurement of local cerebral glucose utilization: Theory, procedure and normal values in the conscious and anesthetized albino rat. *J Neurochem* 28:897–916, 1977.

Valk, P.E.; Jagust, W.J.; Derenzo, S.E.; Huesman, R.H.; Geyer, A.B.; and Budinger, T.F. Clinical evaluation of a high resolution (2.6 mm) positron emission tomograph. *Radiology* 176:783–790, 1990.

Wik, G.; Borg, S.; Sjogren, I.; Wiesel, F.-A.; Blomqvist, G.; Borg, J.; Greitz, T.; Nyback, H.; Sedvall, G.; Stone-Elander, S.; and Widen, L. PET determination of regional cerebral glucose metabolism in alcohol-dependent men and healthy controls using ¹¹C-glucose. *Acta Psychiatr Scand* 78:234–241, 1988.

Wolfe, N.; Linn, R.; Babikian, V.L.; Knoefel, J.E.; and Albert, M.L. Frontal systems impairment following multiple lacunar infarcts. *Arch Neurol* 47:129–132, 1990.

Wolfson, L.I.; Leenders, K.L.; Brown, L.L.; and Jones, T. Alterations of regional cerebral blood flow and oxygen metabolism in Parkinson's disease. *Neurology* 35:1399–1405, 1985.

21

PET STUDIES OF THE MYOCARDIUM: PROSPECTS FOR APPLICATIONS TO STUDIES OF ALCOHOLIC INJURY

James E. Holden, Ph.D.¹

Radionuclide tracer methods have served for many decades as one of the most prevalent and productive means of conducting biomedical research. Positron emission tomography (PET) allows tracer methods and models that have been developed and validated in the basic laboratory to be extended to studies in intact subjects. Ultimately, the same tracer principles first applied in tissue culture, in isolated organs, or in animal studies can be applied in humans, for both the basic study of diseases and therapies and for the management and care of patients.

This chapter is concerned with applications of PET to the study of the heart. It is not intended to provide a general review of the field, rather to convey a particular perspective about the role of PET in the study of disease processes. Whereas the applications of PET to the study of cardiac injury induced by alcohol have been limited to

date, references to the association between the methods under discussion and alcohol research are preliminary and speculative.

OVERVIEW OF PET DATA INTERPRETATION

Although PET does represent an extension of the conventional tracer methods applied in the basic science laboratory, important differences between PET and bench-top tracer studies must not be

ACRONYMS

ATP	<i>adenosine triphosphate</i>
2DG	<i>2-deoxy-D-glucose</i>
2FDG	<i>2-deoxy-2-fluoro-D-glucose</i>
FDNB	<i>[¹⁸F]1-fluoro-2,4-dinitrobenzene</i>
IPPA	<i>iodophenylpentadecanoic acid</i>
LCFA	<i>long-chain fatty acids</i>
PET	<i>positron emission tomography</i>
TCA	<i>tricarboxylic acid</i>

¹Department of Medical Physics, University of Wisconsin, Madison, WI 53706

overlooked. The object of PET imaging is to determine the time course of radioactivity concentration in specified anatomical regions. However, with PET, as opposed to conventional tracer studies, direct determination of the various subdivisions of total radioactivity concentration is not possible.

In conventional studies, subdivision of the total quantity of tracer label can be accomplished by destructive assays: the experiment is terminated, and the tissue is separated into its physical and chemical constituents by a variety of centrifugation, filtration, and chromatographic methods. In PET, these distinctions can only be inferred from the behavior of the total radioactivity time course. Such a requirement puts clear limits on the degree of complexity of a tracer study performed with PET. However, this limitation is mitigated to some degree by the fact that the delivery of tracer label to tissue is via the arterial blood. Conventional assay methods applied to sequential blood samples can allow the decomposition of blood tracer label into its various components. This kind of adjunct information is often critically important for the proper interpretation of the PET image data.

Two major classes of study have emerged as being simple enough for unique interpretation, yet complex enough to provide powerful information. The first is the determination of a process rate by measuring the accumulation of irreversibly trapped reaction products.

An important example of this approach is the deoxyglucose method (Sokoloff et al. 1977), described in greater detail later in the chapter. This approach can be generalized to include situations in which the reaction product is lost from the reaction site; however, it is limited to those rare situations in which the kinetic behavior of the reaction product makes it uniquely identifiable in the data. In such cases, reentry of reaction product from blood back into the tissue must be considered.

The second major class of study involves the evaluation of equilibrium distribution spaces. These measures relate the capacity for a specific compound in 1 g of tissue to the capacity for the same compound in 1 mL of perfusing fluid, usually plasma, with which the tissue is equilibrated. These equilibrium measures can provide information about the kinetic processes that determine their values. Furthermore, they can often be estimated without true equilibrium having been attained. The assay of noradrenergic innervation using labeled hydroxyephedrine (Schwaiger et al. 1990) described in a later section provides an excellent example of this approach.

It is important to note that many PET tracers are not true tracers, rather they are analogues of the compounds of actual interest that may behave quite differently from them. In some cases, these differences are intentional; in fact, they are the whole basis of the tracer method. Whether the differences

are intentional or not, the inference of the behavior of the parent compound from the behavior of the tracer is a component of PET methodology that requires independent attention and effort. The development of a basic understanding of the lumped constant that allows the net rate of glucose utilization to be derived from the measured phosphorylation rate of deoxyglucose (Sokoloff et al. 1977; Holden et al. 1991; Ng et al. 1991) provides the best-known example of this kind of consideration.

Finally, and perhaps most important of all, even the completely accurate derivation of physiological and biochemical information from PET data has negligible value unless it is performed as part of a well-designed experimental investigation. Posing the proper questions is at least as important as technical skill for providing answers. Furthermore, although PET is often called an interdisciplinary field, it cannot be conducted successfully if roles and responsibilities are too compartmented. People trained to be experts in PET technique must be prepared to learn a great deal about the context of a particular application, and the experts in that context must reciprocate.

PET STUDIES OF THE MYOCARDIUM

The versatility of PET is reflected in the remarkable variety of measurements that have been performed either with PET itself or with tracers labeled with positron-emitting

radionuclides in isolated heart preparations. We have selected three major categories of studies for expanded discussion in this chapter:

- (1) The metabolism of energy-producing substrates;
- (2) Tissue innervation and neurotransmitter turnover; and
- (3) The activity of detoxification systems.

Each of these categories has clear potential relevance to the study of alcoholic injury to the heart.

The list excludes several major categories of myocardial PET studies, for example, studies of tissue perfusion, *in vivo* receptor pharmacology, tissue oxygenation, and rates of synthesis of structural proteins. Limiting the discussion to three categories was required both by space limitations and by the goal of bringing an immense variety of material to a single focus. Future investigations of the myocardial response to acute and chronic alcohol exposure could, in fact, benefit from all past and current developments of PET methods in the heart.

CARDIAC PET FOR THE STUDY OF ALCOHOL-INDUCED INJURY

The relationship between chronic alcohol consumption and heart disease has been recognized for more than 100 years. Although the myocardial abnormalities induced by alcohol may progress to actual cardiomyopathy, the incidence of

congestive cardiomyopathy, even among severe chronic alcoholics, is low (Kupari and Suokas 1989). The subtle preclinical derangements believed to be present in as many as 80 percent of chronic alcoholics are clearly of greater importance, from both the perspective of developing a basic understanding of pathogenesis and that of assessing the true morbidity associated with alcohol consumption.

Long before progression to actual cardiomyopathy, the alcoholic heart demonstrates clear abnormalities of contractility, diastolic compliance, and electrical conduction (Klatsky 1987; Kupari and Suokas 1989). Abnormal catecholamine release (Kupari and Suokas 1989) and changes in the β -adrenergic receptor system (Hoffman et al. 1987; Kupari and Suokas 1989) are also associated with chronic alcohol exposure. In the worst case, sudden death may result either from fibrillation or from coronary spasm. The progression of abnormality to actual myopathic disease is believed to be influenced by factors that determine the degree of prior susceptibility (Kupari and Suokas 1989). Nearly all the changes, including even myopathy, will respond favorably to total abstinence from alcohol (Klatsky 1987). On the basis of this background, we propose the following roles for PET in the study of the effects of alcohol in the heart:

- The early detection and elucidation of alcoholic derangements

of metabolism, innervation, neurotransmitter and receptor pharmacology, and the activity of detoxification systems in cardiac tissue.

- The application of what is learned in those studies to the development of models of the mechanisms of pathogenesis. PET would allow the progression of a particular investigation, from cell culture and *in vitro* methods to isolated hearts to the imaging of intact animals and finally the imaging of human subjects under controlled conditions.
- Clinical patient care for those with the most advanced disease, e.g., in the management of acute withdrawal.

TECHNICAL CHALLENGES SPECIFIC TO CARDIAC PET

A thorough discussion of the technical difficulties unique to PET studies of the heart are beyond the scope of this chapter. The most important problems arise from two primary sources: cardiac motion and the proximity of the intraventricular blood pool, which often contains tracer label at high concentration, to the muscle tissue of interest. Some control of the first problem is afforded by gating PET data acquisition with an electrocardiographic signal. The mean interval between successive R waves is subdivided into 10–16 time bins, and a separate image is acquired for each; each thus corresponds to the heart, relatively immobilized at a

unique cardiac phase. The only drawback is that several hundred different heart cycles must be averaged into each image; however, this was equally true without gating. The ambiguity between radioactivity signal arising from muscle and from ventricular blood pool can be controlled to a degree by post-study image processing. In addition, new approaches to data analysis may be less sensitive to these problems (Holden et al. 1990). A review by Schelbert and Schwaiger (1986) provides a comprehensive overview of the technical challenges encountered in PET studies of the heart.

THREE CATEGORIES OF PET STUDIES OF THE MYOCARDIUM

Metabolism of Energy-Providing Substrates

Response to the demand for energy set by both external mechanical workload and biosynthetic regeneration of structures gives the heart one of the highest mass-specific energy consumption rates among the body's tissues. This energy is provided to the site of need almost entirely in the form of the high-energy phosphate bonds of adenosine triphosphate (ATP). This ATP is, in turn, nearly all produced by oxidative phosphorylation in the respiratory assemblies located in the inner membrane of the mitochondria. The formation of ATP in such assemblies occurs as electrons are transferred from NADH or FADH₂ to O₂ by a series of electron carriers. These reduced com-

pounds that drive the phosphorylation reaction can be produced from several different sources (Taegtmeyer 1984).

Available to the heart is an immense variety of enzymatic and transport mechanisms, which work together to allow the heart to adjust, at least in the short term, to the conditions externally imposed by combinations of mechanical workload, sympathetic and parasympathetic control, circulating hormones, substrate availability (including that of oxygen), and the accumulation of exogenous and endogenous toxins. Often described in terms of substrate "preferences," these adaptations are more accurately the net result of complex couplings and interactions among the cycles and systems of enzymes, intermediates, and cofactors involved in the provision of myocardial energy. When the heart is presented with a particular challenge, e.g., the chronically elevated arterial acetaldehyde and acetate levels of alcoholism, its physiological and biochemical adaptations may be stable and benign. On the other hand, the challenge may impose a particular biochemical disruption such that long-term damage is induced. PET offers the potential for four particular probes for the study of metabolic adaptations to alcoholic insult:

- (1) The phosphorylation rate of exogenous glucose;
- (2) The β -oxidation rate of exogenous long-chain fatty acid;

- (3) The rate of incorporation of exogenous long-chain fatty acid or acetate into complex lipids; and
- (4) The kinetic rate *constant* (as opposed to the turnover flux rate itself) of the pools of intermediates and exchangeable side pools of the tricarboxylic acid (TCA) cycle.

The following subsections provide additional detail about each of these possibilities.

Glucose

The study of glucose metabolism has been the dominant PET study performed in human heart, just as in human brain. As in brain, the studies are based on the deoxyglucose method of Sokoloff (1977). Small alterations of the structure of the glucose molecule can have very large effects on the affinities between glucose and the enzymes and carriers involved in the glycolytic and other metabolic pathways. Affinities of the two major analogue compounds, 2-deoxy-D-glucose (2DG) and 2-deoxy-2-fluoro-D-glucose (2FDG), for membrane transporters and for hexokinase are comparable to those for D-glucose itself. However, the 6-phosphate compounds that are the products of hexokinase-catalyzed phosphorylation are not significant substrates for the enzymes that drive glucose-6-phosphate into the three major subsequent pathways--glycolysis, glycogen synthesis, and the pentose phosphate shunt. The accumulation of phosphorylated

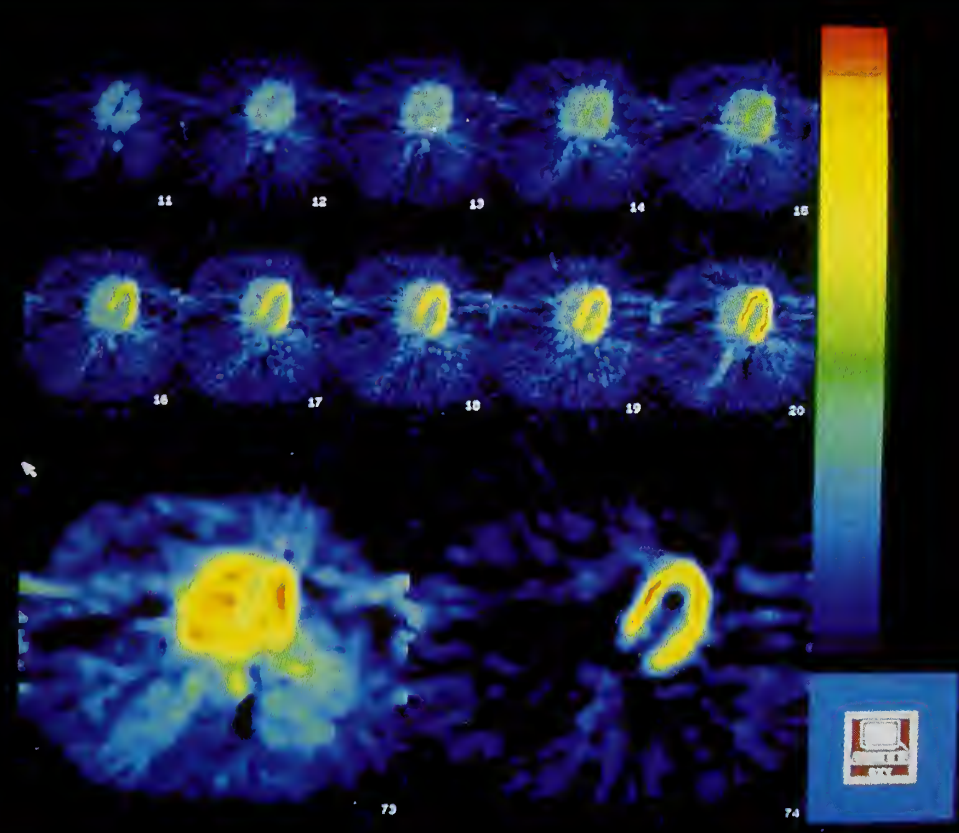
product thus reflects the total phosphorylation rate of the analogue. Knowledge of the relationships between the affinities of the tracer and of glucose itself for the primary transport carriers and for hexokinase can then allow the rate of glucose phosphorylation to be inferred from that of the analogue (Sokoloff et al. 1977; Holden et al. 1991).

Considerable misunderstanding about the value of glucose studies in the heart is based on the assumption that glucose is a secondary or "disfavored" substrate in the heart. Determination of total energy production rate is not necessarily the most important goal of myocardial metabolic studies; the phosphorylation rate of glucose, when combined with other information, may provide very powerful insight into the metabolic status of heart muscle, even if glucose is providing a minority of the mechanical energy required. For example, the failure of elevated plasma fatty acids to suppress glucose phosphorylation may provide information about regional abnormalities of fatty acid metabolism. Furthermore, the phosphorylation of glucose is the first step not only of glycolysis but of the synthesis of glycogen stores and of the pentose phosphate shunt. The pentose phosphate shunt is a major source of the reduced pyridine nucleotide NADPH, which is the primary means of reduction of the oxidized form of glutathione, a tripeptide known to be critically involved in the detoxification of the heart.

Figure 1 demonstrates a particular approach to 2FDG studies in the heart that is under development in our laboratory (Holden et al. 1990). The 2FDG tracer is administered by programmed infusion designed to provide a time-invariant level of radioactivity in arterial plasma. The top section of the figure shows a sequence of 10 images of 5-minute duration each, acquired continu-

ously during a 50-minute infusion. The images are displayed with a common color scale. The steady accumulation of radioactivity in the ventricular walls and the constancy of the concentrations in the right and left cardiac chambers are clearly seen. The linear accumulation of radioactivity with time reflects the rate of phosphorylation in each image region. Because of the

FIGURE 1



2FDG study in the normal human heart. The images all correspond to the same transverse-axial plane, with the subject's anterior at the top, and the subject's left to the right. The arterial concentration of 2FDG was held constant by programmed infusion of the tracer. Phosphorylation of 2FDG (taken to be proportional to that of glucose) is therefore readily visualized as the steady accumulation of radioactivity in each image region. The 10 images at the top of the figure correspond to a dynamic sequence of 5-minute frames continuously collected over a 50-minute period. The time course in each pixel is fitted to a straight line using conventional least-squares methods; the best fit intercepts and slopes estimated in each pixel are shown as pixel maps at the lower left and right, respectively.

high quality of the data, slopes and intercepts of the linear accumulation over time can be estimated in each PET image pixel using conventional least-squares methods.

The slope image (figure 1, lower right) represents a map of local phosphorylation rate. The combination of the slope information with pixel-by-pixel estimates of the intercept (figure 1, lower left) may in fact provide information about local variations in the lumped constant required to infer the rate of glucose phosphorylation rate from the rate of 2FDG phosphorylation provided by the slope image (Ng et al. 1991; Holden et al. 1991). Validation of this important concept remains one of our primary research interests.

Fatty Acids

Under most circumstances, the majority of the metabolic energy produced in the heart is from the β -oxidation of long-chain fatty acids (LCFA). Disruption of fatty acid metabolism is believed to be one of the earliest alcohol-induced abnormalities (Regan 1979; Kondrup et al. 1989). The kinetics of the label following bolus administration of labeled LCFA into myocardial tissue have been shown to be sharply dependent on the identity of the fatty acid studied and the position of the radioactive label.

The single-pass extraction of most fatty acid analogues in heart is quite high, sometimes as high as 50 percent. In many cases, the subsequent fate of the extracted label can be well understood in terms of a small number of kinetic behaviors.

First, the unchanged, nonesterified compound is free to return from tissue back to plasma. Second, the compound may be complexed to acyl coenzyme A, a complex that in turn has two primary fates. In some cases, the labeled analogue will enter the mitochondrial β -oxidation pathway, which is reflected in the kinetics by the clearance of labeled catabolic products from the tissue. Alternatively, the complexed compound can be incorporated into pools of compounds that have longer dwell times in the heart tissue, such as structural lipid or local stores of triacylglycerol.

Long-chain saturated acids such as palmitate represent the majority of the LCFA metabolized for energy production in the heart. It would seem, therefore, that palmitate labeled with ^{11}C would represent the ideal "natural" tracer of LCFA kinetics in heart. Indeed, the patchy, highly variable deposition of $[^{11}\text{C}]$ palmitate has been validated as a marker for congestive cardiomyopathy (Geltman et al. 1983; Schelbert et al. 1986). However, its application for the quantitative estimation of the rate of β -oxidation of exogenous LCFA has met with a serious obstacle: the kinetic behaviors of the nonesterified tracer and the CO_2 -bicarbonate reaction products of β -oxidation may not be definitively distinguishable from each other (Schelbert et al. 1986). Despite this obstacle, $[^{11}\text{C}]$ palmitate may be the ideal tracer to demonstrate and perhaps even to quantify the rate of incorporation of circulating LCFA into complex lipids.

(Bergmann et al. 1982). Abnormalities of fatty acid incorporation have been well established as a fingerprint of early alcoholic injury (Regan 1979; Kondrup et al. 1989). An attribute of $[^{14}\text{C}]$ palmitate that was an obstacle to the original goal of estimating β -oxidation rates thus may be beneficial for alcohol studies.

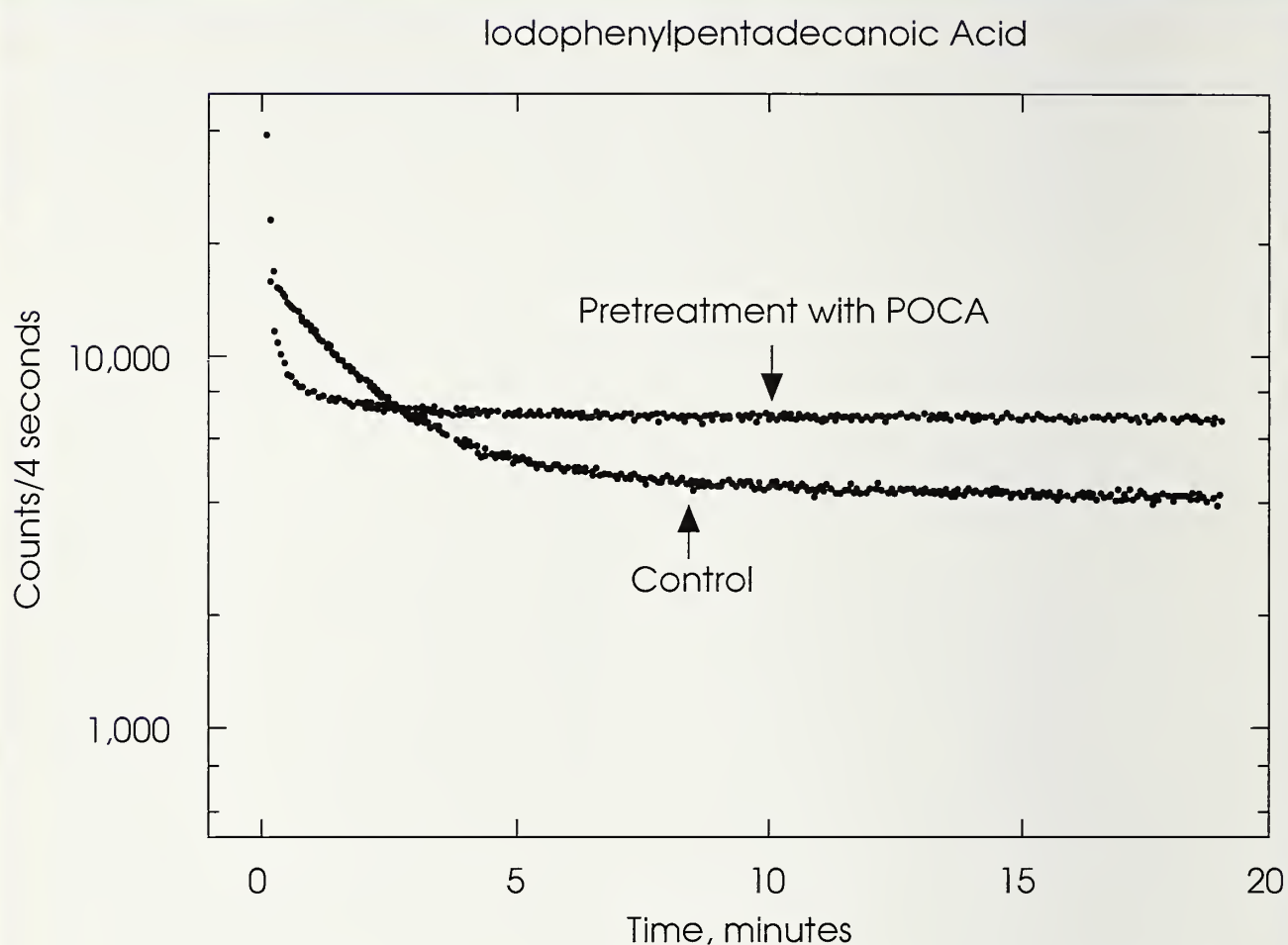
When the nonesterified tracer and its catabolic products are kinetically distinguishable, fatty acid analogues can identify the β -oxidation process. A method of identification was demonstrated in our laboratory using iodophenylpentadecanoic acid (IPPA) in isolated rat heart (DeGrado et al. 1988; DeGrado et al. 1989). Bolus injection of labeled IPPA into isolated hearts was followed by detection of total heart radioactivity residue in external detectors. Some hearts were obtained from animals pretreated with the palmitoyl carnitine transferase I inhibitor POCA, which inhibits the transport of acyl CoA into the mitochondrion, thus inhibiting β -oxidation. The intermediate clearance phase, between the rapid early peak showing clearance of the unchanged tracer and the late residue "tail" reflecting incorporation into complex lipids, was strongly diminished in the POCA study (figure 2). The same figure also shows the enhanced incorporation of tracer into complex lipid when β -oxidation is compromised.

Acetate

Acetate is readily metabolized by the heart and will displace other

energy-providing substrates if present at high concentrations (Taegtmeier et al. 1980). Basic studies performed by several groups (Brown et al. 1987; Buxton et al. 1989; Henes et al. 1989) support the suggestion that acetate is rapidly complexed to acetyl CoA, which enters the TCA cycle. The myocardial kinetics of the radioactive label during the first few tens of minutes following bolus administration of $[^{14}\text{C}]$ acetate thus are presumed to reflect the turnover of the TCA intermediates and possibly the side pools of compounds in equilibrium with these intermediates. Because characteristic clearance times are more than 10 minutes, it is likely that the label has access at least to the glutamate and aspartate pools that are equilibrated with the pools of the TCA intermediates α -ketoglutarate and oxaloacetate, respectively. The interpretation of this measured turnover rate constant in terms of an actual cycle flux would require knowledge of the pool sizes being turned over; these, unfortunately, may be quite variable, and even dynamic, quantities.

The experimental inotropic excitation of the heart with dobutamine caused the expected increase in the measured turnover rate constant, but also exposed significant incorporation of label into a very slowly clearing kinetic component (Henes et al. 1989), which may correspond to the fixing of the label in proteins. Interestingly, the incorporation of the $[^{14}\text{C}]$ label into triglyceride following administration of $[^{14}\text{C}]$ acetate in alcohol-treated hearts has been observed (Kondrup et al. 1989). This

FIGURE 2

Total radioactive content of isolated working rat heart following bolus administration, with no recirculation, of an ^{125}I -labeled analogue of pentadecanoic acid. Each curve corresponds to data from a single heart. Under control conditions, a kinetic component corresponding to efflux of the catabolic products of β -oxidation is clearly visible. The component disappears in hearts from animals pretreated with an inhibitor of β -oxidation. In both cases, a very slow-clearing component of the tissue radioactivity residue is visible, corresponding to incorporation of the fatty acid tracer into complex lipids; this component is significantly enhanced following inhibition of β -oxidation.

process does not involve the TCA cycle, but rather probably reflects the carboxylation of acetyl CoA to malonyl CoA. The presence of an anomalous slowly clearing kinetic component following administration of labeled acetate could reflect a metabolic disruption similar to that reflected in the abnormal incorporation of LCFA into complex lipid. Regardless of the partial

ambiguity of the quantitative interpretation of the early turnover, acetate clearly has potential as a powerful tool for the assessment of both the acute and chronic response to alcohol.

Tissue Innervation

It had long been recognized that the neurotransmitter acetylcholine

existed in tissue in both free and bound forms when DeRobertis and Bennett (1955) first definitively demonstrated the existence of granular storage vesicles in the presynaptic terminals of cholinergic nerves. Since then, the importance of similar nerve terminal storage mechanisms has also been established for catecholamine neurotransmitters. The vesicles in the noradrenergic terminals and varicosities of the sympathetic innervation of the heart represent an example of this storage function.

A particular class of sympathomimetic drugs have actions based on the elevation of extracellular norepinephrine by displacement of the natural transmitter from its storage vesicles (Weiner 1985). Chronic displacement would ultimately result in a depletion of neurotransmitter from the treated tissue. The pioneering work of Wieland and his coworkers (1989) has led the way in the labeling of such catecholamine analogues for the noninvasive evaluation of regional sympathetic nerve integrity in heart.

Some analogues have binding affinities for the storage vesicles that are higher than that of norepinephrine itself. The uptake of label may thus enhance identification of the number of such storage sites per unit mass of tissue, rather than reflect turnover of natural ligand. Those densities may in turn reflect the number of noradrenergic terminals. Schwaiger et al. (1990) have validated this concept by demonstrating the greatly dimin-

ished equilibrium distribution space of [^{11}C]hydroxyephedrine in recently transplanted heart, which is devoid of sympathetic innervation. Preliminary studies have demonstrated loss of distribution space in patients with cardiomyopathy (personal communication, M. Schwaiger, March 1991).

If, on the other hand, the stored compound is more nearly similar to norepinephrine itself, its kinetics may provide information about neurotransmitter turnover. Dopamine labeled with ^{18}F has been shown to be readily taken up by heart, and studies performed in dogs in conjunction with desipramine, ganglionic blockade, and the infusion of tyramine all support the model assumption that the labeled tracer is hydroxylated to the corresponding norepinephrine analogue, stored, and released at rates that characterize turnover of the natural neurotransmitter (Goldstein et al. 1990).

While sympathetic innervation and norepinephrine turnover are believed to be involved in the progress of alcohol-induced injury, no clear picture has yet emerged (Hoffman et al. 1987; Klatsky et al. 1987; Kupari and Suokas 1989). Noninvasive assays of sympathetic innervation and norepinephrine turnover rates represent major advances for the study of alcoholic injury. Whereas alcoholic cardiomyopathy is in some cases reversible (Klatsky 1987), longitudinal studies performed during the resolution of symptoms following total abstinence would be a powerful source of

information about the proper interpretation of these tracers.

Mechanisms of Detoxification

Glutathione is a tripeptide present in high concentrations in most tissues of the body; the thiol moiety of the cysteinyl residue allows it to function both as an electron donor and as a nucleophilic compound. Glutathione thus can serve in the enzyme-catalyzed reduction of toxic peroxides and superoxides and in the enzyme-catalyzed conjugation of electrophilic toxins. The depression of liver glutathione levels to as low as 50 percent of normal in chronic alcoholism has been reported (Speisky et al. 1989). Whether other tissues suffer a comparable depression has not been established.

We have investigated the use of labeled substrates for glutathione detoxification as a means of tracing tissue detoxification activity (Kornguth et al. 1989). [¹⁸F]I-fluoro-2,4-dinitrobenzene (FDNB) is a known substrate of glutathione-S-transferase, the enzyme that catalyzes the conjugation of glutathione to toxic electrophiles. The conjugation process releases the fluorine as free fluoride ion, and the dinitrobenzene-glutathione complex is cleared from the cell. As in the case of fatty acid, the distinct kinetics of intact FDNB and fluoride facilitate estimation of the rate of the defluorination process. Figure 3 shows the total heart radioactivity, together with its model decomposition, following bolus administration of labeled FDNB with-

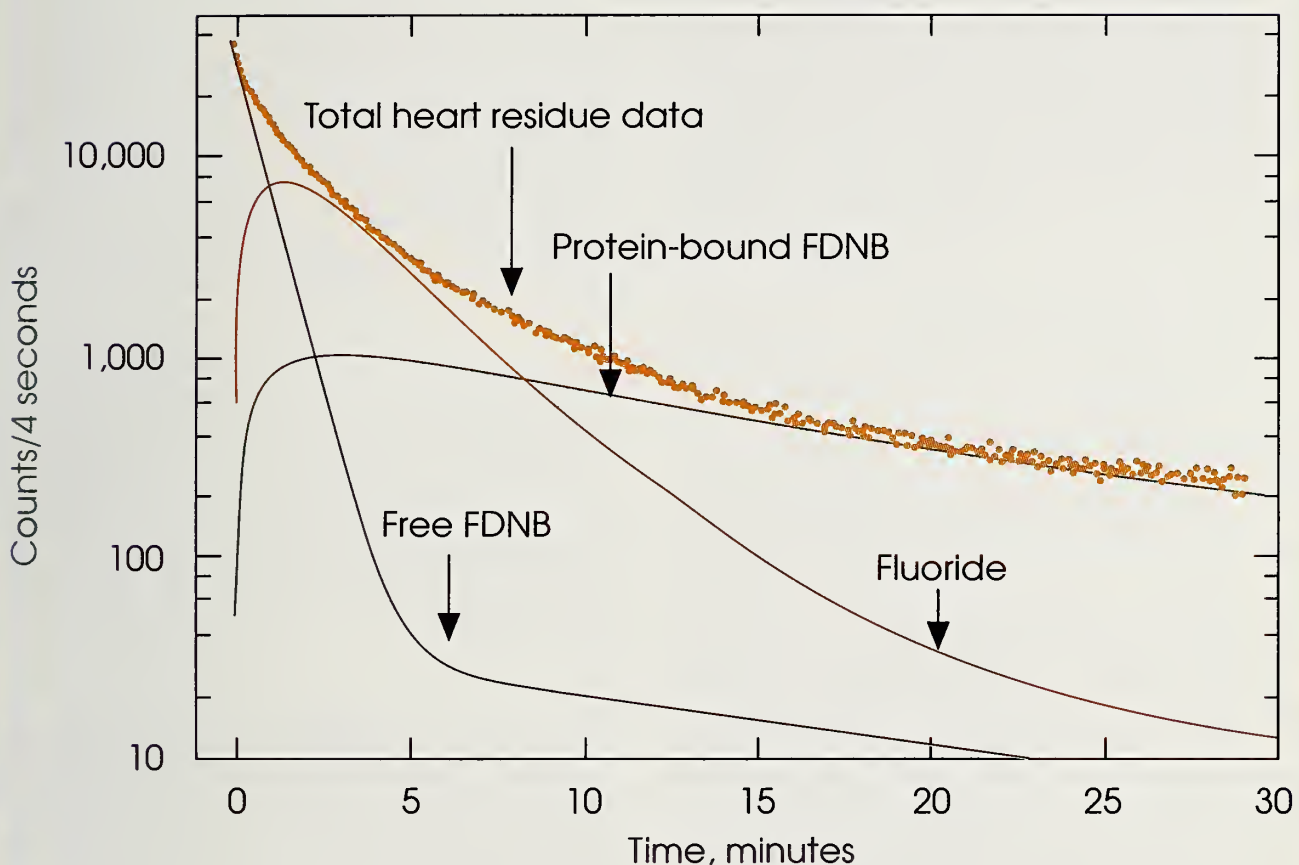
out recirculation into isolated working rat heart. In this case, whole-heart radioactivity was measured by coincidence detection mimicking PET imaging. The presence of nonspecific protein binding was validated by assays of extracted tissue and of venous effluent.

The characteristic clearance of fluoride that reflects the detoxification process is seen to be less rapid than the component reflecting efflux of unchanged FDNB, yet is distinguishable from the slow kinetics associated with the protein-bound components. This concept was confirmed in separate experiments in which the tissue glutathione stores were depleted by infusion of the toxin t-butyl-hydroperoxide. Time course data showed that the intermediate kinetic component between the most rapidly and the most slowly clearing components was clearly diminished.

Unfortunately, trials of FDNB in intact rats quickly uncovered an important problem: Administered as a venous bolus, the compound cannot reach the organ of interest due to rapid defluorination during the first passage through lung, presumably by the high activities of pulmonary glutathione. However, the data from isolated heart demonstrate the assay of a detoxification system using the measured kinetics of tracer quantities of a known toxin. In specific cases, the ability to assay glutathione detoxification activity without biopsy may be sufficient justification for invasive arterial administration.

FIGURE 3

FDNB model compartmental time courses



Total heart radioactivity, together with its model decomposition, following bolus administration of labeled FDNB without recirculation into isolated working rat heart. The presence of nonspecific protein binding was validated by assays of extracted tissue and of venous effluent. The characteristic clearance of fluoride (clearance rate 0.3/min) reflects the detoxification process.

CONCLUSIONS

PET allows physiological, metabolic, and neurochemical investigations based on tracer methodology to be extended to nondestructive studies in intact subjects. Process rates and the tissue distribution spaces of chemical species can be noninvasively estimated on an anatomically specific basis. In this chapter, three particular categories of PET studies of the myocardium were described. These were chosen on the basis of

both their current states of development and their potential for contributing to the future study of alcoholic injury.

Because PET is an extension of conventional tracer methods, the development and validation steps required for the design of an imaging protocol may begin with *in vitro* enzymology and membrane transport studies in cell culture, then progress to tracer kinetics in isolated organs or small animals, using external radiation detection, and

finally result in actual time course measurements via PET imaging. This chapter described several examples of the use of preliminary tracer studies in the isolated rat heart. Measurements performed in conjunction with specifically controlled interventions can be used to develop models that allow physiological, biochemical, or neurochemical conclusions to be drawn from the PET image sequence.

Although alcohol-induced injury can progress to actual cardiomyopathy, this condition is rare even in the most chronic conditions. The true burden of morbidity imposed by alcohol appears in the form of preclinical derangements of energy metabolism, biosynthesis, neurotransmitter kinetics, and receptor properties. These biochemical and neurochemical changes in turn induce structural and electrophysiological changes that reduce cardiac performance and reserve. PET offers the opportunity to study these changes systematically in both acute and chronic models. Ultimately, measurements in patients can be applied to the early detection of alcoholic changes, to the development of models of pathogenesis, and to management of the withdrawal process.

REFERENCES

Bergmann, S.R.; Nomura, H.; Rand, A.L.; Sobel, B.E.; and Lange, L.G. Externally detectable changes in fatty acid utilization by perfused hearts from rabbits exposed to alcohol. *Circulation* 66(II):II-109, 1982.

Brown, M.; Marshall, D.R.; Sobel, B.E.; and Bergmann, S.R. Delineation of myocardial oxygen utilization with carbon-11 labeled acetate. *Circulation* 76:687-696, 1987.

Buxton, D.B.; Nienaber, C.A.; Luxen, A.; Ratib, O.; Hansen, H.; Phelps, M.E.; and Schelbert, H.R. Noninvasive quantitation of regional myocardial oxygen consumption in vivo with [^{11}C]acetate and dynamic positron emission tomography. *Circulation* 79:134-142, 1989.

DeGrado, T.R.; Holden, J.E.; Ng, C.K.; Raffel, D.M.; and Gatley, S.J. Comparison of 16-iodohexadecanoic acid (IHDA) and 15-p-iodophenyl-pentadecanoic acid (IPPA) metabolism and kinetics in the isolated rat heart. *Eur J Nucl Med* 14:600-606, 1988.

DeGrado, T.R.; Holden, J.E.; Ng, C.K.; Raffel, D.M.; and Gatley, S.J. Quantitative analysis of myocardial kinetics of 15-p-[iodine-125] iodophenylpentadecanoic acid. *J Nucl Med* 30:1211-1218, 1989.

DeRobertis, E., and Bennett, H.S. Some features of the submicroscopic morphology of synapses in frog and earthworm. *J Biophys Biochem Cytol* 1:47-58, 1955.

Geltman, E.M.; Smith, J.L.; Beecher, D.; Ludbrook, P.A.; Ter-Pogossian, M.M.; and Sobel, B.E. Altered regional myocardial metabolism in congestive cardiomyopathy detected by positron tomography. *Am J Med* 74:773-785, 1983.

Goldstein, D.S.; Chang, P.C.; Eisenhofer, G.; Miletich, R.; Finn, R.; Bacher, J.; Kirk, K.L.; Bacharach, S.; and Kopin, I.J. Positron emission tomographic imaging of cardiac sympathetic innervation and function. *Circulation* 82:359-368, 1990.

- Henes, C.G.; Bergmann, S.R.; Walsh, M.N.; Sobel, B.E.; and Geltman, E.M. Assessment of myocardial oxidative metabolic reserve with positron emission tomography and carbon-11 acetate. *J Nucl Med* 30:1489–1499, 1989.
- Hoffman, P.L.; Valverius, P.; Kwast, M.; and Tabakoff, B. Comparison of the effects of ethanol on beta-adrenergic receptors in heart and brain. *Alcohol Alcohol suppl 1*:749–754, 1987.
- Holden, J.E.; Mori, K.; Dienel, G.; Cruz, N.F.; Nelson, T.; and Sokoloff, L. Modeling the dependence of hexose distribution volumes in brain on plasma glucose concentration: Implications for estimation of the local 2-deoxyglucose lumped constant. *J Cereb Blood Flow Metab* 11:171–182, 1991.
- Holden, J.E.; Ng, C.K.; Endres, C.J.; Perlman, S.B.; Stone, C.K.; Raffel, D.M.; and Bianco J. Approach to the fluorodeoxyglucose method in heart with programmed infusion (Abstract). *J Nucl Med* 31:778, 1990..
- Klatsky, A.L. The cardiovascular effects of alcohol. *Alcohol Alcohol suppl 1*:117–124, 1987.
- Kondrup, J.; Grunnet, N.; and Dich, J. Interactions of ethanol and lipid metabolism. In: Crow, K.E., and Batt, R.D., eds. *Human Metabolism of Alcohol*. Vol. III. Boca Raton, FL: CRC Press, 1989. pp. 97–113.
- Kornguth, M.L.; Holden, J.E.; DeGrado, T.R.; Ng, C.K.; Raffel, D.M.; and Gatley, S.J. Kinetics of [¹⁸F] 1-fluoro-2,4-dinitrobenzene, a potential probe for the glutathione detoxification system, in perfused working rat heart. *Nucl Med Biol* 16(5):519–524, 1989.
- Kupari, M., and Suokas, A. Effects of ethanol and its metabolites on the heart. In: Crow, K.E., and Batt, R.D., eds. *Human Metabolism of Alcohol*. Vol. III. Boca Raton, FL: CRC Press, 1989. pp. 50–98.
- Ng, C.K.; Holden, J.E.; DeGrado, T.R.; Raffel, D.M.; Kornguth, M.L.; and Gatley, S.J. Sensitivity of myocardial fluorodeoxyglucose lumped constant to glucose and insulin. *Am J Physiol* 260:H593–H603, 1991.
- Regan, T.J. Animal models and varied clinical presentations of alcoholic cardiomyopathy. In: Jennings, R.B., and Morgan, H.E., eds. *Workshop on Cardiomyopathies*. NIH Pub. No. 79–1608. Bethesda, MD: National Institutes of Health, 1979. pp. 5–6.
- Schelbert, H.R.; Henze, E.; Sochor, H.; Grossman, R.; Huang, S.C.; Barrio, J.R.; Schwaiger, M.; and Phelps, M.E. Effects of substrate availability on myocardial C-11 palmitate kinetics by positron emission tomography in normal subjects and patients with ventricular dysfunction. *Am Heart J* 111(6):1055–1064, 1986.
- Schelbert, H.R., and Schwaiger, M. PET studies of the heart. In: Phelps, M.E.; Mazziotta, J.C.; and Schelbert, H.R., eds. *Positron Emission Tomography and Autoradiography: Principles and Applications for the Brain and Heart*. New York: Raven Press, 1986. pp. 581–563.
- Schwaiger, M.; Kalff, V.; Rosenspire, K.; Haka, M.S.; Molina, E.; Hutchins, G.D.; Deeb, M.; Wolfe Jr., E.; and Wieland, D.M. Noninvasive evaluation of sympathetic nervous system in human heart by positron emission tomography. *Circulation* 82(2):457–464, 1990.
- Sokoloff, L.; Reivich, M.; Kennedy, C.; DesRosiers, M.H.; Patlak, C.S.; Pettigrew, K.; Sakurada, O.; and Shinohara, M. The

$[^{14}\text{C}]$ deoxyglucose method: Theory, procedure, and normal values in the conscious and anesthetized albino rat. *J Neurochem* 28:897–916, 1977.

Speisky, H.; Orrego, H.; and Israel, Y. Hepatic glutathione metabolism: Alterations induced by alcohol consumption. In: Crow, K.E., and Batt, R.D., eds. *Human Metabolism of Alcohol*. Vol. III. Boca Raton, FL: CRC Press, 1989. pp. 125–139.

Taegtmeyer, H.; Hems, R.; and Krebs, H.A. Utilization of energy-providing substrates in the isolated working rat heart. *Biochem J* 186:701–711, 1980.

Taegtmeyer, H. Six blind men explore an elephant: Aspects of fuel

metabolism and the control of tricarboxylic acid cycle activity in heart muscle. *Basic Res Cardiol* 79:322–336, 1984.

Weiner, N. Norepinephrine, epinephrine, and the sympathomimetic amines. In: Gilman, A.G.; Goodman, L.S.; Rall, T.W.; and Murad, F., eds. *The Pharmacological Basis of Therapeutics*. 7th ed. New York: MacMillan Publishing Co., 1985. pp. 169–171.

Wieland, D.M.; Rosenspire, K.C.; Hutchins, G.D.; Vandort, M.; Rothley, J.M.; Mislankar, S.G.; Lee, H.T.; Massin, C.C.; Gildersleeve, D.L.; Sherman, P.S.; and Schwaiger, M. Neuronal mapping of the heart with $6-[^{18}\text{F}]$ fluorometaraminol. *J Med Chem* 33:956–964, 1990.

THE APPLICATION OF METABOLIC MAPPING METHODS TO THE IDENTIFICATION OF THE NEURAL SUBSTRATES OF THE EFFECTS OF ALCOHOL

Linda J. Porrino, Ph.D.¹

Ethanol is a substance that has complex physiological, behavioral, and biochemical actions. It has long been held that the effects of ethanol are due to its nonspecific actions on neuronal cell membranes (Meyer and Gottlieb 1926). Changes in the fluidity of membrane lipids have been shown to correlate well with ethanol's sedative and intoxicating effects (Chin and Goldstein 1977). However, recent evidence suggests that ethanol's actions may be far more specific than previously thought. Selective effects of ethanol on specific receptor types, including GABA-benzodiazepine (Allan and Harris 1986; Suzdak et al. 1986; Hoffman et al. 1987; Mehta and Ticku 1988) and NMDA receptors (Hoffman et al. 1989; Lovinger et al. 1989), have recently been demonstrated. Likewise, ethanol interac-

tions with receptor second messenger systems (Rabin and Molinoff 1981; Luthin and Tabakoff 1984) have been shown to be highly selective in that they depend on the neuroanatomical sites of the affected receptors. Other work has shown that ethanol can increase the release of neurotransmitters such as dopamine (Imperato and DiChiara 1986), but again these effects occur only at specific neuroanatomical sites.

The diversity of ethanol's neurochemical and behavioral effects complicates the identification of the substrates of its effects in the central nervous system (CNS). It is

ACRONYMS

CNS	central nervous system
2DG	[2^{-14}C]deoxyglucose

¹Department of Physiology and Pharmacology, Bowman Gray School of Medicine, Winston Salem, NC 27157

unlikely that physiological or behavioral responses to ethanol result from single actions at single loci. Therefore, to determine the neuroanatomical substrates of the effects of a drug like ethanol, it is necessary to measure neural events in circuits and pathways throughout the brain. The [$2-^{14}\text{C}$]deoxyglucose (2DG) method developed by Louis Sokoloff and his colleagues (1977) is one means of simultaneously investigating changes in functional activity that are related to physiological, pharmacological, and behavioral states throughout the brain. Extensively used in neuropharmacology to identify the neural circuits that mediate the effects of a wide variety of pharmacological agents (for reviews, see McCulloch 1982, Porrino and Pontieri 1991), the 2DG method is particularly applicable to the study of the effects of ethanol.

The 2DG method measures rates of local cerebral glucose utilization, demonstrating biochemically the rates at which energy is consumed in neuroanatomically defined regions throughout the CNS of conscious animals. In the brain, as in other tissues that do physicochemical work, the amount of energy used is correlated with the amount of work done in that tissue. Because glucose is virtually the exclusive substrate for energy metabolism, glucose utilization in the brain is a measure of energy use under normal physiological conditions. The rationale for using the 2DG method is that functional activity in any given brain region is directly related to energy metabolism in that

region, thus changes in glucose utilization rates can identify brain regions in which functional activity is altered during various experimental manipulations.

A number of energy-requiring processes in the brain contribute to basal rates of glucose utilization--transmitter synthesis, release and reuptake, and protein synthesis. However, most CNS energy is used to maintain and restore ionic gradients; an estimated 80 percent of the energy generated in the brain is used for this purpose (Kurumaji et al. 1991). Changes in glucose utilization rates evoked by experimental manipulation are thought to result mainly from increases or decreases in CNS electrical activity or synaptic activity. These electrical activity changes produce corresponding increases or decreases in the activity of Na^+ , K^+ -ATPase, the energy-consuming enzyme involved in the restoration of neuronal ionic gradients to their resting state. Experiments with deoxyglucose have shown that the coupling of glucose utilization to functional activity is dependent on Na^+ , K^+ -ATPase activity. An ATPase inhibitor, ouabain, can block the increases in glucose utilization that accompany electrical stimulation (Mata et al. 1980).

The basic principles for measurement of the rate of any reaction using a radioactive tracer (figure 1) apply to the measurement of glucose utilization rates. The amount of product formed over an interval of time is determined, related to the integrated specific activity (i.e.,

FIGURE 1**Functional Anatomy of the Operational Equation of the (¹⁴C) Deoxyglucose Method****General Equation for Measurement of Reaction Rates with Tracers:**

$$\text{Rate of Reaction} = \frac{\text{Labeled Product Formed in Interval of Time, 0 to } T}{\left[\begin{array}{l} \text{Isotope Effect} \\ \text{Correction Factor} \end{array} \right] \left[\begin{array}{l} \text{Integrated Specific Activity} \\ \text{of Precursor} \end{array} \right]}$$

Operational Equation of (¹⁴C) Deoxyglucose Method:

$$R_i = \frac{\text{Labeled Product Formed in Interval of Time, 0 to } T}{\left[\begin{array}{c} \text{Total } ^{14}\text{C in Tissue} \\ \text{at Time, } T \end{array} \right] - \left[\begin{array}{c} ^{14}\text{C in Precursor Remaining in} \\ \text{Tissue at Time, } T \end{array} \right]} = \frac{C_i^*(T) - k_1^* e^{-(k_2^* + k_3^*)T} \int_0^T C_p^* e^{(k_2^* + k_3^*)t} dt}{\left[\begin{array}{c} \frac{\lambda \cdot V_m^* \cdot K_m}{\Phi \cdot V_m^* \cdot K_m} \\ \text{Isotope Effect} \end{array} \right] \left[\begin{array}{c} \int_0^T \left(\frac{C_p^*}{C_p} \right) dt \\ \text{Integrated Plasma} \\ \text{Specific Activity} \end{array} \right] - e^{-(k_2^* + k_3^*)T} \left[\begin{array}{c} \int_0^T \left(\frac{C_p^*}{C_p} \right) e^{(k_2^* + k_3^*)t} dt \\ \text{Correction for Lag in Tissue} \\ \text{Equilibration with Plasma} \end{array} \right]} = \frac{C_i^*(T) - k_1^* e^{-(k_2^* + k_3^*)T} \int_0^T C_p^* e^{(k_2^* + k_3^*)t} dt}{\text{Integrated Precursor Specific Activity in Tissue}}$$

Operational equation of the radioactive deoxyglucose method and its functional anatomy. T represents the time at the termination of the experimental period; C_i^* represents the total ¹⁴C concentration in brain tissue; C_p^* and C_p represent the concentrations of (¹⁴C)deoxyglucose and glucose in the arterial plasma, respectively. The constants k_1^* , k_2^* , and k_3^* represent the rate constants for carrier-mediated transport of (¹⁴C)deoxyglucose from plasma to tissue, for carrier-mediated transport back from tissue to plasma, and for phosphorylation by hexokinase, respectively; λ equals the ratio of the distribution space of deoxyglucose in the tissue to that of glucose; 0 is the fraction of glucose which, once phosphorylated, continues down the glycolytic path. K_m^* and V_m^* and K_m and V_m represent the Michaelis-Menten kinetic constants of hexokinase for deoxyglucose and glucose, respectively (from Sokoloff 1982).

the ratio of labeled precursor to total precursor pooled over the time of measurement), and corrected for kinetic differences between labeled and unlabeled compounds. Local cerebral glucose utilization rates are measured with a radioactively labeled analogue of glucose, [$2-^{14}\text{C}$]deoxyglucose, which is transported into cerebral tissue by the same carrier as glucose and phosphorylated by hexokinase. Unlike glucose, 2DG is not metabolized further and is, therefore, trapped within cells. This sequestration within cells enables the use of quantitative autoradiography to measure actual rates of glucose utilization in specific brain regions. In contrast, glucose is eventually metabolized via the glycolytic and tricarboxylic acid pathways or the pentose phosphate pathway to CO_2 , which is cleared rapidly from cerebral tissue. The use of [1^4C]glucose as a tracer for the measurement of cerebral glucose utilization can be inaccurate because it is difficult to estimate correctly the amount of labeled CO_2 lost from tissue during measurement. Because of CO_2 loss, the amount of label in tissue measured autoradiographically with [1^4C]glucose does not necessarily reflect the amount of glucose used in that tissue. In fact, direct comparison of 2DG and [1^4C]glucose showed underestimation of glucose utilization rates in visually stimulated animals when [1^4C]glucose was used as the tracer (Collins et al. 1987).

Calculation of glucose utilization rates by the 2DG method (figure 1) involves two kinds of measure-

ments: First, the concentration of radioactivity in the tissue is measured autoradiographically. The radioactivity in the tissue comprises both the product formed ($[2-^{14}\text{C}]$ deoxyglucose-6-phosphate) and unmetabolized precursor (2DG); the two cannot be distinguished autoradiographically. The percentage of unmetabolized precursor, estimated from the amount of 2DG remaining in the blood at the end of the experimental period, must be subtracted from the total radioactivity to obtain an accurate reaction rate. Second, the levels of glucose and 2DG in plasma are measured during the experimental period. These levels are required to determine the integrated specific activity of the precursor in tissue. Because it is impossible to make direct tissue measurements, plasma glucose and 2DG levels are corrected for the lag in tissue equilibration with plasma. The rate of glucose utilization is described mathematically by the operational equation of the 2DG method (figure 1). The mathematical derivation of this method and extensive discussion of its theoretical basis are beyond the scope of this paper; for further discussion, see Sokoloff et al. (1977), Sokoloff (1982), and Sokoloff and Porrino (1986). The techniques used for application of the 2DG method have been described in detail elsewhere (Porrino and Crane 1990).

ADVANTAGES AND DISADVANTAGES

Like other neurobiological methods, the 2DG method offers specific advantages, as well as disadvantages,

for use in neuropharmacological investigations. The remainder of this paper will address these issues and discuss some of the factors that can influence interpretation of the results of 2DG experiments.

One of the primary advantages of the 2DG method is the capability of examining the entire CNS. Table 1 shows representative values for local glucose utilization in a variety of cerebral structures in normal conscious rats and primates. Autoradiography allows a broad survey of possible effects at all levels of the brain, rather than limiting investigations to loci in which effects are "expected." Examination

of the whole brain reveals effects of experimental manipulation that might otherwise go unnoticed. Eckardt and his coworkers (1988) mapped the effects of acute ethanol administration in 53 regions of the rat brain, identifying significant glucose utilization rate changes in structures at several brain levels and in a number of brain systems, including sensory, motor, and limbic. Such an approach enables the assessment of effects in a number of systems without using different sets of animals.

Another advantage of autoradiography is anatomical resolution that allows visualization not only of indi-

Table 1. Representative values for local cerebral glucose utilization in normal conscious rat and monkey ($\mu\text{mol}/100 \text{ g}/\text{minute}$)

Structure	Rat* (n=4)	Monkey† (n=4)
Prefrontal cortex	66 \pm 3	57 \pm 2
Motor cortex	94 \pm 1	47 \pm 2
Auditory cortex	154 \pm 3	73 \pm 2
Visual cortex	102 \pm 2	69 \pm 1
Caudate	107 \pm 2	64 \pm 4
Nucleus accumbens	87 \pm 2	37 \pm 2
Globus pallidus	55 \pm 1	25 \pm 1
Lateral hypothalamus	55 \pm 1	28 \pm 1
Ventral thalamus	95 \pm 1	43 \pm 2
Medial geniculate	113 \pm 4	61 \pm 2
Lateral geniculate	92 \pm 2	39 \pm 2
Substantia nigra compacta	72 \pm 2	46 \pm 1
Inferior colliculus	167 \pm 2	133 \pm 6
Superior colliculus	91 \pm 1	52 \pm 1
Locus coeruleus	71 \pm 1	36 \pm 3
Cerebellum	58 \pm 1	37 \pm 2

* Values from Porrino et al. (1988).

† Values from Porrino et al. (1987).

vidual structures within the brain, but also of small subnuclei and anatomical subdivisions within a given structure. The limiting factors are the diffusion and migration of the labeled compound in the tissue during freezing and cutting of the brain. Resolution of the 2DG method is approximately 100 μm ; cellular resolution is not possible at this time. Yet autoradiography provides a considerable degree of anatomical resolution, which is apparent from now-classic 2DG studies of the primate visual system: Following the occlusion of one eye, a pattern of light and dark striations in the visual cortex is visible as columns that correspond to ocular dominance columns identified electrophysiologically and anatomically (Kennedy et al. 1978).

With many other neurochemical methods such as *in vivo* microdialysis or neurotransmitter turnover determinations, it is not possible to ascribe effects to particular divisions or subdivisions of brain regions because the areas sampled are by necessity rather large. In 2DG studies, the use of quantitative autoradiography makes it possible to evaluate changes in functional activity within circumscribed brain regions. For example, studies in this laboratory have shown that the acute administration of low doses of ethanol selectively increases rates of glucose utilization in the most anterior portions of the olfactory tubercle (figure 2; Lewis et al. 1990). These effects might have been obscured if the ventral striatum had been examined as a whole.

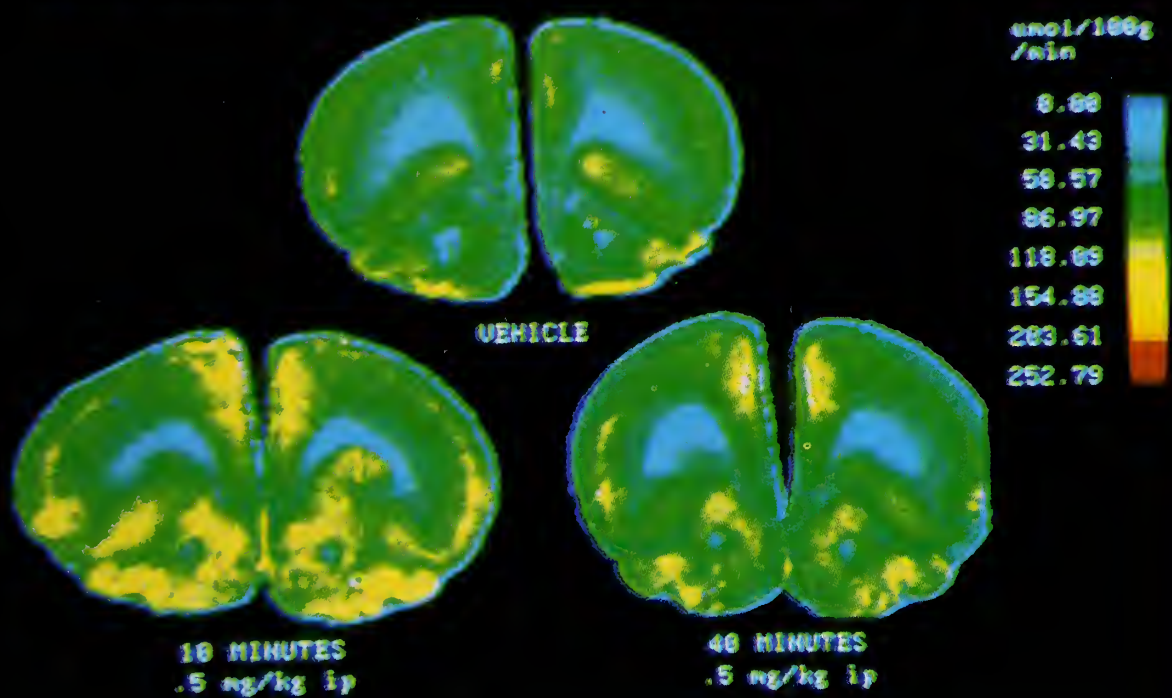
Another example is a study of the effects of withdrawal from alcohol in rats, in which Campbell and colleagues (1982) observed a distinct columnar pattern in the distribution of rates of glucose uptake in frontal cortex. Alternating regions of high and low uptake demonstrate the level of anatomical analysis possible with the 2DG method.

Although experiments with the 2DG method were originally conducted in restrained or partially restrained animals, recently developed techniques permit the use of the 2DG method in freely moving conscious animals (Crane and Porrino 1989). This approach allows the application of the method to the study of behavior. Animals lever-pressing for electrical brain stimulation have been studied (Porrino et al. 1984, 1990), as have the effects of psychostimulants on locomotor activity (Porrino et al. 1988; Pontieri et al. 1990). With these modifications, it should be possible to study the effects of ethanol in specific behavioral paradigms such as oral ethanol self-administration. Such studies will facilitate a more direct analysis of the substrates of the reinforcing properties of ethanol.

The 2DG method has a number of limitations that should be considered, particularly with regard to the interpretation of experimental results. First is the inability to differentiate between direct and indirect effects of a given stimulus. An entire pathway or circuit may be metabolically activated even though the direct action of the

FIGURE 2

EFFECTS OF ETHANOL ON METABOLIC ACTIVITY IN THE VENTRAL STRIATUM



Effects of acute intraperitoneal administration of ethanol (0.5 g/kg) on local cerebral glucose utilization in rats measured 10 and 40 minutes after ethanol administration. Shown are color-coded transformations of autoradiograms of coronal sections of rat brain at the level of the anterior ventral striatum in which each color represents a range of rates of local cerebral glucose utilization in micromoles per 100 grams per minute, according to the calibration scale to the right of the autoradiograms. Note: The highest levels of metabolism are present 10 minutes after ethanol administration, while lower rates, particularly in the olfactory tubercle, are seen at 40 minutes.

stimulus may occur only at the origin of or at some point along the pathway. The 2DG method does not identify the sites at which a drug binds or the sites at which a drug initiates its actions. For example, apomorphine, a dopaminergic receptor agonist, has widespread effects on rates of cerebral glucose

utilization (figure 3). The areas in which glucose utilization is altered include some brain regions that are devoid of dopaminergic receptors. Furthermore, rates of metabolism are unchanged in regions in which high concentrations of dopaminergic receptors are found, e.g., the nucleus accumbens (McCulloch et al.

FIGURE 3

Schematic representations of three coronal sections of rat brain at the levels of the nucleus accumbens (top), caudate-putamen (middle), and substantia nigra (bottom). Areas rich in dopamine receptors are shown on the left of each section; regions in which alterations in cerebral metabolism were observed following apomorphine administration are shown on the right of each section (data from McCulloch et al. 1982).

1982). Although this lack of specificity may be a limitation in some instances, as in the case of determining the primary site of action of a drug, it is an advantage when the goal is to identify the neural circuits or pathways that mediate the effects of a drug like ethanol, which has a broad range of nonspecific actions on the CNS.

Another limitation is the inability to distinguish between inhibitory and excitatory processes on the basis of increases or decreases in 2DG uptake. Excitation and inhibition at the neuronal level involve similar metabolic processes: Maintenance and restoration of ionic gradients have similar energy requirements, regardless of whether excitatory or inhibitory neurotransmitters are secreted at synaptic terminals. In an elegant study, Ackermann and his colleagues (1984) demonstrated that when either the fimbria-fornix or perforant paths were stimulated electrically, the resulting increases in 2DG uptake within the hippocampus were a consequence of the long-lasting recurrent inhibitory processes rather than the brief excitatory potentials that also accompanied the stimulation. The increased 2DG uptake in that study resulted from the increased activity of afferents to the hippocampus. Neither excitation nor inhibition was the critical determinant of the direction of changes in glucose utilization rates. Since ethanol enhances GABAergic neurotransmission, which is mainly inhibitory, some increases in rates of glucose utilization associated with

ethanol administration may, in fact, reflect increased inhibitory processing rather than excitation.

Because constant or steady-state conditions are considered necessary for measurement of glucose utilization rates (Sokoloff et al. 1977), the long experimental time required by the 2DG method can significantly limit its use in drug studies. Physiological and behavioral responses to drug administration can vary significantly during the 45-minute 2DG procedure; however, the uptake and phosphorylation of 2DG in brain reflect predominantly its metabolism in the first 5–10 minutes after injection, when tissue concentrations of free 2DG available for metabolism are highest (Sokoloff et al. 1977).

If drug administration is timed so that the maximum drug response coincides with the time of maximum incorporation of 2DG, the method can be very sensitive to changes in the effects of drugs across time. This sensitivity is illustrated by a study in which rates of glucose utilization were measured 10 and 40 minutes after the administration of a low dose of ethanol (Lewis et al. 1990). The time points were chosen so that metabolic activity was measured while levels of blood alcohol were rising (10 minutes) and while they were declining (40 minutes). At both time points, glucose utilization was increased above vehicle control levels in a number of regions, including the nucleus accumbens, medial prefrontal cortex, substantia nigra reticulata, globus pallidus, and cau-

date nucleus. However, in one structure--the olfactory tubercle--increased metabolic rates were observed during the ascending portion of the blood alcohol curve, but rates of glucose utilization returned to control levels during the descending portion (figure 2). Because ethanol's reinforcing effects have been specifically associated with the ascending but not the descending portion of the blood alcohol curve, the selective effects of ethanol in the olfactory tubercle suggest a unique role for this region in the processing of ethanol's reinforcing effects.

FACTORS INFLUENCING INTERPRETATION

Application of the 2DG method to map the changes in functional activity associated with the administration of any drug, but particularly ethanol, can pose some unique problems. Significant changes in physiological variables such as body temperature or respiratory status, both of which frequently are affected by pharmacological agents, can confound the interpretation of the results of 2DG experiments. Problems arise because the uptake of 2DG is dependent upon the physiological status of the subject. Overall differences in uptake based on blood pressure or plasma glucose levels, for example, can sometimes obscure differences between groups that are actually the result of changes in functional activity. Small changes in these variables are generally taken into account in the

calculation of absolute rates of glucose utilization with the 2DG method except with nonquantitative or semiquantitative modifications of the method. Use of the fully quantitative 2DG method facilitates making valid comparisons between groups by allowing both identification of brain areas with altered functional activity and measurement of the magnitude of these changes.

On the other hand, if the changes in physiological status are large, the basic assumptions of the method may be violated, and significant errors in the calculation of glucose utilization rates may occur. For example, moderate to high doses of ethanol can produce increases in plasma glucose levels that may be great enough to require the use of a different set of rate constants and lumped constant (Orzi et al. 1988) for the calculation of glucose utilization rates. Furthermore, when plasma glucose concentrations change by more than 20 or 25 percent during the experimental period (a frequent occurrence with pharmacological manipulations), a modified operational equation is required to compensate for the lack of constant or steady-state glucose levels (Savaki et al. 1980). Ethanol administered in any dose range may cause such changes.

Another problem that can arise particularly with moderate to high ethanol doses is hypercapnia. Increased pCO_2 levels produce generalized depressions in metabolic rates throughout the whole brain. These nonspecific effects

may also mask alterations in glucose utilization due to actual changes in functional activity.

One of the most important considerations in the interpretation of alterations in glucose utilization rates is the choice of measure in and of itself. Because it is sometimes difficult to design experimental procedures for sampling the blood of freely moving, behaving animals, modifications of the 2DG method that eliminate the necessity for catheterization and blood collection have led to the use of alternatives to glucose utilization rates as measures of functional activity. A number of these modifications compromise the validity of the method and, in effect, result in errors, as discussed by Sokoloff et al. (1983). Some investigators (Collins 1978; Sharp et al. 1983) have used relative rates of glucose utilization or the ratio of optical densities or tracer concentrations of a given structure to that of white matter. The validity of gray-white matter ratios as a measure of glucose utilization depends on the assumption that optical densities or tracer content in white matter is constant across conditions. This assumption may be valid at times, but many pharmacological treatments can cause changes that invalidate it. The choice of the particular white matter measured may also be critical; for example, the fornix or the internal capsule, may be more sensitive to such drug-induced changes than is the corpus callosum or the optic tract. Moreover, the relationship of tracer concentration in tis-

sue to optical density is not a linear one, and this relationship varies with exposure time (Kelly and McCulloch 1983). The exposure times chosen must be on the linear portion of the curve for that particular film type.

CONCLUSIONS

Quantitative autoradiographic methods have made it possible to visualize structural and functional changes in the CNS, as well as to quantify these changes and to localize them to specific anatomical sites. The application of imaging methods to the study of ethanol's effects can provide important new information regarding the sites and mechanisms of ethanol's complex effects in the brain.

REFERENCES

- Ackermann, R.F.; Finch, D.M.; Babb, T.L.; and Engel, J. Increased glucose metabolism during long-duration recurrent inhibition of hippocampal pyramidal cells. *J Neurosci* 4:251–264, 1984.
- Allan, A.M., and Harris, R.A. Gamma-aminobutyric acid and alcohol actions: Neurochemical studies. *Life Sci* 39:2005–2015, 1986.
- Campbell, G.A.; Eckardt, M.J.; Majchrowicz, E.; Marietta, C.A.; and Weight, F.F. Ethanol-withdrawal syndrome associated with both general and localized increases in glucose uptake in rat brain. *Brain Res* 237:517–522, 1982.
- Chin, J.H., and Goldstein, D.B. Drug tolerance in biomembranes: A spin

- label study of the effects of ethanol. *Science* 196:684–685, 1977.
- Collins, R.C. Kindling of neuroanatomic pathways during recurrent focal penicillin seizures. *Brain Res* 150:503–517, 1978.
- Collins, R.C.; McCandless, D.W.; and Wagman, I.L. Cerebral glucose utilization: Comparison of [^{14}C]deoxyglucose and [$6\text{-}^{14}\text{C}$]glucose quantitative autoradiography. *J Neurochem* 49:1564–1570, 1987.
- Crane, A.M., and Porrino, L.J. Adaptation of the quantitative 2-[^{14}C]deoxyglucose method for use in freely moving rats. *Brain Res* 499:87–92, 1989.
- Eckardt, M.J.; Campbell, G.A.; Marietta, C.A.; Majchrowicz, E.; and Weight, F.F. Acute ethanol administration selectively alters localized cerebral glucose metabolism. *Brain Res* 444:53–58, 1988.
- Hoffman, P.L.; Rabe, C.S.; Moses, F.; and Tabakoff, B. N-Methyl-D-aspartate receptors and ethanol: Inhibition of calcium flux and cyclic GMP production. *J Neurochem* 52:1937–1940, 1989.
- Hoffman, P.L.; Tabakoff, B.; Szabo, G.; Suzdak, P.D.; and Paul, S.M. Effect of an imidazobenzodiazepine, RO 15-4513, on the incoordination and hypothermia produced by ethanol and pentobarbital. *Life Sci* 41:611–619, 1987.
- Imperato, A., and DiChiara, G. Preferential stimulation of dopamine release in the nucleus accumbens of freely moving rats by ethanol. *J Pharmacol Exp Ther* 239:219–228, 1986.
- Kelly, P.A.T., and McCulloch J. A critical appraisal of semi-quantitative analysis of 2-deoxyglucose autoradiograms. *Brain Res* 269:165–167, 1983.
- Kennedy, C.; DesRosiers, M.H.; Sakurada, O.; Shinohara, M.; Reivich, M.; Jehle, J.W.; and Sokoloff, L. Metabolic mapping of the primary visual system of the monkey by means of the autoradiographic [^{14}C]deoxyglucose technique. *Proc Natl Acad Sci USA* 73:4230–4234, 1978.
- Kurumaji, A.; Dewar, D.; and McCulloch, J. Metabolic mapping with deoxyglucose autoradiography as an approach for assessing drug action in the central nervous system. In: London, E.D., ed. *Imaging of Functional Neuroanatomy of Drug Action*. Caldwell, NJ: Telford Press, 1991, in press.
- Lewis, M.J.; Perry, L.B.; June, H.L.; Garnett, M.L.; and Porrino, L.J. Regional changes in functional brain activity with ethanol stimulant and depressant effects. *Soc Neurosci Abstr* 16(1):459, 1990.
- Lovinger, D.M.; White, G.; and Weight, F.F. Ethanol inhibits NMDA-activated ion current in hippocampal neurons. *Science* 243:1721–1724, 1989.
- Luthin, G.R., and Tabakoff, B. Activation of adenylate cyclase by alcohol requires the nucleotide-binding protein. *J Pharmacol Exp Ther* 228:579–587, 1984.
- Mata, M.; Fink, D.J.; Gainer, H.; Smith, C.B.; Davidsen, L.; Savaki, H.E.; Schwartz, W.J.; and Sokoloff, L. Activity-dependent energy metabolism in rat posterior pituitary primarily reflects sodium pump activity. *J Neurochem* 34:213–215, 1980.
- McCulloch, J. Mapping functional alterations in the CNS with [^{14}C]deoxyglucose. In: Iverson, L.; Iverson, S.; and Snyder, S., eds. *Handbook of Psychopharmacology*. Vol. 15. New York: Plenum, 1982. pp. 321–410.

McCulloch, J.; Savaki, H.E.; McCulloch, M.C.; Jehle, J.; and Sokoloff, L. The distribution of alterations in energy metabolism in the rat brain produced by apomorphine. *Brain Res* 243:67-80, 1982.

Mehta, A.K., and Ticku, M.K. Ethanol potentiation of GABAergic transmission in cultured spinal cord neurons involves gamma-aminobutyric acid A-gated chloride channels. *J Pharmacol Exp Ther* 246:558-564, 1988.

Meyer, H.H., and Gottlieb, R. Theory of narcosis. Translated by V.E. Henderson. In: *Experimental Pharmacology as a Basis for Therapeutics*. 2nd ed. Philadelphia: Lippincott, 1926. pp. 116-129.

Orzi, F.; Lucignani, G.; Dow-Edwards, D.; Namba, H.; Nehlig, A.; Patlak, C.S.; Pettigrew, K.D.; Schuier, F.; and Sokoloff, L. Local cerebral glucose utilization in controlled graded levels of hyperglycemia in the conscious rat. *J Cerebr Blood Flow Metab* 8:346-356, 1988.

Pontieri, F.E.; Crane, A.M.; Seiden, L.S.; Kleven, M.S.; and Porrino, L.J. Metabolic mapping of the effects of intravenous methamphetamine administration in freely moving rats. *Psychopharmacology* 102:175-182, 1990.

Porrino, L.J.; Burns, R.S.; Crane, A.M.; Palombo, E.; Kopin, I.J.; and Sokoloff, L. Changes in local cerebral glucose utilization associated with Parkinson's syndrome induced by l-methyl-4-phenyl-1,2,3,6-tetrahydropyridine (MPTP) in the primate. *Life Sci* 40:1657-1664, 1987.

Porrino, L.J., and Crane, A.M. Metabolic mapping of the effects of drugs of abuse with the [2^{-14}C]deoxyglucose method. In: Adler, M.W., and Cowan, A., eds. *Modern Methods in Pharmacology*:

Testing and Evaluation of Drugs of Abuse. New York: Alan R. Liss, 1990. pp. 147-164.

Porrino, L.J.; Domer, F.R.; Crane, A.M.; and Sokoloff, L. Selective alterations in cerebral metabolism within the mesocorticolimbic dopaminergic system produced by acute cocaine administration in rats. *Neuropsychopharmacology* 1:109-118, 1988.

Porrino, L.J.; Esposito, R.U.; Seeger, T.F.; Crane, A.M.; Pert, A.; and Sokoloff, L. Metabolic mapping of the brain during rewarding self-stimulation. *Science* 224:306-309, 1984.

Porrino, L.J.; Huston-Lyons, D.; Bain, G.; Sokoloff, L.; and Kornetsky, C. The distribution of changes in local cerebral metabolism associated with brain stimulation reward to the medial forebrain bundle of the rat. *Brain Res* 511:1-6, 1990.

Porrino, L.J., and Pontieri, F.E. Metabolic mapping of the effects of psychomotor stimulants in rats. In: London, E.D., ed. *Imaging the Functional Neuroanatomy of Drug Action*. Caldwell, NJ: Telford Press, 1991, in press.

Rabin, R.A., and Molinoff, P.B. Activation of adenylate cyclase by ethanol in mouse striatal tissue. *J Pharmacol Exp Ther* 216:129-134, 1981.

Savaki, H.E.; Davidsen, L.; Smith, C.; and Sokoloff, L. Measurement of free glucose turnover in brain. *J Neurochem* 35:495-502, 1980.

Sharp, F.R.; Kilduff, T.S.; Bzorgchamp, S.; Heller, H.C.; and Ryan, A.F. The relationship of local cerebral glucose utilization to optical density ratios. *Brain Res* 263:97-103, 1983.

Sokoloff, L. The radioactive deoxyglucose method: Theory, procedure, and applications for the measurement of local glucose utilization in the central nervous system. In: Agranoff, B.W., and Aprison, M.H., eds. *Advances in Neurochemistry*. Vol. 4. New York: Plenum, 1982. pp. 7-36.

Sokoloff, L.; Kennedy, C.; and Smith, C.B. Metabolic mapping of functional activity in the central nervous system by measurement of local glucose utilization with radioactive deoxyglucose. In: Bjorklund, A., and Hokfelt, T., eds. *Methods in Chemical Neuroanatomy*. Vol. 1. Amsterdam: Elsevier Scientific, 1983. pp. 416-441.

Sokoloff, L., and Porrino, L.J. Some fundamental considerations in the

application of the deoxyglucose method to pharmacological studies. In: Kriegelstein, I., ed. *Pharmacology of Cerebral Ischemia*. Amsterdam: Elsevier, 1986. pp. 65-76.

Sokoloff, L.; Reivich, M.; Kennedy, C.; DesRosiers, M.H.; Patlak, C.S.; Pettigrew, K.D.; Sakurada, O.; and Shinohara, M. The [^{14}C]deoxyglucose method for the measurement of local cerebral glucose utilization: Theory, procedure and normal values in the conscious and anesthetized albino rat. *J Neurochem* 28:897-916, 1977.

Suzdak, P.; Glowa, J.R.; Crawley, J.N.; Schwartz, R.D.; Skolnick, P.; and Paul, S.M. A selective imidazodiazepine antagonist of ethanol in the rat. *Science* 234:1243-1247, 1986.

METHODOLOGICAL ISSUES IN THE USE OF PET TO STUDY DRUGS OF ABUSE

H. de Wit, Ph.D.,¹ J. Metz, Ph.D.,¹ K. Luh, Ph.D.,² and M. Cooper, M.D.²

Positron emission tomography (PET) holds great promise as a technique for studying the effects of drugs of abuse on brain function (Mathew and Wilson 1991). PET may be used to measure alterations in regional and global cerebral metabolic rate or cerebral blood flow after either chronic or acute administration of drugs. The technique may be used to detect long-term alterations in brain function resulting from chronic exposure to high doses of abused drugs (e.g., in chronic drug abusers), or it may be used to evaluate transient changes in brain activity after acute administration of psychoactive drugs. Using radiolabeled ligands that are chemically similar to abused drugs, PET may also identify the presumed sites of action of drugs of abuse. Our laboratory has used PET to study the acute effects of mood-altering drugs on metabolic activity in normal volunteers (de Wit et al. 1990, 1991).

Several features make PET particularly well suited for studying the acute effects of drugs in humans.

First, it is a relatively noninvasive technique that can be used safely, and with a minimum of discomfort, with normal volunteers. It can be used repeatedly with the same subjects, enabling researchers to use powerful within-subject designs to study cerebral metabolic activity under various conditions (e.g., in the drugged versus non-drugged state). Most important for the studies to be discussed here, PET reflects ongoing brain activity in fully conscious, awake subjects who may be engaged in predetermined and controlled mental activities and who can report on their current subjective state.

ACRONYMS

CMR _{glu}	cerebral metabolic rate of glucose
FDG	[2- ¹⁸ F]deoxyglucose
PET	positron emission tomography
POMS	Profile of Mood States
VMT	visual monitoring task

Departments of Psychiatry¹ and Radiology², University of Chicago, Chicago, IL 60637

The focus of our studies has been to assess the correlation between the effects of drugs on metabolic rate and their effects on mood state. This chapter will discuss some methodological issues that arise in the use of PET for studying the mood-altering effects of drugs in human subjects. The issues will be illustrated using examples from our studies.

METHODS

Our laboratory has conducted a series of PET studies using [$2-^{18}\text{F}$]deoxyglucose (FDG) as the tracer to investigate the effects of acute doses of alcohol and other drugs of abuse in normal healthy volunteers. Two primary goals have directed this research: One is to characterize the effects of relatively low, psychoactive doses of abused drugs on regional and global cerebral metabolic rate in normal healthy volunteers; the other is to investigate the relationship between the drugs' effects on metabolic rate and their effects on mood or subjective state. The three drugs we have studied thus far are ethanol, diazepam, and amphetamine. Within each study, subjects undergo several PET scans, one after administration of a placebo and the others after different doses of a drug (e.g., alcohol, 0.5 and 0.8 g/kg; diazepam, 5 and 10 mg; or *d*-amphetamine, 5 and 10 mg). The drugs' effects on the subjects' self-reported mood states are monitored throughout each scan, with the aim of correlating the

drug-induced changes in metabolic rate with changes in mood state.

The subjects in these studies are typically normal healthy males recruited from the university community. They are light-to-moderate social drinkers. We exclude individuals who are totally abstinent from alcohol or who report any history of drug- or alcohol-related problems. Subjects are given thorough medical and psychiatric screening prior to participation.

Each subject's scans are scheduled at weekly intervals at the same time of day. Drugs are administered under double-blind, "double-dummy" conditions (i.e., capsules and beverages are administered in each study), and the order of the experimental conditions (i.e., placebo and two doses of drug) is counterbalanced across subjects. Subjects are informed that they might receive a stimulant, a tranquilizer, alcohol, or a placebo. Drug pretreatment times are selected so that the drugs' onset and/or peak effects coincide with the period of highest FDG uptake.

The PET studies are conducted using a three-ring PETT VI scanner (Ter-Pogossian et al. 1982), which provides five transaxial image slices with an intraslice spatial resolution of 8 mm (full width at half maximum) and an interslice distance of 14 mm. Although the studies are performed in the "dynamic" mode (Huang et al. 1980), the data thus far have been reported using the autoradiographic method (Phelps et al. 1979; Reivich et al. 1979). The cerebral metabolic rate of glucose

(CMRglc) is assessed bilaterally in seven regions of interest, including four cortical regions (temporal, parietal, occipital, and frontal), basal ganglia, thalamus, and cerebellum. The regions of interest are identified on each subject's reconstructed images by a technician who is blind to the drug condition. Global CMRglc is calculated by averaging all 14 regions, and regional CMRglc is calculated as a ratio of CMRglc in each region to CMRglc in the whole brain. Regional ratios from drug sessions are compared to regional ratios obtained after placebo.

The subjects' mood states are monitored using the Profile of Mood States (POMS; McNair et al. 1971) and a visual analog questionnaire of drug effects. The POMS is a 72-item adjective checklist that has been factor-analyzed into 10 subscales corresponding to mood states such as anxiety, depression, and elation. The questionnaire has been found to be highly sensitive to the effects of psychoactive drugs (Johanson and Uhlenhuth 1980*a,b*). The visual analog questionnaire measures a subject's liking of a drug. Questionnaires are completed at baseline (i.e., before taking capsules or beverages) and again 20 and 60 minutes following the FDG injection. The questions are presented via Macintosh computer suspended in front of subjects while they are in the scanner. The subjects respond using a mouse.

For the 40-minute FDG uptake period, during which they are in the scanner, the subjects perform a visual monitoring task intended to

stabilize their attentional state. Their performance on this task also provides an objective indication of any drug-induced psychomotor impairment. The task consists of brief presentations of a bright and a dim light; subjects are to press a hand-held button only when the dim light is presented. Accuracy and reaction times are recorded.

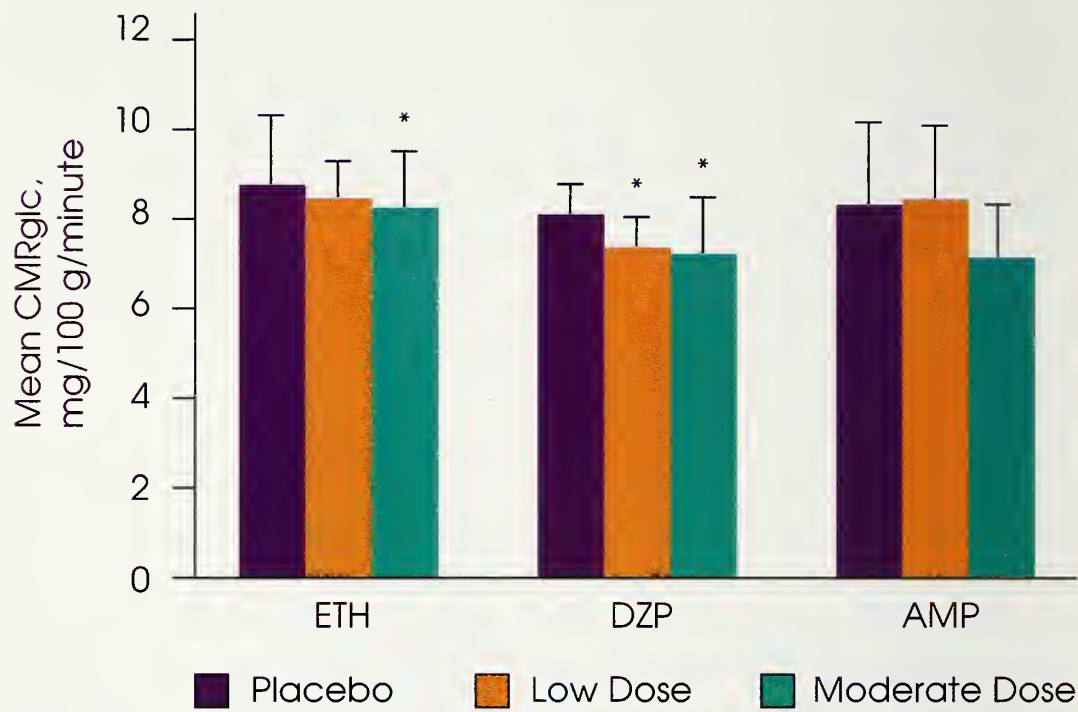
RESULTS

Drug Effects on CMRglc

Averaging global CMRglc across the eight subjects in each study showed that the higher dose of ethanol (0.8 g/kg) and both doses of diazepam (5 and 10 mg) significantly decreased CMRglc (figure 1). The group average CMRglc also appeared to decrease after amphetamine (10 mg), but this decrease occurred only in a few subjects and did not reach statistical significance. The hypometabolic effects of ethanol and diazepam were observed in all regions of the brain, although mid-brain areas (thalamus and basal ganglia) were somewhat less affected by the drugs than were cortical regions. When global changes in metabolic rate were taken into account, none of the individual regions was affected differentially by the drug.

Drug Effects on Mood

Ethanol and diazepam produced some drug-typical changes in mood (figure 2). For example, ethanol increased positive mood and friendliness, while diazepam decreased anxiety scales on the POMS.

FIGURE 1

Mean global CMRglc after ethanol (placebo, 0.5 or 0.8 g/kg; $n=8$), diazepam (placebo, 5 or 10 mg; $n=8$), or *d*-amphetamine (placebo, 5 or 10 mg; $n=8$). Standard deviations are shown by vertical bars; asterisks indicate which drug conditions differed significantly ($p<0.05$) from respective placebo conditions.

However, compared with previous non-PET drug studies conducted in our laboratory (Johanson and Uhlenhuth 1980a,b; de Wit et al. 1986), the subjective effects of diazepam were very much attenuated. A dose of amphetamine (10 mg) that had produced clear stimulant effects in previous studies failed to produce any subjective effects at all in the PET study. Notably, the subjects in the PET studies reported sedative-like subjective effects during the sessions when placebos were administered, suggesting that the PET setting itself had an effect on subjects' mood states, which may have confounded the observed drug effect.

Drug Effects on Psychomotor Performance

None of the three drugs significantly impaired performance or altered reaction times on the monitoring task. This result confirmed that the subjects remained in an alert and uniform behavioral state throughout the scanning periods.

Relationships Between Regional Metabolic Rate and Subjective/Behavioral Measures

Because of variability across subjects in the drugs' effects on both metabolic rate and mood states, correlational analyses were per-

formed to determine whether any regional changes in CMRglc were consistently related to specific mood changes. Although isolated correlations were observed between metabolic rate and mood within each drug study, the relationships appeared to be random across the three drug studies.

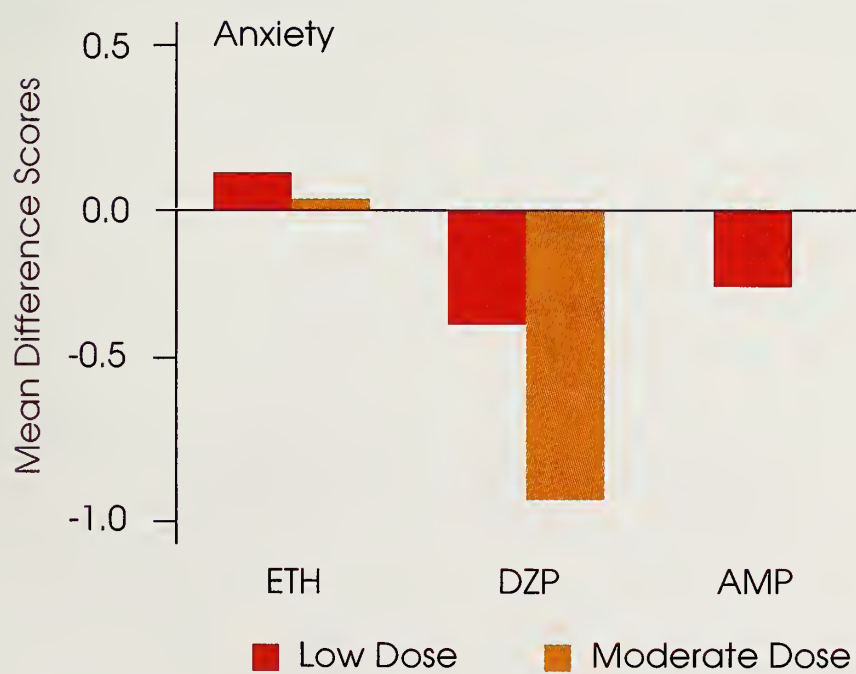
METHODOLOGICAL ISSUES

Correlational Nature of Results

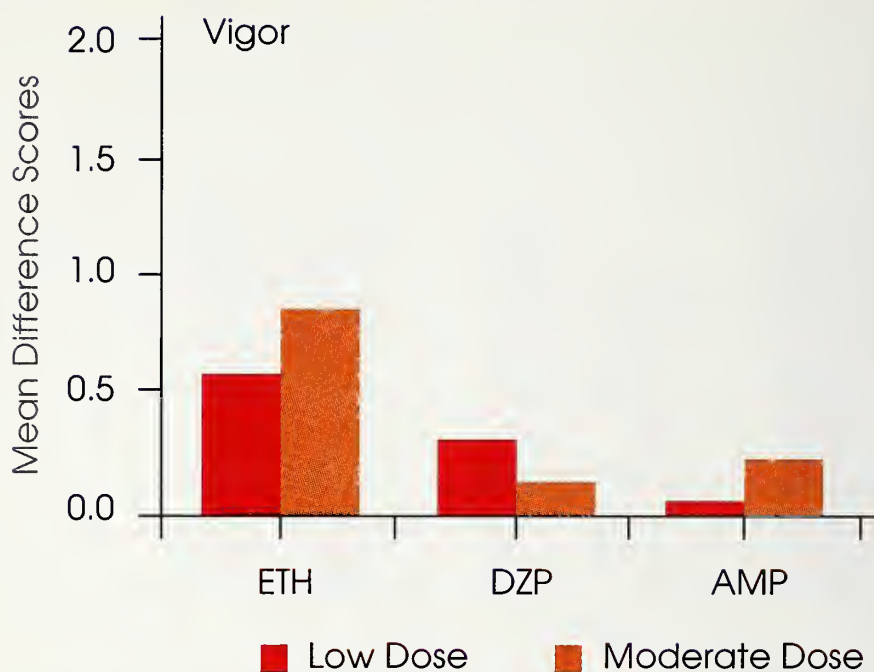
Even if significant and orderly relationships between mood and metabolic rate had been obtained in the studies described above, the findings would be conceptually

difficult to interpret for two reasons: One is that most psychoactive and abused drugs have multiple actions on several biological substrates, producing many effects that are not relevant to the drugs' euphorogenic or dependence-producing properties. This multiplicity of effects compounds another conceptual limitation of the studies, the correlational nature of the data. It is extremely difficult to determine causal relationships among multiple, simultaneously occurring drug effects on brain and behavior. Thus, metabolic rate in a certain brain region may be correlated with a particular mood state,

FIGURE 2a



Mood effects of low and moderate doses of ethanol, diazepam, and *d*-amphetamine on POMS scale for anxiety. Data presented are mean difference scores obtained by subtracting predrug from postdrug scores on each session (i.e., change scores) and subtracting the change scores on placebo sessions from the change scores on drug sessions (i.e., double-difference scores).

FIGURE 2b

Mood effects of low and moderate doses of ethanol, diazepam, and *d*-amphetamine on POMS scale for vigor. Data presented are mean difference scores obtained by subtracting predrug from postdrug scores on each session (i.e., change scores) and subtracting the change scores on placebo sessions from the change scores on drug sessions (i.e., double-difference scores).

but it is not clear whether the drug's action on that brain region produced the changes in subjective state, or whether the changes in mood states (elicited by some other action of the drug) produced changes in metabolism. Alternatively, the changes in metabolic rate and mood may be causally unrelated, each attributable to other actions of the drug. Despite the complexity of interpreting the results of individual studies, however, a convergence of correlational results across different studies (e.g., studies using different classes of drugs, or studies manipulating mood nonpharmacologically)

may indicate possible functional relationships. Thus, the convergence of data across studies is the ultimate long-term objective of brain function studies using PET.

Spatial/Temporal Resolution of PET Images

PET technology is limited by the relatively poor spatial and temporal resolution of the instruments and technology. In our studies, which use a PETT VI scanner and FDG as the tracer, the spatial resolution is about 8 mm. Although newer machines could provide improved spatial resolution, there are several ways to maximize the information

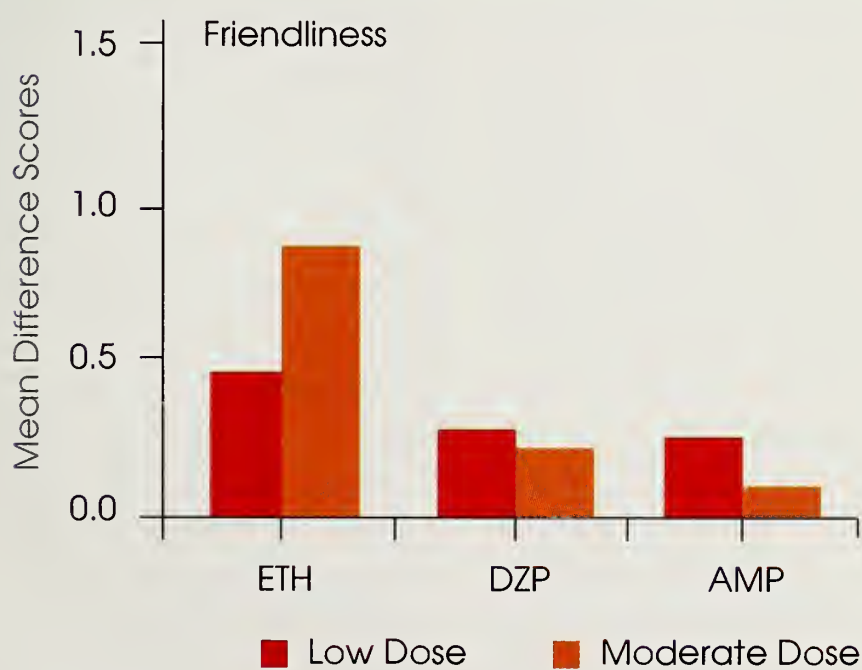
obtained from the existing instruments. One is to superimpose the PET image onto a structural image of the subject's brain. In our laboratory, for example, magnetic resonance images of brain structures can be precisely matched in computer space with PET images of brain functions. This technique substantially improves our ability to identify brain structures activated on the PET image.

Another way to maximize data from PET images is to average data across subjects, using image subtraction techniques. Other investigators have shown that pixel-by-pixel subtraction of sequential

PET slices can greatly improve the localization of focally activated brain regions (Fox et al. 1986). So far this technique has been applied only for studies of cerebral blood flow where sequential measurements are made in the same PET session. Improved methods of image registration, however, may make this method applicable to FDG studies (Pelizzari et al. 1989).

A third way to optimize the information available from PET images is to group regions of interest into areas that have been identified by neuropsychological studies as functionally distinct, an approach taken in our laboratory. Previous

FIGURE 2c



Mood effects of low and moderate doses of ethanol, diazepam, and *d*-amphetamine on POMS scale for friendliness. Data presented are mean difference scores obtained by subtracting predrug from postdrug scores on each session (i.e., change scores) and subtracting the change scores on placebo sessions from the change scores on drug sessions (i.e., double-difference scores).

studies in our laboratory as well as in other laboratories have used fairly large regions of interest that can be identified on single slices and that are defined by clearly recognizable structures and neuroanatomical "landmarks." The large size of the regions of interest (i.e., up to 1,820 mm²) ensured that we did not exceed limitations on the spatial resolution of the machine.

Recently, we reanalyzed some of our previous metabolic data, using a different approach: Relatively small fixed-size regions of interest (190 mm²) were outlined on the images according to neuroanatomical landmarks. These smaller regions were then recombined often across slices into larger, functionally related areas. For instance, the prefrontal cortex was defined as the three most anterior regions on the top two slices. Preliminary analyses of the ethanol data, using these newly defined areas, suggest that the drug decreases metabolic rate nonspecifically in all cortical regions and that it has negligible effects on metabolic rate in the basal ganglia, thalamus, and cerebellum.

Stability of Mood Effects of Drugs

It is well known in the field of psychopharmacology that the subjective, or mood-altering, effects of drugs are transitory and easily disrupted by a host of environmental and subject-related factors. The subjective effects of drugs vary widely across individuals; even within the same individual, drug effects often depend on the setting

and the manner of drug administration. Intersubject variability is illustrated by the results of a behavioral study with ethanol conducted in our laboratory (de Wit et al. 1987), in which a moderate dose of ethanol produced stimulant-like subjective effects in some of the subjects but opposite, sedative-like effects in others. Individual differences such as these are not understood and may result from prior experience with drugs, preexisting differences in physiology, or differences in behavioral history.

Intersubject variability in mood effects of drugs has two important implications for studies of the neural basis of drug effects. First, it points to the importance of careful selection of subject populations and of thorough description of their demographic characteristics. Consideration should be given to subjects' age, gender, race, weight, mental status, and, in particular, current and lifetime history of recreational drug use. Furthermore, to the extent that intersubject variability cannot be predicted and controlled by subject selection and description, it becomes very important to confirm, in each study and in each subject, that the drugs are indeed producing their purported mood-altering effects.

The mood-altering effects of drugs may also vary widely within the same subject, depending on such factors as expectations and the environmental setting in which the drug is administered. Expectations may be partially controlled in laboratory studies by

instructions to subjects and by the double-blind administration of drugs. Subjects in all of our studies are informed that they might receive a stimulant, a tranquilizer, alcohol, or a placebo. Even if subjects are told that they might receive either a placebo or a single other drug (e.g., amphetamine), drug-specific expectations could influence and confound the results. To preserve the double-blind administration of drugs, subjects in our studies always receive both a capsule and a beverage (double-dummy), regardless of the drug administered. Neither the subject nor the staff who interact with the subjects knows the identity of the drug being administered.

The setting in which a drug is administered is also known to have profound effects on subjective experiences. This has been of particular concern in the PET studies in which relatively low doses of psychoactive drugs are used. Drugs may produce lesser, or different mood effects in the PET environment than in a recreational drug-taking environment, limiting the generalizability of the PET data. Concern about this issue led us to compare, using the same subjects, the effects of ethanol in a recreational setting to its effects in the PET setting. The mood-altering effects of ethanol were first assessed in a behavioral study conducted in a comfortable, social environment. The subjects were then tested with the same dose of ethanol in a PET study, using the same questionnaires to assess the drug's effects

on mood. Ethanol produced remarkably similar subjective effects (i.e., increased positive mood) in both settings. However, the effects of other drugs (i.e., diazepam and amphetamine) were markedly attenuated in the PET setting, relative to their effects in the recreational environment. We have also found that the PET environment can alter subjects' moods (i.e., increase ratings of fatigue and sedation), independent of drug administration. Thus the effects of the PET environment may interact with and confound the pharmacological effects of drugs on mood.

Pharmacological Factors

Many drug effects, including subjective drug effects, are known to depend upon pharmacological factors such as the dose and route of administration. These factors are also likely to affect cerebral metabolism. At low doses, some drugs, including ethanol, produce behavioral and subjective effects that are qualitatively different from, and even opposite to, their effects at higher doses. Other drugs, such as opiates, have biphasic effects in which one effect (e.g., depressant) is followed by a different effect (e.g., stimulant). Subjects report that intravenously administered or inhaled cocaine produces a "rush" and a drug "high," whereas the same dose administered orally produces a gradual onset with considerably less euphoria.

These pharmacological factors are important considerations in studying the neural basis of drug euphoria. Our laboratory has

focused on the effects of relatively low oral doses of psychoactive drugs for ethical reasons (subjects are normal healthy volunteers) and because the low doses minimize the possibility of global disruption of brain function and behavioral state which would complicate the investigation of subtle mood effects. Ultimately, it will be important to study a wide range of doses and to characterize the full profile of the drugs' subjective, behavioral, and physiological effects.

Role of Cognitive/Behavioral State of Subjects

Another variable that may influence measurements of cerebral metabolism is the subject's cognitive behavioral state. In an extreme instance (but one that is relevant to studying drugs with potent sedative effects), a subject who is asleep clearly may be expected to have a lower metabolic rate than a subject who is fully awake and alert (Buchsbaum et al. 1989). Similarly, the amount and complexity of a subject's cognitive activity may influence measurements of metabolic activity (Duara et al. 1987). Our experience with normal healthy volunteers indicates that subjects vary widely in their cognitive state during the scans: Some subjects appear passive and indifferent to the PET procedures, whereas others may be anxious or highly involved and curious about the ongoing activities. These naturally occurring individual differences in reactivity to the study procedures may be further complicated by the adminis-

tration of either stimulant or sedative drugs.

One way to reduce variability in cognitive activity is to engage subjects in a standard, simple cognitive task. In our studies, we have used a simple visual monitoring task (VMT) in which brief flashes of a bright or dim light are projected in front of the subjects. The subjects are instructed to press a hand-held button after presentation of the dim light but not the bright light. Performance of the VMT ensures that subjects remain attentive and in a stable cognitive state throughout the period of tracer uptake. Incidentally, the task also provides useful measures of the psychomotor effects of the drugs that are administered (e.g., reaction time and accuracy on the task).

To investigate this issue further, we have recently conducted a study to determine how performing the VMT after administration of amphetamine affected metabolic rate. We were also interested in determining whether performing the VMT affected subjective responses to amphetamine. Five subjects were tested under four experimental conditions: with and without performing the VMT task and with placebo or amphetamine (20 mg) pretreatment. Somewhat to our surprise, global metabolic rate was not significantly elevated with the VMT versus without the VMT condition. However, it was observed that the subjective effects of amphetamine were attenuated during sessions when subjects performed the VMT, relative to the

sessions when they did not. Thus, while performance of a task may reduce unwanted variability, it may also mask potentially important mood-altering effects of the drug.

CONCLUSIONS

PET is potentially a very powerful tool with which to investigate brain activity associated with the euphorogenic effects of drugs. The limitations in temporal and spatial resolution that characterize existing PET technology are rapidly being overcome by new developments in imaging technology. In addition, our understanding of the behavioral and subjective effects of mood-altering drugs and our techniques for measuring these sometimes ephemeral effects are constantly improving. Together, technical and methodological developments will greatly improve the power of PET as a tool for studying brain function.

ACKNOWLEDGMENTS

This research was supported by the Alcoholic Beverage Medical Research Foundation and by National Institute on Drug Abuse grants DA02812 and DA06176 and Department of Energy grant DE-AC02-86ER60438. The authors acknowledge the expert technical assistance of Betsy Bodker and the entire PET center staff.

REFERENCES

- Buchsbaum, M.S.; Gillin, J.C.; Wu, J.; Hazlett, E.; Sicotte, N.; Dupont, R.M.; and Bunney, W.J. Regional cerebral glucose metabolic rate in human sleep assessed by positron emission tomography. *Life Sci* 45:1349-1356, 1989.
- de Wit, H.; Metz, J.T.; Wagner, N.; and Cooper, M.D. Behavioral and subjective effects of ethanol: Relationship to cerebral metabolism using PET. *Alcoholism* 14:482-489, 1990.
- de Wit, H.; Metz, J.; Wagner, N.; and Cooper, M.D. Effects of diazepam on cerebral metabolism and mood in normal volunteers. *Neuropharmacology* 1991, in press.
- de Wit, H.; Uhlenhuth, E.H.; and Johanson, C.E. Individual differences in the reinforcing and subjective effects of amphetamine and diazepam. *Drug Alcohol Depend* 16:341-360, 1986.
- de Wit, H.; Uhlenhuth, E.H.; Pierri, J.; and Johanson, C.E. Individual differences in behavioral and subjective responses to alcohol. *Alcoholism* 11:52-59, 1987.
- Duara, R.; Gross-Glenn, K.; Barker, W.W.; Chang, J.Y.; Apicella, A.; Loewenstein, D.; and Boothe, T. Behavioral activation and the variability of cerebral glucose metabolic measurements. *J Cereb Blood Flow Metab* 7:266-271, 1987.
- Fox, P.T.; Mintun, M.A.; Raichle, M.E.; Miezin, F.M.; Allman, J.M.; and Van Essen, D.C. Mapping human visual cortex with positron emission tomography. *Nature* 323:806-809, 1986.
- Huang, S.C.; Phelps, M.E.; Hoffman, E.J.; Sideris, K.; Selin, C.J.; and Kuhl, D.E. Noninvasive determination of local cerebral metabolic rate of glucose in man. *Am J Physiol* 238:E69-E82, 1980.
- Johanson, C.E., and Uhlenhuth, E.H. Drug preference and mood in humans:

d-amphetamine. *Psychopharmacology* 71:275-279, 1980a.

Johanson, C.E., and Uhlenhuth, E.H. Drug preference and mood in humans: Diazepam. *Psychopharmacology* 71:269-273, 1980b.

Mathew, R.J., and Wilson, W.H. Substance abuse and cerebral blood flow. *Am J Psychiatry* 148:292-305, 1991.

McNair, D.; Lorr, M.; and Dropelman, L. *Profile of Mood States (Manual)*. San Diego: Educational and Industrial Testing Service, 1971.

Pelizzari, C.A.; Chen, G.T.Y.; Spelbring, D.R.; Weichselbaum, R.R.; and Chen, C.-T. Accurate 3-dimensional registration of CT, PET, and MR images of the brain. *J Comput Assist Tomogr* 13:20-26, 1989.

Phelps, M.E.; Huang, S.C.; Hoffman, E.J.; Selin, C.J.; Sokoloff, L.; and Kuhl, D.E. Tomographic measurement of local cerebral glucose metabolic rate in humans with [F-18]fluoro-2-deoxy-d-glucose: Validation of method. *Ann Neurol* 6:371-388, 1979.

Reivich, M.; Kuhl, D.; Wolf, A.P.; Greenberg, J.; Phelps, M.; Ido, T.; Casella, V.; Fowler, J.; Hoffman, E.; Alavi, A.; Som, P.; and Sokoloff, L. The 18-F-fluorodeoxyglucose method for the measurement of local cerebral glucose utilization in man. *Circ Res* 44:127-137, 1979.

Ter-Pogossian, M.M.; Ficke, D.C.; Hood, J.T.; Yamamoto, M.; and Mullani, N.A. PETT VI: A positron emission tomograph utilizing cesium fluoride scintillation detectors. *J Comput Assist Tomogr* 6:125-133, 1982.

NIAAA 21

c.2

NIDA DIR LIBRARY

P.O. BOX 5180

BALTIMORE, MD 21224



Amazing Research.
Amazing Help.

<http://nihlibrary.nih.gov>

10 Center Drive
Bethesda, MD 20892-1150
301-496-1080

NIH LIBRARY



3 1496 01022 8115